AIT Series

Trends in earth observation

Volume 1

Earth observation advancements in a changing world

Edited by Chirici G. and Gianinetto M.

Earth observation advancements in a changing world

Edited by

Gherardo Chirici and Marco Gianinetto

AIT Series: Trends in earth observation

Volume 1 - Published in July 2019
Edited by Gherardo Chirici and Marco Gianinetto
Published on behalf of the Associazione Italiana di Telerilevamento (AIT)
Via Lucca 50
50142 Firenze, Italy

ISSN 2612-7148
ISBN 978-88-944687-1-7
DOI: 10.978.88944687/17

All contributions published in the Volume "Earth observation advancements in a changing world" were subject to blind peer review from independent reviewers.

Publication Ethics and Publication Malpractice Statement
Editors, Reviewers and Authors agreed with Publication Ethics and Publication Malpractice Statement

Preface

Since 1986 the Italian Remote Sensing Society (Associazione Italiana di Telerilevamento – AIT) aims to disseminate remote sensing culture, disciplines and applications in Italy. Specifically, AIT's mission is to:

- Create a network of people from Research, Academia and hi-tech Companies interested in analysis, development and application of a wide range of remote sensing methods and techniques;
- Promote and coordinate initiatives to expand the use of remote sensing technologies in Italy and across the European Union;
- Foster the exchange of knowledge and cooperation between its members to "shorten" the chain: research→innovation→new applications/markets→research;
- Support the dissemination of remote sensing methods through the organization of congresses, conferences, working groups, including international thematic courses;
- Represent and take care of scientific and cultural interests in remote sensing for institutions, agencies, companies and similar associations, at national and international level.

Recently, AIT was included in the Italian Copernicus User Forum among the representatives of the IV sector. AIT is also the official Society of the European Journal of Remote Sensing, an open-access scholarly journal published by Taylor & Francis.
Until 1995, AIT was used to organise National Conferences, but in 1997, the Society joined a wider Federal Association (Associazioni Scientifiche per le Informazioni Territoriali e Ambientali - ASITA) related to Cartography, GIS, Topography, Photogrammetry and Remote Sensing, which organises annual national conferences to share and diffuse the Geomatic advancements.

In 2016 AIT decided to bring back its tradition to organize its national conferences with a more distinctive research trait. In addition, always in that year, AIT started to organize its annual International Summer Schools for the exploitation of Copernicus data and programmes.
In this framework, we decided to take the opportunity to create a new book series, officially supported by AIT, entitled *Trends in Earth observation*. These volumes want to present to the readers a snapshot of the state-of-the-art in several different application fields.
I hope that *Trends in Earth observation* can contribute to the scientific progress and the continuous innovation of Earth Observation.

AIT President
Livio Rossi

Contents

Introduction

Earth observation advancements in a changing world

Chirici G., Gianinetto M.

Trends in Earth observation (ISSN 2612-7148) is a new series supported by the Italian Society of Remote Sensing (AIT) which purpose is to provide a new media for publishing the outcomes of high-quality researches. This series accompanies the well-established European Journal of Remote Sensing, which is the official journal of AIT, and shares its blind peer-review process. However, while the journal is general purpose, Trends in Earth observation addresses specific emerging topics organized into thematic chapters.

This first volume of Trends in Earth observation is entitled Earth observation advancements in a changing world and includes 47 contributions from colleagues belonging to 10 different countries, organized in 6 chapters. Compared to similar volumes which often focus on the techniques and methods, Trends in Earth observation also describes case histories. In this sense, it provides the present state-of-the-art of many real-world remote sensing applications.

The first chapter is specifically oriented to agriculture applications of remote sensing and authors present innovative applications for monitoring problems of different cultivations (coffee, rice, olive, maize, tomato, oil palm) in different environmental conditions and with different Earth Observation technologies.

The second chapter covers the very wide area of forest monitoring and environmental studies. Two of the most common issues are the recognition of tree species and/or forest types and the multi-temporal analysis of vegetation trends and disturbances.

The third chapter is focused on disaster risk and geomorphologic applications, also including some applications using UAVs which is a relatively recent new area of remote sensing applications.

The fourth chapter describes applications in the field of water management and protection, with a specific focus on the mapping of water resources with different data and different resolutions.

The fifth chapter addresses the monitoring of coasts and the last chapter reports new advancements in the monitoring of urban environments using either optical or radar images.

We gratefully acknowledge the contributions of all authors and hope you will enjoy reading this first volume of the new series Trends in Earth observation.

Remote sensing advancements to support modern agriculture practices

USING HYPERSPECTRAL DATA TO DIFFERENTIATE SHADE COFFEE VARIETIES WITH AND WITHOUT RUST AND OTHER CANOPY SPECIES

N. Corona-Romero*, J. M. Madrigal Gómez, M. González-Stefanoni
Centro de Investigación en Ciencias de Información Geoespacial, 137 Contoy Street, Mexico City, Mexico –
(ncorona, jmadrigal, mstefanoni)@centrogeo.edu.mx,

KEY WORDS: Coffea arabica, rust, hyperspectral data, spectral reflectance, spectral signatures

ABSTRACT:

In Mexico coffee, mainly Coffea arabica L., is one of the main industrial crops, the second most exported product and a great generator of foreign currency. Chiapas is the largest producer, giving high quality grains resulting mainly from shaded agroforestry systems. However, since 2013 this activity has presented great losses both in quantity and quality due to rust infestation (Hemileia vastatrix), which causes lesions on the leaves of the coffee tree, affecting seed production. In order to bring knowledge that will help to support research on hyperspectral data usefulness in coffee crop identification and therefore its health status monitoring, we tested whether there are significant differences between the spectral reflectance of healthy coffee leaves and coffee leaves with rust. Spectral signatures of leaves of different varieties of coffee (Arabica, Catimorro, Marago and Bourbon) with and without rust and several species associated with the shade coffee crop, were collected with the FieldSpec 4 spectrumradiometer. Then the spectral data were averaged and processed with a derivative analysis using the Savitzky-Golay filtering method. The one-way analysis variance (ANOVA) with a Scheffe multiple comparison method with *P* value of 0.05 was conducted to examine differences between the means of reflectance bands' varieties and healthy and ill varieties. We found that Spectral reflectance data at leaf level provided useful information to identify a set of bands to discriminate between varieties of healthy coffee and coffee infested by rust.

1. INTRODUCTION*

Coffee, mainly Coffea arabica L., is a product of global importance and it is part of a significant fraction of the export economy of several countries. In Mexico, it is one of the main industrial crops, the second most exported product and a great generator of foreign currency where it is cultivated in 14 states with more than 717 thousand hectares, which makes it an impeller of the regional economy and sustenance for more than half a million families. Of the 32 states of Mexico, Chiapas is the largest producer and in particular, the Sierra Madre of Chiapas, which has a history of coffee production for almost 200 years, giving high quality grains resulting mainly from shade agroforestry systems (Nestel, 1995).

The cultivation of shade-grown coffee and the use of traditional systems has gained great importance in recent years, because it promotes conservation of biodiversity by bringing on native species permanence and forest cover and, therefore numerous environmental services, since it generally grows in an elevation gradient that represents key areas of biological transition. However, since 2013 this activity has presented great losses both in quantity and quality due to rust infestation (Hemileia vastatrix), which causes lesions on the leaves of the coffee tree, affecting the foliage and less seed production (coffee). In order to reduce this impact, coffee producers have introduced coffee varieties resistant to rust that are not compatible with shade agroforestry systems resulting in the removal of forest cover in order to grow corn or for livestock. All of these at least put at risk thousands of families and the ecosystem services that agroecosystems provide (Libert and Paz, 2017; Gordon et al., 2007; Moguel and Toledo, 1999; Nestel 1995).

Due to the economic, social and environmental relevance of coffee cultivation and the effects caused by rust, it is important to generate mechanisms that allow monitoring health status of coffee crops. Normally, this is done through fieldwork, involving high costs in both time and money, and exposure to different risks for the people in charge for carrying this out. Therefore, methodologies that allow identification of crops with and without rust should be considered, thus reducing monetary and temporary investment, as well as risk associated with it.

In this sense, remote sensing has been widely used for vegetation monitoring, showing high reliability for homogeneous coverages, but not at identifying different species in heterogeneous vegetation cover (Roberts et al., 1993). Shade-grown coffee is an example of this case, because it needs a cover of trees to protect it from sunlight, hence limiting the detection of the plant of coffee by spatial and aerial commercial sensors and therefore, commonly used techniques of remote sensing have shown poor results for its identification. However, in recent years the effectiveness of advanced methods, such as spectral de-mixing and the use of hyperspectral data have proven effective in identifying species and components found in mixed coverages such as tropical forests and soil minerals, but not in crops such as coffee (Quintano et a., 2012; Keshava and Mustard, 2002). The aim of this paper is to test whether there are significant differences between the spectral reflectance of shade coffee leaves and coffee leaves with rust. Hence, it is intended to bring knowledge that will help support research on hyperspectral data usefulness in coffee crop identification, and therefore its health status monitoring through satellite or aerial data (such as those obtained by drones). All of these to reduce the vulnerability of the producers from implementation of strategies from this monitoring.

2. STUDY AREA AND METHODS

2.1 Study area

The spectral data was taken on June 8, 2017 in a coffee zone of the Monterrey Ejido located in the buffer zone of the El Triunfo Biosphere Reserve, Municipality of Jaltenango de la Paz,

* Corresponding author

Chiapas. Its altitude is 1,484 meters and the predominant vegetation is cloud forest and coniferous forest. This area was chosen since the main activity is coffee cultivation, in addition to having different varieties of coffee and the presence and absence of rust, as well as shade vegetation.

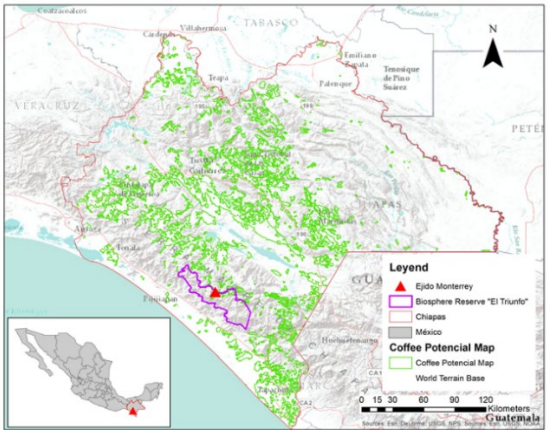

Figure 1. Study area. The Monterrey Ejido located in the buffer zone of the El Triunfo Biosphere Reserve, Municipality of Jaltenango de la Paz, Chiapas, Mexico.

2.2 Materials and methods

Spectral signatures of leaves were collected with the high resolution portable FieldSpec 4 Standar-Res spectroradiometer, with a spectral resolution of 3 nm in the VNIR (350-1000 nm) and 10 nm in the SWIR (1001-2500 nm) and with a bandwidth of 1.4 nm in the VNIR and 1.1 in the SWIR (Malvern Panalytical Ltd, 2019). The spectral data were taken on June 8, 2017 when rain season is starting and before coffee plant flowering begins. The rust infestation was on the first phase or slow phase (Rivillas et al., 2011). Five spectral signatures per leaf per variety of coffee (Arabica, Marago, Catimorro and Bourbon) with and without rust and, species associated with the crop (shade trees and shrubs) were taken by the plant probe (which provides non-destructive data collection from live vegetation), having 59 reflectance signatures. Just the Arabica and Marago varieties were infested by rust, with a grade of infestation between 3 and 10%, the leaves on other hand, showed around 20% severity of infestation, according to the Scale of Severity of coffee rust in leave and plant (SINAVEF, 2013).

2.2.1 Processing spectral reflectance data. Spectral reflectance data were averaged and processed with a derivative analysis using the Savitzky-Golay filtering method, which uses a simplified least-squares convolution for smoothing and computing derivatives of a set of consecutive values to remove noise produced by environment. It is done by a mean filter using a simple average of points within the filter window. It removes sources of variability associated with broad band ratios, then they are more sensitive measures of stress than broad band measurements and it allows the components of the spectrum to be more clearly separated (Liu et al., 2008; Tsai and Philot, 1998).

A one-way analysis of variance (ANOVA) was conducted to examine if differences exist between means of second derivative reflectance bands of coffee varieties and between healthy coffee varieties and coffee varieties with rust. In order to reduce the Type I error, a Scheffe multiple comparisons method was applied with a *P* value of 0.05 (McDonald, 2014).

3. RESULTS

Comparing the obtained reflectance spectra from all the varieties of healthy coffee resulting from the Savitzky-Golay filtering method, it was found that in the red edge, the curve inflection becomes broader between 680-740nm. In addition, from 650 to 775nm, it shifts towards longer wavelengths. At last the signal of the spectrum decreases around 500 and 680nm. For all cases, Bourbon presented the greatest values, while Arabica has the lowest values (Figure 2).

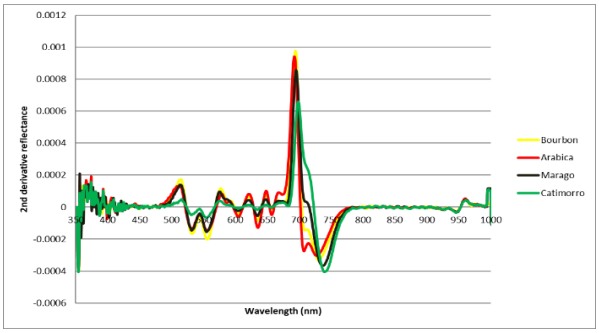

Figure 2. 2nd derivative spectral reflectance from coffee leaves varieties.

The 2nd derivative analysis of the obtained reflectance spectra of healthy coffee and coffee rust infested (Arabica y Marago) shows the same spectral development in the range of 650 to 725nm for both healthy coffee and coffee infested with rust. At 680 to 740nm in Arabica with rust, the reflectance is less than without rust and the inflection in Marago with rust starts around 650. In addition, around 500nm, in both the spectral reflectance is smaller in leaves with rust than healthy coffee (Figure 3).

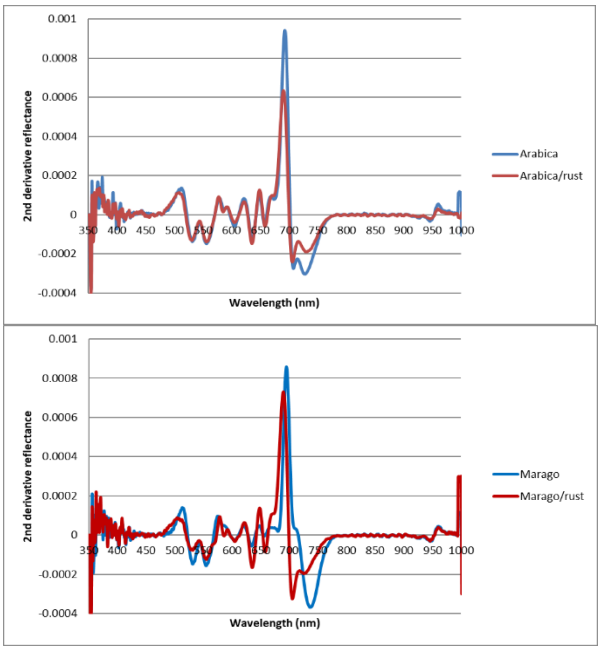

Figure 3. 2nd derivative spectral reflectance from coffee leaves varieties with and without rust. Upper: Arabica; Bottom: Marago.

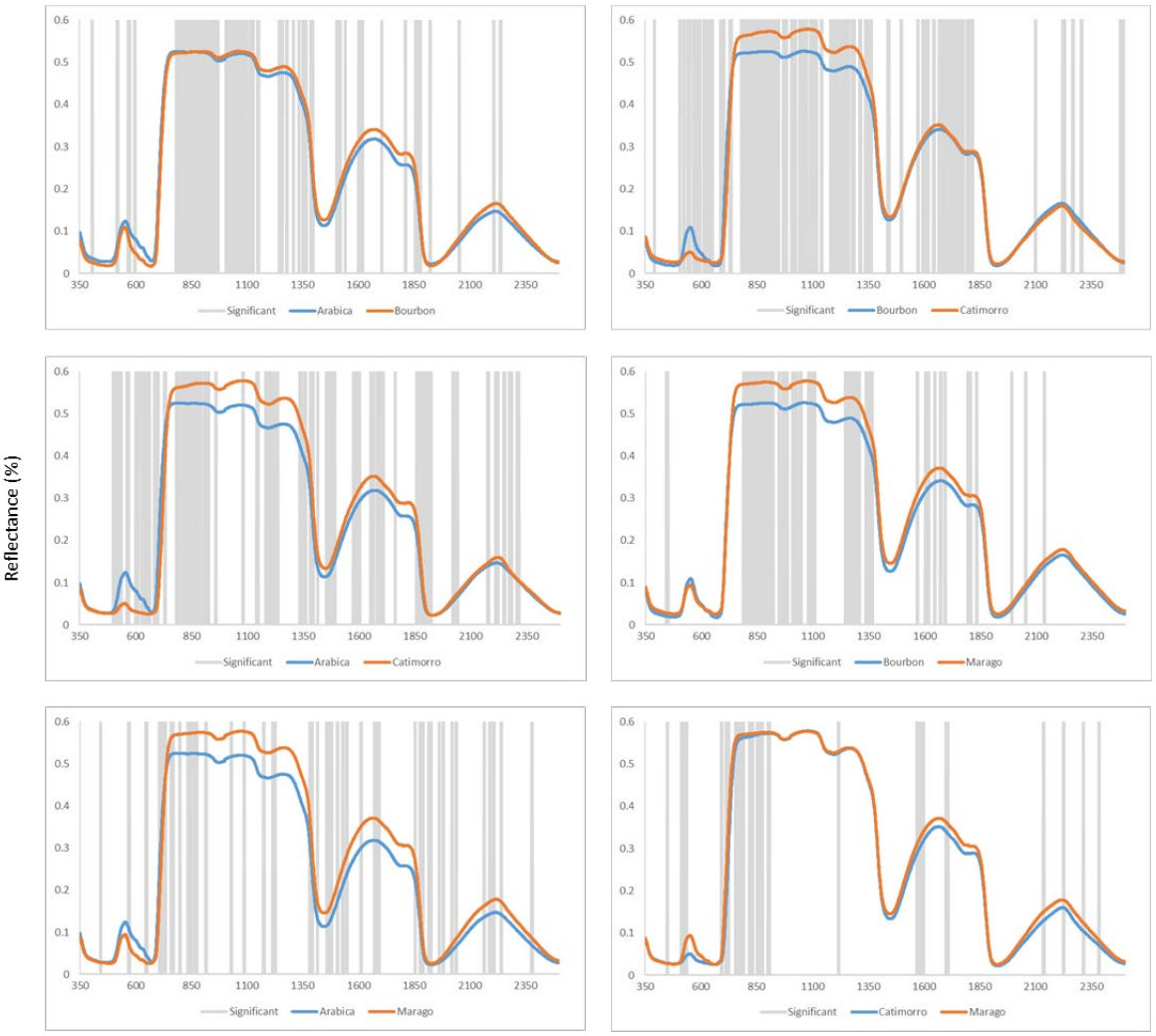

Figure 4. Significant differences between the spectral reflectance of leaves of coffee varieties

The one-way analysis of variance (ANOVA) with the Scheffe multiple comparisons method found several differences between the 2nd derivative spectral reflectance of coffee leaves varieties, being Arabica and Bourbon, Arabica and Catimorro and Bourbon and Catimorro the ones that showed greater differences.On the other hand, these differences are more frequent around red edge, NIR and mid-infrared (Figure 4).

The analysis between healthy coffee leaves and coffee leaves with rust shows that Arabica has more differences around 1109 and 1175nm and 1483 to 1531nm while Marago shows differences between 668 and 689nm (Figure 5).

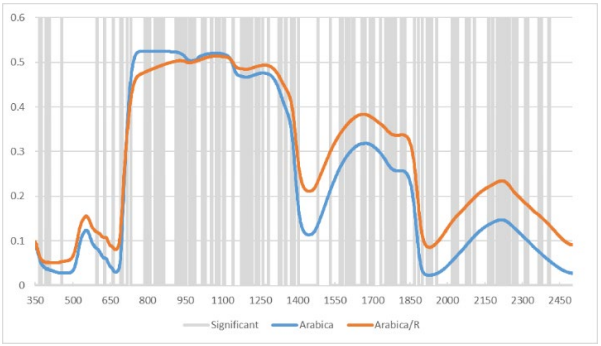

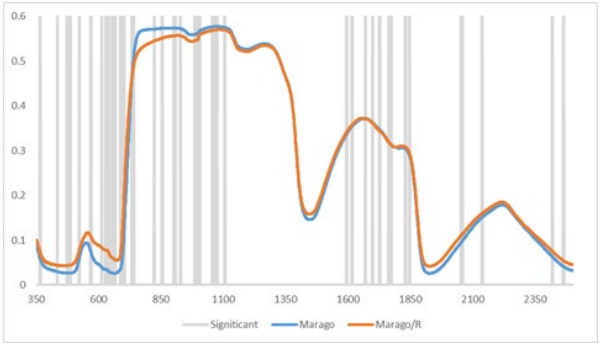

Figure 5.Significant differences between healthy coffe leaves and coffee leaves with rust derived by the one-way analysis of variance (ANOVA) with the Scheffe multiple comparisons method. Left: Arabica, Upper: Marago.

3. DISCUSSION

The behavior of reflectance spectra from all the varieties of healthy coffee resulting from the Savitzky-Golay filtering method around the red ege and betwee 650 and 775nm suggest that Bourbon leaves contain more chlorophyll than the other varieties, while Arabica leaves contain less chlorophyll. The analysis in leaves infested by rust shows a different behavior

which could indicate that Arabica leaves without rust contain more chlorophyll than those that are infested. The same was observed for Marago leaves with rust, but the reduction of reflectance around 500nm could be due to a reduction in the content of carotenoid pigments (Gitelson, 2016; Buschmann and Nagel, 1993).

The coffee varieties that show more significant differences are Bourbon and Catimorro. Of them, Bourbon is more desired because of its flavor and production but unlike Catimor, it is not resistant to rust (Rodrigues et al, 1975). It should be important to study the photosynthetic differences between coffee varieties in order to understand the effect that it could be in the degree of rust infestation.

Most of the significant differences between healthy coffee leaves and leaves with rust was found in the mid-infrared. It should be because of the cellular lyses and filling of intercellular space with cellular debris, caused by the rust infestation which is located in the stoma of the leave. As a result, the capability of respiration and transpiration is reduced and the water content in the broken leaves decreases damaging the intecellular air spaces, cells with chloroplasts and the mesophyll tissue which is the region where the internal reflectance is measured in the mid-infrared (Zhan-yu et al., 2008; Silva et al., 1999; Tsai and Philot, 1998; Buschman and Nagel, 1993).

3. CONCLUSIONS

Spectral reflectance data at leaf level provided useful information to identify a set of bands to discriminate between varieties of healthy coffee and coffee infested by rust.

It is necessary to improve the sampling method increasing the number of samples by varieties and for varieties infested by rust.

This study case can provide useful information to improve monitoring systems that ensure the productive capacity of coffee agroecosystems and the economy of coffee producers.

REFERENCES

Buschmann, C., & Nagel, E. (1993). In vivo spectroscopy and internal optics of leaves as basis for remote sensing of vegetation. *International Journal of Remote Sensing*,14(4), 711-722.

Gitelson A. (2016). Non destructive estimation foliar pigment (chlorophylls, carotenoids, and anthocyanins) Contents: evaluating a semianalytical three-band model. In Thenkabail, P. S., & Lyon, J. G. (2016). *Hyperspectral remote sensing of vegetation*. CRC Press.

Gordon, C., Manson, R., Sundberg, J., & Cruz-Angón, A. (2007). Biodiversity, profitability, and vegetation structure in a Mexican coffee agroecosystem. *Agriculture, ecosystems & environment*, 118(1-4), 256-266.

Keshava, N., & Mustard, J. F. (2002). Spectral unmixing. *IEEE signal processing magazine*, *19*(1), 44-57.

Libert, A., A., Paz, F., P. (2017). La campaña de investigación-acción interdisciplinaria del Programa Mexicano del Carbono ante la crisis socio-ecológica de la epidemia de roya del cafeto. *Una REDD para SALVAR la SOMBRA de la Sierra Madre de Chiapas. Programa Mexicano del Carbono.*

Liu, Z. Y., Huang, J. F., & Tao, R. X. (2008). Characterizing and estimating fungal disease severity of rice brown spot with hyperspectral reflectance data. *Rice Science*, *15*(3), 232-242.

McDonald, J.H.(2014). Handbook of Biological Statistics. 3rd ed.

Moguel, P., & Toledo, V. M. (1999). Biodiversity conservation in traditional coffee systems of Mexico. *Conservation biology*, 13(1), 11-21.

Nestel, D. (1995). Coffee in Mexico: international market, agricultural landscape and ecology. *Ecological Economics*, 15(2), 165-178.

Quintano C., Fernández-Manso, A., Shimabukuro, Y., Gabriel, P. (2012). Spectral unmixing. *International Journal of Remote Sensing*. 33:17, 5307-5340.

Rivillas, C. A., Serna, C. A., Cristancho, M. A., & Gaitan, A. L. (2011). *La roya del cafeto en Colombia: Impacto manejo y costos del control*.

Roberts, D. A., Smith, M. O., & Adams, J. B. (1993). Green vegetation, nonphotosynthetic vegetation, and soils in AVIRIS data. *Remote Sensing of Environment*, *44*(2-3), 255-269.

Rodrigues Jr, C. J., Bettencourt, A. J., & Rijo, L. (1975). Races of the pathogen and resistance to coffee rust. *Annual Review of Phytopathology*, *13*(1), 49-70.

Silva, M. C., Nicole, M., Rijo, L., Geiger, J. P., & Rodrigues, Jr, C. J. (1999). Cytochemical aspects of the plant–rust fungus interface during the compatible interaction Coffea arabica (cv. Caturra)–Hemileia vastatrix (race III). *International Journal of Plant Sciences*, 160(1), 79-91.

Sistema Nacional de Vigilancia Epidemiológica Fitosanitaria (SINAVEF). *Ficha técnica. Roya del Cafeto. Hemelia vastatrix Berkeley & Broome*.

Tsai, F., & Philpot, W. (1998). Derivative analysis of hyperspectral data. *Remote Sensing of Environment*, 66(1), 41-51.

WAITING FOR "INSTITUTIONAL" MONITORING SERVICES OF RICE CROPS BY REMOTE SENSING: IS CADASTRAL PARCEL THE PROPER REFERENCE GEOMETRY?

G. Corvino*, A. Lessio, E. Borgogno Mondino.
DISAFA, University of Torino, Dept. of Agriculture, Forest and Food Sciences.
Largo Braccini, 2, 10095 Grugliasco (TO), Italy –
(gianmarco.corvino, andrea.lessio, enrico.borgogno)@unito.it

KEY WORDS: Rice crop monitoring, Sentinel 2, Landsat 8, Cadastral parcels, CAP, Monitoring Services

ABSTRACT:

Monitoring of agricultural areas in Europe is generally operated at cadastral parcel level. Nevertheless, especially in Italy, many parcels are internally inconsistent in terms of crop type or management techniques. In this work, based on free satellite data (Landsat 8 and Sentinel 2), authors tested differences between a parcel- and segment-based approach for rice monitoring. Consequently, ordinary cadastre-based tessellation scheme was compared with a different one obtained by image segmentation operating in the multitemporal NDVI spectral domain. With reference to these two approaches, the available time series of spectral measures (NDVI and NDWI) were processed aggregating spectral information at parcel and segment level by averaging. NDI and NDWI differences were tested computing: a) $MAE_{x,y}(t)$ to measure the "average" spectral difference over the scene at the generic date; it was intended to explore seasonality of differences; b) $MAE_t(x,y)$ to measure the average local spectral difference along time; it was intended to explore spatial distribution of differences. The analysis concerned the 2016 rice growing season in the study area (Piemonte Region, NW Italy). Differences proved to be significant and seasonal showing that, if not considered, can lead to wrong deductions concerning both area computations (important for CAP payments) and time of water releases. Authors retain that this approach should be mandatory for whatever institutional remote sensing driven service aimed at monitoring crops at regional level. Once more, it is clear that standardized and certified procedures are presently needed to make the ongoing technology transfer reliable and robust for Institutional Administrators.

1. INTRODUCTION

Nowadays remote sensing techniques are imagined to be widely used in agricultural applications due to the high availability of free pre-processed dataset. In particular a great challenge is the adoption by Institutional players of remote sensing-based (web) services to support their ordinary tasks, mainly devoted to controls and alerting. Presently, in the EU context, even if an innovative trend is started, the most commonly adopted reference land unit for controls and payments is the cadastral parcel. It is worth to remind that, this land tessellation scheme is merely administrative: a single parcel can, in fact, be made of different parts, whose spectral properties can be significantly different, being often different their content due to different crop type or timing of operation, or both. While monitoring such a geometry, many of the proposed pilot services tend to operate at parcel level, i.e. by aggregating (averaging) over the parcel the available spectral signal from the included pixels, or, oppositely, maintaining information at pixel level with no regards about information synthesis (Erden &Töreyen, 2015). Examples come from the EU FP7 ERMES project (www.ermes-fp7space.eu/it/homepage/), that was specifically aimed at developing a prototype of downstream service dedicated to the rice sector based on active and passive satellite data and ground observations. Or, similarly, from the Space4Agri (www.space4agri.irea.cnr.it) project, developed by the General Direction of Agriculture Office of Lombardia Region and the Italian National Research Council (CNR), rice crops monitoring was achieved integrating Earth Observation (EO) data and ground data as well. Both the projects were intended for supporting local public authorities in monitoring and mapping crops with the aim of managing various related risks along the whole growing season. It is not surprising that cadastral parcel was initially assumed as reference land unit, being a stable geometry in time with a strong administrative meaning, suitable for economic concerns. Moreover, the choice of aggregating the spectral signal by averaging the local spectral response of the pixels included in the parcel to generate a single value is certainly an easy way to translate a complex spectral information into a single attribute value that can be associated to a vector layer representing the cadastral parcels. Unfortunately, this strategy is reliable only if the parcel is effectively homogeneous from an agronomic point of view; otherwise, the computed aggregated spectral value is highly unreliable and inconsistent with real conditions. With the aim of overcome this undesired situation, in the EU regulation no. 809/2014 was explicitly stated that payment claims related to CAP (Common Agricultural Policy) must be based on the actual managed areas independently from cadastre. Applicants are now required to apply for CAP payments using an GIS-based electronic format called "Geo-Spatial Aided Application Form (GSAAF)". GSAAF requires that applicant draws field border in a GIS-like environment, aiming at limiting errors by beneficiaries when declaring their agricultural areas and making administrative cross-checks more efficient. In addition, more accurate spatial information provided by GSAAF will provide more reliable data to monitor and evaluate agronomic practices, since the effective spatial distribution and extension of crops within, or over, cadastral parcels will be considered and declared by applicants. The focus of this work was to evaluate differences between cadastral- and segment- based tessellation scheme, comparing maps of average spectral behaviour generated by aggregation of signal at both cadastral and segment level. Tested differences concerned a time series of NDVI (*Normalized*

* Corresponding author

Difference Vegetation Index, Rouse et al., 1974) and NDWI (*Normalized Difference Water Index*, McFeeters, 1996) spectral indices along the 2016 rice growing season.

2. MATERIALS AND METHODS

This work was based on twenty-four optical satellite images calibrated into at-the-ground reflectances; 14 ESA (*European Space Agency*) Sentinel-2 Level 2A (S2) and 10 NASA (*National Aeronautics and Space Administration*) Landsat-8 C1 Level 2 (L8) collections were jointly used. The L8 dataset was over-sampled (nearest-neighbor) at a geometrical resolution of 10 m to be consistent with the S2 one (Lessio, A. et al., 2017; Munyati, C. 2017).

Table 1. L8 and S2 images used in this work.

Mission	Dates (2016)
L8 (Path 194, Row 28-29)	18/03, 19/04, 21/05, 22/06, 24/07, 25/08, 10/09, 12/10, 13/11, 31/12
S2 (Tile 32TMR)	05/02, 03/03, 21/07, 24/07, 03/08, 10/08, 23/08, 19/09, 29/09, 12/10, 29/10, 08/11, 08/12, 28/12

A cadastral map (1:2000 nominal map scale) was available in vector format, representing the administrative boundaries of rice fields as declared by farmers to the Regional Administration for the year 2016. The study area (Fig.1), sizing about $8.7 \cdot 10^3$ ha is part of the rice PDO (*Protected Designation of Origin*) area of "Consorzio di Bonifica della Baraggia Biellese e Vercellese" sited in the Piemonte Region (NW Italy). From the agricultural point of view, this area is mainly devoted to rice cultivation; ISTAT (*Italian National Institute for Statistics*) estimated that in 2016, rice crops took 116325 ha with a production of 499273 tons within the whole Vercelli province, where the study area is sited. The area was investigated along the 2016 rice growing season with reference to the correspondent NDVI and NDWI image time series.

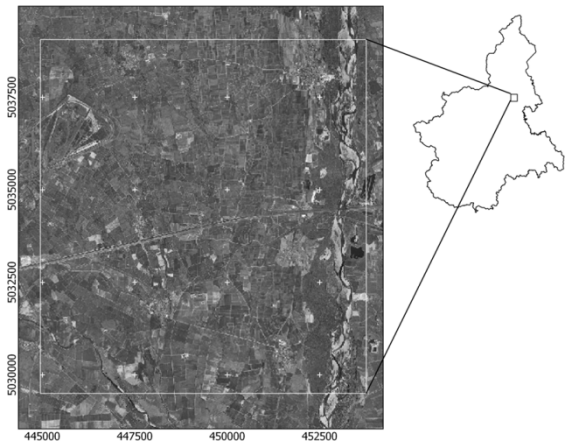

Figure 1. Study area in the Piemonte Region. Reference frame is WGS-84 UTM 32N.

NDVI was assumed as proxy of rice vegetative vigour after plants exit the water; NDWI was differently used to detect water content dynamics with particular concerns about the rice pre-seeding flooding period (McFeeters S. K., 1996).
NDVI/NDWI computations from at-the-ground reflectance calibrated S2 and L8 bands were performed at pixel level, generating the correspondent raster maps (GSD=10m).
Segments, possibly aggregating pixels with similar spectral properties, were generated running a region growing segmentation algorithm exploring the NDVI image time series. NDVI was therefore selected as discriminant for mapping similarly behaving areas over the scene.
Image segmentation (Mean Shift algorithm) (Comaniciu & Meer, 2002) was achieved by Orfeo ToolBox (OTB, v. 6.4.0) with the following parameters: spatial radius = 5 pixels (50 m), range radius = 0.1, minimum region size of 25 pixels (i.e. 0.25 ha consistent with the statistical distribution of area values: about 95% of parcels, in fact, were found to be smaller than 3 ha, 83.1% smaller than 1 ha. A geometrical assessment aimed at enhancing differences in cadastral and segmented polygons was performed at this point. Numerousness, average area size and Shape Index (*SI*, Forman & Godron, 1986, [1]) of polygons from both cadastral and segmented vector maps were computed in SAGA GIS and compared.

$$SI = \frac{P}{(2 \cdot \sqrt{\pi \cdot A})} \quad [1]$$

where P is polygon perimeter and A is its area. SI =1 for circular polygons, SI =1.128 for squared polygons and it tends to increase for more anisotropic polygons with complex borders (a long perimeter in respect of a limited area). Successively, according to the two tessellation schemes, for each single date, the average value of NDVI/NDWI was computed considering all the pixels included within each polygon.

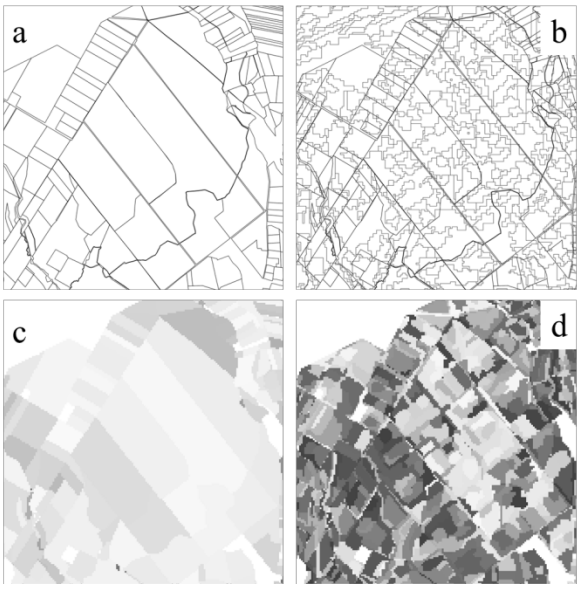

Figure 2. Land tessellation schemes: a) cadastral parcels; b) segments; c) example of NDVI aggregated map (parcels); d) example of NDVI aggregated map (segments). Greyscale values represent the parcel/segment NDVI average value for the selected date.

Two pairs of image time series were consequently obtained for respectively NDVI and NDWI, hereinafter called SM_i and PM_i if respectively segment- or parcel-based. In Fig. 2 the parcel- and segments-based tessellation schemes are shown together with an example of NDVI aggregated maps for the two situations (parcel/segment average value). The *Mean Absolute Error* (MAE, Willmott, C. J., & Matsuura, K., 2005) for each index was used as statistical measure to quantify differences. To explore "how" differences were averagely spatially distributed, a map of MAE (computed locally along the image time series) was generated according to [2]:

$$MAE_t(x,y) = \frac{\sum_1^n |SM(x,y)_i - PM(x,y)_i|}{n} \quad [2]$$

where $SM(x,y)_i$ and $PM(x,y)_i$ are the average values of the spectral index computed respectively in the segment and in the parcel at the generic time t, n is the number of images.
A further investigation was aimed at testing MAE behaviour along the rice growing season. In this case three temporal profiles of $MAE_{x,y}(t)$ were computed, [3]: the average, the minimum and the maximum MAE value of each available scene (only rice fields were considered). This resulted in a temporal profile consisting of 24 $MAE_{x,y}(t)$ values measuring average, maximum and minimum differences between a cadastral and segment based approach.

$$MAE_{x,y}(t) = \frac{\sum_1^m |SM(x,y)_i - PM(x,y)_i|}{m} \quad [3]$$

where $SM(x,y)_i$ and $PM(x,y)_i$ are the average values of the spectral index computed respectively in the segment and in the parcel at the generic time t, m is the number of rice pixels in the image at the time t. To locally enhance significance of differences a reference rice parcel was finally selected as paradigm and explored to demonstrate authors' hypothesis about the need of working at segment level.

3. RESULTS AND DISCUSSIONS

After segmentation, a first analysis concerned the geometric features of the two series of polygons (cadastre vs segmentation). Both size and shape were taken into account.
Segmentation results showed a higher number of polygons: more than 8000 in respect of the 5787 cadastral parcels. The average polygon size was 9594.38 m^2 and 6823.49 m^2 for parcel and segments respectively. The correspondent SI average values was 1.71 for cadastral polygons and 1.84 for segmented ones, demonstrating that segments are more anisotropic than the parcels. This effect is mostly due to the capability of segments of isolating parcel edges/roads in which the average NDVI value is sensitively different from the central part of the same parcel. Moreover it can be assert that the SI can be a good discriminant to automatically map and exclude terrain infrastructures (headlands, service roads, etc.) from the analysis. Comparison between SM_i and the PM_i maps for the year 2016 proved that differences between the two approaches are significant. As far as maps of $MAE_t(x,y)$ are concerned (Fig. 3), they proved to be able to detect anomalous areas where differences are very high. $MAE_t(x,y)$ highest values if found within a parcel, in general represent headlands, service roads, or tree lines separating fields. These features, while using cadastral parcel as reference mapping unit, can move the average parcel spectral signal from the pure one of the crop, leading to wrong conclusions in monitoring. Differently, a segmentation-based approach can properly take into account this problem. The shape index (SI) can be effectively used, in this context, to automatically separate these two types of occurrences from $MAE_t(x,y)$. Elongated polygons can be easily related to infrastructures (headlands, service roads), eventually not mapped by cadastral cartography, permitting their exclusion from the computations directly related to crops phenology. Moreover $MAE_t(x,y)$ allows to map potentially different rice cultivars (or crops) managed within the same cadastral parcel. NDWI differences proved to better stress these anomalous situations, that can be ordinarily related to a different water management within the parcel that strictly depends on rice cultivar (or crop). Regarding to $MAE_{x,y}(t)$, i.e. the temporal profile of the rice pixels "average" difference along the season, the maximum values were sensitively higher than the expected index measure accuracy (i.e. ≈ 0.02, Borgogno Mondino et al., 2016). They count 0.07 for NDVI and 0.11 for NDWI, respectively (Fig. 4). NDVI maximum difference was detected on the 19/04/2016, i.e. at the starting of the growing season, when crop proceeds on with different velocities at different times especially in its germination and tillering phases.

Figure 3. Maps of $MAE_t(x,y)$ of respectively NDVI (left) and NDWI (right). Dark areas correspond to the highest difference values.

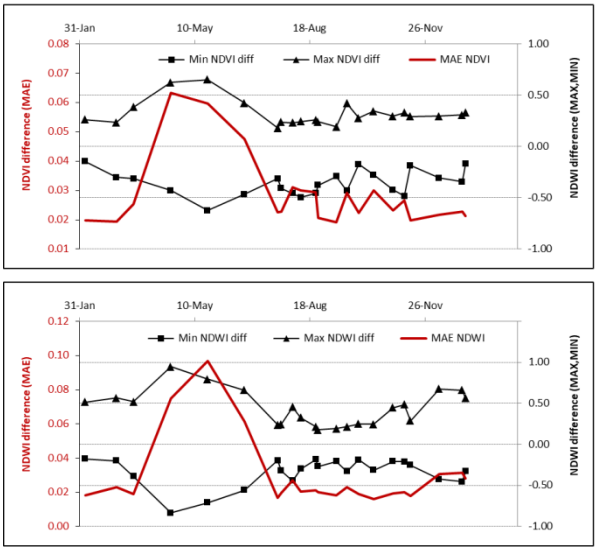

Figure 4. NDVI (above) and NDWI (below) $MAE_{x,y}(t)$ trends along the year (red = image average value, triangles = image max value, squares = image min values).

NDWI maximum difference occurred on 21/05/2016, i.e. when water releases from the local Irrigation Consortium enter the fields to operate the submersion, suggesting a not homogeneous distribution of water at parcel level.
No rigorous ground data were obtained to test this deduction, whose reliability was not so important at this point. Nevertheless, water dynamics investigation was preliminarily verified by an informal survey involving technicians of the local Irrigation Consortium, that confirmed the most of deductions.
To further emphasize the importance of a segmentation-based approach in monitoring crop with satellite data, a reference parcel was selected as paradigm to prove that within the same parcel, different segments can significantly represent different growing situations (Fig. 5), with particular concerns about farming operations, flooding phases and plants development. According to Fig. 5 (graphs) it can be easily noticed that the parcel average trends of NDVI/NDWI (red line) especially in Spring (starting of the growing season) is poorly representative of the actual ongoing situations within the parcels, that segments are able to peculiarly recognize.
Temporal profiles explicit these significant differences. In particular water-related dynamics of crops are badly

represented by the NDWI average profile of the whole parcel, especially in spring when the biggest water releases occur in the area. Differences can be observed both in time (things happen at different times) and in strength (index value sometimes never reaches the same values in all the segments).

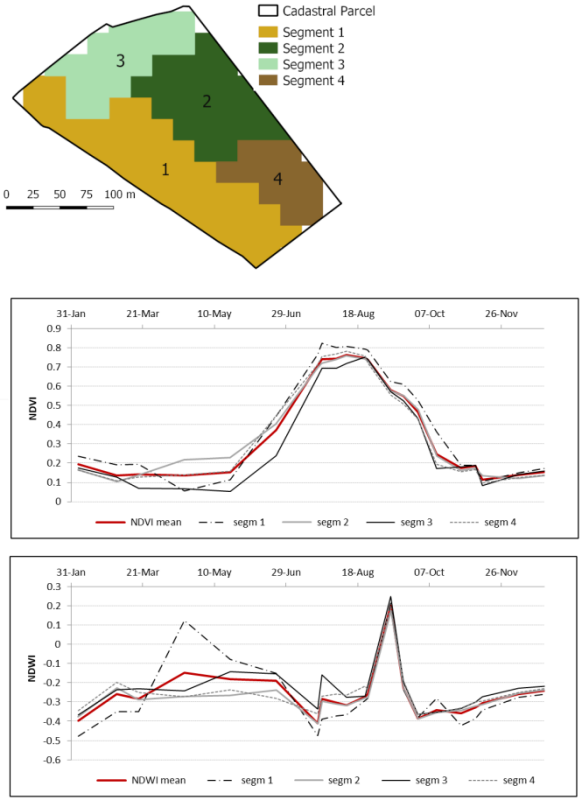

Figure 5. Example of segmented parcel. In the graphs the average spectral indices profiles, NDVI (above), NDWI (below) of segments are compared with the one of the whole parcel (red line).

4. CONCLUSIONS

The availability of an increasing number of free remotely sensed datasets, makes nowadays possible the development, engineering and supplying of web-based geo-services for agriculture based on the continuous monitoring of crops.
This work explores some critical aspects of crop monitoring at regional level, which is based on the assumption that the minimum mapping unit is the cadastral parcel. Unfortunately this land tessellation is merely administrative: a single parcel can, in fact, be made of differently managed parts whose spectral properties can be significantly different, being often different their content. In this condition, aggregation of spectral signal of pixel at parcel level can generate incorrect interpretation of the actual behaviour of crops. In this work, focusing on time series of NDVI and NDWI spectral indices S2 and L8 datasets, a cadastral-based landscape tessellation scheme is compared with an image segmentation-based one. Image segmentation proved to be able to isolate sub-parcel homogeneous areas whose spectral content is internally consistent and referable to a common macro-phenology and water content dynamic of crops. Differences between cadastral- and segmentation-based aggregation of NDVI and NDWI time series were tested at both spatial and temporal level. Results showed that differences area seasonal (see $MAE_{x,y}(t)$) with the highest values in Spring, exactly when rice management requires a more accurate and complete information to operate according to a Precision Farming philosophy. This makes crucial the possibility of correctly interpret land tessellation and the consequent spectral information aggregation, suggesting that a segments-based approach is more desirable than a parcel-based one. Concerning the spatial analysis of differences (see $MAE_t(x,y)$), it was found that highest values are located or in correspondence of infrastructural land features like service roads, tree lines, etc. (linear features) or where the parcel is managed differently in terms of agronomic techniques and/or rice cultivars (polygon features). In the area, the latter can possibly be related to local dry seeding techniques, characterized by different water management during the agronomic season, thus resulting in different spectral behaviour. Authors retain that a segmentation-based approach is mandatory in a processing workflow oriented to the development of a reliable monitoring service, constantly updated (because based on regularly acquired images). Segments, whose shape has to be constantly updated along the years should represent the reference mapping unit for agricultural services based on remotely sensed data. Cadastral parcel still can enter the process supplying all those administrative information to relate crop to farmer. This can be easily obtained by ordinary GIS tools (geoprocessing) able to intersect the cadaster and the segmentation layers. In the meantime, cadastral maps can be constantly updated taking care of the actual managed crop whose declaration, at the moment in the Italian context, is static and steady at its original value (often not anymore correct). In this condition, a service of this type can enter the official and institutional procedures of both Regional and European CAP administrators making controls and payments more complete and consistent. One crucial point is anyway missing at this point: standardized and certified procedures (approved by scientific community, administrators and farmers) are required to make all results consistent and relatively comparable.

REFERENCES

Borgogno-Mondino, E., Lessio, A., & Gomarasca, M. A. 2016. A fast operative method for NDVI uncertainty estimation and its role in vegetation analysis. *European Journal of Remote Sensing*, 49(1), pp 137-156.

Comaniciu, D., & Meer, P. 2002. Mean shift: A robust approach toward feature space analysis. *IEEE Transactions on pattern analysis and machine intelligence*, 24(5), pp 603-619.

Erden, H., Töreyen, G. 2015. "Parcel Based Crop Production Yield Model." In Agro-Geoinformatics, 2015 Fourth International Conference on, pp. 109-112. IEEE.

Forman R.T.T., Godron M. Landscape Ecology. Cambridge University (1986).

Lessio, A., Fissore, V., & Borgogno-Mondino, E. 2017. Preliminary Tests and Results Concerning Integration of Sentinel-2 and Landsat-8 OLI for Crop Monitoring. *Journal of Imaging*, 3(4), pp 49.

McFeeters S. K. 1996. The use of the Normalized Difference Water Index (NDWI) in the delineation of open water features. *International journal of remote sensing*, 17(7).

Munyati, C. 2017. "The potential for integrating Sentinel 2 MSI with SPOT 5 HRG and Landsat 8 OLI imagery for monitoring semi-arid savannah woody cover." International journal of remote sensing, 38(17), 4888-4913.

Rouse Jr, J.W., Haas R. H., Schell J. A., Deering D. W., Harlan J. C. 1974. Monitoring the vernal advancement of retrogradation of natural vegetation. Final report. NASA/GSFC

Willmott, C. J., & Matsuura, K. 2005. Advantages of the mean absolute error (MAE) over the root mean square error (RMSE) in assessing average model performance. *Climate research*, 30(1), pp 79-82.

A PLOT SAMPLING STRATEGY FOR ESTIMATING THE AREA OF OLIVE TREE CROPS AND OLIVE TREE ABUNDANCE IN A MEDITERRANEAN ENVIRONMENT

M. Grotti[1]*, N. Puletti[1], F. Chianucci[2*], W. Mattioli[1], A. Floris[1], F. Clementel[1], C. Torresan[1], M. Marchi[1], A. Gentile[3], M. Pisante[4], A. Marcelli[5], P. Corona[1]

[1] CREA, Research Centre for Forestry and Wood, Arezzo, Italy – mirkogrotti@gmail.com, (nicola.puletti, walter.mattioli, antonio.floris, fabrizio.clementel, chiara.torresan, maurizio.marchi, piermaria.corona)@crea.gov.it
[2] CREA, Research Centre for Agriculture and Environment, Rome, Italy – fchianucci@gmail.com
[3] University of Catania, Department of Agricultural and Food Science, Catania, Italy – gentilea@unict.it
[4] University of Teramo, Teramo, Italy – mpisante@unite.it
[5] University of Siena, Department of Economics and Statistics, Siena, Italy – agnese.marcelli@student.unisi.it

KEY WORDS: Olea europaea; tessellation stratified sampling; olive crops inventory

ABSTRACT:

Accurate inventory and mapping of olive (*Olea europaea* L.) tree attributes represents a central issue to support the olive production system. With reference to the cultivation, there is a high heterogeneity and complexity in the cultivation of olive trees, which is reflected in the large variability in olive grove surfaces. This poses some challenge in accurately estimating olive tree attributes via traditional inventory approaches, as commonly adopted in national forest inventory. From a methodological point of view, the complexity and heterogeneity of olive tree groves can be comparable to the problem of accurately estimating tree outside forests (TOF) attributes. In this study, we tested whether a plot sampling approach formerly developed for TOF is suitable for estimating olive tree attributes at large scale. We tested this approach in a case study where the census of the olive crop area and the number of olive groves was conducted from photo-interpretation of high resolution aerial orthoimagery, used as benchmark to test the effectiveness of the plot sampling approach. The main result of this study is that the plot sampling method can be applied for estimating olive tree attributes. Our obtained RSEs were below 20%, with a limited sampling effort of about 6% of the studied population; the obtained RSEs were below 6% when increasing sampling up to about 21% the studied population. Using robust statistical procedures among countries, should allow obtaining harmonized and comparable information, which can increase the knowledge of olive geographical distribution and structure at its relevant Mediterranean scale.

1. INTRODUCTION

The olive tree (*Olea europaea* L.) is a long-living evergreen plant with relevant cultural, economic and landscape relevance (Loumou and Giourga, 2003). The cultivation of olive started in Greece 3500 years ago, and, with the support of the Romans, it spread to the entire Mediterranean basin. Currently, there are approximately 750 million productive olive trees worldwide, with the countries of the Mediterranean basin concentrating 95% of the global cultivation area (about 10.5 Mha; International Olive Oil Council, 2016). In recent years, the olive production area has increased worldwide, due to the introduction of innovations in the farming systems and cultivars (Leon et al., 2007; Caruso et al., 2014). Olive tree crops have also a strong potential in mitigating climate, since as permanent crops they provide carbon storage in soils (Montanaro et al. 2010; Las Casas et al. 2014). In addition, the use of olive residues as alternative fossil fuel provides additional reductions in greenhouse gas emissions. Accurate inventory and mapping represents a central issue to support the olive production system since it plays a key role in the sustainable management of farming, irrigation and other intervention (Biasi et al. 2017; Puletti et al. 2018).
With respect to the cultivation, there is a high heterogeneity and complexity in the cultivation of olive trees. This is mainly due to the different agricultural systems, farming techniques, and genetic variability. The main cultivation methods can be summarized as:

- a traditional or extensive production systems, which is characterized by low-density crop (less than 140 trees per hectare) with irregular tree spatial distribution and minimum interventions as resources inputs;
- a semi-intensive method, with higher number of trees (140-400 trees per hectare);
- a super-intensive method, with very high-density crop (up to 2,500 trees per hectare) located on flat areas and super-intensive agronomical interventions and inputs.

In addition, olive tree is cultivated in a wide variety of soils and can tolerate a broad range of physicochemical conditions. Such heterogeneity in production systems is reflected in the large variability in olive crop size, whose average ranges from 1.3 ha in Italy and 1.5 ha in Greece, up to 5.5 ha in Spain (Eurostat 2016). The heterogeneity of its cultivation poses some challenge in accurately estimating the olive grove area and the olive tree density via traditional approaches of tree inventory, like those e.g, commonly adopted for national forest inventories (McRoberts and Tomppo, 2007). Because complete censuses of all trees on all forest lands are prohibitively expensive and time-consuming, national forest inventory usually relies on sample-based procedures to produce estimates of forest area and wood volume per unit area. A wide variety of sampling designs have been used, although most now have systematic components that prescribe sampling units on either regularly spaced grids or in regular polygons that tessellate the area of interest (Fattorini et

* Corrisponding author

al., 2016). Remotely-sensed information is integrated in the sampling procedure to support the retrieval of inventoried attributes.

From a methodological point of view, the complexity and heterogeneity of olive grove area and olive tree density can be comparable to the problem of accurately estimating trees outside forests (TOF) attributes. TOFs are defined as small groups of trees within rural and urbanized areas not classified as forests (De Foresta et al., 2013). Only relatively recently the importance of including TOF to integrate forest inventory estimates have been addressed by some studies (Corona et al., 2015; Johnson et al., 2015; Fattorini et al., 2016; De Foresta, 2017). Similarly, to traditional forest inventory, TOF inventory strategies are usually based on environmental sampling scheme such as point and plot sampling, and its combination with information derived from remotely sensed imagery. Fattorini et al. (2016) investigated the performance of various point and plot sampling approaches on TOF estimation and concluded the "PLIS" (plot intercept sampling) was effective for large-scale TOF inventorying.

In this study, we verified whether the statistical approach proposed by the authors above is suitable for estimating olive grove area and olive tree density. For the purpose, the approach was tested in a case study where the census of the olive grove area and abundance (number of olive groves) was manually conducted from photo-interpretation of high resolution aerial orthoimagery and used as benchmark to test the effectiveness of the plot sampling approach in olive tree inventory. Tree abundance has been also estimated using the same sampling procedure, although no manual benchmarking was available for this variable.

1. MATERIAL AND METHODS

In this study, we adopted the one-phase tessellation stratified sampling (TSS) estimation as indicated by Fattorini et al. (2016) to be the more effective strategy for large-scale TOF inventories. In TSS, the reference area A* is overlaid by a grid of R polygons (hexagons). A point is randomly selected within each polygon and a circular plot centered on the point is drawn. Compared to uniform random sampling (URS), TSS gave mathematically lower variance than URS. For details, see Fattorini et al. (2016).

The study was carried out in the municipality of Calenzano (43° 51' N; 11° 9' E), Central Italy (Figure 1). The area of interest (AOI) covers 76.9 km^2, which is mainly constituted by urban and hilly areas. The utilised agricultural area comprised about 25%, while the wooded area comprised about 36% the total surface (National Agricultural Census, 2010). The census of olive variables (olive grove area and) was conducted by photo-interpretation of high resolution (20 cm ground pixel resolution) aerial orthoimagery carried out by trained photo-interpreters. Each polygon identifying an olive grove was manually delineated on-screen and a unique identification number was assigned to that polygon in a polygon layer file; the area of each polygon was then assessed.

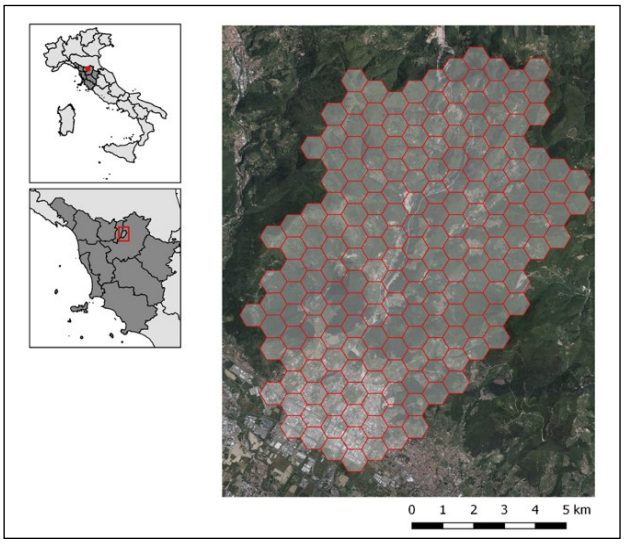

Figure 1. Study area tessellated by 0.5 km^2 hexagons to perform the plot intersect sampling strategy adopted to estimate olive tree attributes

The plot intersect sampling (PLIS) proposed by Fattorini et al. (2016) was adopted to select units. The AOI was overlaid by a grid of hexagons covering the area. The hexagon size proposed by the previous study was 1 km^2, as recommended for TOF sampling. However, by definition TOF units have a maximum surface of 0.5 ha, for which the use of 1 km^2 hexagon size is justified. In case of olive groves, a larger variability in size can occur; after a preliminary check, we observed that a hexagon size of 0.5 km^2 for olive inventory is more appropriate for capturing the variability of olive groves. Therefore, we tessellated the study area by 0.5 km^2 hexagons (Figure 1).

The sampling procedure requires randomly selecting a point in each hexagon. Circular plots centered on the selected points were then derived. To test the accuracy of the PLIS method with different sampling efforts (which depends on plot size), the circular plots were derived using three different radii (r=50 m; r=100 m; r=150 m). All the olive groves intersected by the plot were included in the sampling; this method was hereafter abbreviated as PLIS50, PLIS100 and PLIS150 depending on the plot radius. This sampling strategy was used to get the estimated number of olive groves (polygons), the total area of olive groves and the total number of olive trees.

The adopted estimators of the totals and their variances are those reported by Fattorini et al. (2016). The relative standard error (RSE) was determined as the ratio of the estimated variance square root to the total under estimation.

2. RESULTS

The olive census led to 1,161 polygons representing the number of olive groves, which covered a total surface of 662.41 ha (about the 9% of the AOI surface). Using a hexagon size of 0.5 km^2 to tessellate the AOI, the total number of hexagons was 194. The sampling scheme allowed selecting 58, 133 and 244 olive groves polygons using respectively 50, 100 and 150 circular plot radius. The estimates obtained for olive variables are summarized in Table 1. For the three target estimates, the sampling scheme yielded estimates whose RSE was always below 20%, regardless the plot radius. The best performance was obtained using the PLIS150 scheme, which required a sampling effort of 21% of the target population. Under this scheme, the RSE was below 6% in

the three estimated variables and the absolute difference between estimates and censuses was below 20%.

Method	Total number of olive groves	Total area of olive groves	Total number of olive trees
	N	ha	N
PLIS50	216	160.20	23,490
RSE (%)	9.6%	11.6%	13.9%
PLIS100	514	325.91	49,310
RSE (%)	3.1%	5.5%	8.7%
PLIS150	960	566.84	88,124
RSE (%)	2.0%	3.9%	5.9%
Census	1161	662.41	-

Table 1. Summary statistics of obtained estimates using the PLIS50, PLIS100 and PLIS150 sampling scheme and hexagons size of 0.5 km^2

3. DISCUSSION

The main result of this study is that the PLIS method, formerly developed for TOF inventorying (Fattorini et al., 2016), can be effectively applied for estimating olive tree attributes. In our case study, we obtained accurate estimates of such attributes, with RSEs below 10%, with a limited sampling effort of about 11% of the studied population (olive grove polygons) under the PLIS100; the obtained RSEs were below 6% when increasing sampling up to about 21% under the PLIS150. The PLIS150 was the most accurate overall, as the absolute difference between estimated and censored variables were below 20%, and thus it appears more suited to estimate olive groves attributes. Worst results were obtained using the PLIS50.

Overall, PLIS demonstrated the effectiveness of estimating olive tree attributes with considerable reduction in cost and time efforts required compared with total census. This procedure can be carried out without *a-priori* knowledge of land classes spatial distribution, by post-classifying just the areas intersected by the sampling plots. While we recommend the PLIS150 method, as the most accurate scheme, future applications should define the circular plot size, which determines sampling efforts, as a compromise between the sampling efforts required and the desired accuracy of produced estimates.

The proposed procedure is proven to be effective to estimate both the total number and the total area of olive groves. With regards to olive tree abundance, we have no (manually derived) benchmark to compare against with the PLIS estimates, since manual delineation of all trees at the large scale of the study is unpractical. However, the PLIS allowed getting low RSE also for olive tree abundance estimation. To the best of our knowledge, no previous studies have attempted to estimate these olive variables at large scale at such a level of detail (i.e, tree abundance). The output is interesting as it can foster large-scale assessment of olive grove attributes which are relevant for supporting both the policy and the production system in olive – e.g, estimating olive tree density can allow defining strategies for improving the olive farming system, including irrigation, fertilization, and mechanization. From a wider point of view, the need to produce robust estimate using robust statistical procedures among countries should allow to obtain harmonized, evidence-based and comparable information (Corona, 2015), which can increase the knowledge of olive geographical distribution and structure at its relevant Mediterranean scale.

ACKNOWLEDGEMENTS

The study has been funded by the research project “Mappatura dei fabbisogni di investimento e monitoraggio dell'olivicoltura italiana (OLIVEMAP)” funded by the Italian Ministry of Agricultural, Food and Forestry Policies (MiPAAF).

REFERENCES

Biasi, R., Brunori, E., Ferrara, C., Salvati, L., 2017. Towards sustainable rural landscapes? a multivariate analysis of the structure of traditional tree cropping systems along a human pressure gradient in a mediterranean region. Agroforestry Systems 91, 1199-1217.

Caruso, T., Campisi, G., Marra, F.P., Camposeo, S., Vivaldi, G.A., Proietti, P., Nasini, L., 2014. Growth and yields of the cultivar Arbequina in high density planting systems in three different olive growing areas in Italy. Acta Hortic 1057, 341–348.

Corona, P., 2015. Forestry research to support the transition towards a bio-based economy. Annals of Silvicultural Research 38, 37-38.

Corona, P., Fattorini, L., Pagliarella, M.C., 2015. Sampling strategies for estimating forest cover from remote sensing-based two-stage inventories. Forest Ecosystems 2, 18.

De Foresta, H., 2017. Where are the trees outside forest in Brazil? Pesquisa Florestal Brasileira 37 (91), 393-401.

De Foresta, H., Somarriba, E., Temu, A., Boulanger, D., Feuilly, H., Gauthier, M., 2013. Towards the assessment of trees outside forests. Forest Resources Assessment Working Paper 183, FAO, Rome, pp. 335.

Eurostat. Agricultural Production–Orchards, 2016. Available online: https://ec.europa.eu/eurostat/statistics-explained/index.php/Agricultural_production_-_orchards (accessed on 15 April 2018).

Fattorini, L., Puletti, N., Chirici, G., Corona, P., Gazzarri, C., Mura, M., Marchetti, M., 2016. Checking the performance of point and plot sampling on aerial photoimagery of a large-scale population of trees outside forests. Canadian Journal of Forest Research 46, 1264-1274.

International Olive Oil Council, 2016. Available online: http://www.internationaloliveoil.org/ (accessed on 15 April 2018).

Johnson, K.D., Birdsey, R., Cole, J., Swatantran, A., O’Neil-Dunne, J., Dubayah R, Lister A., 2015. Integrating LiDAR and forest inventories to fill the trees outside forests data gap. Environmental monitoring and assessment 187(10), 623-631.

Las Casas, G., Scollo, F., Distefano, G., Continella, A., Gentile, A., La Malfa, S., 2014. Molecular characterization of olive (Olea europaea L.) Sicilian cultivars using SSR markers. Biochemical Systematics and Ecology 57, 15-19.

León, L., de la Rosa, R., Rallo, L., Guerrero, N., Barranco, D., 2007. Influence of spacing on the initial production of hedgerow 'Arbequina' olive orchards. Span. J. Agric. Res. 4, 554–558.

Loumou, A., Giourga, C., 2003. Olive groves: "The life and identity of the Mediterranean". Agriculture and Human Values, 20, 87-95.

McRoberts, R.E., Tomppo, E.O., 2007. Remote sensing support for national forest inventories. Remote Sensing of Environment, 110, 412-419.

Montanaro, G., Celano, G., Dichio, B., Xiloyannis, C., 2010. Effects of soil-protecting agricultural practices on soil organic carbon and productivity in fruit tree orchards. Land Degrad. Dev. 21, 132–138.

National Agricultural Census, 2010 http://www.istat.it/it/censimento-agricoltura/agricoltura-2010 (accessed on 06 March 2018).

Puletti, N., Chianucci, F., Castaldi, C., 2018. Use of Sentinel-2 for forest classification in Mediterranean environments. Annals of Silvicultural Research 42(1), 32-38, doi: 10.12899/ASR-1463.

PHENOLOGY AND YIELD ASSESSMENT IN MAIZE SEED CROPS USING SENTINEL 2 VIs' TIME SERIES

M. Croci[1,3*], F. Calegari[1], P. Morandi[2], S. Amaducci[3], M. Vincini[1]

[1] CRAST Centro Ricerca Analisi geoSpaziale e Telerilevamento, Università Cattolica del Sacro Cuore, Italy - (michele.croci, ferdinando.calegari, massimo.vincini) @unicatt.it

[2] Syngenta Italia, Italy - paolo_venceslao.morandi@syngenta.com

[3] DiPROVES Dipartimento Produzioni Vegetali Sostenibili, Università Cattolica del Sacro Cuore, Italy - stefano.amaducci@unicatt.it

KEY WORDS: Sentinel-2, Vegetation Indexes, Maize, Time series analysis, Yield forecast, Phenological metric

ABSTRACT:

Vegetation indexes (VIs) Time-Series (TS) data can be used to deliver in-season yield forecasts and to extract key phenological metrics. The present work addresses the TS analysis of different VIs, obtained from Sentinel 2 data for the 2015-17 growing seasons, for yield assessment and for the determination of the beginning of the reproductive stage (silking) of maize seed crops cultivated in the Po plain. Yields (expressed as green ears weight and grain weight) and silking dates (DoY - Day of Year) were collected for 17 maize seed crops (2 crops for the 2015 growing season, 11 for 2016, 4 for 2017) and correlated with different temporal parameters extracted from VIs' field average TS by fitting different functions (Gaussian, Asymmetric Gaussian, Double Logistic, Double Sigmoid and Growth function). Extracted parameters included large integrals and small integrals between the fitted curve and the Greenness baseline as determined by the tangent at the first inflection point or by an arbitrary VI threshold. Results showed best linear correlations of yields with the small integrals of EVI (Enhanced Vegetation Index) field average TS, fitted by the Gaussian function and with an arbitrary EVI threshold in the 0.15-0.25 range. The date of maximum Green-up at the first inflection point of the Double Logistic fitting was the best silking date estimator, regardless of the VI used.

1.INTRODUCTION

The analysis of high-spatial and temporal resolutions optical data provided by the Sentinel 2 constellation is a powerful tool for crops monitoring. The analysis of Vegetation indexes (VIs) Time-Series (TS) data can deliver in-season yield forecasts and extract key phenological metrics. Despite its sensitivity to saturation at higher leaf area index (LAI), atmospheric conditions and soil background, the Normalized Difference Vegetation Index (NDVI, Rouse et al., 1974) is mostly used for crop monitoring by TS analysis. TS of medium and coarse resolution data AVHRR and MODIS (Moderate Resolution Imaging Spectroradiometer) have been used to extract vegetation phenology either by using a predefined VI threshold (Reed et al. 1994; Jonsson and Eklundh, 2004; Boschetti et al., 2009) or using the inflection points of a function fitted to the VI TS (Zhang et al., 2003). Phenological metrics obtained in such studies include the onset of greenness (start of season), time of peak VI, maximum VI, rate of green-up, length of season, rate of senescence and time-integrated area under the curve. A specific software tool (TIMESAT) has been developed by Jonsson and Eklundh (2004) to analyze VIs TS data based on asymmetric Gaussians and Double Logistic fitting functions. The approach developed by Zhang et al. (2003, 2015) using a hybrid piecewise logistic function has been used to obtain the MODIS phenology data product since 2001. An a priori shape-model of Wide Dynamic Range Vegetation Index (WDRVI) defined for maize and soybean was used by Sakamoto et al., (2010, 2011) to map crop progress in the U.S. Corn Belt using MODIS data (Sakamoto et al., 2011) and to estimate corn grain yield at the state level (Sakamoto et al., 2013). Zhao et al., (2012) pointed out the relevance of TS temporal resolution for the accuracy of the phenology estimation. To improve temporal resolution and mapping crop phenology, Gao et al. (2017) used VI TS generated by fusing Landsat and MODIS surface reflectance. High-spatial and temporal resolutions optical data provided by the Sentinel-2 are expected to markedly improve the accuracy of both phenological metrics and yield prediction based on VI TS analysis. The ESA Sentinel-2 used for Agricultural projects (Udroiu et al., 2017) provides vegetation status products during the season generated weekly (i.e. starting date of the growing season, date of maximum growth rate, length of the growing season, date of end of the growing season) by using a Double Logistic fit of Sentinel-2 NDVI TS. In literature, TS features used for yield prediction include maximum recorded VI, VI value at a specific phenological stage, model-derived maximum VI and time-integrated VIs' area. Sakamoto et al. (2013) used the WRDVI value collected before the reproductive stage to estimate corn grain yield. Rahman and Robson (2016) used model-derived maximum GNDVI for sugarcane yield prediction in Australia. The present work addresses a comparison of different VIs obtained from Sentinel 2 data, different TS fitting functions and different TS-extracted parameters for yield assessment and for the determination of the beginning of the reproductive stage (silking) in maize seed crops cultivated in the Po plain during the 2015-17 growing seasons.

2. METHODS

2.1. Crops' Data and VIs' Time Series (TS)

The multi-temporal 2015-17 study was carried-out on 17 seed maize crops (2, 11 and 4 for 2015, 2016 and 2017 respectively) cultivated in the Po plain area for Syngenta, a major maize seed producer company. For the study, Syngenta has made available accurately measured crops' yield (grain and green ears weight) and phenological (sowing and silking date) data. The three VIs used for TS analysis include the Normalized Difference VI -

* Corresponding author

NDVI, the Optimized Soil-Adjusted VI - OSAVI and the Enhanced VI -EVI (Table 1). OSAVI and EVI are more resistant than NDVI to soil background and atmospheric effect but tend to saturate for higher green biomass levels. The VIs field-averaged TS values have been extracted from all cloud-free S2 image available in the 2015-17 growing seasons and, at the start of the 2015 season, from two Landsat 8 images. Level 1C S2 data for TNQ, TNR and TQQ granules were atmospherically corrected using Sen2Cor (Louis et al., 2016), whereas S2 L2A data with sensing date after March 2017 for the same granules were directly downloaded from the Copernicus Open Access Hub.

Index	Formula	Reference
NDVI	(B8- B4)/(B8+B4)	Rouse et al., 1973
OSAVI	(1+0.16)*(B8-B4)/(B8+B4+0.1)	Rondeaux et al., 1996
EVI	2.5*((B8-B4)/(1+B8+6*B4-7.5*B2))	Huete et al., 2002

Table 1. Vegetation indexes and Sentinel 2 bands used for their calculation (B8 NIR, B4 red and B2 blue)

Landsat 8 OLI surface reflectance were obtained from the USGS ESPA (EROS Center Science Processing Architecture) after the application of the OLI atmospheric correction procedure (Vermonte et al., 2016).

2.2.TS Fitting and extraction of temporal parameters

Five different functions (Figure 2) were used to fit the three VIs' TS for each growing season and for each crop using the Phenex R-package for phenological data analysis (Lange and Doktor, 2017). The five functions are Gaussian (Press et al., 1992), Asymmetric Gaussian (Press et al., 1992), Double Logistic (Fischer, 1994), Double Sigmoid (Zhang et al., 2003) and Growth function (Richter et al., 1991).

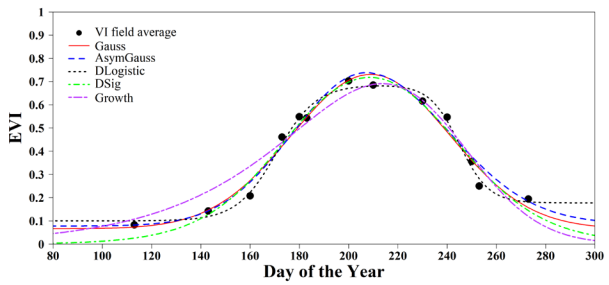

Figure 2. TS Fittings with different functions

The following parameters were extracted from the VIs TS fittings:

1. Date (Day of Year) of maximum Green-up at the first inflection point determined as the maximum of the first derivative of the fitted function (Figure 3, top);
2. Start and End of Season (SOS and EOS) dates (DoY), determined by the intersection of the tangents at the inflection points with the time axis (Figure 3, top), or by an arbitrary VI threshold (Figure 3, bottom);
3. Date (DoY) of the model-derived maximum VI (Peak of the Season);
4. Model-derived maximum VI value (Greenness Peak)
5. Greenness baseline between SOS and EOS as determined by the intersection of the tangents at the inflection points with the time axis (Figure 3, top), or by an arbitrary VI threshold (Figure 3, bottom);
6. Small integral (S) over the SOS-EOS interval and between the fitted curve and the Greenness baseline as determined by the tangent at the first inflection point (*a* in Figure 3, top), or by an arbitrary VI threshold (*a* in Figure 3, bottom);
7. Large integral (L) between the fitted curve and the time axis over the SOS-EOS interval, as determined by the tangent at the first inflection point (*a*+*b* in Figure 3, top), or by an arbitrary VI threshold (*a*+*b* in Figure 3, bottom);
8. Large integral (L total) between the fitted curve and the time axis over the whole growing season TS, regardless of EOS and SOS.

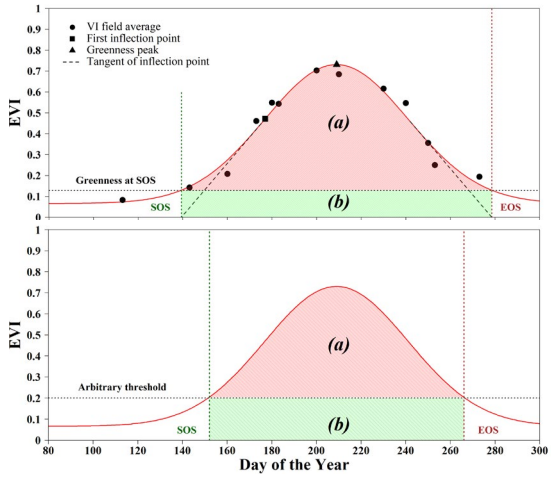

Figure 3. Greenness baseline determined by the tangents at the inflection points (top), or by an arbitrary VI threshold (bottom)

3.RESULTS

3.1. Correlation with Yields

The time-integrated VIs showed the highest linear correlation levels with yields among all the parameters extracted from TS. Especially, Time-integrated EVI with arbitrary baseline EVI = 0.2 (S(0.2)) fitted by the Gaussian function recorded the maximum R^2 value of 0.82 for grain, and of 0.80 for green ears yield. Greenness Peak as expressed by Model-derived maximum VI values showed lower linear correlation levels with maximum R^2 values of 0.29 for grain, and of 0.32 for green ears vs. Model-derived maximum EVI. Figure 4 reports the RMSE values of grain (left) and green ears yields (right), estimated by linear regressions vs. time-integrated VIs (i.e. L - or S - integrals with baseline determined by the tangents at the inflection points or by an arbitrary VI threshold) for the three VIs and for the five fitting functions. In general, the correlations with the yields were high for the parameters extracted from EVI TS, intermediate for OSAVI TS and the lowest for NDVI TS. This trend is also visible in Figure 4, showing the low RMSE values associated with EVI for all kinds of integrals. The Gaussian function showed the highest accuracy levels for both grain and green ears yields. However, the Growth or the Double Sigmoid functions outperformed the other fitting functions for some large or small integrals in terms of accuracy. The lowest RMSE values overall for both grain (0.34 Mg/ha) and green ears (0.58 Mg/ha) yields were obtained by the EVI small integral with 0.2 threshold fitted

by the Gaussian function - S(0.2) as showed in Figure 4. The EVI small integrals with threshold in the 0.2-0.3 range outperformed EVI large integrals, which, in turn, showed improved accuracy by using larger EVI thresholds for the determination of the start and of the end of the season (i.e. the integral limits). Such trends are not similarly detectable for the other three fitting functions. The use of the tangent at the inflection points for the determination of the start and the end of the season (L by tangent in Figure 4) and for the baseline delineation (S by tangent) markedly increased the RMSE obtained by the two best functions fitting the EVI TS both for grain (left) and green ears (right) yields. Higher RMSE values are also visible for the large integral (L total in Figure 4) between the fitted curve and the time axis over the whole growing season.

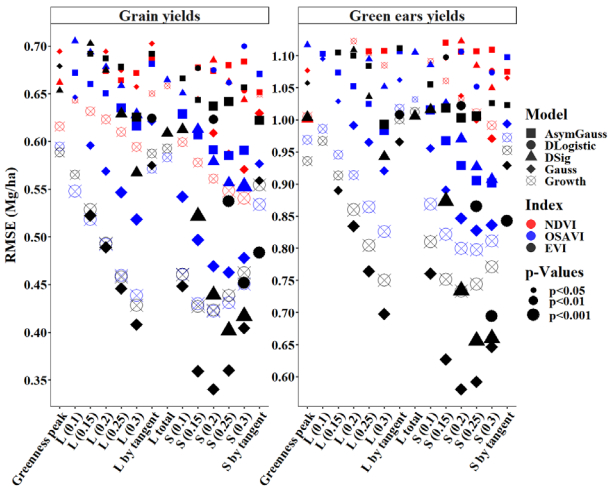

Figure 4. RMSE (Mg/ha) values of grain (left) and green ears yields (right), of the correlations with a p-Value lower than 0.05, estimated by linear regressions vs. time-integrated VIs (i.e. L - or S - integrals between SOS and EOS and baseline determined by the tangents at the inflection points or by an arbitrary VI threshold) for the three VIs and the five fitting functions.

The EVI is a more effective yield estimator thanks to its lower sensitivity to atmospheric conditions (compared to the OSAVI and the NDVI) and soil spectral behaviour (compared to the NDVI). However, the visual analysis of TS fittings and the lower performance of the Asymmetric Gaussian function seem to suggest that the higher performances of the Gaussian fitting function rely on a lower sensitivity to the variability of VIs' values at the EOS (e.g. variable VI values of maize stubbles, weeds, tilled soil…), which is not connected to the productivity of the preceding crop. This variability can largely affect the integral values for "asymmetric" fitting functions at the SOS and at the EOS. The RMSE decrease obtained from the "asymmetric" Double Logistic and Double Sigmoid functions by using higher VIs (0.25-0.3 in Figure 4) baseline thresholds (i.e. cutting both SOS and EOS tails) supports this hypothesis. The Double Sigmoid function with 0.25 threshold obtained the second lowest RMSE values overall for both grain (0.40 Mg/ha) and green ears (0.66 Mg/ha) yields. Finally, a possible interpretation of the overall good performances of the Growth function could be based on its higher fitting accuracy of TS high frequency variations compared to the Double Logistic or Sigmoid functions. Similarly, to the Gaussian function, the Growth function showed its lowest RMSE values using the 0.2 EVI baseline threshold for both grain and green ears yields.

3.2. Phenological metrics

In Figure 5 are reported the RMSE (Days) values of silking (left) and sowing (right) dates estimated by linear regressions vs. the date of maximum Green-up at the first inflection point for the three VIs and the five fitting functions. As visible in Figure 5 (left), the lowest silking date RMSE values, similar for the three VIs tested (2.64, 2.73 and 2.81 Days for OSAVI, EVI and NDVI), were obtained by the Double Logistic function while the Growth and the Gaussian functions showed comparable RMSE values only for the EVI.

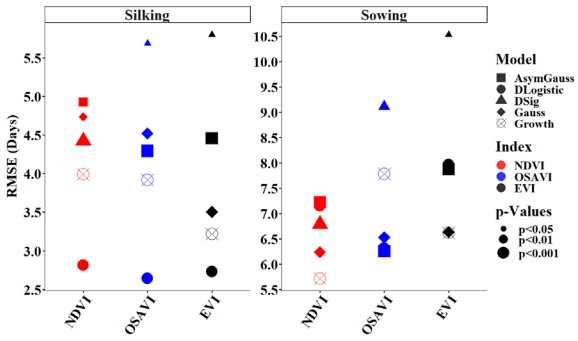

Figure 5. RMSE (Days) values of silking (left) and sowing (right) dates, of the correlations with a p-Values lower than 0.05, estimated by linear regressions vs. the date of maximum Green-up at the first inflection point for the three VIs and the five fitting functions.

As expected, considering that the thermal variability over the large test area affected germination and emergence durations, which were not detected by spectral data, the sowing date RMSE (Figure 5, right) were markedly higher than those of the silking dates. Such large errors confirm that the analysis of spectral-only time series data is unsuitable for the assessment of the sowing date.

4.CONCLUSIONS

Results of a comparison addressing yield assessment of seed maize crops in the Po plain using most common fitting functions for the extraction of several parameters from 2015-17 Time Series of NDVI, OSAVI and EVI spectral indexes, obtained from Sentinel 2 data, highlights that: i) The EVI index is more effective than OSAVI and NDVI in yield and phenology assessment; ii) Among commonly used fitting functions, those that are symmetric at the start and at the end of the season, such as the Gaussian function, are less affected by VIs' variability at the end of the season and can model more effectively the seasonal productivity of the crop; iii) Gaussian-fitted EVI TS small integrals with arbitrary greenness baseline threshold in the range 0.15-0.25 seem to be the best yield predictors obtainable by VIs' TS analysis. Even though correlation with yield and parameters extracted by VIs' TS analysis in the present study is very high (maximum R^2=0.82) for being based only on spectral data, it should be noted that, most datas analysed only refer to 2016.

Further work and datas of more years are required to assess the seasonal specificity of relationships between yield and the different parameters obtainable by the analysis of crops VIs' Time Series.

5. REFERENCES

Boschetti, M., Stroppiana, D., Brivio, P.A., and Bocchi, S., 2009. Multi-year monitoring of rice crop phenology through time series analysis of MODIS images. International Journal of Remote Sensing, 30 (18), pp.4643-4662. 10.1080/01431160802632249.

Fischer, A., 1994. A Model for the Seasonal Variations of Vegetation Indices in Coarse Resolution Data and Its Inversion to Extract Crop Parameters. Remote Sensing of Environment, 48(2), pp.220-230. 10.1016/0034-4257(94)90143-0

Gao, F., Anderson, M.C., Zhang, X., Yang, Z., Alfieri, J.G., Kustas, W.P., Mueller, R., Johnson, D.M. and Prueger, J.H., 2017. Toward Mapping Crop Progress at Field Scales through Fusion of Landsat and MODIS Imagery. Remote Sensing of Environment, 188, 9-25. https://doi.org/10.1016/j.rse.2016.11.004.

Huete, A., Didan, K., Miura, T., Rodriguez, E., Gao, X, Ferreira, L.G., 2002. Overview of the Radiometric and Biophysical Performance of the MODIS Vegetation Indices. Remote Sensing of Environment. 83. 195-213. 10.1016/S0034-4257(02)00096-2.

Johnson, P. and Eklundh, L., 2004. TIMESAT - a program for analysing time-series of satellite sensor data. Computers and Geosciences, 30, 833-845 pp. https://doi.org/10.1016/j.cageo.2004.05.006.

Lange, M., and Doktor D., 2017. phenex: Auxiliary Functions for Phenological Data Analysis. R package version 1.4-5. https://CRAN.R-project.org/package=phenex

Louis, J., Debaecker, V., Pflug, B., Main-Knorn, M., Bieniarz, J., Mueller-Wilm, U., Cadau, E., Gascon, F., 2016. Sentinel-2 SEN2COR: L2A processor for users. In: *Conference: ESA Living Planet Symposium 2016*. European Space Agency-ESA, Special Publication, vol. SP-740, pp. 9-13.

Press, W.H., Flannery, B.P., Teukolsky, S.A., and Vetterling, W.T., 1992. Numerical Recipes in C (2nd Ed.): The Art of Scientific Computing. Cambridge University Press, New York, NY, USA.

Rahman, M.R. and Robson, A.J., 2016. A Novel Approach for Sugarcane Yield Prediction Using Landsat Time Series Imagery: A Case Study on Bundaberg Region. Advances in Remote Sensing, 5(02), pp. 93 -102. http://dx.doi.org/10.4236/ars.2016.52008

Reed, B.C., Brown, J.F., Vander Zee, D., Loveland, T.R., Merchant, J.W., and Ohlen D.O.,1994. Measuring phenological variability from satellite imagery. Journal of Vegetation Science, 5(5), pp.703-714.http://www.jstor.org/stable/3235884.

Richter, O., Spickermann, U. and Lenz, F., 1991. A new model for plant-growth. Gartenbauwissenschaft, 56(3), pp.99-106.

Rondeaux, G., Steven, M.D., Baret,F., 1996. Optimization of Soil-Adjusted Vegetation Indices. Remote Sensing of Environment. 55. 95-107. 10.1016/0034-4257(95)00186-7.

Rouse, J.W., Haas, R.H., Schell, J.A. Deering, D.W., 1974. Monitoring Vegetation Systems in the Great Plains with ERTS. In: Proceedings of 3rd Earth Resources Technology Satellite-1.Symposium, Greenbelt, NASA SP-351, pp. 3010-3017.

Sakamoto, T., Gitelson, A. A., Arkebauer, T. J., 2013. MODIS-based corn grain yield estimation model incorporating crop phenology information. Remote Sensing of Environment, 131, pp.215-231. http://dx.doi.org/10.1016/j.rse.2012.12.017

Sakamoto, T., Wardlow, B.D., and Gitelson, A.A., 2011. Detecting Spatiotemporal Changes of Corn Developmental Stages in the U.S. Corn Belt Using MODIS WDRVI Data. IEEE T. Geoscience and Remote Sensing, 49. pp.1926-1936.

Sakamoto, T., Wardlow, B. D., Gitelson, A. A., Verma, S. B., Suyker, A. E., and Arkebauer, T. J., 2010. A Two-Step Filtering approach for detecting maize and soybean phenology with time-series MODIS data. Remote Sensing of Environment, 114(10), pp.2146-2159. http://dx.doi.org/10.1016/j.rse.2010.04.019

Udroiu, C., Grosu, A., Popescu, R., Manda, R., Savinaud, M., Bontemps, S., 2017. Sentinel-2 Agriculture: Software User Manual. 2. pp.1–117.

Vermote, E., Justice, C., Claverie, M., and Franch, B., 2016. Preliminary analysis of the performance of the Landsat 8/OLI land surface reflectance product. Remote Sensing of Environment, 185, pp. 46-56 http://dx.doi.org/10.1016/j.rse.2016.04.008.

Zhang, X., Friedl, M.A., Schaaf, C.B., Strahler, A.H., Hodges, J.C.F., Gao, F., and Reed, B.C, 2003. Monitoring vegetation phenology using MODIS. Remote Sensing of Environment, 84(3), pp.471-475. http://dx.doi.org/10.1016/s0034-4257(02)00135-9

Zhang, X., 2015. Reconstruction of a complete global time series of daily vegetation index trajectory from long-term AVHRR data. Remote Sensing of Environment, 156, pp.457-472. https://doi.org/10.1016/j.rse.2014.10.012

Zhao, Y., Chen, S., Shen, S., 2013. Assimilating remote sensing information with crop model using Ensemble Kalman Filter for improving LAI monitoring and yield. Ecological Modelling, 270, pp.30-42. https://doi.org/10.1016/j.ecolmodel.2013.08.016

Zhao, H., Yang, Z., Di, L., and Pei, Z., 2012. Evaluation of temporal resolution effect in remote sensing based crop phenology detection studies. Computer and Computing Technologies in Agriculture V the series IFIP Advances in Information and Communication Technology, 369, pp.135-150.https://doi.org/10.1007/978-3-642-27278-3_16

USE OF SENTINEL-2 IMAGES FOR WATER NEEDS MONITORING: APPLICATION ON AN INDUSTRIAL TOMATO CROP IN CENTRAL ITALY

B. Rapi[1], L. Angeli[2], P. Battista[1], M. Chiesi[1], R. Magno[1,2], A. Materassi[1], M. Pieri[1,2], M. Romani[1], F. Sabatini[1], F. Maselli[1*]

[1] CNR – Institute of Biometeorology, Via Madonna del Piano 10, 50019 Sesto Fiorentino (FI), Italy
(b.rapi, p.battista, m.chiesi, r.magno, a.materassi, maurizio.pieri, m.romani, f.sabatini, f.maselli) @ibimet.cnr.it
[2] LaMMA Consortium, Via Madonna del Piano 10 – 50019 Sesto Fiorentino (FI), Italy

KEY WORDS: High resolution images; NDVI; SWC; crop coefficients.

ABSTRACT:
The improvement of remote sensing techniques can provide a significant contribution to the use of more sustainable and efficient agronomic procedures in Mediterranean regions, especially in low and medium-tech farming systems. The availability of high spatial and temporal resolution images enables to deliver information on crop coverage and plant condition, useful to evaluate seasonal trends and to estimate water and nutrient requirements. This work investigates the potential advantage of using Sentinel-2 high resolution images both to estimate tomato field internal variability and to retrieve its related crop coefficients (Kc), for a more reliable definition of water requirements during different phenological stages. Satellite data were included into an integrated irrigation management system based on soil moisture sensors, meteorological data and agrometeorological model, to monitor and evaluate the irrigation efficiency of an Italian industrial tomato farmer. The results obtained confirm the utility of NDVI-derived Kc values in areas homogeneously managed, to estimate actual evapotranspiration at operational level and the suitability of Sentinel-2 images derived information for producing a detailed estimation of plant growth and soil water content.

1. INTRODUCTION

In many Mediterranean regions, information derived from satellites and unmanned aerial vehicles already supports farmers and water managers in the evaluation of plant growth and water requirements under different field and climatic conditions; this is pursued at any spatio-temporal resolution, integrating on-field measurements and observations. Some services have developed advanced computing and data processing functions for near real-time integration of data collected from various sources and agrometeorological models, delivering advices calibrated to specific agricultural sectors (e.g. Nemani et al., 2009).
Satellite data are also used to directly estimate evapotranspiration and soil moisture, to evaluate crop development and coverage, as well as to provide information supporting a large number of farmers in short, medium and long-term analysis (Calera et al., 2017). Agricultural weather networks, such as the California Irrigation Management Information System (CIMIS, https://cimis.water.ca.gov/), AgriMet (https://www.campbellsci.eu/agrimet), and the Arizona Meteorological Network (AZMET, https://cals. arizona.edu/crop/irrigation/azsched/azsched.html) provide hourly information on weather conditions and plant water requirements, starting from meteorological observations and agrotechnical information. Nowadays, advances in remote sensing and sensor network products offer the opportunity to develop new tools to obtain higher quantity of data, which can be used into tested procedures and operational support systems.
Taking into consideration Italian user requirements, some studies were carried out in Tuscany (Central Italy) to develop an automatic procedure for local and remote sensing data integration into a dedicated system for actual evapotranspiration (AET) estimation and irrigation control of different annual and perennial crops.
To this aim, water balance methods are often utilised at different spatial and temporal scales, using fully-equipped agrometeorological stations, with a limited amount of soil moisture detection points and a series of satellite images, for a frequent updating of crop growth and for independent ET estimation (Zeleke and Wade, 2012). These methods, however, are particularly sensitive to possible problems arising from the poor representativeness of soil moisture data and are also affected by inaccuracy in the measurements or sensor drift (Chiesi et al., 2018). In this operational framework, classical ET estimation formulas can be used to: i) evaluate the weight of environmental conditions; ii) define reasonable limits of soil water content (SWC) variation; iii) highlight the representativeness of point measurements with respect to the general condition of the crop and iv) detect any anomalies in soil moisture data. High spatial and temporal resolution images, in turn, provide reliable information on plant growth and water uptake, useful to derive the actual crop coefficients (NDVI_Kc) and compute AET (Maselli et al., 2014). The aim of this work is to test this method for the operational estimation of the irrigation requirements in different sectors of a typical industrial tomato field, located in a water-limited Mediterranean environment.

2. MATERIAL AND METHODS

2.1 Study area and data

The investigation was carried out in a tomato field with an extent of about 360 x 320 m^2, located near Grosseto, Central Italy (42.83° N, 11.11° E). The area is characterized by a Mediterranean climate, with hot, dry summers and mild, wet winters. The mean annual temperature over the period 1995-2018 was 15.9 °C and the mean annual precipitation was about 650 mm. Soil texture is clay-loam, with a field capacity (FC) of 0.36 m^3/m^3 and a wilting point (WP) of 0.22 m^3/m^3.
A fully equipped agrometeorological station was installed close to the field. This station included a CR6 Campbell Scientific data-logger and a Delta Ohm multiparameter probe mod. HD52.3DP147to collect standard hourly meteorological data (i.e. air temperature and humidity, precipitation, solar radiation and wind speed and direction). SWC was also measured in ten sampling points at two different soil depths (15 and 30 cm), by means of 10HS Decagon sensors. All

* Corresponding author

measurements were collected during the 2018 crop growing cycle (i.e. from the end of April until the end of July). The phenological stages and the crop canopy cover were also monitored in the field with a 15-days temporal interval.
During the growing season, the available Sentinel-2 normalised difference vegetation index (NDVI) images (10 m spatial resolution) were also collected.
The experimental trial was carried out on two parcels of the same field, sowed with two tomato cultivars (HEINS H1015 and Delfo, identified with A and B respectively); for each cultivar, two differently managed and irrigated plots were monitored (i.e. A1 and A2 for A and B1 and B2 for B, Table 1). At the end of the growing season, each plot was characterised in terms of biomass production by sampling both green tissues and fruits.

Plot	Area (m^2)	Tomato Cultivar	Irrigation (mm)	Transpl. date
A1	35400	HEINS H1015	255	21/04
A2	31200	HEINS H1015	255	23/04
B1	31200	Nunhems Delfo	234	22/04
B2	600	Nunhems Delfo	213	22/04

Table 1. Main characteristics of the plots.

2.2 Data processing

All collected information was remotely supervised and integrated with local data (e.g. geographic, edaphic, agronomic, etc.) to identify plant water demand during different phenological stages. This allowed to provide the required irrigation amount, estimating and comparing AET derived both from field and satellite data (Figure 1).

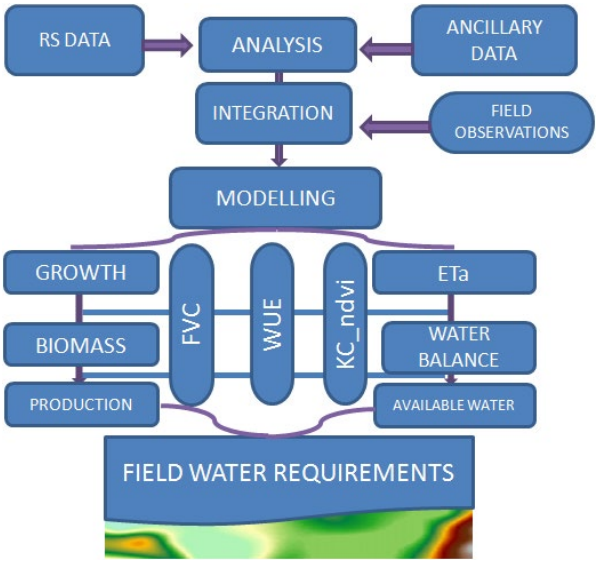

Figure 1. Flow chart describing components and procedures used to control on-field tomato irrigation management.

The general criterion was to limit irrigation when watering (i.e. the total water reaching the plants, being it rainfall, irrigation, etc.) exceeded predefined experimental thresholds, identified by means of the classical Kc approach (Allen et al., 1998). The novelty was the use of Sentinel-2 images to derive the AET estimates. This was obtained applying the NDVI-Cws (water stress Coefficient) method (Maselli et al., 2014), which is capable of separating the contribution of transpiration from green tissues and evaporation from soil by means of the remotely sensed fractional vegetation cover (FVC). Therefore, AET is computed as:

$$AET = ET_0 (FVC\ Kc_{veg} + (1\text{-}FVC)\ Kc_{soil}) \quad (1)$$

where ET_0 is the potential evapotranspiration estimated as proposed by Jensen and Heise (1963); FVC is obtained from the Sentinel-2 NDVI images following the method applied by Maselli et al. (2014); Kc_{veg} and Kc_{soil} are the maximum crop coefficients Kc related to vegetation and soil, respectively. More specifically, Kc_{veg} is set to 1.2 and Kc_{Soil} is set to 0.2.

3. RESULTS AND DISCUSSION

The comparison between synthetic indices of crop growth and water use efficiency (WUE) at two spatial scales (point and gridded) offers the opportunity to evaluate the representativeness of the sampling points with respect to the general field conditions (Table 2).

Parcel	NDVI aver. ±st.d.	Kc at NDVI max	Total AET (mm)	Fruit biomass (g/m^2)	IWUE (g/L)
A	0.70 ±0.05	0.88	236	10819	42.3
B	0.74 ±0.05	0.95	251	11938	51.1
Plot	**NDVI**	**Kc**	**AET**	**Fruit**	**IWUE**
A1	0.82	1.1	282	12129	47.5
A2	0.72	0.91	244	9508	37.2
B1	0.75	0.95	247	11735	50.2
B2	0.74	0.95	251	10553	49.5

Table 2. Satellite NDVI-derived indices related to field conditions at the maximum crop development and related field indices (fruit biomass and Irrigation Water Use Efficiency, IWUE = Fruit Dry Matter/Irrigation) detected at the end of the growing season.

Despite the general correspondence between biomass and NDVI values at pixel level, the use of satellite images for monitoring crop condition on the field requires a careful analysis of some technical and agronomic components, like sowing dates, soil and nutritional variability, irrigation and tillage scheduling.
During the growing season, NDVI_Kc and FVC were able to distinguish the peculiarity of each sampling area, despite the limited number of images collected in optimal weather conditions (only 8/20). Moreover, according to the agronomic practices conducted by the farmer, tomato growth from satellite appeared quite regular, and differences detected during the key phenological phases remained representative of the relative conditions, also during intermediate periods. For this reason, even using a limited number of sampling points and images, satellite information appears in agreement with the in-situ vegetation cover observations (Figure 2) and can be used as a proxy of the whole field conditions. Due to this relation, it is also possible to estimate plant water requirements pixel by pixel.
The analysis of water uptake by the root system (i.e. by means of the SWC measurements collected by the two-depths sensors) allows to split the growing cycle in three main periods with different AET behaviour: after transplanting, mid-season and end of the season (Figure 3).

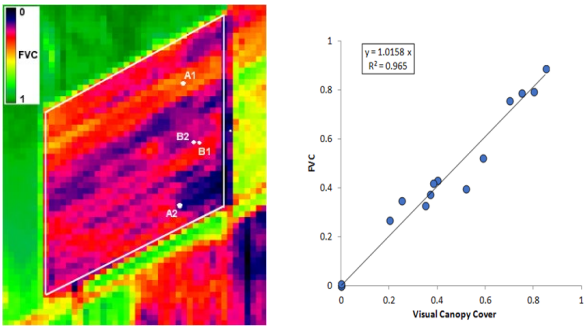

Figure 2. FVC image derived from Sentinel-2 on 03.06.2018 (left) and correlation between FVC and canopy cover from in situ photo analysis (right; Maselli et al., 2014).

During the first growing period, after transplanting (Figure 3a), water uptake was quite limited and the root system was active only at the surface soil layer (15 cm).
In the middle of the season (Figure 3b), both sensors detected a similar AET activity, showing as the contribution of each layer was the result of the relative efficiency of the root system at each soil layer.
At the end of the cycle, the deeper layer (30 cm) registered lower SWC and relatively larger excursions, due to the greater absorption of water by the roots (Figure 3c).

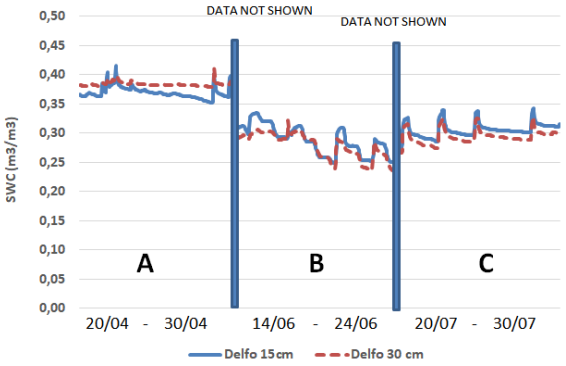

Figure 3. SWC (m^3/m^3) of Delfo cultivar during three separated 10-day periods: a) after transplanting; b) mid-season; c) end of the season.

The comparison between AET derived from sensors (Chiesi et al., 2018) and estimated applying equation [1] showed a correlation affected by crop conditions, i.e. R^2 is lower when plants are less developed (Table 3). The highest correlation observed in A1 is probably due to a higher field homogeneity. Good correlations are also found both analysing single cultivars (A - HEINS H1015: $R^2 = 0.49$; B - Nunhems Delfo: $R^2 = 0.30$) and averaging values for the whole field (A+B: $R^2 = 0.38$).

Plot	Canopy cover	Linear equation	R^2
A1	Very Good	0.729 x + 0.8122	0.52
B1	Good	0.344 x + 2.0597	0.41
B2	Good	0.3613 x + 1.9291	0.36
A2	Poor	0.3595 x + 1.9327	0.21

Table 3. AET comparison: soil moisture sensor-derived vs satellite-derived estimates (zero AET is not considered).

Similarly, NDVI_Kc describes existing differences among the detected areas, both at pixel level and on the whole field. These differences seem to be significant and variable during the season, suggesting heterogeneous plant growth and related water requirements. In particular, A1 starts with higher coverage, B1 and B2 show a regular growth rate and A2 presents a low growth rate after transplanting.
The different degree of plant cover with respect to the potential values affects the accuracy of the water balance model in the estimation of SWC (Gardin et al., 2014). In fact, observing the relative variation of this parameter for the last 20 days of the crop cycle (Figure 4), the underestimation of the model based on classic Kc is evident, as well as the significant improvement obtained utilising the NDVI_Kc.

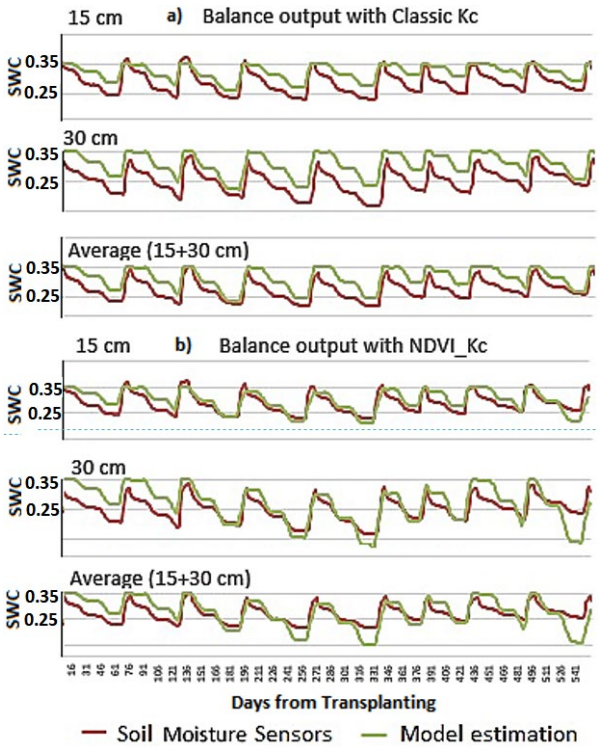

Figure 4. Relative variation of SWC (m^3/m^3) estimated during the last 20 days of the tomato cycle at 15 cm, 30 cm and as weighted balance. Sensors SWC vs Water Balance Model outputs (Gardin et al., 2014) with Classic Kc (4a), and Sensors SWC vs Model outputs with NDVI_Kc (4b).

Moreover, the observation of model reliability seems to change in relation to the considered soil depth. In Table 4, preliminary indications on the capability of the model to describe soil water behaviour during the whole season are given. Once again, these results suggest a different contribution of NDVI_Kc in function of plant growth and management.
In principle, except for A2 plot at 30 cm, the model can provide quite good estimation of SWC during the growing season, approaching the average values and maintaining satisfactory statistical relationships.
Using a percentage error index as a summary indicator of model efficiency (Ali, 2014), the following considerations can be made: i) the model works very well in plots with good canopy cover (parcel A and plot A1; ≤ 5% of average error), both as 15 and 30 cm of depth ; ii) the estimation satisfies final user operational requirements in 83% of cases (≤ 10% of average error); iii) even in the worst cases the error is maintained below 15% of average error.
Among the factors affecting soil water balance, AET appears the most important in the determination of model efficiency, even if its relative weight must still be investigated.

Parcel	SWC Measured	SWC Estimated	R^2	Std. Err.	Err. %
15 cm					
A	0.315 ± 0.03	0.303 ±0.04	0.60	0.020	5.0
B	0.312 ± 0.03	0.315 ± 0.04	0.60	0.022	5.3
A1	0.325 ± 0.02	0.326 ± 0.03	0.55	0.012	3.4
A2	0.306 ± 0.05	0.292 ± 0.06	0.61	0.031	8.6
B1	0.295 ± 0.02	0.295 ± 0.04	0.66	0.012	6.8
B2	0.286 ± 0.03	0.295 ± 0.04	0.42	0.021	10.2
30 cm					
A	0.287 ± 0.02	0.295 ± 0.04	0.40	0.018	4.6
B	0.303 ± 0.04	0.303 ± 0.07	0.61	0.031	8.0
A1	0.316 ± 0.02	0.319 ± 0.04	0.68	0.013	3.1
A2	0.259 ± 0.04	0.299 ± 0.06	0.24	0.034	13.1
B1	0.286 ± 0.06	0.273 ± 0.07	0.53	0.021	9.7
B2	0.321 ± 0.03	0.303 ± 0.07	0.66	0.021	5.2
Average (15-30 cm)					
A	0.313 ± 0.03	0.312 ± 0.04	0.61	0.021	5.7
B	0.309± 0.03	0.307 ± 0.06	0.57	0.026	6.5
A1	0.325 ± 0.02	0.321 ± 0.03	0.76	0.010	3.8
A2	0.301 ± 0.05	0.307 ± 0.05	0.61	0.034	10.8
B1	0.290 ± 0.02	0.277 ± 0.06	0.61	0.016	8.2
B2	0.286 ± 0.03	0.276 ± 0.06	0.52	0.021	9.5

Table 4. Measured vs estimated SWC (m^3/m^3) using NDVI-Kc for the detected areas (Average ± St.dev.), with some common statistical indices used for model evaluation.

4. CONCLUSIONS

Soil moisture measurements are affected by many external factors and lose their representativeness during significant rainfall and irrigation events, when soil saturation is reached, and water percolation occurs. In fact, soil system and moisture sensors require variable time to reach stable conditions and the use of collected data should take into consideration these different behaviours. At the same time, the analysis of the soil moisture variations derived by sensors between two watering events can provide quite reliable information on plant evapotranspiration; the integration of this information with modelling and spatial data can support irrigation management in different, advanced agricultural systems. Moreover, the integration between data collected by Sentinel-2 and field observations showed the opportunity to utilise agronomic information, like cultivar types and tillage, to weight field conditions and to understand relative variability in some critical periods of the growing season. The preliminary results of this study suggest the opportunity of using Sentinel-2 high spatio-temporal resolution images for estimating the water requirements of industrial tomato in central Italy, taking into account some operational conditions, like:

- the availability of a complete agronomic and environmental dataset updated in near real-time respect to field conditions;
- the presence of a local well managed monitoring agrometeorological network collecting and timely transmitting reliable data;
- the possibility to use advanced data management and geoprocessing tools and procedures, validated for a specific local company.

Under these conditions, the proposed integrated system could be a useful tool for local irrigation scheduling, providing detailed and quasi-real time information on plant growth and water requirements, able to improve traditionally based irrigation practices and to reduce water wasting.

REFERENCES

Ali M. H. (2014). A new novel index for evaluating model performance. *Journal of Natural Resources and Development*, 04: 1-9. DOI number: 10.5027/jnrd.v4i0.01.

Allen R. G., Pereira L. S., Raes D., Smith, M. (1998). Crop evapotranspiration - Guidelines for computing crop water requirements - *FAO Irrigation and drainage paper 56*. Rome.

Calera A., Campos I., Osann A., D'Urso G., Menenti M. (2017). Remote sensing for crop water management: from ET modelling to services for the end users. *Sensors*, 17, 1104; doi:10.3390/s17051104.

Chiesi M., Battista P., Fibbi L., Gardin L., Pieri M., Rapi B., Romani M., Maselli F. (2018). A semi-empirical method to estimate actual evapotranspiration in Mediterranean environments. *Advances in Meteorology*, Vol. 2018: 1-13 doi: 10.1155/ 2018/ 9792609.

Gardin L., Battista P., Bottai L., Chiesi M., Fibbi L., Rapi B., Romani M., Gozzini B., Maselli F. (2014). Improved simulation of soil water content by the combination of ground and remote sensing data. *European Journal of Remote Sensing*, 47: 739-751. DOI: 10.5721/EuJRS20144742.

Jensen M. E., & Haise H. R. (1963). Estimating evapotranspiration from solar radiation. *Journal of the Irrigation and Drainage Division ASCE*, 89, 15-41.

Maselli F., Papale D., Chiesi M., Matteucci G., Angeli L., Raschi A., Seufert G. (2014). Operational monitoring of daily evapotranspiration by the combination of MODIS NDVI and ground meteorological data: application and validation in Central Italy. *Remote Sensing of Environment*, 152, 279-290.

Nemani R., Hashimoto H., Votava P., Melton F., Wang W., Michaelis A., Mutch L., Milesi C., Hiatt S., White M. (2009). Monitoring and forecasting ecosystem dynamics using the Terrestrial Observation and Prediction System (TOPS). *Remote Sensing of Environment*, 113, pp.1497-1509.

Pardossi A., Incrocci L., Incrocci G., Malorgio F., Battista P., Bacci L., Rapi B., Marzialetti P., Hemming J., Balendonck J. (2009). Root zone sensors for irrigation management in intensive agriculture. *Sensors,* 9(4), 2809-2835.

Zeleke K.T., Wade L.J. (2012). Evapotranspiration estimation using soil water balance, weather and crop data. Evapotranspiration - Remote Sensing and Modeling, Ayse Irmak (Ed.), ISBN: 978-953-307-808-3, InTech.

ACKNOWLEDGEMENTS

The authors wish to thank Mr. Silvano Dragoni, for the local technical support and to let us conduct the experiment in his field.

MODIS EVI TIME SERIES TO ASSESS NEW OIL PALM PLANTATION DYNAMICS IN BORNEO

S. De Petris[1]*, P. Boccardo[2], E. Borgogno-Mondino[1]
[1] DISAFA, Department of Agricultural, Forest and Food Sciences, University of Torino, Largo Paolo Braccini 2, 10095, Grugliasco – samuele.depetris@edu.unito.it; enrico.borgogno@unito.it
[2] DIST, Interuniversity Department of Regional and Urban Studies and Planning, Politecnico di Torino, Viale Pier Andrea Mattioli 39, 10125, Torino - piero.boccardo@polito.it

KEY WORDS: MODIS EVI, Time series, Oil palm, Palm age, Palm detection, Borneo.

ABSTRACT:

Palm oil is the highest yielding oil crop of the world. Oil palms are extensively planted in the equator zone, especially in Indonesia where plantations have been spreading in response of the increasing market demand. Cultivation of oil palm in tropical countries it has already proved of endangering biodiversity and degrading environment with a global impact related to forest loss. From this point of view, remote sensing can support a more efficient plantation management that takes into account its effects over environment. In this work a time series of EVI (Enhanced Vegetation Index) maps, covering the period 2000–2018, was generated from the MODIS Vegetation Index product (MOD13Q1-v5) with the aim of automatically detecting new oil palm plantations and possibly giving an estimate of their age. To achieve these goals a self-developed routine was implemented to automatically operate the EVI time series analysis. Accuracy assessment showed an overall accuracy in new palm oil plantations detection of about 94%. Starting age estimation proved to be accurate enough: 76% of estimates were placed in a time range of ±1 year in respect of the actual plantation date, as communicated by farmers. The method was thought to be reliable and simple enough to be easily engineered in a web based geo service useful for the main players of the sector.

1. INTRODUCTION*

Oil palm is planted extensively in South-East Asia, especially in Indonesia, Malaysia, and Thailand. Oil palm is a perennial tree and well fits the humid tropical climate with a high precipitation rate, high solar radiation and warm temperature (24–32 °C) (Corley and Tinker, 2008). Plantations generally have a triangular pattern (9 m row spacing) resulting in a uniform pattern at the ground; this makes oil palms different from other trees or forest in satellite imagery (Shafri et al., 2011). Palm oil is the world highest yielding oil crop with an increasing consumption through the years: 50 Million tons in 2012-2013, over 60 Million tons in 2015-2016 (Chong et al., 2017). Especially in Indonesia, plantations showed a steeper positive linear trend that brought the 4 million hectares in 2000 up to 11 million ha in 2015. These tropical countries represent the 11% of the world remaining tropical forests, containing numerous endemic or rare species, many of which are restricted to forest habitats (Mittermeier et al., 2004; PIN KOH, 2007). For this reason cultivation of oil palm, in these countries, endangers biodiversity and degrades the environment with a global impact (Koh and Wilcove, 2008). But, on the other hand, it is an important economic factor for those Countries. Additionally, logged-over forests are often seen by governments as degraded habitats, only waiting for farm practices. This fact has encouraged the conversion of secondary (logged) forests to oil palm plantations, especially in Malaysia and Indonesia. From this point of view, remote sensing can support a more efficient plantation management that takes into account their effects over environment. Moreover, plantations monitoring by remote sensing well fits requirements of precision farming that many stakeholders are currently approaching, especially to assess crop conditions and monitoring the state of the national natural/crop capital. In this work a time series of EVI maps obtained from the MODIS Vegetation Index products (MOD13Q1) (Huete et al., 1999) for the period 2000–2018 was processed to automatically detect new oil palm plantations and giving an estimation of plantation age.

2. MATERIALS AND METHODS

2.1 Study area

The study area is sited in the South of Kalimantan Tengah (Central Kalimantan, Fig. 1), a province of Indonesia located on Borneo island (5°00'43.92"S, 115°41'04.92"E, WGS-84 reference frame). Study area borders were arbitrarily selected on landscape markers basis (rivers, coast, etc.) resulting in about 2.95 million hectares. According to USDA (United States Department of Agriculture) Soil Taxonomy (Hall et al., 2004; Hengl et al., 2017, 2014) local soil is labeled as *Oxisol* with a high aluminum and low phosphate content that could hinder plant growth. Morphology is generally flat without significant reliefs, for this reason, edaphic conditions can be retained constant at the small scale.

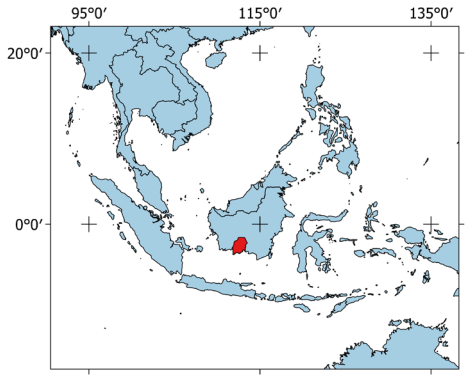

Figure 1. Borneo island (Indonesia). In red the study area (Geographic WGS84 reference frame).

* Corresponding author

2.2 Dataset used

An EVI (Enhanced Vegetation Index) image time series (hereinafter called ETS), composed of 415 images, and covering a period between 18/02/2000 at 18/02/2018 was generated from the MOD13Q1 (version 5) dataset available from the NASA LPDAAC collection (Solano et al., 2010). MOD13Q1 data are provided every 16 days at 250 m spatial resolution as a gridded level-3 product. The EVI maps are retrieved from, atmosphere-corrected, bidirectional surface reflectance; blue, red, and near-infrared reflectances, centred at 469-nanometers, 645-nanometers, and 858-nanometers, respectively, are used to determine the MODIS daily EVI. The algorithm chooses the best available pixel value from all the acquisitions from the 16 day period. The criteria adopted by the provider is low clouds, low view angle and the highest EVI value (Didan, 2015). The Global Forest Change (GFC) 2000–2016 dataset-v1.4 (Hansen et al., 2013), obtained for free from the Hansen/UMD/Google/USGS/NASA system, was validation set. It was supplied in raster format unsigned 8-bit values with a spatial resolution of 1 arc-second per pixel (approximately 30 meters per pixel at the equator). From GFC the following two layers were extracted and projected into the WGS84 UTM 49 S reference system, with a Ground Sampling Distance (GSD) of 30m: a) the Global Forest Cover Loss 2000–2016 layer (hereinafter called GFC-L); it represents the forest loss in the period 2000–2016; loss is defined as a stand-replacement disturbance, or a change from a forest to non-forest state. Encoding is 1 for loss and 0 for no loss; b) the Year of Gross Forest Cover Loss event layer (hereinafter called GFC-YL); it is defined as the disaggregation of total forest loss to annual time scales. Encoding is 0 for no loss and a number in the range 1-16 for loss detected in the correspondent progressive year in the range 2001 (1)–2016 (16).

2.3 Mapping new oil palm plantations

Starting from the EVI time series a new methodology for oil palm detection and characterization was developed and implemented in the IDL 8.0 programming language based on temporal profile analysis of EVI pixels. Candidate pixels, representing newly planted oil palms, were detected using the gain value of the 1st order polynomial approximating, by linear regression EVI, local values in the whole reference period.

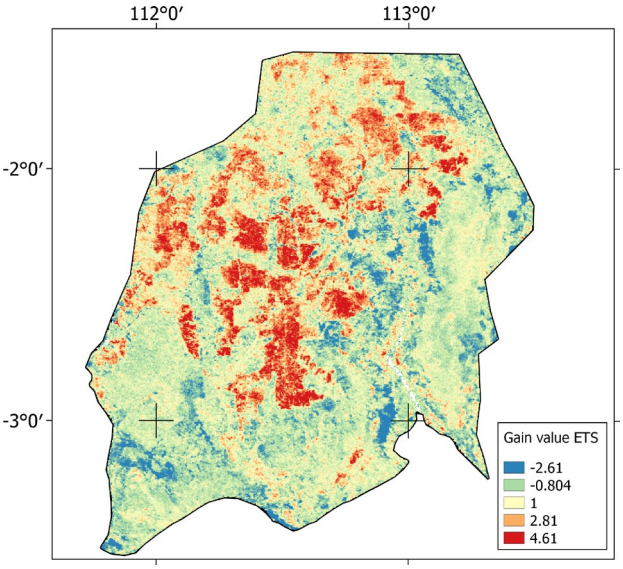

Figure 2. Map of ETS gain values. Orange and red patterns (gain value > 2) are new oil palm plantations.

Theoretical assumption is that, in tropical areas, palm cover shows a gain higher than natural vegetation, being the EVI values of the new cover significantly higher than the one ordinarily expressed by natural vegetation. This reference value was found exploring 200 control points (CPs) testing in the area locations with and without oil palms. CPs were obtained by photointerpretation of available Sentinel-2 RGB true color composites (R: band 4, G: band 3; B: band 2) from the T49MFS tile acquired on 2018/02/08. 100 CPs were placed in evident OP areas and 100 in NOP ones (Fig. 3a). The local gain value was therefore extracted for each CP, determining two groups (OP and NOP) of gain values. In general, can be observed that, when natural vegetation is present, yearly EVI trend is slightly varying with no remarkable profile steep trait, determining gain value close to zero. Differently, if a new plantation occurs, EVI temporal profile suddenly decreases at the moment of forest cut, but after a transitional period, it reaches a new state of vigour corresponding to higher EVI values correlated with plantation growing. If an abrupt change occurs on ETS, then oil palm planting and growing determines a significant increasing of gain, in general higher than 2.0 (Fig. 3b). Concerning the threshold selection, the mean (μ) and standard deviation (σ) values of gain map were computed for NOP points. NOP μ and σ resulted respectively 0.109 and 0.913. Considering a confidence interval of 95 %, corresponding to $\mu+2\sigma = 1.935$, we admitted that OP pixels could be identified looking for local gain values higher than this number. To extract ETS pixels that potentially suffered from vegetation change, from natural vegetation to oil palm, the above mentioned gain value image layer was therefore thresholded with reference to this value, obtaining a rough map of new oil palm plantations (Fig. 2) with the following classes: 1= Oil Palm (OP), 0 = Not-OP (NOP). A further refinement was operated by vectorising the previous raster classification and deleting all those areas smaller than 100 ha, being declared plantation average size in general higher of this value, typically following a rectangular pattern of 1000 m x 300 m.

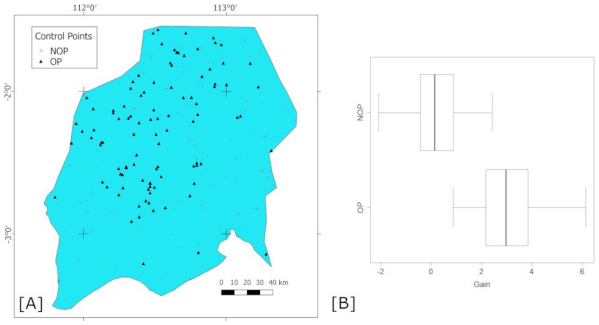

Figure 3. A) Map showing the CPs position in the study area (WGS84 Reference Frame). B) Box plot of CPs gain value for OP and NOP pixels (box plot lines from left to right are respectively: minimum value, 1st quartiles, median, 3rd quartile, maximum value).

2.4 Estimating starting date and age of plantations

The age of oil palm plantation is an important parameter for crop management: it is a good predictor of yearly yield and conditions the quality and quantity of the fresh fruit bunches (FFB). To achieve an estimation of plantation age, time distribution of changes in the area was analyzed, focusing on the selected pixels from the previous step. ETS profiles of all the OP pixel were analyzed, at year level, looking for the moment of vegetation loss preceding oil palms plantation. The minimum EVI value along the local ETS was assumed as predictor for new plantations starting date. Unfortunately, many outliers along ETS made not possible to operate on the raw ETS, making desirable a preliminary ETS filtering aimed at minimizing effects of local EVI anomalous variations (Fig. 3). To achieve this problem, the following analysis was conducted exploring the local EVI temporal profile with a customized filter (sliding window) running along the time and including 7 images preceding and 7 following the middle one (kernel). Filter customization consisted in a selective application of the mean filter according to the distance between the EVI center value of the sliding window and the regression line computed including all the 15 observations of the local kernel position.

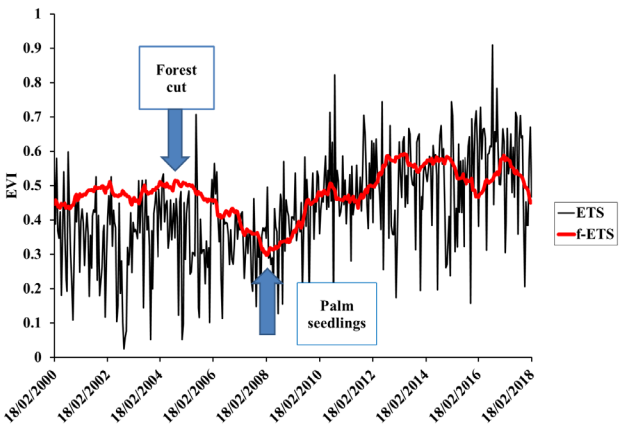

Figure 4. Oil palm ETS and f-ETS. The minimum value of f-ETS was assumed as indicator for plantation starting moment. Note the time lag (about 1÷2 year) between forests cut and palm starting moment.

This selective smoothing permitted to cut off short-term ETS fluctuations, enhancing long-term ones. With respect to the filtered ETS (f-ETS), for each OP pixel, the minimum EVI value was found and the correspondent progressive year number saved in a new image layer. It was found that the minimum EVI value of the local series was a reasonable indicator of the time of changes for that pixel.

According to this minimum value criterion, for each candidate oil palm pixel, an estimate of the year when the new plantation started was computed. Estimated starting date was saved for each pixel and a new image layer generated, finally giving a representation of new plantation trends and spatial distribution in the investigated period. The age of plantations was consequently computed at each position by differencing the estimated planting year with present.

3. RESULTS AND DISCUSSION

Classification accuracy assessment was achieved with reference to GFC-L. Refined vector map of our classification was converted back to the raster format by nearest neighbour resampling, making it consistent with GCF-L and GCF-YL (GSD = 30m). The GFC-L layer represents the forest loss occurred in the period 2000-2016, that authors assumed to be potentially and totally due to new oil palm plantations in the same period. In fact, in this region new palm plantations are the first reason of forest loss (Curran et al., 2004), making this assumption reasonable. The new oil palm plantation classification, based on the thresholding of the gain value of the regression line computed along the whole ETS, proved to be effective: overall accuracy was found to be equal to 94% showing about 545394 ha (18.5% of the whole study area) of converted area from forest to oil palm plantations in the reference period (2000-2018).

Concerning the estimation of plantations age, a transition matrix was calculated by differencing the map of plantations age estimates and GCF-YL. The result was therefore analyzed and the correspondent cumulative frequency distribution of absolute differences was generated (figure 4). It shows that 47% of detected plantations present differences equal to 0, i.e. correctly dated.

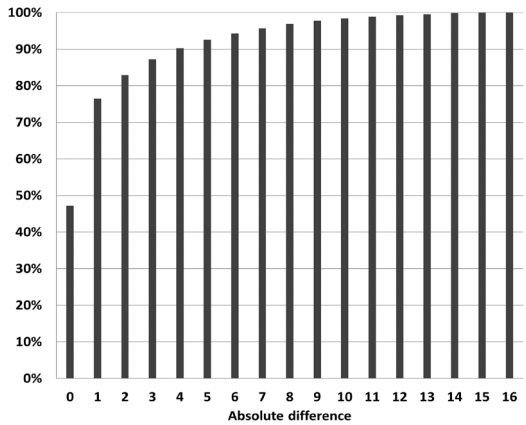

Figure 5 – Cumulative frequency distribution of absolute differences between estimated and reference (GFC-YL) starting year of new plantations.

Nevertheless, it must be considered that the proposed method gives an estimate of the moment when soil preparation/new seedlings occurred. Differently, the reference dataset (GCF-LY), maps the moment of forest loss determining a time lag between the two estimates. Considering that a time delay of one year between the cut of the previously existing vegetation and the planting of new oil palm seedlings is reasonable (Fig. 3), all

differences included in the range ±1 year can be reasonably considered as not significant. According to this approach, it can be noted from figure 4 that 76% of the observations are included in this range, making the estimates of age of plantations satisfactorily accurate.

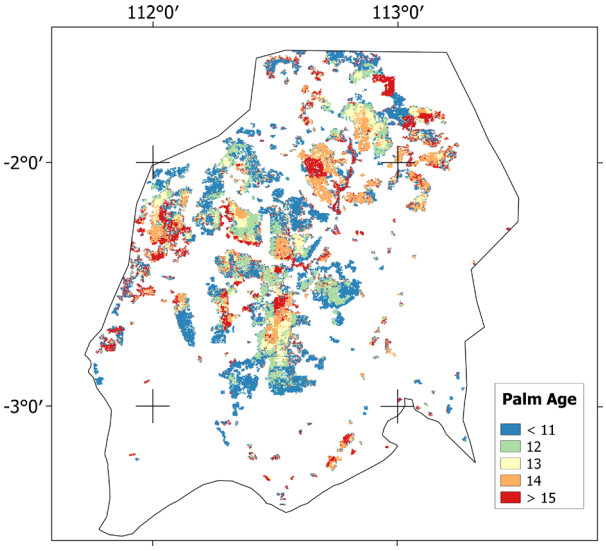

Figure 6. Age map of new oil palm plantations started between 2000-2018.

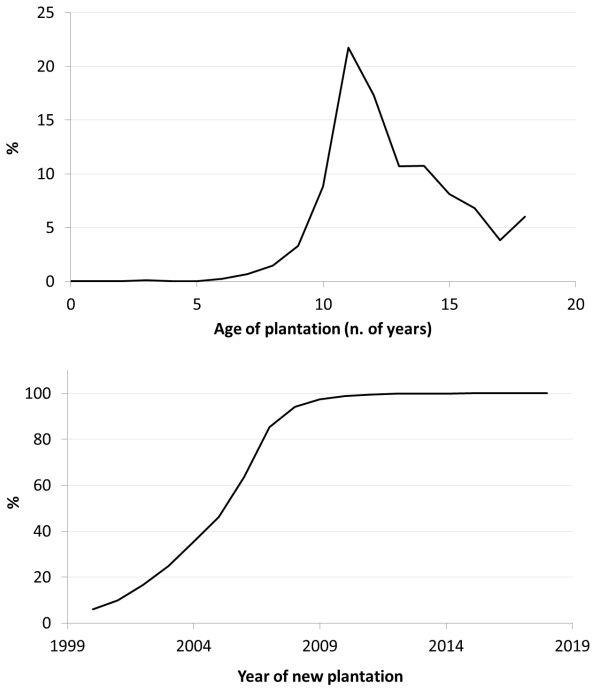

Figure 7. (above) Age of plantations at 2018 as estimated by the proposed algorithm. (below) Cumulative percentage of new plantations along time in the reference period (2000-2018). All percentages refer to the total area detected as oil palm plantations between 2000 and 2018 (545394 ha).

With these premises concerning uncertainty of estimates, the following operational information can be extracted: a) a map showing the spatial distribution of new plantations with reference to the estimated starting year (Fig. 5); b) temporal trend of new oil palm plantations (expressed as percentage of new planted area at the considered year in respect of the total OP area, Fig. 6).

Figure 5 clearly shows as the area was turned to oil palm plantations along the years, describing when and where farming companies concentrated their efforts.

Graphs of Fig. 6 instead clearly synthesize the temporal dynamics of plantations. In particular, in the area, a sudden deceleration of the phenomenon has been occurring since 2010, fortunately telling a well sounding story for the environment. Production is expected to have almost reached its maximum being the 8th year from plantation the one in which oil palm is said to reache its maximum productivity (Ismail and Mamat, 2002). From figure 6 the most of new plantations seem to have passed this point.

4. CONCLUSIONS

MODIS derived EVI time series proved to be effective to map and characterize new oil palm plantations. Detection of new plantations based on EVI local temporal profile analysis revealed to be accurate enough (overall accuracy = 94 %), suggesting that time discriminant is basic in assessing vegetation cover. It also proved to make possible to give a good estimation of the starting year of new plantations. Many limitations, at the moment, still persist: a) detected changes in vegetation cover can be also related to abiotic or biotic disturbance like wildfire, plant diseases, human clear cut. Auxiliary data from other map or institutional source could help to make result more reliable from this point of view; b) at the moment, the approximation of plantation age, in our study area, shows 76% of accuracy using Hansen (2013) dataset as reference map. The GFC map is known to be affected by biases estimates due to both definition of forest changes and the tree cover detection before the 2000 (Tropek et al., 2014). At the moment, it cannot be said if the residual estimate error is due to GFC or the here proposed method. Nevertheless, GFC dataset it is currently the only available and reliable one for tropical vegetation change detection; c) future experiences trying to apply the same methodology are expected to be based on MOD13Q1 version 6 datasets, since the version 5 is going to be dismissed from LPDAAC.

In spite of these limitations the proposed method is quite simple, easy to be engineered in a future web-based service and internally consistent to generate some interesting operative information useful for both economical/commercial and environmental/landscape applications.

REFERENCES

Chong, K.L., Kanniah, K.D., Pohl, C., Tan, K.P., 2017. A review of remote sensing applications for oil palm studies. Geo-spatial Information Science 20, 184–200. https://doi.org/10.1080/10095020.2017.1337317

Corley, R.H.V., Tinker, P.B., 2008. The oil palm. John Wiley & Sons.

Curran, L.M., Trigg, S.N., McDonald, A.K., Astiani, D., Hardiono, Y.M., Siregar, P., Caniago, I., Kasischke, E., 2004. Lowland forest loss in protected areas of Indonesian Borneo. Science 303, 1000–1003.

Didan, K., 2015. MOD13Q1 MODIS/Terra vegetation indices 16-day L3 global 250m SIN grid V006. NASA EOSDIS Land Processes DAAC.

Hall, S., Asner, G., Kitayama, K., 2004. Substrate, climate, and land use controls over soil N dynamics and N-oxide emissions in Borneo. Biogeochemistry 70, 27–58. https://doi.org/10.1023/B:BIOG.0000049335.68897.87

Hansen, M.C., Potapov, P.V., Moore, R., Hancher, M., Turubanova, S.A.A., Tyukavina, A., Thau, D., Stehman, S.V., Goetz, S.J., Loveland, T.R., 2013. High-resolution global maps of 21st-century forest cover change. science 342, 850–853.

Hengl, T., de Jesus, J.M., Heuvelink, G.B., Gonzalez, M.R., Kilibarda, M., Blagotić, A., Shangguan, W., Wright, M.N., Geng, X., Bauer-Marschallinger, B., 2017. SoilGrids250m: Global gridded soil information based on machine learning. PLoS one 12, e0169748.

Hengl, T., de Jesus, J.M., MacMillan, R.A., Batjes, N.H., Heuvelink, G.B., Ribeiro, E., Samuel-Rosa, A., Kempen, B., Leenaars, J.G., Walsh, M.G., 2014. SoilGrids1km—global soil information based on automated mapping. PloS one 9, e105992.

Huete, A., Justice, C., Van Leeuwen, W., 1999. MODIS vegetation index (MOD13). Algorithm theoretical basis document 3, 213.

Ismail, A., Mamat, M.N., 2002. The optimal age of oil palm replanting. Oil palm industry economic journal 2, 11–18.

Koh, L.P., Wilcove, D.S., 2008. Is oil palm agriculture really destroying tropical biodiversity? Conservation letters 1, 60–64.
Mittermeier, R.A.A., Gil, P.R., Hoffman, M., 2004. Hotspots Revisited: Earth's biologically richest and most endangered ecoregions. CEMEX/Agrupacion Sierra Madre. Sierra Madre.

PIN KOH, L., 2007. Potential habitat and biodiversity losses from intensified biodiesel feedstock production. Conservation Biology 21, 1373–1375.

Shafri, H.Z., Anuar, M.I., Seman, I.A., Noor, N.M., 2011. Spectral discrimination of healthy and Ganoderma-infected oil palms from hyperspectral data. International journal of remote sensing 32, 7111–7129.

Solano, R., Didan, K., Jacobson, A., Huete, A., 2010. MODIS vegetation index user's guide (MOD13 series). Vegetation Index and Phenology Lab, The University of Arizona 1–38.

Tropek, R., Sedláček, O., Beck, J., Keil, P., Musilová, Z., Šímová, I., Storch, D., 2014. Comment on "High-resolution global maps of 21st-century forest cover change." Science 344, 981–981.

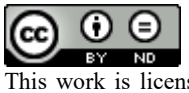

REMOTE SENSING CHARACTERIZATION OF CROP VULNERABILITY TO FLOOD

T. Pacetti[1]*, E. Caporali[1], M.C. Rulli[2]

[1] University of Florence - Department of Civil and Environmental Engineering - (tommaso.pacetti, enrica.caporali)@unifi.it
[2] Politecnico di Milano - Department of Civil and Environmental Engineering - mariacristina.rulli@polimi.it

KEY WORDS: MODIS Aqua; UNITAR UNOSAT; NDVI, SRTM; Water Footprint; Human Energy Requirements; Bangladesh; Pakistan

ABSTRACT:

The analysis of connections between natural disaster and food security is extremely relevant, especially in developing countries where food availability can be highly jeopardized by extreme events that damage agricultural areas and food stocks. In particular, flood events are the most impacting natural disasters on agriculture, with a percentage share of damage around 60%.
This work focuses on the food-flood nexus, developing a methodology for evaluating the effects of floods on food supply by integrating remote sensing data, agricultural statistics, and water footprint databases. Based on the existing literature about extreme floods, the Bangladesh flood in 2007 and the Pakistan flood of 2010 have been selected as exemplar case studies that can highlight the effects of flood events on food availability.
The analysis focused on rice as the most spread crop in Bangladesh, while it considers the national crop mix in Pakistan analysis.
Results showed that the use of remote sensing data combined with other sources of onsite information is particularly useful to assess the effects of flood events on food availability. The damages caused by floods on agricultural areas are estimated in terms of crop losses and then converted into lost calories and water footprint as complementary indicators.

1. INTRODUCTION

The inner connections among natural disaster and food security are extremely relevant especially in developing countries where the food availability (one of the four pillars food security together with access, utilization and stability, FAO 2009) can be highly jeopardized by extreme events that damage the primary access to food, i.e. agriculture.
The objective of this study is to analyze the impact of flood events on food security, taking advantage of remote sensing data to develop a methodology to rapidly determine crop losses due to submergence.
Based on the existing literature related to extreme floods, the events in Bangladesh (2007) and in Pakistan (2010) have been selected. Bangladesh and Pakistan have been chosen as exemplar case studies, because of their vulnerability to floods and the importance of agriculture in their territories. These case studies are characterized by significant differences in their agricultural production (mainly rice in Bangladesh and rice, sugarcane and wheat in Pakistan) allowing us to evaluate the effects of flooding on crops with different resistance to submergence.
The adopted method integrates remote sensing data, agricultural statistics, and water footprint values in order to (i) evaluating the potentially affected agricultural areas; (ii) converting the affected areas into crop loss; (iii) estimating the associated calories and embedded water losses.

2. METHODS AND DATA

Intersecting remote sensed flood maps with administrative and land use maps and then integrating the information regarding crops yields is possible to determine the potential crop losses.

Flood maps can be obtained by following one of the many existing classification algorithms on the basis of raw available satellite data or taking advantage of available remote sensing products, already classified for flood identification (Sanyal and Lu, 2004).
The conversion of potential crop losses into effective crop loss can be done taking into consideration the peculiarities of topography, land use and crops characteristics for the selected study areas. Additional information, such as specific crop resistance to submergence in terms of time and water depth might be added to refine the crop losses evaluation (Figure 1).

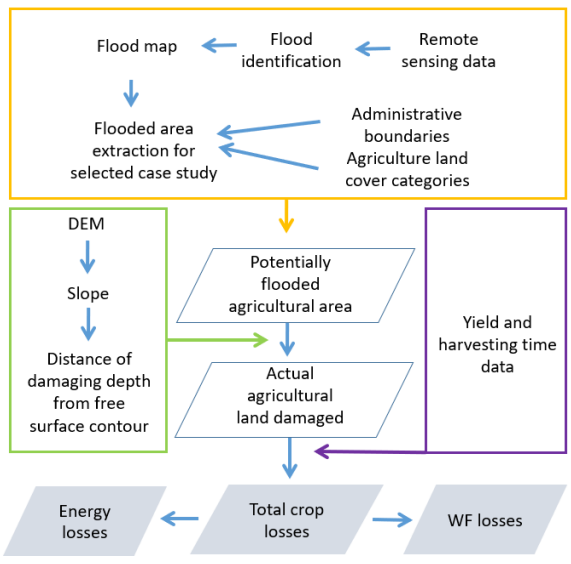

Figure 1. Methodology scheme

* Corresponding author

The final results are here expressed in terms of lost calories through the use of Human Energy Requirements indicator (HER, FAO 2001) or in terms of lost water through Water Footprint indicator (WF, Hoekstra et al. 2011) losses. Both these expressions are useful to convert the analysis into synthetic indicators: lost calories are a direct estimation of the crop losses while the WF allows an indirect evaluation of land use management criticalities both for supporting a complete diet and preserving local water resources.

2.1 Pakistan: multi crop losses

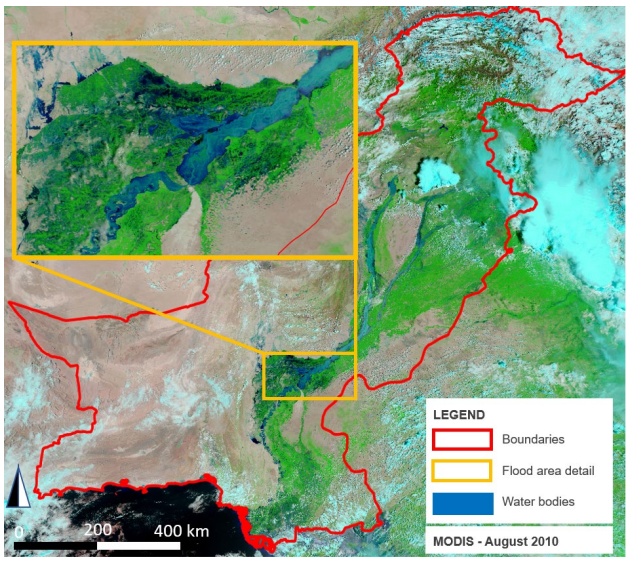

Figure 2. Flood areas identification (source MODIS, August 2010) Pakistan

For the Pakistan case study, the agricultural territories affected by flood are estimated making use of remote sensing derived data that are provided by Suparco and FAO, based on MODIS Aqua Satellite and SPOT VGT data (1 km spatial resolution, Suparco and FAO (2010)).
The flood involved an area with an extension of 58,797 km^2 with duration of around three months, from the end of July until the end of October (Figure 2).
All the main Pakistan crops have been considered together with wheat stocks. The characteristics of the crops in terms of yield are derived from FAOSTAT database (FAO, 2016). Using the FAOSTAT, the crops production data for the 10 years before the flood event, it is possible to calculate an average agricultural yield for the main crops lost (i.e. sugarcane and rice), as well as to estimate the actual crop losses (in term of weight). By knowing the energy content in kcal/ kg of the different crops, it is then possible to estimate the associated food energy losses, both in terms of vegetal and animal calories.

2.2 Bangladesh: focus on rice vulnerability

For Bangladesh case study, UNOSAT map of the flooded areas based on MODIS Aqua satellite data were used. It includes 30233 satellite detected water bodies with a spatial extent of 72,972 km^2 derived from the MODIS-Aqua image (250 m for band1–2500 m for band3–7 and 1000 m for band8–36) acquired on August 2007 and analyzed by a water detection algorithm for rapid flood mapping based on NDVI evaluation UNITAR UNOSAT (2007), Figure 3.
The land use data adopted are distributed by the Pacific Disaster Center, as institution reference of the Global Hazards Information Network (GHIN, 2008).

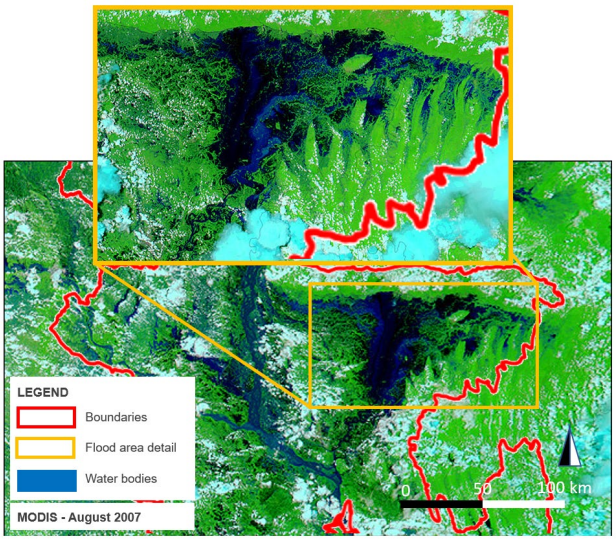

Figure 3. Flood areas identification (source MODIS, August 2007) Bangladesh

In the Bangladesh case study, the assumption that in the flooded area identified by the remote sensing all the crops are destroyed is not applicable because floods affect rice production proportionally to flood hydraulic height and length of the submergence period. Therefore, a threshold in time and space has been adopted to take into account the resistance of submergence of rice: 1-meter depth (according to deep water areas defined by Huke and Huke, 1997) and a period of submergence greater than three weeks (according to the International Rice Research Institute, 1976) have been assumed, as the limiting factors to rice growth.
The water depth in the flooded area was estimated integrating MODIS satellite images of 20 August with SRTM remote sensed topography data (van Zyl, 2001). In order to calculate the area included within the 0-1 meter depth, the slope of the DEM (SRTM) is calculated and used to estimate the average distance from the points where the water depth is 1 meter to the flood perimeter. The cultivated area not destroyed by the flood is therefore the product of the flood perimeter, times the average distance introduced before. The use of MODIS images from 20 August (six weeks after the beginning of the flood), guarantees that the time constraint is included.

3. RESULTS AND DISCUSSION

In the Bangladesh case study, the results depict an average loss of 103 kcal/capita due to flooded rice, representing 5.3% of the potential energy usually provided by this crop. If we consider the effects of flood only on the population of the affected districts, the result increases dramatically to 398 kcal lost (Table 1).

Rice type	Production losses for human use [103 ton]	per capita energy lost [kcal/cap/day] *	per capita energy lost [kcal/cap/day] **
Aus	76.1	5	20
Aman	1413.9	98	377
Total	1490	103	398

* evaluated considering the total population as affected
** considering only the population of the affected areas (i.e. 37, 908,436)

Table 1 Estimation of food energy losses in Bangladesh

The energy deficit due to the rice production lost, compared to the annual energy provided by the entire food production of Bangladesh in 2006, using the total kcal/cap/day supply of 2006 (i.e. 2417 kcal/cap/day) is 4.3% considering the total population as affected and it raises to 16.5%, if only the population of the affected areas is considered.

In order to properly understand the meaning of these percentages, it is important to highlight that the lack of food (and thus energy) caused by the flood is contributing to worsen the already critical situation of food supply in Bangladesh that was already suffering a 19.4% deficit.

Based on the existing statistics on WF in Bangladesh, lost food results have been converted in terms of water footprint to have another measurement of the flood effects on the territory. The results show a total WF of 4.72E+09 m^3 that is equal to 4.4% of the national WF (Table 2).

Rice type	Green WF [m3]	Blue WF [m3]	Grey WF [m3]	Total WF [m3]
AUS	1.79E+08	2.61E+07	3.61E+07	2.41E+08
AMAN	3.33E+09	4.85E+08	6.71E+08	4.48E+09
TOTAL	3.51E+09	5.12E+08	7.07E+08	4.72E+09

Table 2 Water Footprint of rice lost due to Bangladesh flood of 2007

In Pakistan, the results show a reduction of production that is about 19% for sugarcane and 40% for rice that is associated to a significant loss of energy available. The sum of crops and stocks destroyed amounts to a total of 205 kcal/cap/day lost, due the flood and it is equal to a loss of 8.5% of the Pakistan average food supply (10.7% if we consider only the energy derived from vegetal products).

As in the previous case study, the food losses results have been converted into WF resulting in total loss of 1.84 E+10 m^3 that is equal to 13.5% of the Nation WF.

The results highlight the countries vulnerability to flood, being both countries strongly dependent on local agricultural production. The 2007 flood event reflected badly upon Bangladeshi food security, almost doubling the existing food deficit. The same happened in Pakistan where an already scarce food supply has been worsened by the 2010 flood.

The results can be combined with other spatial analysis in order to provide a broader picture of the flood effects on a territory. An integration of flood extent with population poverty distribution is hereby proposed to identify the hotspots areas where flood strikes the poorest areas (Figure 4).

The strategies for disaster management and planning against flood risk should battle social disparities and focus on these areas that are often more vulnerable and less resilient to flood (Vojinovic and Abbott, 2012). This kind of analysis can provide useful information that help the definition of the priorities of intervention to support the poorest areas in case of flood events.

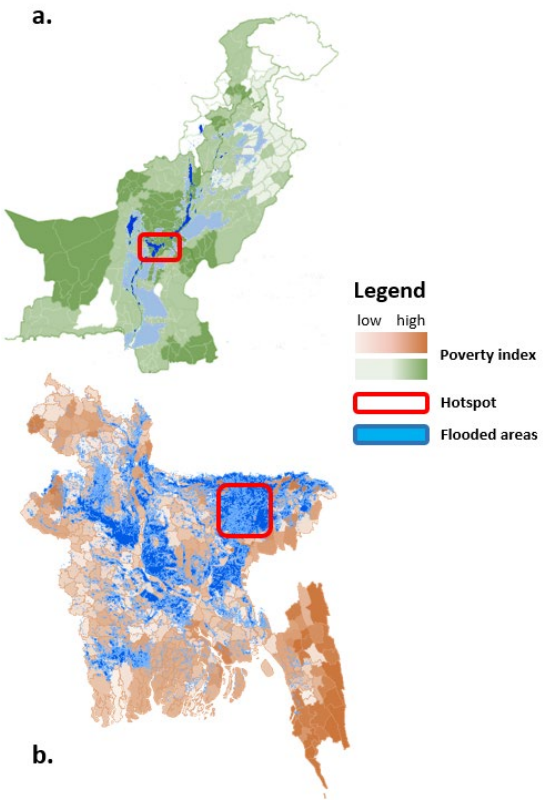

Figure 4. Identification of the poorest area affected by flood (a) Pakistan, (b) Bangladesh

4. CONCLUSION

The proposed framework, taking advantage of the integration of remote sensing data and agricultural statistics, provides a rapid assessment of flood effects on food security on the short term. Moreover, if combined with other spatial information, it can provide useful information that can be applied to spatially identify the hotspots and support long term planning.

Method results are fully repeatable; whereas, for remote sensed data the sources of data are valid worldwide and the data regarding land use and crops characteristics are strongly site specific, which need to be carefully evaluated.

This analysis focuses on direct flood damages to crops or food stocks. Food security could be strongly reduced by flood damages on pasture land, livestock, fisheries affecting directly

or indirectly the animal calories and protein food intake (Davis et al, 2014). Additional side effects of flood events, such as the deposition of sediments on fields, the erosion of agricultural soil, the loss of soil nutrients as well as microbial and fungal activities are not explicitly considered here but could be an obstacle for future cropping possibilities and should be taken in account, too (Pimentel et al., 1995; Zhang et al., 2017). Other factors influencing future production may be the spread of insects that could be dangerous to cultivation due to the presence of stagnant water (Rosenzweig et al., 2001).

The combination with other spatial analysis provides a broader picture of the flood effects on a territory. In fact, the integration of flood extent with population poverty distribution here proposed, allow to identify the hotspots areas where flood strikes the poorest areas. This kind of analysis can provide useful information that help the definition of the priorities of intervention to support most vulnerable areas in case of flood events.

Flood risk has many hidden connections with environmental, social and economic spheres that need to be analyzed to develop effective integrated water-land management strategies. Our study makes a little step in this direction showing how remote sensing data can be mixed with on-site information to assess the effects of the flood on agriculture and how this information can be useful to enhance the resilience of local food production systems.

REFERENCES

Davis, K. F., M. C. Rulli, F. Garrassino, D. Chiarelli, A. Seveso, P. D'Odorico, 2017, Water limits to closing yield gaps, Advances in water resources, vol. 99, pp. 67-75, http://dx.doi.org/10.1016/j.advwatres.2016.11.015

FAO - Food and Agriculture Organization, 2001. Human energy requirements. Report of a Joint FAO/WHO/UNU Expert Consultation. Food and Agriculture Organization of the United Nations, ISBN 92-5-105212-3

Hoekstra, A.Y., Chapagain, A.K., Aldaya, M.M., Mekonnen, M.M., 2011. The Water Footprint Assessment Manual, The Water Footprint Network. doi:978-1-84971-279-8

FAO – Food and Agriculture Organization. How to Feed the World in 2050 High level expert forum, Rome 12-13/10/2009 Available at http://www.fao.org/wsfs/ forum2050/wsfs-background-documents/issues-briefs/en/ . Accessed September 2016.

FAO - Food and Agriculture Organization, 2016. FAOSTAT Country profile and balance sheet, from http://www.fao.org/faostat/en/#home.

GHIN, 2008. Global Hazards Information Network, Bangladesh Land use.
Available at:
http://ghin.pdc.org/ghin/catalog/search/resource/details.page?uuid={BA897FFD-C63F-432B-B278-20B862B4D4CE}.

Huke RE, Huke EH., 1997. Rice area by type of culture: South and Southeast Asia. Los Baños (Philippines): International Rice Research Institute.

International Rice Research Institute, 1976. Proceedings of the Symposium on Climate and Rice, IRRI, 306-307.

Pimentel, D., C Harvey, P Resosudarmo, K Sinclair, D Kunz, M McNair, S Crist, L Shpritz, L Fitton, R Saffouri, R Blair, 1995 Environmental and economic costs soil erosion and conservation benefits. Science, 267, pp. 1117–1123.

Rosenzweig, C., Iglesias, A., Yang, X. B.; Epstein, Paul R.; and Chivian, Eric, "Climate change and extreme weather events - Implications for food production, plant diseases, and pests" (2001). NASA Publications. Paper 24. http://digitalcommons.unl.edu/nasapub/24

Sanyal, Joy, and Lu, X. X., 2004 "Application of remote sensing in flood management with special reference to monsoon Asia: a review." Natural Hazards 33.2, 283-301.

SUPARCO and FAO, 2010. Pakistan Floods/Rains 2010, Rapid Crop Assessment: Series No.1.Karachi: Pakistan Space and Upper Atmosphere Research Commission and Food and Agriculture Organization, pp. 1-34.

UNITAR-UNOSAT, 2007. United Nations Institute for Training Research.
Available at: https://data.humdata.org/dataset/fl20070802bgd-flood-vectors-modisaqua-20-august-2007

Van Zyl, J. J., 2001. The Shuttle Radar Topography Mission (SRTM): A breakthrough in remote sensing of topography. Acta Astronautica, 48(5-12),559−565.

Vojinovic, Z., Abbott, M. B, 2012. Flood risk and social justice: From quantitative to qualitative flood risk assessment and mitigation. IWA Publishing, London.

Zhang, Q., Wu, J., Wang, F., Lei, Y., Zhang, Q., Cheng, X., 2017, Alterations in soil microbial community composition and biomass following agricultural land use change, Scientific Reports, http://dx.doi.org/10.1038/srep36587.

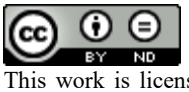

Earth observation for monitoring forest resources and environmental processes

TREE SPECIES CLASSIFICATION WITH SENTINEL-2 DATA IN EUROPEAN PART OF RUSSIA

E.A. Kurbanov*, O.N. Vorobev, S.A. Menshikov, M.S. Ali

Volga State University of Technology, Centre of Sustainable Forest Management and Remote Sensing, 424000 pl. Lenina, 3, Yoshkar-Ola, Mari El, Russian Federation – (kurbanovea, vorobievon, alims)@volgatech.net; plata_ms@mail.ru

KEY WORDS: Remote Sensing, Sentinel-2, Forest ecosystems, Tree species, Monitoring, Supervised classification, Russian forests.

ABSTRACT:

The study presents the results of iterative process of classification using Maximum Likelihood algorithms to estimate the potential of multitemporal Sentinel-2 (summer-autumn) images for mapping tree species in two forest districts of Penza Oblast of Russian Federation. For classification and validation of thematic maps of tree species distribution we used 298 test sites with independent field data, as well Canopus-V and Resurs-P satellites images of high spatial resolution. The authors also analysed the forest polygons and compared them to the state forest inventory data. Based on the field studies 10 classes of land/forest cover were identified to assess the spatial-temporal structure of the forest areas. In both forest districts tree species were distinguished at 10 m spatial resolution. The use of Sentinel-2A autumn data (October) maximized allocation of forest polygons by species that are more difficult to obtain on summer images due to similarity in spectral characteristics of deciduous species (alder, lime, birch and aspen). The beginning of the change in the phenological conditions of the forest stands allowed distinguishing all estimated tree species. Cross-validated overall accuracies, ranged between 74-85%, showed high degree of agreement between the tree species maps and the ground truth data. Research results can be applied for the long term forest monitoring and development of forest management plan for the investigated region.

1. INTRODUCTION

Remote Sensing data and techniques in combination with GIS and field inventory data are essential to analyse forest cover and its changes on vast areas (Loboda et al., 2017). Precise information about tree species distribution is important for sustainable forest management, forest inventory (Bergseng et al., 2014; Moreno et al., 2016), and assessment of potential impacts of climate change on biological productivity of forest ecosystems (Barbati et al., 2014; Han et al., 2016).

Remote sensing-based classification of tree species also include applications related to biodiversity assessment (Petrou et al., 2015; Bochenek et al., 2018), disturbances and stress management (Cohen et al., 2014; Kurbanov et al, 2017), monitoring of invasive species (Boschetti et al., 2007; Kimothi, Dasari, 2010; Hernández et al., 2014), as well as monitoring of reforestation on the abandoned agricultural lands and burned areas (Prishchepov et al., 2012; Hope et al., 2012; Chen et al., 2014). All these activities require fine mapping techniques and monitoring of different forest tree species, which has been limited previously by the temporal, spectral, and spatial resolution available from open access data (e.g. Landsat, MODIS).

1.1. Sentinel-2A images

With the launch in 2015 of a second Sentinel-2A satellite with Multi Spectral Instrument (MSI) on board, a new opportunity in finer scale forest cover mapping became possible, especially for the most complex mixed stands with higher degree of fragmentation and age structure. The 13 spectral bands of Sentinel-2 MSI sensor with fine spatial resolution (10, 20, 60 m depending on the spectral band) give unique perspectives for classification and monitoring of vegetation (Immitzer et al., 2016). The combination of high spectral resolution (up to 10 m) and several near infrared wavelength intervals (three bands in the red-edge plus two bands in the SWIR) with wide coverage (swath width of 290 km) were expected to provide an advanced image analysis and land cover mapping at regional and local levels (Hagolle et al., 2015; Wanga, Atkinson, 2018).

Despite these advantages compared to the previous sensors, only few studies have estimated the capacity of Sentinel-2 MSI images in forest mapping, tree species classification and monitoring (Laurin et al., 2016; Majasalmi, Rautiainen, 2016; Korhonen et al., 2017). There are some practical results based on the Sentinel-2 red-edge vegetation indices in forests. Fernández-Manso et al. (2016) found that MSI red-edge spectral indices are adequate and improve the accuracy to discriminate four burn severity levels for burned area mapping in Spain. According to Chrysafis et al. (2017), who compared Sentinel-2 and Landsat-8 data in the mapping of growing stock volume in a Mediterranean forest, the use of the Sentinel-2 first red-edge band improved the magnitude of correlation with growing stock volume. However, empirical studies demonstrating advantages of using MSI data in mapping forest species are very rare.

The purpose of this research was to assess the suitability of using Sentinel-2A satellite images and forest inventory data for mapping tree species composition on the example of forest stands in Penza Oblast (region) of Russian Federation. The paper examines whether improved multitemporal images at high spatial resolution (10 m) with field data actually improves our knowledge on tree species classification in forest ecosystems. For this we compared the use of Sentinel-2A data (summer–autumn) for the discrimination of forest species, and estimated improvement of forest classification accuracy by analysing the separability of forest classes.

2. STUDY AREA AND METHODS

2.1. Study area

The study were focused on forest stands on the territory of Yursovo and Leninsky forest districts of Penza Oblast (region) (Figure 1), which are part of the forest-steppe region of the European part of the Russian Federation. The land of the territory

* Corresponding author

range from hilly to plain, the height variations being almost unnoticeable (from 45 to 275 m above the sea level), and transitions from the lower to the higher parts being quite gradual. The climate of the region is considered to be temperate-continental with a relatively stable weather in winter and summer, but considerably changing conditions in spring and autumn. The average amount of precipitation is 450-500 m, of which 250-300 falls during the vegetation period (spring and summer).

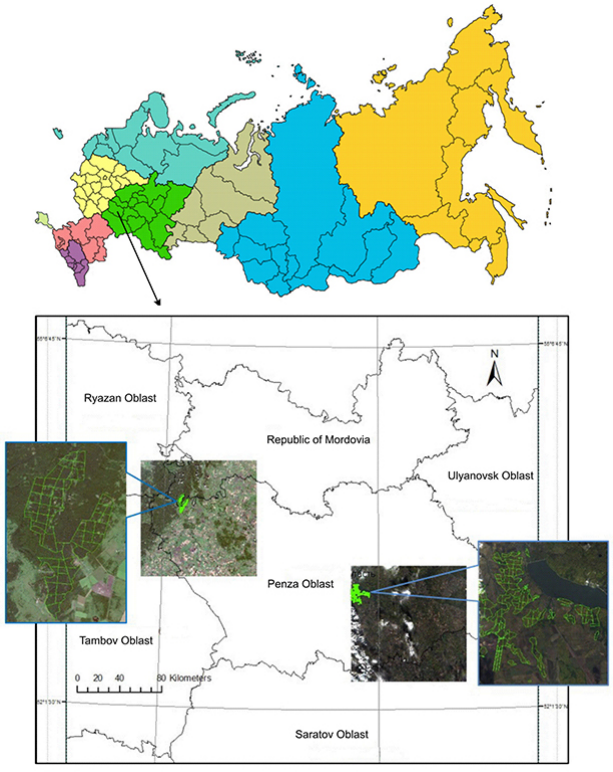

Figure 1. Penza Oblast on the map of Russian Federation. Two investigated forest districts on the Sentinel-2 images.

Broadleaf forest species predominate in the forest stands of the region, with 64% (Yursovo) and 48% (Leninskoye). Coniferous stands occupy 24% and 13% respectively and hardwoods - 11% and 38% of the total area. Among the forest-forming species the Scotch pine (*Pinus sylvestris*) (98% and 89%) is predominant, among hardwood species - oak is represented by (*Quercus robur*) (68% and 87%). Among soft-leaved species a considerable proportion is covered by birch tree (*Betula pendula*) (69% in the Yursovo forest district) and the aspen (*Populus tremula*) (58% in the Leninskoye).

2.2. Remote-sensing and field data

In the research we used Sentinel-2A (Table 1) satellite images acquired in August, early September, and October 2017 for the area of investigated forest districts. The images went through radiometric and atmospheric correction, are Level 1C (Top-of-atmosphere reflectance). Satellite images of Sentinel-2A, visually correlated with existing raster data (Landsat-8, Resurs-P, Canopus-V), and showed good agreement of both spatial and spectral characteristics. Only spectral bands (RGB and NIR) with spatial 10 m/pix and radiometric resolution of 12 bits/pix were used in the work, respectively.

Tile	Date	Cloud %	Pixel size (m)
T38UND	2017.10.10	0	10 (band 8,4,3,2)
T37UGV	2017.09.21	10	10 (band 8,4,3,2)
T38ULE	2017.08.19	10	10 (band 8,4,3,2)
T38UMD	2017.09.15	5	10 (band 8,4,3,2)

Table 1. Sentinel-2 image details for the study area

Two field campaigns were carried out in 2016-2017 between 11 June and 22 August in the forest districts of Penza Oblast. Test sites with an area of at least 100x100m for the validation of thematic mapping were selected along transects to represent the full range of the main forest cover classes and species typically occurring in these ecosystems (Figure 2).
The selection of test sites for validation and assessment of the accuracy of the thematic forest cover maps created was carried out on the base the existing forest inventory materials (polygon descriptions and forest plans) and high resolution satellite imagery (Canopus-V, Resurs-P). The main condition for the selection of test sites was their representation in all classes of land cover and even distribution over the territory of the investigated forest areas.

Figure 2. Field plots in typical forest stands of the study area: a) Birch trees, b) Mixed stand with oak, c) Scotch pine, d) Lime trees (*Tilia Cordata*)

The area of the test site on the ground was at least 1 ha, which allows its identification on Sentinel-2A image. Estimation of forest stands was carried out using the forest inventory methods of ground-based measurements. For each test site the trees composition (not less than 7 units of the main species), the average height and diameter of the stand, and the age of the dominant species were estimated. For two field seasons, 298 test sites were established, most of which (70%) were used to create a training sample. The remaining 30% were included in the database for the accuracy assessment of thematic mapping.
The spectral separability of the forest cover classes, studied in the summer and autumn images of the Sentinel-2A MSI, were estimated using the Jeffries-Matusita distance (J-M) for composition of the Sentinel-2 spectral bands. The J-M for quantitative expressions of the data separability is based on the covariance and weighted distance between the mean values of the classes (Chuvieco, 2016). The values of the J-M criterion, indicating the degree of statistical separability of the pairs, range from 0 to 2.0. The zero value of the J-M criterion shows no difference, and a value higher than 1.41 indicates a good separation of the studied classes (Niblack, 1986).

Based on the results of the field surveys and J-M separability criteria 10 forest cover classes (Table 2) were distinguished to estimate the tree species on the study area. These thematic classes were used to conduct a supervised classification (Maximum Likelihood-ML) to perform classification of each resulting Sentinel-2 scenes of 2017 (Figure 3).

№	Class Description
1	Pine (*Pinus Sylvestris*), middle-aged (41-60 years). The pine covers more than 65% of the stand area. Bonitet I-II.
2	Pine, under mature (61-80 years), mature (81-120) and over mature (120 and over). The pine covers more than 75% of the stand area. Bonitet I-II.
3	Birch *(Betula Pendula*), under mature (40-60 years) and mature (61-80). Bonitet I-III. Birch covers 70% of the stand area.
4	Aspen (*Populus Tremula*), undermature (31-40 years) and mature (41-60). Bonitet II-III. Aspen covers 70% of the stand area.
5	Lime (*Tilia Cordata*), under mature (40-60 years) and mature (61-80). Bonitet I-II. Covers 65% of the area.
6	Oak (*Quercus robur*), middle-aged (40-60 years), under mature (60-80) and mature (81-120). Bonitet 1-II. Oak covers 65-75% of the stand area.
7	Young stands of conifers and broadleaved species of natural and artificial origin (5-40 years).
8	Alder (*Alnus incana),* mature (60-80) and overmature (80 and over). Bonitet 1-II. Alder covers 75% of the area.
9	Bare. Not covered with vegetation.
10	Swamp area (Marsh)

Table 2. Classes of forest cover

3. RESULTS

The obtained J-M values for most compared pairs of thematic classes were higher than the accepted boundary of separability (1.41) (Table 3). The weak J-M separability was observed between hardwoods represented by aspen, birch and alder.

Pair of classes	J-M
Birch – Pine mature	1,73
Birch– Pine middle aged	1,96
Birch– Aspen	1,07
Birch – Oak	1,99
Birch – Alder	1,18
Birch – Young stands	1,93
Birch– Swamp area	1,71
Birch– Open space	2,00

Table 3. The J-M separability of estimated main tree species of the Yursovo forest district (as example)

The maximum separation of J-M in Sentinel images shows the ratio of deciduous and coniferous species, as well as deciduous and hardwood stands.

In the case of the tree species classifications, however, it was difficult to identify and classify mixed forests stands at 10 m spatial resolution. Therefore in our study we used combined series of Canopus-V and Resurs-P images of high resolution, which also contributes to delineation of textual attributes of the forest cover.

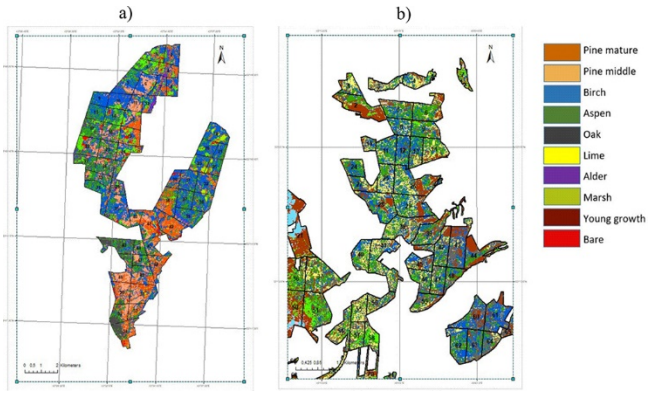

Figure 3. The result of Maximum Likelihood classification: a) Yursovo, b) Leninskoye forest districts

The overall supervised classification accuracy was 81%, kappa = 0.76. The decrease in accuracy was observed for young forest and birch stands. Cross-validated overall accuracies ranging between 74-82% shows high degree of agreement between the tree species maps and the ground truth data.

4. CONCLUSIONS

The results of this research shows that the Sentinel-2A MSI imagery could further strongly support activities for forest inventory and mapping. For forest classifications, images acquired later (beginning of autumn) lead to higher classification accuracies.

The use of the autumn Sentinel-2 data allows distinguishing the forest species with more accuracy, which in some cases are difficult to do on the summer images due to similarity in spectral characteristics of deciduous species (alder, lime, birch and aspen).

The classification algorithms have to be chosen according to the forest cover characteristics. We have chosen ML algorithm for the investigated area where the forest cover features were with clearly spectral behaviour. The resulted forest cover maps have a high level of detail as they are produced at 10 m resolution.

The four spectral bands, the training sets and classification algorithm represent key factors for the forest stand (tree species) map production. Multi-temporal images provide various spectral signatures of the forest cover features in different seasons (summer –autumn) of the same year. Using multiple spectral bands from Sentinel-2A images acquired in two seasons, improves the accuracy of the classification as the spectral separability between tree species increases.

ACKNOWLEDGEMENTS

This work was supported by the Erasmus+ Jean Monnet program of the European Union (Project № 574894-EPP-1-2016-1-RU-EPPJMO-CoE). The European Commission support for the production of this publication does not constitute an endorsement of the contents which reflects the views only of the authors, and the Commission cannot be held responsible for any use which may be made of the information contained therein.

REFERENCES

Barbati, A., Marchetti, M., Chirici, G., Corona P. 2014. European forest types and forest Europe SFM indicators: tools for monitoring progress on forest biodiversity conservation. *Forest Ecology and Management*, 321, pp. 145-157.

Bergseng, E., Ørka, H.O., Næsset, E., Gobakken, T. 2014. Assessing forest inventory information obtained from different inventory approaches and remote sensing data sources. *Annals of Forest Science*, 1432, pp. 1–13.

Bochenek, Z., Ziolkowski, D., Bartold, M., Orlowska, K., Ochtyra, A. 2018. Monitoring forest biodiversity and the impact of climate on forest environment using high-resolution satellite images, *European Journal of Remote Sensing*, 51:1, pp. 166-18.

Boschetti, M., Boschetti, L., Oliveri, S., Casati, L., Canova, I., 2007. Tree species mapping with airborne hyper-spectral MIVIS data: The Ticino Park study case. *International Journal of Remote Sensing*, 28 (6), pp. 1251–1261.

Chen, W., Moriya, K., Sakai, T., Koyama, L., Cao, C. 2014. Monitoring of post-fire forest recovery under different restoration modes based on time series Landsat data, *European Journal of Remote Sensing*, 47, pp. 153-168.

Chrysafis, I., Mallinis, G., Siachalou, S., Patias, P., 2017. Assessing the relationships between growing stock volume and Sentinel-2 imagery in a Mediterranean forest ecosystem, *Remote Sensing Letters*, 8, pp. 508–517.

Chuvieco, E. 2016. Fundamentals of satellite remote sensing: An environmental approach. Second Edition. Boca Raton/ London/New York: CRC Press Taylor & Francis.

Cohen, W.B., Yang, Z., Stehman, S.V., Schroeder, T.A., Bell, D M., Masek, J.G., Huang, C., Meigs, G.W. 2016. Forest disturbance across the conterminous United States from 1985–2012: The emerging dominance of forest decline. *Forest Ecology and Management*, 360, pp. 242-252.

Hagolle, O., Sylvander, S., Huc, M., Claverie, M., Clesse, D., Dechoz, C., Lonjou, V., Poulain, V. 2015. SPOT-4 (Take 5): Simulation of Sentinel-2 time series on 45 large sites, *Remote Sensing,* 7, pp. 12242-12264.

Fernández-Manso, A., Fernández-Manso, O., Quintano, C., 2016. SENTINEL-2A red-edge spectral indices suitability for discriminating burn severity, *International Journal of Applied Earth Observations and Geoinformation*, 50, pp. 170–175.

Han, F., Kang, S., Buyantuev, A., Zhang, Q., Niu, J., Yu, D., Ding, Y., Liu, P., Ma, W. 2016. Effects of climate change on primary production in the Inner Mongolia Plateau, China, *International Journal of Remote Sensing*, 37:23, pp. 5551-5564.

Hernández, L., Fernández, J.M., Cañellas, I., de la Cueva, V.A. 2014. Assessing spatio-temporal rates, patterns and determinants of biological invasions in forest ecosystems. The case of Acacia species in NW Spain. *Forest Ecology and Management,* 329, pp. 206–213.

Hope, A., Albers, N., Bart, R. 2012. Characterizing post-fire recovery of fynbos vegetation in the Western Cape Region of South Africa using MODIS data, *International Journal of Remote Sensing*, 33(4), pp. 979-999.

Immitzer, M., Vuolo, F., Atzberger, C. 2016. First experience with Sentinel-2 data for crop and tree species classifications in Central Europe, *Remote Sensing*, 8(3): 166.

Kimothi, M.M., Dasari, A. 2010. Methodology to map the spread of an invasive plant (Lantana camara L.) in forest ecosystems using Indian remote sensing satellite data. *International Journal of Remote Sensing*, 31 (12), pp., 3273 – 3289.

Korhonen, L, Hadi, Packalen, P., Rautiainen, M. 2017. Comparison of Sentinel-2 and Landsat 8 in the estimation of boreal forest canopy cover and leaf area index, *Remote Sensing of Environment*, 195, 259-274.

Kurbanov, E., Vorobyev, O., Leznin, S., Polevshikova, Y., Demisheva, E. 2017. Assessment of burn severity in Middle Povozhje with Landsat multi-temporal data. *International Journal of Wildland Fire*. 26(9). pp. 772-782.

Laurin, G.V., Puletti, N., Hawthorne, W, Liesenberg V., Corona, P., Papale, D., Chen, Q., Valentini, R. 2016. Discrimination of tropical forest types, dominant species, and mapping of functional guilds by hyperspectral and simulated multispectral Sentinel-2 data. *Remote Sensing of Environment,* 176: 163-176.

Loboda, T., Krankina, O., Savin, I., Kurbanov, E., Joanne, H. 2017. Land Management and the Impact of the 2010 Extreme Drought Event on the Agricultural and Ecological Systems of European Russia. *In Land-Cover and Land-Use Changes in Eastern Europe after the Collapse of the Soviet Union in 1991*, pp. 173-192, doi=10.1007/978-3-319-42638-9_8

Majasalmi, T., Rautiainen, M. 2016. The potential of Sentinel-2 data for estimating biophysical variables in a boreal forest: a simulation study, *Remote Sensing Letters*, 7, pp. 427–436.

Moreno, A., Neumann, M., Hasenauer, H. 2016. Optimal resolution for linking remotely sensed and forest inventory data in Europe. *Remote Sensing of Environment,* 183, pp. 109–119.

Niblack, W.1986. *An Introduction to Digital Image Processing,* Englewood CliVs: Prentice Hall, New Jersey.

Petrou Z.I., Manakos I., Stathaki T. 2015. Remote sensing for biodiversity monitoring: a review of methods for biodiversity indicator extraction and assessment of progress towards international targets, *Biodiversity and Conservation*, 24(10), pp. 2333-2363.

Prishchepov, A.V., Radeloff, V.C., Dubinin, M., Alcantara, C. 2012. The effect of Landsat ETM/ETM+ image acquisition dates on the detection of agricultural land abandonment in Eastern Europe, *Remote Sensing of Environment*, 126, pp. 195–209.

Wanga, Q., Atkinson, P.M. Spatio-temporal fusion for daily Sentinel-2 images. 2018. *Remote Sensing of Environment*, 204, pp. 31–42.

A GIS-BASED ASSESSMENT OF LAND COVER CHANGE IN AN ALPINE PROTECTED AREA

M. Zurlo[1,2] *, B. Bassano[2], M. Caccianiga[1]

[1] Dept. of Biosciences, University of Milan, Via Celoria 26, 20133 Milan, Italy – mikelezurlo@gmail.com marco.caccianiga@unimi.it

[2] Gran Paradiso National Park, Via Pio VII 9, 10128 Turin, Italy – bruno.bassano@pngp.it

KEY WORDS: Aerial photos, Alps, GFOSS, Land cover change, Minimum mapping unit, Object-based approach, Protected areas

ABSTRACT:

The European semi-natural landscape was markedly changed by the simultaneous effects of different land use processes. In this context, aerial photos are still a valuable means to detect this change delineating the fine-scale pattern over large areas. Furthermore, this remote sensed data is available in decades where other remote sensed data were still not available. Conversely, data availability, software cost, image preparation and data mining affect the effective usability of this supports. In this case study we used only free and open source geographical software (GFOSS) focusing on image preparation to improve data mining phase. Aerial images of a mountainous protected area were orthorectified, smoothed and similar neighbouring pixels were grouped in meaningful objects through a semi-automatic unsupervised parameter optimization procedure. Pixel groups were manually labelled creating a spatial explicit database. Using *a priori* defined minimum mapping unit (MMU), the different landscape configurations were compared showing a change in protected area. Implemented method ensured a strong repeatability and suitability over different aerial images and represented scenes, but there are strong limitations in the use of this remote sensed data as data availability, an important amount of work for data pre-process and the need to easily automatize the classification step.

1. INTRODUCTION

The change in socio-economical drivers, started in 1950s, had drastic effects on European Alps landscape structure (Fuchs et al., 2015) designed trough millennia by a widely diffuse human presence. The abandonment of shaping primary activities is independent from planned conservation strategies and it is seriously affecting biodiversity pattern (Zimmermann et al., 2010). This rapid change concerns sensitive areas such as the Alps characterized by extremely, fragmented and complex habitats with a particular pattern of biodiversity along the altitudinal gradient.

In the change assessment, methods based on inventories, statistical models and remote sensing data over large spatial scale often do not fulfil the local stakeholders need of quantitative explicit information extracted with simple and robust tools (Schirpke et al., 2017). In addition, the use of proprietary software in published methodologies set limits where lack of resources is a prominent constraint (Rocchini and Neteler, 2012).

Aerial images are a fundamental tool to reconstruct landscape pattern in decades when other remote sensed data were still not available. The high spatial resolution over a broad scale of analysis allows to understand the structure and the physiognomy of spatial elements via direct interpretation (Rocchini et al., 2006). Indeed, the first public administration GIS databases were image-derived due to their relative ease of use. Nevertheless, the combination of data accessibility and lack of rigorous data preparation steps could lead an unexperienced GIS user to extract erroneous and misleading information through subjective and time inefficient manual photo interpretation.

Despite the wide spread of these supports in last decades a robust and rigorous workflow to extract objective information from different images in different context is still lacking.

In this paper we present an open source workflow to retrieve quantitative data from aerial images. Different pre-process steps were listed according to image characteristics and to retrieve objective spatial units an unsupervised parameter optimization in image segmentation process was implemented. Moreover, to perform a robust overlay analysis of information derived from different data source we proposed the use of an objective definition of the minimum mapping unit (MMU). Care was taken to maintain the process ease, customizable and adaptable to different context and expertise.

2. MATERIALS AND METHODS

2.1 Study area

To study the long-term monitoring applicability in particularly challenging conditions, the topographical complex Alpine protected areas of Gran Paradiso National Park (GPNP) was selected. To test the method under different conditions, an altitudinal transect (45°28’20" N; 7°17’20" E WGS84, 1249-2440 m a.s.l) was chosen, consisting of 7 circular plots (r=100 m) with an altitudinal difference, from each centre, of approx. 200 m (Figure 1). Each plot is representative of one of three altitudinal belts: Montane, below the timberline; Subalpine, between the timberline and the tree line, beyond which no upright tree occurs; Alpine, the zone above the tree line. The selected transect is representative of Orco Valley, one of the 5 valleys that compose the GPNP. The south exposed valley undergone a strong rural depopulation and encompasses different vegetation types along the altitudinal belts, like broadleaf forest derived from wood re-

* Corresponding author

establishment, low-altitude meadows/pastures, shrublands and high-altitude grasslands (Viterbi et al, 2013).

2.2 Materials

Driven from the need to apply the method on different types of support, rather than temporal necessities, to represent the typical heterogeneity of aerial image archives we selected:

- a panchromatic aerial image belonging to 1975 *RATI Piemonte* flight distributed as scanned un-rectified aerial photo (600 dpi flatbed scanner, nominal scale of 1:15000) from *Settore cartografico Regione Piemonte* through the *Geoportale Piemonte* under Creative Commons Attribution CC BY 2.5;
- a digital CIR orthoimage (NIR, red, green bands) with a spatial resolution of 0.25 m belonging to 2006 Provincia Piemonte flight, retrieved under the same conditions of panchromatic image;
- a digital RGB orthoimage with a spatial resolution of 0.40 m retrieved from the 2011 *ICE Piemonte* flight, owned by the GPNP.

2.3 Tools

Due to high demand of reproducibility research, the entire image preparation and change detection processes, if not specified, have been realized in the open source GRASS GIS software (GRASS Development Team, 2018). This choice was done to not limit the method replicability and its improvement (Rocchini and Neteler, 2012). In addition, it is a complete and robust software suite for geospatial data management analysis and image processing with over 30 years of development (Neteler et al., 2012).

2.4 Data preparation

Due to the high aerial image heterogeneity and the complex topography of Alpine environment, which increase the variability at sensor response, it was not possible to have a standardized workflow to pre-process all supports; however, it was possible to define a key step. In this case study the application of Mumford-Shah model variational model, significantly increases the data quality stored in aerial photos. In the following sections, when we refer to *smoothing* we mean to run r.smooth.seg module on each image band, using λ and α coefficients of 1 and 500, as explained in detail by Vitti (2012).

2.4.1 The panchromatic aerial image was orthorectified in the i.ortho.photo module using as references the 2011 RGB image and TINITALY/01 DEM (Tarquini et al., 2015). The smoothed image band has a spatial resolution of 0.85 m/px and a spatial accuracy of 3.54 m expressed as $RMSE_r$ (Acc. 95%) following the ASPRS guidelines (ASPRS 2015).

2.4.2 The CIR orthoimage was only smoothed due the high quality of stored information.

2.4.3 The RGB orthoimage was smoothed and the high correlated RGB space was converted in HIS color model through the r.rgb.his module.

2.5 Image classification

2.5.1 Unsupervised parameter optimization and image segmentation

To characterize the extremely fragmented habitats, the object-based approach was used to delineate, in a repeatable way, contiguous group of spectrally similar neighbouring pixels (Blaschke, 2010). To perform the image segmentation we used the region growing algorithm implemented in i.segment module, that requires a standardized threshold between pixel reflectance value in each objects and their sizes. To avoid the tedious and too subjective trial and error segmentation parameter selection, the i.segment.uspo addon was used (Grippa et al., 2017); selected values are listed in Table 1.

plot	Threshold		
	1975	2006	2011
gpa	0.11	0.11	0.07
gpb	0.11	0.11	0.07
gpc	0.1	0.11	0.09
gpd	0.1	0.07	0.04
gpe	0.09	0.12	0.05
gpf	0.1	0.09	0.05
gpg	0.11	0.1	0.05

Table 1. Table list the best statistical thresholds assessed through the f-function (Johnson et al. 2015) using: α =1.25, a minimum object size of 5m^2 and a threshold list comprised between 0.01 to 0.51.

2.5.2 Object labelling

Objects were converted in vector format and manually labelled in QGIS (QGIS Development Team, 2018) using the 3rd level of Corine Land Cover legend, to assure the process ease and the comparison between different data sources.

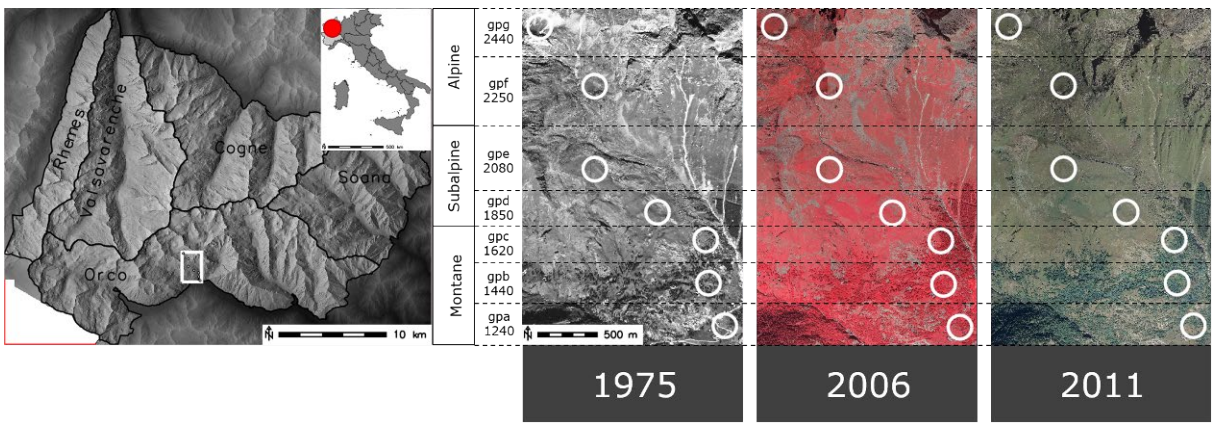

Figure 1. Study area. On the left the altitudinal transect location within GPNP (white square on hillshade relief). On the right side are listed the elevation (m a.s.l.) and the altitudinal belt of each plot (white circle) overlaid on 1975, 2006 and 2011 images.

2.6 Map comparison

Following the consideration of Rocchini et al. (2006) and to avoid subjective considerations in MMUs establishment, we used an a priori defined MMU in map comparison. Maps were aggregated using a majority filter (r.mode module) defining a 5x5 m grid on the basis of image resolution and their spatial displacement.

2.7 Change detection

Change was assessed using the r.change.info addon selecting the proportion of change method, a cell-based method expressing the number of changed cell in a moving windows divided by the theoretical maximum number of changes. Its nature was identified using a tabulate intersection analysis through the r.coin module and the magnitude accounting for the net change.

3. RESULTS

The aggregated final outputs of classified and resampled ortho-imagery products are represented in Figure 2. The proportion of change map quantitatively shows the number of changes for each cell highlighting that the structural changes occurred on a larger extent in Montane belt plots and on a minor extent in Alpine belt ones.

The tabulate intersection (Table 2) revealed the nature of change in two predominant phenomena: i) an up-to double increase of broad-leaved forest cover from 1975 to 2011 reflecting a drastic decrease of pastures and ii) a slight increase of natural grasslands upon bare rocks. Other minor changes are: i) a slight increase in discontinuous urban fabric and a decrease of road surfaces due to spread of tree cover; ii) a reduction and high instability of moors and heathland class; iii) a general instability of peat bogs and water courses classes.

1975	2011									
	112	**122**	**232**	**311**	**321**	**322**	**332**	**412**	**511**	**TOT**
112	**83**	0	7	14	0	6	0	0	0	**110**
122	0	**76**	43	107	0	0	3	0	0	**229**
232	35	9	**1198**	2391	0	94	76	0	0	**3803**
311	3	1	50	**1872**	0	5	11	0	0	**1942**
321	0	0	0	0	**6105**	2	528	76	8	**6719**
322	0	0	19	439	0	**8**	27	0	0	**493**
332	1	1	116	582	1089	33	**2124**	6	5	**3957**
412	0	0	0	0	88	0	10	**68**	2	**168**
511	0	0	0	0	28	0	17	0	**34**	**79**
TOT	**122**	**87**	**1433**	**5405**	**7310**	**148**	**2796**	**150**	**49**	**17500**

Table 2. The tabulate intersection. Table shows the change from 1975 (horizontal) to 2011 (vertical). The stable area are the diagonal values while the *change* the out-diagonal ones (values in 5 m cell). For CLC class codes, see Figure 2.

In terms of relative change, the predominant change registered in the altitudinal transect was the overall gain of broad-leaved forest (Table 3).

CLC	Cell (5x5 m)			Net change (5x5 m)		
	1975	**2006**	**2011**	**1975-2006**	**2006-2011**	**1975-2011**
112	110	122	122	+12	0	+12
122	229	56	87	-173	+31	−142
232	3803	1749	1433	-2054	-316	-2370
311	1942	5016	5405	**+3074**	**+389**	**+3463**
321	6719	7103	7310	+384	+207	+591
322	493	36	148	-457	+112	-345
332	3857	3255	2796	-602	-459	-1061
412	168	121	150	-47	+29	-18
511	79	42	49	-37	+7	-30

Table 3. Net change. Table lists results as number of cells in considered time span. For CLC class codes, see figure 2.

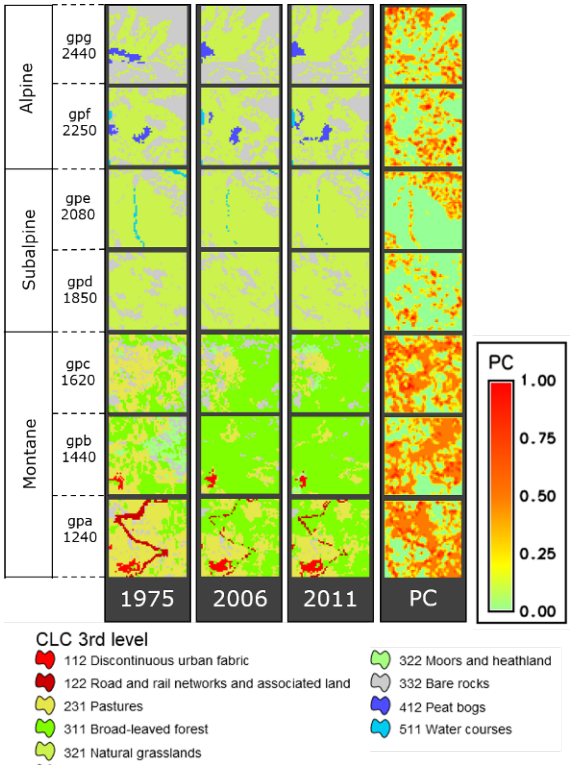

Figure 2. Results. 1975, 2006, 2011 classified and resampled products according to CLC legend. The elevation (m a.s.l.) and the altitudinal belt of each plot are listed. The proportion of change (PC) is a heat map where higher numbers correspond to major cell changes.

4. CONCLUSIONS

4.1 Method considerations

The open source workflow was implemented to deal with the aerial images and to generate land cover maps from diachronical aerial images.

To allow an unbiased overlay of maps derived from images collected with different spectral and spatial characteristics a rigorous pre-process, carried out with robust and peer-reviewed algorithms, is a mandatory step and the most expensive part of the case study, in terms of time resources. The application of Mumford-Shah variational model allowed to enhance the data quality removing image noise and speeding up the segmentation step.

The use of an unsupervised segmentation parameter optimization step allowed: i) to speed up the process, to ii) increase the method repeatability and iii) to retrieve clear and well-defined objects in fragmented complex habitats, iv) to avoid the over- or under-segmentation.

The manual object labelling kept the entire process ease reaching a trade-off between required classification time and plot spatial extent. Furthermore, working on prepared objects avoids the users to perform too subjective considerations on thematic class assignment and spatial extent of homogeneous spatial units.

The use of a priori defined MMU considering pixel resolutions and spatial displacements allowed i) to spatially integrate information derived from different supports; ii) to avoid scale effects in map comparison; iii) to obtain detailed land cover maps with a spatial resolution of 5 m in according to the need of detailed and reliable spatial information.

Nonetheless, the method requires fine tuning in pre-process phase (e.g. i.topo.corr module) and an automatic object labelling will be considered to speed up object-labelling of larger spatial extents.

4.2 Management implications

Many changes that the European landscape had to face in the last 50 years are related to the re-establishment of natural forest succession with loss of semi-natural habitat and cultural heritage (Fuchs et al., 2015).
The image process was developed to fulfil the need of detailed quantitative spatial explicit information, to deal with these unplanned changes affecting biodiversity pattern (Zimmermann et al., 2010).
The entire workflow was adapted to promote the invaluable data source of older aerial images to address ecological questions. Care was taken to make the process ease and robust and accessible both to well skilled technician (CLI approach) and to beginners (GUI approach).

4.3 Future perspectives

The remote sensing approach used to characterize a mountain protected area appeared to be a reliable tool to evaluate the vegetation pattern change occurred in the last few decades. Nevertheless, the applications of temporal GIS analysis are constrained by data distribution and their availability, therefore the integration with other dataset is a mandatory step (Petit and Lambin, 2001; Amici et al., 2017).
The study carried out along an altitudinal transect showed robust results, and it was immediately injected in the "Long term Alpine Biodiversity monitoring program of GPNP, a priority site identified by LTER network (LTER Code: LTER_EU_IT_109).

Concerning the improvement of retrieved quantitative data, the overlay with cadastral data, the integration with quali-quantitative protected area data, and an insertion within a restoration workflow will be considered in order to create a comprehensive management plan taking into account biodiversity conservation, landscape protection and continuity of traditional human activities.

REFERENCES

Amici, V., Maccherini, S., Santi, E., Torri, D., Vergari, F., and Del Monte, M., 2017. Long-Term Patterns of Change in a Vanishing Cultural Landscape: A GIS-Based Assessment. *Ecological Informatics, 37,* 38–51, doi:10.1016/j.ecoinf.2016.11.008.

ASPRS, 2015. ASPRS Positional Accuracy Standards for Digital Geospatial Data. *Photogrammetric Engineering & Remote Sensing,* 81(3), 1–26, doi:10.14358/PERS.81.3.A1-A26.

Blaschke, T., 2010. Object Based Image Analysis for Remote Sensing. *ISPRS Journal of Photogrammetry and Remote Sensing,* 65(1), 2–16, doi:10.1016/j.isprsjprs.2009.06.004.

Fuchs, R., Herold, M., Verburg, P.H., Clevers, J.G.P.W., and Eberle, J., 2015. Gross Changes in Reconstructions of Historic Land Cover/use for Europe between 1900 and 2010. *Global Change Biology,* 21(1), 299–313, doi:10.1111/gcb.12714.

GRASS Development Team, 2018. Geographic Resources Analysis Support System (GRASS) Software, Open Source Geospatial Foundation http://grass.osgeo.org.

Grippa, T., Lennert, M., Beaumont, B., Vanhuysse, S., Stephenne, N., and Wolff, E., 2017. An Open-Source Semi-Automated Processing Chain for Urban Object-Based Classification. *Remote Sensing,* 9(4), doi:10.3390/rs9040358.

Neteler, M., Bowman, M.H., Landa, M., and Metz M., 2012. GRASS GIS: A Multi-Purpose Open Source GIS. *Environmental Modelling & Software,* 31(May), 124–30, doi:10.1016/j.envsoft.2011.11.014.

Petit, C.C., and Lambin, E.F., 2001. Integration of Multi-Source Remote Sensing Data for Land Cover Change Detection. *International Journal of Geographical Information Science,* doi:10.1080/13658810110074483.

QGIS Development Team (2018). QGIS Geographic Information System, Open Source Geospatial Foundation Project. http://qgis.osgeo.org

Rocchini, D., and Neteler, M., 2012. Let the Four Freedoms Paradigm Apply to Ecology. *Trends in Ecology and Evolution,* 27(6), 310–11, doi:10.1016/j.tree.2012.03.009.

Rocchini, D., Perry, G.L.W., Salerno, M., Maccherini, S., and Chiarucci, A., 2006. Landscape Change and the Dynamics of Open Formations in a Natural Reserve. *Landscape and Urban Planning*, 77(1–2), 167–77, doi:10.1016/j.landurbplan.2005.02.008.

Schirpke, U., Kohler, M., Leitinger, G., Fontana, V., Tasser, E., & Tappeiner, U., 2017. Future impacts of changing land-use and climate on ecosystem services of mountain grassland and their resilience. Ecosystem Services, 26, 79-94, doi:10.1016/j.ecoser.2017.06.008

Tarquini, S., Vinci, S., Favalli, M., Doumaz, F., Fornaciai, A., and Nannipieri, L., 2012. Release of a 10-M-Resolution DEM for the Italian Territory: Comparison with Global-Coverage DEMs and Anaglyph-Mode Exploration via the Web. *Computers and Geosciences,* 38(1), 168–70, doi:10.1016/j.cageo.2011.04.018.

Viterbi, R., Cerrato, C., Bassano, B., Bionda, R., von Hardenberg, A., Provenzale, A., Bogliani, G., 2013. Patterns of Biodiversity in the Northwestern Italian Alps: A Multi-Taxa Approach. *Community Ecology*, 14(1), 18–30, doi:10.1556/ComEc.14.2013.1.3.

Vitti, A., 2012. The Mumford-Shah Variational Model for Image Segmentation: An Overview of the Theory, Implementation and Use. *ISPRS Journal of Photogrammetry and Remote Sensing,* 69, 50–64, doi:10.1016/j.isprsjprs.2012.02.005.

Zimmermann, P., Tasser, E., Leitinger, G., and Tappeiner, U., 2010. Effects of Land-Use and Land-Cover Pattern on Landscape-Scale Biodiversity in the European Alps. *Agriculture, Ecosystems and Environment,* doi:10.1016/j.agee.2010.06.010.

PRESENCE OF EUROPEAN BEECH IN ITS SPANISH SOUTHERNMOST LIMIT CHARACTERIZED WITH LANDSAT INTRA-ANNUAL TIME SERIES

C. Gómez[1]*, P. Alejandro[2], I. Aulló-Maestro[1], L. Hernández[1], R. Sánchez de Dios[3], H. Sainz-Ollero[4], J.C. Velázquez[3], F. Montes[1]

[1] INIA, Forest Research Centre, Dept. of Silviculture and Forest Management, Ctra. La Coruña km 7.5, 28040 Madrid, Spain (gomez.cristina, isabel.aullo, fmontes)@inia.es

[2] Quasar Science Resources, Ctra. La Coruña km 22.3, Las Rozas, 28232 Madrid, Spain - palejandro@quasarsr.com

[3] Dept. Plant Biology, Facultad de Biología, Universidad Complutense de Madrid, 28040 Madrid, Spain – rut.sanchez@bio.ucm.es

[4] Dept. of Biology, Facultad de Ciencias, Universidad Autónoma de Madrid, 28049 Madrid, Spain – helios.sainz@gmail.com

KEY WORDS: *Fagus sylvatica* L., Spain, Landsat, SVM, Spectro-phenological characterization

ABSTRACT:

The Spanish Central Range hosts some of the southernmost *Fagus sylvatica* L. (European beech) populations, which relict character is under scientific debate. There is a lack of detailed and updated cartography of European beech dominated stands in this area. In this work the current location and distribution of European beech dominated stands in the Spanish Central Range was mapped based on intra-annual series of Landsat OLI and ETM+ images acquired in 2015 and field verification over 108,000 ha. The distinctive early opening of the European beech leaves, which occurs in this area by mid-May, was captured by an ETM+ image acquired May 11th 2015. Surface reflectance and vegetation indices derived from four images distributed over the year were classified with a support vector machine algorithm. The spectro-phenological behaviour during period June 2013 - December 2017 of European beech and five other vegetation types present in the area was characterized to get insights of the landscape spectral response, and the most distinct traits of each vegetation type were identified. Comparison with previous cartographic records and current dendrometric measurements enabled characterization of the established or expansive condition of individual stands. In recent times European beech has increased its distribution by 12.5 % in area, gaining land to heather bushes, *Quercus pyrenaica* Willd. forests, and pine plantations. Landsat intra-annual time series has shown to be a valuable source of data to get insights of the distribution of phenologically distinct species.

1. INTRODUCTION

The Spanish Central Range hosts some of the southernmost populations of *Fagus sylvatica* L. (European beech). European beech has high water requirements and its Mediterranean distribution is limited by summer temperatures, drought, and moisture availability (Huston Durrant et al., 2016). Change in the use of land and short term climate oscillations are the main drivers of beech populations' recent dynamics in Spain. Furthermore, the character of the European beech in the Spanish Central Range as a relict species is currently under scientific debate.

Records from the second half of the 20th century partially mapped European beech distribution in the Central Range (Hernández Bermejo and Sáinz Ollero, 1978; Arranz and Allué, 1993) based on field observations and digitization on aerial photography or topographic maps. However, there is no detailed and comprehensive current cartography of the species. Knowledge of the current location and extension of European beech populations may contribute to better understanding of its recent dynamics.

Remote sensing of medium spatial resolution (10-30 m pixel size) enables identification and mapping of dominant species distribution (Fassnacht et al., 2016). The current availability of compatible Landsat ETM+ and OLI images, with one record every 8 days enables phenological characterization of habitat and vegetation formations (Pasquarella et al., 2016).

This work aims to map the current distribution of European beech populations in the Central Range of Spain. Our objectives are to characterize the species spectro-phenological behaviour in the area with a series of intra-annual Landsat images, and to classify the most distinctive spectral data to serve as base information for mapping.

2. METHODS

2.1 Location of study area

The study area covers 108,000 ha of the Central Range in Spain (Figure 1) encompassing all to-date mapped European beech populations. Annual rainfall is over 1000 mm with a two-month dry period in summer, and mean annual temperature is 8ºC (Gonzalo, 2010), allowing the presence of Atlantic broadleaved species (Ruiz-Labourdete et al., 2010). European beech groves are found between 1400 and 1900 m on acidic soils formed from metamorphic materials and frequently conform the tree line, growing over Pyrenean oak (*Quercus pyrenaica* Willd.) forests, mounting streams, and intermingled with pine plantations.

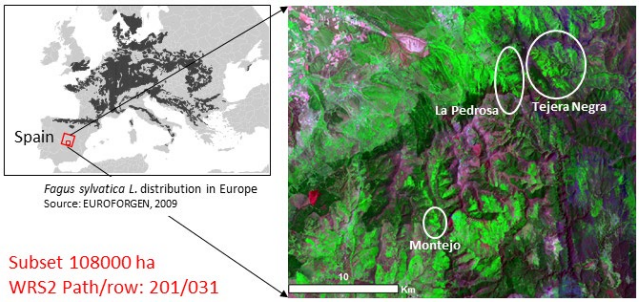

Figure 1. Location of the study area with main groves indicated.

* Corresponding author

European beech trees in this area have an earlier leave-on than other companion broadleaved species, normally by mid-May (Gil et al., 2010), although this may be hampered by late frosts.

2.2 Landsat data availability

From 2013 the United States Geological Survey (USGS) holds all Landsat acquisitions by Landsat 7 ETM+ and Landsat 8 OLI. Metadata of all available images were investigated and images with less than 70% cloud coverage were considered usable for this work (Figure 2).

Figure 2. Landsat data (path row 201/031) with less than 70% cloud cover available in the USGS archive.

Surface reflectance (SR) products were ordered via ESPA (https://espa.cr.usgs.gov/). ETM+ images (67) and OLI images (81) were downloaded when ready as SR products. Landsat collection 1 level 2 SR products are geometrically co-registered, radiometrically corrected and directly comparable, that is, ready for time series analysis. Vegetation indices—Normalized Difference Vegetation Index (NDVI, Tucker 1979), Tasselled Cap Wetness (TCW, Crist, 1985), and Tasselled Cap Angle (TCA, Powell et al., 2008)—were calculated for all images.

2.3 Single year spectral characterization

Year 2015 was selected for single year characterization of the vegetation spectral behaviour due to the good quality of well-timed imagery. In particular an image acquired May 11th seemed to be adequate to capture European beech leaf-on condition whilst other species were still leaf-dormant. Fourteen images of good quality observations (i.e. with a minimum of clouds and cloud shadows in the study area) were employed for this purpose.

Single pixel samples (178) were chosen based on Mapa Forestal Español (MFE), other ancillary cartography, and existing field inventories (Gil et al., 2010) irregularly distributed among six vegetation formations herein named: Fagus sylvatica, Quercus pyrenaica, Quercus ilex, and pine forests, as well as shrubs and pastures. Spectral values of the intra-annual time series (SR, NDVI, TCA, TCW) were averaged per class and explored, aiming to identify differences and similarities at different dates.

2.4 Classification and verification

Four epochs were selected based on previous analysis to make a Support Vector Machine (SVM) multi-temporal classification of SR, TCA, and TCW values. Dates chosen corresponded with DOY 12, 132, 172, and 268. A total of 32 variables were classified. To obtain complete observations free of atmospheric obstructions, a pixel-based compositing approach (White et al., 2014) was implemented complementing 2015 observations with better quality observations of years 2013 and 2014 (Table 1). The same pixels (178) employed for spectral characterization of vegetation formations were used as training samples for classification.

Table 1. Data employed for pixel-based compositing and variables included in the multi-temporal classification

Main image year, DOY, sensor	Auxiliary image year, DOY, sensor	Variables
2015 012 OLI	2015 316 OLI	SR, TCA, TCW
2015 132 ETM+	2014 137 OLI	SR, TCA, TCW
2015 172 OLI	2014 169 OLI	SR, TCA, TCW
2015 268 OLI	2013 262 OLI	SR, TCA, TCW

The classification was refined with an altitude mask, eliminating areas classified as European beech below 1200 m. The map verification process was based on an intensive field campaign during years 2016-2018. Field work included visual inspection of areas identified as European beech and potential locations overlooked by Landsat-based results. Field plots (122) were also measured to study structure, demography, regeneration, and tree growth of the largest populations. To derive accurate cartography all locations defined by the medium spatial resolution (30 m pixel size) spectral data were refined by onscreen digitization supported by aerial photography acquired in 2015.

We compared the current distribution of European beech with ancillary cartography (1978, 1993) co-registered to current aerial photography (2015), to help infer the dynamic character of the stands. European beech stands were labelled *established* when appearing in previous cartographic records and *expansion* when not. When old maps indicated the presence of spread trees and our classification assigned European beech we considered this a densified area and labelled as *expansion*.

2.5 Multi-year spectral characterization

European beech dominated areas as well as other vegetation formations were characterized with five years of NDVI and TCA series (148 records, that is, an average of 29 records per year). The series were completed to 8-day frequency with a spline interpolation, and then visually inspected and analysed with TIMESAT (Eklundh and Jönsson, 2017) to infer phenological parameters. TIMESAT enables extracting of seasonality parameters such as season start, season duration, or peak time from a fitted series.

3. RESULTS

3.1 Single year spectral characterization

European beech dominated stands reflectance over the year, represented by fourteen repetitions of the six Landsat optical bands (Figure 3) is characterized by low values (< 2000) during the winter period. NIR values increase progressively since May and peaks staying high during the summer time. The VIS spike characteristic of pigment activity is noticed between DOY140 and DOY268.

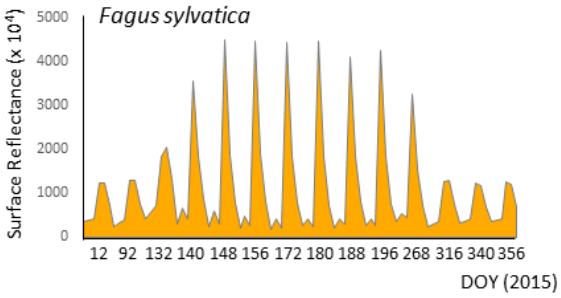

Figure 3. Surface reflectance of *Fagus sylvatica* L. (European beech) over year 2015 characterized by Landsat optical bands.

The highest water content of European beech showed by a strong reflectance on the SWIR in summery images, being the reflectance of other broadleaved species like *Quercus petraea* (Matt.) Liebl. or *Quercus pyrenaica* Willd. just below on average. Pines showed lower reflectance values on average and a more stable response over the year, whilst shrubs and pastures showed high variations in reflectance over the phenological year.

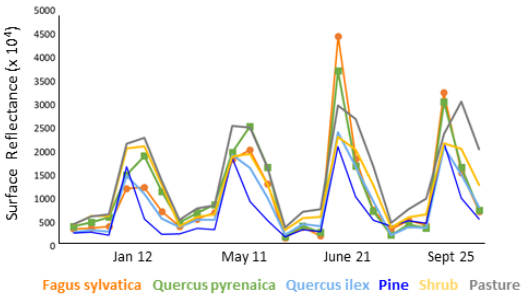

Figure 4. Spectral characterization of six vegetation formations

3.2 Classification and verification

A SVM classifier with Radial Basis Function kernel (Gamma 0.031, penalty 100) yielded best classification results. Overall, the spectral classification identified all European beech locations appearing in old cartography and spotted some new ones, in polygons with size between 1 and 874 pixels. The European beech dominated area was overestimated, with most of the overestimations laying below 1200 m, and therefore removed by the classification improvement rule (> 1200 m mask). *Fraxinus angustifolia* Vahl. on pastures was a frequent source of spectral confusion readily refined. More difficult to discern was the confusion with *Fraxinus excelsior* L. and *Sorbus aucuparia* L. on humid slopes, and *Betula* spp. or aspen along streams, which sometimes have phenological spectral behaviour comparable to *Fagus sylvatica*. The intense field campaign with onsite visual verification enabled confirmation of locations where European beech trees are sparse and frequently mixed with other broadleaved species.

Some areas previously mapped as scattered beech individuals were identified with beech-dominated spectral behaviour, and verified on the field as densified beech stands (Figure 5). These and newly spotted areas were considered as *expansion* areas in our cartography. Compared with ancillary cartography (1978, 1993) our results demonstrate there has been considerable densification and evident expansion of previously established European beech dominated stands, gaining land to other tree species but mostly to shrub lands, and a few new locations in pine shelters or following water streams.

3.3 Current distribution of *Fagus sylvatica* L.

European beech populations are located at altitudes between 1200-1970 m, preferably in shaded orientations and steep slopes. There is a tendency towards connection of groves and certain dispersion down the streams (Figure 5).

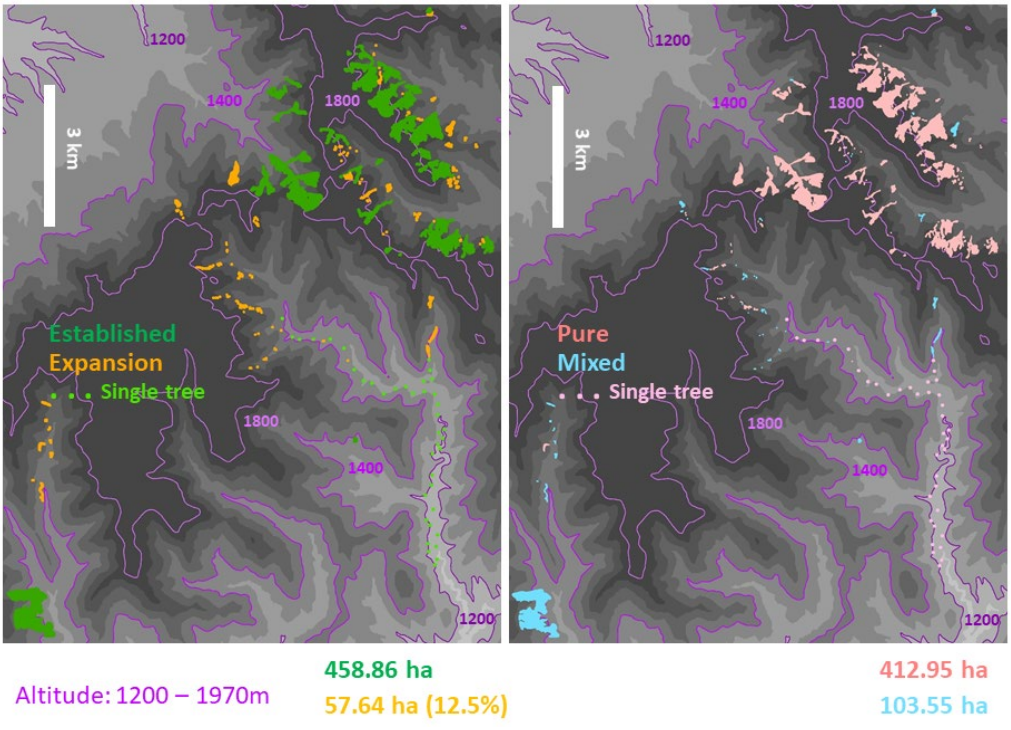

Figure 5. Current distribution of *Fagus sylvatica* L. populations in the Spanish Central Range

3.4 Multi-year spectro-phenological characterization

TCA and NDVI time series were best fitted with Savitzky Golay functions. During the period analysed European beech phenological season started consistently earlier than other companion species like *Q. pyrenaica* (Figure 5). The duration of these two species season was on average similar, with varying ending ranking. TIMESAT analysis demonstrated TCA phenological series were shorter than NDVI and showed a later start of the season.

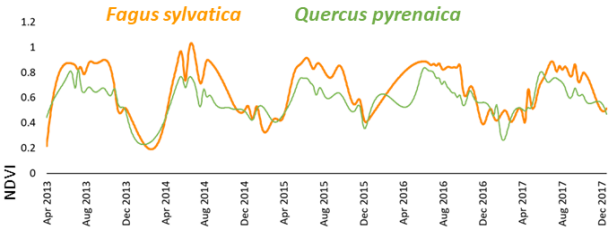

Figure 5. Spectral of *F. sylvatica* and *Q. pyrenaica*

4. CONCLUSIONS

Landsat intra-annual time series, with the high frequency enabled by Landsat 7 ETM+ and Landsat 8 OLI coexistence characterizes distinctive phenological traits of *Fagus sylvatica* L. species in the Spanish Central Range. Combined with ecological knowledge Landsat data have enabled better understanding of the species dynamics in this Mediterranean region. There has been a recent expansion of European beech with a tendency to connect existing populations. The recovery of European beech forests after the disappearance of traditional land uses points out the resilience of the species in its southern limit. Overall, the remote sensing based approach was a reliable method for identification of European beech dominated stands, as well as a tool to identify areas in a process of densification.

5. ACKNOWLEDGEMENTS

This work was funded by the Spanish Ministry of Science, Innovation and University through projects: AGL2013-46028-R "Forest management facing the change in forest ecosystems dynamics: a multiscale approach (SCALyFOR)" and AGL2016-76769-C2-1-R "Influence of natural disturbance regimes and management on forests dynamics, structure and carbon balance (FORESTCHANGE)". Field work assistance by Diego Galán, Belén Oñate, and Gregorio Cerezo is much appreciated.

REFERENCES

Arranz, J.A., Allué, M., 1993. Enumeración, descripción y cartografía de los enclaves de Fagus sylvatica L. en la vertiente segoviana del macizo de Ayllón. *Ecología,* 7, pp. 149-177.

Crist, E.P., 1985. A TM Tasseled Cap equivalent transformation for reflectance factor data. *Remote Sensing of Environment*, 17, pp. 301-306.

Eklundh, L., and Jönsson, P., 2017. Timesat 3.3 Software Manual, Lund and Malmö University, Sweden.

Fassnacht, F.E., Latifi, H., Stereńczak, K., Modzelewska, A., 2016. Review of studies on tree species classification from remotely sensed data. *Remote Sensing of Environment*, 186, pp. 64-87

Gil, L., Náger, J.A., Aranda-García, I., González Doncel, I., Gonzalo Jiménez, J., López de Heredia, U., Millerón, M., Nanos, N., Perea García-Calvo, R., Rodríguez Calcerrada, J., Valbuena Carabaña, M., 2010. El Hayedo de Montejo: una gestión sostenible. Dirección General del Medio Ambiente, Spain, 151 pp.

Gonzalo J. 2010. Diagnosis fitoclimática de la España peninsular. Hacia un modelo de clasificación funcional de la vegetación y de los ecosistemas peninsulares españoles. Serie Técnica: Naturaleza y Parques Nacionales. Ministerio de Medio Ambiente y Medio Rural y Marino. Organismo Autónomo Parques Nacionales.

Hernández Bermejo, J.E., Sainz Ollero, H., 1978. Introducción a la ecología de los hayedos meridionales ibéricos: el macizo de Ayllón. Publicaciones de la Secretaría General Técnica del Ministerio de Agricultura. Serie Recursos Naturales. Madrid, 145 pp.

Huston Durrant, T., de Rigo, D., Candullo, G., 2016. Fagus sylvatica in Europe: distribution, habitat, usage and threats in San Miguel Ayanz, J., de Rigo, D., Candullo, G., Huston Durrant, T., Mauri, A. (eds.) European Atlas of Forest Tree Species. Publication Office of the European Union, Luxembourg

Pasquarella, V.J., Holden, C.E., Kaufman, L., Woodcock, C.E., 2016. From imagery to ecology: leveraging time series of all available Landsat observations to map and monitor ecosystem state and dynamics. *Remote Sensing in Ecology and Conservation,* 2(3), pp. 152-170

Powell, S.L., Cohen, W.B., Healey, S.P., Kennedy, R.E., Moisen, G.G., Pierce, K.B., Ohmann, J.L., 2010. Quantification of live aboveground biomass dynamics with Landsat time-series and field inventory data: a comparison of empirical modeling approaches. *Remote Sensing of Environment*, 114, pp. 1053-1068.

Tucker, C.J., 1979. Red and photographic infrared linear combinations for monitoring vegetation. *Remote Sensing of Environment*, 8(2), pp. 127-150

Ruiz-Labourdette, D., Nogués-Bravo, D., Sainz Ollero, H., Schmitz, M.F., Pineda, F.D., 2012. Forest composition in Mediterranean mountains is projected to shift along the entire elevational gradient under climate change. *Journal of Biogeography*, 39, pp.162-176

White, J.C., Wulder, M.A., Hobart, G.W., Luther, J.E., Hermosilla, T., Griffiths, P., Coops, N.C., Hall, R.J., Hostert, P., Dyk, A., Guindon, L., 2014. Pixel-based image compositing for large-area dense time series applications and science. *Canadian Journal of Remote Sensing,* 40(3), pp. 192-212

POST-HURRICANE FOREST MAPPING IN BORY TUCHOLSKIE (NORTHERN POLAND) USING RANDOM FOREST-BASED UP-SCALING APPROACH OF ALS AND PHOTOGRAMMETRY- BASED CHM TO KOMPSAT-3 AND PLANETSCOPE IMAGERY

P. Wężyk*, P. Hawryło, K. Zięba-Kulawik

University of Agriculture in Krakow, Faculty of Forestry, Institute of Forest Resource Management; Department of Forest Inventory, Geomatics and Forest Economics; Krakow, Poland - p.wezyk@ur.krakow.pl

KEY WORDS: Airborne laser scanning, Forest damage, Nanosatellites, LiDAR point cloud, Remote sensing

ABSTRACT:

Assessing the extent of hurricane damage in forest areas is a difficult task in case of field-based inventory. In this context, remote sensing technologies are an attractive alternative to fast, inexpensive, and objective mapping of forest damage. The huge hurricane took place in Bory Tucholskie (Poland) on the night of 11/12 August 2017, at the belt with a length of approx. 300 km. The main goal of the study was to determine the suitability of PlanetScope (Dove) and KOMPSAT-3 satellite imageries for post-hurricane inventory of forest damage. The differences in Canopy Height Models (CHM; 1.0 m GSD) generated from the pre-hurricane ALS-based point clouds (density 4 pts/m^2) and post-hurricane aerial photos-derived point clouds (RGB; 0.15 m GSD) have been used as reference data for forest damage degree assessment. That has been determined using continuous scale ranging from 0.0 (no damages) to 100.0 (complete damage; 100%). Predictive models of forest damage degree were built at image segment and forest stand levels using the Random Forests method. The mean values of KOMPSAT-3 as well as PlanetScope spectral bands (NIR, Red, Green and Blue) and NDVI were used as predictor variables. RMSE for predicted damage degree values calculated at stand level based on KOMPSAT-3 and PlanetScope imagery amounted to 8.0% (R^2 = 0.81) and 7.1% (R^2 = 0.82) accordingly. The obtained results indicate that post-hurricane forest damage can be reliably and efficiently up-scaled from limited local area where precise reference data (like aerial photos) is available to wider areas using high resolution satellite images and Random Forest regression.

1. INTRODUCTION

In the face of observed climate changes, extreme weather events causing large destruction of forest areas occur with greater frequency. Such phenomena include, among others, strong winds which are a big threat to the sustainability and stability of forest ecosystems. For the past several years in Poland we have frequently observed the presence of hurricane winds damaging tree stands (Ciesielski et al. 2016). A recent event was the hurricane which took place in northern Poland on the night of August11/12, 2017 and caused destruction on a massive scale. Hurricane had negative impact on total 79.700 ha of forest, destroying completely (100% of damage) of 39.200 ha. The Polish State Forests National Holding (PGL LP) assessed the losses in wood biomass as 9.8 million m^3 of fallen and broken trees. In the event of forest damage occurring on such a large scale, it is extremely important to quickly conduct inventory of the damage in order to take proper economic decisions and specific actions. In such circumstances, the traditional assessment of forest wind-damage by means of field-based inventory is quite expensive, rather ineffective and, in many cases, also dangerous due to difficult and hazard environment. Obtaining high-resolution aerial photographs for the whole windfall area and then interpreting them on a computer screen is also a costly and time-consuming solution (Wezyk 2006; Wezyk et al. 2018) and subjective as well. There is the need to develop new, more efficient and less expensive methods.

In the scientific literature there are known examples of using remote sensing techniques in the post-hurricane forest damage inventory. Previous studies have focused mainly on the change detection in the forests using the changes in spectral characteristics observed on satellite imageries obtained before and after the wind storm. Various satellite imagery has been used for this purpose, both low- (Wang et al. 2010), medium- (Wang & Xu 2010; Ciesielski et al. 2016) and high-resolution (Chehata et al. 2014). In this kind of research, a very important issue is the correct acquisition of reference data on damaged forest stands, which takes place mostly on the basis of the field inventory. In the case of the availability of very high spatial resolution data, reference values of tree damages can be obtained directly from remote sensing data, without field work (Honkavaara et al. 2013). The ideal situation is when the high-resolution digital surface models (like: DSM or nDSM = Canopy Height Models; CHM) are available for the period before and after the occurrence of the disaster. The CHM model with the high spatial resolution (GSD 1.0 m) can be generated on the basis of 3D point clouds gathered with Airborne Laser Scanning (ALS) techniques or derived from automatic adjustment (matching) of digital aerial photos (Image Based Point Clouds; IPC; Honkavaara et al. 2013). However, in the case of wide wind-storms, obtaining ALS or IPC data for the whole area is both highly costly and time-consuming.

The main goal of the study was to determine the suitability of PlanetScope (Dove nanosatellites) and KOMPSAT-3 satellite imageries for post-hurricane inventory of forest damage. The idea was to up-scale the forest damage degree calculated from precision reference data (CHM) but available only for a limited region of the investigated area to the whole area of interest. This can be achieved by creating predictive models of forest damage degree based on spectral information obtained from satellite imageries.

* Corresponding author

2. METHODS

2.1 Study area

The study area of about 7500 ha was selected within Bory Tucholskie forest complex in Northern Poland where the huge windstorm took place on the night 11/12 August 2017 (Figure 1). The selected study area was covered mainly by Scots pine (*Pinus sylvestris* L.) dominated stands (approx. 95%).

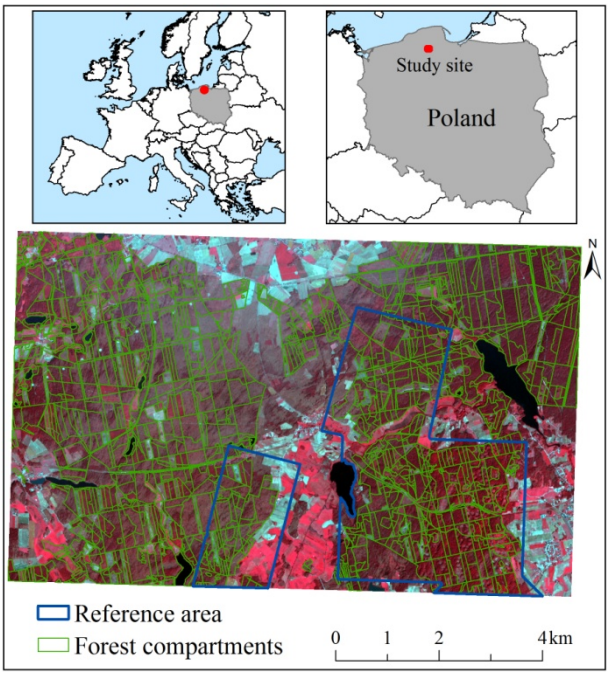

Figure 1. Location of the study area and AOI (in blue). The post-hurricane PlanetScope satellite imagery (15.08.2018) in the background. The blue polygons show the reference area for which the CHMs (pre- and post- hurricane) were available.

2.2 Input data

To achieve the goal of the study, several different remote sensing imageries were used, i.e. pre-hurricane PlanetScope (Aug. 16, 2017), post- hurricane PlanetScope (Aug. 15, 2017) and post-hurricane KOMPSAT-3 image (Aug. 30, 2017). The PlanetScope nano-satellites constellation (+175) acquires images in four spectral bands (BLUE, GREEN, RED, NIR) with 3.1 m GSD. The KOMPSAT-3 data has analogical 4 spectral bands as well (2.8 m GSD) and additional panchromatic (PAN) band at 0.7 m GSD. The satellite imageries covered the whole study area. Additionally, for the reference area of about 1.845 ha the pre-hurricane ALS point clouds and post-hurricane IPC were available. The IPC were generated from digital aerial photos (0.15 m GSD) using the Structure from Motion (SfM) approach (Turner et al., 2012) in PhotoScan Professional (Agisoft) software.

2.3 Creating pre-hurricane forest mask

The first step of analysis was to create the pre-hurricane forest mask based on PlanetScope image. The forest mask was created using the GEOBIA approach (Geographic Object Based Image Analysis; Hay and Castilla, 2008) and Random Forests (RF) classification method (Breiman, 2001). After initial SLIC image segmentation (Achanta et al., 2012), the segments with NDVI values >= 0.8 were classified as healthy vegetation using eCognition Developer 9.3.1 (Trimble Geospatial) software. Next, the training samples for forest and non-forest classes were selected based on visual image interpretation. Finally, the RF classification was performed using the randomForest package for R (Liaw and Wiener, 2002). The overall accuracy of forest mask classification assessed with 500 bootstrap iterations amounted to 97%.

2.4 Calculating reference damage degree

The CHMs (1.0 m GSD) were generated for the reference area (Figure 1) based on ALS and IPC using the FUSION software (CanopyModel; (McGaughey, 2015). In the next step the SLIC image segmentation was performed using the post-hurricane Planet Scope image (Figure 2). The areas covered by pre-hurricane forest mask (PlanetScope) with pre-hurricane CHM values >= 4.0 m and post-hurricane CHM values <= 4.0 m were considered as damaged. For each image segment and forest stand within the reference area the damage degree in 0-100 % range was calculated and treated as dependent variable.

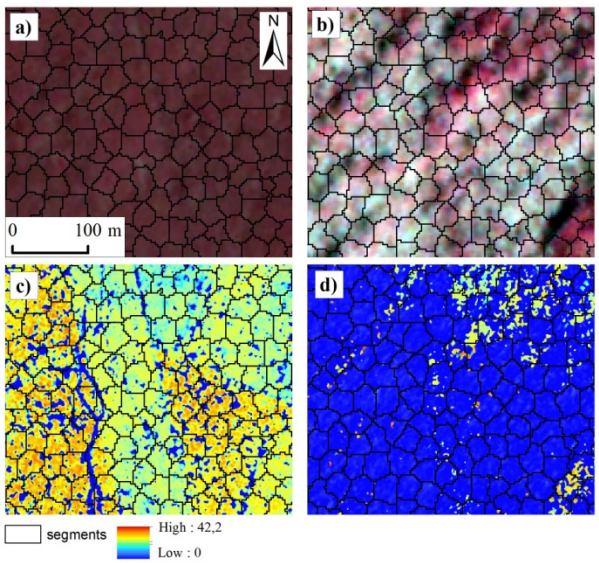

Figure 2. Results of SLIC segmentation and datasets used for building predictive models for PlanetScope imageries: a) pre-hurricane PlanetScope image; b) post-hurricane PlanetScope image; c) pre-hurricane CHM derived from ALS point cloud; d) post-hurricane CHM derived from SfM of aerial images.

2.5 Calculating predictor variables

The mean values of NDVI and DN of all spectral bands were calculated for each segment (results of SLIC segmentation) and forest stand (forest compartments from Digital Forest Map; Figure 1) and then used as predictor variables. In the case of PlanetScope-based models the pre- and post-hurricane images were used. For KOMPSAT-3 only post-hurricane image was available. In addition, the temporary class "image damage" was created for both satellite images sets. In the case of KOMPSAT-3 imagery the pixels with RED band values higher than certain threshold (RED > 1310) were considered as damaged forest. In the case of PlanetScope the raster layer with difference between pre- and post-hurricane RED values divided by the pre-hurricane RED value was created. The pixels of such a created raster layer with values lower than a certain threshold (RED difference <= -

0.18) were classified as "image damage". The threshold values used for creating the temporary class were selected based on visual on-screen interpretation of satellite images. Finally, the percentage cover of "image damage" class for each segment and stand was calculated and used as the predictor variable.

2.6 Creating predictive models

The random forest regression (Liaw and Wiener, 2002) models were created for segment and stand levels separately for KOMPSAT-3 and PlanetScope. The reference segments and stands were divided into training and testing sets. It was assumed that equal number of observations (segments, stands) from different forest damage degree classes should be used for training the predictive models. Thus the reference observations (segments and stands) were stratified to damage classes with 20% step what resulted in five damage classes. In the next step the maximum possible number of observations which guarantees the equal number of observation for each damage class was selected by stratified random sampling. The reference observations non-selected for training set were considered as testing observations. The test sets were finally used for model validation by calculating selected model performance metrics: root mean squared error (RMSE), mean error (ME) and coefficient of determination (R^2).

3. RESULTS

To fulfil the assumed precondition about the equal number of training observations from 5 forest damage degree classes (20% range) 1.000 (200 per class) observations were used at the segment level and 295 (59 per class) at the stand level. The proportion of training to testing observations amounted to 6/94 and 25/75 at the segment and the stand level accordingly.

Model validation showed that the best accuracy can be obtained when using PlanetScope pre- and post-hurricane images at the stand level (RMSE = 7.1%, R^2 = 0.82; Table 1). However, the obtained values of model performance metrics (Table 1) and analysis of scatterplots of observed vs. predicted values (Figure 3) showed that reliable prediction can be achieved in the case of each of the evaluated model. The ME for all tested models was higher than 0.0 indicating some overestimation of forest damages. The lowest ME was observed also for PlanetScope-based stand level model (ME = 1.9%).

Metrics	KOMPSAT-3		PLANETSCOPE	
	segments	stands	segments	stands
RMSE [%]	12.8	8.0	12.2	7.1
ME [%]	4.3	3.2	4.4	1.9
R^2	0.81	0.81	0.83	0.82

Table 1. Results of model validation on test sets.

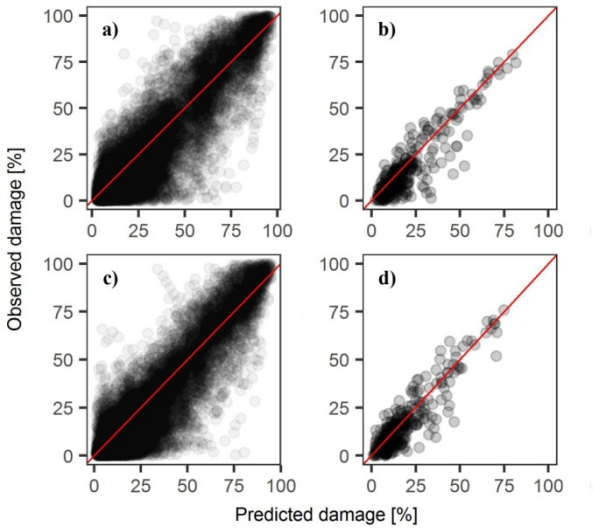

Figure 3. Observed vs. predicted values of forest damage degree at segment and stand levels for test sets: a) KOMPSAT-3 segments; b) KOMPSAT-3 stands; c) PlanetScope segments; d) PlanetScope stands.

4. CONCLUSIONS

The obtained results indicate that post-hurricane forest damage degree can be reliably assessed for wide forest areas using KOMPSAT-3 and PlanetScope satellite images. The performed analysis shows that forest damage degree can be successfully up-scaled to the whole investigated area using random forest regression method from a smaller local region where precise reference data (CHM) is available. The proposed approach is attractive in the context of practical applications since the usually expensive reference data in the form of point cloud-based CHMs is necessary only for a certain region of the wide investigated area.

ACKNOWLEDGEMENTS

Special thanks go to the satellite data providers: Planet Labs and SI Imaging Services as well as the Regional Directorate of Polish State Forests National Holding in Gdańsk for sharing aerial photos taken in September 2017 and for the Forest Data Bank for providing a Digital Forest Map (DFM).

REFERENCES

Achanta, R., Shaji, A., Smith, K., Lucchi, A., Fua, P., Süsstrunk, S., 2012. SLIC Superpixels Compared to State-of-the-Art Superpixel Methods. IEEE Trans. Pattern Anal. Mach. Intell. 34, 2274–2282. doi:10.1109/TPAMI.2012.120

Breiman, L., 2001. Random Forests. Mach. Learn. 45, 5–32. doi:10.1023/A:1010933404324

Ciesielski, M., Bałazy, R., Hycza, T., Dmyterko, E., Bruchwald, A., 2016. Szacowanie szkód spowodowanych przez wiatr w drzewostanach przy wykorzystaniu zobrazowań satelitarnych i danych Systemu Informatycznego Lasów Państwowych. Sylwan, 160(5), pp. 371–377

Chehata, N., Orny C., Boukir, S., Guyon, D., Wigneron, J.P., 2014. Object-based change detection in wind storm-damaged

forest using high-resolution multispectral images. International Journal of Remote Sensing, 35(13), pp.4758–4777

Hay, G.J., Castilla, G., 2008. Geographic Object-Based Image Analysis (GEOBIA): A new name for a new discipline, In: Blaschke, T., Lang, S., Hay, G.J. (Eds.), Object-Based Image Analysis: Spatial Concepts for Knowledge-Driven Remote Sensing Applications, Lecture Notes in Geoinformation and Cartography. Springer Berlin Heidelberg, Berlin, pp. 75–89. doi:10.1007/978-3-540-77058-9

Honkavaara, E., Litkey, P. & Nurminen, K., 2013. Automatic storm damage detection in forests using high-altitude photogrammetric imagery. Remote Sensing, 5(3), pp.1405–1424

Liaw, A., Wiener, M., 2002. Classification and Regression by randomForest. R News 2, 18–22.

McGaughey, R.J., 2015. FUSION/LDV: Software for LIDAR Data Analysis and Visualization. USDA Forest Service, Pacific Northwest Research Station: Seattle, WA, USA.

Turner, D., Lucieer, A., Watson, C., 2012. An automated technique for generating georectified mosaics from ultra-high resolution Unmanned Aerial Vehicle (UAV) imagery, based on Structure from Motion (SFM) point clouds. Remote Sens. 4, 1392–1410. doi:10.3390/rs4051392

Wang, F. & Xu, Y.J., 2010. Comparison of remote sensing change detection techniques for assessing hurricane damage to forests. Environmental Monitoring and Assessment, 162(1–4), pp.311–326

Wang, W., Qu, J.J., Hao, X., Liu, Y., Stanturf, J.A., 2010. Post-hurricane forest damage assessment using satellite remote sensing. Agric. For. Meteorol. 150, 122–132. doi:10.1016/j.agrformet.2009.09.009

Wezyk, P., 2006. Integration of geoinformation technologies in analyses of hurricane damages in the Pisz Primeval Forest. Archive of Photogrammetry, Cartography and Remote Sensing, Vol. 16, pp. 547- 556

Wezyk, P., Hawrylo, P., Janus, B., Weidenbach, M., Szostak M., 2018. Forest cover changes in Gorce NP (Poland) using photointerpretation of analogue photographs and GEOBIA of orthophotos and nDSM based on image-matching based approach. European Journal of Remote Sensing, Volume 51 Issue 1, pp. 501-510. doi: 10.1080/22797254.2018.1455158

FOREST TYPE CLASSIFICATION USING MORPHOLOGICAL OPERATORS AND FOREST PA METHOD

M. Ustuner[1] *, F. B. Sanli[1], S. Abdikan[2]

[1] Dept. of Geomatic Engineering, Yildiz Technical University, Istanbul, Turkey - (mustuner, fbalik)@yildiz.edu.tr
[2] Dept. of Geomatic Engineering, Bulent Ecevit University, Zonguldak, Turkey – sabdikan@beun.edu.tr

KEY WORDS: Morphological Operators, Forest PA, Support Vector Machines, Random Forests

ABSTRACT:

Morphological operators have obtained great attention in the fields of image processing and pattern recognition due to the providing relevant spatial information for the classification. This study evaluates the impacts of morphological operators from dual-polarized, Advanced Land-Observing Satellite (ALOS) and Phased Array L-band Synthetic Aperture Radar (PALSAR) data for the classification of forested areas. To this aim, the opening and closing operators with different size of structuring elements were exploited as morphological features in our study. For the classification of the forested areas, three different classification models (Support Vector Machines, Random Forests and Forest PA) were performed. The experimental results show that morphological features have increased the classification accuracy by 6.82% and 10.36% for Forest PA (Forest by Penalizing Attributes) and Random Forests (RF), respectively, while decreased the accuracy by 1.43% for Support Vector Machines (SVM). Furthermore, Forest PA yields the highest accuracy with morphological features followed by RF.

1. INTRODUCTION

The temporal monitoring of forest distribution and accurate mapping of forest types are essential for decision makers in climate regulation, environmental planning and management for forest biodiversity. Due to the high coverage of clouds in the tropical to sub-tropical regions, SAR (Synthetic Aperture Radar) sensors are only optimal way to monitor the large forestry areas in those regions with the advantages of penetration through clouds. L-band SAR data have been found more applicable for forestry application rather than X and C bands since longer wavelength and deeper penetration capability. Deeper penetration into the canopy provides greater characterisation of the multiple scattering mechanism. (Baltzer et al., 2003). Microwave signals are more sensitive to forest canopy size and structure and therefore SAR sensors have been found more useful and advantageous for forestry applications (forest type classification, detection of deforestation, forest volume estimation etc.) compared to optical sensors.

Many studies have been reported the use of L-band SAR data for forest cover/type mapping. Thiel et al. (2006) used the L-band SAR data (JERS-1) for forest cover mapping in five different test sites. Liesenberg and Gloaguen (2013) investigated the polarimetric, interferometric and textural features from the ALOS PALSAR data for forest classification. Mitchell et al. (2014) tested the C and L-band SAR images for forest cover mapping and also investigated their interoperability. Middinti et al. (2017) explored the L-band SAR data and textural features for the classification of forest types by using support vector machines. Abdikan (2018) assessed the performance of optical and L-band SAR data for the classification of forested areas.

To able to benefit from the spatial characteristics of the objects for the classification process, several methods have been used so far like image segmentation and mathematical morphology which is a non-linear image processing technique. The morphological operators (opening, closing, erosion and dilation) try to model the spatial characteristics of the object (shape, orientation etc.) given in a structuring element. (Bioucas-Dias et al., 2013). Many research have been carried out for the spatial-spectral classification of high-resolution multi/hyperspectral by using the morphological operators however, seldom performed for SAR (dual or quad pol) data, especially for forest classification.

Only few studies explored the benefits of morphological operators for the classification purposes of SAR/PolSAR data. Du et al. (2015) combined the polarimetric and spatial features for the land use classification of PolSAR data by using RF, rotation forest and SVM. Wang et al. (2017) proposed a new method called “composite kernel” that benefits from both spatial and polarimetric information for the PolSAR data classification. Wurm et al. (2017) investigated the spatial features (textural, morphological and polarimetric) for slum mapping using dual-polarized SAR data. Recently, Samat et al. (2018) explored the potential use of polarimetric signatures and morphological features for mapping the halophyte plants in wetland environments by using their newly proposed classifiers. Samat et al. (2018) also reported that higher classification accuracies were obtained when using morphological features. All these above studies illustrated the spatial features by exploiting of mathematical morphology for the classification purposes however none of them addressed the forest type classification.

The main objective of this research is to test the impacts of the morphological operators on the classification accuracy for the classification of forested areas (including forest types). For this purpose, we implemented three different model (SVM, RF and Forest PA). To the best of our knowledge, this is the first study exploiting Forest PA method for SAR data classification in the field of remote sensing and pattern recognition.

The major contributions of our experimental study can be shortly summarized as follows.

* Corresponding author

(1) We tested Forest PA for the first time in remote sensing for the classification of SAR imagery.
(2) The performance of Forest PA in comparison to RF and SVM was evaluated for classification of forested areas using morphological features

2. MATERIALS AND METHODS

2.1 Study Area and Dataset

The study area is located in Zonguldak city of Turkey. There are several hard coal mining areas in the region and city is surrounded by dense forests.

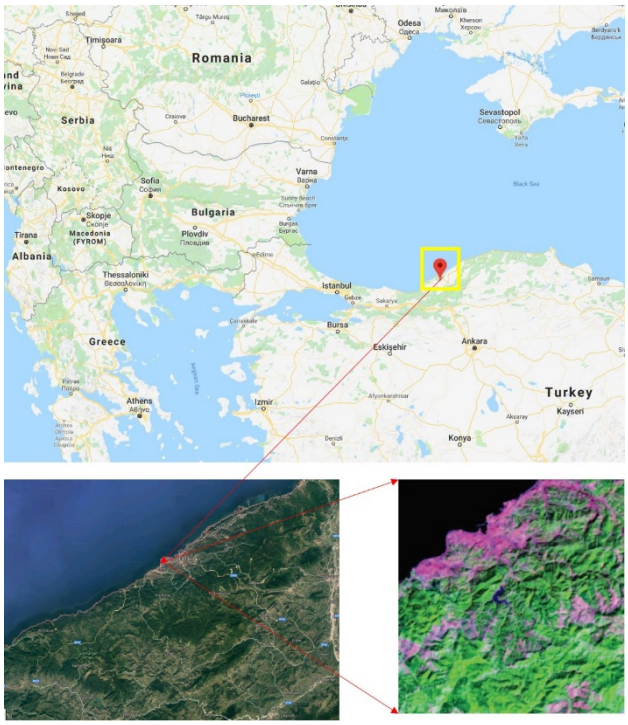

Figure 1. Study area (ALOS PALSAR composite image)

Since L-band SAR data can penetrate deeply due to its long wavelength (23 cm), it was preferred for this experimental study. The data has dual polarization (HH and HV, H: Horizontal, V: Vertical). The specifications of the data are presented in Table 1.

Specifications	Description
Date	10.09.2009
Sensor	PALSAR/FBD
Spatial Resolution	15 m
Flight Direction	Ascending
Polarization	HH+HV
Wavelength	23 cm (L-Band)

Table 1. Data Specifications

The data was acquired in Single-Look-Complex (SLC) format that needs to be processed before the classification. The pre-processing of the data includes the following steps: multi-looking, speckle filtering (3x3 Gamma Map), terrain correction (30 m ASTER GDEM) and scaling the data into decibel. As a final step of pre-processing, the data was exported as GeoTIFF format with 15 meter spatial resolution. Two different dataset were exploited to test the impact of morphological features (Table 2). Dataset I has two bands and Dataset II has ten bands. Morphological features were defined by using the opening profile and closing profile with different size of structuring elements. The size of the structuring elements are 3×3 and 5×5.

Dataset	Description
I	Original Bands (HH+HV)
II	Original Bands + Morphological Features

Table 2. Dataset description

Our study area consists of five classes, including bare land, deciduous forest, deciduous mixed forest, mixed forest and urban areas. Table 3 demonstrates the corresponding number of training and test samples for the classes.

Class Name	Number of Samples	
	Training	Test
Bare land	400	392
Deciduous forest	1467	1451
Deciduous mixed forest	1741	1452
Mixed forest	1366	846
Urban Areas	737	492

Table 3. The number of training and testing samples

The accuracy of classified images was assessed using error matrix that is used to calculate overall accuracy. Overall accuracy which is calculated by summing correctly classified values and dividing it by the total number of values is formulated as follows.

$$Overall\ Accuracy = \frac{Correctly\ classified\ values}{Total\ number\ of\ values}$$

2.2 Morphological Operators

For the extraction of relevant spatial information prior to image classification, there are several approaches employed so far and mathematical morphology (morphological operators, morphological profiles, extended morphological profiles etc.) is one of these approaches. The main purpose of the mathematical morphology is to understand the spatial relationship between the pixels within a structuring element that is also known as a kernel (e.g. a 5×5 square). The fundamental operators of mathematical morphology are erosion and dilation. The erosion basically enlarges the particular (selected) objects which is darker than their surroundings, however dilation makes them smaller. Through the combination of erosion and dilation, both opening and closing operators are derived. The opening operator is defined as the erosion following by dilation and the closing operator is defined as first dilation and then the erosion for a particular pixel of an image (Fauvel et al., 2013; Bioucas-Dias et al., 2013; Samat et al., 2018). In this research, we used 3×3 and 5×5 size of structuring elements for both opening and closing operators.

2.3 Image Classification

In this study, we implemented three different classification models (SVM, RF and Forest PA). SVM and RF, which are two of the popular machine learning algorithms, have been extensively used for the classification and regression problems in the fields of pattern recognition and remote sensing. Forest PA which is a new decision forest algorithm has been proposed by Adnan and Islam (2017) and was tested for the classification of the freely available data sets from the UCI Machine Learning Repository. In the following paragraph, the short overview of the classification models are presented. More details for SVM and RF can be found in Melgani and Bruzzone (2004) and Pal (2005), respectively.

Support vector machine which is one of the kernel-based learning algorithms tries to separate the two classes by defining the optimal hyperplane. SVM uses the kernel tricks for non-linear

classification and needs user-defined parameters to be set for kernels (Melgani and Bruzzone, 2004). We implemented radial basis function (RBF) kernel for SVM classification. Optimum parameters for RBF kernel (gamma and cost parameters) were determined by using grid search algorithm. Random Forest which is one of the decision tree-based ensemble classifiers produce multiple decision trees and utilize the majority voting strategy to assign a class label to the unknown instance. RF uses a random subset of training samples and variables for producing the multiple decision trees. RF is popular for the classification and regression problems because of its high classification accuracy and low computational cost (Pal, 2005). Forest PA (Forest by Penalizing Attributes) is a novel decision forest algorithm, recently introduced to the community by Adnan and Islam (2017). Forest PA benefits from the power of all the non-class attributes in a dataset to create the high accurate decision trees and has novel features like weight assignment strategy and bootstrap sampling. More technical details for Forest PA can be found in Adnan and Islam (2017) and Siers and Islam (2018). SVM and RF classifications were performed using the open-source Scikit-learn module in Python v3.6.4 (Pedregosa et al., 2011) and Forest PA classification was performed using the open-source data mining software Weka 3.8.2 (Frank et al. 2016).

3. RESULTS AND DISCUSSION

Each classification model has different sensitivity and attributes in terms of classification accuracy for the same dataset due to the main differences at learning phase of the model. In this section, we will present the classification results for the dataset-I and dataset-II and discuss them with underlying reasons. The overall accuracies varied from 39.33% to 50.66%. The overall accuracies for dataset-I were presented in Figure 3. The highest accuracy was obtained by SVM while the lowest one was received by RF for the dataset-I. The highest accuracy for dataset-I was reached up to 44.53% which is still less than 50% and may not be acceptable for the practical applications.

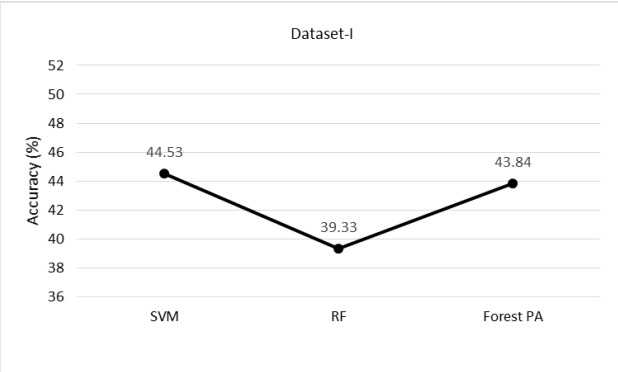

Figure 2. Classification accuracies for Dataset-I

The possible reason of this low accuracy for dataset-I is the spectral confusion between the forest types in the training set and insufficient spectral information to discriminate the classes. When morphological features were added to the original bands, the classification accuracies were changes. Figure 3 shows the classification results for dataset-II and obviously the overall accuracy of Forest PA is the highest among the other methods. SVM obtained the lowest accuracy for dataset-II while it performed better than the other methods for dataset-I. The possible reason of this decline might be the overfitting problem of SVM based upon the choice of cost parameters. In principle, SVM is a robust method against the overfitting problem however it's really based upon the choice of kernel parameters in practical applications.

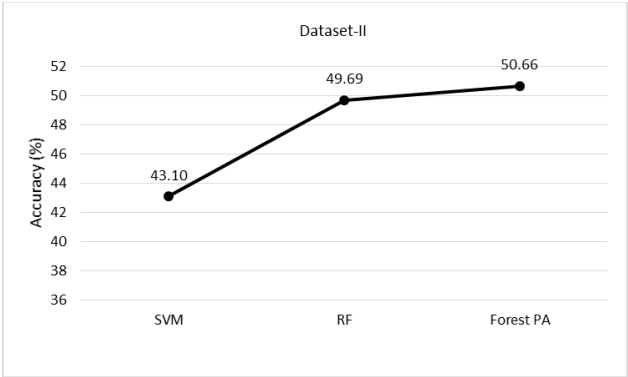

Figure 3. Classification accuracies for Dataset-II

When Figure 4 is examined, it's clear that morphological operators have increased the classification accuracy for Forest PA and RF. However the accuracy of SVM is decreased by 1.43%. The best improvement (sharp increase in graph) in terms of classification accuracy was observed by RF as 10.36%, followed by Forest PA. The classification accuracy for dataset-II was exceed the 50% by Forest PA, which is still insufficient rate for practical applications in remote sensing.

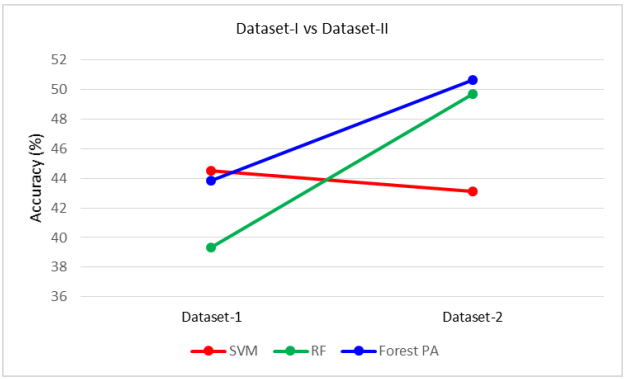

Figure 4. Comparison of classification accuracies

4. CONCLUSION

This study assessed the morphological operators from dual-polarized ALOS-PALSAR data for the classification of forested areas. To investigate the impacts of morphological operators on classification accuracy, two different dataset and three machine learning models were utilized. Our experimental results show that morphological operators increased the accuracy by 6.82% and 10.36% for Forest PA and RF, respectively, while decreased the accuracy by 1.43% for SVM. Any method could not reach up to the 50% accuracy for Dataset-I. The spectral confusion between the forest classes caused to low classification accuracy. Sharp increase was observed on RF when morphological features were incorporated. Only Forest PA exceed the 50% accuracy however such level of accuracy still cannot be acceptable for most practical applications in remote sensing. Our results concluded that dual-polarized ALOS-PALSAR, either by itself or with morphological features is insufficient for the classification of forested areas. We believe that multispectral optical data should be incorporated to able to reach up to the desirable accuracy level. Our future work will focus on the multiple/integrated use of vegetation indices obtained from

multispectral data and SAR data for the classification of forested areas with advanced ensemble classifiers.

ACKNOWLEDGEMENTS

The first author of the paper was granted by TUBITAK (The Scientific and Technological Research Council of Turkey) 2214/A International Doctoral Research Fellowship Programme and experiments were held while he visited the Department of Geography at Friedrich-Schiller University Jena, Germany as a guest researcher. He would like to thank TUBITAK (Grant No #1059B141700579) for the support.

REFERENCES

Abdikan, S., 2018. Exploring image fusion of ALOS/PALSAR data and LANDSAT data to differentiate forest area. *Geocarto International*, 33, pp. 21–37.

Adnan, M.N., Islam, M.Z., 2017. Forest PA: Constructing a decision forest by penalizing attributes used in previous trees. *Expert Systems with Applications*, 89, pp. 389–403.

Balzter, H., Skinner, L., Luckman, A., Brooke, R., 2003. Estimation of tree growth in a conifer plantation over 19 years from multi-satellite L-band SAR. *Remote Sensing of Environment,* 84, pp. 184–191.

Bioucas-Dias J. M., Plaza A., Camps-Valls G., Scheunders P., Nasrabadi N., Chanussot J., 2013. Hyperspectral Remote Sensing Data Analysis and Future Challenges. *IEEE Geoscience and Remote Sensing Magazine,* 1, pp. 6–36.

Du, P., Samat, A., Waske, B., Liu, S., Li, Z., 2015. Random Forest and Rotation Forest for fully polarized SAR image classification using polarimetric and spatial features. *ISPRS Journal of Photogrammetry and Remote Sensing*, 105, pp. 38–53.

Fauvel M., Tarabalka Y., Benediktsson J. A., Chanussot J., Tilton J. C., 2013. Advances in Spectral-Spatial Classification of Hyperspectral Images. *Proceedings of the IEEE*, 101, pp. 652–675.

Hall, M., Frank, E., Holmes, G., Pfahringer, B., Reutemann, P., Witten, I.H., 2009. The WEKA data mining software: an update. *ACM SIGKDD explorations newsletter*, 11, 10–18.

Liesenberg, V., Gloaguen, R., 2013. Evaluating SAR polarization modes at L-band for forest classification purposes in Eastern Amazon, Brazil. *International Journal of Applied Earth Observation and Geoinformation,* 21, pp. 122–135.

Melgani F., Bruzzone L., 2004. Classification of hyperspectral remote sensing images with support vector machines. *IEEE Transactions on Geoscience and Remote Sensing* 42, pp. 1778–1790.

Middinti, S., Jha, C.S., Reddy, T.B., 2017. Forest type classification with combination of advanced polarimetric decompositions and textures of L-band synthetic aperture radar data. *Journal of Applied Remote Sensing,* 11, 016035.

Mitchell, A.L., Tapley, I., Milne, A.K., Williams, M.L., Zhou, Z.-S., Lehmann, E., Caccetta, P., Lowell, K., Held, A., 2014. C- and L-band SAR interoperability: Filling the gaps in continuous forest cover mapping in Tasmania. *Remote Sensing of Environment*, 155, pp. 58–68.

Pal, M., 2005. Random forest classifier for remote sensing classification. *International Journal of Remote Sensing,* pp. 26, 217–222.

Pedregosa, F., Varoquaux, G., Gramfort, A., Michel, V., Thirion, B., Grisel, O., Blondel, M., Prettenhofer, P., Weiss, R., Dubourg, V., 2011. Scikit-learn: Machine learning in Python. *Journal of Machine Learning Research*, 12, 2825–2830.

Samat, A., Gamba, P., Liu, S., Miao, Z., Li, E., Abuduwaili, J., 2018. Quad-PolSAR data classification using modified random forest algorithms to map halophytic plants in arid areas. *International Journal of Applied Earth Observation and Geoinformation* 73, pp. 503–521.

Samat A., Persello C., Liu S., Li E., Miao Z., Abuduwaili J., 2018. Classification of VHR Multispectral Images Using ExtraTrees and Maximally Stable Extremal Region-Guided Morphological Profile. *IEEE Journal of Selected Topics in Applied Earth Observations and Remote Sensing* 11, pp. 3179–3195.

Siers, M.J., Islam, M.Z., 2018. Novel algorithms for cost-sensitive classification and knowledge discovery in class imbalanced datasets with an application to NASA software defects. *Information Sciences* 459, pp. 53–70.

Thiel, C., Drezet, P., Weise, C., Quegan, S., Schmullius, C., 2006. Radar remote sensing for the delineation of forest cover maps and the detection of deforestation. *Forestry: An International Journal of Forest Research,* 79, pp. 589–597.

Wang, X., Cao, Z., Ding, Y., Feng, J., 2017. Composite Kernel Method for PolSAR Image Classification Based on Polarimetric-Spatial Information. *Applied Sciences,* 7.

Wurm, M., Taubenböck, H., Weigand, M., Schmitt, A., 2017. Slum mapping in polarimetric SAR data using spatial features. *Remote Sensing of Environment,* 194, pp. 190–204.

USING GOOGLE EARTH ENGINE FOR THE ANALYSIS OF FOG AND FOREST LANDSCAPE INTERACTIONS IN HYPER-ARID AREAS OF SOUTHERN PERU

E. Forzini[1], G. Castelli[1,2]*, F. Salbitano[1], E. Bresci[1]

[1] Department of Agriculture, Food, Environment and Forestry (DAGRI), Università degli Studi di Firenze, Firenze, Italy
eleonora.forzini@stud.unifi.it; (giulio.castelli, fabio.salbitano, elena.bresci)@unifi.it
[2] Ingegneria Senza Frontiere - Firenze, Firenze, Italy

KEY WORDS: Fogscapes, Reforestation, Remote Sensing, NDVI, Landscape Restoration, Climate Change, Cloud based GIS, Sustainable Water Management

ABSTRACT:

Hyper-arid dryland ecosystems are particularly vulnerable to climate change and human influences, due to their dependence on advection fog as main water source. In these so-called 'fogscapes', human-induced fog collection represents a sustainable technology for fostering reforestation and, thus, increasing soil fertility and combating desertification. Along Atacama Desert coastal line, the effect of the Humboldt Current generates large scale fog events on the coastal belt, lasting from June to December, and the vegetation of the first hilly ridges (locally "lomas ecosystems") may favour of the water content of fog. The University of Florence has set up a long-term research on fog collection associated to reforestation actions in two experimental plots in South Peru at the site of the Lomas de Mejia. 20 Large Fog Collectors were installed in 1996 to collect water from fog, for irrigating the trees and shrubs planted in the experimental plots. The irrigation lasted two years, then the established trees and shrubs were left to collect fog by themselves. The paper presents the results of a long-term remote sensing monitoring of the area, based on the use of Google Earth Engine platform. More than 20 years of NDVI time series for the two reforested parcels and portions of an external control area, were generated and analysed. NDVI time series analysis shows the evolution of the parcels from bare soil to vegetated portions and its development in time. Results show the important role of advection fog for inducing the re-vegetation of areas where forest was previously present, the significant increments of vegetation cover for the reforested parcels in time, encouraging the implementation of fog collection projects for land rehabilitation in areas with similar characteristics.

1. INTRODUCTION

As world population and demand for fresh water are increasing, new water resources are needed, especially in fragile and vulnerable ecosystems, particularly threatened by climate changes and human actions (Djuma et al., 2016). Fog water harvesting can represent a sustainable source of water in hyper-arid coastal areas, where rainfall and groundwater are limited or unavailable (Fessaye et al., 2014).

Fog collection is a water harvesting technique used in arid tropical and subtropical areas, characterized by low rainfall amounts but frequent fog events, due to local weather conditions (Schemenauer and Cereceda, 1991). This technique has been tested in the South Eastern part of Africa, Hawaii islands and in the South American coastal area, especially along the entire cost of Peru and the northern part of Chile (the world's most arid regions). It takes inspiration from trees which can improve up to 25% the rain water income, by concentrating at their base (via throughfall and stem flow) the fog water which impacts and deposits on their canopy and trunk (Qadir et al., 2018).

Fog collected water can be used for human and animal consumption, subsistence agricultural activities, afforestation and environmental restoration, as in our case; it can supplement the average quantity of water per capita in these areas, where normally the water for human uses is carried in villages by trucks (Dodson and Bargach, 2015).

Concerning afforestation and environmental restoration, fog is particularly important because of its contribution of water, especially in the dry seasons or dry periods. Moreover, fog-collected water can be used for irrigation of seedlings and young plants that, otherwise, could not survive in so hard water deficit conditions (Certini et al. 2019). The objective of the irrigation is to support growth of tree and shrub seedlings and facilitate their establishment until they become able to sustain themselves by intercepting fog water (Valiente et al., 2011; Calamini et al., 1998).

The kind of fog suitable for being captured is the advection one: it forms when there is a strong horizontal advection of relatively warm moist air over cold water, as it often happens on regions characterized by strong sea surface temperature gradient, such as the Humboldt, Benguela and Labrador currents, and horizontal winds able to push the fog towards coastal mountains are present. As advection fog droplets have a diameter of some 10s μm, it is possible for the wind to move them (Cereceda et al., 2008). Fog collection is implemented by using vertical plastic meshes, supported by two wooden posts and exposed to the atmosphere; a part of water droplets carried by the wind deposits by impaction on these nets and, as they converge, they run down the meshes into underlying plastic gutters and then into storage tanks (Bresci, 1999).

These structures made by meshes and posts are called "fog collectors" (in Spanish called "atrapaniebla"). There are two main types of fog collectors: Standard Fog Collectors (SFC) have a mesh area of 1 m^2 and are used mainly in pilot experiments to evaluate the amount of water that can be obtained at given sites, and consequently to choose the most suitable areas for fog collection projects. They are equipped with a pluviometer and a meteorological station. Large Fog Collectors (LFC) have a mesh area ranging from 40 to 48 m^2 and are composed by two layers of mesh whose ribbons are 1 mm wide (Bresci, 1998) (Figure 1). Both the SFC and the LFC should be installed perpendicularly to the predominant wind direction for optimal performance (Schemenauer and Cereceda, 1994).

The University of Florence set up a project to study the influence of fog in Lomas ecosystem of Mejia (South Peru) and the possibility of restoring these areas through the plantations of trees and shrubs for their reforestation. A third of the plants was irrigated for 3 years, another third was

* Corresponding author

irrigated for 2 years, while the remaining third received no treatment after the plantation. The experimental afforestation belonged to the project "Fog as a new water resource for a sustainable development of the Peruvian and Chilean coastal desert", funded by the EU from 1995 to 1998.
The present short communication proposes the analysis of the evolution of the two experimental afforested areas, by analyzing long-term time series of Normalised Difference Vegetation Index (NDVI), also comprehending an untreated nearby area. The analysis has been conducted using remote sensing images, through the new platform Google Earth Engine (GEE) (Gorelick et al., 2017).

Figure 1. A Standard Fog Collector and a Large one in the Lomas the Mejia

2. MATERIALS AND METHODS

2.1 Study Area

The study area of Lomas de Mejia is located in South-Western Peru, 17° 02' 10'' S and 17° 2' 37''S and between 71° 50' 00'' W and 71° 51' 00''W at an altitude of 823 m a.s.l., in the Department of Arequipa, province of Islay and district of Deán Valdiviva (Figure 2).

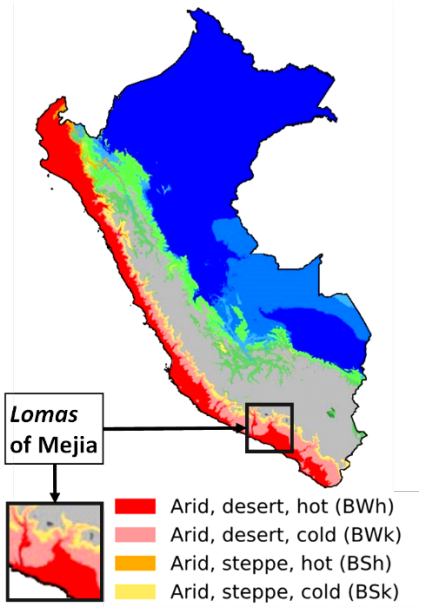

Figure 2. Location of the study area and climate zones of the Lomas of Mejia, processed from Beck et al., 2018.

The area has been deforested after the Spanish Colonization, leading to a severe desertification process (Belknap and Sandweiss, 2014).
From the twenty LFC installed, a PVC pipe (10 cm in diameter), was used to collect water falling from the mesh, stored in two reservoirs.
Two plots of 71 x 51 m, at 740 and 600 m a.s.l., respectively, and distant from each other almost 200 m, were afforested with 864 trees belonging to 5 species: two cohorts of native *Caesalpinia spinosa*, (seedings of 6 months and 12 months), *Prosopis pallida* and allochthones *Acacia saligna, Casuarina equisetifolia,* and *Parkinsonia aculeata*. The two plots were divided into two 51 x 33 m blocks, and each block into six 15 x 15 m parcels, separated by 3 m stripes in between (Figure 3).

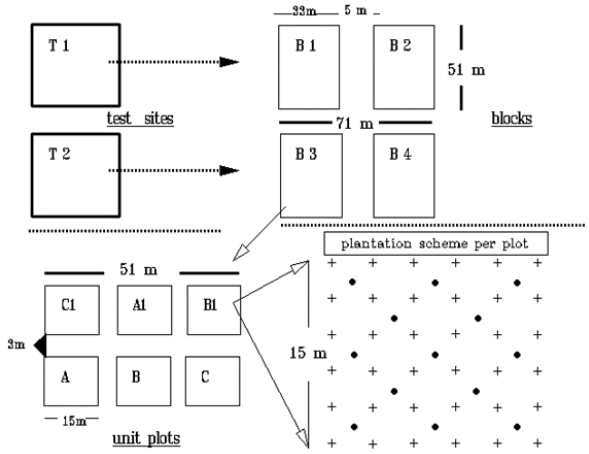

Figure 3. Scheme of the experimental plots in the Lomas de Mejia

The trees were planted in 1996 and, irrigated with fog water until 1998.
The evolution of vegetation in these 2 experimental plots (Figure 4) was observed and evaluated by analyzing NDVI time series, considering a smaller, vegetated target area, since the original framing was no longer visible after 22 years. An untreated control plot was also analyzed, as benchmark.

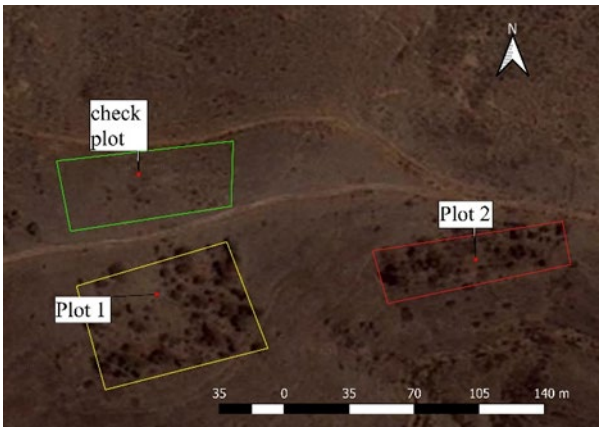

Figure 4. A view of the 2 target areas, representative of the experimental plots and the untreated area.

2.2 Remote sensing of afforested plots

NDVI is an indicator used to assess if the target of a remote sensing analysis contains green vegetation or not.
The index is based on the property of photosynthetically active vegetation of absorbing red radiation and reflecting infrared one. In its mathematical formulation, it can vary from -1 to +1 (Equation 1), while NDVI of vegetated areas can vary from 0 (bare or scarcely vegetated) to 1 (fully vegetated rainforest)

$$NDVI = \frac{\rho_{NIR} - \rho_{RED}}{\rho_{NIR} + \rho_{RED}} \qquad (1)$$

Where:

- ρ_{NIR} is the reflectance of the target pixel in Near infrared wavelength (0.7 – 1.1 µm)
- ρ_{RED} is the reflectance of the target pixel in visible wavelength (0.4 – 0.7 µm)

Satellite data were downloaded through GEE, a cloud-based geospatial processing platform for environmental data analysis on planetary-scale. GEE grants access to many remote sensing datasets and processing algorithms, directly on Google servers. Moreover, it allows rapid integration and sharing of new algorithms and processing tools.
Landsat 5, 7 and Sentinel-2 satellite data were downloaded and processed through GEE online code editor. Landsat NDVI time series were obtained from "Landsat 5 TM 8-day NDVI Composite" and "Landsat 7 8-day NDVI Composite" Image Collections, processed at level 1 T.
Sentinel-2 NDVI time series were calculated from the bands available from the "Sentinel-2 MSI: MultiSpectral Instrument, Level- 1C" collection on GEE database.
Landsat 5 data were utilized to analyse NDVI Before and After the Afforestation (BA, AA), while Landsat 7 images were used to extend the Landsat time series after 2011 (when Landsat 5 satellite was dismissed). Sentinel-2 NDVI data are elaborated to compare them with Landsat time series (Table 1). In fact, while these latter have a resolution of 30 m, Sentinel-2 images have resolution 10 m. Images characterized by cloud cover were removed from the analysis.

Satellite	Before Afforestation (BA)	After Afforestation (AA)	Number of Images
Landsat 5	1984-1997	2011-2015	1110
Landsat 7	-	2012-2017	264
Sentinel-2	-	2016-2018	220

Table 1. Satellite data series considered for the NDVI time analysis

All data were analysed in terms of average of the NDVI on the pixels placed under the parcel shape, averaging the pixels cut by the parcel border of each target area. Temporal averages of these values were calculated for the periods BA and AA and compared.
Monthly averages of NDVI were also analyzed to check if there is a relation between the fog period and NDVI values increase.

3. RESULTS

The NDVI mean values for the two plots for the AA period are higher than those for the BA period (Table 2), including an increase also in the check plot for Landsat 7 AA period. This confirm the initial hypothesis of vegetation being self-capturing, once the irrigation was finished.
The analysis of monthly means of Landsat 5 NDVI time series values, here synthetically presented by averaging the values of the two plots, show an increase for the period September, October, November and December only for AA period. The same months for the BA period showed a slight variation (Figure 5).

Plot	Mean NDVI Landsat 5 (BA)	Mean NDVI Landsat 5 (AA)	Mean NDVI Landsat 7 (AA)	Mean NDVI Sentinel-2 (AA)
1	0.081	0.113	0.157	0.147
2	0.081	0.099	0.150	0.150
check	0.073	0.071	0.135	0.071

Table 2. Average NDVI values for the two experimental plots and the check plot

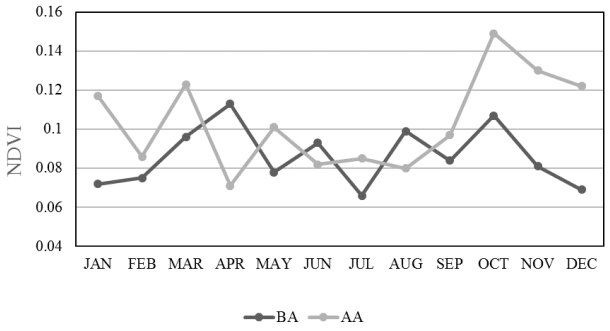

Figure 5. Mean monthly NDVI values from Landsat 5 data. Average value of Plot 1 and Plot 2.

The same temporal pattern is exhibited by the average of NDVI time series calculated with Sentinel-2 data, that showed a peak, but of lower entity, also for the check plot (Figure 6).

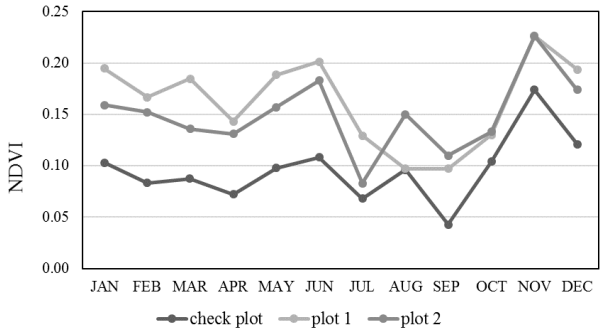

Figure 6. Mean monthly NDVI values for Sentinel-2 AA period in the two afforested plots and check plot after 2016

4. DISCUSSION AND CONCLUSIONS

The NDVI for afforested plots is about 0.1-0.2, the typical values for sparse vegetation and dry savannas. This is because a consistent part of the plots' surface is still uncovered by vegetation, while the alive individuals form low density groups.
The analysis of global averages of NDVI values (Table 2) showed a remarkable increase also in the check plot for the Landsat 7 AA period (2012 – 2017), that can be explained with the frequent occurrence of El Niño-Southern Oscillation (ENSO) in the period of analysis (NOAA, 2017), leading to

higher precipitation, and thus to an increase of green cover and of the vegetation health status also in drylands.
Plot 1 has moderately higher NDVI values with respect to plot 2, because its higher altitude, allowing a major fog collection by the planted trees. This characteristic is robustly confirmed by the comparison with the time series of fog water collected by SFC installed in the study sites from 1995 to 1997 (Figure 7). From the analysis of SFC time series, the occurrence of fog from August to November is evident, explaining the increase of NDVI for the September – January period (Figures 5 and 6).

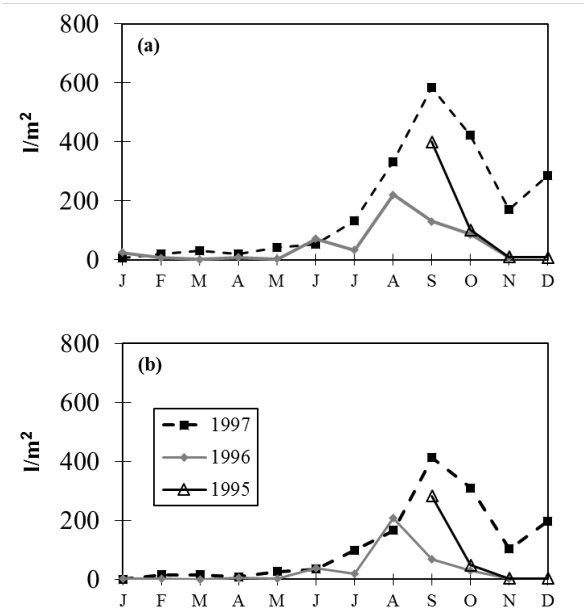

Figure 7. Total monthly SFC fog water (in liter per square meter) for the 1995-1997 period at the experimental plot sites (a) plot 1; (b) plot 2. (Bresci, 1999).

The present remote sensing analysis confirmed that an evident, even if scattered, reforestation is present and persisted in the area after the end of the project. Our results confirmed that the planted vegetation is sensitive to the occurrence of advection fog in autumn, exhibiting higher NDVI in the months from September to January.

REFERENCES

Beck H.E., Zimmermann N. E., McVicar T. R., Vergopolan N., Berg A., Wood E. F., 2018. Present and future Köppen-Geiger climate classification maps at 1-km resolution". *Sci. Data*, 5, 180214.

Bresci, E., 1999. Field Measurements and Wind Tunnel Trials on Fog Collectors. PhD Thesis, Università degli Studi di Firenze.

Bresci, E., 1998. Fog collectors capturing spatial variability. 1st Int. Conf. on Fog & Fog Collection. Vancouver, Canada, 19-24 July 1998. IDRC, pp. 465-468.

Belknap D.F., Sandweiss D.H. 2014. Effect of the Spanish Conquest on coastal change in Northwestern Peru. PNAS, 111, pp. 7986-7989.

Calamini, G., Falciai, M., Giacomin, A., Salbitano, F., 1998. Growth pattern and survivorship in a tree plantation trial under fog dependent environmental conditions. 1st Int. Conf. on Fog & Fog Collection. Vancouver, Canada, 19-24 July 1998. IDRC, pp. 485-488

Cereceda, P., Larrain, H., Osses, P., Fariàs M., Egaña, I., 2008 The spatial and temporal variability of fog and its relation to fog oases in the Atacama Desert, Chile. *Atmospheric Research* 87 (3-4), pp. 312-323.

Certini G., Castelli G., Bresci E., Calamini G., Pierguidi A., Villegas Paredes L. N., Salbitano F., 2019. Fog collection as a strategy to sequester carbon in drylands. *Sci. Total Environ.* 657, pp. 391–400.

Dodson, L.L., Bargach, J., 2015. Harvesting Fresh Water from Fog in Rural Morocco: Research and Impact Dar Si Hmad's Fogwater Project in Ait Baamrane. *Procedia Engineering*, 107, pp. 186–193.

Djuma, H., Bruggeman, A., Eliades, M., Lange, M.A. 2016. Non-conventional water resources research in semi-arid countries of the Middle East. *Desalination Water Treat*., 57, pp. 2290–2303.

Fessehaye, M., Abdul-Wahab, S.A., Savage, M.J., Kohler, T., Gherezghiher, T., Hurni, H., 2014. Fog-water collection for community use. *Renew. Sustain. Energy Rev*., 29, pp. 52–62.

Gorelick, N., Hancher, M., Dixon, M., Ilyushchenko, S., Thau, D., Moore, R., 2017. Remote Sensing of Environment Google Earth Engine: Planetary-scale geospatial analysis for everyone. *Remote Sens. Environ*., 202, pp. 18–27.

National Oceanic and Atmosphere Administration (NOAA) of the Unites States. Historical El Nino / La Nina episodes (1950-present).
http://origin.cpc.ncep.noaa.gov/products/analysis_monitoring/ensostuff/ONI_v5.php (26/10/2018)

Qadir, M., Jiménez, G.C., Farnum, R.L., Dodson, L.L., Smakhtin, V., 2018. Fog Water Collection: Challenges beyond Technology. *Water*, 10(4), pp. 1–10.

Schemenauer, R,S, Cereceda, P., 1991. Fog-water collection in arid coastal locations. *Ambio*, 20, pp. 303–308.

Schemenauer, R.S., Cereceda, P., 1994. A proposed standard fog collector for use in high-elevation regions. *J Appl Meteorol Climatol*., 33, pp. 1313–1322.

Valiente, José A., Estrela Maria J., Corell D., Fuentes D., Valdecantos A., Baeza, M.J., 2011. Fog water collection and reforestation at a mountain location in a Western Mediterranean basin region: air-mass origins and synoptic analysis. *Erdkunde,* Vol. 65, n. 3, pp. 277-290.

DETECTING TREE HEDGEROWS IN AGROFORESTRY LANDSCAPES

F. Chiocchini*, M. Ciolfi, M. Sarti, M. Lauteri, M. Cherubini, L. Leonardi, P. Paris

Istituto di Ricerca sugli Ecosistemi Terrestri**, Consiglio Nazionale delle Ricerche, Porano, Italy
(francesca.chiocchini, marco.ciolfi, maurizio.sarti, marco.luteri, marcello.cherubini, luca.leonardi, piero.paris)@cnr.it

KEY WORDS: Remote sensing, GIS, NDVI, Sentinel2, Ecological connectivity

ABSTRACT:

The practice known as *agroforestry* concerns land use systems involving trees in combination with agricultural crops and/or livestock. Scattered or linear trees (planted or naturally growing) constitute the woody component of agroforestry systems, which can be located either inside the field or along the field boundaries, as tree hedgerows. Such tree systems, belonging to the category of *Trees Outside Forest* (TOF), serve important ecological and economic functions. Only recently, the recognition of TOF in natural resource assessments has emerged as an important research issue. However, due to the complexity of surveying, scarce information is available concerning the current extent of agroforestry systems.
Agroforestry is increasingly perceived as providing ecosystem services, environmental benefits, and economic commodities as part of a multifunctional working landscape. These services and benefits occur over a range of spatial and temporal scales: from the farm/local scale, through the landscape/regional scale up to the global scale. Additionally, the value of ecosystems services of an agroforestry system is strongly dependent on trees number, size and spatial distribution. The use of Remote Sensing and GIS spatial analysis is of the utmost importance for detecting the landscape patterns, for understanding the interactions between biological and physical components, and for assessing, mapping and quantifying the social and economic value of the agroforestry ecosystem services.

1. INTRODUCTION

A decline of traditional agroforestry systems occurred during the 20th century in different places of Europe, due to the farming mechanization and crop expansion (Eichhorn et al., 2006; Mosquera-Losada et al., 2009). To reverse the decreasing of such good practices, the European Common Agricultural Policy is currently supporting the preservation of pre-existing agroforestry systems and the establishment of new ones, because of their high ecological and socio-economic value (Facciotto et al., 2015). Agroforestry is a combined land use system where the woody vegetation (trees/shrubs) is cultivated on the same land unit as agricultural crops and/or animals. Usually the woody component consists of scattered trees or linear forest formations, located either inside the field or along the field boundaries as tree hedgerows (THRs). Besides, scattered trees or linear forest formations are classified as *Trees Outside Forest* (TOF), as reported by FAO (1998, 2001). TOF are important elements of rural landscape, they contribute to the ecological connectivity and functioning of the landscape, providing environmental and economic benefits (Bellefontaine et al., 2002). Schnell et al. (2015) reported that the present monitoring of TOF is extremely variable across different countries, and systems that routinely monitor TOF are often missing or incomplete. Since the recognition of TOF over a wide spatial extent is time-consuming, the current extension of the linear forest formations of most Italian agroforestry systems is not known. Therefore, the magnitude of ecosystems services, strongly depending on trees number, dimension and spatial distribution (Shibu, 2009), cannot be easily estimated. Agroforestry landscapes are widespread in Italy, resulting by the complex interactions between natural processes and human activities, driven by the environmental, geomorphological and climatic conditions, and the historical and cultural land management practices. It is therefore necessary to define and test a methodology that allows the identification and quantification of TOF in the Italian agroforestry landscapes.

In this study, we focused our attention on tree hedgerows growing in an agroforestry landscape, located in Umbria region (central Italy). We combined different methodologies including, other than Remote Sensing, photo interpretation, GIS analysis and field survey (ground truth) to detect the forest linear formations, map their spatial distribution, estimate their extent, in order to understand the spatial interactions between the crop and tree components of the agroforestry system at the plot–farm scale.

2. MATERIALS AND METHODS

2.1 The study area

We investigated a farm managing over 600 ha of arable land and woods (Figure 1). The main land uses include herbaceous crops, tree hedgerows, shelterbelts and forest belts. In these systems, trees grow only at the edges of the fields, within hedgerows, or on scarps and drainage ditches between the fields; the trees provide established positive effects on soil erosion, wind shielding and ecological enrichment as well as aesthetic enhancement of the landscape.

2.2 Satellite imagery pre-processing

A Sentinel-2 image Level 1C[1] covering the entire study area was downloaded from the ESA's Sentinel Scientific Hub (ESA, 2016a). Pre-processing of the Level-1 image was performed using the SNAP Sentinel Application Platform toolbox (ESA, 2016b). The ESA Sen2CoR processor (ESA, 2016c) was used for atmospheric and terrain correction of the Sentinel-2 Top-Of-Atmosphere Level 1C data to generate a Level-2A Bottom-Of-Atmosphere reflectance image.

* Corresponding author
** Formerly IBAF (Istituto di Biologia Agroambientale e Forestale)
[1] Image S2A_MSIL2A_ 20170620T100031_N0205_R122_T32TQN_ 20170620T100453

2.3 Land use classification

We classified the main land uses of the farmland by visual photo interpretation (Data source: AGEA 2011, from UmbriaGEO online resources[2]) using QGIS software (http://qgis.osgeo.org) and we identified two experimental sites (ES) to study the continuous and discontinuous THRs along the margins of the cultivated fields. Each site contains a plot of annual crops and THRs along at least one of the borders consisting of oaks, mainly *Quercus pubescens* and *Quercus cerris,* with a high aesthetic value (Figure 2).
Through the aerial photos and Google Earth images (Google Earth Pro V.7.3.2.5491, 2017), we identified two test areas (TA) of 100 ha (1 km x 1 km squares) each one containing an ES (Figure 1).

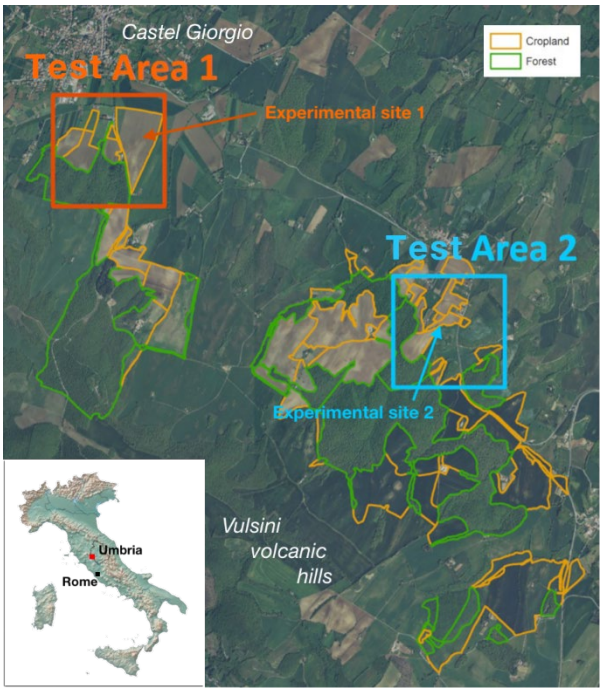

Figure1. Geographical location of the study area and identification of the experimental sites and the test areas. Map of the main land uses of the farmland

2.4 GIS Inventory of THRs

We tested a procedure for the GIS inventory of THRs over the two TAs, consisting in: 1) field survey of THRs with a GPS device in the ES, for the proper georeferencing and actual measurement of the tree linear systems; 2) recognition of THRs by photo interpretation of aerial and satellite images; 3) comparison of field measurements against estimates by photo interpretation for the error evaluation; 4) estimation of the incidence of THRs per hectare of cultivated area over the two TAs and over the whole farmland.
1) We collected geographical coordinates for each tree of THRs by GPS. We measured height (H), diameter at breast height (DBH) for each tree of the THRs and the distance between adjacent individuals.
2) The recognition of THRs was based on the interpretation of high-resolution multispectral Sentinel2 (HRS2) images[3].
The Normalized Difference Vegetation Index[4]:

$$\mathrm{NDVI} = \frac{\mathrm{NIR} - \mathrm{RED}}{\mathrm{NIR} + \mathrm{RED}} \quad (1)$$

allows the discrimination between areas with dense vegetation coverage (0.6 < NDVI < 0.9, tree covered) and areas with low/zero vegetation cover (cultivated areas or bare soil areas). Starting from the HRS2 images and using the raster algebra capabilities of the Sentinel Application Platform toolbox (ESA, 2016b), the NDVI was derived and the corresponding raster file was generated for the TAs. The vectorization of the raster file outputted a vector file of polygonal elements that were classified according to the NDVI.
3) We used the field measurements of THRs as control points to assess the ground truth for the THRs identified by photo interpretation.
4) We estimated the incidence of THRs per hectare / perimeter of cultivated area with linear element along the boundaries, over the two TAs.
Based on the previous steps, we applied the same procedure throughout the study area to estimate the incidence of total THRs per hectare of the whole farm.

3. RESULTS AND DISCUSSIONS

3.1 Land use classification

Based on visual photo interpretation, we classified 330.10 ha of the study area as arable land and 298.13 ha as forested land (other than THRs), with prevalence of mixed broad-leaved woods, corresponding respectively to the 53% and the 47% of the whole land surface (Figure 1).

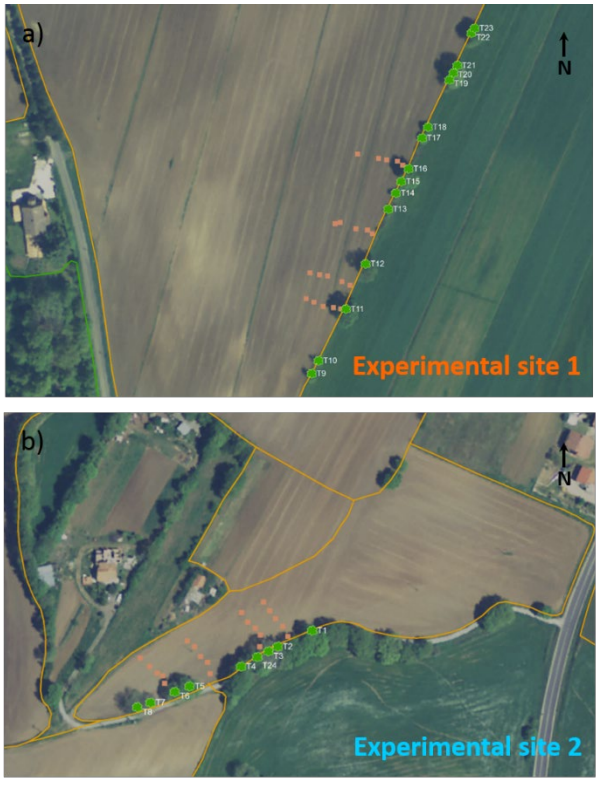

Figure 2. Experimental sites with tree codes (Tx) along field margin and sampling transects (orange squares)

[2] http://www.umbriageo.regione.umbria.it/pagine/servizi-wms-attivi (active WMS services).

[3] https://sentinel.esa.int/web/sentinel/missions/sentinel-2/data-products

[4] Where RED and NIR are the spectral reflectances in the red band (Sentinel2 MSI band 4, 665 nm) and the near-infrared band (band 8, 842 nm), 10 m spatial resolution, 5 days revisit time (https://earth.esa.int/ web/sentinel/user-guides/sentinel-2-msi/).

Figure 2 shows the experimental sites: the first ES (Figure 2a) has a surface of 17.8 ha of arable land and a perimeter of 1992 m. Fifteen oak trees make up a THR oriented NNE–SSW, with an average H = 14 m, an average DBH = 50 cm and an average distance between individuals of about 36 m. We classified this THR as discontinuous. The second ES (Figure 2b) covers an area of 1.98 ha of arable land, with a perimeter of 791 m. The THR of site 2, classified as continuous, is oriented ENE–WSW and consists of nine oak trees having an average H = 20 m, DBH = 62 cm and an average distance between individuals of about 15 m.

3.2 GIS Inventory of THRS

Based on NDVI we discriminated between areas with dense vegetation coverage (0.6 < NDVI < 0.9, tree covered areas) and areas with low/zero vegetation cover (cultivated areas or bare soil areas). The 10 m spatial resolution of HRS2 scenes allowed the identification of long and narrow polygons corresponding to the crowns of the tree rows, as shown in Figure 3.

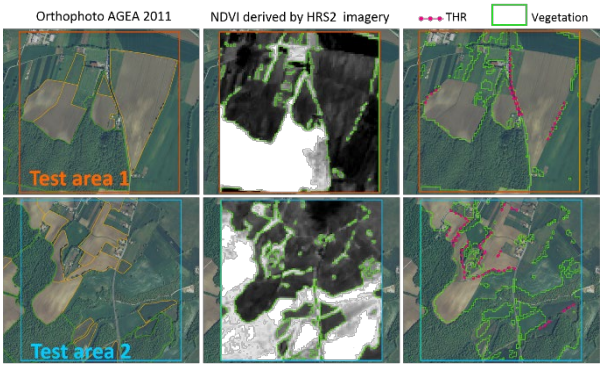

Figure 3. Detection of vegetated area and of tree hedgerows in the two test areas

THRs detected by the NDVI based procedure are in accordance with the field survey of THRs.
The results for the GIS inventory throughout the study area agree with the results over the two test areas, as reported in Table 1. THRs length corresponds to the 14% of the total perimeter of the cultivated fields with THRs along the boundaries and the crowns of THRs cover the 3% of the total cultivated area, with an incidence of 67 m of tree rows for each hectare of cultivated land.

	Study area	TA 1	TA 2
THRs L (m)	6241.3	826.9	1272.6
Fields P (m)	44885.4	5234.5	9075.9
THRs L/Fields P (%)	13.9	15.8	14
THRs L/A (m/ha)*	67	56	58
THRs A (ha)	7	0.9	1.4
Fields A (ha)	237	32.6	38.7
THRs A/Fields A (%)	2.9	2.7	3.6

Table 1. THRs Inventory summary statistics.
THRsL = length of THRs; Fields P = perimeter of fields with THRs, THRs A = area covered by THRs; Fields A = area of fields with THRs. * Mean values

In conclusion, our results show that, in the study area, the 14% of the total fields' perimeter is covered by THRs dominated by oaks, consisting mostly of adult trees with a high added aesthetic value. The linear density of THRs is variable, amounting to an average value of 67 m/ha. THRs' spatial distribution provides a partial connection between forested patches in the study area, enhancing landscape connectivity.
Combining different methodologies such as Remote Sensing, photo interpretation, GIS analysis and field survey we have detected the forest linear formations, mapped their spatial distribution, estimated their extent. The Sentinel 2 spatial resolution seem to be suitable for the detection of THRs at the typical farm scale. Further development of this technique could be useful for mapping and quantifying the current status of Italian agroforestry system at regional and national scale.

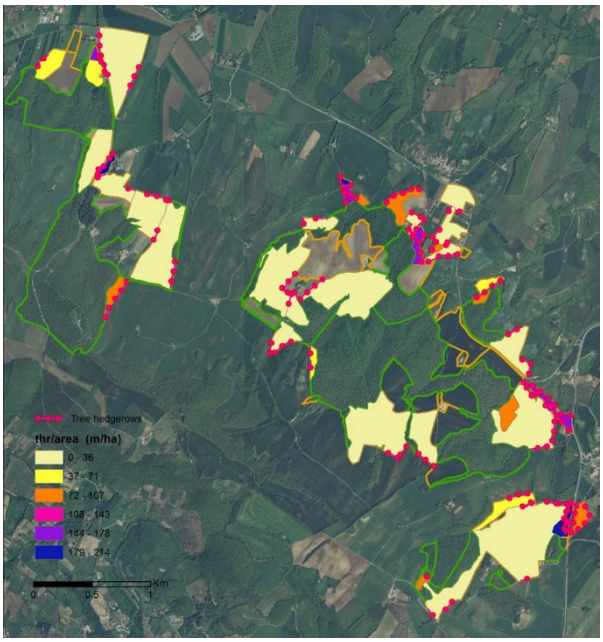

Figure 4. THR incidence per hectare of cultivated land in the study area

ACKNOWLEDGEMENTS

Research supported by SidaTim project in the framework of the EU's Horizon 2020 research and innovation programme under grant agreement No 652615 (FACCE-JPI). www.sidatim.eu/en/.

REFERENCES

Bellefontaine R, Petit S, Pain-Orcet M, Deleporte P, Bertault JG (2002) Trees outside forests. Towards better awareness. FAO Conservation Guide 35, Roma, Italy.

Eichhorn, M.P., Paris, P., Herzog, F. et al. (2006) Silvoarable Systems in Europe – Past, Present and Future Prospects. Agroforest Syst 67: 29-50. https://doi.org/10.1007/s10457-005-1111-7

European Space Agency (2016a). Sentinel scientific hub. Retrieved May 2016 https://scihub.copernicus.eu/dhus/#/home.

European Space Agency (2016b). Sentinel application platform. Retrieved July 2016 http://step.esa.int/main/toolboxes/snap.

European Space Agency (2016c). Sen2Cor. Retrieved June 2016 http://step.esa.int/main/third-party-plugins-2/sen2cor.

Facciotto G., Minotta G., Paris P., Pelleri F., 2015 – Tree farming, agroforestry and the new green revolution. A necessary alliance. In: Proceedings of the Second International Congress of Silviculture. Designing the future of the forestry sector. Florence, 26-29 November, 2014. Firenze: Accademia Italiana di Scienze Forestali. Vol. 2, p. 658-669. ISBN 978-88-87553-21-5. http://dx.doi.org/10.4129/2cis-gf-tre

FAO. 1998. FRA 2000 – terms and definitions. Forest Resources Assessment Programme Working Paper No. 1. Rome.

FAO (2001). Global forest resources assessment 2000. Main report. Food and Agriculture Organization of the United Nations, Rome.

Mosquera-Losada MR, McAdam JH, Romero-Franco R, Santiago-Freijanes JJ, Rigueiro-Rodríguez A (2009) Definitions and Components of Agroforestry Practices in Europe. In A. Rigueiro-Rodríguez et al. (eds.), Agroforestry in Europe: Current Status and Future Prospects.

QGIS Development Team (2018). QGIS Geographic Information System. Open Source Geospatial Foundation Project. http://qgis.osgeo.org.

Schnell, S., Kleinn, C. & Ståhl, G. Environ Monit Assess (2015) 187: 600. https://doi.org/10.1007/s10661-015-4817-7.

Shibu J (2009) Agroforestry for ecosystem services and environmental benefits: an overview. Agroforest Syst (2009) 76:1–10. DOI 10.1007/s10457-009-9229-7.

EVALUATING ACCURATE POPLAR STEM PROFILES BY TLS

N. Puletti[1*], M. Grotti[1], R. Scotti[2]

[1] Consiglio per la ricerca in agricoltura e l'analisi dell'economia agraria (CREA), Research Centre for Forestry and Wood – Viale Santa Margherita 80, Arezzo, - nicola.puletti@crea.gov.it, mirko.grotti@gmail.com
[2] NuoroForestrySchool-DipAgr-UniSS.it, scotti@uniss.it

KEY WORDS: Spacing; Plant density; Terrestrial laser scanner; Taper functions; Bole eccentricity

ABSTRACT:

The value of wood for different timber assortments can vary by a factor of ten, optimization of stems assortment is hence a key element in the wood products supply chain, particularly for plantations. 'Taper functions' are commonly used in other countries to tackle this issue. In Italy, this approach has not yet entered operational use. These functions are developed based on measures of stem diameters taken at different distances from the base. Such measurements are commonly taken felling the tree and using a tape meter and the tree calliper, clearly assuming some approximations. This research assesses the advantages, in terms of assortments evaluation, that can be obtained if the diameters at different heights are extracted adequately processing Terrestrial Laser Scanning (TLS) output. TLS data have been collected, in a poplar plantation, on 36 trees distributed on three stands with different plantation densities in Padana Plane, Italy. The estimated profiles display a very high variability with an average of 1.8 cm of lateral compression. The results from this study demonstrate the potential and feasibility of estimating bole eccentricity by TLS, providing preliminary tools that will hopefully favour the diffusion of taper functions in operational environments.

1. INTRODUCTION

The value of wood for different timber assortments can vary by a factor of ten. Optimal assortments allocation is thus a key element in the wood products supply chain, particularly for plantations. Stem profile is the first element to consider for assortments allocation.

The so called 'taper functions', geometric approaches commonly used to produce smoothed stem profiles (i.e. a vertical section of a tree stem), has not yet entered operational use in Italy. These functions are based on measures of stem diameters taken at different distances from the base. Such measurements are commonly taken felling the tree and using a tape meter and the tree calliper, clearly assuming some approximations.

More accurate measurement of tree parameters and detailed three-dimensional modelling of forest stands can be obtained by high density point clouds obtained using Terrestrial Laser Scanners (TLS). An overview on methods used for stem diameter estimation by means of TLS was given by Pueschel et al. (2013). In addition, the development of smallest and light-weighted devices makes their use in forest environments feasible (Eitel et al., 2013).

Three approaches for point-cloud data acquisition have been reported for TLS-based forest inventories: single-scan, multi-scan and multi-single-scan (see e.g. Liang et al., 2016). For stem diameters estimation, both multi-scan and single-scan have been used (Kelbe et al., 2015).

Traditional methods for diameter estimation by TLS are mainly based on circle-fitting methods from point clouds (see e.g. Koreň et al. 2017; Liang et al., 2014; Pueschel et al., 2013; Moskal and Zheng, 2012; Brolly and Király, 2009). This approach, assuming that all cross-sections are circles, obviously hides eventual bole eccentricities. Processing the most valuable assortments the bole must be reduced to a cylinder to initiate the peeling process. For these assortments, greater eccentricity implies more waste. The study has hence tested a different approach to diameter estimation better exploiting TLS data.

The general aim of this research is to improve assortments estimation of standing poplar plantation trees. Specific objective of this experiment is to assess poplar profiles sensitivity to competition anisotropy and to plantation density by FARO TLS. Lateral compression of horizontal stem cross sections (bole eccentricity) has been evaluated. In this plantation distances to neighbouring trees differ, depending on direction. Lateral compression is interpreted as an effect of this anisotropic competition.

2. MATERIAL AND METHODS

2.1 Data collection

TLS data were acquired using a Focus3D X 130 (FARO Technologies Inc., Florida, USA). The instrument uses a phase-shift based technology with a maximum range of 120 m and acquires data with a scan angle of 360°. It collects the x, y and z coordinates and the intensity of laser returns with a scan ranging noise of ± 1 mm (FARO, 2011). A complete description of the instrument can be found in Giannetti et al. (2018).

TLS data have been acquired in a 10 years old poplar plantation located in Viadana, Mantova, Northern Italy. The general layout of the plantation includes two poplar rows alternated with a row of other valuable (but less fast growing) species. (Figure 1, right). Distance between rows is fixed (9 m) while it varies along the rows, defining different stands: 4 m (*V-400*), 4.5 m (*V-450*) and 5 m (*V-500*). The stands grow in a flat and uniform terrain, cultivated since long time, they evidence no relevant site potential differences.

The data have been collected in these 3 neighbouring stands, one plot per stand, 12 trees per plot, for a total of 36 trees. Nine stations were used in each plot. At least four stations have a complete view of each studied tree (Figure 1, left).

* Corresponding author

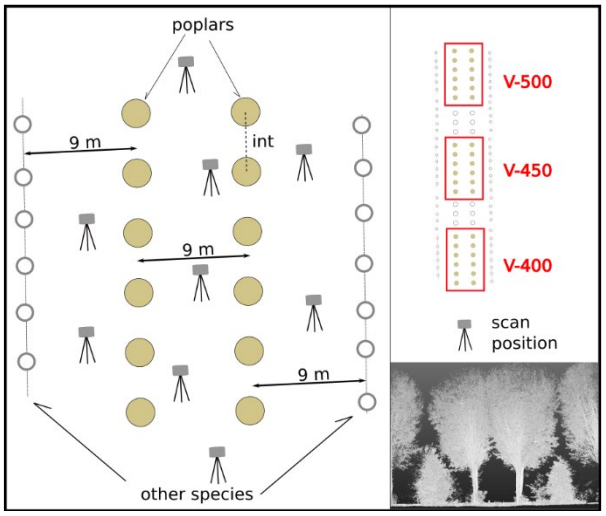

Figure 1 - Experimental design. Distance within rows ('int') is 400, 450 and 500 cm, respectively. In the lower right side, a point cloud profile in V-450 stand

2.2 Point cloud processing

2.2.1 Phase 1 – Isolation of individual boles

1. Merge of all TLS multi-scan point clouds for each plot, using Trimble Real Works® software (TRW, 2018);
2. rotate stand-level point clouds, setting tree-rows parallel to Y axes;
3. from stand-level point clouds, visually separate individual tree stems from the rest;
4. delimit boles considering stem portions up to 6 m height.

2.2.2 Phase 2 - Estimation of directional diameters

This phase was performed using R statistical software (R Core Team, 2018).

1. Isolate a 3 cm high slice every 10 cm from the base;
2. compute slice ranges, i.e. *xmin*, *xmax*, *ymin*, *ymax*;
3. to reduce the effects of minor local irregularities, instead of considering absolute extremes (max and mins), all points within 1 cm radius from each extreme have been considered to compute the local averages: *xmin_bar, xmax_bar, ymin_bar, ymax_bar*;
4. compute diameters in the two directions
    a. along the rows = *xmax_bar - xmin_bar*
    b. between rows = *ymax_bar - ymin_bar*

3. RESULTS

The analysis considers the lower part of the stems, up to 6 m height (Figure 2). The typical neiloidic shape, due to butt swell, and the transition to the paraboloidic shape of the central part of the bole are well recognizable in all the selected profiles. Single curves present some irregularities that are due to data extraction issues.

All stems exhibit some level of difference between the profile based on measurements taken along the row direction, where competition is higher because the neighbours are nearer (and bigger), and the orthogonal measurements, in the direction with the lowest competition.

Statistical analysis of breast height diameters quantitatively documents the effects of stand density and anisotropic competition (Table 1). Average diameter for the 4 m spacing is over 37 cm. Increasing the distance between trees along the row from 4 m to 4.5 m, average diameter increases 2 cm, further increasing to 5 m, average diameter grows almost one centimetre more.

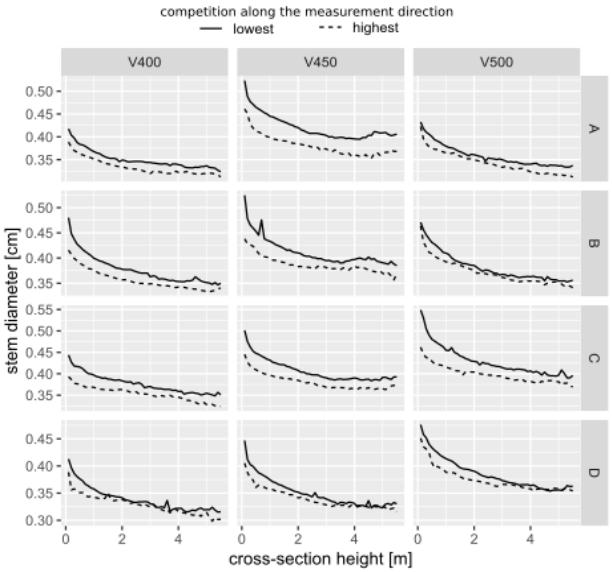

Figure 2 - Selected profiles, diameter measures are taken facing competitors

Moreover, the analysis evidences that, on average, breast height cross sections are compressed in the row direction: they are about 1.8 cm smaller than the orthogonal ones (Table 1).

Treatment	Estimate	std. error	statistic	*p-value*
V-400	37.54	0.54	69.56	0.0000
V-450	37.54+2.09	0.66	3.16	0.0024
V-500	37.54+2.60	0.66	3.93	0.0002
competition anisotropy	**-1.84**	**0.54**	**-3.40**	**0.0011**

Table 1. Lateral compression of dbh and plantation density effects

Average values and average variability have been computed pooling data from all profiles for each treatment. Cross section compression is evidenced considering the differences between the diameters measured in the two orthogonal directions: *i) along the rows*, where competition is higher and variable (4 to 5 meters to nearest competitor), and *ii) between rows* (lowest competition, 9 m to nearest competitor). The average differences for the treatment with less competition (5 m along the row) is consistently less than for cases with higher competition (4 m and 4.5 m to next competitor). Some irregularities appear in the lower part of the stem where, in the 4 m treatment, cross section compression is, on average, less than for the 4.5 m treatment (Figure 3).

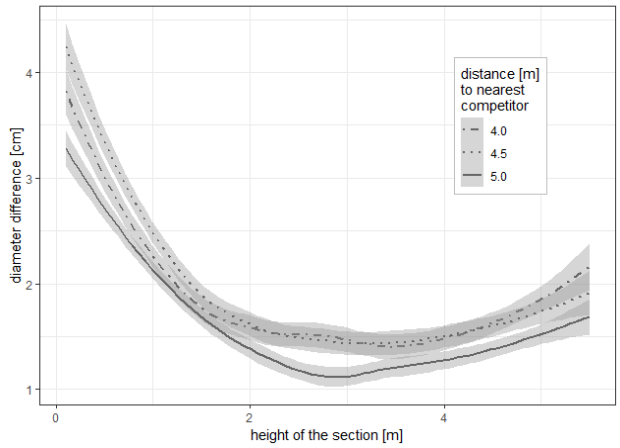

Figure 3 - Compression of the stem's horizontal cross sections, difference between diameter in low-competition-direction and that in high-competition-direction

4. DISCUSSION

Compared to traditional stem-profiles measurement methods, TLS evidently offers much greater precision and accuracy. This advantage has already been exploited for taper functions development and calibration (e.g. Holopainen et al 2011, White et al. 2016) but finer yet technologically limiting characteristics, such as lateral compression or bole straightness, have received little attention.

The considered plantation offered the opportunity to start exploiting TLS data in greater detail since the stands present different densities and an anisotropic competition structure. Present study concentrates on the evaluation of lateral compression of stem horizontal cross sections.

Procedures reliably estimating cross section's contours without pre-establishing its shape (namely assuming a circular shape) have to be better refined. Nonetheless proposed approximation allowed to evidence significant effects.

Namely the effects of plantation density as well as that of the difference in competitors distances placed at orthogonal directions have been quantified. Diameters difference, on average, are in the order of centimetres, a significant quantity in terms of volume.

5. CONCLUSIONS

Optimal management of the wood products supply chain is a very complex objective, even within plantation forestry. Trees growth requires years or decades and implies a great exposure to many different risks. The quality of the final products and hence timber prices depend on many internal and exogenous factors. Nonetheless precise evaluation of the shape and of the dimensions of the bole of standing trees is an inevitable step in the production process.

It is well known, for example, that stand density significantly reduces stem diameters but forecasting the extent of the reduction is not well developed. Moreover, there is a quality-quantity trade-off. Although, for an assessment in terms of total volume production, more detailed processing is required but the effect in terms of value is surely relevant: the price for a volume unit multiplies by a factor up to ten, as dimension exceed given thresholds. The analysis has produced a quantitative evaluation of this effect: having one meter more between trees along the rows, breast height diameters increase, on average, almost three centimetres. TLS enables a much more detailed evaluation of stem profiles than what was achievable with previous instruments. In the present analysis, considering the bole up to 6 m height, lateral compression has been significantly evidenced: an average of 1.8 cm compression has been observed on the sides facing the highest competition compared to the orthogonal direction.

Estimated profiles display a very high variability, possibly the estimation procedure needs to be refined. Extending the analysis to include an even less dense stand could be of interest.

The study has set the grounds for the development of 'competition aware' taper functions extending the exploitation of TLS data potential. Refining the diameters estimation procedure, it will be possible to develop functions estimating stem tapering (with eccentricity and straightness) considering plantation schema and inter-tree distances.

REFERENCES

Brolly, G., Király, G., 2009. Algorithms for stem mapping by means of terrestrial laser scanning. Acta Silv. Lign. Hung. 5, 119–130

Eitel, J.U.H., Vierling, L.A., Magney, T.S., 2013. A lightweight, low cost autonomously operating terrestrial laser scanner for quantifying and monitoring ecosystem structural dynamics. Agricultural and Forest Meteorology. Vol. 180, 5 October 2013, Pages 86-96. DOI: 10.1016/j.agrformet.2013.05.012

FARO, 2011. User Manual FARO Laser Scanner Focus 3D. available on-line at: https://doarch332.files.wordpress.com/2013/11/e866_faro_laser_scanner_focus3d_manual_en.pdf (1 July 2018)

Giannetti, F., Puletti, N., Quatrini, V., Travaglini, D., Bottalico, F., Corona, P., Chirici, G., 2018. Integrating terrestrial and airborne laser scanning for the assessment of single-tree attributes in Mediterranean forest stands. European Journal of Remote Sensing, 51:1, 795-807, DOI: 10.1080/22797254.2018.1482733

Holopainen, M., Vastaranta, M., Kankare, V., Räty, M., Vaaja, M., Liang, X., Yu, X., Hyyppä, J., Hyyppä, H., Viitala, R, Kaasalainen, S., 2011. Biomass estimation of individual trees using stem and crown diameter TLS measurements. ISPRS-International Archives of the Photogrammetry, Remote Sensing and Spatial Information Sciences. Volume XXXVIII-5/W12, 2011

Kelbe, D., Van Aardt, J., Romanczyk, P., Van Leeuwen, M., Cawse-Nicholson, K., 2015. Single-scan stem reconstruction using low-resolution terrestrial laser scanner data. IEEE Journal of Selected Topics in Applied Earth Observations and Remote Sensing. Vol. 8, Issue 7, 1 July 2015, Article number 7080835, Pages 3414-3427

Koreň, M., Mokroš, M., Bucha T., 2017. Accuracy of tree diameter estimation from terrestrial laser scanning by circle-fitting methods.

Liang, X., Kankare, V., Hyyppä, J., Wang, Y., Kukko, A., Haggrén, H., & Holopainen, M., 2016. Terrestrial laser scanning in forest inventories. ISPRS Journal of Photogrammetry and Remote Sensing, 115, 63–77

Liang, X., Kankare, V., Yu, X., Hyyppa, J., & Holopainen, M., 2014. Automated stem curve measurement using terrestrial laser scanning. IEEE Transactions on Geoscience and Remote Sensing, 52, 1739–1748

Moskal, L.M., Zheng, G., 2012. Retrieving forest inventory variables with terrestrial laser scanning (TLS) in urban heterogeneous forest. Remote Sens. 4 (1), 1–20. http://dx.doi.org/10.3390/rs4010001

Pueschel, P., Newnham, G., Rock, G., Udelhoven, T., Werner, W., Hill, J., 2013. The influence of scan mode and circle fitting on tree stem detection, stem diameter and volume extraction from terrestrial laser scans. ISPRS J. Photogramm. Remote Sens. 77 (March), 44–56. http://dx.doi.org/10.1016/j.isprsjprs.2012.12.001.

R Core Team (2018). R: A language and environment for statistical computing. R Foundation for Statistical Computing, Vienna, Austria. URL https://www.R-project.org/

Trimble Real Works, 2018. Trimble Real Works 6.5 User Guide All modules. Available on line at ftp://www.myconnectedsite.com/TCC/surveysalesam/SeanChard/Spatial%20Imaging/Trimble%20Realworks/TrimbleRealWorks%206.5%20User%20Guide%20-%20ALL%20MODULES.pdf (1 September 2018)

White, J.C., Coops, N.C., Wulder, M.A., Vastaranta, M., Hilker T., Tompalski, P., 2016. Remote sensing technologies for enhancing forest inventories: A review Canadian Journal of Remote Sensing 42 (5), 619-641 DOI: 10.1080/07038992.2016.1207484

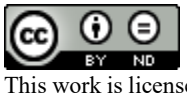

CLASSIFICATION OF DOMINANT FOREST TREE SPECIES BY MULTI-SOURCE VERY HIGH RESOLUTION REMOTE SENSING DATA

B. Del Perugia[1*], D. Travaglini[1], A. Barbati[2], A. Barzagli[1], F. Giannetti[1], B. Lasserre[3], S. Nocentini[1], G. Santopuoli[4], G. Chirici[1]

[1] DAGRI, Università degli Studi di Firenze, Firenze, Italy, - (barbara.delperugia, davide.travaglini, andrea.barzagli, francesca.giannetti, susanna.nocentini, gherardo.chirici)@unifi.it
[2] DIBAF, Università degli Studi della Tuscia, Viterbo, Italy, e-mail: barbati.sisfor@unitus.it
[3] DiBT, Università degli Studi del Molise, e-mail: lasserre@unimol.it
[4] Dip. A.A.A., Università degli Studi del Molise, e-mail: giovanni.santopuoli@unimol.it

KEY WORDS: Forest management, Tree species composition, RGB, LiDAR, Random forest, k-NN

ABSTRACT:

In this study we classified dominant forest tree species in a Mediterranean study area that hosted forest stands dominated by seven tree species, both coniferous and broadleaf, plus two mixed formations, for a total of nine classes. Airborne laser scanning data with a point density of 10 pts/m^2 and multispectral data (RGB and NIR) with 20 cm spatial resolution were taken using a helicopter. We divided the study area into a grid of quadrats of side 23 m and each quadrat was assigned to a dominant forest tree species class by visual inspection of remote sensing data. For each quadrat multispectral features and point cloud-derived metrics were extracted. For classification purposes, the quadrats were divided into training sites (35%) and test sites (65%). Two supervised classifiers were tested: Random Forest (RF) and k-NN. Several combinations of data sources were used. The accuracy of the supervised classifications was assessed against the visual one. The best accuracy of dominant forest tree species was obtained with RF using all data sources, achieving an overall accuracy of 71%. The overall accuracy increased up to 83% when forest categories (coniferous, broadleaf and mixed forest) instead of forest tree species were considered.

1. INTRODUCTION

Tree species composition is important to study forest ecosystems, to assess forest resilience and vulnerability and to estimate the forest's economic value (Abdollahnejad et al., 2017). Forest tree species composition is usually classified using largely subjective methods based upon ground-based visual observations by a surveyor. However, such approaches are time consuming and can suffer from a lack of consistency between surveyors. Airborne remote sensing platforms equipped with multispectral and/or laser scanning sensors provide very high spatial resolution data useful for forest classification and for the quantification of forest variables.

For land cover classification with remote sensing data, it is desirable to use multi-source data in order to extract as much information as possible. Remote sensing-assisted classification of tree species and land cover has been increased in the last decades, as it is prompted by a wide variety of applications from forest management, such as resource inventories (European Environmental Agency, 2007) and conservation sectors, including wildlife habitat mapping, biodiversity assessment and monitoring (Corona et al., 2011), but also in relation to the increased availability of airborne hyperspectral and LiDAR data (Fassnacht et al., 2016).

Several studies on tree species classification have been conducted in temperate forest ecosystems and in boreal forests (Fassnacht et al., 2016). Most of the temperate forest ecosystem's studies have been conducted in North America and in Central and Northern Europe (Chan and Paelinckx, 2008; Gislason et al., 2006), especially in Scandinavia, while the Mediterranean forests have been less investigated (Rodriguez-Galiano et al., 2012; Puletti et al., 2016).

Most studies have used multispectral and hyperspectral data (Chan and Paelinckx, 2008; Fassnacht et al., 2016; Dechesne et al., 2017), which range from moderate spatial resolution satellites (Gislason et al., 2006; Rodriguez-Galiano et al., 2012; Puletti et al., 2016) to very-high spatial resolution satellites and airborne sensors (Fu et al., 2017). Several studies combined more sensors type (Dalponte et al., 2014; Pelletier, 2016), like an active system (LiDAR) with a passive optical system (airborne multispectral and hyperspectral systems); in addition, some studies investigated the combination of multiple data sources, for example auxiliary (environmental) data for prediction of tree species (Gislason et al., 2006; Abdollahneiad et al., 2017).

Supervised classifiers are widely used since they are more robust than model-based approaches (Niemeyer et al., 2014). These classifiers are able to learn the characteristics of target classes from training samples and to identify these learned characteristics in the unclassified data (Belgiu et Dra, 2016). The Random Forest (RF) classifier is a reliable classification that uses predictions derived from an ensemble of decision trees (Breiman, 2001), while the k-Nearest Neighborn (k-NN) method is one of the simplest and most popular data-mining algorithms for classification and regression based on multidimensional distance search (Hudak et al., 2007; McRoberts, 2009).

The objective of this study is to compare the use of very high spatial resolution multispectral images and LiDAR point cloud data to classify dominant forest tree species in Mediterranean forests using two classifiers: RF and k-NN. The overall goal is to investigate how the combination of multi-source remote sensing data is helpful to increase the accuracy of forest tree species classification in the Mediterranean region.

2. MATERIALS AND METHOD

The work was carried out in the public forest district of Rincine (Tuscany, Italy). The study area extends over 275 ha. Elevation ranges between 520 m and 890 m a.s.l. Apennine Mountain forests can be very complex and challenging to classify. Relief

* Corresponding author

complexity and high anthropogenic influence result in a very heterogeneous forest landscape, thus seven dominant forest tree species and two mixed classes can be distinguished in the study area. The most common species are Douglas fir, Turkey oak, Black pine and Sweet chestnut.

In May 2015 a flight was carried out by GEOCART society using an Eurocopter AS350 B3 equipped with a Riegl LMS-Q680i laser scanner and a Digicam H39 RGB and NIR optical instrument. A full-waveform airborne laser scanner (ALS) data was registered and discretized to a point density of 10 pts/m^2. The maximum laser scanning angle was 60° resulting in an average SWAT of 1100 m, the pulse frequency was 300 kHz with 80 lines per second and 2500 lines per line. The wavelength used was 1550 nm. Standard pre-processing with LAStools software was used to remove noise in the ALS data and echoes were classified as ground/non-ground. From this data, a Digital Terrain Model (DTM) with a spatial resolution of 1 m was produced. The DTM was used to normalize the heights of non-ground points in order to convert heights above sea level into relative heights above the ground.

Digital orthophotos with 20 cm spatial resolution were taken with a pair of cameras, an RGB and a color infrared (CIR) camera. From the digital orthophotos, the Normalized Difference Vegetation Index (NDVI) with a spatial resolution of 20 cm was obtained using the red and NIR bands.

Auxiliary data on forest tree species composition were obtained by categorical map and forest inventory plots. A pre-existing forest types map (scale 1:10,000) of the forest district of Rincine was acquired. A local forest inventory was carried out in the study area in 2016. A sample of 50 inventory plots was selected using the one per stratum stratified sampling scheme (Fattorini et al., 2015). To do this, the study area was divided into a grid of quadrats of side 23 m, corresponding to the size of the inventory plots (529 m^2). The study area was partitioned into 50 strata of the same size, and one sample plot (i.e., one quadrat) was independently and uniformly selected in each stratum. The x,y coordinates of the plot centre were collected using the Trimble Juno 3B receiver with a positional error of 2-5 m. In each plot, all trees with DBH > 2.5 cm were inventoried. For each tree the species was noted and the DBH was measured.

We used the grid of quadrats of the forest inventory sampling scheme as spatial reference for the classification of the forest tree species. Each quadrat was classified into forest and non-forest by visual inspection of digital orthophotos. Non-forest quadrats were excluded from the analysis.

A two levels hierarchical classification system was adopted. The first level (Level 1) refers to the classification of dominant forest tree species and consists of nine classes, seven pure and two mixed classes; the second level (Level 2) refers to the classification of forest categories and consists of three classes, two pure and one mixed class (Table 1). Each quadrat was classified into one class of Level 1 and Level 2 by visual inspection. Mixed classes were considered when individual species were less than 75% of crown cover.

The semiautomatic classification was carried out using the multi-source data acquired by helicopter. For each quadrat both multispectral features and point cloud-derived metrics were computed. QGIS 2.14.13 software (QGIS developing team 2016) was used to extract multispectral features from RGB, NIR and NDVI images (for a total of 10 multispectral features). LAStool (rapidlasso GmbH developing team 2016) and R 3.4.1 statistical software (r-project developing team 2016) were used to compute point cloud-derived metrics (a total of 57 metrics). Several combinations of data sources were tested: RGB, NIR, NDVI and point cloud alone, and all data sources.

For classification purposes, the quadrats were divided into training sites and test sites with the following percentage breakdown: 35% training and 65% test (Table 1). Two supervised classifiers were tested: RF and k-NN.

We used the randomForest package within the statistical software R (Rodriguez-Galiano et al., 2012; Ghosha et al., 2014; Belgiu and Dra, 2016). Based on previous studies (Liaw and Wiener, 2002; Gislason et al., 2006) and after some tests, we set the RF parameters for our study as m = 12 (m=√p, where p is the number of input variables considered) and *Ntree* = 500.

The k-NN algorithm present in the caret package was used. According to McRoberts (2009), a value of k ranging between 1 and 20 is the best option for using the k-NN algorithm. In our study, the optimal k value for k-NN algorithm was k = 5.

Species		Leve 1 - 9 classes			Level 2 - 3 classes		
Code	**Tree species / forest categories**	**N of quadrats**	**Training (%)**	**Test (%)**	**N of quadrats**	**Training (%)**	**Test (%)**
1	Sweet chestnut	464	37	63	-	-	-
2	Turkey oak	575	44	56	-	-	-
3	Douglas fir	1239	33	67	-	-	-
4	European beech	48	40	60	-	-	-
5	Coniferous and broadleaf mixed forest	306	29	71	306	29	71
6	Broadleaf mixed forest	1290	31	69	-	-	-
7	European alder	43	47	53	-	-	-
8	Black pine	789	39	61	-	-	-
9	Downy oak	46	39	61	-	-	-
10	Coniferous	-	-	-	2028	35	65
11	Broadleaf	-	-	-	2466	36	64
Total		4800	35	65	4800	35	65

Table 1. Percentage of training sites and test sites divided by level.

The accuracy of the classification by photointerpretation was assessed using the forest inventory plots (50 quadrats) as ground truth while the accuracy of the classification by semiautomatic methods (RF and k-NN) was assessed using the test sites as ground truth.

We used four indices to assess the accuracy of the classification: overall accuracy (OA), producer's accuracy (PA), user's accuracy (UA) and kappa index of agreement (KIA).

3. RESULTS

The OA of the classification by photointerpretation was 92% for dominant forest tree species and 96% for forest categories.

The OA and KIA of the semi-automatic classification by RF and k-NN are presented in Table 2. The RF algorithm had a slightly higher performance compared to k-NN algorithm for classification of both dominant forest tree species (Level 1) and forest categories (Level 2).

	Level 1				Level 2			
	RF		k-NN		RF		k-NN	
	OA (%)	KIA	OA (%)	KIA	OA (%)	KIA	OA (%)	KIA
All data	70.5	0.628	67.3	0.589	83.4	0.777	82.3	0.732
RGB	64.7	0.553	60.4	0.488	82.2	0.673	80.3	0.608
NIR	46.7	0.318	44.1	0.286	73.6	0.504	72.5	0.445
NDVI	43.8	0.281	42.1	0.264	68.0	0.381	67.1	0.346
Point cloud	62.5	0.523	58.5	0.472	78.5	0.652	77.5	0.600

Table 2. Overall accuracy (OA) and Kappa Index of Agreement (KIA) of the classification by thematic level.

Using source variable individually for classification of dominant forest tree species by RF, the OA ranges between 43.8% and 64.7%. RGB images were the best data source among the variables taken by helicopter. However, the best OA was obtained by RF using all multi-source variables (OA = 70.5%). As expected, the accuracy of the classification increased when only forest categories were considered (OA = 83.4%). For dominant forest tree species, the UA was > 70% for five out of nine species: turkey oak, Douglas fir, European alder, Black pine and Downy oak. The worst result was for Coniferous and broadleaf mixed forest class. PA was > 70% for Douglas fir, Black pine and the Broadleaf mixed forest class. Regarding the forest categories classification, UA and PA were greater than 70% for pure classes of Coniferous and Broadleaf. Figure 2 shows the spatially explicit distribution of the dominant forest tree species in the study area obtained with RF algorithm using multi-source data from helicopter.

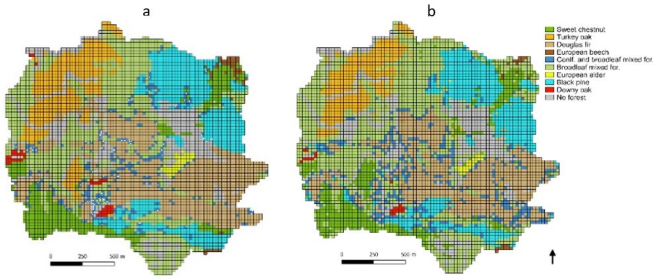

Figure 2. Spatial distribution of tree species by photointerpretation (a) and by RF classification using multi-source data (b).

4. DISCUSSION

Our results confirm that the combination of multi-source remote sensing data is helpful to increase the accuracy of the classification of dominant forest tree species. When multispectral variables were combined with LiDAR point cloud-based metrics the accuracy of the classification increased by 9%. The best OA for the classification of nine dominant forest tree species (Level 1) was 71% using multi-source data with RF algorithm. The results reported by other authors for tree species classification in boreal forests are higher than those we obtained in the Mediterranean environment, where the number of species to be classified is usually higher. However, our results are similar to those of other authors who have attempted to classify more than five species. For instance, Dechesne et al. (2017) in France, lead a study on segmentation and classification of forest stands with six tree species combining airborne LiDAR data and very high-resolution multispectral imagery, achieving an OA = 73% using RF classifier. Abdollahnejad et al. (2017) in Iran, predicted seven dominant forest tree species using very high-resolution multispectral satellite images and environmental data with 64% accuracy using RF algorithm. For the classification of three forest categories (Level 2) the best result was obtained using multi-source data with RF, which gave 83% overall accuracies. Puletti et al. (2016) in the Apennines mountain used RF to classify coniferous and broadleaf with hyperspectral images from Hyperion satellite obtaining an OA of 94%.

5. CONCLUSIONS

This study proves the contribution of very high spatial resolution multispectral images and point cloud data for classification of dominant forest tree species in the Mediterranean environment. The combination of spectral features with height, textural and density metrics increase classification accuracy when compared to spectral data only. The Random Forest algorithm provided slightly higher performances compared to k-NN algorithm for classification of forest tree species. The best overall accuracy was achieved with Random Forest by combining multispectral information and point cloud data.

ACKNOWLEDGEMENTS

Work carried out under the FRESh LIFE project: “Demonstrating Remote Sensing integration in sustainable forest management” (LIFE14_ENV/IT/000414).

REFERENCES

Abdollahnejad, A., Panagiotidis, D., Joybari, S.S., Surový, P., 2017. Prediction of Dominant Forest Tree Species Using QuickBird and Environmental Data. Forests 8(2):19. doi: 10.3390/f8020042

Belgiu, M., Dra, L., 2016. A review of applications and future directions ISPRS 114:24–31. doi: 10.1016/j.isprsjprs.2016.01.011

Breiman, L.E.O., 2001. Random Forests. Machine Learning, 45, 5–32

Corona, P., Chirici, G., McRoberts, R. Winter, S., Barbati, A., 2011. Contribution of large-scale forest inventories to biodiversity assessment and monitoring. Forest Ecology and Management 262, 11, 2061-2069

Chan, J.C.W., Paelinckx, D., 2008. Evaluation of Random Forest and Adaboost tree-based ensemble classification and spectral band selection for ecotope mapping using airborne hyperspectral imagery. Remote Sens Env 112 2999–3011

Dalponte, M., Ørka, H.O., Gobakken, T., Gianelle, D., Næsset, E., 2013. Tree species classification in boreal forests with

hyperspectral data. IEEE Trans. Geosci. Remote Sens. 51 (5), 2632–2645.

Dechesne, C., Mallet, C., Le Bris, A., Gouet-Brunet, V., 2017. Semantic segmentation of forest stands of pure species combining airborne lidar data and very high-resolution multispectral imagery. Journal of Photogrammetry and Remote Sensing 126 129–145

European Environmental Agency, 2007. European Forest Types: Categories and Types for Sustainable Forest Management Reporting and Policy. (No. EEA Terchnical Report No 9/2006). http://www.env-edu.gr/Documents/European%20forest%20types.pdf

Fassnacht, F., E., Latifi, H., Stereńczak, K., Modzelewska, A., Lefsky, M., Waser, L., Straub, C., Ghosh, A., 2016. Review of studies on tree species classification from remotely sensed data. Remote Sensing of Environment, 186, 64–87. Doi: 10.1016/j.rse.2016.08.013

Fattorini, L, Corona, P, Chirici, G, Pagliarella, MC., 2015. Design-based strategies for sampling spatial units from regular grids with applications to forest surveys, land use and land cover estimation. Environmetrics, 26, 216-228.

Fu, B., Wang, Y., Campbell, A., Lia, Y., Zhanga, B., Yind, S., Xinga, Z., Jina, X. 2017. Comparison of object-based and pixel-based RF algorithm for wetland vegetation mapping using high spatialresolution GF-1 and SAR data. Ecological Indicators 73, 105–117

Ghosh, A., Ewald, F., Joshi, P., K., Koch, B., 2014. A framework for mapping tree species combining hyperspectral and LiDAR data: Role of selected classifiers and sensor across three spatial scales. Int J Appl Earth Obs Geoinf 26:49–63.

Gislason, P.O., Benediktsson, J.A., Sveinsson, J.R, 2006. Random Forests for land cover classification. Pattern Recognition Letters 27

Hudak, A., Crookston, N., L., Evans, J., S., Hall, D., E., Falkowski, M., J., (2007). Nearest neighbor imputation of species-level, plot-scale forest structure attributes from LiDAR data. Remote Sensing of Environment 112 (2008) 2232–2245 doi: 10.1016/j.rse.2007.10.009

Liaw, A., Wiener, M., 2002. Classification and Regression by randomForest. R News, Vol. 2, No. 3. (2002), pp. 18-22.

McRoberts, R., 2009. Diagnostic tools for nearest neighbors techniques when used with satellite imagery. Remote Sens Env 113

Niemeyer, J., Rottensteiner, F., Soergel, U., 2014. ISPRS Journal of Photogrammetry and Remote Sensing Contextual classification of lidar data and building object detection in urban areas. ISPRS J Photogramm Remote Sens 87:152–165. doi: 10.1016/j.isprsjprs.2013.11.001

Pelletier, C., Valero, S., Inglada, J., Champion, N., Dedieu, G., 2016. Remote Sensing of Environment Assessing the robustness of Random Forests to map land cover with high resolution satellite image time series over large areas. Remote Sens Env 187:156–168.

Puletti, N., Camarretta, N., Corona, P., 2016. Evaluating EO1-Hyperion capability for mapping conifer and broadleaved forests, European Journal of Remote Sensing, 49:1, 157-169, DOI: 10.5721/EuJRS20164909

Rodriguez-Galiano, V.F., Ghimire, B., Rogan, J., Chica-Olmo, M., Rigol-Sanchez, J.P., 2012. An assessment of the effectiveness of a random forest classifier for land-cover classification. ISPRS Journal of Photogrammetry and Remote Sensing 67, 93–104.

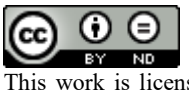

ALS DATA FOR DETECTING HABITAT TREES IN A MULTI-LAYERED MEDITERRANEAN FOREST

G. Santopuoli[1,2,3]*, M. Di Febbraro[2], C. Alvites[2], M. Balsi[4], M. Marchetti[2,3], B. Lasserre[2]

[1]Dipartimento di Agricoltura, Ambiente e Alimenti, Università degli Studi del Molise, Via De Sanctis snc, 86100 Campobasso, Italy – giovanni.santopuoli@unimol.it

[2] Dipartimento di Bioscienze e Territorio, Università degli Studi del Molise, Cda Fonte Lappone snc, 86090 Pesche (IS), Italy – (mirko.difebbraro, cesar.alvites, lasserre)@unimol.it

[3] Centro di ricerca per le Aree Interne e gli Appennini (ArIA), Università degli Studi del Molise, Via De Sanctis snc, 86100 Campobasso, Italy – (giovanni.santopuoli, marchettimarco)@unimol.it

[4] Dipartimento di Ingegneria dell'Informazione, Elettronica e Telecomunicazioni, Università degli Studi di ROMA "La Sapienza", Via Eudossiana 18, 00184 Roma – marco.balsi@gmail.com

KEY WORDS: Habitat Trees; Forest Biodiversity, LiDAR, Tre-Related Microhabitat; Sustainable Forest Management

ABSTRACT

Among the wide pool of ecosystem services provided by forests to human wellbeing, biodiversity conservation represents one of the most important topics of Sustainable Forest Management. Monitoring forest biodiversity is a challenging task as it includes all the life forms that can be found in a forest. However, the availability of inventory data is often inadequate to assess the biodiversity value of forests, therefore requiring improvements in monitoring activities and methods. In the last decades, several improvements have been made to reduce costs for collecting data and supporting monitoring and management activities. Particularly, remote sensing techniques have provided a significant contribution to forest and natural resource management and planning. Nevertheless, most of the information concern to the forest canopy and photosynthesis responses quantified through vegetation indices. Few information are available about tree habitats and other important ecological features. This study aims to demonstrate how ALS data can contribute to assess forest biodiversity through the detection of Habitat Trees. We use the Tree-Related Microhabitats, such as cavities, dead branches, injuries and woods, as a proxy to identify Habitat Trees and correlate them to the ALS metrics. Four statistical models were implemented to assess and map the biodiversity value in a mixed and multi-layered forest in Central Apennine.

1. INTRODUCTION

Monitoring forest biodiversity is not only linked to the tree species diversity, but refers to all the life forms that can be found in the forests (Conference Of the Parties; COP 2 Decision II/9).

Several authors focused on developing methods to assess and correlate forest structure and biodiversity. Nevertheless, the most common set of Indicators for Sustainable Forest Management, and in particular those related to criterion 4 "*Maintenance, conservation and appropriate enhance-ment of biological diversity in forest ecosystems*" (MCPFE 2002), are mostly concerned with the assessment of tree species diversity, regeneration, naturalness, introduced tree species, deadwood, genetic resources, forest fragmentation, threatened forest species and protected forests. These Indicators represent the most common tool to assess forest biodiversity across Pan-European countries, although information is rather limited to assess the habitat value of forests for several reasons. Firstly, field inventory activities are strongly expensive and time consuming. Moreover, there are no information about "all life forms", as Indicators focused only on the trees species.

As regards the first point, remote sensing techniques have been recognized as very valuable tool in supporting biodiversity monitoring. In fact, they provide significant contribution to monitor and assess forest biodiversity, especially for forest fragmentation (Chirici *et al.*, 2012; Santi *et al.*, 2017) and naturalness (McRoberts *et al.*, 2012) with relative low costs.

As concerns the amount of information provide by Indicators, many authors agreed on the fact that Tree-Related Microhabitats (TreMs) are strongly important to increase forest biodiversity as they represent ecological niches of several living organisms (Bütler *et al.*, 2013; Kraus and Krumm, 2013; Larrieu *et al.*, 2018). Since 1993, different classification systems have been developed across Europe in order to assess their occurrence, frequency and habitat value (Winter and Möller, 2008; Kraus *et al.*, 2016; Larrieu *et al.*, 2018). For these reasons, it is strongly important to develop automatic methods to recognize and assess the habitat values of both single trees and forests. For this purpose, monitoring activities should move from the forest structure to the tree structure target, as many living organisms live in the particular niches that are present on the tree' trunks and crowns.

Since monitoring single trees is a demanding challenge, we describe an experimental approach to detect the abundance of TreMs using LiDAR could points. The frequency and abundance of these particular niches allow to identify Habitat Trees, which play a significant role for the conservation of biodiversity. Thus, the aim of this study is to verify whether or not Airborne Laser Scanner (ALS) data can support the prediction of Habitat Trees within a mixed and multi-layered Mediterranean forest. Habitat Trees are trees hosting TreMs as cavities, injuries and wounds, bark structure, deadwood, growth form or epiphytes.

Although Habitat Trees are not included in the indicators set for SFM developed by Forest Europe process, they could be considered as valid ecological indicators. In the last decade, the topic of TreMs has become common among forest researchers, with several studies evaluating the occurrence and abundance of TreMs, and correlating their frequency with different forest management systems or with the forest ownership regimes, developing practical classifications systems currently used at the European level. Importantly, TreMs are not only linked to the deadwood, which is the most common biodiversity indicator used at European scale, but also to the living trees. This is very important as Habitat Trees are among the largest trees occurring in a forest, also representing potentially conflictual trees because of their value for biodiversity and timber production. Data on the TreMs occurrence and frequency can support forest technicians to balance timber production and conservation of biodiversity and thus to address the selection of trees for harvesting activities.

* Corresponding author

2. MATERIALS ANS METHODS

2.1. Study area

The study was carried out in Bosco Pennataro (Figure 1), a mixed and multilayer forest in Molise Region, Central Apennine, Italy. Bosco Pennataro is characterised by a high number of trees species (Figure 1), though *Quercus cerris* L. and *Fagus sylvatica* L. are the most frequent ones. At regional level, the forest plays a significant ecological and cultural role as it is one of the five regional forests, it is part of the Natura 2000 site (code IT7212124), and it has been recognized as a core area of the *Collemeluccio - Montedimezzo Alto Molise* Man and Biosphere reserve. Currently, the forest management system is high forest with continuous canopy cover and uneven aged trees.

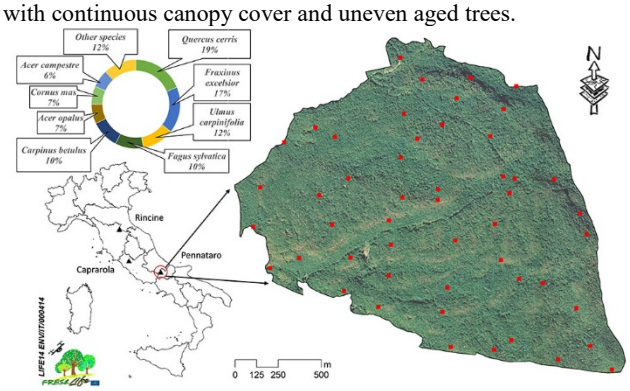

Figure 1. Study area. Geographical location of Bosco Pennataro and the other sites of FRESh LIFE project. Distribution of sampling plots across Bosco Pennataro (red squares). Tree species composition of forest (top-left).

2.2. Field data collection

We collected field data of tree diameter at breast height, tree height, crown length, tree vitality and tree position using Field-Map technology (http://www.fieldmap.cz). TreMs were observed using the classification system by Winter and Möller (2008), considering only the TreMs of standing trees and leaving out the TreMs on fallen deadwood (Figure 2). Data was collected during the demonstration FRESh Life project (*LIFE14 ENV/IT/000414*).

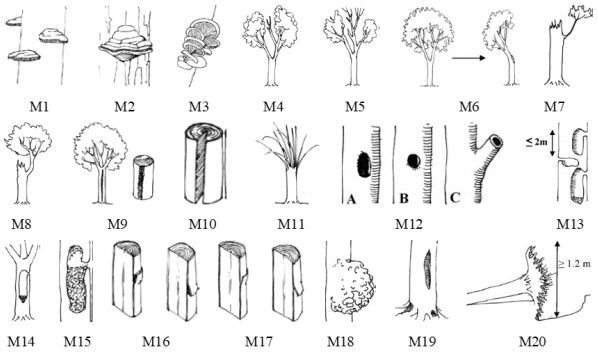

Figure 2. Tree-related Microhabitats (TreMs) classification used for the field survey. Further detail on the TreMs description can be found in Winter and Möller 2008.

2.3. ALS data acquisition

The ALS dataset was collected using YellowScan LiDAR, mounted on a light conventional helicopter. Data were taken in a single flight, on March 2016 and the LiDAR instrument was operated by Oben srl (www.oben.it). Dimensions, weight and autonomy of YellowScan LiDAR are 17 × 21 × 15 cm^3, 2.1 kg, and 3 h, respectively. The system provides up to three echoes per shot, allowing to get topographic information under vegetation cover.

The sensor was set with a maximum scan angle of +/-50°, and a pulse frequency of 20 KHz, resulting in an average density of 30 pulses/m^2. The raw ALS data were elaborated using LAStools software (https://rapidlasso.com).

From the original points cloud, 38 canopy metrics were extracted using LAStools to be correlated with biodiversity variables such as Habitat Trees and TreMs.

2.4. Modelling approach to estimate forest biodiversity variables

From the initial set of 38 ALS metrics, we applied a multicollinearity filter by retaining only variables exhibiting a variance inflation factor ≤ 5 (Zuur, Ieno and Elphick, 2010), and obtained the following ten ALS metrics: *min, std, kur, b10, b90, c00, c02, d00, dns_gap and max*, which were scaled to unit variance. Since the selected forest attributes were calculated as count data, we tested their statistical relationship with the ALS metrics by using Generalized Linear Models (GLM). In particular, we fitted two GLMs (Figure 3) for each forest biodiversity attribute, i.e. one with a Poisson and another with a Negative Binomial distribution of errors, both including linear and quadratic terms. For each GLM, we run a stepwise variable selection procedure based on the Akaike Information Criterion (AIC; Akaike, 1974), as implemented in the R package "MASS" (Venables and Ripley, 2002). In addition, we evaluated the effect of potential outliers on the resulting GLMs by calculating the Cook's distance *D* (Cook, 1977). Specifically, we dropped all the observations showing a Cook's *D* greater than three times the average *D* value calculated among all the observations (Cook, 1977), then refitting GLMs with the remaining data. For each GLM, we evaluated the goodness-of-fit by calculating the coefficient of determination (R^2) and the Root Mean Square Error (RMSE). RMSE was also used in a *leave-one-out* procedure to quantify GLMs predictive performance.

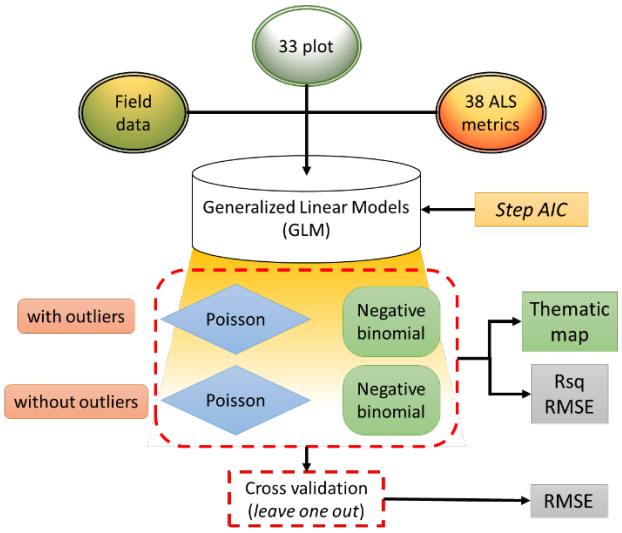

Figure 3. Modelling framework.

Subsequently, for each forest biodiversity variable, a raster map was provided for displaying the biodiversity value of Bosco Pennataro.

2.5. Results and discussion

Tree species composition partly confirms Bosco Pennataro biodiversity value. In fact, forest biodiversity is also stressed by the high variability of tree density, mean tree height and mean tree diameters among plots as well as basal area (G) and tree volume (Table 1). The past forestry interventions favoured an increase of complexity in forest structure across the forest. Historically, Bosco Pennataro represented an important source of timber and Non-Timber Forest Products, even if over the years,

particularly after the shift of forest ownership from the State to regional administration, forestry interventions have decreased. Nowadays, harvesting activities regards only fire prevention, sanitation cutting to allow recreational activities and few forestry interventions for scientific purposes. The abandonment of forestry interventions has contributed to the aged of forest stands with consequent shifting of forest structure from even-aged to uneven-aged and a high variability of number of trees per hectare among forest stands.

Nevertheless, beyond the forest structure, tree structure offers a deeper evaluation of forest biodiversity. Results show that there is also a high variability of Habitat Trees, ranging from 4 to 32 per plot, abundance of TreMs ranging from 6 to 61 per plot, and TreMs types, which range from 2 to 8 per plot.

The most frequent TreMs encountered in the forest are: cavities, broken stems and trees with <50% of the crown broken.

	Min	1st Qu	Median	Mean	3rd Qu	Max
Tree (N/plot)	24.00	43.25	57.00	68.94	93.25	196.00
Tree (N/ha)	454.0	817.5	1077.5	1303.2	1762.8	3705.0
Tree species (plot)	3.00	7.00	7.50	7.68	9.00	11.00
Average DBH (cm)	10.00	13.00	16.00	16.42	19.00	27.00
H max (m)	17.60	24.80	28.40	28.10	31.07	39.60
G (m^2/ha)	19.90	33.17	37.60	37.62	42.20	53.10
V (m^3/ha)	142.0	311.2	372.5	387.2	447.8	647.0
Habitat Trees	4.00	11.00	15.00	16.56	20.75	32.00
TreMs	6.00	17.25	23.50	25.14	30.00	61.00
TreMs Type	2.00	5.00	5.00	5.38	6.00	8.00

Table 1. Ground data summary results. Descriptive statistics of the main forest structure and biodiversity variables from the ground.

As regards the modelling approach, results show that outliers affect models implementation, providing better results when GLMs have been fitted without outliers (Table 2). Moreover, Negative Binomial is the best performing modelling approach in all the cases.

	Model	df	AIC	R^2	RMSE	Pred. RMSE
Habitat Trees	*M_pois*	13	222.5	0.7	4.5	179.2
	M.NO_pois	**15**	**201.8**	**0.8**	**3.4**	**333.8**
	M_nb	14	223.8	0.6	4.5	14.8
	M.NO_nb	**16**	**203.8**	**0.8**	**3.4**	**12.5**
TreMs	*M_pois*	17	252.4	0.7	6.4	164.1
	M.NO_pois	**15**	**226.2**	**0.8**	**5.9**	**25.1**
	M_nb	14	248.9	0.6	6.9	16.0
	M.NO_nb	**12**	**225.6**	**0.7**	**6.3**	**16.3**
TreMs Type	*M_pois*	1	136.4	0.0	1.3	
	M.NO_pois	1	123.7	0.0	1.2	
	M_nb	2	138.4	0.0	1.3	
	M.NO_nb	2	125.7	0.0	1.2	

Table 2. Modelling approach summary results. Main statistical results of the model approaches implementation. M_pois "Poisson model"; M_nb is "Negative Binomial model"; NO is "no outliers". Bold character indicates the best performant model.

In detail, for detection of Habitat Trees, both Poisson and Negative Binomial GLMs show similar performances (Figure 4) in terms of RMSE and R^2 (3.4 and 0.8 respectively). Nevertheless, the AIC values seem to tend towards the Poisson rather than the Negative Binomial approach (201.8 and 203.8 respectively), while the difference is significantly relevant for prediction accuracy (333.8 and 12.5 respectively). Thus, the Negative Binomial is better than Poisson model at predicting Habitat Trees (Figure 5).

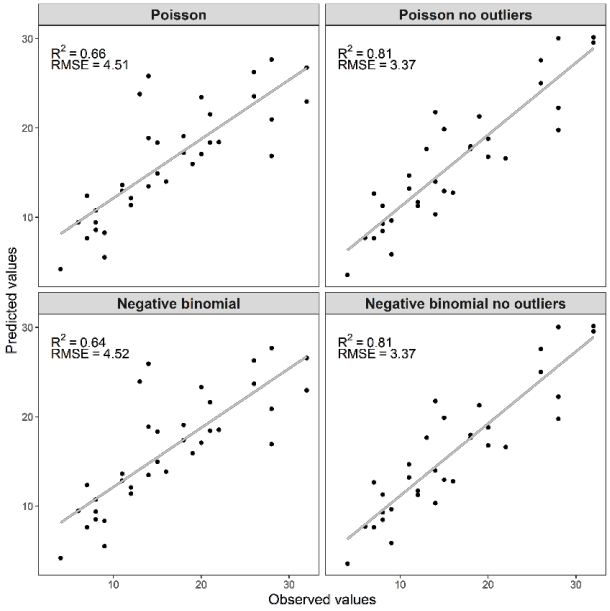

Figure 4. Goodness-of-fit for Habitat Trees. Comparison of the observed vs. predicted values for the 4 modelling approaches for detection of Habitat Trees.

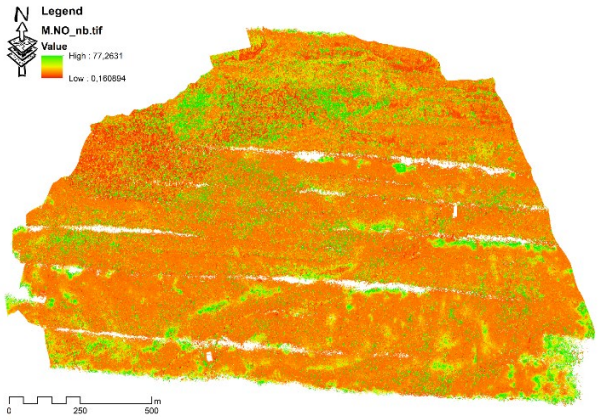

Figure 5. Habitat Trees prediction. Prediction of the Habitat Trees according the Negative Binomial no outliers approach.

As regards the detection of TreMs, the Poisson approach shows value of R^2 and RMSE slightly better than Negative Binomial (Figure 6). Nevertheless, the Negative Binomial results are somewhat better performing to prediction of TreMs (Figure 7), since the RMSE is moderately lower.

Finally, as regard the detection of TreMs Type, the study reveals that all the modelling approaches failed. We have two main reasons for this. Firstly, to image that ALS data can distinguish different type of cavities or different type of fruiting bodies on the trees is rather difficult. Second, the scarcely occurrence for some TreMs hinder their detection and of course their prediction.

By contrast, this non-result demonstrates that the approach is robust because it works only with a consistent quantity of data.
This leave a light to think that a deeper investigation could provide more detailed data allowing a better detection of single TreMs. Maybe the integration of ground data, with ALS, Terrestrial laser scanning data and multispectral images could improve the detection and prediction of TreMs and thus support the SFM.

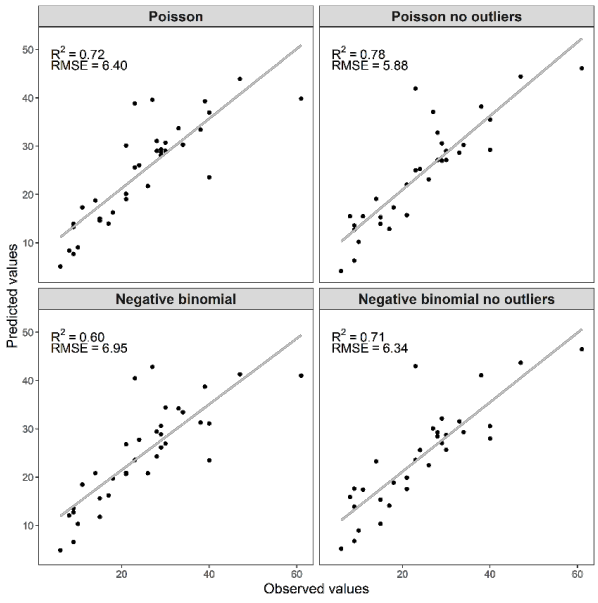

Figure 6. Goodness of fit for TreMs. Comparison of the observed vs predicted values for the 4 modelling approaches for detection of TreMs.

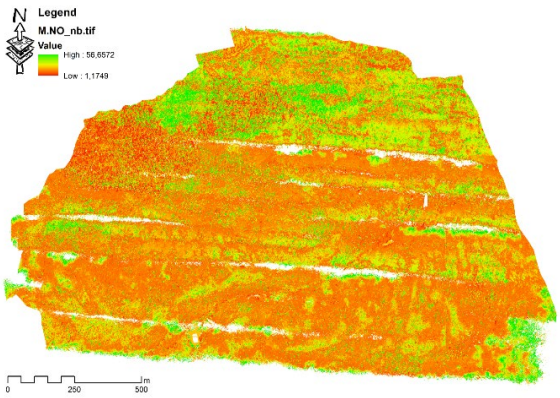

Figure 7. TreMs prediction. Prediction of the TreMs according the Negative bionomial no outliers approach.

3. CONCLUSION

This study introduces an approach to assess forest biodiversity based on the occurrence and abundance of Tree-Related Microhabitats.
Some weaknesses are still present and a deeper investigation is necessary. Maybe the integration of different source of remote sensing data could improve the detection approach. However the study shows a good results for Habitat Trees, and frequency of TreMs. Nevertheless, it was observed that the prediction of single microhabitats depends from their frequency, because without a significant number of occurrences the analysis failed.
In conclusion, ALS data are useful to detect Habitat Trees, and thus to support forest decision makers and managers in the assessment of forest biodiversity.

ACKNOWLEDGEMENTS

This research was supported by the LIFE program and the Italian Academy of Forest Sciences, in the framework of the project "FRESh LIFE—Demonstrating Remote Sensing integration in sustainable forest management" (LIFE14 ENV/IT/000414). We thank Marco di Cristofaro, Paolo Picone, Igino Di Schiavi and Micael Petruccioli for their support in the collection of ground data. Finally, we thank the former Ufficio Territoriale per la Biodiversità di Isernia, for their support and assistance during the fieldwork.

REFERENCES

Akaike, H. (1974) 'A new look at the statistical model identification', *Automatic Control, IEEE Transactions on*, pp. 716–723. doi: 10.1109/TAC.1974.1100705.

Bütler, R. *et al.* (2013) 'Habitat trees: key elements for forest biodiversity', *Integrative approaches as an opportunity for the conservation of forest biodiversity*, p. 84.

Chirici, G. *et al.* (2012) 'National forest inventory contributions to forest biodiversity monitoring', *Forest Science*, 58(3), pp. 257–268. doi: 10.5849/forsci.12-003.

Cook, R. D. (1977) 'Detection of Influential Observation in Linear Regression', *Technometrics*. Taylor & Francis, Ltd.American Statistical AssociationAmerican Society for Quality, 19(1), p. 15. doi: 10.2307/1268249.

Kraus, D. *et al.* (2016) *Catalogue of tree microhabitats – reference field list*. Freiburg (Germany).

Kraus, D. and Krumm, F. (eds) (2013) *Integrative approaches as an opportunity for the conservation of forest biodiversity*. Freiburg: European Forest Institute. Available at: http://www.efi.int/files/attachments/publications/integrate_2013.pdf.

Larrieu, L. *et al.* (2018) 'Tree related microhabitats in temperate and Mediterranean European forests: A hierarchical typology for inventory standardization', *Ecological Indicators*. doi: 10.1016/j.ecolind.2017.08.051.

McRoberts, R. E. *et al.* (2012) 'Assessing forest naturalness', *Forest Science*. Society of American Foresters, 58(3), pp. 294–309.

Santi, E. *et al.* (2017) 'The potential of multifrequency SAR images for estimating forest biomass in Mediterranean areas', *Remote Sensing of Environment*, 200, pp. 63–73. doi: 10.1016/j.rse.2017.07.038.

Venables, W. N. and Ripley, B. D. (2002) *Modern Applied Statistics with S*. New York (US): Springer.

Winter, S. and Möller, G. C. (2008) 'Microhabitats in lowland beech forests as monitoring tool for nature conservation', *Forest Ecology and Management*, 255(3), pp. 1251–1261. doi: 10.1016/j.foreco.2007.10.029.

Zuur, A. F., Ieno, E. N. and Elphick, C. S. (2010) 'A protocol for data exploration to avoid common statistical problems', *Methods in Ecology and Evolution*, 1(1), pp. 3–14. doi: 10.1111/j.2041-210X.2009.00001.x.

CREATING A MAP OF REFORESTATION ON ABANDONED AGRICULTURAL LANDS IN MARI EL REPUBLIC USING SATELLITE IMAGES

S.A. Lezhnin, R.L. Muzurova

Volga State University of Technology, Yoshkar-Ola, Russia – lejninsa@volgatech.net

KEY WORDS: Abandoned agricultural lands, Satellite images, Republic of Mari El, Spectral channel, Thematic maps, Accuracy assessment, Landsat

ABSTRACT:

The study and evaluation of growing agricultural areas is an important task for the national economy of the Russian Federation. The use of satellite information in similar studies is a priority. Modern development of technologies allows to estimate the big areas at the minimum financial and human efforts. The study was based on the analysis of thematic maps obtained by the controlled classification of satellite images Landsat 8 with a spatial resolution of 30 m in various combinations of spectral channels that were obtained from the NASA database. Evaluation of the accuracy of the developed thematic maps allowed to identify the optimal combination of spectral channels of satellite imagery and the time of survey.

During the thematic mapping, 10 maps were obtained for several time periods. The evaluation of the resulting thematic maps was carried out using control points obtained in the test areas, with the Kappa coefficient (k) being determined. The highest accuracy was shown by the thematic map, obtained from the spring image in combination of the 6-5-2 (SWIR2 - NIR - BLUE) spectral channels. The Kappa coefficient, which has a value of 0.66-0.67 for spring shots, indicates good consistency of thematic maps and field data. On the final thematic map of the agricultural lands of the Republic of Mari El for 2017, the areas of the sites of abandoned agricultural lands, overgrown with coniferous and deciduous species, were determined.

1. INTRODUCTION

The economic situation in Russia and abroad in recent years has led to the fact that on large areas of uncultivated agricultural land there is a change of ecosystems from agricultural to forest vegetation. This process has both negative (reduction of areas for growing crops in the context of the global food problem) and positive aspects (tree species restore water and soil balance in the territory, there is an opportunity for the development of side forest use: picking mushrooms, berries, hunting).

The study and assessment of overgrown agricultural areas is an important task for the national economy of the Russian Federation (Federal Law "On Amendments to the Code of the Russian Federation on Administrative Offenses"). The use of satellite information in such studies is a priority, since modern technology development allows us to estimate large areas with minimal financial and human labor costs (Hostert et al., 2011; Kurbanov et al., 2015; Plungmacher et al., 2014., Xin et al., 2013). For the study of former agricultural land, medium- and high-resolution images of different periods, various vegetation indices and other approaches are usually used (Johansson, 2007; Lucas et al, 2007; Pinto, Fernandes, 2011; Prishchepov, 2012; Loboda et al, 2016; Meng et al., 2015; Sulla-Menashe et al., 2014).

The research team of the Center for Sustainable Forest Management and Remote Sensing under the guidance of prof. E.A. Kurbanov (Kurbanov et al., 2010a) made a wide efforts in studying the overgrowing deposits. They investigated the area of overgrowing of abandoned agricultural lands of the Middle Volga region by tree species (accumulation of phytomass) using remote sensing methods (Kurbanov et al., 2010b; Kurbanov et al., 2011; Lezhnin, Akbarov, 2014; Lezhnin, 2015). Nevertheless, the problem of finding the optimal method for solving the problem of studying overgrown deposits remains open.

* Corresponding author

2. MATERIALS AND METHODS

The aim of the study was to find the optimal combination of Landsat 8 satellite imaging channels for identifying saplings of young trees on the abandoned agricultural lands of the Republic of Mari El. To achieve this, the following tasks were solved:

- selected cloudless images of the Landsat 8 satellite to the study area over several time periods;
- several combinations of spectral channels of Landsat 8 images were used to identify their optimum for research;
- thematic mapping of selected three-channel images was carried out;
- conclusions were drawn on the most optimal combination of spectral channels of Landsat 8 satellite images for identifying woody vegetation in agricultural areas.

The object of the study was the deposits of the Republic of Mari El.

The study was based on the analysis of thematic maps obtained by the method of controlled classification of Landsat 8 satellite images with a spatial resolution of 30 m in various combinations of spectral channels that were obtained from the NASA database (USGS Global ...). Evaluation of the accuracy of the developed thematic maps made it possible to identify the optimal combination of spectral channels of satellite images and the time of shooting.

Landsat 8 satellite images (scene 171-20) were selected for work over three time periods and several combinations of spectral channels: spring images (early May 2017), summer images (July 2017) and autumn images (September 2017) (Table 1, Figures 1, 2). All images were subjected to the atmospheric correction procedure in the FLASH module of the ENVI-5.2 software to reduce the influence of atmospheric phenomena on the accuracy of the study.

Name	Date	The combination of spectral channel*
Spring_652	May 2017	6-5-2
Spring_654		6-5-4
Spring_751		7-5-1
Summer_652	July 2017	6-5-2
Summer_654		6-5-4
Summer_751		7-5-1
Autumn_652	September 2017	6-5-2
Autumn_654		6-5-4
Autumn_751		7-5-1

*Note: 1 - spectral channel "coast and aerosols" (wavelength 0.433—0.453); 2 - the blue channel (0,450—0,515); 4 - red channel (0,630—0,680); 5 - near infrared, NIR (0,845—0,885); 6 - shortwave near infrared, SWIR2 (1,560—1,660); 7 - shortwave near infrared, SWIR3 (2,100—2,300).

Table 1. The combinations of Landsat 8 satellite channels used in the study (scene 171-20)

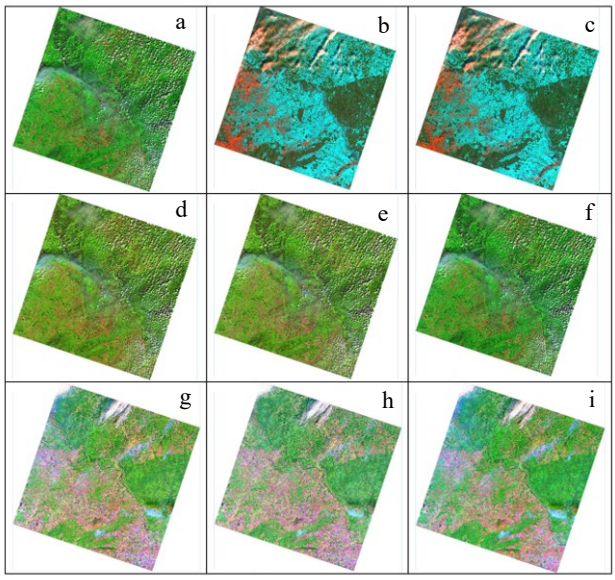

Figure 1. The combinations of Landsat 8 satellite channels used in the study (scene 171-20): a) Spring_652; b) Spring_654; c) Spring_751; d) Summer_652; e) Summer_654; f) Summer_751; g) Autumn_652; h) Autumn_654; i) Autumn_751

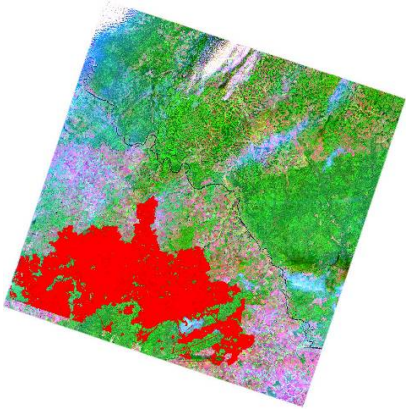

Figure 2. An example of a Landsat 8 image with a mask of the study area (red)

The spectral channels were selected on the basis of their optimal applicability for the study of crops (6-5-2), forest communities (6-5-4) and open soils (7-5-1) (Interpretation of channel combinations ...).

For thematic mapping using the method of managed classification (maximum likelihood) and evaluation of the obtained maps, data collected for the 2007-2015 field season on the Mari El Republic deposits were used.

Prior to the beginning of the multiple uncontrolled classification, on the prepared Landsat satellite scene, in the form of a mask, parts of the terrain were cut out that do not belong to agricultural objects — forest lands (forest fund), settlements and water bodies. The result of the first stage of the uncontrolled classification was a thematic map of land cover in the agricultural land of the Mari El Respublic, consisting of 25 classes. A large number of classes of the map obtained is due to the fact that the classes of young forest from agricultural land can be separated as accurately as possible (Lezhnin, 2015).

In the process of thematic mapping, three classes were identified in each of the images studied: agricultural land proper (including unused), coniferous young forest and deciduous young forest.

3. RESULTS

During the thematic mapping, 10 maps were obtained over several time periods (Figure 3).

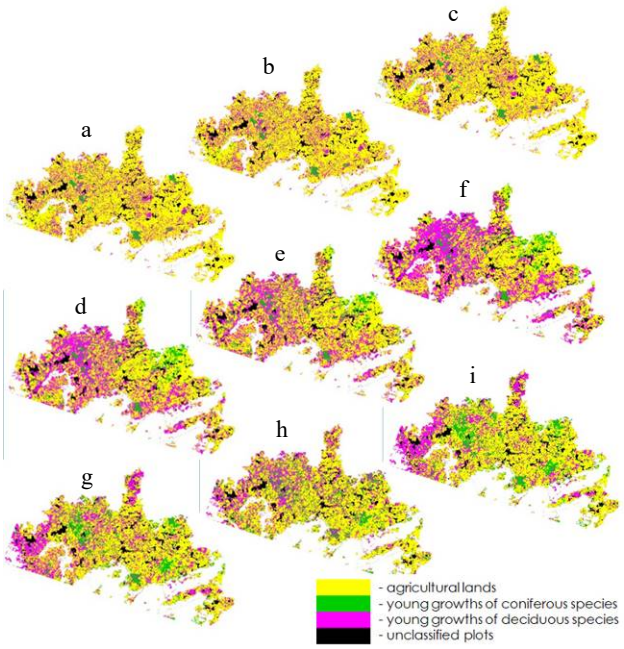

Figure 3. Thematic maps obtained from the corresponding Landsat 8 satellite images: a) Spring_652; b) Spring_654; c) Spring_751; d) Summer_652; e) Summer_654; e) Summer_751; g) Autumn_652; h) Autumn_654; i) Autumn_751

The assessment of the obtained thematic maps was carried out using the confusion matrix method in the ENVI-5.2 software package. To calculate the accuracy of thematic maps and the Kappa coefficient (k) (Table 2), control points obtained at test sites were used.

Thematic map	Total accuracy,%	Kappa ratio (k)
Spring_652	87,89	0,67
Spring_654	86,87	0,66
Spring_751	87, 55	0,67
Summer_652	79,67	0,41
Summer_654	79,62	0,39
Summer_751	74,9	0,34
Autumn_652	65,93	0,16
Autumn_654	65,20	0,15
Autumn_751	67,42	0,19

Table 2. Accuracy of the received thematic maps

As can be seen from the table, the greatest accuracy was shown by the thematic map obtained from the spring images in the combination of 6-5-2 spectral channels. This is explained by the fact that in the spring photos the grassy vegetation is either covered with snow cover, or it differs significantly from the tree vegetation in its spectral characteristics. In addition, in spring there are areas of deposits, where vegetation is absent due to autumn plowing. The Kappa coefficient, which has a value of 0.66-0.67 for spring shots, indicates a good consistency of thematic maps and field data.

Thematic maps based on summer images have a high overall accuracy, but a rather low Kappa ratio. This situation can be explained by the fact that in the middle of summer the herbaceous vegetation reaches the peak of its vegetative activity, therefore its spectral characteristics will be close to those of young woody vegetation. In the process of classification, the spectral values of the thematic map classes are mixed. Satellite imagery combined with 6-5-2 spectral channels on Landsat-8 summer images shows better consistency with field data. (k> 0.4)

Weak results showed autumn maps. They have an average overall accuracy, and the Kappa coefficient indicates a low consistency of thematic maps with field data (k <0.4).

In addition to evaluation using the Kappa coefficient, the obtained thematic maps were compared with the "reference" map of the overgrowing of the Mari El deposits, obtained in previous studies using the unmanaged classification of satellite images after the MNF-transformation (Figure 4).

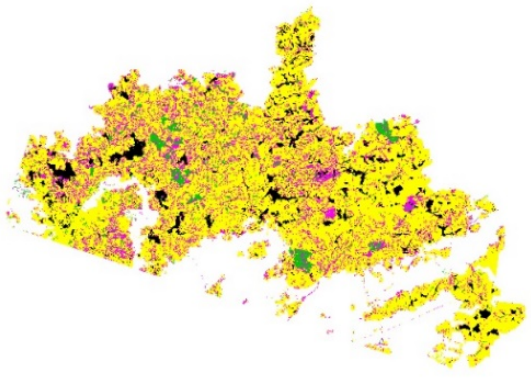

Figure 4. "Reference" map (2016)

The comparison of the "reference" card with the thematic maps obtained in the study was carried out using the Change Detection module of the ENVI-5.2 software. This procedure made it possible to evaluate not only the correspondence of the obtained thematic classes to the natural data, but also to reveal the spatial mixing of the thematic classes. With this estimate, the best accuracy was again shown by a thematic map based on a spring image in a combination of 6-5-2 spectral channels (Figure 5).

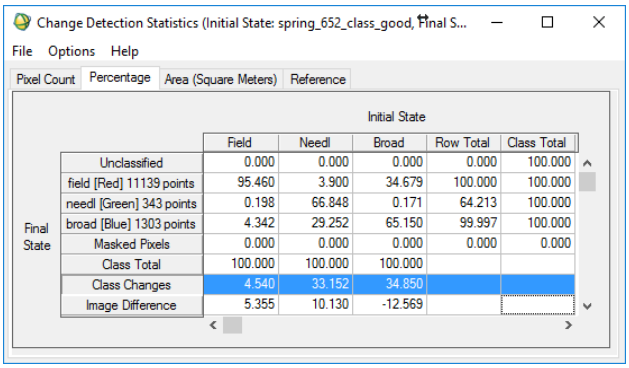

Figure 5. Comparison of the "reference" card with the Spring_652 map

As can be seen from Figure 5, the Field class (agricultural land proper) almost completely coincides on both maps (accuracy of falling into the class of 95.46%), while the classes Needle (coniferous young forest) and Broad (deciduous young forest) have a lower accuracy of falling into its class (66.85% and 65.15%, respectively). At the same time, it is clear that young coniferous are well divided with agricultural crops (mixing classes only 3.9%), but have spectral characteristics similar to deciduous youths, which is reflected in 29.25% mixing classes. Deciduous youths, on the contrary, have high mixing with the class of agricultural land due to similar spectral characteristics, which is also confirmed by previous studies.

The remaining thematic maps showed large discrepancies with the "reference" map, but the general trend was also there: according to their spectral characteristics, coniferous young stands out well on agricultural lands, and deciduous youths, on the contrary, are more susceptible to mixing with both coniferous youths and crops.

4. CONCLUSIONS

Research and assessment of deposits overgrown with woody vegetation is a priority for both agriculture and forestry. The most important information that can be used to solve this problem is satellite information, which allows for the assessment of large areas of agricultural land in a short time and at minimal cost. The most accurate was the thematic map obtained by the spring snapshot in combination 6-5-2 (SWIR2 - NIR - BLUE) spectral channels. It is in this combination that young trees have good spectral separation with agricultural areas without the use of additional transformations.

The developed thematic maps testify to a stable process of mass overgrowing of young tree vegetation in the territory of the Republic of Mari El. Thematic mapping of young forests on deposits allowed to determine the area of overgrowth for 2017. The total area of agricultural land according to the obtained thematic map reaches 763694.46 hectares, while overgrowing of young growths of deciduous species up to 123776.19 hectares (1.6%), respectively, and overgrowth by young conifers species reaches 52557.12 ha (7%), respectively. The created thematic maps of coniferous and deciduous species on the Respublic of Mari EL deposits can be used as a basis for their further study and monitoring.

ACKNOWLEDGEMENTS

The work was supported by The Jean Monnet Centre of Excellence and a grant from the President of the Russian Federation for state support of young Russian scientists - candidates of science No. MK-6343.2018.11.

REFERENCES

Federal Law "On Amendments to the Code of the Russian Federation on Administrative Offenses" of 03.02.2014

Hostert, P. Kuemmerle, T., Prishchepov, A., Sieber, A., Lambin, E. F., Radeloff, V.C., 2011. Rapid land use change after socio-economic disturbances: the collapse of the Soviet Union versus Chernobyl. In: *Environmental Research Letters*, №6(4), 8 p.

Interpretation of the Landsat TM / ETM + data channel combination. http://gis-lab.info/qa/landsat-bandcomb.html

Johansson, T., 2007. Biomass production and allometric above- and below-ground relations for young birch stands planted at four spacings on abandoned farmland. In: *Institute of Chartered Foresters*, 12 p.

Kurbanov, E. A., Vorobiev, O. N., Gubaev, A. V., Lezhnin, S. A., Nezamaev, S. A., Aleksandrova, T.A., 2010a. Evaluation of the overgrowing of lands of the Mari El Republic by forest vegetation using satellite imagery. In: *Vestnik MarSTU*, № 2 (9), pp. 14-20. (in Russian)

Kurbanov, E. A., Vorobev, O. N., Gubaev, A. V., Lezhnin, S. A., Polevshchikova, Yu. A., Demisheva, E. N., 2014. Four decades of forest research from Landsat. In: *Bulletin of the Volga State Technological University. Ser .: Forest. Ecology. Nature use,* № 1 (21), pp. 18-32. (in Russian)

Kurbanov, E. A., Nureeva, T. V., Vorobev, O. N., Gubaev, A. V., Lezhnin, S. A., Miftakhov, T. F., Nezamaev, S. A., Polevshchikova, Yu. A., 2011. Remote monitoring of the dynamics of violations of forest cover, reforestation and reforestation in the Mari trans-Volga region. In: *Bulletin of the Volga State University of Technology. Series: Forest. Ecology. Nature use*, № 3, pp. 17-24. (in Russian)

Kurbanov, E. A., Vorobev, O. N., Lezhnin, S. A., Gubaev, A. V., Polevshchikova, Yu. A., 2015. Thematic mapping of vegetation cover using satellite images: validation and assessment of accuracy. *Monograph.* Yoshkar-Ola, 131 p. (in Russian)

Kurbanov, E. A., Vorobev, O. N., Gubaev, A. V., Lezhnin, S. A., 2010b. Use of ALOS satellite images to identify areas of former agricultural land overgrown with forest. *Geomatics*, №4, pp. 68-72. (in Russian)

Lezhnin, S. A., 2015. Determination of overgrowing of deposits of the Mari Trans-Volga by tree vegetation according to remote sensing data. In: *Forest Ecosystems in a Changing Climate: Biological Productivity and Remote Monitoring: Proceedings of the International Conference*. Yoshkar-Ola: Volga State Technical University, pp. 114-118. (in Russian)

Lezhnin, S. A., Akbarov, O. M., 2014. The use of the analysis of the main components in the identification of young hardwood on fallows. In: *Proceedings of the Volga State Technological University. Technological series*, Yoshkar-Ola, pp. 33-38. (in Russian)

Loboda, T., Krankina, O., Savin, I., Kurbanov, E., Joanne. H., 2016. Land Management and the Impact of the 2010 Extreme Drought Event on the Agricultural and Ecological Systems of European Russia. in book *"Land-Cover and Land-Use Changes in Eastern Europe after the Collapse of the Soviet Union in 1991"*. Eds. G. Gutman, R. Volker, Springer International Publishing, pp. 173—192.

Lucas, R., Rowlands, A., Brown, A., Keyworth, S., Bunting, P., 2007. Rule-based classification of multi-temporal satellite imagery for habitat and agricultural land cover mapping. In: *ISPRS Journal of Photogrammetry & Remote Sensing*, №62, pp. 165–185.

Meng, R., Dennison, P., Huang, C., Moritz, M., D'Antonio, C., 2015. Effects of fire severity and post-fire climate on short-term vegetation recovery of mixed-conifer and red fir forests in the Sierra Nevada Mountains of California. *Remote Sensing of Environment*, Vol. 171, pp. 311-325.

Pinto, L., Fernandes, L., 2011. Multitemporal analyses of the vegetation cover of coastal sand dune ecosystems in Natal/RN, based on NDVI index. In: *Anais XV Simposio Brasileiro de Sensiamento Remoto - SBSR*, Curitiba, PR, Brasil, p. 1895.

Plungmacher, D., Cohen, W., Kennedy, R., Yang, Z., 2014. Using Landsat-derived disturbance and recovery history and lidar to map forest biomass dynamics. *Remote Sensing of Environment*, Vol. 151, pp. 124-137.

Prishchepov, A. V., Radeloff, V. C., Dubinin, M., Alcantar, C., 2012. The effect of Landsat ETM/ETM + image acquisition dates on the detection of agricultural land abandonment in Eastern Europe. *Remote Sensing of Environment*, Vol. 126, pp. 195-209.

Sulla-Menashe, D., Kennedy, R. E., Yang, Z. et al., 2014. Detecting forest disturbance in the Pacific Northwest from MODIS time series using temporal segmentation. *Remote Sensing of Environment*, № 151, pp. 114–123.

USGS Global Visualization Viewer. http://glovis.usgs.gov/.

Xin, Q., Olofsson, P., Zhu, Z., Tan, B., Woodcock, C., 2013. Toward near real-time monitoring of forest disturbance by fusion of MODIS and Landsat data. *Remote Sensing of Environment*, Vol. 135, pp. 234-247.

MONITORING THE GROWTH DYNAMICS OF WATER HYACINTH (*EICHHORNIA CRASSIPES*)

J.F. Mas *

Centro de Investigaciones en Geografía Ambiental, Universidad Nacional Autónoma de México, Morelia, México – jfmas@ciga.unam.mx

KEY WORDS: Monitoring, Water hyacinth, Eichhornia crassipes, Invasive species

ABSTRACT:

The water hyacinth (*Eichhornia crassipes*) is a a highly invasive aquatic plant which has negative impacts in bodies of water as declines in pH, temperature, oxygen, nutrient levels and an increase of evapotranspiration. In this study, multispectral images from the PlanetScope constellation were used to assess the growth of the water hyacinth in the dam of Cointzio, in central Mexico. The analysis showed that, after the mechanical removal of the weeds in June 2017, re-invasion began to emerge in September. In a period of three months, the area covered by *E. crassipes* increased from 40 to 200 ha, which corresponds to a relative increase of 400%, with an average growth of 1.5 ha/day. Based on the field measurements, a density of 200 tons of fresh biomass per hectare was found, corresponding to 23.2 t/ha of dry matter. These water hyacinth infestations are likely related with pollution from agricultural run-off and rural and urban drainage. Due to its high temporal and spatial resolutions, PlanetScope imagery enabled the monitoring of the growth of the water hyacinth cover in a small reservoir with a large number of observations. The data obtained can be used to support water management actions and validate models.

1. INTRODUCTION

1.1 Short presentation of water hyacinth

The water hyacinth (*Eichhornia crassipes*) is a a highly invasive aquatic plant native of South America. Its ability for growth and propagation enabled it to spread on all the continents except Antarctica and causes huge problems in many regions of the word (Coetzee et al., 2017). In Europe, its distribution is limited to the warmer southern regions. In Mexico, it is estimated that *Eichhornia crassipes* covers 40,000 ha of lakes, dams and canals (Gutiérrez et al., 1996; CONABIO, 2009). Some of the impacts of the water hyacinth in bodies of water are declines in pH, temperature, oxygen, nutrient levels and water flow as well as an increase of water loss by evapotranspiration. It also affects human activities as fishing and water transport. *Eichhornia crassipes* reproduces by budding, a type of asexual reproduction, and through the spreading of seeds. Due to these characteristics, it has an exponentially high growth rate, particularly when under ideal conditions, such as warm temperatures (Mean temperature for between 25°C and 27°C) and high nutrient levels (calcium, phosphates, and nitrates) in the water (François, 1970).

This study aims at assessing the growth of the water hyacinth in the dam of Cointzio, near the city of Morelia, in central Mexico.

1.2 Study area

The dam of Cointzio (19.62°N, 101.26°W) is located in the Mexican Central Plateau near the city of Morelia in the state of Michoacán, in the center of Mexico. The Cointzio watershed drains an area of 650 km^2 and corresponds to the south-western portion of the Cuitzeo lake watershed. It supplies drinking water to Morelia and is also used for irrigation purposes during the dry season.

The reservoir is located at an altitude of 1990 m.a.s.l. The surrounding region presents a sub-humid climate with mean annual precipitation of 830 mm and temperature of 17.8°C. Precipitations are concentrated from June to October while the period between November and May is dry.

In the watershed, main activities are agriculture and cattle ranching. An analysis of land use / land cover change in the watershed over the period 1975-2003 showed that the large majority of the changes occurred during the 1986-1996 period (López-Granados et al., 2013). However, agricultural practices have likely changed during a more recent period. For instance, since the last decade, avocado plantations, which use huge quantities of fertilizers, herbicides and fungicides, appeared in the area. The reservoir is facing various problems including low water levels, sediment accumulation and eutrophication, and, recently, water hyacinth invasion.

1.3 Material

In this study, PlanetScope imagery, provided by the Planet Education and Research Program, was used (www.planet.com). The PlanetScope constellation is composed by more than 120 micro-satellites which image the entire surface of the Earth with both high spatial and temporal resolutions. Images present four spectral bands: Blue (455-515 nm), green (455-515 nm), red (590-670 nm) and NIR (780-860 nm) at a 3 m spatial resolution. 31 cloud free images were acquired during a period beginning just after the mechanical removal of the weeds, in May 2017, and concluding in October 2018. Images were chosen taking into account the availability of cloud free data and trying to have at least one image each 15 days. Sequences

* Corresponding author

of images on consecutive days were also selected to assess the variability of the estimates of water hyacinth's area due to variations of the weed density and issues with image classification.

R was utilized to carry out image processing and statistical analysis (Mas, 2018), in particular the packages raster (Hijmans, 2018), drc (Ritz et al., 2015) and Rstoolbox (Leutner et al., 2018) with the endmember spectral mixture analysis function implemented by Schwalb-Willmann (2018).

2. METHODS

2.1 Image processing

Digital numbers (DN) of the images were converted to Top of Atmosphere Reflectance, multiplying the DN value by the reflectance coefficient found in the image metadata. Spectral unmixing is a technique for analysing the mixture of components in remotely sensed images (Quintano et al., 2012). In this study, multispectral images were unmixed using the multiple endmember spectral mixture analysis (MESMA) function and spectral endmember profiles for water, water hyacinth cover and area without vegetation. This function is based upon a non-negative least squares solver which is a statistical technique to fit model parameters to data, that assumes that the parameters are always positive and expressed linearly to unknown parameters (Franc et al., 2005). Endmember profiles were obtained, for each date, from training points selected through visual interpretation of the RGB image composites. After spectral unmixing, three fraction images were obtained. Pixels which maximum unmixed values corresponded to the class water hyacinth were reclassified to obtain an image mask and calculate water hyacinth cover area.

2.2 Field measurements

The biomass of *E. crassipes* was sampled in April 2018 using five 1 x 1 m quadrats. All the individuals inside the quadrat were collected and transported to the laboratory in plastic bags. The samples were dried and biomass was determined as tons of dry matter per hectare (t/ha).

3. RESULTS

Figure 1 shows RGB false colour composites of two images acquired in May 2018. It can be observed that, as the water hyacinth is a free floating plant, the wind blows it from one part of the reservoir to another, creating patches with different densities of plants. Figure 2 shows the fraction image for the water hyacinth.

The multidate analysis showed that, after the mechanical removal of the weeds in May 2017, re-invasion began to emerge in September. In May 2018, near 300 ha (40% of the reservoir area) was covered by water hyacinth (Figure 1).

As shown in figure 3, cover growth was rapid: Between the 15/10/17 and the 27/1/2018, the area covered by *E. crassipes* increased from 40 to 200 ha, which corresponds to a relative increase of 400%, with an average growth of 1.5 ha/day. This growth can be approximately modelled by a logistic function. It can be observed a slow initial growth rate followed by a high absolute growth rate and then a decline of area. Wilson et al. (2005) have modelled water hyacinth population growth, expressed as biomass density (kg/m^2), using a logistic model based on an intrinsic daily growth rate and a carrying capacity. At low plant densities, the population increases at its intrinsic growth rate. When the plant density comes nearer to the carrying capacity, the growth rate tends to zero. In case of densities above the carrying capacity, the population decreases to the carrying capacity.

Based on the field measurements, a density of 200 tons of fresh biomass per hectare was found, corresponding to 23.2 t/ha of dry matter. This estimate is an approximation because the samples were not randomly distributed and their number was low. Moreover, as shown in figure 2, the estimates of the area covered by the water hyacinth present large variations (see the variation for consecutive days in figure 3). This was due to i) the variation of vegetation density depending on the action of wind and, ii) misclassifications of the image. For instance, disperse water hyacinth can have been classified as water and vegetated area of the edge of the reservoir as water hyacinth (Figure 2).

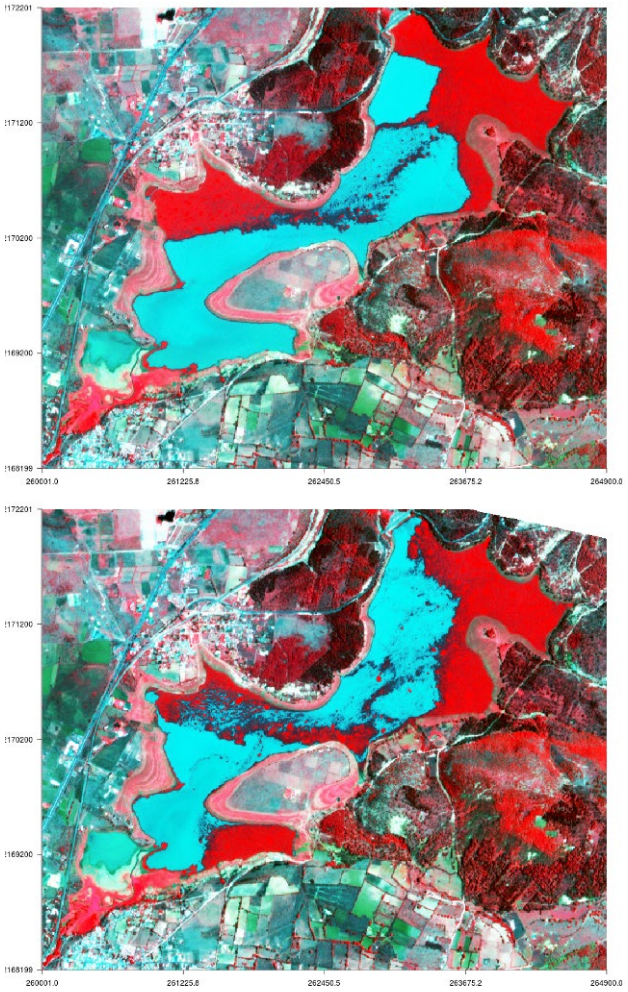

Figure 1. PlanetScope images dated 27/05/2018 (top) and 29/05/2018 (bottom).

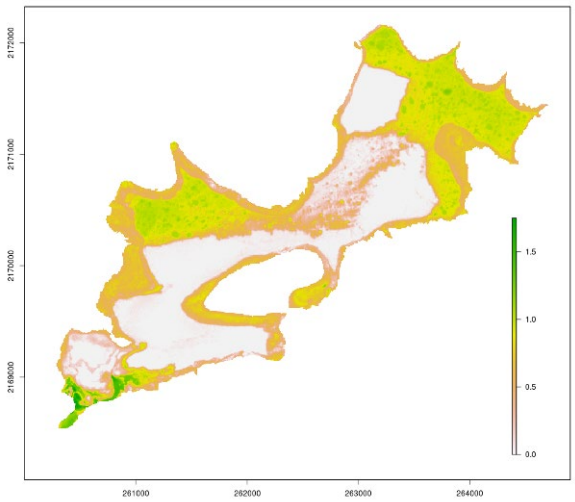

Figure 2. Water hyacinth image fraction (29/05/2018).

Various studies identified wastewater discharges as the major nutrient inputs into this Cointzio reservoir, over runoff waters from croplands (López López and Dávalos-Lind, 1998; Ramírez-Olvera et al., 2004; Némery et al., 2014). However, *E. crassipes* invasion in the reservoir is a recent phenomenon (about 2014) and it is likely related to change in agricultural practices and agriculture intensification in the watershed which may have caused an increase of nutrient concentrations in the reservoir in addition to wastewater discharges.

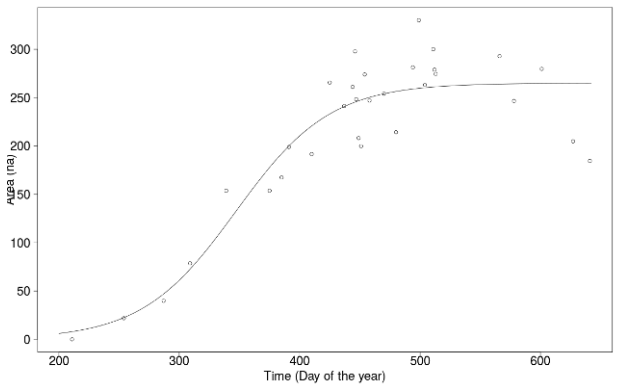

Figure 3. Area covered by water hyacinth as a function of time.

4. CONCLUSIONS

As concluding remarks, remote sensing has proven to be a useful tool for studying plant community dynamics in aquatic ecosystems (Khanna et al., 2012). In particular, due to its high temporal and spatial resolutions, PlanetScope images enabled the monitoring of the growth of the water hyacinth cover in a small reservoir with a large number of observations. The data obtained from the imagery can be used to monitor the weed invasion, support water management actions and validate models (Eid and Shaltout, 2017). These water hyacinth infestations are related with pollution from agricultural run-off and rural and urban drainage. However, water hyacinth can be used for the removal of pollutants (Gutiérrez et al., 1996; Malik, 2007; Carrión et al., 2012; Gómez Durán, 2015).

This study was limited to the monitoring of water hyacinth growth in the Cointzio reservoir. Future researches will focus on identifying the sources of the nutrients in the reservoir through water field measurements and land use/land cover change assessment in the watershed and on proposing a control and use management strategy.

ACKNOWLEDGEMENTS

Juliette Mas Caussel Pérez helped in the field measurements. PlanetScope imagery was obtained in the framework of the Planet Education and Research Program. This research was supported by the program *Programa de Apoyos para la Superación del Personal Académico de la UNAM* (PASPA-DGAPA), UNAM.

REFERENCES

Carrión, C., Ponce-de León, C., Cram, S., Sommer, I., Hernández, M. and Vanegas, C., 2012. Aprovechamiento potencial del lirio acuático (*Eichhornia crassipes*) en Xochimilco para fitorremediación de metales. *Agrociencia*, 46(6), pp. 609-620.

Coetzee, J.A., Hill, M.P., Ruiz-Téllez, T., Starfinger, U. and S. Brunel, 2017. Monographs on invasive plants in Europe N° 2: *Eichhornia crassipes* (Mart.) Solms. *Botany Letters,* 164(4), pp. 303-326, doi.org/10.1080/23818107.2017.1381041.

CONABIO, 2009. *Eichhornia crassipes* (Mart.) Solms. http://www.conabio.gob.mx/malezasdemexico/pontederiaceae/eichhornia-crassipes/fichas/ficha.htm (10 October 2018).

Eid, E.M. and Shaltout, K.H., 2017. Growth dynamics of water hyacinth (*Eichhornia crassipes*): a modeling approach. *Rendiconti Lincei. Scienze Fisiche e Naturali,* 28, pp. 169-181.https://doi.org/10.1007/s12210-016-0589-4.

Franc, V., Hlaváč, V., and Navara, M., 2005. Sequential coordinate-wise algorithm for the non-negative least squares problem. In: *International Conference on Computer Analysis of Images and Patterns*, pp. 407-414. Berlin, Heidelberg.

François, J., 1970. Recherches expérimentales sur l'écologie de la jacinthe d'eau *Eichhornia crassipes* (Mart.) Solms. Dissertation, Faculté Sci Agronom Gembloux, Belgium.

Gómez Durán, T., 2015. Lirio acuático, más que una plaga. *TecReview*, 10, pp. 79-85.

Gutiérrez, E., Delgadillo, R., Saldaña, P. and Arreguín, F., 1996. Strategies for waterhyacinth (*Eichhornia crassipes*) control in Mexico. *Hydrobiologia*, 340, pp. 181-185. doi.org/10.1007/BF00012752.

Hijmans, R.J., 2018. Raster: Geographic Data Analysis and Modeling. R package version 2.7-15. https://CRAN.R-project.org/package=raster (10 October 2018).

Khanna, S., Santos, M.J., Hestir, E.L. and Ustin, S.L., 2012. Plant community dynamics relative to the changing distribution of a highly invasive species, *Eichhornia crassipes*: a remote sensing perspective. *Biological Invasions*, 14(3), pp. 717-733. doi.org/10.1007/s10530-011-0112-x.

Leutner, B., Horning, N., Schwalb-Willmann, J. and Hijmans, R.J., 2018. Package Rstoolbox, https://cran.r-project.org/web/packages/RStoolbox/RStoolbox.pdf (10 October 2018).

López López, E. and Dávalos-Lind, L., 1998. Algal growth potential and nutrient limitation in a tropical river-reservoir system of the Central Plateau, Mexico. *Aquatic Ecosystem Health & Management*, 1, pp. 345–351.

López-Granados, E., Mendoza, M.E. and González, D.I., 2013. Linking geomorphologic knowledge, RS and GIS techniques for analyzing land cover and land use change: a multitemporal study in the Cointzio watershed, Mexico. *Revista Ambiente & Água*, 8(1), pp. 18-37. doi.org/10.4136/ambi-agua.956.

Malik, A., 2007. Environmental challenge vis a vis opportunity: The case of water hyacinth. *Environment International*, 33, pp. 122-138.

Mas, J-F., 2018, Análisis espacial con R: Usa R como un Sistema de Información Geográfica, European Scientific Institute, 114 p, ISBN: 978-608-4642-66-4. eujournal.org/files/journals/1/books/JeanFrancoisMas.pdf.

Némery, J., Gratiot, N., Doan, P. T. K.,Duvert, C., Alvarado-Villanueva, R. and Duwig, C., 2016. Carbon, nitrogen, phosphorus, and sediment sources and retention in a small eutrophic tropical reservoir. *Aquatic Sciences*, 78(1), pp.171-189. doi.org/10.1007/s00027-015-0416-5.

Quintano, C, Fernández-Manso, A. Shimabukuro, Y. and Pereira, G., 2012. Spectral unmixing. *International Journal of Remote Sensing*. 33(17), pp. 5307-5340. doi.org/10.1080/01431161.2012.661095.

Ramírez-Olvera, M.A., Díaz-Argüero, M. and López-López, E., 2004. Planktonic crustacean assemblages in a system of three reservoirs in the Mexican Central Plateau: seasonal and spatial patterns. *Journal of Freshwater Ecology*, 19(1), pp. 25-34 doi.org/10.1080/02705060.2004.9664508.

Ritz, C., Baty, F., Streibig, J. C. and Gerhard, D., 2015. Dose-Response Analysis Using R. *Plos One*, 10(12), e0146021. doi.org/10.1371/journal.pone.0146021.

Ruiz Téllez, T., Martín de Rodrigo López, E., Lorenzo Granado, G., Albano Pérez, E., Morán López, R. and Sánchez Guzmán, J.M., 2008. The Water Hyacinth, Eichhornia crassipes: an invasive plant in the Guadiana River Basin (Spain), *Aquatic Invasions*, 3(1) pp. 42-53. doi.org/ 10.3391/ai.2008.3.1.8.

Schwalb-Willmann, J., 2018. Spectral unmixing in R, http://students.eagle-science.org/spectral-unmixing-in-r/ (10 October 2018).

Wilson, J.R., Holst, N. and Rees, M., 2005. Determinants and patterns of population growth in water hyacinth. *Aquatic Botany*, 81(1), pp. 51–67. doi.org/10.1016/j.aquabot.2004.11.002.

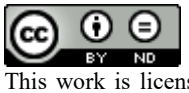

LONG-TERM COMPARISON OF *IN SITU* AND REMOTELY-SENSED LEAF AREA INDEX IN TEMPERATE AND MEDITERRANEAN BROADLEAVED FORESTS

C. Tattoni[1,2*], F. Chianucci[3], M. Grotti[4], R. Zorer[2], A. Cutini[4], D. Rocchini[1,2]

[1] University of Trento, Trento, Italy - clara.tattoni@gmail.com, duccio.rocchini@unitn.it
[2] Research and Innovation Centre, Fondazione Edmund Mach, San Michele all'Adige, Trento, Italy - roberto.zorer@fmach.it
[3] CREA, Research Centre for Agriculture and Environment, Rome, Italy – f.chianucci@gmail.com
[4] CREA, Research Centre for Forestry and Wood, Arezzo, Italy - andrea.cutini@crea.gov.it, mirkogrotti@gmail.com

KEY WORDS: Forest canopy, MODIS, LAI-2000/2200, time-series

ABSTRACT:

Monitoring vegetation structure and functioning is critical for modelling terrestrial ecosystems and energy cycles. Leaf area index (LAI) is an important structural property of vegetation used in many land-surface, climate, and forest monitoring applications. Remote sensing provides a unique way to obtain estimates of leaf area index at spatially extensive areas. However, the analysis and extraction of quantitative information from remotely-sensed data require accurate cross-calibration with *in situ* forest measurements, which are generally spatially- and temporally-limited, thereby limiting the ability to compare the seasonal dynamic patterns between field and remotely-sensed time series. This is particularly relevant in temperate broadleaved forests, which are characterized by high level of complexity, which can complicate the retrieval of vegetation attributes from remotely-sensed data.
In this study, we performed a long-term comparison of MODIS LAI products with continuous *in situ* leaf area index measurements collected monthly in temperate and Mediterranean forests from 2000 to 2016. Results indicated that LAI showed a good correlation between satellite and ground data for most of the stands, and the pattern in seasonal changes were highly overlapping between the time-series. We conclude that MODIS LAI data are suitable for phenological application and for up-scaling LAI from the stand level to larger scales.

1. INTRODUCTION

Monitoring forest structure and functioning is critical for understanding changes in forest coverage and health in response to management and climate, and for modelling terrestrial carbon and energy cycles. Remote sensing provides a unique way to obtain estimates of forest attributes at spatially extensive areas, from local to the global scale. In addition, the availability of standardized information over time allows to make projections under different forest management and climate change scenarios (Ciolli et al., 2012, Ferretti et al., 2018, Ciolli et al., 2018).
Among the measured variable, leaf area index (LAI), defined as half the total green leaf area per unit ground surface area (Chen and Black, 1992), is an important structural property of vegetation used in many land-surface, climate, and monitoring programs. LAI directly influences the radiative transfer of sunlight in vegetation, determining the amount of radiation measured by optical (passive) remotely-sensed sensors in the visible and infrared portions of the electromagnetic spectrum (Asnar et al., 1984; Zhen and Moskal, 2009).
Optical remote sensing of leaf area index requires accurate calibration with *in situ* measurements (Boer et al. 2008; Prospatin and Panferov, 2013; Xu et al., 2018). This is particularly relevant in temperate and Mediterranean forests, which are characterized by high level of complexity, which can complicate the retrieval of vegetation attributes from optical remotely-sensed sensors (Angelini et al. 2015; Leroux et al., 2018; Munier et al., 2018; Puletti et al., 2018). However, *in situ* datasets are mainly available in boreal forests (e.g., Kuusk et al., 2009) and austral forests (e.g., Woodgate et al., 2015), while such datasets in temperate and Mediterranean forests are scarce. In addition, the majorities of previous studies build relationships exploiting *in situ* measurements performed in a single period (typically a single field campaign), since the availability of long-term ground-truth data series has been limited by the cost and time required by field sampling. The operational Moderate Resolution Imaging Spectroradiometer (MODIS) sensors have provided an opportunity for opening a new horizon of satellite LAI products (Myneni et al., 2015). The latest version (Collection 6, C6) provides continuous LAI data since 2000. To date, no previous studies have performed a comprehensive temporal investigation of LAI time series, since the preliminary evaluations were temporally limited (Xu et al., 2018).
In this study, we performed a long-term comparison between MODIS LAI products with continuous *in situ* leaf area index measurements collected in temperate and Mediterranean forests from 2000 to 2016. Our specific objectives were:

- Evaluate the temporal consistency of (latest) MODIS LAI product along its operational range;
- Checking the ability of MODIS to detect trend, intra-annual variations, seasonal cycle of LAI as compared with *in situ* measurements in Mediterranean and temperate forests
- Evaluate the applicability of MODIS LAI products at the forest stand scale.

2. MATERIAL AND METHODS

2.1 Study area

The data have been collected within the framework of a wider project (LIFE 14 ENV/IT/000514 "FutureForCoppiceS"; www.futureforcoppices.eu) aimed to demonstrate the effect of different management options on sustainable forest management criteria and indicators in temperate and Mediterranean coppice forests. In the project, 45 stands were surveyed in seven forest districts located in two Italian regions (Sardinia and Tuscany) the area sampled was on average about 2800 m² (800-10000 m²) . Thirteen stands located in Tuscany were amongst selected to be included in this study due to their larger temporal availability of leaf area index data and extent comparable with MODIS resolution. The stands are located in large homogeneous forest stand areas and are representative of two European Forest Types (EFT; Barbati et al., 2014): thermophilus deciduous forests

* Corresponding author

dominated by Turkey oak (*Quercus cerris* L.) (EFT 8.2) and mountainous beech (*Fagus sylvatica* L.) forests (EFT 7.3). The data are available from an open repository (Chianucci et al., 2018). Table 1 lists the characteristics of the studied stands.

Forest district	EFT	Stand density n ha^{-1}	Basal area m^2 ha^{-1}
Alpe di Catenaia	7.3	412	29.77
Alpe di Catenaia	7.3	2046	48.15
Alpe di Catenaia	7.3	419	39.45
Alpe di Catenaia	7.3	108	19.9
Alto Tevere	8.2	436	20.21
Alto Tevere	8.2	1222	33.26
Colline Metallifere	8.2	4509	30.17
Colline Metallifere	8.2	54	1.37
Colline Metallifere	8.2	682	16.31
Foresta di Caselli	8.2	2667	38.89
Foresta di Caselli	8.2	2167	44.11
Foresta di Caselli	8.2	3417	41.66
Foresta di Caselli	8.2	2922	42.67

Table 1. Main characteristics of the studied stands

2.2 *In situ* leaf area index

LAI measurements were performed monthly every year, from 1999 to 2016, in the studied stands, just after dawn or close to sunset and under uniform sky conditions using the LAI-2000. Plant Canopy Analyzer (LI-COR, Lincoln, NE, USA). The optics of LAI-2000 consists of a fisheye lens divided into five concentric rings. Each ring simultaneously integrates incoming radiation in the 320 - 490 nm wavelength (blue light) range.
During each sampling session, one above-canopy reference measurement was recorded in clearings near each stand. Nine to 15 below-canopy measurements were then collected for each stand. The fisheye lens of the instrument was covered by a 90° view cap to avoid the influence of surrounding trees on the reference measurements. Gap fraction was estimated as the fraction of below- to above-canopy readings. Leaf area index corrected for apparent clumping (Ryu et al., 2010) was then calculated using the Miller's (1967) theorem.

2.3 Remotely sensed leaf area index

Remotely sensed LAI measurements for the studied stands were obtained from the MODIS sensor (Moderate Resolution Imaging Spectroradiometer) available on Terra and Aqua satellites, formerly known as EOS AM-1 and EOS PM-1.
MODIS Land Products Subset MOD15A2 was chosen because it provided readily available 8-day composite LAI measurements starting from the year 2000 to present. Data were downloaded from the Distributed Active Archive Center (ORL DAAC, 2018). Data were downloaded for a window of 7x7 km centered on the forest district average coordinates with a resolution of 1km (Myneni, et al., 2015).

2.4 Statistical analyses

Data were processed in R environment (R Core Team 2015). First, the time-series alignment between field and remote sensed data was performed using the 'eXtensible' package (Ryan and Ulrich 2017) and interpolation for missing data. The data were then checked for cross-correlation using the 'CCF' function of the 'nlme' package (Pinheiro and Bates, 2017). CCF was run also on the difference between LAI value at time t and the previous value at time *t-1* to account for the correlation about the direction of change rather than considering the absolute values. A paired T test was then performed to assess the difference in the two time-series for both absolute values and differences between subsequent times, using a significant threshold of $p<0.01$.

3. RESULTS

The studied stands were characterized by relatively-high canopy density, as indicated by the high LAI values observed in summer (vegetation-peak period). Field measurements yielded LAI values ranging between 0.75 and 6.73 in beech stands (average ± standard deviation: 4.4 ± 1.6) and between 0.33 to 7.97 in thermophilous oak stands (3.5 ± 1.1) considering all the seasonal data series. MODIS LAI values ranged between 0.10 and 5.66 in beech stands (4.3 ± 1.2) and ranged between 0.10 to 6.37 in thermophilous oak stands (4.01 ± 1.3).
The analysis was performed for separate districts where the starting year of sampling and the number of field LAI measurements was (brackets): Alpe di Catenaia (1999, 298), Alto Tevere (1999, 178), Colline Metallifere (1999, 259) and Foresta di Caselli (1999, 255). Results showed a significant agreement in trend between field and remotely sensed data considering either the aligned data series (Figure 1) and the data averaged on monthly basis (Figure 2) in the considered forest district ($p<0.01$), with the exception of Foresta di Caselli ($p=0.089$, thermophilous oak forests) and Alpe di Catenaia ($p=0.14$, mountainous beech forests) districts, where the alignment was not significant.
The CCF analysis showed a significant agreement between field and remotely-sensed LAI values (T test) meaning that the LAI changed in the same direction in both types of measurements.

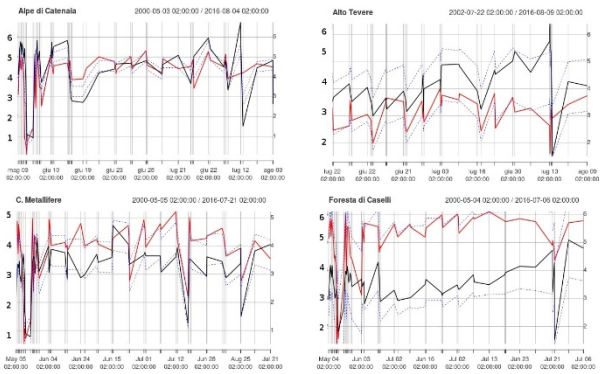

Figure 1 Aligned time series for field (black) and remotely sensed (red) LAI measurements with 95% confidence intervals (blue dashed lines) in the following districts: a) Alpe di Catenaia, b) Alto Tevere, c) Colline Metallifere and d), Foresta di Caselli, Italy.

4. DISCUSSION AND CONCLUSIONS

The main results imbue confidence in the consistency of long-term MODIS LAI time series. The advantage of MODIS products is its large temporal and spatial resolution, which has often been used for large scale studies on LAI across biomes (Weiss et al., 2007). Our results also indicated that MODIS LAI products can be used for medium spatial scale (forest stand level) applications, based on the agreement between satellite and field measurements. The repeated seasonal field measurements also allowed to verify that MODIS LAI can capture the seasonality pattern of LAI at the stand scale, as the speed and sign of change are comparable between field and satellite time-series data.

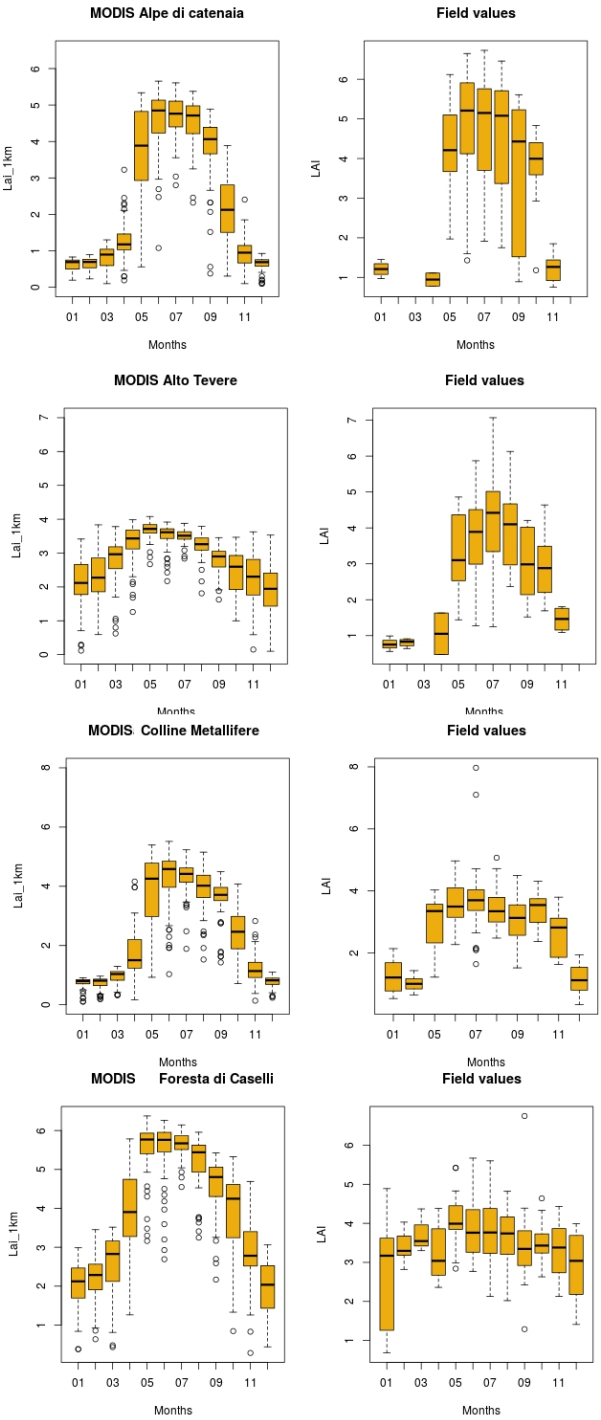

Figure 2 Average monthly values (2000-2016) of LAI measured from MODIS (left) and LAI measured on site (right) for each district, from top to bottom: Alpe di Catenaia, Alto Tevere, Colline Metallifere and Foresta di Caselli, Italy.

While consistent with another study performed in an open canopy stand (Ryu et al., 2012), the results extend the applicability of MODIS LAI in temperate and Mediterranean forests, which are often characterized by very high canopy density (LAI>5 m^2 m^{-2}, Alivernini et al., 2018; Cinnirella et al., 2002; Thimonier et al., 2010; this study) which can limit the retrieval of optical information from satellite data. Indeed, optical measures often saturate at leaf area index values of about 5 (Thenkabail et al., 2000), while vegetation indices using near-infrared bands may saturate at lower values (Davi et al., 2006; Turner et al., 1999). In addition, Mediterranean forests exhibits different phenological patterns according to forest categories and types, and therefore accurate temporal resolution data are strongly required for discriminating different forest types in these environments. Taken together, results indicated that temporal MODIS LAI are suitable for modelling and up-scaling LAI from the stands to larger areas. The discrepancy in the average of LAI measurements from the two sources, which can be observed in some points of the series, can be explained by the different spatial resolution of the data (Rocchini 2007, Geri et al., 2011, Xu et al., 2018). MODIS LAI has the resolution of 1 km, and despite the field measurements were taken in stands that are representative of the surroundings, the above-mentioned limits in measures taken in temperate forest is compatible with the observed pattern. We conclude that the availability of long time-series satellite products with quick revisiting time enabled a reliable investigation of seasonal patterns dynamics, which can support finer application on forests ecology and management and phenological monitoring.

ACKNOWLEDGEMENTS

Financial support was provided by the EU LIFE Project "Shaping future forestry for sustainable coppices in southern Europe: the legacy of past management trials" - LIFE FutureForCoppiceS (LIFE14 ENV/IT/000514). The MOD15A2 was retrieved from the online MODIS/VIIRS Subsetting and Visualization services at https://modis.ornl.gov, courtesy of the NASA EOSDIS Land Processes Distributed Active Archive Center (LP DAAC), USGS/Earth Resources Observation and Science (EROS) Center, Sioux Falls, South Dakota, https://eros.usgs.gov.

REFERENCES

Alivernini, A., Fares, S., Ferrara, C., Chianucci, F., 2018. An objective image analysis method for estimation of canopy attributes from digital cover photography. Trees 32, pp. 713-723.

Angelini, A., Corona, P., Chianucci, F., Portoghesi, L., 2015. Structural attributes of stand overstory and light under the canopy. Annals of Silvicultural Research, 39: 23-31 doi: 10.12899/ASR-993.

Asrar, G.Q., Fuchs, M., Kanemasu, E.T., Hatfield, J.L., 1984. Estimating Absorbed Photosynthetic Radiation and Leaf Area Index from Spectral Reflectance in Wheat 1. Agronomy journal, 76(2), pp. 300-306.

Barbati, A., Marchetti, M., Chirici, G., Corona, P., 2014. European forest types and forest Europe SFM indicators: tools for monitoring progress on forest biodiversity conservation. Forest Ecology and Management, 321, pp. 145-157.

Boer, M.M., Macfarlane, C., Norris, J., Sadler, R.J., Wallace, J., Grierson, P.F., 2008. Mapping burned areas and burn severity patterns in SW Australian eucalypt forest using remotely-sensed changes in leaf area index. Remote Sens. Environ. 112, pp. 4358-4369.

Brus, D., Hengeveld, G. M., Walvoort, D. J. J., Goedhart, P. W., Heidema, A. H., Nabuurs, G. J., Gunia, K., 2011. Statistical mapping of tree species over Europe. European Journal of Forest Research, 131, pp. 145-157.

Chen, J.M., Black, T.A., 1992. Defining leaf area index for non-flat leaves. Plant Cell Environ. 15, pp. 421-529.

Chianucci, F., Ferrara, C., Bertini, G., Fabbio, G., Tattoni, C., Rocchini, D., Corona, P., Cutini, A., 2018. Multi-temporal

dataset of stand and canopy structural data in temperate and Mediterranean coppice forests. Mendeley Data, v1, [Dataset] http://dx.doi.org/10.17632/z8zm3ytkcx.1

Ciolli M., Tattoni C., Ferretti F., 2012 Understanding forest changes to support planning: A fine-scale Markov chain approach. Developments in Environmental Modelling 25 pp 355-373

Ciolli M., Bezzi M., Comunello G., Laitempergher G., Gobbi S., Tattoni C., Cantiani M. 2018. Integrating dendrochronology and geomatics to monitor natural hazards and landscape changes. Applied Geomatics, DOI:10.1007/s12518-018-0236-0

Cinnirella, S., Magnani, F., Saracino, A., Borghetti, M., 2002. Response of a mature *Pinus laricio* plantation to a three-year restriction of water supply: structural and functional acclimation to drought. Tree Physiology 22(1), pp. 21-30.

Davi, H., Soudani, K., Deckx, T., Dufrene, E., Le Dantec, V., Francois, C., 2006. Estimation of forest leaf area index from SPOT imagery using NDVI distribution over forest stands. International Journal of Remote Sensing 27, pp. 885–902.

Geri F., Amici V., Rocchini D., 2011. Spatially-based accuracy assessment of forestation prediction in a complex Mediterranean landscape. Applied Geography, 31 (3) pp881-890

Ferretti F., Sboarina C., Tattoni C., Vitti A., Zatelli P., Geri F. Pompei E., Ciolli M., 2018. The 1936 Italian Kingdom Forest Map reviewed: a dataset for landscape and ecological research. Annals of Silvicultural Research, 42(1) pp 3-19 doi: 10.12899/asr-1411

Kuusk, A., Kuusk, J., Lang, M., 2009. A dataset for the validation of reflectance models. Remote Sensing of Environment, 113(5), pp. 889-892.

Leroux, D., Calvet, J.C., Munier, S. and Albergel, C., 2018. Using Satellite-Derived Vegetation Products to Evaluate LDAS-Monde over the Euro-Mediterranean Area. Remote Sensing, 10(8), p. 1199.

Miller, J.B., 1967. A formula for average foliage density. Australian Journal of Botany 15, pp. 141-144.

Munier, S., Carrer, D., Planque, C., Camacho, F., Albergel, C. and Calvet, J.C., 2018. 17 years. Remote Sensing, 10(3), p. 424.
Myneni, R., Knyazikhin, Y., Park, T., 2015. MOD15A2H MODIS Leaf Area Index/FPAR 8-Day L4 Global 500m SIN Grid V006. NASA EOSDIS Land Processes DAAC. http://doi.org/10.5067/MODIS/MOD15A2H.006 (Terra).

ORNL DAAC, Oak Ridge National Laboratory, Distributed Active Archive Center, 2008. Modis collection 5 land products global sub-setting and visualization tool. ORNL, Tennessee, USA. Accessed November 03, 2016. Subset obtained for MOD15A2 product at 43.2152N,10.6864E, 43.7423N,12.045E, 42.6492N,11.1022E, 39.2713N, 9.4299E, 39.0505N,8.837E time period: 2000-02-18 to 2016-10-15, and subset size: 7x7 km.
Pinheiro, J., Bates, D., DebRoy, S., Sarkar, D., R Core Team, 2017. _nlme: Linear and Nonlinear Mixed Effects Models_. R package version 3.1-131, https://CRAN.R-project.org/package=nlme

Prospatin, P., Panferov, O., 2013. Retrieval of remotely sensed LAI using Landsat ETM+ data and ground measurements of solar radiation and vegetation structure: Implication of leaf inclination angle. Int. J. Appl. Earth. Obs. Geoinf. 25, pp. 38-46.

Puletti, N., Chianucci, F., Castaldi, C., 2018. Use of Sentinel-2 for forest classification in Mediterranean environments. Annals of Silvicultural Research 42, pp. 32-38 http://dx.doi.org/10.12899/asr-1463

R Core Team, 2015. R: A language and environment for statistical computing. R Foundation for Statistical Computing, Vienna, Austria. URL https://www.R-project.org/

Rocchini D., 2007. Effects of spatial and spectral resolution in estimating ecosystem α-diversity by satellite imagery. Remote sensing of Environment, 111(4) pp 423-434

Ryan, J.A., Ulrich, J.M., 2017. xts: eXtensible Time Series. R package version 0.10-0. https://CRAN.R-project.org/package=xts

Ryu, Y., Nilson, T., Kobayashi, H., Sonnentag, O., Law, B.E., Baldocchi, D.D., 2010. On the correct estimation of effective leaf area index: Does it reveal information on clumping effects? Agric. For. Meteorol. 150, pp. 463-472.

Ryu, Y., Verfaillie, J., Macfarlane, C., Kobayashi, H., Sonnentag, O., Vargas, R., Ma, S. and Baldocchi, D.D., 2012. Continuous observation of tree leaf area index at ecosystem scale using upward-pointing digital cameras. Remote Sensing of Environment, 126, pp. 116-125.

Thenkabail P.S., Smith R.B., De Pauw E., 2000. Hyperspectral vegetation indices and their relationships with agricultural crop characteristics. Remote Sensing of Environment 71, pp. 158-182.

Thimonier A., Sedivy I., Schleppi P., 2010. Estimating leaf area index in different types of mature forest stands in Switzerland: a comparison of methods. European Journal of Forest Research 129, pp. 543-562.

Turner P.D., Cohen W.B., Kennedy R.E., Fassnacht K.S., Riggs J.M., 1999. Relationships between leaf area index and Landsat TM spectral vegetation indices across three temperate zone sites. Remote Sensing of Environment 70, pp. 52–68.

Weiss, M., Baret, F., Garrigues, S. and Lacaze, R., 2007. LAI and fAPAR CYCLOPES global products derived from VEGETATION. Part 2: validation and comparison with MODIS collection 4 products. Remote sensing of Environment, 110(3), pp. 317-331.

Woodgate, W., Disney, M., Armston, J.D., Jones, S.D., Suarez, L., Hill, M.J., Wilkes, P., Soto-Berelov, M., Haywood, A., Mellor, A., 2015. An improved theoretical model of canopy gap probability for Leaf Area Index estimation in woody ecosystems. Forest Ecology and Management, 358, pp. 303-320.
Xu, B., Park, T., Yan, K., Chen, C., Zeng, Y., Song, W., Yin, G., Li, J., Liu, Q., Knyazikhin, Y., Myneni, R.B., 2018. Analysis of Global LAI/FPAR Products from VIIRS and MODIS Sensors for Spatio-Temporal Consistency and Uncertainty from 2012–2016. Forests, 9(2), p.73.

Zheng, G. and Moskal, L.M., 2009. Retrieving leaf area index (LAI) using remote sensing: theories, methods and sensors. Sensors, 9(4), pp. 2719-2745.

EVALUATION OF THE ATMOSPHERIC UPWARD THERMAL EMISSION TOWARDS SSS RETRIEVAL AT L BAND

A.V. Bosisio[1]*, G. Macelloni[2], M. Brogioni[2]

[1] Institute of Electronics, Computer and Telecommunication Engineering - IEIIT-CNR, Milan, Italy –adavittoria.bosisio@ieiit.cnr.it
[2] Institute of Applied Physics - IFAC-CNR, Florence, Italy - (g.macelloni, m.brogioni)@ifac.cnr.it

KEY WORDS: Microwave radiometry, Sea surface salinity, Atmospheric attenuation, SMOS, Radiosonde

ABSTRACT:
In the framework of actual and future L-band satellite radiometric missions devoted to ocean observation, and in particular to the retrieval of sea surface salinity, it is important to accurately evaluate every single contribution to the signal that can affect the retrieval algorithm. This paper presents the results of the comparison between the atmospheric contribution to the signal, as computed by the SMOS Surface Sea Salinity (SSS) algorithm, and that predicted by a multi-layer forward model driven by radio sounding data. This preliminary analysis focuses on two years of radiosonde measurements collected in a specific test site (Kauai Island, HI, USA) to estimate the Top of Atmosphere (TOA) brightness temperature T_B under well-controlled conditions. As expected, while the two predicted sets of T_B are statistically in good agreement, differences occur under high humidity hot weather conditions. In these cases, the difference between the two methods exceeds 0.2 K and 0.5 K at V and H polarization, respectively. Such fluctuations have an impact on SSS estimate.

1. INTRODUCTION

The development of the L-band missions SMOS (ESA) and Aquarius (NASA) occurred in the last decade has offered the opportunity to map the sea surface salinity from satellite-borne sensors with both spatial and temporal accuracy unattained before. Indeed, L-band is the most suitable frequency band available to the remote sensing community for this specific topic. As reported in (Le Vine et al., 2010), the sensitivity of the brightness temperature T_B to the sea surface salinity has a dynamic range of about 5K; thus every further contribution to the T_B in the observed scenario must be taken into account accurately. Among these contributions, one may recall the cosmic microwave background, the sun-emitted and the moon-reflected radiation, and the self-emission of the atmosphere (Wentz et al., 2012). Whereas the first three contributions are well assessed and they can be estimated with the required accuracy, the last one is variable in itself as it depends on the continuously changing atmospheric conditions in term of water content, in both vapor or liquid phase, and occurrence of precipitation. A fluctuation of 0.5K due to the atmosphere can have an appreciable impact on the Sea Surface Salinity (SSS) estimations (Yueh et al., 2001).
The aim of this study is to compare the atmospheric contribution, as computed by the SSS algorithm of SMOS (ICM-CSIC et al., 2011), to a multi-layer model (Schroeder et al., 1991) driven by real radio sounding data. In particular, we compare the TOA (Top of Atmosphere) brightness temperature T_B computed by a radiative transfer model applied to radiosonde profiles with SMOS predictions at the same locations. The atmospheric state is taken from radiosonde profiles collected during 2015 and 2016 at Kauai Island, HI, USA (http://weather.uwyo.edu/upperair/sounding.html). The first layer of each radiosonde profile is taken as input for SMOS algorithm to mimic measurements.
The sea surface brightness temperature T_{Bsea} is computed by means of the two scale model (Johnson, 2006) for a typical range of wind speed and thermodynamic temperature at fixed salinity value, i.e. 35 psu, at observation angles comprised between 0 and 60° off nadir and both polarizations. As expected, the preliminary results of this analysis show that the multilayer model and the SMOS algorithm predictions are in good agreement in statistical sense but they differ under specific atmospheric condition such as high humidity level.
The paper is organized as follows. Section 2 states the problem, briefly reminds the two computation methods and describes both the atmospheric and the sea brightness temperature database. The numerical results and their discussion are addressed in section 3, whereas section 4 reports the final remarks.

2. MATERIAL AND METHODS

The analysis focuses on the possible impact of a finer modeling of the atmospheric contribution to the TOA brightness temperature. The underlying sea contribution is modeled only for a limited set of parameters.
The multilayer forward model computes the TOA brightness temperature as follows:

$$T_B(\theta, pol) = T_{Bsea}(\theta, pol)\cdot e^{-\tau_{atm}(\theta, pol)} + T_{Bup}(\theta, pol) + \Gamma(\theta, pol)\cdot T_{Bdn}(\theta, pol)\cdot e^{-\tau_{atm}(\theta, pol)} \quad (1)$$

Where:
T_{Bup} and T_{Bdn} = atmospheric self-emitted brightness temperature values in upward and downward direction
τ_{atm} = atmospheric optical thickness.
T_{Bsea} = sea surface brightness temperature computed as (Johnson, 2006)
Γ = sea reflection coefficient which is derived from emissivity ε computed as the ratio of the simulated T_{Bsea} brightness temperature and its thermodynamic temperature (sea surface temperature, SST)
All quantities are angle and polarization dependent, but for sake of simplicity in the following explicit notation is omitted.
Instead, SMOS algorithm applies empirical laws to obtain the brightness temperature. In particular, SMOS algorithm assumes:

$$T_{Bdn} \approx T_{Bup} = T_{Batm} = T_{BO_2} + T_{BH_2O} \quad (2)$$

* Corresponding author

and

$$\tau_{atm}^{*} = \tau_{BO_2} + \tau_{BH_2O} \quad (3)$$

The emission of each atmospheric constituent, dry and water vapor, is computed as follows:

$$T_{Bgas} = (T_0 - \Delta T_{Bgas}) \cdot \tau_{gas} \quad (4)$$

where:

τ_{gas} (τ_{H_2O} or τ_{O_2}) = optical thickness

T_0= surface thermodynamic temperature

ΔT_{Bgas} (ΔT_{BH_2O} or ΔT_{BO_2}) = difference between T_0 and T_{Bgas} (T_{BH_2O} or T_{BO_2})

τ_{gas} and ΔT_{Bgas} are obtained through empirical laws. The latter is useful to define an equivalent thermodynamic temperature to compute the brightness temperature T_{Bgas}.

Then, T_{BSMOS} TOA is obtained as:

$$T_{BSMOS} = T_{Bsea} \cdot e^{-\tau_{atm}^{*}} + T_{Batm}(1 + \Gamma \cdot e^{-\tau_{atm}^{*}}) \quad (5)$$

being T_{Batm} the overall contribution of the two gaseous constituents and τ_{atm}^{*} the optical thickness. In this paper we focus the analysis on the difference $\Delta T = T_B - T_{BSMOS}$ between the two estimated TOA brightness temperature values.

2.1 Atmospheric database

The atmospheric database is composed of the radiosonde profiles collected during 2015 - 2016 at the test site of Lihue airport, Kauai Island, HI, USA, whose geographic coordinates are 21° 58' N, 159° 20' W, and it includes 804 dry and 673 with non-precipitating clouds atmospheric scenarios. The quantities of interest, i.e. pressure, height a.s.l., thermodynamic temperature and relative humidity, were used as input to the radiative transfer forward model, known as *Tbmodel* (Schroeder et al., 1991), to estimate the atmospheric contribution T_B under well-controlled conditions. Figure 1 reports the histograms of the Integrated Water Vapor content (IWV) and of the integrated Liquid Water Path (LWP). IWV shows an almost Gaussian distribution with an average value equal to 30.2 mm and S.D. of about 8 mm, whereas the maximum modeled LWP in the cloudy profiles is 0.5 mm.

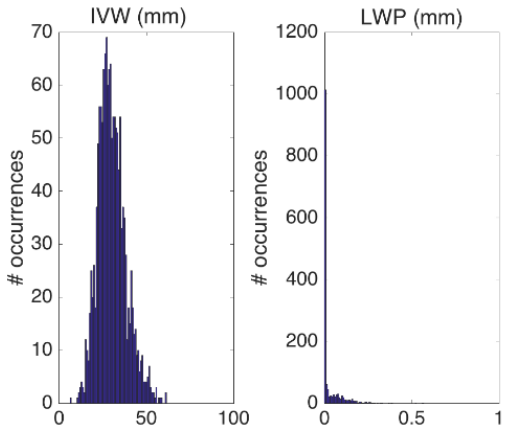

Figure 1. Histograms of Integrated Water Vapor content (left) and of Liquid Water Path (right).

2.2 Atmospheric modeling: multilayer forward and SMOS algorithm

Tbmodel computes the atmospheric contribution under scatter-free hypothesis, i.e. only emission and absorption mechanisms involving water vapor and liquid water are taken into account, related to the atmospheric database. The gaseous absorption is computed according to Rosenkranz model (Rosenkranz, 1999), whereas cloud liquid was added to radiosonde profiles and absorption computed accordingly by using Salonen criterion (Salonen and Uppala, 1991).

Figure 2 shows the difference between the two self-emitted temperatures, T_{Bdn}, and T_{Bup} along the five directions of observation. As expected, the difference increases with increasing observation angle due to the longer geometric path. Although they are slight differences, the average ΔT value along 60° direction is about 0.02 K with S.D. = 0.003 K and a maximum value of 0.05 K, they are not null as postulated in SMOS algorithm.

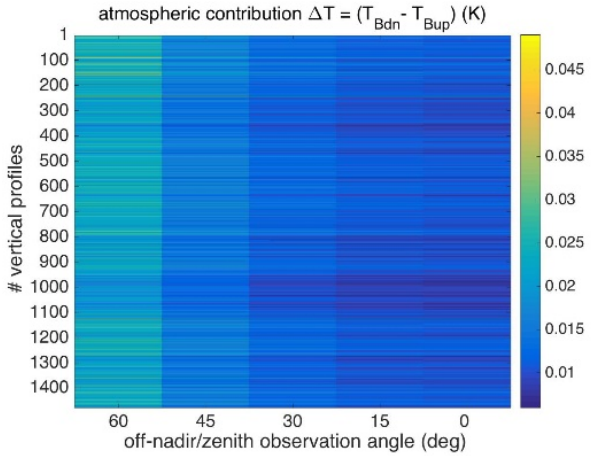

Figure 2. Atmospheric self-emitted temperature difference between downward and upward direction along the observation direction.

The TOA T_{BSMOS} is computed according to L2B ATBD (ICM-CSIC et al., 2011) interpreting the first radiosonde level as ground measurements. τ_{gas} and T_{Bgas} are computed by means of empirical laws that assume, for dry atmosphere, a quadratic fit and, for water vapor, a linear fit:

$$\tau_{0_2} = \left\langle \{\bar{c}_{tau}\}, \{\bar{d}_{O_2}\} \right\rangle \quad (6)$$

$$\Delta T_{0_2} = \left\langle \{\bar{c}_T\}, \{\bar{d}_{O_2}\} \right\rangle \quad (7)$$

$$\tau_{H_2O} = \left\langle \{\bar{k}_{tau}\}, \{\bar{d}_{H_2O}\} \right\rangle \quad (8)$$

$$\Delta T_{H_2O} = \left\langle \{\bar{k}_T\}, \{\bar{d}_{H_2O}\} \right\rangle \quad (9)$$

The numerical values of the coefficients in the columnar vectors $\bar{c}_{tau}$, $\bar{c}_T$, $\bar{k}_{tau}$, $\bar{k}_T$ are taken after the SMOS L2 OS TGRD ((ICM-CSIC et al., 2006), whereas the surface parameters are stored in vectors $\bar{d}_{O_2}$ =[1, T_0, P_0, T_0^2, P_0^2, T_0P_0] and $\bar{d}_{H_2O}$ =[1, P_0, WVC], being WVC the water vapor content (kg/m^2). <{},{}> is the scalar product between vectors.

Figure 3 shows the difference between the two estimates of the single atmospheric brightness temperature, namely T_{Bup}- T_{Batm}. Again, the average value of the difference is about few hundredth of a Kelvin; still, there are conditions that reveal a maximum at about 0.3 K that deserve to be inspected. The largest differences occur at the warmest temperature concurrently with high pressure and humidity values, as shown in Figures 4 and 5.

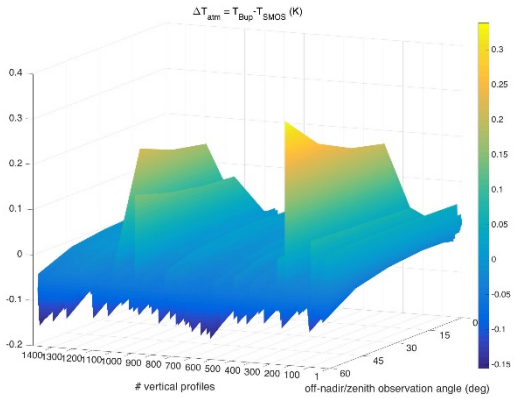

Figure 3. Atmospheric temperature difference between modeled self-emitted upward T_{Bu} and SMOS prediction T_{Batm}.

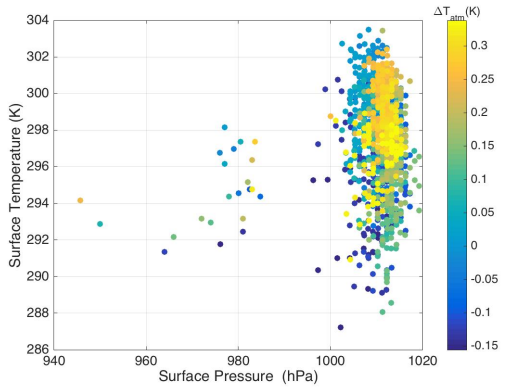

Figure 4. Scatterplot of the atmospheric temperature difference of Figure 2 explained with surface Pressure and Temperature values.

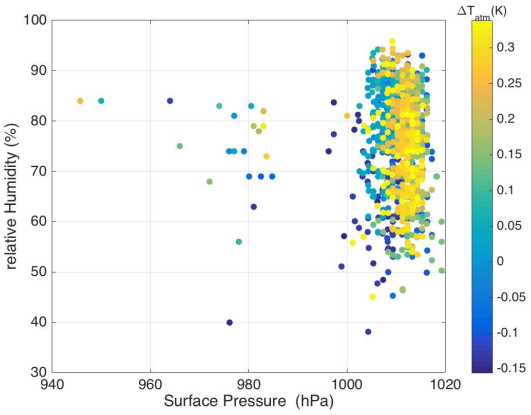

Figure 5. Scatterplot of the atmospheric temperature difference of Figure 3 explained with surface Pressure and relative humidity.

2.3 Sea surface modeling

T_{Bsea} values are computed assuming typical values by using the two-scale model (J. Johnson, 2006). Specifically, salinity value is fixed at 35 psu, whereas SST varies from 275 to 285 K and wind speed is comprised between 0 and 25 km/h.
The two-scale model divides the emission contribution due to the sea waves in two spectral regions, long and short one. The former accounts for the long wave slope variance and the latter describes local variations in terms of facets tilted about the local incidence angle. Polarization and observation angles are the other required parameters to model the sea surface emission. Hence, both polarization are considered and observation angles span from 0 to 60° off nadir.
Figure 6 shows the impact of the polarization on T_{Bsea} for the chosen set of parameters. As expected, T_{Bsea} is higher at vertical polarization but shows a lesser sensitivity to the physical parameters since we observe close to the Brewster's angle, whereas at horizontal polarization the wind speed has a strong impact on the temperature value itself.

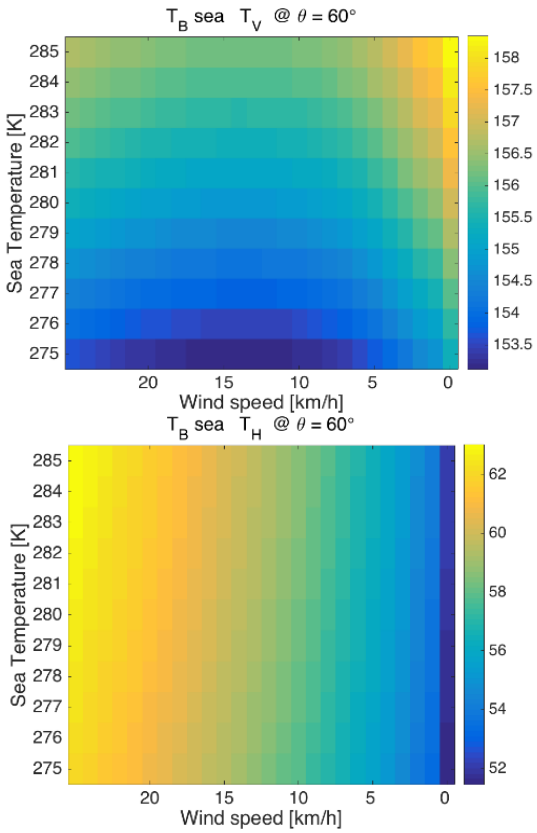

Figure 6. T_{Bsea} computed at 60° off nadir: vertical polarization (top), and horizontal polarization (bottom).

3. NUMERICAL RESULTS

The modeling of the atmospheric contribution to the computation of the TOA brightness temperature plays both an explicit and an implicit role. In the previous section, the analysis has been focused on the computation of the atmospheric brightness temperature itself (explicit contribution). Here, the implicit contribution is included by observing the difference between the two predicted TOA, i.e. T_B, as from (1), and T_{BSMOS}, as from (5). The comparison between the two approaches is based on 4 typical statistical indicators, i.e. average value < >, standard deviation

S.D., minimum and maximum value of the difference (T_B- T_{BSMOS}) at both polarizations and for all the observation angles. Table 1 summarizes the numerical results computed at θ=0°, 30° and 60° that represent the overall trend. The maximum difference is displayed in Figure 7 to highlight the relationship with the parameters that describe the underlying ocean status.

The results of this analysis should be considered preliminary as they are based on a limited atmospheric database. Still, there are some comments that are interesting to single out. Firstly, it appears that SMOS algorithm tends to underestimate the brightness temperature. Then, if the differences are little statistically, as confirmed by the average value and the standard deviation, in few cases the atmospheric conditions bear discrepancies up to about 0.5K. This can have an impact on the SSS retrieval, as reported in (Yueh et al, 2001), because a +0.15K bias on the brightness temperature induces a bias of -0.2 psu at SST= 300K and of -0.6 psu at SST =270 K.

θ=0°	**<>**	**S.D.**	**min**	**max**
T_{Bdn} -T_{Bup}	0.01	0.002	0.006	0.024
T_{Bup}- T_{Batm}.	-0.010	0.011	-0.05	0.05
T_B- T_{BSMOS} (H&V)	0.017	0.015	-0.053	0.09
θ=30°	**<>**	**S.D.**	**min**	**max**
T_{Bdn} -T_{Bup}	0.012	0.002	0.008	0.028
T_{Bup}- T_{Batm}.	-0.016	0.016	-0.065	0.22
T_B- T_{BSMOS} (V)	0.019	0.025	-0.084	0.295
T_B- T_{BSMOS} (H)	0.012	0.023	0.084	0.33
θ=60°	**<>**	**S.D.**	**min**	**max**
T_{Bdn} -T_{Bup}	0.022	0.003	0.013	0.049
T_{Bup}- T_{Batm}.	-0.07	0.026	-0.155	0.34
T_B- T_{BSMOS} (V)	-0.055	0.054	-0.163	0.255
T_B- T_{BSMOS} (H)	-0.09	0.036	-0.21	0.54

Table 1. Comparison between the two modeling approaches. Numerical values are in Kelvin.

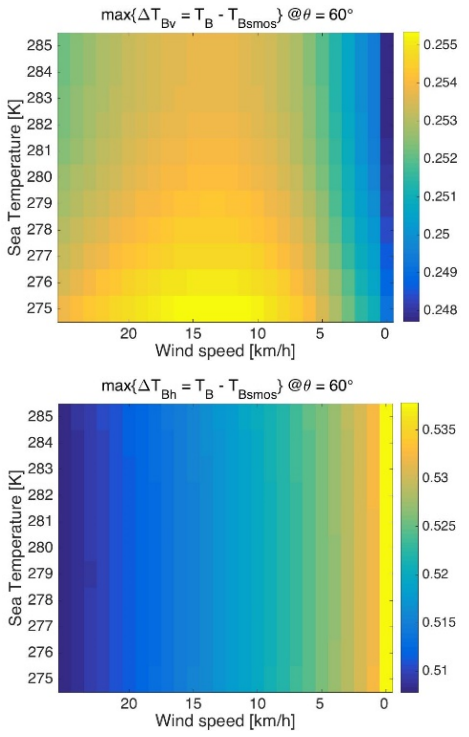

Figure 7. Maximum T_B- T_{BSMOS} difference computed at 60: vertical polarization (top), and horizontal polarization (bottom).

4. CONCLUSIONS

Actual L-band satellite missions SMOS provide ocean observations with both spatial and temporal accuracy unattained before. A deeper insight to every single contribution that can possibly refine the retrieval of geophysical parameters such as SSS or SST is needed. In particular, the effect of the atmospheric correction, predicted with a physically-based multilayer forward model, as opposite to the SMOS algorithm that is based upon empirical laws, is considered here. As a general comment, the multilayer forward modeling approach and the SMOS algorithm are almost in agreement in statistical sense, which was fairly expected. The maximum difference occurs under weather condition characterized by high relative humidity values. Nevertheless, in these cases the difference between the two methods exceeds 0.2 K and 0.5 K at V and H polarization, respectively. These values are relevant for the retrieval of SSS and further analysis are needed to better investigate on this effect.

ACKNOWLEDGEMENTS

The authors gratefully thank Jacqueline Boutin and Clovis Thouvenin-Masson (LOCEAN\CNRS) for the constructive discussions.

REFERENCES

ICM-CSISC, LOCEAN, SA, CETP, IFREMER, "SMOS L2 OS Table Generator Requirements Document", Chapter 2.4.8 Atmosphere Effects, July 2016.

ICM-CSISC, LOCEAN, SA, CETP, IFREMER, "SMOS L2 OS Algorithm Theoretical Baseline Document", Chapter 4.9 Atmospheric Effects, Nov. 2011.

Johnson J.T., "An efficient two-scale model for the computation of thermal emission and atmospheric reflection from the sea surface," IEEE Trans. Geosci. Remote Sens., vol. 44, no. 3, pp. 560–568 March 2006, doi: 10.1109/TGRS.2005.855999.

Le Vine D. M., G. S. E. Lagerloef, S. E. Torrusio, " Aquarius and Remote Sensing of Sea Surface Salinity from Space", Proc. of the IEEE, Vol. 98, No. 5, May 2010, doi: 10.1109/JPROC.2010.2040550.

Rosenkranz P. W. (1999) - Correction to "Water Vapor Microwave Continuum Absorption: A Comparison Of Measurements And Models", Radio Science, 34(4): 1025, doi:10.1029/1999RS900020.

Salonen E., S. Uppala, "New prediction method of cloud attenuation," Electronic Letters, vol. 27, no. 12, pp. 1106–1108, Jun. 1991, doi: 10.1049/el:19910687 ,.

Schroeder J.A., E. R. Westwater, Users' guide to WPL Microwave Radiative Transfer Software, NOOA Technical Memorandum ERL WPL-213, WPL, Boulder, CO, Oct. 1991.

Wentz F. J., D. M. Le Vine, "Version 2: ATBD Aquarius Salinity Retrieval Algorithm", RSS Technical Report 082912, Aug. 2012.

S. Yueh, R. West, W. Wilson, F. Li, E. Njoku, and Y. Rahmat-Samii, "Error sources and feasibility for microwave remote sensing of ocean surface salinity," IEEE Trans. Geosci. Remote Sens., vol. 39, no. 5, pp. 1049–1060, May 2001, doi: 10.1109/36.921423

USE OF SENTINEL-1 AND SENTINEL-3 DATA TO INITIALIZE A NUMERICAL WEATHER MODEL

L. Pulvirenti[1]*, M. Lagasio[1], A. Parodi[1], G. Venuti[2], E. Realini[3], N. Pierdicca[4]

[1] CIMA Research Foundation, via Armando Magliotto 2, 17100 Savona, Italy - (luca.pulvirenti, martina.lagasio, antonio.parodi)@cimafoundation.org

[2] Dept. of Civil and Environmental Engineering, Politecnico di Milano, Piazza Leonardo da Vinci 32, 20133 Milan, Italy – giovanna.venuti@polimi.it

[3] Geomatics Research & Development srl, via Cavour 2, 22074 Lomazzo Italy - eugenio.realini@g-red.eu

[4] Dept. of Information Engineering, Electronics and Telecommunications, Sapienza University of Rome, via Eudossiana 18, 00184 Rome, Italy – nazzareno.pierdicca@uniroma1.it

KEY WORDS: Sentinel-1, Sentinel-3, Soil Moisture, Land Surface Temperature, Sea Surface Temperature, Wind Field, Numerical Weather Prediction Models

ABSTRACT:

This paper deals with an example of synergy between numerical weather models and Sentinel data. The example concerns the incorporation of Sentinel-1 and Sentinel-3 derived products in a high spatial resolution numerical weather prediction (NWP) model operating at cloud resolving grid spacing. The rationale is that NWP models are presently able to produce forecasts with a spatial resolution in the order of 1 km, but unreliable surface information or poor knowledge of the initial state of the atmosphere may produce an inaccurate simulation of the weather phenomena. In this context, the Copernicus Sentinel satellites represent an important source of data, because they provide a set of high spatial resolution observations of physical variables (e.g. soil moisture, land/sea surface temperature, wind speed) used in NWP models runs. This paper presents the first results of one experiment of ingestion/assimilation of surface information derived from Sentinel data into a NWP model. The experiment concerns a flood event occurred in Tuscany (Central Italy) in September 2017.

1. INTRODUCTION

The progresses achieved in numerical weather prediction (NWP) allow the models to produce forecasts with a spatial resolution in the order of 1 km (the so-called cloud resolving grid spacing). However, the problem of providing high-resolution NWP models with suitable surface information represents a critical point. In fact, the representation of surface-atmosphere interactions in weather forecast models has a strong impact on the Planetary Boundary Layer (PBL) and, in turn, on the forecast (Panegrossi et al., 2011). Hence, the knowledge of the initial and boundary conditions is the first and major source of uncertainties in weather modelling. For the knowledge of the initial and boundary conditions, satellite data can be of great importance, because it is expected that weather forecast uncertainties can be significantly reduced by ingesting Earth Observation (EO) derived products into models operated at cloud resolving grid spacing. These products may concern soil moisture, land and/or sea surface temperature, wind speed, as well precipitable water vapour content. From this point of view, data extracted from the Copernicus Sentinel satellites can be very useful in improving the performances of high-resolution numerical models through a spatially accurate determination of land/sea conditions.

In agreement with the previous considerations, in 2017 the European Space Agency (ESA) issued a tender about novel advances in the synergistic use of high-resolution numerical atmosphere models and Earth observation products. The STEAM (SaTellite Earth observation for Atmospheric Modelling) project was finally selected and kick off was held in November 2017. The STEAM project aims at investigating new areas of synergy between numerical atmosphere models and EO data, such as the ingestion of remote sensing products in high-resolution NWP models. Among the available EO data, the project focuses on Sentinel ones.

Several steps should be accomplished in order to assess the effect of incorporating Sentinel data in NWP models, such as the selection of a suitable model according to criteria such as the applicability in the high-resolution limit and the choice of the physical variables ingested in the model. Then, a set of experiments, regarding a number of case studies, has to be carried out to compare the outputs of the model simulations with actual data (e.g., rain rate). Note that, for each case study, several model runs have to be carried out for a complete investigation on the possible utility of EO data in high-resolution NWP applications. Besides the open loop (i.e., no ingestion of any EO derived variable) run, the ingestion/assimilation of one variable at a time should be firstly performed to evaluate the sensitivity of the model to each variable. Successively, the assimilation/ingestion of a combination of variables can be carried out. As a matter of fact, the number of case studies analysed in the project should be forcedly limited. Hence, the case studies have to be significant for an operational point of view (e.g., reliability of the weather alerts), so that it was decided to focus on high impact weather events (HIWEs).

* Corresponding author

This paper gives a general overview of the project and focuses on the first activities performed in its framework. In particular, it discusses the rationale behind the choice of the Numerical Weather Prediction Model and analyses the preliminary results of the first experiment of ingestion of Sentinel derived products into the selected NWP.

2. THE STEAM PROJECT

Despite the technological and scientific advances in recent decades, it is still a challenge to accurately forecast the onset and/or the spatio-temporal evolution of HIWEs, especially in complex topography areas (e.g. Great Alpine Region and Mediterranean Sea coastline). Nowadays, the skill of numerical weather models is certainly being improved thanks to the increasing model resolution from cloud-permitting (5 km) to cloud-resolving (1 km) grid spacing. However, challenges in predictive abilities with respect to HIWE derive from the poor knowledge of the initial state of both atmosphere and surface at small scales, thereby leading to an inevitable model spin-up that often results in an inaccurate simulation of the severe weather phenomena in terms of timing, location and intensity. Satellite data can be of great importance in this context. It is thought that forecast uncertainties can be significantly reduced by ingesting into models, operated at cloud-resolving grid spacing, EO observational data concerning soil moisture, land surface temperature, land cover, as well as precipitable water vapour content.
The objectives of the STEAM project are: 1) the ingestion of high-resolution remote sensing data products in high-resolution numerical weather models; 2) the assessment and improvement of the capability of current high resolution numerical weather models and large-eddy simulations (LES) to characterize the effect of tropospheric turbulence and spatial inhomogeneity of water vapour fields on propagation parameters relevant for SatCom services, Radio Science and Radio Astronomy, and use of GNSS data for meteorology.
The work described in this paper is part of the activities carried out in the framework of objective 1).

3. THE SELECTED NUMERICAL WEATHER MODEL

For a profitable ingestion of high resolution EO data in a NWP model, the latter should: 1) be well-established when applied in the high-resolution limit; 2) have different physics parameterizations for what concerns microphysics, radiation, surface processes and turbulence; 3) have a proven portability on cloud computing environment (because the progress of supercomputing capabilities has strongly influenced the progress in the numerical weather modeling); 4) allow various data assimilation techniques.
Among the available NWP models, COSMO, AROME-HARMONIE, Unified Model (UM) and WRF were considered. As for point 1), the number of research papers involving applications in the high-resolution limit was analyzed (2009-2016, title keywords: model name & high & resolution, source: https://webofknowledge.com/). Looking at Table 1, which summarizes the results of the comparison among the selected NWP models in terms of the aforementioned criteria (i.e., points 1-4), it can be deduced that the Weather Research and Forecasting (WRF) model is the one associated to the highest number of scientific publications during the reference period 2009-2016. In terms of available physical parameterizations, COSMO, HARMONIE-AROME and Unified models are comparable, but they are considerably limited with respect to the WRF model. As for the topic of this paper, it is interesting

	COSMO	Harm. Arome	Unified	WRF
N° of research papers with applications in the high-resolution limit	11	3	5	34
N° of available physics parameteriz.	4	4	4	20
Portability on cloud computing environment	NO	NO	NO	YES
Data assimilation technique	Latent heat nudging Kalman filter	Kalman filter	3DVAR 4DVAR Kalman filter	3DVAR 4DVAR Kalman filter

Table 1. Figure placement and numbering

to note that WRF includes four different land surface models (LSMs), i.e., two versions of the Noah model (Niu et al., 2011), the RUC LSM (Benjamin et al., 2004) and the Pleim-Xiu model (Xiu and Pleim, 2001). Comparing the data assimilation techniques, WRF and UM models show the same types of approaches, namely 3DVAR, 4DVAR and Kalman filter, while COSMO and HARMONIE-AROME are definitely more limited.
Summarizing the results, the model with the highest indicators for all the four criteria is the WRF model, which therefore was selected to carry out the experiments performed in the framework of the STEAM project.

4. FIRST RESULTS OF THE STEAM PROJECT

The first case study selected to assess the impact of the ingestion of Sentinel data into the WRF model concerns the HIWE that occurred in the city of Livorno (Tuscany, Central Italy) on September 9-10, 2017. The rain started to fall during the late hours of Sep. 9, but was at its most intense during the early hours of Sep. 10 giving rise to widespread flooding in the city. The Livorno flood caused nine casualties.
As underlined before, the STEAM project focuses on Copernicus Sentinel-1 data. Assuming a WRF model run starting ~24-36 hours before the onset of the event, S1 and S3 data acquired between the afternoon of Sep. 8 and the afternoon of Sep. 9, 2017 have been searched for. The following data were directly available through the Sentinel catalogues: 1) land and sea surface temperatures derived from the Sea and Land Surface Temperature Radiometer (SLSTR) on board Sentinel-3, generated on a 1×1 km^2 grid; 2) wind vector (speed and direction at 10 m asl) included in the Ocean Wind Field (OWI) component of the Sentinel-1 Level-2 Ocean (OCN) product (again generated on a 1×1 km^2 grid). In particular, for sea surface temperature (SST), S3 data acquired on Sep. 9, 2017 at 20:36 UTC were gathered, while for land surface temperature (LST), S3 data acquired on Sep. 9, 2017 at 09:50 UTC were

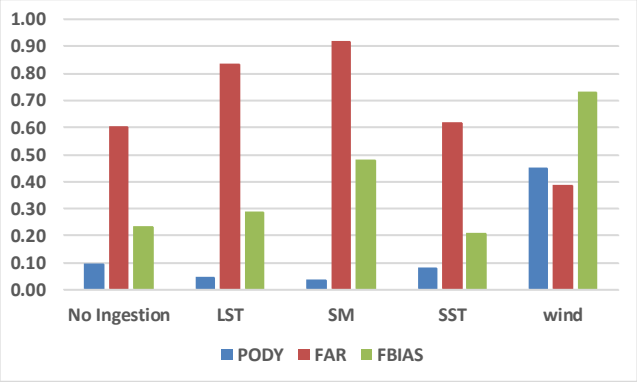

Figure 1. Results of the comparison between reference and WRF derived cumulated rain rate for the Livorno event. Legend: IFS: no ingestion/assimilation (open loop); IFS-LST: ingestion of S3-derived LST; IFS-SM: ingestion of S1-derived SM; IFS-SST: ingestion of S3-derived SST; IFS-wind: assimilation of S1-derived wind vector. IFS indicates that WRF was initialized using the Integrated Forecasting System model derived atmospheric and land-soil variables (except for the EO derived variable).

used. S1 observed the Livorno area on Sep. 8, 2017 at 17:14 UTC.

For what concerns surface soil moisture, it was derived from S1 Ground Range Detected (GRD) Interferometric Wide Swath (IW) products by applying a multi-temporal retrieval algorithm (maximum likelihood) implemented in a software package designed to set up a surface soil moisture mapping service at national (Italian) scale (Pulvirenti et al., 2018). The multi-temporal algorithm assumes that the temporal scale of variation of surface soil moisture (SM) is considerably faster than that of soil roughness. Hence, once vegetation effects on S1 data are corrected, short-term variations of S1 backscattering are related to variations of SM. In order to discriminate the contributions from soil and vegetation to the backscatter (thus correcting for the effect of vegetation), the semi-empirical water cloud model (Attema and Ulaby, 1978) is applied. WCM uses one parameter, i.e. the plant water content, to describe vegetation. This parameter is estimated from the Normalized Difference Vegetation Index (NDVI) derived from optical images through an empirical relationship (Pierdicca et al., 2014). To apply the multi-temporal algorithm, even the S1 data acquired on Sep. 2, Aug. 27, Aug 21 and Aug 15, 2017 were used. All the Sentinel derived data were resampled and reprojected to a reference WRF grid (Geographic Lat/Lon, WGS84, ~1.5 km of pixel size, corresponding to 0.0135°).

The WRF simulation started at the synoptic hour temporally closest to the time of the Sentinel-1 acquisition, i.e., on Sep.8, 2017 at 18:00 UTC and lasted 48h (until Sep.8, 2017 at 18:00 UTC). It was initialized using the atmospheric and land-soil variables available through the Integrated Forecasting System (IFS) global model of the European Centre for Medium-Range Weather Forecasts (ECMWF) (0.125° of resolution). This paper focuses on the analysis of the sensitivity of the WRF model to each surface variable, so that the results of the ingestion of one variable at a time are described.

The values of SM and wind field were assumed as acquired at 18:00 UTC (although S1 acquisition time was 17:40). For the wind field, a 3DVAR assimilation technique was applied, while SM was used for the initialization of the WRF run. It is well-known that SM retrieval is unfeasible in urban, forested and densely vegetated areas. To deal with gaps in the S1 derived SM map, thus initializing the NWP model with a spatially homogeneous moisture map, the calculation of the difference between the retrieved SM values and the original (model) ones in the upper layer was firstly carried out. Then, this difference was spatially interpolated and, finally, the map of interpolated difference was added to the original (model) one. Obviously, in areas where gaps are not present, this procedure has no effect and the retrieved data are maintained. While the LSM included in WRF (the RUC model was used in this case) has six layers, the SAR derived SM is relative to approximately the first 5 cm of soil. To account for this inconsistency, the LSM derived vertical profile of SM was corrected through a linear interpolation of the difference between the S1-derived surface SM and the model one. The difference was assumed as equal to 0 m^3/m^3 at the deepest level.

For what concerns S3 derived SST and LST data, a direct insertion was carried out. For this purpose, the WRF simulation was stopped at the acquisition time of each variable and then restarted after having replaced the WRF derived variable with the S3 derived one.

The spatially interpolated rain cumulated between September 9 at 18:00 UTC and September 10 at 06:00 UTC was considered as benchmark to evaluate the possible improvement in the forecast accuracy brought by the incorporation of Sentinel derived products in WRF. For this purpose, the Method for Object-Based Diagnostic Evaluation (MODE) tool (Davis et al., 2009) was used. Simply speaking, MODE can be considered a basic algorithm for image segmentation and object matching, but developed for meteorological applications. In our experiments, objects in the reference (rain gauge-derived) and WRF-derived rain rate (RR) maps were identified based on a threshold on RR (namely 72 mm). Then, the statistics of the similarities of the objects in the two datasets were computed and the degree of similarity between forecast and observed objects was considered to evaluate the forecast quality. Among the different parameters measuring the similarity between objects available through MODE, the probability of detection (PODY), the frequency bias (FBIAS) and the false alarm ratio (FAR) were chosen. PODY is given by the number of hits divided by the total number of observed rainy events. FBIAS is given by the total number of forecasted rainy events divided by the total number of observed rainy events. FAR is given by the number of false alarms divided by the total number of forecasted rainy events. The values obtained for PODY, FBIAS and FAR are shown in Figure 1.

Looking at Figure 1, it can be noted that the assimilation of S1-derived wind vector yields a FBIAS close to 1 (perfect score), as well as the highest PODY and the lowest FAR. The ingestion of SM data increases the FBIAS, but slightly decreases the PODY with respect to the open loop and increases the FAR. The ingestion of LST and SST does not seem to improve the quality of the WRF simulations.

ACKNOWLEDGEMENTS

This work was funded by the European Space Agency (ESA) under Contract No. 4000121670/17/NL/AF.

REFERENCES

Attema, E.P.W., Ulaby, F.T., 1978. Vegetation modeled as a water cloud. *Radio Sci*. (13), pp. 357–364.

Benjamin, S.G., Grell, G. a., Brown, J.M., Smirnova, T.G., Bleck, R., 2004. Mesoscale Weather Prediction with the RUC

Hybrid Isentropic–Terrain-Following Coordinate Model. *Mon. Weather Rev*. (132), pp. 473–494.

Davis, C.A., Brown, B.G., Bullock, R., Halley-Gotway, J., 2009. The Method for Object-Based Diagnostic Evaluation (MODE) Applied to Numerical Forecasts from the 2005 NSSL/SPC Spring Program. *Weather Forecast*. (24), pp. 1252–1267.

Niu, G.Y., Yang, Z.L., Mitchell, K.E., Chen, F., Ek, M.B., Barlage, M., Kumar, A., Manning, K., Niyogi, D., Rosero, E., Tewari, M., Xia, Y., 2011. The community Noah land surface model with multiparameterization options (Noah-MP): 1. Model description and evaluation with local-scale measurements. *J. Geophys. Res. Atmos*. (116).

Panegrossi, G., Ferretti, R., Pulvirenti, L., Pierdicca, N., 2011. Impact of ASAR soil moisture data on the MM5 precipitation forecast for the Tanaro flood event of April 2009. N*at. Hazards Earth Syst. Sci.* (11), pp. 3135-3149.

Pierdicca, N., Pulvirenti, L., Pace, G., 2014. A prototype software package to retrieve soil moisture from sentinel-1 data by using a bayesian multitemporal algorithm. *IEEE J. Sel. Top. Appl. Earth Obs. Remote Sens*. (7), pp. 153-166.

Pulvirenti, L., Squicciarino, G., Cenci, L., Boni, G., Pierdicca, N., Chini, M., Versace, C., Campanella, P., 2018. A surface soil moisture mapping service at national (Italian) scale based on Sentinel-1 data. *Environ. Model. Softw*. (102), pp. 13-28.

Xiu, A., Pleim, J.J.E.J., 2001. Development of a land surface model. Part I: Application in a mesoscale meteorological model. *J. Appl. Meteorol*. (40), pp. 192–209.

Earth observation for disaster risk and geomorphologic application

MODELLING SOIL EROSION IN THE ALPS WITH DYNAMIC RUSLE-LIKE MODEL AND SATELLITE OBSERVATIONS

M. Aiello[1], M. Gianinetto[1]*, R. Vezzoli[1], F. Rota Nodari[1], F. Polinelli[1], F. Frassy[1], M.C. Rulli[1], G. Ravazzani[2], C. Corbari[2], A. Soncini[2], D.D. Chiarelli[2], C. Passera[2], D. Bocchiola[2]

[1] Dept. of Architecture, Built Environment and Construction engineering, Politecnico di Milano, via Ponzio, 31, 20133 Milano, Italy - (martina.aiello, marco.gianinetto, renata.vezzoli, francesconiccolo.polinelli, federico.frassy, mariacristina.rulli)@polimi.it

[2] Dept. of Civil and Environmental Engineering, Politecnico di Milano, Piazza Leonardo da Vinci, 32, 20133 Milano, Italy – (giovanni.ravazzani, chiara.corbari, andrea.soncini, davidedanilo.chiarelli, corrado.passera, daniele.bocchiola)@polimi.it

KEY WORDS: Satellite time series, Spectral indices, NDVI, RUSLE-LIKE MODEL, Erosion, Natural hazards

ABSTRACT:

Soil water erosion is a creeping natural phenomenon, mostly related to weather and climate, and one of the main hydrogeological risk in Europe. It causes nutrients loss and exposes the environment to landslides, with negative impacts on agriculture, ecosystem services and infrastructures. Conversely, several human activities induce environmental modifications which intensify pressure on soils, thus increasing their predisposition to erosion.

This study describes the integration of satellite observations with a modified version of the well-known Revised Universal Soil Loss Equation (RUSLE) model for estimating soil erosion in an Italian Alpine river basin. Compared to traditional RUSLE formulation, in this study we assigned the cover management factor using a combination of DUSAF land cover classification and NDVI values computed from Landsat time series. Rainfall erosivity was estimated separating liquid precipitation (erosive) and solid precipitation (non-erosive) from hourly data. Soil erodibility for the study area was tuned combining soil maps with total organic carbon (TOC), acidity (pH) and texture (granulometry) from soil samples collected on site. Finally, the slope length and steepness factor was derived using a 30-meter spatial resolution digital elevation model.

Integrating the RUSLE-like model with spectral indices derived from satellite data allows highlighting spatial patterns useful for understanding soil erosion dynamic and forcing. Thus, satellite-derived spectral information, that include both seasonal and long-term land cover changes, opens new ways for modelling the dynamics of soil erosion.

1. INTRODUCTION

1.1 Background and aims

Soil water erosion is a creeping natural phenomenon, mostly related to weather and climate, which leads to loosening, dissolving or removal of earthy or rock materials from the surface. It causes nutrients loss and exposes the environment to landslides, with negative impacts on agriculture, ecosystem services and infrastructures (Boardman and Poesen, 2006). Conversely, several human activities (e.g. land cover changes, agricultural patterns reshaping,intensive grazing and forest management activities) induce environmental modifications which may intensify pressure on soils, thus increasing their predisposition to water erosion.

The European Commission's Soil Thematic Strategy (COM (2012) 46) has identified soil erosion as one of the main hydrogeological risks in Europe. Long dry periods followed by heavy rainfall on steep slopes, make the Southern European countries particularly prone to erosion (Van der Kniff *et al.*, 2000), with the highest soil loss rates in the Alpine region (Panagos *et al.*, 2015b).

With reference to Italy, mass movements and soil erosion are the most widespread forms of soil degradation, which accounts for an annual cost of about 900 million Euros per year (Costantini and Lorenzetti, 2013). Nonetheless, this natural hazard is often underestimated in local planning.

In this scenario, Earth observation offers a unique mean for monitoring land cover and land use changes over large areas, which is extremely useful to understand how those dynamics affect soil erosion processes. This work describes the integration of satellite observations within a modified version of the Revised Universal Soil Loss Equation (RUSLE) model for the estimation of soil erosion in the Italian Alps.

1.2 Study area

The study area is Val Camonica, one of the largest valleys of the central Alps, located in the northern part of Oglio river basin which is embedded in the central alpine and pre-alpine domain of Regione Lombardia (Italy) (Figure 1).

Val Camonica has an area of about 1,800 km^2 and extends from 185 m a.s.l. to 3,585 m a.s.l. of the Adamello Glacier. Almost 90% of the landscape is vegetated (less than 1% crops and 45% forests), highly influenced by altitude variations and rainfall seasonal regime. Precipitation reaches its peak during summer and fall, while snowfall is frequent from October to May and snow cover generally persists at higher altitudes until July.

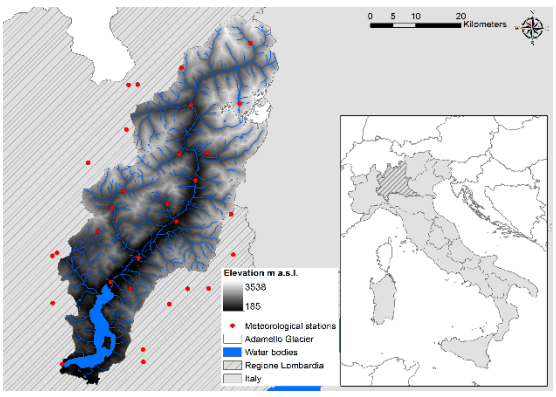

Figure 1. Digital Elevation model of the case study area (Regione Lombardia, Italy).

* Corresponding author

2. MODELING SOIL EROSION

2.1 The RUSLE model

The well-known empirical Revised Universal Soil Loss Equation (RUSLE) (Renard, 1997) estimates the annual potential soil erosion rate A [t ha^{-1} yr^{-1}] as the product of the following quantities:

i) Rainfall erosivity (R-factor) [MJ mm ha^{-1} h^{-1} yr^{-1}]. This is the driving force of erosion and is a function of precipitation rate, air temperature and snow cover dynamics;
ii) Soil erodibility (K-factor) [t ha h ha^{-1} MJ^{-1} mm^{-1}]. This quantity describes the soil properties (i.e. soil structure and organic matter content) that influence the predisposition of soil to erosion;
iii) Topography of the area (LS-factor) [dimensionless]. This parameter mainly depends on slope length and steepness that can further increase soil erosion;
iv) Cover management factor (C-factor) [dimensionless]. This parameter takes into account how land use and land cover management practices protect soils from erosion. Lower C-factor values correspond to higher protection, thus to lower erosion.
v) Control practice factor (P-factor) [dimensionless]. This factor is representative of the capacity of soil conservation practice to reduce the erosion potential of runoff. In this study we assumed the P-factor equal to 1.

2.2 Modification of the RUSLE model

RUSLE is usually applied at yearly scale, neglecting the partitioning between solid precipitation (non-contributing to erosion) and liquid precipitation (active in erosion) and the sheltering effect of snow cover with respect to soil erosion. Besides, the land cover/land use parameter is generally set as a static variable, even when using RUSLE to project future scenarios.
In this study we adopted a RUSLE-like approach which incorporates remotely sensed multispectral images for the dynamic updating of C-factor and estimates rainfall erosivity, as described in Section 2.3. In formal terms, we retained the same equation of RUSLE.

2.3 Data and methods

With respect to traditional RUSLE, the R-factor was estimated as function of liquid precipitation intensity (Sun *et al.*, 2002) and snow presence/absence over the soil; the partitioning between liquid and solid precipitation is a function of air temperature (Aiello *et al.*, in press). Hourly precipitation and air temperature data were recorded from 2003 to 2017 by 26 meteorological stations spread over the study area. The observed meteorological data were spatialized through an inverse distance squared weighting algorithm to compute hourly R-factor on a 30-m grid.
The soil erodibility factor was tuned on the study area, by verifying the agreement between the information extracted from the available soil map and analytical measurements of total organic carbon (TOC), acidity (pH) and texture (granulometry) from a set of soil samples collected on site. Then, each textural class of the soil map were assigned a K-factor value as function of the TOC according to Fantappiè *et al.* (2014).
The LS-factor was derived from a 30-meter spatial resolution digital elevation model, through the method proposed by Desmet and Govers (1996), which captures complex topography and takes into account the upslope contributing area.
Dynamism and seasonality of land cover was introduced in the C-factor using satellite multi-temporal surveys. C-factor values were assigned to each land class using a combination of NDVI computed from Landsat-5, -7 and -8 time series images from 2002 to 2017 and the official thematic maps of the DUSAF (*Destinazione d'Uso dei Suoli Agricoli e Forestali*) for 2000, 2007 and 2015 made available by Regione Lombardia.
Satellite data were pre-processed with standard radiometric calibration and atmospheric correction. All the images were grouped into Summer (from March to August) and Winter (from September to February) subsets and snow cover and clouds were masked before the computation of NDVI. However, Val Camonica has many steep and narrow valleys and during Winter almost half of the study area is completely shadowed or snowed up, thus soil protection from erosion based on NDVI-based C-factor turned out to be an unrealistic estimation (Gianinetto *et al.*, 2018). For this reason, the relationship between NDVI and C-factor was based on Summer NDVI values integrated with DUSAF, while the observed Winter NDVI values were replaced with synthetic values reconstructed from Summer observations and DUSAF land cover classes as follows:
i) For each Winter image, we selected the closest Summer image;
ii) Then, we computed the pixel-based ratio between Winter NDVI and Summer NDVI, excluding shadowed or snowy image pixels;
iii) Next, we computed the average ratio between Winter NDVI and Summer NDVI for each land cover class of DUSAF;
iv) Finally, for each land cover class of DUSAF, we reconstructed the synthetic pixel-based map for Winter NDVI by multiplying the Summer NDVI by the average ratio based computed at the previous step.

Once generated both the Summer and Winter maps of NDVI, we computed the C-factor. To all unvegetated classes of DUSAF we assigned a null C-factor, while for each vegetated class a range of possible values ($C_{min} \leq \mathrm{C-factor} \leq C_{max}$) was given, as suggested by Panagos *et al.* (2015a). Then, for each land cover class we computed the Summer average NDVI (μ_{NDVI}) and its standard deviation (σ_{NDVI}). Finally, for each land cover class we assumed a linear relationship between NDVI (in the range $\mu_{\mathrm{NDVI}} - \sigma_{\mathrm{NDVI}} \leq \mathrm{NDVI} \leq \mu_{\mathrm{NDVI}} + \sigma_{\mathrm{NDVI}}$) and C-factor (in the range $C_{min} \leq \mathrm{C-factor} \leq C_{max}$), both for Winter and Summer. To avoid saturation effects, we assumed $\mathrm{C-factor} = C_{max}$ for $\mathrm{NDVI} < \mu_{\mathrm{NDVI}} - \sigma_{\mathrm{NDVI}}$ and $\mathrm{C-factor} = C_{min}$ for $\mathrm{NDVI} > \mu_{\mathrm{NDVI}} + \sigma_{\mathrm{NDVI}}$.
This method allowed us to: (a) use Winter satellite images despite clouds, shadows and snow cover, (b) link the estimation of C-factor to real land covers, and (c) achieve reasonable estimates for Summer and Winter.

3. RESULTS

3.1 Seasonality in soil erosion rates

Rainfall regime (i.e. R-factor) and land cover variability (i.e. C-factor) are the parameters which convey seasonality within our RUSLE-like model. In our study, we retrieved both annual and seasonal soil loss rates for the simulation period 2003-2017.
While both Summer and Winter show similar spatial patterns of soil erosion, nevertheless during Summer months we simulated slightly lower erosion rates (1.86 [t $ha^{-1}y^{-1}$]) compared to Winter months (2.01 [t $ha^{-1}y^{-1}$]). However, the model is sensitive to the combined effects of seasonality and altitude. As an example, Winter erosion is slightly lower than Summer erosion in the northern section of the basin, which is mainly characterized by the presence of sparsely vegetated areas and moors (Figure 2a-b).

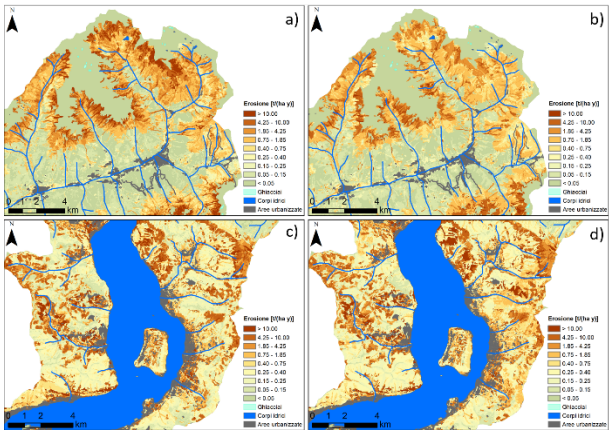

Figure 2. Detail of seasonal soil erosion rates. Top: basin upper section for Summer months (a) and Winter months (b). Bottom: basin lower section for Summer (c) and Winter months (d).

That is probably due to the sheltering effect of snow at higher altitudes. At lower altitudes, where the predominant land covers are broad-leaved and mixed forests, the reduced sheltering effect of vegetation causes higher Winter soil erosion (Figure 2c-d).
The seasonal influence of rainfall and cover management factor on soil erosion was analysed for the most meaningful land cover classes of DUSAF present in the study area. The box-plots of Figure 3a show similar median values for Summer and Winter for the majority of the classes, as the effect of R-factor and C-factor are mostly compensated. A detail of these box-plots for forest classes (311, 312, 313) is presented in Figure 4a. However, this balance is due to a twofold effect:
i) Summer rainfall erosive force exceeds Winter rainfall erosive force, because Summer liquid precipitations are more abundant and more intense (Figure 3b and Figure 4b) but C-factor values are lower due to more prosperous vegetation (Figure 3c and Figure 4c);
ii) On the contrary, during Winter some of the liquid precipitation is replaced by more abundant snowy precipitation (Figure 3b and Figure 4b) and the protective effect of vegetation is attenuated (Figure 3c and Figure 4c).
This compensation effect is also visible in class 333 (Sparsely vegetated areas), which is mainly located at higher altitudes. A similar effect is present in agricultural classes (211, 221, 222, 223) characterized by some of the highest erosion rates. However, it has to be pointed out that the high variability in erosion rates shown by agricultural classes is mostly due to their small size compared to the other classes.

3.2 Comparison with previous studies

The work by Panagos *et al.* (2015b) at the continental scale is a milestone for assessing soil erosion in Europe, thus we used it as reference for comparison. However, they used a 'static' C-factor, derived from the CORINE land cover map of 2006.
The estimation of C-factor through satellite-derived spectral indices, instead of fixed values based on land cover classes, may potentially increase its discretization within different vegetated classes, that may contribute to soil erosion. This is particularly important when studying areas dominated by vegetation, such as on the Alps.
Looking at Figure 5, we can see that hot spots are almost located in the same areas, given the different spatial resolution of the two maps (100-meter (aggregated) for Panagos *et al.*, (2015b) 30-meter for our map), but our fine-tuned modelling suggests that the average potential erosion rate in Val Camonica is only one third (3.87 [t ha^{-1} y^{-1}]) of that estimated with a global modelling (13.71 [t ha^{-1} y^{-1}]).

Our dynamic estimate can help detailing some specific soil loss patterns, particularly when the land cover is subject to natural or artificial changes over time. Besides, our estimate of soil erosion is characterized by a smaller variability with respect to that of Panagos *et al.* (2015b). This holds particularly true for vegetated classes, as shows Figure 6). However, we should mention that Panagos' extremely high variability for classes 332 (bare rocks), 333 (sparsely vegetated areas) and 335 (glaciers and perpetual snow) is biased by the presence of several "no-data" values.

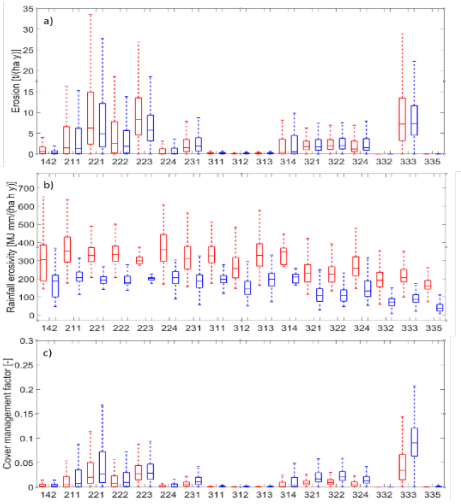

Figure 3. Box-plots of average a) soil erosion rates, b) rainfall erosivity values and c) cover management factor values computed for Summer (red) and Winter (blue). DUSAF land cover classes: 142=Sport and leisure facilities; 211=Non-irrigated arable land; 221=Vineyards; 222=Fruit trees and plantations; 223=Olive groves; 224=Wood arboriculture; 231=Permanent grassland; 311=Broad-leaved forest; 312=Coniferous forest; 313=Mixed forest; 314=Recent reforestation; 321=Natural grasslands; 322=Moors and heatland; 324=Transitional woodland-shrub; 332=Bare rocks; 333=Sparsely vegetated areas; 335=Glaciers and perpetual snow.

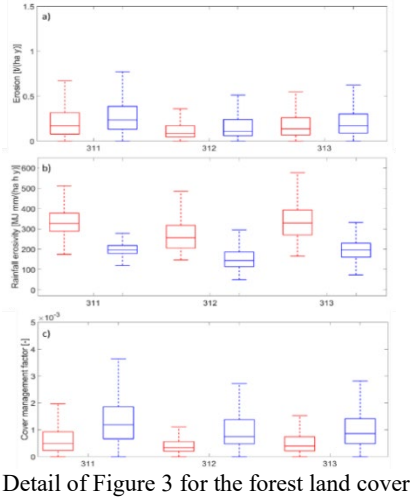

Figure 4. Detail of Figure 3 for the forest land cover classes. DUSAF land cover classes: as in Figure 3 caption.

4. CONCLUSIONS AND FUTURE WORKS

In this study, we proposed a RUSLE-like model based on the integration of traditional on site measures (i.e. meteorological stations), Earth observation (i.e. satellite-derived C-factor), and

on site calibration (i.e. K-factor). The model was tested in central Alps of Italy to study the benefits of a dynamic modelling.
First results shows that a dynamic modelling of soil erosion could highlight different erosive patterns for Summer and Winter, hotspots and land covers which are more susceptible to erosion. Moreover, integrating the erosion model with spectral indices could potentially allow relating phenological and health variations of vegetation with soil loss severity.
This information is required for developing appropriate conservation policies regarding land use and agricultural practices, to avoid irreversible soil loss. Thus, the use of satellite-derived spectral information opens new ways for modelling the dynamics of soil erosion, including both short-term (i.e. seasonal) and long-term land cover changes.
Future steps will include modelling erosion under climate change projections, which foresee relevant changes for the European mountains. Besides, is currently under evaluation the benefit of including Sentinel-2 data in the work flow, both to increase the spatial resolution of the C-factor and to increase the revisit time in Winter, when the cloud cover is higher.

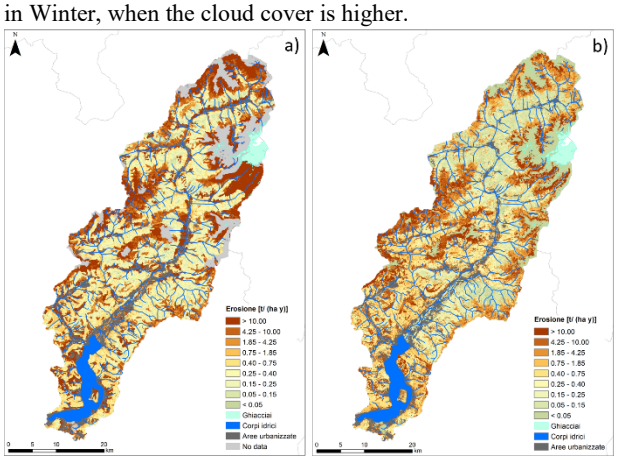

Figure 5. Comparison between (a) the erosion map at European scale by Panagos *et al.* (2015b) and (b) our estimates. While the patterns are similar, our dynamic approach estimates a smaller erosion.

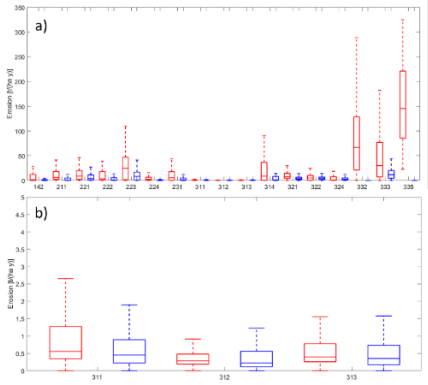

Figure 6. Box-plots of average soil erosion rates. Comparison between the study by Panagos *et al.* (2015b) (red) and our estimates (blue). a) Overall results, b) detail for the forest classes. DUSAF land cover classes: as in Figure 3 caption.

ACKNOWLEDGEMENTS

This study belongs to the research project *Hydrogeological modeling for Erosion Risk Assessment from SpacE* (HERASE), founded by Fondazione Cariplo for the years 2017-2019 (Grant Nr. 2016-0768). Authors also thank: i) Parco dell'Adamello and Comunità Montana della Val Camonica for their support and interest in the project and for supplying useful data; ii) Regione Lombardia-Regional Territorial Office (Brescia) for information and data on the study area; iii) ENEL Production for data on sediment deposition rates within their dams, and iv) Servizio Glaciologico Lombardo for their help.

REFERENCES

Aiello, M., Vezzoli, R. F., Polinelli F., Frassy F., Rota Nodari, Rulli, M.C., Ravazzani G., Corbari C., Soncini A., Chiarelli, D.D., Passera, C., Bocchiola, D., and Gianinetto, M., Analisi di sensitività nella stima dell'erosione di suolo nelle Alpi con misure in situ e serie temporali Landsat, in ASITA 2018 Conference (in press).

Boardman, J. and Poesen, J., 2006. *Soil Erosion in Europe*, John Wiley & Sons Ltd, 855.

Costantini, E.A.C., and Lorenzetti, R., 2013. Soil degradation processes in the Italian agricultural and forest ecosystems. In: *Italian Journal of Agronomy*; 8(28), pp. 233-243.

Desmet, P.J.J., Govers, G., 1996. A GIS procedure for automatically calculating the USLE LS factor on topographically complex landscape units. In: *Journal of soil and water conservation*, 51(5), pp. 427-433.

European Commission, 2012, The implementation of the Soil Thematic Strategy and ongoing activities, COM (2012) 46.

Fantappiè, M., Priori, S., Costantini, E.A.C., 2015. Soil erosion risk, Sicilian Region (1: 250,000 scale). In: *Journal of Maps*, 11(2), pp. 323-341.

Gianinetto, M., Aiello, M., Vezzoli, R., Rota Nodari, F., Polinelli F., Frassy F., Rulli, M.C., Ravazzani G., Bocchiola, D., Soncini A., Chiarelli, D.D., Passera, C. and Corbari C., "Satellite-based cover management factor assessment for soil water erosion in the Alps"., in SPIE Remote Sensing 2018 Conference.

Panagos, P., Borrelli, P., Meusburger, K., Alewell, C., Lugato, E., Montanarella, L., 2015a. Estimating the soil cover-management factor at the European scale. In: *Land Use Policy*, 48,pp. 38-50

Panagos, P., Borrelli, P., Poesen, J., Ballabio, C., Lugato, E., Meusburger, K., Montanarella, L., Alewell, C., 2015b. The new assessment of soil loss by water erosion in Europe. In: *Environmental science & policy*, 54, pp. 438-447.

Renard, K.G., Foster, G.R., Weesies, G.A., McCool D.K., Yoder, D.C., 1997. Predicting soil erosion by water: a guide to conservation planning with the revised universal soil loss equation (RUSLE). Washington, DC:United States Department of Agriculture, Vol. 703.

Sun, H., Cornish, P.S., and Daniell, T. M., 2002. Contour-based digital elevation modeling of watershed erosion and sedimentation: Erosion and sedimentation estimation tool (EROSET). In: *Water resources research*, 38(11).

Van der Knijff, J.M., Jones, R.J.A. & Montanarella, L., 2000. Soil erosion risk assessment in Europe. European Soil Bureau, Joint Research Center of the European Commission.

SOIL DEGRADATION MAPPING USING GIS, REMOTE SENSING AND LABORATORY ANALYSIS IN THE OUM ER RBIA HIGH BASIN, MIDDLE ATLAS, MOROCCO

A. El Jazouli*, A. Barakat, R. Khellouk, J. Rais

Team of Georessources and Environment, Faculty of Sciences and Techniques, Sultan My Slimane University, Béni-Mellal, Morocco (a.eljazouli, a.barakat, r.khellouk, j.rais)@usms.ma

KEYWORDS: Soil degradation, Remote sensing, GIS, Oum Er Rbia high basin, Landsat 8 Oli

ABSTRACT

The main purpose of this research is to assess soil degradation combining GIS, remote sensing data and laboratory analysis. To achieve this aim, the study required Soil samples which were collected at 50 locations in the Oum Er Rbia high basin in the Middle Atlas of Morocco. These samples were dried, sieved at 2 mm and analyzed in a laboratory. Landsat 8 OLI images have been analyzed using physically-based or empirical methods to derive soil properties. The potential deterministic (Spline and Inverse Distance Weighted) interpolation method was used to produce maps of each textural classes and soil properties using GIS software. The severity of land degradation has been quantitatively estimated by analyzing physicochemical parameters in the laboratory to determine saline or salt-free soils and calcareous or sodium soils. WLC method was then used to generate the soil degradation map in a GIS environment, by overlaying indicator weights and thematic maps generated using interpolation method.The study area shows the distribution of the five soil degradation classes ranging from very low (1) to very high (5). From the calculations made, 17.28 % of the area is at low, 34.51 % at moderate, 32.88 % of high and 15.31 % of very high degradation area coverage.

This approach developed in the current research will enhance the perspectives of using remotely sensed data for soil degradation mapping in arid and semi-arid environments.

1. INTRODUCTION

The degradation produces an alteration of the chemical and physical properties of the soil in situ. However, in many cases, soil degradation produces aggravated erosion. This later is a movement of food and organic matter in another place. In the context of water erosion, this displacement is done through runoff (AbdelRahman, Shalaby et al. 2017, Barakat, Ennaji et al. 2017, Orgiazzi 2018, Oldeman 2017).

The major drivers of soil degradation are climate aridization, unsustainable agricultural practices, industrial and mining activities (Dudka 1997), expansion of crop production to fragile and marginal, inadequate maintenance of irrigation and drainage networks, and overgrazing.

The disappearance of the topsoil of Moroccan soils was estimated at about 22 000 ha/year (Knidiri M 1998), and that more than 12 000 000 hectares (of which 1/3 of the arable surface) are threatened with degradation by erosion, salinization, and overexploitation (MAMVA 1995).

The combination of high rainfall, a spectacular extension of soft rocks (marls, schists and clays), rugged terrain, acidification, salinization, imposed on the soil and a high human occupation make the High Oum Er Rbia watershed in the Middle Atlas of Morocco a vulnerable and predisposed area to soil degradation phenomena.

Quite recently, considerable attention has been paid to soil degradation assessment by different methods which include: expert judgment, remote sensing, productivity changes, field monitoring, pilot studies at farm level based on field criteria and expert opinion, and GIS modeling.

The GIS based interpolation techniques became widely used to evaluate the soil quality because they allow rapid generation of thematic maps and area estimates, and combination of different information data to produce suitability maps (ennaji et al. 2018). Several publications have appeared in recent years documenting soil degradation mapping using soil properties, Remote sensing and GIS techniques (Kotb, Ali et al. 2017, Ahmad and Pandey 2018, Ennaji et al. 2018, Žížala et al. 2017).

Therefore, awareness about the spatial and temporal variability of soil is in tremendous value for natural resources management and ecological modeling (Bünemann, Bongiorno et al. 2018).

The aim of this study is to assess the potential of a combined use of GIS, remote sensing data and laboratory analysis.

In this paper, we explore the possibility of integrated remote sensing and GIS technologies; spatial variability in soil pH, organic carbon (OC), electrical conductivity (EC), organic matter (OM), soil texture, slope, and NDVI by interpolation method in agricultural and non-agricultural soils of the study area analyze and improve the understanding of causative factors in land degradation assessment. The presented approach promises to produce a practical method usable in a frequent monitoring of soil degradation in High Oum Er Rbia watershed.

2. MATERIALS AND METHOD

2.1. Study area

The study was carried on the Oum Er Rbia high-basin, which occupies the South of the Middle Atlas Mountain and a part of the Central Moroccan Plateau in the Khenifra Province (Fig.1). The studied basin is delimited in the west by the Hercynian Central Massif, to the north by the Causse of Ajdir and south-east by the plain of the High Moulouya. It occupies an area of 3612.21 Km². The elevation of the area ranged from 662 to 2400 m.

The Middle Atlas has a flat relief, consisting of secondary limestones with large synclines and narrow anticlines, low-level dumped to the northwest. South, in the basin of the SEROU, the relief takes on the appearance of a causse. The valleys are narrow and deep and have sunk into Triassic gypseous terrains and salifiers.

The existence of steep slopes and unconsolidated rocks (clay and marls) represents the main factors affecting land degradation, soil erosion and leaching phenomena that are negative environmental impacts on soil and slope stability and river water quality (Barakat A 2016, Barakat, Meddah et al. 2018). However, one of the major environmental concerns of soil degradation, including soil erosion, waterlogging, landslides, and salinization.

* Corresponding author

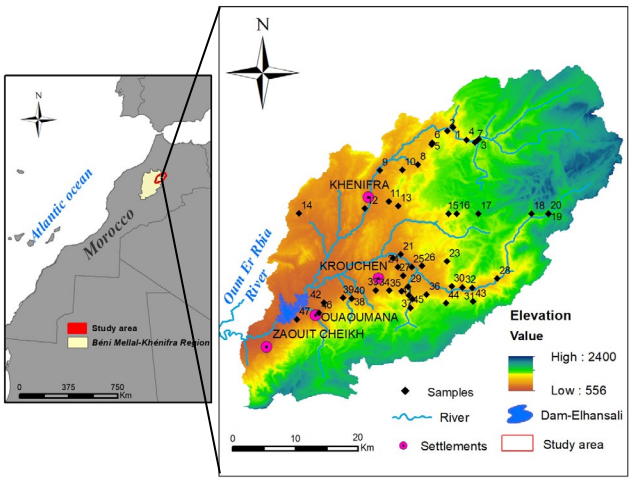

Figure 1. High Oum Er Rbia watershed map location.

2.2. Soil sampling and laboratory analysis

From the study area, a total of 47 sites (Fig. 1) were randomly selected for soil sample collection (at a depth of 10–25 cm) for the analysis of physicochemical parameters in Georessources and Environment Laboratory at the Faculty of Sciences and Techniques of Beni-Mellal. The geographical coordinates of the sampling sites were recorded using a Garmin GPS device. For an accurate assessment of spatial soil fertility, some soil quality indicators frequently used to assess soil quality and suitability for agriculture (El Baroudy 2016, Barakat, Ennaji et al. 2017), i.e., pH, organic carbon (OC), electrical conductivity (EC), organic matter (OM), soil texture, slope, and NDVI, were used to map the soil degradation in the study area. Thematic maps of all analyzed parameters were produced using inverse distance weighting (IDW) interpolation technique. Slope map was obtained using a digital elevation model (DEM) with a 30 × 30 m cell size of the study area. All thematic maps were generated using ArcGIS software.

2.3. Satellite image acquisition, pre-processing and terrain analysis

Satellite images of Landsat 8 OLI sensor were free downloaded, characterized by the absence of rainfall and very slow chlorophyll activity; thus, implicitly declining agricultural activities. This scene was acquired in July 2016, on the official website of NASA http://earthexplorer.usgs.gov/. It was composed of eleven bands covering the electromagnetic spectrum between 0.433 µm and 12.50 µm. The bands stacked are blue, green, red, near infrared, and the two-shortwave infrared with a spatial resolution of 30 meters, while the panchromatic band is at 15 meters.

Pre-processing operations were performed to prepare the images. This step starts with the radiometric calibration and atmospheric corrections by Chavez (1996) low-cost method on each scene. The Normalized Difference Vegetation Index (NDVI) is a unit of the measure designed to factor both red and near-infrared reflectance. NDVI measurements can range from -1 to 1, with higher values indicating greater plant health.
Digital Elevation Model (DEM) with a 30-meter resolution was downloaded from ASTER GDEM (https://asterweb.jpl.nasa.gov/gdem.asp), in order to derive slope map.

2.4. Weighted linear combination (WLC) in mapping soil degradation

Weighted linear combination method is a hybrid between qualitative and quantitative methods. It's based on the qualitative map combination approach (heuristic analysis) (Akgün 2008). This multi-criteria evaluation method allows flexibility and tradeoffs amongst all parameters used. Ranks and weights are assigned depending on their influence on soil degradation. Parameters selected for the study include seven quality indicators, namely soil texture, pH, EC, OC, OM, and remote sensing data such as NDVI and slope were used to assess soil degradation. Each parameter was categorized into classes and assigned ranks from having very low influence on very high, 1 (very low)—5 (very high) (Table1), based on reported norms in published literature (WRB 2006, Schiefer, Lair et al. 2015, Barakat, Ennaji et al. 2017, Mohamed, Belal et al. 2019), The outcome can significantly vary between experts. Each parameter is classed and multiplied with its assigned weight and within a GIS overlay environment. The classes within each parameter are multiplied with the weight and added using the spatial analysis tool to get susceptibility output maps. In WLC, the weight of each parameter considered is added by means of overlay to obtain soil degradation map.

3. RESULTS AND DISCUSSION

In this study, the soil degradation map was produced using WLC method, to achieve this goal, we sampled and analyzed nearly 47 randomly taken points distributed over our study site in Georessources and Environment Laboratory at the Faculty of Sciences and Techniques of Beni-Mellal. Soil degradation severity was shown as the spatial distribution of pH, EC and alkalinity in quantitative terms via IDW interpolation methods the statistical analysis tool, then an overlaying after weighting of seven maps of different parameters using WLC method in the ArcGIS software.

Soil property	**Soil degradation score**					**Indicator weight**
	Very high (4)	High (3)	Moderate (2)	Low (1)	Unit	
Texture	>50	35–50	15–35	<15	%	4
pH		6.5–8	5.5–6.5	<5.5; >8		4
OM		>2	1–2	<1	%	3
OC	>4	2–4	1.5–2	<1.5	%	3
EC	>16	ago-16	4–8	4	ds/m	3
Slope		<10	10–15	15–25	%	5
NDVI	-1			1		2

Table 1. Threshold levels and scoring of land degradation. Score for each indicator is given in parentheses.

pH

pH is a parameter used to define whether a medium is acidic or basic. The pH of each soil sample was determined was measured by a pH-meter in a soil:deionized water suspension (5 mg soil to 20 ml deionized water) after shaking for 12 h. Afterward, the pH meter was calibrated with a standard solution whose pH must be neutral (pH = 7), and an electrode was introduced into the beaker for a few minutes to read the pH. The soil pH value measured in water was ranging between 7.27 and 8.79.

OC

The organic carbon (OC) stocks in the terrestrial ecosystem is about twice as much carbon found in the atmosphere (Lal 2004) and three times the quantity found in vegetation (Zhang 2013). The OC of the study area ranged between 0.09 and 7.51%

EC

Soil salinity refers to the presence of soluble salts within the root zone. It's considered the most ecologically risky that is an obstacle in agricultural productivity especially in arid and semi-arid (FAO 2011)..

Soil salinity is the principal factor causing soil degradation. The high concentrations of salinity affect crop growth.

In this study, the measurement of Electrical Conductivity was done in accordance with IS: 14767- 2000 using EC- Meter (Systronic water analyser 371).

The result showed that the soil is characterized by medium to low saline where it ranges from 0.03 to 0.89 dS/m.

OM

Soil organic matter (OM) is one of the major pools of carbon in the biosphere and is important both as a driver of climatic change and as a response variable to climate change capable of acting both as a source and sink of carbon (Thompson, Miller et al. 2017, Ismail-Meyer 2018). It is mainly located in the superficial horizon of the soil (0 to 20 cm). It's declining in most agricultural ecosystems, impacting multiple ecosystem services including erosion and flood prevention, climate and greenhouse gas regulation as well as other services that underpin crop production, such as nutrient cycling and pest control (Garratt, Bommarco et al. 2018). The obtained results showed that soil organic matter distribution in the study area is heterogeneous.

Measurement of particle size fractions

The percentage of clay and silt is determined based on the Stokes sedimentation principle using the Robinson pipette. The determination of the proportions of sand is made by sieving.

The particle size analysis was carried out on 20 g of fine earth. After the release of the particles from each other by the destruction of the organic and mineral cement, we proceeded to their separation. This separation was made by sedimentation according to Stoke's law for clay and fine silt. The samples of these constituents were made by Robinson pipette. The textural analysis showed that the texture of the study area is dominated by silt loam and silty clay loam. The resilience and performance are especially low in sandy soils.

Slope

Slopes are dynamic systems enabling movement of material downslope at varying speeds from negligibly slow to fast avalanches. It's derived from the DEM with a spatial resolution of 30m using ArcGIS spatial analysis tool, it represents an important parameter in the study and the characterization of the state of degradation of the soil. A steep slope accelerates runoff; therefore, the vulnerability of soil to erosion increases. Slope values of the study area ranged from 0 to 62%, higher angles indicative of abrupt limestone escarpments.

NDVI

The NDVI became one of the widely used indices for predicting surface soil characteristics and vegetation coverage (Blanco, Hardtke et al. 2017, El Jazouli, Barakat et al. 2017). NDVI was derived from pre-processed and enhanced Landsat 8 Oli images using ENVI. In this study, the vegetation coverage is separated into five classes; low vegetation cover (<10%), moderate vegetation cover (30% - 45%), high vegetation cover (45% - 60%), and very high vegetation cover (>60%).

Soil degradation map

The weighted linear combination (WLC) method involving multiple parameters; soil laboratory analysis, GIS techniques and remote sensing data, is used to establish the relational importance and degree of influence of the selected parameters to enable a soil degradation map in the Oum Er Rbia high basin in a GIS environment.

According to the soil degradation map obtained from the WLC method, four classes were identified using the equal interval classification method (Fig. 2). 17.28 % (623 km²) of the total area is found to be of low degraded. Moderate and high degraded zones represent 34.51 % (1244 km²), and 32.88 % (1185 km²) of the total area, respectively. The very high soil degradation area is 15.31 % (552 km²) of the total study area.

Integrating different types of factors affecting soil degradation, the results show that most of the study area falls under moderate soil degradation classes. High land erosion class has been found in areas affected by high soil loss; this is the major reason for biological degradation by removing the plow layer of the topsoil. Erosion decrease soil fertility, reduce crop yield (AbdelRahman, Shalaby et al. 2017, El Jazouli, Barakat et al. 2017), and removes the OM along with other mineral components of the soil resulting in soil biological degradation.

Moreover, we notice that the soil in the study area is poor in MO and clay, and rich in loam. Among other things, this low level of OM can be linked to land degradation caused by intensive logging and irrigation, deep plowing techniques, and crop residues that are picked up at the end of the growing season.

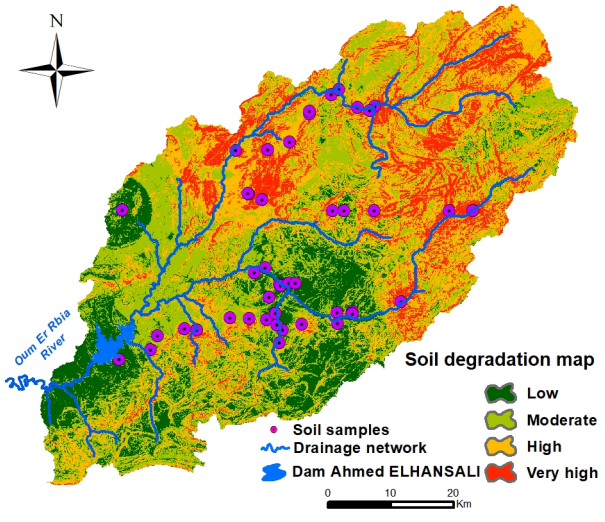

Figure 2. Soil degradation map of High Oum Er Rbia watershed.

According to the previous researches in similar conditions, lands with good soil texture and flat slope which have moderate degradation and are most frequent limiting indicators to categorize a land for sustainable intensive agriculture (Barakat, Ennaji et al. 2017).

4. CONCLUSION

The main goal of this study was to assess the soil degradation in the High Oum Er Rbia watershed which is a mountainous land at a regional scale using, GIS techniques, remote sensing data and laboratory analysis. Seven parameters are used to generate soil degradation map namely, pH, OC, EC, OM, soil texture, Slope and NDVI.

This study reveals that the applied approach enables to be applied to projects of particular interest to soil scientists, environmental scientists and planning agencies that can use the present study as baseline data for combating forest degradation. land and conserve land resources effectively.

In addition, anthropogenic activities have two-sided effect: positive action by right management that leads to mitigate soil degradation, this need to understand the cause of degradation. The human can also accelerate degradation by mismanagement of land resources. Moreover, social and economic factors have significant effects on reducing or accelerating degradation processes.

GIS, remote sensing and soil laboratory analysis manifested great efficiency in the land degradation assessment process, whose results hopefully may help decision makers to take the necessary actions to protect the most degraded spots. These outputs have been analyzed and weighted in terms of degradation classes.

ACKNOWLEDGMENTS

This research was supported by Sultan My Slimane University. Morocco. The authors would like to thank all members of the Georessources and Environnement Team.

REFERENCES

AbdelRahman, M. A. E., et al. (2017). "GIS spatial model based for determining actual land degradation status in Kafr El-Sheikh Governorate, North Nil(Barakat, Ennaji et al. 2017).e Delta." Modeling Earth Systems and Environment 4(1): 359-372.

Ahmad, N. and P. Pandey (2018). "Assessment and monitoring of land degradation using geospatial technology in Bathinda district, Punjab, India." Solid Earth 9(1): 75-90.

Akgün, A., Dag, S., and Bulut, F (2008). " Landslide susceptibility mapping for a landslide prone area (Findikli, NE of Turkey) by likelihood frequency ratio and weighted linear combination models." Environ. Geol., 54, 1127–1143, https://doi.org/10.1007/s00254-007-0882-8, .

Barakat A, E. B. M., Rais J, Aghezzaf B, Slassi M (2016). "Assessment,of spatial and seasonal water quality variation of Oum Er Rbia River (Morocco) using multivariate statistical techniques." Int Soil Water Conserv Res 4(4): 284–292.

Barakat, A., et al. (2017). "Multivariate analysis and GIS-based soil suitability diagnosis for sustainable intensive agriculture in Beni-Moussa irrigated subperimeter (Tadla plain, Morocco)." Modeling Earth Systems and Environment 3(1).

Barakat, A., et al. (2018). "Physicochemical and microbial assessment of spring water quality for drinking supply in Piedmont of Béni-Mellal Atlas (Morocco)." Physics and Chemistry of the Earth, Parts A/B/C 104: 39-46.

Blanco, P. D., et al. (2017). Soil degradation in Peninsula Valdes: Causes, factors, processes, and assessment methods. Late Cenozoic of Península Valdés, Patagonia, Argentina, Springer: 191-213.

Bünemann, E. K., et al. (2018). "Soil quality – A critical review." Soil Biology and Biochemistry 120: 105-125.

Daniel Žížala, Anna Juřicová, Tereza Zádorová, Kateřina Zelenková & Robert Minařík (2018): Mapping soil degradation using remote sensing data and ancillary data: South-East Moravia, Czech Republic, European Journal of Remote Sensing, DOI: 10.1080/22797254.2018.1482524

Dudka, S., et Adriano, D.-C. , (1997). "Environnmental impacts of metal ore mining and processing: ." A review. Journal of Environnmental Quality(26(3) :): 590–602.

El Baroudy, A. A. (2016). "Mapping and evaluating land suitability using a GIS-based model." Catena 140: 96-104.

El Jazouli, A., et al. (2017). "Soil erosion modeled with USLE, GIS, and remote sensing: a case study of Ikkour watershed in Middle Atlas (Morocco)." Geoscience Letters 4(1): 25.

Ennaji, W., Barakat, A., El Baghdadi, M., Oumenskou, H., Aadraoui, M., Karroum, L. A., & Hilali, A. (2018). GIS-based multi-criteria land suitability analysis for sustainable agriculture in the northeast area of Tadla plain (Morocco). Journal of Earth System Science, 127(6), 79.

FAO (2011). "CA Adoption Worldwide, FAO-CA website available online at: (http://www.fao.org/ag/ca/6c.html).".

Garratt, M. P., et al. (2018). "Enhancing soil organic matter as a route to the ecological intensification of European arable systems." Ecosystems: 1-12.

Ismail-Meyer, K., Stolt, M. H., & Lindbo, D. L.. . (2018). "Soil organic matter. In Interpretation of Micromorphological Features of Soils and Regoliths " Elsevier (pp. 471-512).

Knidiri M, T. B. (1998). "Le développement durable dans les pays du sud méditerranéen : enjeux et obstacles. Colloques interculturels méditerranéens. Palerme : COMEN,." 5 p.

Kotb, M. M., et al. (2017). "Use of Remote Sensing and GIS for Land Degradation Assessment of Qarun Lake Coastal Area, El-Fayoum, Egypt." 251-267.

MAMVA (1995). "Direction des Eaux et Forêts et de la Conservation des Sols. La désertification au Maroc : Causes, ampleur et réalisations. Terre et Vie.; 15-16, 17. http :\\www.terrevie.ovh.org/a46.htm.".

Mohamed, E., et al. (2019). "Land Degradation." 159-174.

Oldeman, L. R., Hakkeling, R. T. A., & Sombroek, W. G.. . (2017). "World map of the status of human-induced soil degradation: an explanatory note."

Orgiazzi, A., & Panagos, P. (). (2018). "Soil biodiversity and soil erosion: It is time to get married: Adding an earthworm factor to soil erosion modelling. Global Ecology and Biogeography.".

Schiefer, J., et al. (2015). "Indicators for the definition of land quality as a basis for the sustainable intensification of agricultural production." International Soil and Water Conservation Research **3**(1): 42-49.

Thompson, K., et al. (2017). "Storage of carbon by marine ecosystems and their contribution to climate change mitigation."

WRB (2006). "World Reference Base for Soil Resources A Framework for International Classification, Correlation and Communication,." FAO Rome, World Soil Resources Reports 103.

Zhang, C., Liu, G., Xue, S., Sun, C., . (2013). " Soil organic carbon and total nitrogen storage as affected by land use in a small watershed of the Loess Plateau, China." Eur. J. Soil Biol.: 54, 16–24.

UAV APPLICATION FOR MONITORING THE ANNUAL GEOMORPHIC EVOLUTION OF A COASTAL DUNE IN PUNTA MARINA (ITALY)

E. Grottoli*, P. Ciavola, E. Duo, A. Ninfo

Dipartimento di Fisica e Scienze della Terra, Università di Ferrara, Via G. Saragat 1, 44122, Ferrara, Italy
(grtdrd, cvp, duonrc, nnfndr)@unife.it

KEY WORDS: SfM photogrammetry, High resolution DEM, DoD, Dune geomorphology, Dune conservation, Incipient dune, Drone application.

ABSTRACT:

Unmanned Aerial Vehicles (UAV) allow to gather detailed topographic data at low cost over large survey areas. The study site, located in Punta Marina (Emilia-Romagna), is one of the few regional coastal locations still characterized by "natural" dunes; in 2015 a preservation scheme was realized to protect the dune system and reduce the erosion and vegetation degradation generated by beach users. Four UAV surveys were performed using a commercial DJI Phantom 3 Professional, a quadcopter equipped with the standard digital camera of 12 megapixels (3.6 mm focal length). Drone surveys were supported by a RTK-GNSS, both for GCP measurements and drone-derived DSM validation. Orthophotos were obtained through photogrammetry processing with a geometric resolution of about 3 cm, generating a DEMs with a cell size of 5 cm. Dune morphology was compared by means of DoD processing to understand the geomorphological evolution and quantify the volume of sediments displaced. The most evident result is related to the growth of a small incipient dune fed by aeolian processes and enhanced by preservation measures (planted vegetation and wooden fence). A cumulative vertical growth of 0.5 m was locally measured after the monitoring period. The role played by the growth of pioneer plants in overestimating volume changes was quantified as +11%. The use of drone-derived images, combined with SfM algorithms, allowed to achieve a centimetric accuracy in the incipient dune analysis. This methodological approach can represent an efficient tool for coastal and landscape managers, both for mapping and risk assessment purposes at small spatio-temporal scales.

1. INTRODUCTION

Unmanned Aerial Vehicles (UAVs) are today a common tool adopted by geomorphologist to monitor landform evolution in different environments. The geomorphic evolution of coastal zones is often fast and it requires efficient, low-cost and sufficiently accurate monitoring techniques like UAV that can provide a practical option for multi-temporal surveys (Casella et al., 2016, Turner et al., 2016). In a few years, the commercial market growth, combined to the development of SfM (Structure from Motion) photogrammetry, have assigned UAV the role of low-cost and user-friendly tool for surveying and monitoring landforms where short-term evolution is taking place, like in coastal areas.

In sandy coastal zones, dune morphology is constantly changing due to the sand transport capability exerted by forcing factors such as wind, waves and tides. In the current scenarios of sea level rise and worsening of erosion processes along large portions of coastlines, dune conservation and stability represent essential conditions that have to be maintained by local authorities and citizens. Coastal dunes also represent a natural defence from sea flooding and can protect strategic infrastructures and populated urban areas located behind them. The results of a yearly monitoring programme (from March 2017 to April 2018), performed by means of UAV surveys at seasonal intervals, are presented, focusing on the geomorphic evolution of a coastal dune system, recently subjected (2015) to a preservation scheme by local authorities. The most active dune in the study site is the one closer to the shoreline, which was recently artificially vegetated with pioneer plants (2016). Contrarily, the dense vegetation which covers the stabilized rear dune makes the use of drone-derived images difficult to detect geomorphic changes of loose sediments. For these reasons we chose to focus on the geomorphic evolution of the embryonic incipient dune being covered by pioneering vegetation and easily subjected to geomorphic evolution. Although the development of new dunes is well described, we know little about the factors that determine the speed of early dune development (van Puijenbroek et al., 2017). As highlighted by van Puijenbroek et al. (2017), the contribution of vegetation and dune size depends on seasonality and degree of shelter, therefore it seems important to investigate the effectiveness of the preservation scheme recently built for this dune, in order to propose an appropriate management scheme.

2. STUDY AREA

The study area is located on the Northern Adriatic coast, 12 km NE from the city of Ravenna adjacent to the Punta Marina village (Emilia-Romagna, Italy). The monitored dune reaches 6 m in elevation, it is 600 m long and 150 m wide and is separated from sea by a 40 to 60 m-wide sandy beach. It represents part of the 28% of preserved dune systems still surviving along the whole regional coast (Perini and Calabrese, 2010). The area is an alternation of natural elements and human structures such as bathing installations and recreational activities. The beach facing the dune is bounded at its southernmost limit by a 70 m long groin that traps sand from the littoral drift directed northwards. The wave climate consists of small waves from E occurring for most of the time (about 90% of significant wave height is below 1.25 m). The main storm directions are from SE ("Scirocco" wind) and ENE ("Bora" wind): the latter is the strongest wind that generates the most energetic storms. The microtidal range is 30-40 cm at neap tide and 80-90 cm at spring tide. Despite the small tidal range the combination of high tides and storm surges can be significant for morphological changes of the dune and beach system (Armaroli et al., 2012).

* Corresponding author

2.1 Dune preservation project by local authorities

Between May and June 2015, local municipalities built a preservation scheme for the dune in order to reduce the increasing dune trampling produced by beach users and hold back the geomorphic and vegetation deterioration. The project mainly consisted of a 1-m elevated wooden pathways crossing the dune system (Figure 1). A wooden fence was also built few meters distant from the foredune toe to improve the sand trapping and stabilize the entire dune ridge in its seaward-most line. Deployment of sand-trapping fences is a common adjustment that changes the characteristics of the dune ramp and its role in linking sediment transfers from the backshore to the foredune (Jackson and Nordstrom, 2017). Furthermore, 5500 typical dune plants were planted in autumn 2016 to accelerate sedimentation and growth of the incipient dune.

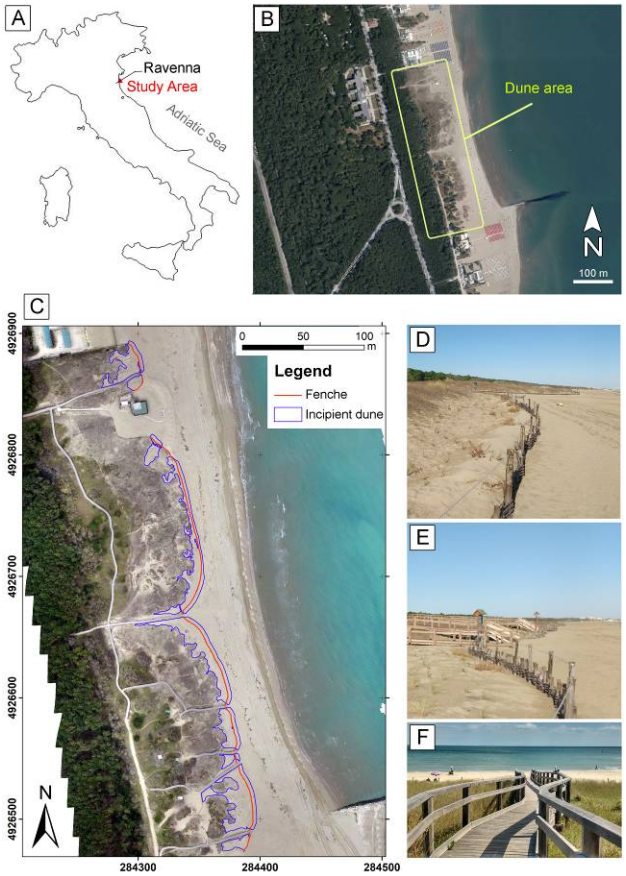

Figure 1 - Study area location (A); monitored dune area (B); overall view of the area of incipient dune (area of interest) and preservation structures (C); frame enlargements of wooden fence and elevated pathways (D, E, F).

3. METHODOLOGY

Topographic surveys have been performed by means of a RTK-GNSS Trimble R6 at the same time of UAV surveys in order to monitor the conservation and geomorphic state of the dune and validate UAV derived results. UAV surveys were carried out with a commercial DJI Phantom 3 Professional, a quadcopter equipped with the standard digital camera of 12 megapixels (4000x3000 resolution, 3.61 mm focal length). As suggested by Duo et al. (2018) the use of automatic flight planning can considerably improve the survey quality due to controlled flight altitude and image overlap. A satisfying overlap between captured images should stay between 70-80% (Dohner et al., 2016; Turner et al., 2016). The flight parameters used for the surveys were: ~ 80 m flight altitude, 72% sidelap, 72% frontlap, fixed focus and automatic pilot mode in order to avoid any shortcoming derived from a manually pilot mode. Those parameters were chosen to have a good compromise between the acquisition time and the cell size resolution (ground resolution of 3.2-3.3 cm) necessary to detect also the subtle morphological changing, as comparably obtained by Giordan et al. (2018). Four surveys were carried out during one year of monitoring (March, September, December 2017 and April 2018; Table 1). Before each flight, twenty ground control points (GCPs), consisting of 60x60 cm wooden squares, painted with a red and white cross, were placed across the study area in order to completely cover the dune system and the facing subaerial beach. GCPs were then measured by means of a RTK-GNSS (range accuracy ~3 cm) linked to the Comacchio GNSS fixed station. The GNSS measurements were performed in geographical coordinates with elevations referred to the WGS84 ellipsoid. Then they were projected to the UTM 33N system with the ETRF2000 geoid.

Survey date	Overlap F/S [%]	Image nr.	Coverage area [Km^2]	Ground res. [cm/pix]
01. 03/03/2017	72/72	297	0.218	3.2
02. 27/09/2017	72/72	154	0.173	3.3
03. 13/12/2017	72/72	150	0.129	3.2
04. 18/04/2018	72/72	150	0.168	3.3

Table 1 - Flight settings of each survey.

The photogrammetric reconstruction (DEM and orthophoto generation) was made in Agisoft PhotoScan Professional. The settings of photogrammetric reconstruction are the following ones: Alignment accuracy (highest); Dense cloud quality (ultrahigh or high); Mesh face count (high); Texture (Mosaic mode).

	Alignment accuracy	Sparse Cloud Points	Dense Point Cloud quality	Dense Point Cloud points	Mesh face count
01	highest	~~113 K	high	~31 M	~6 M
02	highest	~87 K	ultrahigh	~94 M	~19 M
03	highest	~88 K	ultrahigh	~94 M	~19 M
04	highest	~88 K	ultrahigh	~98 M	~20 M

Table 2 - Characteristics of photogrammetric process for each survey.

Since the entire dune area presents high vegetated areas, we only focused on the incipient dune part where the accuracy of drone derived DEMs is sufficient to detect subtle morphological changes. For each survey, a validation of DEM produced by the photogrammetric process was done computing the RMSE (Root Mean Square Error) between its elevation values compared to GNSS measurements along four cross-sections equally spaced along the incipient dune area (area of interest). The DEMs produced for each survey were then analyzed through the Dem of Difference (DoD) method to quantify the amount of sand that fed the incipient dune during the monitoring period. Wave, wind and water level data were retrieved from the closest measuring sites (off-shore Cesenatico, Ravenna and Porto Garibaldi respectively) provided by the regional environmental agency (ARPAe-Dexter database).

In order to compare the incipient dune geomorphic changes, focusing only on natural processes and avoiding artefacts and errors (e.g. shadows), a mask representing the "undisturbed" dune area was digitized in GIS. The mask was created interpreting as landward limit the toe of the stabilized dune from the first orthophoto (March 2017). As seaward limit a vector line was automatically generated, using a buffer distance of 3 m from the wooden fence. The mask was manually refined to remove the largest shadow zones from the orthophotos (mainly generated by walkways) and reshaping the seaward limit where beach portions underwent large human modifications (i.e. beach scraping in winter). This analysis mask was digitized at 1:125 map scale. Stable artificial elements were also excluded from the mask (i.e. roof, walkways, buildings, etc.). The vegetation's contribution to volume variation of the incipient dune was also calculated in a representative portion and resulted to be 9% of the whole incipient dune area. The vegetation's contribution was analysed comparing two DSMs (one with and the other without plants) derived from the drone images, which showed the most increased growth of plants (second survey in September 2017). Plants were excluded from DEM contouring their shape on the orthophoto in ArcGIS software.

4. RESULTS

Orthomosaics obtained from the photogrammetry processing have a grid cell size of ~3 cm, whereas DEMs have a grid cell size of 5 cm. GCPs returned a mean error on their real location (XYZ) below 10 cm for each drone survey (8, 9, 7 and 5, respectively), with a minimum value of 1.8 cm in September 2017 for one single GCP. These values are quite high because include the thick vegetation of the stabilized dune area. In the incipient dune (area of interest) validation of drone-derived DSMs with GNSS measurements returned an error (Root Mean Square Error) between 5 and 7 cm in elevation computed on about 30 points for each survey.

During the monitoring year, all the occurred storms were identified as category I ("Weak"), except one in February 2018 of category II ("Moderate") according to the Mendoza et al. (2011) storm classification (Figure 2). The thresholds for storm identification were those of Armaroli et al. (2012). The storm direction was always from the NE sector and the maximum water level associated to each storm never reached 1 m above mean sea level (Figure 2). Since the lowest measured elevation of the incipient dune is 1.3 m, none of the occurred storms reached the dune foot. Thus, it is reasonable to believe that wind action was the process responsible for the generation and growth of the incipient dune. In particular, between the first and the second survey (from March to September 2017), the wind blew from an E-ESE direction (Figure 2A), being this direction perpendicular to the dune system and inducing the strongest dune growth. In that period there was the greatest vertical growth (mean value 0.1 m), especially in the southern zone where peak values of 0.4-0.45 m were recorded (Figure 3A and 4). The greatest volume increase (+312 m^3) was also measured in this interval (Table 3). Partial erosion affected the incipient dune between the second and the third UAV survey (Figure 3B) with an overall volume decrease of 90 m^3 (Table 3). The period between December 2017 and April 2018, even though remained basically stable as volume variation (only +6 m^3, Table 3), showed a mild increase in elevation and a landward migration of the crest of the incipient dune, especially in the southern zone (Figure 3C and 4). This process is better visible looking at the cumulative DoD (Figure 3D) where the sedimentation portion in the central and southern zone of the incipient dune is marked in Figure 3A with blue if compared to the first time-slice. The landward migration of the incipient dune crest is clearly visible in the profiles in the southern zone in Figure 4, where an overall increase of 0.5-0.55 m in elevation is locally noticeable. As a whole, the volume of incipient dune increased of 228 m^3 after one year. Masking vegetated portions from DoD computation, we found that vegetation overestimates volume increase of about 11% (Table 3). Being the RMSE of four DEMs comprised between 5 and 7 cm an overestimation or underestimation of the actual volume variation has to be taken into account.

	01. March 2017	02. September 2017	03. December 2017	04. April 2018
Incipient dune	5105 m^3	5417 m^3 (+312)	5327 m^3 (-90)	5333 m^3 (+6)
Incipient dune without vegetation	4544 m^3	4821 m^3 (+227)	4741 m^3 (-80)	4746 m^3 (+5)

Table 3 - Volume values of incipient dune measured from each UAV survey. Volume variation compared to previous survey is showed between brackets. Volume values refer to the incipient dune mask visible in Figure 1C.

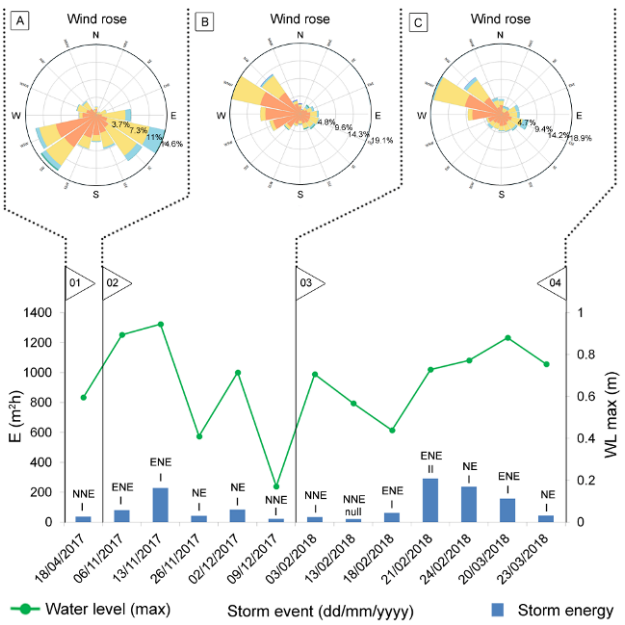

Figure 2 - Climate conditions (wind, storm events and max water level) during the yearly monitoring period: from March to Sep. 2017 (A); from Sep. to Dec. 2017 (B); from Dec. 2017 to Apr. 2018 (C). Storm classes are identified following Mendoza et al., (2011): "null" means under min threshold; "I" means "Weak" energy; "II" means "Moderate" energy. On each storm event the wave direction is also written.

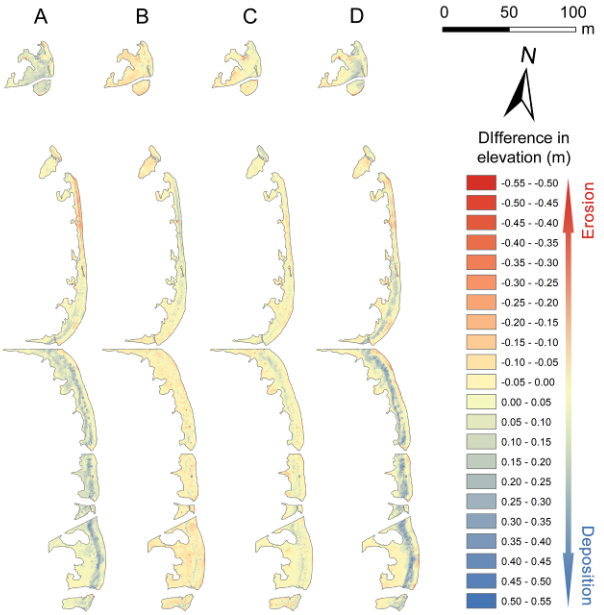

Figure 3 - Geomorphic variation of the incipient dune during the monitoring period: Dem of Difference (DoD) from March to Sep. 2017 (A); from Sep. to Dec. 2017 (B); from Dec. 2017 to Apr. 2018 (C) and cumulative period from March 2017 to Apr. 2018 (D).

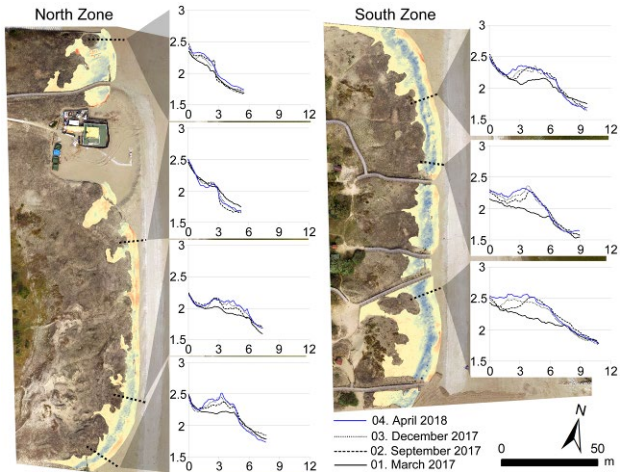

Figure 4 - Cross section variation of the incipient dune at seven locations across the study area. The background DSM is the cumulative DoD for the entire monitoring period: blue color represents sedimentation, red color erosion (see color-scale of Figure 3 as reference).

CONCLUSIONS

During the monitoring period the incipient dune showed the ability to withstand low energy storms and to grow under strong wind action from easterly quadrants in a few months. The buffering role played by the fence and the planted vegetation resulted important for the generation and growth of the dune that locally reached and exceeded 0.5 m of vertical growth. Currently, the incipient dune represents a small sand reservoir ready to feed the beach during a stronger sea storm or potentially able to enlarge the backward foredune during intense and prolonged wind actions from E. With the occurrence of more energetic storms, especially combined with high water levels, the small incipient dune is likely to disappear if not stabilized by vegetation growth or increasing its size further.

Despite vegetation exclusion was a useful test to have an idea on volume overestimation (+11%), to remove plants from the DSM may imply the exclusion of sand amounts placed at plant bases where the accumulation of sediments is more pronounced. We showed that with the right methodological approach (acquisition, processing and accuracy) also low cost commercial UAVs can be used to detect subtle changes of topography and consequently estimate the rate of growth of small landforms with their volume variation. This represents a clear benefit for coastal managers that should take advantage of this low-cost technique for mapping storm impacts (flood limits, damage to buildings or ecosystems, sedimentation and erosion patterns), to improve and update risk assessment at local scale and short-term monitoring of the conservation state of coastal dunes and beaches.

ACKNOWLEDGEMENTS

We are thankful to Yoeri Eijkelhof, Silvia Cilli, Alba María Delfín de la Rosa and Marc Sanuy for their valuable help during the fieldwork activities.

REFERENCES

Armaroli, C., Ciavola, P., Perini, L., Lorito, S., Valentini, A., Masina, M. (2012). Critical storm thresholds for significant morphological changes and damage along the Emilia-Romagna coastline, Italy. Geomorphology 143-144, 34-51, doi:10.1016/j.geomorph.2011.09.006.

Casella, E., Rovere, A., Pedroncini, A., Stark, C. P., Casella, M., Ferrari, M. and Firpo, M. (2016). Drones as tools for monitoring beach topography changes in the Ligurian Sea (NW Mediterranean). Geo-Marine Lett., 36(2), 151-163, doi:10.1007/s00367-016-0435-9.

Dohner, S. M., Trembanis, A. C., and Miller, D. C. (2016). A tale of three storms: Morphologic response of Broadkill Beach, Delaware, following Superstorm Sandy, Hurricane Joaquin, and Winter Storm Jonas, Shore & Beach, 84, 3–9.

Duo, E., Trembanis, A. C., Dohner, S., Grottoli, E., Ciavola, P. (2018). Local-scale post-event assessments with GPS and UAV-based quick-response surveys: A pilot case from the Emilia-Romagna (Italy) coast. Nat. Hazards Earth Syst. Sci. 18(11), 2969-2989, doi:10.5194/nhess-18-2969-2018

Giordan, D., Notti, D., Villa, A., Zucca, F., Calò, F., Pepe, A., Dutto, F., Pari, P., Baldo, M., and Allasia, P. (2018). Low cost, multiscale and multi-sensor application for flooded area mapping, Nat. Hazards Earth Syst. Sci., 18, 1493–1516, doi:10.5194/nhess-18-1493-2018.

Jackson, N. L., Nordstrom, K. F. (2018). Aeolian sediment transport on a recovering storm-eroded foredune with sand fences. Earth Surf. Process. Landforms 43, 1310-1320, doi: 10.1002/esp.4315.

Mendoza, E., Jimenez, J., Mateo, J. (2011). A coastal storms intensity scale for the Catalan sea (NW Mediterranean). Nat. Hazards Earth Syst. Sci. 11, 2453–2462, doi:10.5194/nhess-11-2453-2011.

Perini, L., Calabrese, L. (2010). Le dune costiere dell'Emilia-Romagna: strumenti di analisi, cartografia ed evoluzione. Studi Costieri 17, 71-84.

Turner, I. L., Harley, M. D., Drummond, C. D. (2016). UAVs for coastal surveying, Coast. Eng., 114, 19-24, doi:10.1016/j.coastaleng.2016.03.011.

van Puijenbroek, M. E. B., Nolet, C., de Groot, A. V., Suomalainen, J. M., Riksen, M. J. P. M., Berendse, F., Limpens, J. (2017). Exploring the contributions of vegetation and dune size to early dune development using unmanned aerial vehicle (UAV) imaging. Biogeosciences 14(23), 5533-5549, doi:10.5194/bg-14-5533-2017-supplement.

THERMOGRAPHIC CHARACTERIZATION OF A LANDFILL TROUGH AN UNMANNED AERIAL VEHICLE

F. Capodici, G. Dardanelli, M. Lo Brutto, A. Maltese*

Dept. of Civil, Environmental, Aerospace and Materials Engineering (DICAM), University of Palermo, Italy
(fulvio.capodici, gino.dardanelli, mauro.lobrutto, antonino.maltese) @unipa.it

KEY WORDS: Thermal images, UAV, DSM, Ortho-images

ABSTRACT:
The use of the thermal imaging camera for Unmanned Aerial Vehicle (UAV) survey is to date very common for environmental analysis, especially if high spatial resolution images are required. Some analyses require images to be acquired close to sunrise, to avoid the influence of the incident solar radiation on the surface temperature, as in the case of a landfill survey. Indeed, thermal anomalies due to generated landfill biogas can be characterized once other heat sources are excluded. In this framework, thermal images need to be processed similarly to optical images by typical photogrammetric workflows producing both a Digital Surface Model (DSM) and an ortho-image. The low spatial resolution of thermal cameras, optical distortion and low and homogeneous spatial distribution of radiant exitance at sunrise require, however, an adapted workflow. In this work, some first tests were carried out at a landfill in Palermo (Italy) to evaluate the feasibility of using thermal images to determine the DSM and the thermal ortho-image of the area, aiming to identify thermal anomalies related to landfill heat sources such as biogases.

1. INTRODUCTION

Unmanned Aerial Vehicles (UAVs) have been used for many applications in recent years in the field of cultural heritage, archaeology, 3D mapping and environmental monitoring. In particular, the UAVs have been used to 3D survey and modelling of a historical building (Carnevali *et al.*, 2018; Lo Brutto *et al.*, 2018) and archaeological sites (Lo Brutto *et al.* 2014; Erenoglu *et al.*, 2017). Also in a hazardous situation, the 3D documentation was done with UAVs (Zaragoza *et al.*, 2017). Some works have been carried out for 3D mapping in civil engineering applications (Siebert and Teizer, 2014; Santos de Melo *et al.*, 2018) or for environmental monitoring (Manfreda *et al.*, 2018) and natural hazards monitoring (Gomez and Purdie, 2016).

One of the most recent applications of UAVs is the inspection and monitoring of landfills. For example, some applications were carried out to monitor slow-evolving processes such as waste compactness and landfill subsidence; these processes are recognised as threats in causing the major economic loss to management of rubbish damps (Gasparini *et al.*, 2014).

Some UAVs aerial surveys for landfill monitoring have been conducted using thermal sensors. In Baiocchi *et al.* (2018) first tests have been performed to evaluate the altimetric and thermal accuracy of a UAV landfill survey.

Other recent works have been aimed at measuring gas emissions through thermal imaging cameras pointing out that emissions are localized in hotspots points (Röwer *et al.*, 2011; Xu *et al.*, 2014) due to the mixed nature of the landfills (composed by litters, soil, organic matter, leachate liquid, etc.).

An optimum landfill management requires the detection of landfill gas (LFG) emission hotspots. Thus, thermal images are clearly useful as the gas emissions generally are observable as thermal anomalies. Indeed, the degradation of organic waste produces LFG mainly composed of methane (CH_4) and carbon dioxide (CO_2). The former is generated by an exothermic process which warms up the surrounding area (as these gasses are characterized by temperatures up to 60° C). The detection of thermal anomalies due to generated LFG could be performed once other heat sources are excluded; thus, leading to the need of performing acquisitions close to sunrise, to avoid the warming up of the surface due to the incident solar radiation... Some limitations in the use of the thermal sensors to detect LFG emission hotspots have been highlighted in Lewis *et al.* (2003); these limitations include sunlight, ambient temperatures, wind, surface materials and distance between a sensor and the source. These authors conclude "that unless all the fundamental factors are clearly understood and addressed, the technique (*i.e.*, infrared thermography) currently can only be used as a screening tool rather than as a precise tool to detect landfill gas leakages".

Ground-based surface campaigns for locating emission hotspots are generally difficult as time-consuming and labour-intensive. In addition, landfills are often moderately/largely extended (up to hectares in area) and not always easily accessible. For these reasons, the UAV survey appears to be worthwhile to detect hotspots' emissions.

An aerial infrared thermography approach to identify thermal anomalies with a good resolution over a large region of the landfill surface was showed in Tanda *et al.* (2017). A simplified procedure to evaluate the biogas flow rate emerging from the soil into the atmosphere, based on infrared thermography measurements, was also presented in this paper.

Fjelsted *et al.* (2018) have used an UAV-mounted thermal infrared camera's to delineate landfill gas emission hotspots; the authors have evaluated the methodology in two landfills test areas of 100 m^2. The relationship between landfill gas emissions and soil surface temperatures were investigated in these case studies through several measuring campaigns, in order to cover different atmospheric conditions. Because the extension of the area of the landfills and the high spatial resolution often required for these type of survey, it could be useful to process thermal images similarly to optical images. Thermal images, acquired from UAV, can be processed by applying the typical

* Corresponding author

photogrammetric workflow, and in particular, the photogrammetric/structure-from-motion (SfM) approach, prior to use these data to localize gas emission hotspots.
The use of thermal images in a typical photogrammetric/SfM approach is showed in Mauriello and Froehlich (2014) and in Westfeld *et al.* (2015). These authors have investigated the possibility to efficiently use SfM approach with thermal images for 3D point cloud generation; these works are, however, aimed at buildings survey. In environmental survey, the use of photogrammetric/SfM workflow allows obtaining from thermal data the DSM beyond the thermal ortho-image of the area. However, low spatial resolution of thermal cameras, optical distortion and low and homogeneous radiant exitance spatial distribution impose an adapted workflow.
Within this work, preliminary tests were carried out to evaluate the feasibility to use thermal images acquired from a UAV for DSM extraction and for ortho-image production in a landfill environment. The study area is within the landfill of Bellolampo (close to Palermo, Italy) where landfill managers are interested in thermal behaviour and actual DSM that undergo temporary storage, consolidation, compaction and transfer of waste material. The work was carried out in a quite small area test (about 2.5 hectares) of the landfill. In this operative scenario, we performed optical and thermal flights to compare outcome from the thermal images process with a medium/large UAV (~7 kg weight).

2. STUDY AREA

The "Bellolampo landfill" is used as landfill for the waste of the city of Palermo (Sicily, Italy) and for some municipalities near Palermo. The landfill receives the waste of about one million people; on average about one thousand tonnes of waste per day is stored in the landfill. The "Bellolampo landfill" is located 5 km from the city, in the North-West of Palermo, in a site far away devoted as the landfill of the city (Figure 1). The nearest inhabited settlement is far away just 1 km south of the landfill facilities.
The landfill covers on the whole an area of about 30 hectares and is located at an altitude of about 500 m above sea level (a.s.l.), between Badami Plain and mount Gibilforni (Figure 2).

Figure 1. Positioning of "Bellolampo landfill" (from Google Maps©).

Figure 2. The "Bellolampo" site (from Google Maps©).

In addition to a historical "reclaimed" landfill in which waste was accumulated without controls for almost 3 decades, five more landfills have been built in the last 2-3 decades. More recently, five controlled landfills were built starting from 1990 to 2010; these latter nowadays are closed. A sixth landfill (namely the landfill #6) is under construction since 2015, and it is currently in operation. This latter landfill has an area of about 90,000 m^2 and a volume of about 1,700,000 m^3; it is composed by four sectors (namely sector #1 to sector #4, numbered counter-clockwise from the southeast corner of the landfill #6). Altitudes of the first two sectors range approximately between 510 and 520 m a.s.l., while altitudes of the last two sectors extend up to ≈ 560 m a.s.l.. The first two sectors are already filled and covered by a capping. High-density polyethylene (HDPE) has been used as cap (Figure 3).

Figure 3. HDPE used as cap for the sector #1 and sector #2 of the landfill #6 (from RAP S.p.A. website).

This geomembrane cap contains landfill gas and prevents precipitation becoming leachate, and a floating cover prevents odour emissions. Biogas recovery facility as well as leachate storage and treatment plants are present. The Landfill gas plant is characterized by an installed power of 6.35 MW generated at municipal solid waste (MSW).
The study was limited to only part of the landfill #6; the area of interest is about 130 m x 200 m and is delimited by a red line in figure 4. The area is almost all covered by an impermeable cap; only a small part is partially vegetated and covered with soil.

Figure 4. Flown area (red box) over an image from Google Maps©.

3. DATA ACQUISITION

The area of interest was flown on the 30th of January 2018 by an NT-8 Contras octocopter carrying on-board an Optris PI450 thermal camera and a GoPro HERO Black 4 camera (Figure 5). The Optris PI450 is a microbolometer acquiring in the 7.5 - 13 µm spectral range with 40 mK thermal sensitivity; it produces thermal images with a resolution of 382 pixels x 288 pixels. GoPro HERO Black 4 is a well-known action camera that could be used for photogrammetric image acquisition in contexts where is not required a high level of accuracy (Hastedt *et al.*, 2016).

Figure 5. The NT-8 Contras octocopter used for images acquisition.

Four strips were planned at an average UAV flight height of 50 m above the ground level; the flight direction was parallel to the contour lines (Figure 6). The acquisition was done by two flights; the first acquisition was carried out at 06:20 local time, very close to sunrise (starting at 06:10 local time) under diffuse solar radiation and the second just after sunrise with direct plus diffuse solar radiation (at 07:00 local time).
With thermal camera and GoPro, only videos have been acquired for the area of interest. The resulting thermal images were characterized by a pixel spatial resolution of ≈ 14 cm; about 5 times coarser than the visible images (≈ 3 cm).

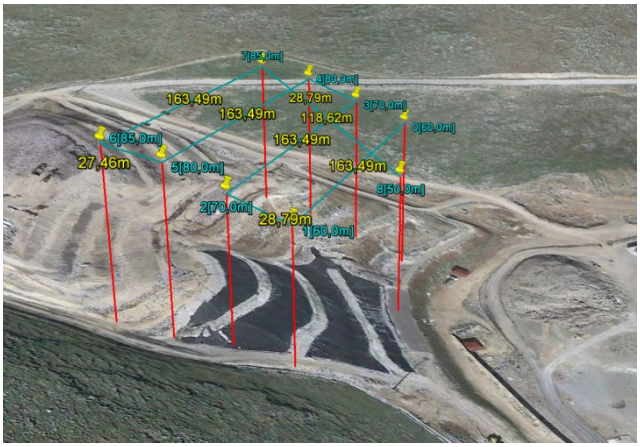

Figure 6. View of UAV acquisition scheme.

Aluminium targets (20 cm x 20 cm) were deployed on the ground as suitable ground control points (GCPs) for thermal images. Aluminium is indeed characterized by very low emissivity (ε=0.04-0.07 for foil and rough surfaces, respectively) resulting in pixels with very low brightness temperature. Even though the night-time thermography was characterized by low homogeneous radiative temperature these targets were clearly detectable within the scene. On the other hand, these aluminium targets were not simply detectable on the visible images due to sparse vegetation mixed to waste emerging from the soil. The coordinates of the targets were measured by a Network Real Time Kinematic (NRTK) survey using a Topcon Hiper V receiver (both GPS and Glonass) (Figure 7). NRTK positioning was carried out using the hardware and software infrastructure of the permanent Netgeo-Topcon network (http://www.netgeo.it/index.php) framed in the reference system ETRF2000 (powered by IGMI, the Italian Military Geographic Institute) and in particular via the VRS (Virtual Reference Station) stream. The survey has a planimetric and altimetric accuracy of the centimetre level.

Figure 7. GNSS survey of the aluminium targets.

4. DATA PROCESSING

The first step in data processing was to extract the single frames from the video sequences. One frame per second was extracted from the videos of both the thermal camera and the GoPro. As the ground-speed of the UAV was 2 m s^{-1} a sequence of images

with a high percentage of coverage was obtained from both flights.

Visible and thermal images were processed using the Agisoft PhotoScan Pro software; the typical photogrammetric/SfM approach was carried out by image alignment and estimation of internal camera parameters, dense point cloud computing, DSM and ortho-image production.

To use thermal images with Agisoft PhotoScan Pro software it was necessary to convert the thermal sequence in TIF images and to reduce the image radiometric resolution to 8 bit.

Three different Agisoft PhotoScan Pro projects have been setup: two with the thermal images of the first and second flight and one with the visible images of the second flight. In this way, it was possible to obtain three DSMs and three ortho-images (two from thermal images and one from visible images) of the test area (Figure 8).

Figure 8. Ortho-image from GoPro data.

5. DATA ANALYSIS

Thermal images are suitable to detect some landfill characteristics not clearly visible elsewhere. Pipelines used for biogas conduction (Figure 9, upper panel) generally show temperatures (Figure 9, lower panel) higher than the surrounding ground, with some pipelines showing values much higher than others. Some temperature features are also clear in landfill zones with and without capping (in this latter case often close to boundaries).

The acquisition at sunrise allows neglecting the ground heat flux due to its inversion at the surface. During the first flight, features due to underground heat sources are clearly visible; although under diffuse solar radiation (Figure 10, left panel) brightness temperature was quite low. During the second flight underground heat source were masked by direct shortwave radiation warming up surface micro-reliefs (Figure 10, right panel) and activating also the vegetation covering the soil (as part of the landfill is not covered with capping). The brightness increase between the two acquisitions was 4.8 °C on the average, with a 2.1 °C standard deviation. Minimum and maximum percentiles, 1 and 99% were P_{01} = 2.8 °C and P_{99} = 6.9 °C, respectively.

A high spatial resolution DSMs characterizing the landfill at the time of the acquisition was obtained by processing both thermal and visible images (Figure 11). These products are useful as active landfills are characterized by morphologies quickly evolving in time due to waste movement and compaction.

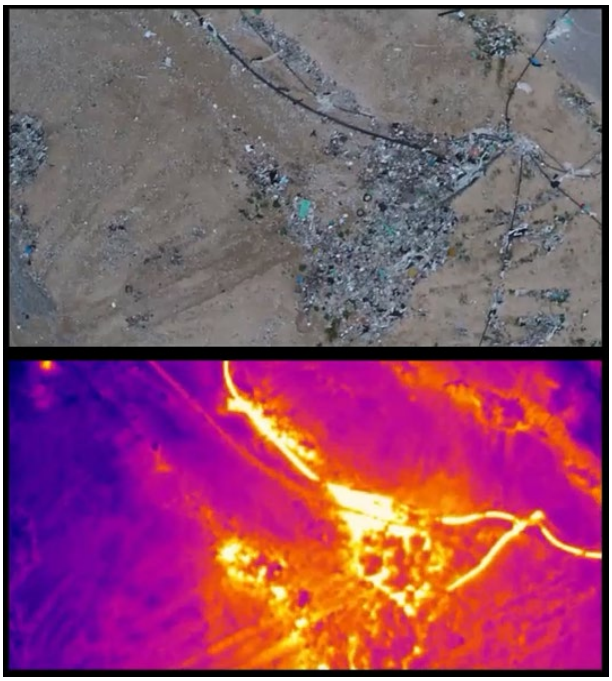

Figure 9. A detail of the landfill including biogas pipelines (upper panel, visible image) and brightness temperature of the same area (lower panel, thermal image).

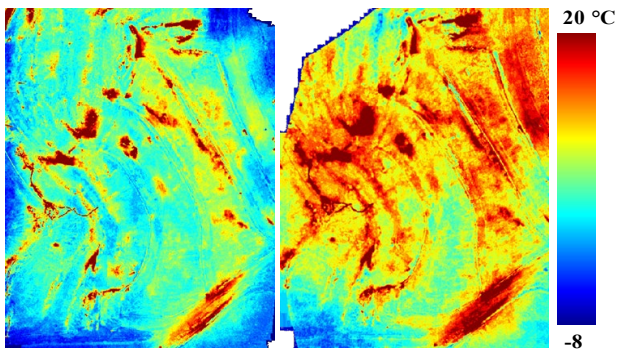

Figure 10. Brightness acquired at 6:20 local time with diffuse radiation (left panel) and at 7:00 under diffuse plus direct radiation (right panel).

DMS obtained by thermal images, DSM_{TIR}, acquired during the first flight was compared to the more standard product from optical image, DSM_{VIS}, to test the reliability of the former one. Altitude values are strongly correlated ($r^2 \approx 0.98$) with no notable over- or under-estimation (the slope was 0.999) and quite low dispersion (MAE ≈ 1.1 m) (Figure 12). Lines characterizing DSM_{TIR} 10° and 90° percentiles are also reported (P_{10} and P_{90}, respectively) to confirm that few pixels fall outside of these extremes. The colour scale (blue to yellow to red) is

proportional to the density of pixels falling within the scatterplot bin element. The colour scale highlights that most of the pixels (in red) are aligned on the 1:1 line (part of the study area covered by ground control points); while a second cluster of pixels is observed over the part of the landfill were no or few aluminium targets were deployed.

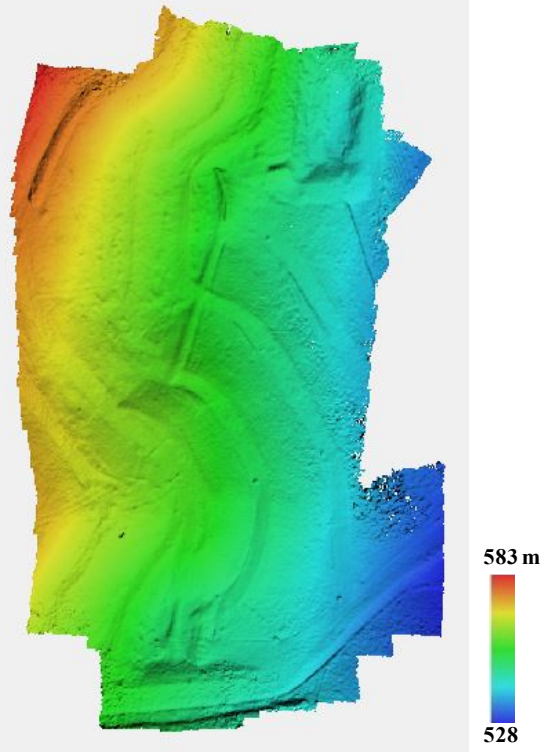

Figure 11. DSM_{VIS} derived from the acquisition under direct plus diffuse solar radiation.

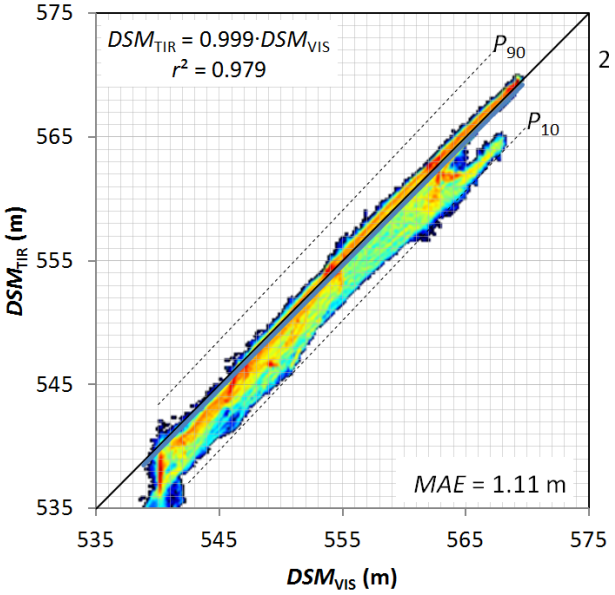

Figure 12. DSM_{VIS} from an overpass under direct plus diffuse solar radiation *versus* DSM_{TIR} from an overpass just after sunrise under diffuse solar radiation.

6. CONCLUSIONS

The work has shown the results of some first tests carried out for the thermographic characterization of a landfill in Palermo (Italy). The thermal images were acquired by a UAV and were used to identify thermal anomalies related to landfill heat sources.

Thermal images acquired close to sunrise, with only diffuse and no direct solar radiation, allow highlights features due to underground heat sources such biogas production, emission or storage; while daily ground heat flux due to net radiation can be neglected due to its daily inversion at the surface. If a thermal image is acquired during daytime or even when direct shortwave radiation hit the surface, underground heat source would be masked by warmed up surface micro-reliefs and by evaporation and transpiration processes of soil and vegetation if occurring. A DSM derived by processing the thermal images has been proved to be an unconventional alternative to that obtainable from visible images although further and more in-depth tests must be done to verify the metric reliability of the DSM produced from thermal images. Furthermore, the processing step highlighted that aluminium targets turn out to be suitable ground control points for DSM and ortho-image production from thermal images; even when, close to sunrise, exitance and reflectance are quite low and standard visible targets cannot be easily detected in thermal and visible images.

ACKNOWLEDGEMENTS

The authors want to thank the support of RAP (*Risorse Ambiente Palermo*) Company S.p.A. for kindly hosting the UAV acquisitions and, Eng. M.T. Masaniello for her precious help during the *in-situ* measurements and data processing. Dr. D. Di Trapani and M. Capodici for measuring biogas emissions *in situ* (measures currently not used within this manuscript). Prof. G. Viviani and Prof. G. Ciraolo for their scientific advices.

REFERENCES

Baiocchi, V., Napoleoni, Q., Tesei, M., Costantino, D., Andria, G. and Adamo, F., 2018. First Tests of the Altimetric and Thermal Accuracy of an UAV Landfill Survey. In: 5th IEEE International Workshop on Metrology for AeroSpace (MetroAeroSpace), Rome, 2018, pp. 403-406. doi: 10.1109/MetroAeroSpace.2018.8453601

Carnevali, L., Ippoliti, E., Lanfranchi, F., Menconero, S., Russo, M., and Russo, V., 2018. Close-range mini-UAVs photogrammetry for architecture survey. In: *The International Archives of the Photogrammetry, Remote Sensing and Spatial Information Sciences*, Vol. XLII-2, pp. 217-224, https://doi.org/10.5194/isprs-archives-XLII-2-217-2018, 2018.

Erenoglua, R. C., Akcaya, O., Erenoglub, O., 2017. An UAS-assisted multi-sensor approach for 3D modeling and reconstruction of cultural heritage site. *Journal of Cultural Heritage*, 26, pp. 79–90. http://dx.doi.org/10.1016/j.culher.2017.02.007

Fjelsted, L., Christensen, A.G., Larsen, J.E., Kjeldsen, P. and Scheutz, C., 2018. Assessment of a landfill methane emission screening method using an unmanned aerial vehicle mounted thermal infrared camera – A field study. *Waste Management*, in press, available online from 28 May 2018. https://doi.org/10.1016/j.wasman.2018.05.031

Gasperini, D, Allemand; P., Delacourt, C. and Grandjean, P., 2014. Potential and limitation of UAV for monitoring subsidence in municipal landfills. *International Journal of Environmental Technology and Management*, Vol. 17, 1, pp. 1-13. DOI: 10.1504/IJETM.2014.059456

Gomez, C., Purdie, H., 2016. UAV- based Photogrammetry and Geocomputing for Hazards and Disaster Risk Monitoring – A Review. *Geoenvironmental Disasters*, 3:23, pp. 1-11. DOI 10.1186/s40677-016-0060-y.

Hastedt, H., Ekkel, T., and Luhmann, T., 2016. Evaluation of the quality of action camera with wide-angle lenses in UAV photogrammetry. In: *The International Archives of the Photogrammetry, Remote Sensing and Spatial Information Sciences*, Vol. XLI-B1, pp. 851-859. https://doi.org/10.5194/isprs-archives-XLI-B1-851-2016, 2016.

Lewis, A.W., Yuen, S.T.S., Smith, A.J.R., 2003. Detection of gas leakage from landfills using infrared thermography – applicability and limitations. *Waste Management & Research*, 21, pp. 436–447. https://doi.org/10.1177/0734242X0302100506.

Lo Brutto, M., Ebolese, D., and Dardanelli, G., 2018. 3D modelling of a historical building using close-range photogrammetry and Remotely Piloted Aircraft System (RPAS), In: *The International Archives of the Photogrammetry, Remote Sensing and Spatial Information Sciences*, Vol. XLII-2, pp. 599-606, https://doi.org/10.5194/isprs-archives-XLII-2-599-2018, 2018.

Lo Brutto, M., Garraffa, A., and Meli, P., 2014. UAV platforms for cultural heritage survey: first results. In: *ISPRS Annals of the Photogrammetry, Remote Sensing and Spatial Information Sciences*, Vol. II-5, pp. 227-234, https://doi.org/10.5194/isprsannals-II-5-227-2014, 2014.

Manfreda, S., McCabe, M.F., Miller, P.E., Lucas, R., Pajuelo Madrigal, V., Mallinis, G., Ben Dor, E., Helman, D., Estes, L., Ciraolo, G., Müllerová, J., Tauro, F., de Lima, M.I., de Lima, J.L.M.P., Maltese, A., Frances, F., Caylor, K., Kohv, M., Perks, M., Ruiz-Pérez, G., Su, Z., Vico, G. and Toth, B., 2018. On the Use of Unmanned Aerial Systems for Environmental Monitoring. *Remote Sensing*, 10(4), 641, pp. 1-28. https://doi.org/10.3390/rs10040641

Mauriello, M. L. and Froehlich J. E., 2014. Towards Automated Thermal Profiling of Buildings at Scale Using Unmanned Aerial Vehicles and 3D – Reconstruction. In: *Adjunct Proceedings of the 2014 ACM International Joint Conference on Pervasive and Ubiquitous Computing*, Seattle, Washington - September 13 - 17, 2014, pp. 119-122. DOI: 10.1145/2638728.2638731.

Santos de Melo, R.R., Bastos Costa, D., Sampaio Álvares, J., Irizarry, J., 2017. Applicability of unmanned aerial system (UAS) for safety inspection on construction sites. *Safety Science*, 98, pp. 174-185. https://doi.org/10.1016/j.ssci.2017.06.008.

Siebert, S., Teizer, J., 2014. Mobile 3D mapping for surveying earthwork projects using an Unmanned Aerial Vehicle (UAV) system. *Automation in Construction*, 41, pp. 1-14. https://doi.org/10.1016/j.autcon.2014.01.004.

Röwer, I.U., Geck, C., Gebert, J., Pfeiffer, E.-M., 2011. Spatial variability of soil gas concentration and methane oxidation capacity in landfill covers. *Waste Management,* 31, 5, pp. 926–934. https://doi.org/10.1016/j.wasman.2010.09.013.

Tanda, G., Migliazzi, M., Chiarabini, V., Cinquetti, P., 2017. Application of close-range aerial infrared thermography to detect landfill gas emissions: a case study. In: *Journal of Physics: Conference Series*. Vol. 796, 0120. https://doi.org/10.1088/1742-6596/796/1/012016.

Westfeld, P., Mader, D., Maas, H.-G., (2015). Generation of TIR-attributed 3D Point Clouds from UAV-based Thermal Imagery. *PFG Photogrammetrie, Fernerkundung, Geoinformation*, N. 5/2015, pp. 381-393. DOI: 10.1127/1432-8364/2015/0274.

Xu, L., Lin, X., Amen, J., Welding, K., McDermitt, D., 2014. Impact of changes in barometric pressure on landfill methane emission. *Global Biogeochemical Cycles*, 28, pp. 679–695. https://doi.org/10.1002/2013GB004571.

Zaragoza, I.M.-E., Caroti, G., Piemonte, A., Riedel, B., Tengen, D. and Niemeier, W., 2017. Structure from motion (SfM) processing of UAV images and combination with terrestrial laser scanning, applied for a 3D-documentation in a hazardous situation. *Geomatics, Natural Hazards and Risk*, Vol. 8:2, pp. 1492-1504. DOI: 10.1080/19475705.2017.1345796

UAV DIGITAL PHOTOGRAMMETRIC ANALYSIS FOR SOIL EROSION EVALUATION IN THE RIVO CATCHMENT: PRELIMINARY RESULTS

A. Minervino Amodio[1]*, P.P.C. Aucelli[2], G. Di Paola[1], V. Garfì[1], M. Marchetti[1], C.M. Rosskopf[1], S. Troisi[2]

[1] Dept. of Biosciences and Territory. University of Molise, 86090 Pesche (IS), Italy – (a.minervinoamodio@studenti.unimol.it) (gianluigi.dipaola, vittorio.garfi, marchettimarco, rosskopf.)@unimol.it

[2] Dept. of Science and Technology, University of Parthenope, 80143 Naples, Italy – (pietro.aucelli, salvatore.troisi)@uniparthenope.it

KEY WORDS: Cultivated land, Photogrammetry, SfM, Soil erosion, Terrain mapping, UAV

ABSTRACT:

Soil erosion is one of the main factors responsible for land degradation in nature. Its quantification in field conditions is very difficult. Here we present the development of a simple, sensitive and inexpensive field method for the quantification of soil loss. The goal is to produce high precision digital elevation models (DEMs) of the soil surface that is investigated repeatedly (after days, months, years, events). The volumetric quantification of soil erosion will be the result of DEM overlapping over time. According to the developed methodological procedure, high-resolution aerial images are acquired by a small unmanned aerial vehicle (UAV) flying at low altitude (15 meters) on test areas smaller than 2 hectares to assure a very high image resolution. For each test area, at least four, homogenously distributed GCPs (Ground Control Points) are measured with GPS for geo-referencing. The images are processed with methods from photogrammetry and computer vision; the structure from motion (SfM) software is applied for this purpose. The results show the validity of the method for the calculation of volumes eroded in rills and gullies, but not so when there is only sheet-washing.

1. INTRODUCTION

Soil erosion is one of the main concerns of bare lands, both when it affects cultivated lands, but also when it involves territories after fire. In fact, when fire severity is high, the arboreal/shrub/herbaceous layer is eliminated and the soil erosion rate increases (Moench, 2003). The rate of erosion after a fire depends on many factors, including the type of soil. If the erosion is concentrated in linear elements, after a fire its rate can increase due to the poor vegetation protection, in addition to the material coming from the slope.

Field measurement of soil erosion using fixed instruments is not easy due to the elevated costs and the technical personal to be involved. The main tools used to investigate the geomorphological processes related to soil erosion are field plots. This field method has provided different results, depending on the characteristics of the plots, on their suitability to reflect the ecosystems' characteristics, and on the objectives of the single research (Boix-Fayos et al., 2006). Modelling is another most used method for erosion prediction. Indeed, a wide variety of models is currently available, ranging from fairly simple approaches (Wischmeier and Smith, 1978) to physics-based schemes (Williams, 1985). However, these models share a common requirement: they all need basic data for calibration and validation of the model,

The recent development of photogrammetric Unmanned Aerial Vehicle (UAV) technologies is offering new opportunities for field survey and monitoring. This technology allows obtaining accurate and effective Digital Elevation Models (DEMs) with relative simplicity and reduced times.

UAVs are easy to be transported also in rural areas due the small dimensions and weights and are useful for frequent flights after significant land cover changes and/or rainfall events. In general, fixed wing drones are particularly effective for remote topographic analyses of wide areas, but are less suitable to obtain high-accuracy DEMs due to their elevated flight height. Multirotor drones can work very close to the ground surface maintaining a fixed position and are extremely suitable for producing high resolution DEMs and micro-morphological surface analyses.

Here we present the first results of the development of a simple, sensitive and inexpensive field method for the quantification of soil loss based on the use of a DJI Phantom 3 drone system. The goal is to produce high precision DEMs of the soil surface that is investigated monthly and after significant rainfall events. The volumetric quantification of soil erosion is evaluated by overlapping the high precision DEMs produced over time.

2. STUDY AREA

The study area is located in the southern Apennines, in the hilly, Adriatic sector of Molise region. It falls in the headwater portion of the Rivo Stream basin, a small (80 km^2) 6th order sub-catchment of the Trigno River, one of the three major rivers of this Region (Aucelli et al., 2006) (Fig. 1).

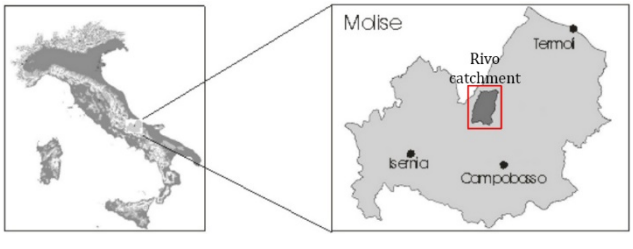

Figure 1. Location of the study area

Prevailing clayey, marly and arenaceous rocks underlie the Rivo basin. Particularly, the arenaceous-pelitic successions of the

* Corresponding author

Tufillo Unit and S. Bartolomeo Flysch, along with the clayey-marly terrains of the varicolored scaly clays referring to the Sannio Unit are dominating. Regarding the soil cover, Inceptisols are prevailing (63%), followed by Vertisols, Entisols and Mollisols. The Rivo basin is under the influence of a warm temperate, Mediterranean climate with annual precipitations of 650 to 800 mm, and monthly temperatures ranging between 5 and 30° (Marker et al., 2010).
In the study area, crop cultivation is prevailing and typically represented by cereals and fodder that well reflect the traditional agriculture of the Molise region and, in general, of the Central-Southern hilly Apennines.
To apply the developed method, one parcel (test area) has been taken into consideration, characterized by a surface area of approximately two hectares and average slope gradients of 40 to 50%. To monitor the precipitations, the study area has been equipped with a rain gauge station and data logger.

3. METHODS

We used the Structure from Motion (SfM) method to generate 3D terrain models starting from photography (Howland et al., 2014; James et al., 2012). SfM builds a cloud of 3D points that represents the photographed surface using a series of photographs. Starting from this point cloud, we obtained a DEM of our test area. However, the acquisition of the photos must follow precise instructions and the processing of the model must follow certain steps.

3.1 Data collection

In this study, the UAV DJI Phantom 3 Std (quadricopter) was used to acquire the images. The drone mounts a stabilized camera to compensate involuntary movements due to the wind. In this way, photos are assured with the correct orientation with respect to the ground. To assure a very high image resolution, the drone flies at low elevation above the ground level (15 meters). The drone records the coordinates for each photo through an internal GPS. This is very important because the drone with the GPS can follow the points (waypoints) previously drawn in the flight plan. The characteristics of the camera (Table 1) represent an essential factor for a good flight plan in addition to the resolution and the size of the sensor, especially the camera viewing angle (FOV – Field of View).

Feature	Value
Sensor	1/2.3” CMOS
Resolution	12 Mpx
Lens	FOV 94° 20 mm (35 mm format equivalent) f/2.8
Electronic Shutter Speed	8 - 1/8000 s
Image Size	4000×3000

Table 1 Features of the DJI Phantom 3 Std camera

In the flight plan, we set the FOV value, the flight altitude and the percentage of overlap between one swipe and another (side overlap). We calculated the shutter speed value to have a good percentage of longitudinal overlap (frontal overlap). We set a 60% side overlap and a frontal overlap of 80%. With these characteristics, the study area was covered with about 550 photos. The same flight plan was used on January 5th and on March 8th. For the study area, at least seven, homogenously distributed GCPs (Ground Control Points) have been acquired using a DGPS Trimble device.

3.2 Processing

The SfM-software Agisoft photoscan (http://www.agisoft.com/) was used to generate 3D models after the images acquisition. The SfM algorithm calculated the position of the photos and the geometry of the scene, comparing all the images and finding the common points (Westoby et al., 2012). This process involved different steps. In the first step, homologous image points (Tie points) between images were matched. In this way, the images were oriented in the space and a cloud of low density points, named dense sparse cloud, was created. Starting from this scattered cloud, a dense cloud of points (Fig. 2) was built in the next step.

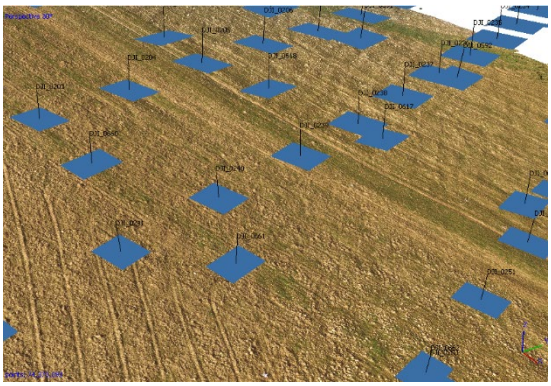

Figure 2. Dense Cloud Point of the study area (in blue the position of the photo in the space)

In the last step, the DTM of the study area was built starting from the dense cloud of points. The resulting DTMs have a resolution of 1.6 cm^2 (Fig. 3).

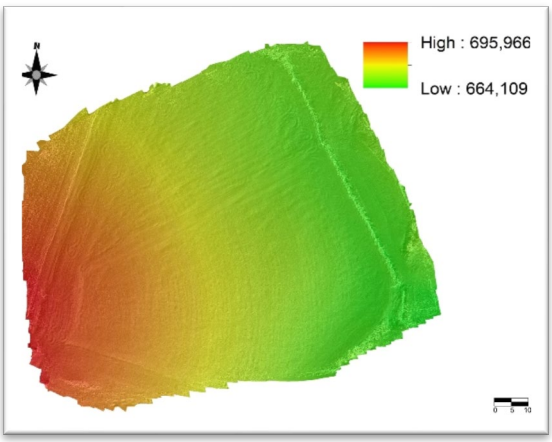

Figure 3. Digital elevation model (DTM) generated by unmanned aerial vehicle (UAV)

4. DISCUSSION

Two DEM of a field were obtained and compared. Model 1 (5th January 2018) and model 2 (8th March 2018)). A relevant topographic variation along the field profile was observed due to processes that induce the lowering of the topographic surface, such as soil erosion and compaction, and topographic raising mainly due to soil accumulation processes (Fig. 4).

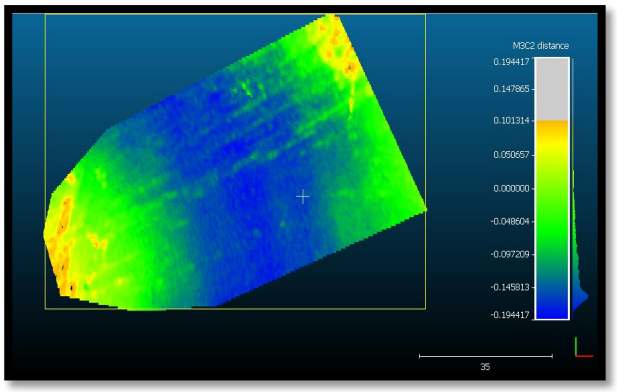

Figure 4. Difference in altitude between the model 1 (January 5th) and model 2 (March 8th). Scale and legend are in meters

We identified three areas with different features moving downslope the field:

- Top area characterized by positive topographic variation due to the growing of vegetation. Here negligible soil loss was expected (fig. 6).
- Central area with the major soil loss, due to both compaction and erosion. Here a depletion of the topography was observed (fig. 7).
- Foot area where soil loss is lower. Here the accumulation of the soil coming from the central part of the field exceeds the soil loss due to running waters producing a positive variation of topography (fig. 8).

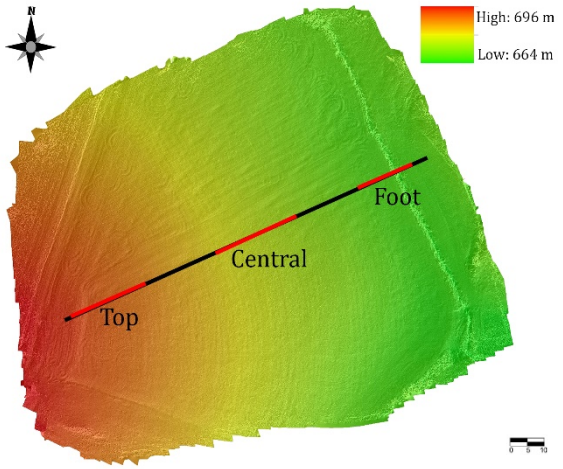

Figure 5. DEM of model 1, with profile (Black line) and the traces of the topographic profile Top, Central and Foot (Red lines).

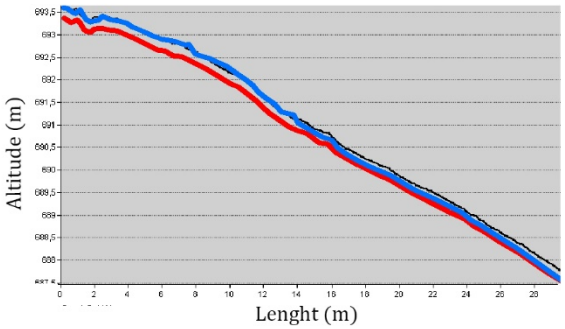

Figure 6. Top profile (red line is model 1, blue line is model 2)

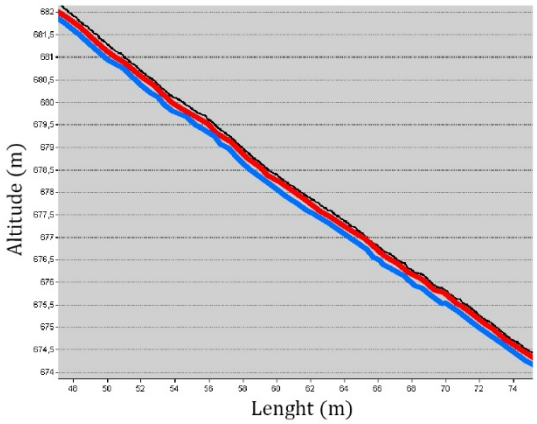

Figure 7. Central profile (red line is model 1, blue line is model 2)

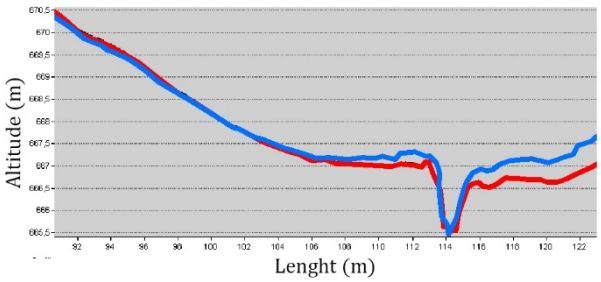

Figure 8. Foot profile (red line is model 1, blue line is model 2)

5. CONCLUSIONS

In conclusion, the SfM method is very useful for building high-resolution DEMs. In our case, we have obtained DEMs with a pixel resolution of 1.6 cm^2, which is appropriate to estimate soil loss due to rill and gully erosion.

The topographic variations due to the compaction component and the sheet-washing component are difficult to distinguish by comparing only the DEMs, and some additional field analysis are required to achieve this purpose.

REFERENCES

Aucelli, P.P.C., Caloiero, T., De Angelis, A., Gaudio, R., Rosskopf, C.M., 2006. Analisi del rapporto afflussi-deflussi in alcuni piccoli bacini idrografici molisani impostati su litologie a forte componente pelitica (Italia Meridionale) attraverso la misura diretta e la modellazione. Proceeding of the final Workshop of the PRIN/COFIN 2002 project “Water erosion in

Mediterranean environment: direct and indirect assessment in test and catchments", 2004.

Boix-Fayos, C., Martinez, M.M., Arnau, E., Calvo, A.C., Castillo, V.M., Albaladejo, J., 2006. Measuring soil erosion by field plots: Understanding the sources of variation. Earth-Science Reviews. 78(3), 267-285

Moench, R., Fusaro, J., 2003. Soil erosion control after wildfire. University of Colorado. Fact sheet N° 6308.

Howland, M.D., Kuester, F., Levy, T.E., 2014. Structure from motion: twenty-first century field recording with 3D technology. Near Eastern Archaeol. 77 (3), 187–191.

James, M., Robson, S., 2012. Straightforward reconstruction of 3D surfaces and topography with a camera: accuracy and geoscience application. Journal of Geophysical Research 117.

Marker, M., Rosskopf, C.M., Aucelli, P.P.C., 2010. Erosion processes mapping using datamining technologies: the Rivo Basin example (Molise, Central Italy). 1th Italian-Russian Workshop on Water Erosion At: Mosca, Russia.

Westoby, M., Brasington, J., Glasser, N., Hambrey, M., Reynolds, J., 2012. Structure-from motion photogrammetry: a low-cost, effective tool for geoscience applications. Geomorphology 179, 300–314.

Williams, J.R., 1985. The physical components of the EPIC model. In: El-Swaify, S., Moldenhauer, W.C., Lo, A., Soil Erosion and Conservation. Soil Conservation Society of America, Ankeny, Iowa, 272–284.

Wischmeier, W.H., Smith, D.D., 1978. Predicting Rainfall Erosion Losses. US Department of Agriculture. Agricultural Research Service Handbook 537, Washington, 58.

EXPLOITATION OF GNSS FOR CALIBRATING SPACE-BORNE SAR FOR THE STUDY OF LANDSUBSIDENCE

G. Farolfi[1,2]*, M. Del Soldato[1], S.Bianchini[1], N. Casagli[1]
[1] Earth Science Department, University of Firenze, Firenze, Italy –
(gregorio.farolfi, matteo.delsoldato, silvia.bianchini, nicola.casagli)@unifi.it
[2] Department of Geo-information, Italian Military Geographic Institute, Firenze, Italy

KEY WORDS: GNSS; SAR; Persistent Scatterers Interferometry; deformation map; Calibration, InSAR

ABSTRACT:

Nowadays advanced multi-temporal interferometric approaches such as PSI (Persistent Scatterers Interferometry) derived from the processing of space-borne SAR (Synthetic Aperture Radar) images represent an effective tool to detect terrain movements and provide millimetric ground measurements over large scenes thanks to their wide-area coverage, non-invasiveness, and high accuracy. Nevertheless, PSI data lack of absolute reference both in time and space, as they are relative estimates measured along the sensors-to-target line of sight and referred to a chosen stable motionless reference point. In this work, a methodology to fix relative InSAR results into conventional geodetic reference systems through calibration with GNSS (Global Navigation Satellite System) data acquired from permanent stations is proposed. In particular, mean yearly velocities of PSI radar benchmarks are corrected with GNSS values by means of procedures commonly used in geodesy for combining crustal and local deformation studies. The operative method is tested in the area of Ravenna and Ferrara cities on the north-western Adriatic coast within the eastern alluvial plain of Po River, extensively affected by subsidence with strong spatial and temporal variations. The outcomes reveal the usefulness of the presented methodology for generating unique ground deformation maps over wide are using geodesy for aligning PSI data before SAR maps stacking.

1. INTRODUCTION

Land subsidence is commonly defined as sudden sinking or gentle and gradual lowering or sudden sinking of the ground surface (Galloway & Burbey, 2011). Natural or anthropogenic processes, as well as their combination, and endogenic or exogenic phenomena, which refer to geological-related motions and the removal of underground materials, respectively, (Prokopovich, 1979) can be caused subsidence, sometimes with consequences. Subsidence phenomena mainly affect urban and greenhouses or nurseries areas (Tomas et al., 2014; Del Soldato et al., 2018) because of water overexploitation, with serious consequences such as damage to linear infrastructures, e.g., bridges, roads or railways, and building stability issues due to differential settlement (Del Soldato et al., 2016; Tomas et al., 2012). The monitoring of these phenomena plays a key role in the management of natural hazards for mitigating and minimizing the disaster losses and consequences. For land subsidence monitoring, classical techniques such as levelling networks (Teatini et al., 2005) or GNSS/GPS (Global Positioning System) techniques (Béjar-Pizarro et al. 2016) are traditionally used. In the last several decades, the Earth Observation (EO) technique, especially SAR (Synthetic Aperture Radar) remote sensing methods have rapidly grown. These techniques can profitably support risk reduction strategies by taking advantage of their wide area coverage associated with a high cost/benefit ratio. The PSI (Persistent Scatterers Interferometry) techniques (e.g. Ferretti et al., 2001and 2011), has been successfully adopted for a wide range of applications in disaster management, and it has extensively proven to be a valuable tool to detect ground deformations due to landslides (Solari et al., 2018; Del Soldato et al., 2018a; Ciampalini et al., 2016) or subsidence (Bonì et al., 2017; Da Lio & Tosi, 2018a).

PSI is commonly applied to satellite SAR images based on the recognizing on ground points characterized by long-term stability of the electromagnetic backscattered signal and high reflectivity Persistent Scatterers (PS) (Ferretti et al., 2001, Crosetto et al. 2016). By using the interferometric technique on the signal phase reflected by PS, the velocities of these points can be studied thought the time-series analysis of their displacements. Such as all the interferometric techniques, the velocity measured are relative to some points of the SAR image that is supposed to be stable.The lack of an absolute reference frame can be supplied by GNSS (Global Navigation Satellite System) measurements (Farolfi et al., 2018, 2019) as this is a geodetic network that provides rates and precise geographic location. In literature, many works exploited both SAR and GNSS data (i.e. Bovenga et al., 2012; Casu et al., 2006; Del Soldato et al., 2018b) for local terrain movements. In this work, we exploit SAR data acquired by historical ENVISAT data supported and calibrated by means of GNSS data throughout a methodological procedure for combining the two source datasets. We apply this approach to Ravenna and Ferrara cities located in the Po Plain in Central Italy, as this area is historically affected by subsidence due to natural and anthropogenic causes (Carminati and Martinelli, 2002). The merging of SAR products with GNSS reveals to be fundamental especially in the case of land subsidence where the velocity rates play an important role to understand and quantify the phenomena.

1. AREA OF STUDY

The paper focuses on the eastern portion of the Po River plain, a narrow area of Italian peninsula between Northern Apennines, Southern Alps and along the northern Adriatic coast where Ravenna and Ferrara cities are located. The Po River sedimentary basin is filled by Alpine and Apennine sediments. From the structural point of view, the north-verging Apennine fold-and-

* Corrisponding author

thrust belt system is overlapped by Plio–Quaternary sediments (Carminati, 2002). In this area, vertical deformation is known and the subsidence is driven by the combination of anthropogenic, geological and tectonic processes. The main factor responsible for land subsidence in the Po plain is the human extraction of deep no-rechargeable ground waters (Gambolati et al., 1999). The industrial growth, the modern extensive agricultural and zootechnical techniques and the population increase that took place in the second half of the 20th century in Italy induced a dramatic intensification in groundwater demand. Some authors state that these factors produced a near quadrupling of groundwater withdrawal compared with the first half of the century (Gonella et al., 1998). In addition to water pumping, gas exploitation is also greatly performed in this area during the last century (Teatini et al. 2005, Tosi et al. 2010). Regarding the components of natural subsidence in the Po Plain, the ground lowering is also sediment loading and compaction (Sclater and Christie, 1980) as well as post-glacial rebound and tectonic loading. Geologically, Holocene sediments include sandy and clayey silty level often rich in organic matter and they can suffer from compaction problems by loads and in case of water over-pumping (Rizzetto et al., 2003). Moreover, the effects of the last deglaciation, still impacting the Po Plain (Mitrovica and Davis, 1995), and active tectonics linked to a buried anticline under the Ferrara area are considered additional factors to the long-term geological subsidence (Carminati et al. 2003).

2. DATASETS

2.1 GNSS Dataset

The velocity field for the eastern Po Plain area was derived by the combination of two independent solutions (Palano 2014, Farolfi et al., 2016, 2017) consists of a subset of 35 sites determined for a period that runs from 2008 to 2014. The two velocity solutions were combined involving a rigid Helmert transformation that minimizes the differences of GNSS site velocities that the two datasets have in common, by using a least squares approach. The resulting horizontal velocity field were referred into the European Terrestrial Reference Frame ETRF2008.

2.2 PS dataset

The velocity field determined with SAR satellites were calculated by involving with using PSInSAR technique (Ferretti et al., 2001) by using all available ENVISAT data from the Italian peninsula resulting from the program "Not-Ordinary Plan of Remote Sensing" developed by the Italian Ministry of the Environment available from the Italian Geoportale Nazionale (www.pcn.minambiente.it). The European ENVISAT mission covered a long-term continuous period from 2003 to 2010 with a temporal solution or satellite's repeating cycle of 35 days.

3. METHODOLOGY

The PS displacements and velocities calculated with GNSS and SAR show differences due to the different LOS direction in which they are recorded. Since the deformation PS velocity is acquired a LOS of the satellites with determined parameters, it must be re-projected and decomposed in vertical and horizontal components to be compared with the velocity components derived by GNSS. For this reason, the LOS displacements and velocities of the ENVISAT PS data was decomposed into horizontal and normal components with respect to the international ellipsoid. After this procedure, the InSAR displacements and velocities can be compared to GNSS dataset.

The velocityv_{LOS} measured by the SAR satellite for a ground velocity v with components $v = [v_N, v_E, v_V]$ is determined by the direction cosine or unit vector $S = [S_N, S_E, S_V]$ in the direction from the ground to the satellite along the LOS direction:

$$v_{LOS} = V_N S_{N,LOS} + V_E S_{E,LOS} + V_V S_{V,LOS} \,. \quad (1)$$

The unit vector S for ascending (S_A) and descending (S_D) orbits are derived by the inclination of the orbits with respect to the equator $\delta = 98.5°$, and the mean off-nadir θ:

$$\begin{pmatrix} S_A \\ S_D \end{pmatrix} = \begin{pmatrix} -\sin\theta_A \cos\delta & -\sin\theta_A \sin\delta & \cos\theta_A \\ \sin\theta_D \cos\delta & \sin\theta_D \sin\delta & \cos\theta_D \end{pmatrix} \quad (2)$$

For ENVISAT mission the LOS angles for both ascending and descending geometry is given the same value of θ =23.3° Eq. 1 can be written for the ascending (V_A) and descending (V_D) velocities with the direction cosine:

$$\begin{pmatrix} V_A \\ V_D \end{pmatrix} = \begin{pmatrix} S_{N,A} & S_{E,A} & S_{V,A} \\ S_{N,D} & S_{E,D} & S_{V,D} \end{pmatrix} \begin{pmatrix} V_N \\ V_E \\ V_V \end{pmatrix} \quad (3)$$

Eq. 3 is a system of two equations with three variables and is thus not solvable. Considering that the displacements along the north–south direction are almost parallel to the ENVISAT satellite orbit and for this reason cannot be detected along the LOS for both the ascending and descending orbits, then eq. 3 can be approximated as:

$$\begin{pmatrix} V_A \\ V_D \end{pmatrix} \cong \begin{pmatrix} S_{E,A} & S_{V,A} \\ S_{E,D} & S_{V,D} \end{pmatrix} \begin{pmatrix} V_E \\ V_V \end{pmatrix} \quad (4)$$

and be solved. The two components of velocity v can be derived as follows:

$$V_E \cong \frac{V_D - V_A}{2.|S_E|}, \qquad V_V \cong \frac{V_D + V_A}{2.|S_V|} \quad (6)$$

where the modules of unit vectors of S for ENVISAT are $S = [S_N, S_E, S_V] = [0.05, 0.38, 0.92]$. The availability of GNSS site velocity in the Area of Interest (AoI) permits to align the PS velocities to the ETRS89 reference frame. In fact, PS velocities are calculated respect to one or more reference points chosen during the processing phase of the SAR images.

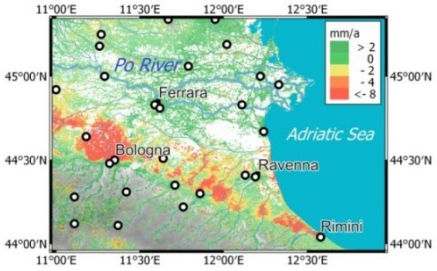

Figure 1 - Map of PS vertical velocity from InSAR images. Green represents represents stable points, yellow represents points with mild downward movement around -2mm/a, and red represents points of downward movement lower than -8.0 mm/a. Black circles represent the position of GNSS sites.

The lack of an absolute reference frame of PS dataset can be supplied by the comparison of ground point velocities determined using both techniques (Fig.2). The differences between the two velocity datasets were interpolated with an exponential inverse distance weighting to determine the map of correction for PS velocities (Fig.3).

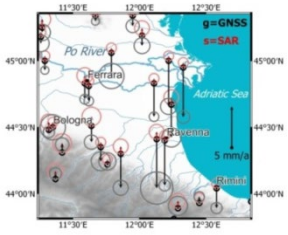

*F*igure 2 - Comparison of vertical velocities and their circles of uncertainties determinate with GNSS (black arrows) and PSInSAR (red arrows) for each GNSS site (black circles).

4. RESULTS

The GNSS stations displaced in the Po River Delta and in the city of Ravenna record important values lower than -5 mm/a of subsidence. The limit of this lowering ~ -2 mm/a is close to Ferrara. The GNSS stations present in Bologna are stable since they are located out from the wide subsidence area. Rimini show mild values of subsidence ~ - 2mm/y. The comparison between the PS and GNSS vertical velocity shows different rates (Fig. 2) that reach -5 mm/a in the area of Po River Delta and Ravenna, -2 mm/a around Ferrara and Rimini.

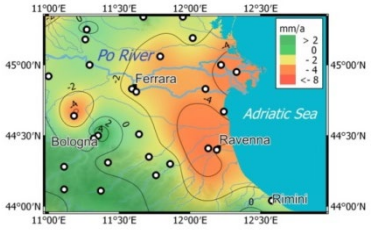

Figure 3 - Calibration map for PS vertical velocity to apply to PS to obtain "absolute" and corrected vertical velocity rates.

The area of the Po River Delta shows subsidence rate with values ~ - 5 mm/y (Figure 4). The coastal area from the north of Ravenna town to the city of Rimini shows a bend of subsidence with values variable from -8 mm/a to -4 mm/a confined by stable sector. In the western area of Bologna, is located a big bowl with subsidence rates lower than - 10 mm/a. The area of Ferrara town and its surrounding show values of velocity of displacement into the stable span (~2 mm/a).

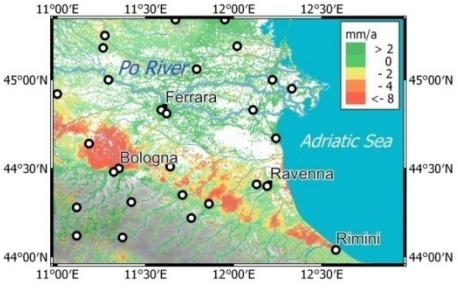

Figure 4 - Vertical velocities of PSI points after the calibration performed by GNSS (absolute velocity). Green represents points with a stable or light uplift, yellow represent points with a mild downward movement, orange represent points with downward movement less than -4 mm/a and red represents points of downward movement less than -8.0 mm/a.

5. CONCLUSIONS

The combination of the GNSS with the PS data deeply improved the investigation of the displacement of the ground. In this way, all the problem of the choice of a stable points for PS processing based on geological and signal features, can be an overpass. The determination of correct vertical velocity rates play an important role in subsiding areas for avoiding damage to structures and infrastructure (e.g. Bianchini et al., 2015; Del Soldato et al., 2016). Moreover, the combination of GNSS and SAR produces new maps of surface movements where velocities at both a detailed and a wider scale are geodetically correct.

CONTRIBUTIONS

Intellectual content to conception and project coordination are contributions of G. Farolfi and N. Casagli. G. Farolfi developed mathematical models and performed the geodetic analysis. S. Bianchini and M. Del Soldato provide SAR analysis, geological settings, geodynamic analysis and the writing of the manuscript. Drafting the article came from the contribution of all the authors.
This work received the support of the Department of Earth Sciences, University of Firenze and Istituto Geografico Militare Italiano (IGM). We thank EPN, ASI, INGV and all public and private agencies who run and maintain GNSS networks that publicly share the data. We thank the Ministry of Environment for the SAR datasets used in this study.

REFERENCES

Bianchini, S., Moretti, S. Analysis of recent ground subsidence in the Sibari plain (Italy) by means of satellite SAR interferometry-based methods. International Journal of Remote Sensing, 2015, 36.18: 4550-4569.

Béjar-Pizarro, M., Guardiola-Albert, C., García-Cárdenas, R.P., Herrera, G., Barra, A., López Molina, A.,Tessitore, S., Staller, A., Ortega-Becerril, J.A., García-García, R.P. Interpolation of GPS and geological data using InSAR deformation maps: Method and application to land subsidence in the Alto Guadalentín aquifer (se Spain). Remote Sens. 2016, 8, 965.

Bonì, R., Meisina, C., Cigna, F., Herrera, G., Notti, D., Bricker, S., McCormack, H., Tomás, R., Béjar-Pizarro, M., Mulas, J. Exploitation of satellite a-DInSAR time series for detection, characterization and modelling of landsubsidence. Geosciences 2017.

Bovenga, F., Wasowki, J., Nitti, D.O., Nutricato, R., T. Chiaradia, M, Using COSMO/SkyMed X-band and ENVISAT C-band SAR interferometry for landslides analysis. Remote Sensing of Environment 119 (2012): 272-285.

Carminati, E., and G. Martinelli. Subsidence rates in the Po Plain, northern Italy: the relative impact of natural and anthropogenic causation. Engineering Geology 66.3-4, 2002: 241-255.

Carminati, E., G. Martinelli, and P. Severi. "Influence of glacial cycles and tectonics on natural subsidence in the Po Plain (Northern Italy): Insights from 14C ages." Geochemistry, Geophysics, Geosystems 4.10 (2003).

Casu, F., M. Manzo, and R. Lanari. "A quantitative assessment of the SBAS algorithm performance for surface deformation retrieval from DInSAR data." Remote Sensing of Environment 102.3-4 (2006): 195-210.

Ciampalini, A., Raspini, F., Frodella, W., Bardi, F., Bianchini, S., Moretti, S. The effectiveness of high-resolution lidar data

combined with PSInSAR data in landslide study. Landslides 2016, 13, 399–410.

Crosetto, M., Monserrat, O., Cuevas-González, M., Devanthéry, N., and Crippa, B. 2016, Persistent Scatterer Interferometry: A review. International Journal of Photogrammetry and Remote Sensing, 115, 78-89.

Da Lio, C., Tosi, L. Land subsidence in the Friuli Venezia Giulia coastal plain, Italy: 1992–2010 results from sar-based interferometry. Sci. Total Environ. 2018, 633, 752–764.

Da Lio, C., Teatini, P., Strozzi, T., Tosi, L. Understanding land subsidence in salt marshes of the Venice lagoon from SAR interferometry and ground-based investigations. Remote Sens. Environ. 2018, 205, 56–70.

Del Soldato, M., Tomás, R., Pont Castillo, J., Herrera García, G., Lopez-Davalillos, G., Carlos, J., & Mora, O. (2016). A multi-sensor approach for monitoring a road bridge in the Valencia harbor (SE Spain) by SAR Interferometry (InSAR).

Del Soldato, M., Riquelme, A., Bianchini, S., Tomàs, R., Di Martire, D., De Vita, P., Moretti, S., Calcaterra, D. Multisource data integration to investigate one century of evolution for the Agnone landslide (Molise, Southern Italy). Landslides 2018.

Del Soldato, M., Farolfi, G., Rosi, A., Raspini, F., Casagli, N. Subsidence Evolution of the Firenze–Prato–Pistoia Plain (Central Italy) Combining PSI and GNSS Data. Remote Sens. 2018, 10, 1146.

Farolfi, G., Del Ventisette, C. 2016, Contemporary crustal velocity field in Alpine Mediterranean area of Italy from new geodetic data. GPS Solutions, 204, pp.715-722. ISSN Print 1080-537, doi: 10.1007/s10291-015-0481-1.

Farolfi, G., Del Ventisette, C. Monitoring the Earth's ground surface movements using satellite observations: Geodinamics of the Italian peninsula determined by using GNSS networks. In Metrology for Aerospace (MetroAeroSpace), 2016 IEEE (pp. 479-483). IEEE.

Farolfi, G. and Del Ventisette, C. 2017, Strain rates in the Alpine Mediterranean region: insights from advanced techniques of data processing. GPS Solutions, 21(3), pp.1027-1036, doi:10.1007/s10291-016-0588-z.

Farolfi, G., Bianchini, S., Casagli, N. 2018 Integration of GNSS and satellite InSAR data: derivation of fine-scale vertical surface motion maps of Po Plain, Northern Apennines and Southern Alps, Italy, IEEE Transactions on Geoscience and Remote Sensing (TGRS), doi: 10.1109/TGRS.2018.2854371.

Farolfi, G., Piombino, A., Catani, F. 2019 Fusion of GNSS and satellite radar interferometry: determination of 3D fine-scale map of present-day surface displacements in Italy as expressions of geodynamics processes, Remote Sensing.
Ferretti, A., Prati, C. and Rocca, F.2001, Permanent Scatterers in SAR Interferometry. IEEE Trans. On Geosci. Remote Sens., 39, p. 8-20.

Galloway, Devin L., and Thomas J. Burbey. Regional land subsidence accompanying groundwater extraction. Hydrogeology Journal 19.8, 2011: 1459-1486.

Gambolati, G., Teatini, P., Tomasi, L., Gonella, M. Coastline regression of the Romagna region, Italy, due to natural and anthropogenic land subsidence and sea level rise. Water Resources Research 35.1 (1999): 163-184.

Gonella, M., Gambolati, G., Giunta, G., Putti, M., Teatini, P. Prediction of land subsidence due to groundwater withdrawal along the Emilia-Romagna coast. CENAS. Springer, Dordrecht, 1998. 151-168.

GeoportaleNazionale. www.pcn.minambiente.it (20 august 2018).

Mitrovica, Jerry X., and James L. Davis. Present-day post-glacial sea level change far from the Late Pleistocene ice sheets: Implications for recent analyses of tide gauge records. Geophysical Research Letters 22.18 (1995): 2529-2532.

Palano, M. 2014, On the present-day crustal stress, strain-rate fields and mantle anisotropy pattern of Italy. Geophysical Journal International, 200(2), 969-985.

Prokopovich, Nikola P. Genetic classification of land subsidence. Evaluation and Prediction of Subsidence. ASCE, 1979.

Sclater, John G., and Phillip AF Christie. Continental stretching: An explanation of the post-mid-Cretaceous subsidence of the central North Sea basin. Journal of Geophysical Research: Solid Earth 85.B7 (1980): 3711-3739.

Solari, L., Raspini, F., Del Soldato, M., Bianchini, S., Ciampalini, A., Ferrigno, F., Tucci, S., Casagli, N. Satellite radar data for back-analyzing a landslide event: The ponzano (central Italy) case study. Landslides 2018, 15, 1–10.

Teatini, P., Ferronato, M., Gambolati, G., Bretoni, W., Gonella, M., Morelli, M., Severi, P. 2005 Land subsidence due to groundwater withdrawal in the Emilia-Romagna coastland, Italy. In Land Subsidence. Proceedings of the Seventh International Symposium on Land Subsidence, Vol. I.

Teatini, P. Tosi, L., Strozzi, T., Carbognin, L., Wegmüller, U., Rizzetto, F. Mapping regional land displacements in the Venice coastland by an integrated monitoring system. Remote Sens. Environ. 2005, 98, 403–413.

Tomás, R., García-Barba, J., Cano, M., P Sanabria, M., Ivorra, S., Duro, J., Herrera, G.. Subsidence damage assessment of a gothic church using Differential Interferometry and field data. Structural Health Monitoring 11.6,2012, 751-762.

Tomás, Roberto, Romero, R., Mulas, J., Marturià, J.J., Mallorquí, J.J., Lopez-Sanchez, J.M, Herrera, G., Gutiérrez, F., González, P.J., Fernández, J., Duque S., Concha-Dimas, A., Cocksley, G., Castañeda, C., Carrasco, D., Blanco, P. Radar interferometry techniques for the study of ground subsidence phenomena: a review of practical issues through cases in Spain. Environmental earth sciences 71.1 (2014): 163-181.

Tosi, L., Teatini, P., Strozzi, T., Carbognin, L.,Brancolini, G., and Rizzetto, F. 2010,Ground surface dynamics in the northern Adriatic coastland over the last two decades. Rend. Fis. Acc. Lincei., 21; S115–S129.

CONTRIBUTION OF SPATIAL MULTI-SENSOR IMAGERY TO THE CARTOGRAPHY OF STRUCTURAL LINEAMENTS: CASE STUDY OF THE PALEOZOIC MASSIF OF REHAMNA (MOROCCAN MESETA)

I. Serbouti[1]*, M. Raji[1], M. Hakdaoui[2]

[1] Dept. of Geology, Laboratory of geodynamics of the old chains, Faculty of Sciences Ben M'Sik, Hassan II University of Casablanca, Casablanca, Morocco (imaneserbouti, mhedraji)@gmail.com

[2] Dept. of Geology, Laboratory of Applied Geology, Geomatic and Environment, Faculty of Sciences Ben M'Sik, Hassan II University of Casablanca, Casablanca, Morocco – hakdaoui@gmail.com

KEY WORDS: Landsat 8, Sentinel 1, Interferometry, SRTM, Automatic extraction, Lineaments, Rehamna, Morocco

ABSTRACT

Lineaments constitute an interesting approach in the geological mapping and the exploration of resources such as minerals, energy and groundwater. With the use of remote sensing technology structural lineaments can be better detected, due to strong advances in using data and methods that enable us to exceed the usual classical procedures and achieve more precise results. The aim of this work is combining and comparing different techniques of automatic extraction of lineaments in the Palaeozoic massif of Rehamna located in the western Moroccan Meseta. Three methods were used to extract lineaments from Landsat 8 Oli, Sentinel 1 and DEM images. In the first method, four derived images were generated by applying frequential directional filters, in all possible directions (NS, NE-SW, EW, and NW-SE), to RGB composite images and the principal component analysis (PCA) of Landsat 8 OLI. These filters increase the image contrast and allow mapping a large number of lineaments. The second method consists to extract lineaments automatically by using level 1 GRD (Ground Range Distance) of Sentinel 1, according to IW mode with the polarizations (VH) and (VV). Finally, shaded relief images were generated from DEM created by radar interferometry with the resolution of 13m, made by two Single Look Complex (SLC) of sentinel 1 images, and the DEM SRTM with a resolution of 30m. The results were compared with pre-existing geological data and Google Earth images, and were satisfying.

1. INTRODUCTION

Lineaments are the linear or curvilinear discontinuities such as faults and fractures, which reflect the tectonic history, groundwater potential, oil and mineral resources on the earth's surface (Das and Pardeshi 2018).

The fundamental concept of lineaments was introduced by Hobbs (1903, 1912) and define them as a significant lines of landscape which reveal the hidden architecture of the rock basement, since then several definitions have been carried out by a number of researchers namely O'Leary and al. (1976), Spencer (1988), Sabin (1996).

Linear features can be derived from remote sensing sources in particular optical imagery, radar imagery or digital elevation model. Therefore, the extraction of geological lineaments from remote sensing data can be grouped into at least three approaches: manual extraction (Jordan and Schott 2005) and semi-automatic extraction (Lim et al 2001, Jordan et al., 2005) that are influenced by the experience of the interpreter, whereas the automatic extraction (Mostapha and Bishta 2005, Anwar et al., 2013, Ghazi 2013) depends chiefly on the performance of the methods and data used, hence it gives information of both the geological fractures as well as surface features of a given area, suchlike natural objects as boundaries between different lithological units or vegetation covers and artificial objects like roads, bridges, railway...

The purpose of this work is to compare and combine the structural lineaments obtained using Landsat-8 and Sentinel 1 (GRD) data sensors in automatic lineament extraction, in addition to the shaded relief images that were generated from the DEM of radar interferometry with the resolution of 13m, made by two Single Look Complex (SLC) of sentinel 1 images, and the DEM SRTM with a resolution of 30m.

2. STUDY AREA

2.1 Location

For a detailed presentation of the results obtained, we have zoomed on the North Hercynian massif of Rehamna. It is located in the Moroccan West Meseta, between North Latitudes 32°49'28.69" – 32°29'53.79" and West longitudes 8° 0'16.72" – 7°49'41.62" (Fig.1).

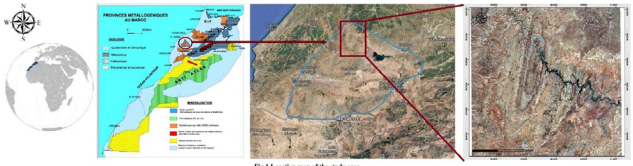

Figure 1. Location map of the study area

2.2 Geological and structural settings

The Rehamna Massif is located in the western Meseta. It is divided into three blocks of meridian direction: a western block (coastal mole) and an eastern bloc, more or less moderately deformed framing a central, sedimentary area in the North Rehamna and metamorphic with granitic intrusions in the South. The boundaries between these blocks are traced by two major accidents:

the shearing accident of the western Meseta (or median fault) in the West and the accident of Foum el Mejez_Ouled Zednes in the East. While the Imfout syncline is characterized by shear faults related to the folding event (Fig.2). (Michard et al. 1978; EI Kamel 1987).

* Corresponding author

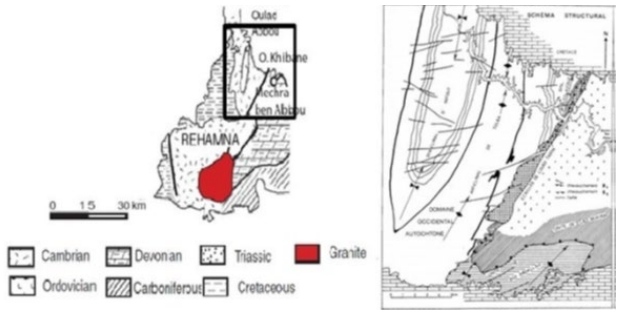

Figure 2. Geology of the study area (Michard and al. 2008)

3. MATERIALS AND METHODS

The general flowchart of methodology is given in Figure 3, wherein the first stage consists on the pre-processing of the datasets that includes the geometric correction and projection of all data in the same geographic space using the universal Transverse Mercator (UTM) zone 29 North Morocco, and a World Geodetic System (WGS84). The second stage pertains to the automatic extraction of lineaments using the shaded relief images that were generated from the DEM of radar interferometry and the DEM SRTM, the frequential directional filters of the coloured composite and the principal component analysis of Landsat 8 OLI and the level 1 GRD of Sentinel 1, according to IW mode with the polarizations (VH) and (VV). In the next stage the lineaments obtained were combined, the duplicate and non-geological lineaments were eliminated to generate and analyse the final lineament map of the study area.

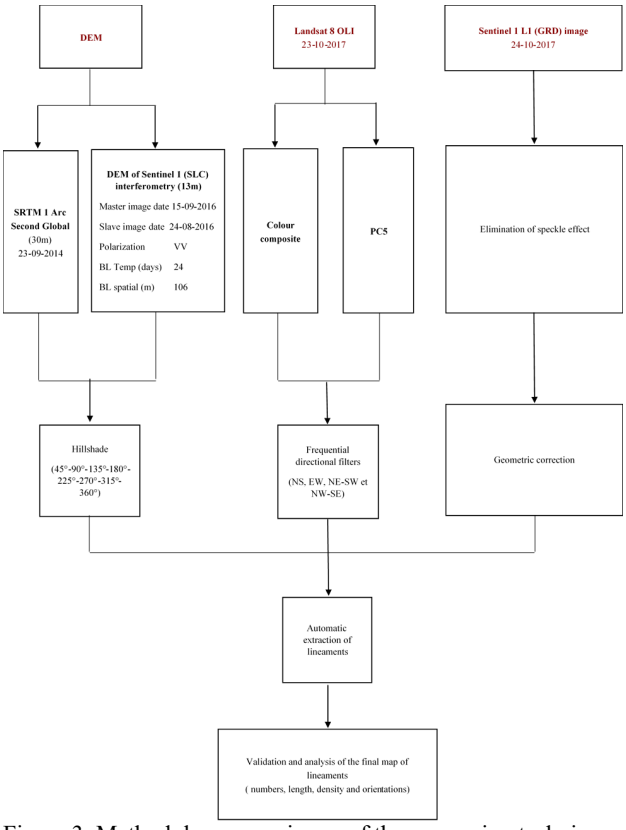

Figure 3. Methodology organigram of the processing techniques applied in this study

4. RESULTS AND DISCUSSION

Comparing the SRTM and the DEM of Sentinel 1, it is observed that the latter provides a high-resolution DEM with low coherence in some areas, this can be explained by the two consecutive Sentinel 1 acquisitions (24 days), while the SRTM used a single pass interferometry, which means that the two images have been acquired at the same time (*https://www2.jpl.nasa.gov*).

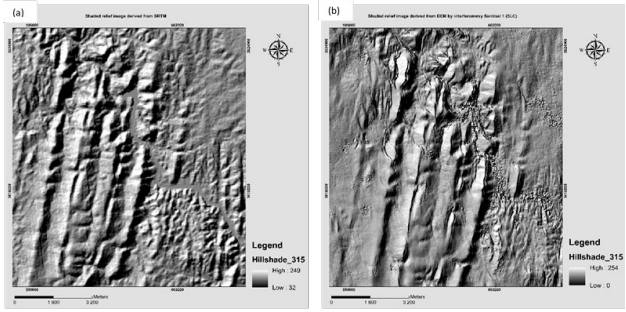

Figure 4. Comparison between the hillshade of (a) SRTM, and (b) DEM of Sentinel 1

4.1 Lineaments mapping

The results of automatic lineament extractions are shown in Fig.5 and Fig.6.

For the ones extracted from the shaded relief images of Sentinel 1 DEM (Fig.5.b) are more precise in the areas with high coherence while the lineaments extracted from the shaded relief images of the SRTM (Fig.5.a) are characterized by a random distribution that occupies the entire study area.

Otherwise, the resulting lineaments of the Colour Composite (Fig.6.c) and the PCA (Fig.6.d) of OLI and the two VV (Fig.6.e) and VH (Fig.6.f) images of the radar Sentinel 1 are superimposed on the Colour Composite (CC) RGB ($PC_4/PC_5/PC_2$) in order to analyse the distribution of the resulted lineaments with regard to the colour differences between the boundaries of contrasting lithological units (Solomon and Ghebreab,2006).

The analysis of the results obtained reveal that the lineaments extracted from the OLI sensor are longer and have a high concentration compared to those resulting from the Sentinel 1 images. This can be explained by the sensitivity of the optical images to the soil's occupation such as lithological units, vegetation and roads. conversely, radar data are not influenced by the nature of land use.

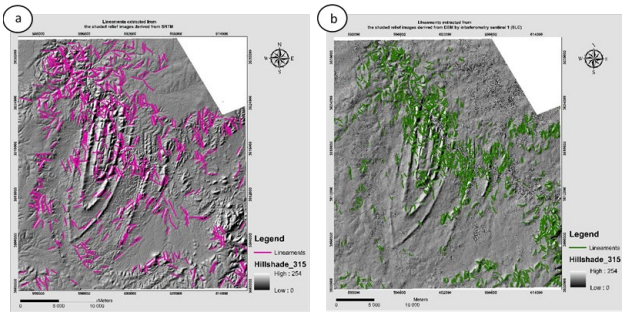

Figure 5. Lineaments extracted from the shaded relief images derived from (a) SRTM (b) DEM of Sentinel 1 interferometry.

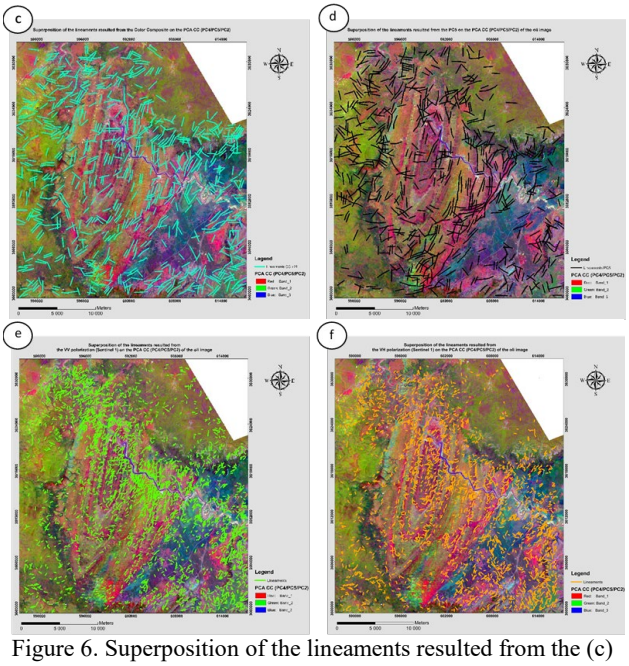

Figure 6. Superposition of the lineaments resulted from the (c) Colour Composite and (d) the PC5 of Landsat 8 OLI in addition to the (e) VV and (f) VH polarizations (Sentinel 1) on the PCA CC (PC4/PC5/PC2) of the OLI image.

4.2 Statistical analysis of lineaments

To understand the orientation of lineaments, rosette diagrams were constructed, it is clearly shown in Figure 7 that the most dominant directions of lineaments extracted from SRTM (Fig.7.a) and Sentinel 1 DEM (Fig.7.b) are those of East-West, which correspond perfectly to that of the shear faults related to the folding event, however the directions indicated by the Colour Composite (Fig. 7c) and PC5 (Fig. 7d) of OLI image, are characterized by NE-SW and NE-SW as majority directions, while the most dominant directions of lineaments extracted from the radar polarizations, VV (Fig.7.e) and VH (Fig.7.f), are those of NE-SW which correspond with the orientation of the major accidents.

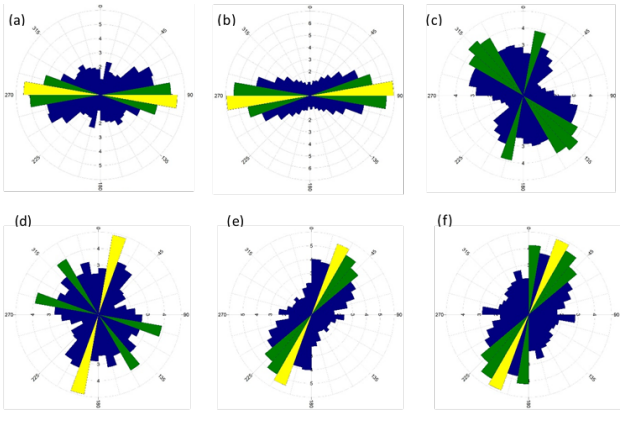

Figure 7. Orientations of lineaments obtained from the (a) SRTM, (b) DEM of Sentinel 1 interferometry, (c) the colour composite and (d) the PC5 of Landsat 8 OLI as well as (e) the VV and (f) VH polarizations (Sentinel 1).

In order to compare the obtained results, Fig. 8 represent the number of the obtained lineaments as a function of the length (in Meters), in addition to some statistics relating to the length for each of the used data. Concerning those of SRTM (Fig.8.a) the values range from around 196 m to a maximum of 2261 m while the value of Sentinel 1 DEM image (Fig.8.b) are between 170 m and 1377 m. Regarding the OLI image, the values of the colour composite (Fig.8.c) vary between 108 m and 2649 m, while they are between 60 m and 2395 m for PC5 (Fig.8.d). Whereas the VV (Fig.8.e) and VH (Fig.8.f) of Sentinel 1 images extend from around 16 m to 750 m.

This difference can be explained by the different natures of the images (optical and radar), which reveal the efficiency of the radar data that are independent of the soil's occupation.

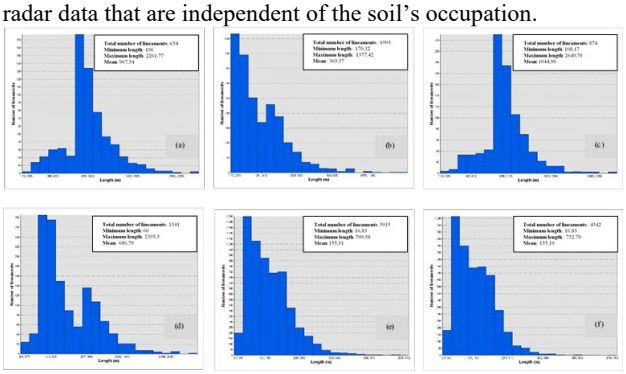

Figure 8. Distribution histograms showing the number of lineaments according to the length for the (a) SRTM (b) DEM of Sentinel 1 interferometry, (c) the colour composite and (d) the PC5 of Landsat 8 OLI, (e) VV and (f) VH polarizations (Sentinel 1).

The density of lineaments provides valuable information regarding the intensity of tectonic events (Hung et al.2002; Das et al.2003), and rock fracturing and shearing (Chandrasekhar et al.2011). For the SRTM (Fig.9.a) the high values randomly occupy most of the study area, while those of Sentinel 1 DEM (Fig.9.b) are concentrated in the north-western part of the study area, otherwise, the result obtained from the colour composite of OLI sensor (Fig.9.c) shows a random distribution over unit area, on contrary of those obtained from the PC5 (Fig.9.d) are concentrated in the SW-NE and in the NW, which correspond perfectly to the major faults of the study area. For the Sentinel 1 images (Fig.9.e) and (Fig.9.f) the high values are concentrated in the NW.

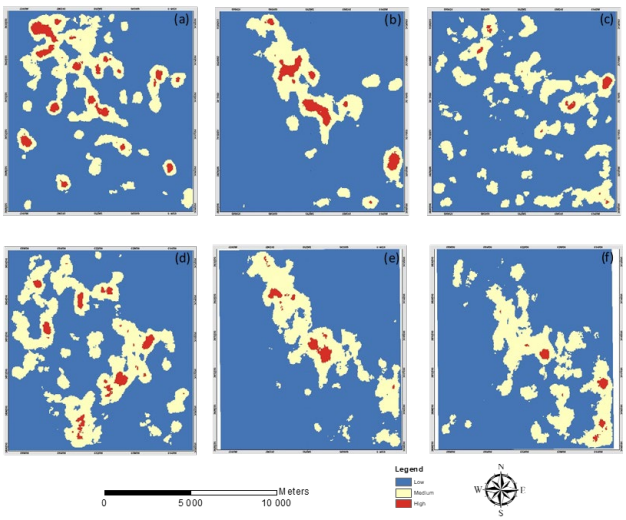

Figure 9. Lineaments density of the (a) SRTM (b) DEM of Sentinel 1 interferometry, (c) the colour composite and (d) the PC5 of Landsat 8 OLI, (e) VV and (f) VH polarizations (Sentinel 1).

4.3 Final result

The final map (Fig.10.a) was carried out by combining all the results obtained from the different data used, in addition to the elimination of non-geological and redundant lineaments.
The analysis of the synthetic result indicated that the high values of lineament density (Fig.10.b) are concentrated in the SW-NE which completely matches with the major faults of the study area, whereas the length of lineaments (Fig.10.c) vary from around 60 m to 2650 m, furthermore the rose diagram (Fig.10.d) shows that the most dominant directions of lineaments are East-West and NE-SW the thing that correspond exactly with the shear faults related to the folding event and the major faults of the study area.

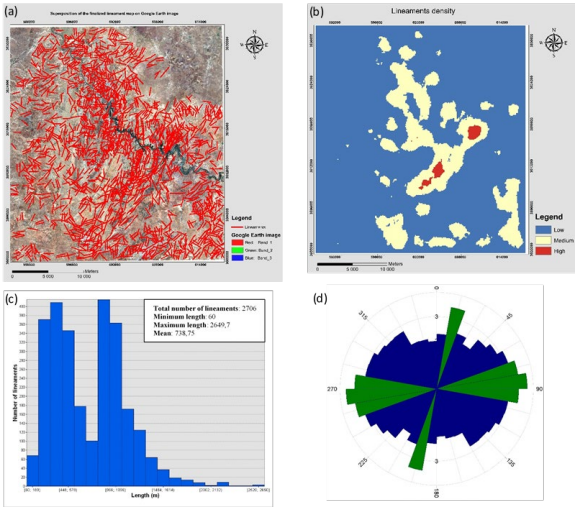

Figure 10. (a)Superposition of the finalized lineament map on Google Earth image, (b) lineaments density, (c) the distribution histogram and (d) the rose diagram of the final map.

5. CONCLUSIONS

In this study, the DEM obtained from Radar interferometry, SRTM, the colour composite, the PC of Landsat-8 OLI and the Sentinel 1 (GRD) images, were assessed in automatic extraction lineaments task.
The DEM resulted from sentinel 1 interferometry gives more information about the small fractures in areas with high coherence compared to those resulting from SRTM.
The lineaments extracted from the OLI sensor are more numerous and have a high concentration compared to those resulting from DEM and Sentinel 1 images. This can be explained by the sensitivity of the optical images towards the soil occupation such as lithological units, roads and rivers, contrary to radar data that are sensible to the geomorphology.

REFERENCES

Anwar Abdullah, Shawki Nassr, Abdoh Ghaleeb, 2013. Landsat ETM-7 for lineament mapping using automatic extraction technique in the SW part of Taiz area, Yemen. Global Journal of human social science geography, geo-science, environmental and disaster management.13, ISS 3, VER 1.0, 2013.

Chandrasekhar P, Martha TR, Venkateswarlu N, Subramanian SK, Kamaraju MVV (2011) Regional geological studies over parts of Deccan Syneclise using remote sensing and geophysical data for understanding hydrocarbon prospects. Curr Sci 100(1):95–99

Das S, Pardeshi SD (2018) Comparative analysis of lineaments extracted from Cartosat, SRTM and ASTER DEM: a study based on four watersheds in Konkan region, India. Spat Inf Res 26(1):47–57. https://doi.org/10.1007/s41324-017-0155-x

Das DP, Chakraborty DK, Sarkar K (2003) Significance of the regional lineament tectonics in the evolution of the Pranhita-Godavari sedimentary basin interpreted from the satellite data. J Asian Earth Sci 21:553–556. https://doi.org/10.1016/S1367-9120(02)00025-1

Hung LQ, Dinh NQ, Batelaan O, Tam VT, Lagrou D (2002) Remote sensing and GIS-based analysis of cave development in the Suoimuoi catchment (son la - NW Vietnam). J Cave Karst Stud 64(1):23–33

Hobbs WH (1903) Lineaments of the Atlantic border region. Geol Soc Am Bull 15:483–506. https://doi.org/10.1130/GSAB-15-483

Hobbs WH (1912) Earth features and their meaning. McMillan, New York

Jordan, G., Meijninger, B.M.L., Van Hinsbergen, D.J.J., Meulenkamp,J.E., Van Dijk, P.M.,2005. "Extraction of morphotectonic features from DEMs: Development and applications for study areas in Hungary and NW Greece", Int. J. Appl. Earth Obser. Geoinform. 7, 163–182.

Jordan, G., Schott, B.,2005. "Application of wavelet analysis to the study of spatial pattern of morphotectonic lineaments in digital terrain models: a case study",Remote Sens. Environ. 94, 31–38.

Lim, C.S., Ibrahim, K., Tjia, H.D., 2001. "Radiometric and Geometric information content of TiungSat-l MSEIS data", in: TiungSAT-1: From Inception to Inauguration, pp. 169–184.

Michard, A. (1969). "Fracturations profondes et décrochement dans les Rehamna (Maroc hercynien) ; C.R. somm. Séance soc.géol.fr. pp. 89-90.
Michard et al., Continental Evolution: The Geology of Morocco. Lecture Notes 65 in Earth Sciences 116, c_ Springer-Verlag Berlin Heidelberg 2008.

Mostafa, M.E., A.Z. Bishta, 2005. Significance of lineament patterns in rock unit classification and designation: a pilot study on the Gharib-Dara area, northern Eastern Desert. Egypt. Int. J. Remote Sens., 26(7): 1463–1475, 2005.

Rayan Ghazi Thannoun, 2013. Automatic Extraction and Geospatial Analysis of Lineaments and their tectonic significance in some areas of Northern Iraq using remote sensing techniques and GIS. International journal of enhanced research in science technology and engineering, 2(2), FEB, 2013.

Solomon, S., Ghebreab, W., 2006. Lineament characterization and their tectonic significance using Landsat TM data and field studies in the central highlands of Eritrea. J. Afr. Earth Sci. 46, 371–378.

https://www.esa.int (23/09/2018)

https://www2.jpl.nasa.gov (23/09/2018)

Use of remote sensing for water management and protection

COSMO-SKYMED SPACE DATA SUPPORTING DISASTER RISK REDUCTION

F. Lenti, M.L. Battagliere*, M. Virelli, A. Coletta

ASI, Agenzia Spaziale Italiana, Via del Politecnico, 00133 Roma, Italy – (maria.battagliere, alessandro.coletta)@asi.it - (fabrizio.lenti, maria.virelli)@est.asi.it,

KEY WORDS: COSMO-SkyMed, SAR, X-Band, Disaster Risk Reduction, InSAR.

ABSTRACT:

Today, improving the understanding of disaster risks is an important key point to define emergency preparedness and planning measures. Generally, natural hazards such as earthquakes, floods, drought and cyclones cannot be prevented but the number of lives they take and the damage they cause can be greatly reduced thanks to space systems for Earth Observation. Since 2008, COSMO-SkyMed mission is playing a key role in emergency response activities being one of the most exploited SAR mission during disaster events. In this context, the constellation is able to monitor efficiently the different phases of crisis: early warning, recovery operations and post-crisis, representing an efficient approach for managing and limiting the effects of natural and man-made disasters.

1. INTRODUCTION

COSMO-SkyMed (COnstellation of small Satellites for Mediterranean basin Observation) represents the largest Italian investment in space systems for Earth Observation (EO). The COSMO-SkyMed (CSK) Constellation, composed of four satellites, is based on a dual-use (civilian and defence) system aimed at establishing a worldwide service providing data to a wide range of purposes, such as natural and man-made disasters, environmental monitoring, scientific and commercial applications.

This paper is proposed with the goal to provide an overview of the CSK data exploitation in supporting Disaster Risk Reduction (DRR). The DRR strategies includes disciplines like disaster risk management, disaster mitigation and disaster preparedness with the aim to reduce the impact of damages and to strengthen the resilience of communities (European Commission, 2017). In the first part of the paper, the CSK mission and its technical capabilities are summarised. In the second part, the CSK contributions in monitoring and supporting natural and man-made disasters are grouped into five kind of emergencies: floods, volcanoes, oil-spills, earthquakes and landslides.

2. COSMO-SKYMED: MISSION STATUS AND TECHNICAL CAPABILITIES

The COSMO-SkyMed programme has been developed by ASI, supported by the Ministry of Education, Universities and Research (MIUR), and the Italian Ministry of Defense (It-MoD). The mission is based on a constellation of four Low Earth Orbit (LEO) mid-sized satellites, located on the same orbital plane and each equipped with a multi-mode high-resolution SAR operating in the X-Band. The constellation became operational with all the four satellites in May 2011, with the first satellite launched in June 2007 and the fourth one in November 2010. The CSK mission is able to operate in different mission configurations, each characterized by a specific orbital geometry which directly characterizes system capabilities and performances.

Three different System operative modes have been defined (routine, crisis and very urgent) allowing to respond to different needs in term of required programming latency. In the first mode (routine) the requests of the users pertaining image acquisitions are planned and sent to the constellation once a day. In the second mode (crisis) this operation is done twice a day. The third mode (very urgent) is asynchronous, allowing the servicing of an image acquisition request with the minimum possible latency.

The system is capable to satisfy a user request is within 72 hours for the system working in routine mode, 36 hours for the crisis mode and 18 hours for very urgent mode. In order to obtain a greater planning flexibility and an improvement of the system performances, the transfer from once a day planned acquisitions to twice a day in routine chronology has been introduced. It pander to the needs expressed by civilian users, that are considerably benefiting from the double daily planning.

The system is able to acquire images all over the world in every atmospheric condition, during day and night, without latitude limitations. In order to guarantee a wide versatility, the SAR payload has been designed to acquire data in different modes according to the image area and the resolution that can be obtained (Virelli et al., 2014). The following table describes the main features of different sensor modes available.

Sensor Mode	Swat Extension (km x km)	Geometric Resolution (m x m)
ENHANCED SPOTLIGHT	10x10	1x1
STRIPMAP HIMAGE	40x40	5x5
STRIPMAP PING PONG	30x30	20x20
SCANSAR WIDE	100x100	30x30
SCANSARHUGE	200x200	100x100

Table 1. CSK Sensor modes

In the next years, the operational life of the COSMO-SkyMed system will be guaranteed by a second generation of satellites: the COSMO-SkyMed Second Generation (CSG) programme, currently scheduled to be launched in the first quarter of 2019.

3. CSK CONTRIBUTION IN FLOOD EMERGENCIES

Floods are among the most catastrophic natural disasters globally in terms of impact on human life and the economic damages. Developed nations are not immune in fact, according to the

* Corresponding author

European Space Agency (ESA), about 85% of all European civil protection measures are concerned with floods. Furthermore, in the next years, the damages done by flooding are expected to increase because of climate change impacts and by human activities such as land use changes, deforestations and water leakage from utilities. Flooding can occur due to various phenomena: heavy rainfall in short period of time, a sudden release of dams, groundwater level rise, storm or tsunami wave, sea or lake level rise (Teodorescu et al., 2014).
In this context, COSMO-SkyMed mission is particularly suitable for flood mapping, thanks to the synoptic view, the capability to operate in almost all-weather conditions, during both day-time and night-time, and the sensitivity of the X-Band to water. Although the temporal repetitiveness of SAR imagery is a critical issue for other SAR missions, COSMO-SkyMed constellation allows collecting a large amount of daily radar data (Pulvirenti et al., 2014). A data set is used to produce several inundation maps (revisit time in the order of some hours) characterized by high spatial resolution and based on change detection analysis in order to improve operational flood management systems.

Year	Flood
2009	Istanbul - Turkey
2010	Indo River - Pakistan
2014	Veneto - Italy
2016	Georgia - USA
2017	Emilia Romagna - Italy
2017	Houston - USA

Table 2. Some examples of COSMO-SkyMed contribution in flood emergency events.

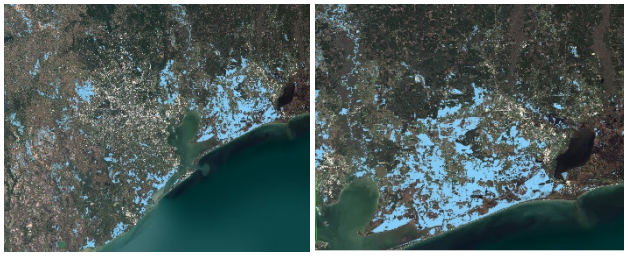

Figure 1. In the framework of COPERNICUS Programme, Flooding in Houston (USA) caused by Hurricane Harvey: the CSK images of August 30, 2018 shows the flood mapping and a detail of the city area most affected. [COSMO-SkyMed© ASI, processed by e-GEOS S.p.A]

4. CSK CONTRIBUTION IN VOLCANOES MONITORING

Remote sensing plays a critical role in operational volcanoes monitoring. In fact, InSAR (Interferometric Synthetic Aperture Radar) represents one of the most powerful tools because it is a technique that maps millimeter-scale deformations of the Earth's surface. Combined with the use of CSK high-resolution SAR images, InSAR technique shows spatial patterns of deformation in remarkable detail. The deformation analyzed can then be estimated to build up displacement models, creating an early change warning system when it senses a change in surface height or ground stability (Massonnet and Feigl, 1998).
This information, in combination with ground-based monitoring, gives unprecedented insight into an eruption processes satisfying two basic needs: examining the volcano topography and mapping surface changes such as lava flows or deformations. In particular, ground deformations detected by CSK satellites can be a good indicator of eruptions in order to recognize volcanoes "bulging with magma". This information provides a safe environment as well as decreasing the amount of on-site data needed.
In this context, CSK features improve the knowledge of volcanoes dynamic processes, allowing scientists to identify precursor elements to potentially disastrous eruptions and giving support in the emergency plan definition (Sacco et al., 2015). In the framework of CSK Background Mission (CSK data archive), 163 volcanoes are regularly acquired with a frequency of observation of 16 days. In addition, supporting CEOS initiatives, such as Geohazard Supersites Natural Laboratories (GSNL) projects and Disaster Risk Management (DRM) Volcano Pilot Project, ASI has planned to provide about 10.000 CSK products until 2018 (Battagliere et al., 2017). Therefore, also in the framework of this international cooperation, the potentially most dangerous volcanic areas will be continuously monitored.

Volcano	Country
Etna	Italy
Sinabung	Indonesia
Kilauea	Hawaii (USA)
El Hierro	Canary Island
San Miguel	El Salvador
Eyjafjöll	Iceland

Table 3. Some examples of COSMO-SkyMed contribution in volcanoes monitoring.

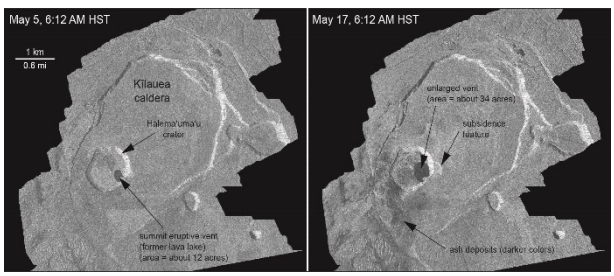

Figure 2. In the framework of ASI-CEOS initiatives, Kilauea Volcano eruption (Hawaii–USA): monitoring of lava, subsidence and ash deposits. The first CSK Image of May 5, 2018 compared to the second CSK image of May 17, 2018. [COSMO-SkyMed© ASI, processed by e-GEOS S.p.A].

5. CSK CONTRIBUTION IN OIL-SPILLS EMERGENCIES

Large spills of oil related petroleum products in the marine environment cause serious biological and economic impacts. In this framework, remote sensing is playing an increasingly important role to monitor the oil patch. Microwave beam it is an actually effective tool, which can penetrate clouds, rain and less restricted by the weather respect to optical satellites.
SAR scenes are composed of pixels and each pixel represents the amount of backscatter from that area on the ground (Chan and Koo, 2008). In this case, marine oil spills are visible as dark patches because of low backscatter power in SAR images then, thanks to coherent mechanisms, it is possible to discriminate oil from seawater.
The CSK constellation can be used to fulfil the strategic roles within a surveillance programme during an oil spill response, including the initial detection support, conducting ongoing assessment based on synoptic monitoring and providing pre-spill and baseline data. For a useful oil spill response, the data delivery, within a required time frame, is often the most critical

requirement, as the value of satellite data is greatly diminished by delays incurred between its receipt and the production of actionable intelligence. The low revisit time and the radiometric characteristics of COSMO-SkyMed point to good suitability of the instrument for management of oil spill detection (Cheng et al., 2014).

Year	Oil-Spill
2010	Italy- Lambro River
2010	USA- Gulf of Mexico
2011	UK- North Sea
2015	Italy- Adriatic Sea
2015	Japan- Sea of Japan
2018	PRC- East China Sea

Table 4. Some examples of COSMO-SkyMed contribution in oil-spill emergency events.

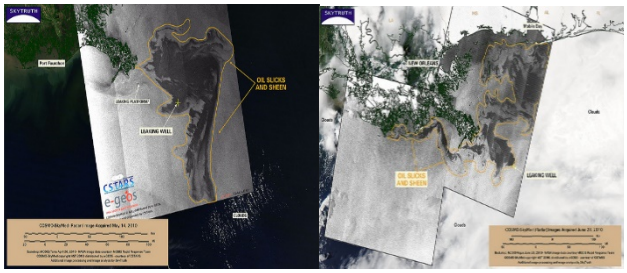

Figure 3. In the framework of ASI-University of Miami cooperation, the Deepwater Horizon oil-spill patch evolution (Gulf of Mexico-USA). The first CSK Image of May 14, 2010 compared to the second CSK image of June 28, 2010 [COSMO-SkyMed© ASI, processed CSTARS/e-GEOS].

6. CSK CONTRIBUTION IN EARTHQUAKES EMERGENCIES

Unlike hazards such as tropical storms, it is not yet possible an earthquake short-term prediction, however their impacts can be mitigated through improved understanding of the distribution of earthquake hazard and concerted actions by planners to facilitate the response to emergencies.

In this framework, new techniques and satellite systems would provide an operational global seismic risk contribution, especially improving response and recovery management. Indeed, in the aftermath of a major earthquake, critical infrastructures like roads, rail, and airports are often degraded or destroyed, including systems used by emergency managers to rapidly assess damages. SAR instruments, operating in X-Band like CSK Constellation, have demonstrated in several occasions their utility to support seismic emergency management operations.

In particular, with reference to SAR interferometry application such as the Differential Interferometry Synthetic Aperture Radar (DInSAR) and Permanent Scatterers (PS), a millimeter level of accuracy can be achieved. Specifically, DInSAR is based on the exploitation of the phase difference between pairs of SAR images to produce displacement maps with sub-wavelength accuracy characterized by a high density of measurement points. Combined with the use of CSK high-resolution SAR images, this technique is extensively proved as valuable tool to detect ground deformations. Permanent Scatterers (PS) is also a powerful remote sensing technology that help conduct a long time series of synthetic aperture radar data for any deformations. Its accuracy is on a millimetric level with high spatial density grid of pointwise targets (Bamler and Hartl, 1998). Combined with a high-resolution CSK SAR images, the PS-InSAR technique creates countless permanent scatterers on individual buildings that can be analyzed for any complex movement within the concrete.

These kind of data are mainly used for change detection and mapping analysis as complementing ground information. Displacements can indicate activity in underground faults and such information can support the analyses of vulnerability and site-specific hazards as well as to improve understanding of the tectonic processes (Milillo et al., 2016).

Year	Country
2009	L'Aquila - Italy
2010	Port-au-Prince - Haiti
2011	Christchurch - New Zeland
2014	Iquique - Chile
2015	Gorkha - Nepal
2016	Amatrice/Norcia - Italy
2017	Ischia - Italy

Table 5. Some examples of COSMO-SkyMed contribution in earthquake emergency events.

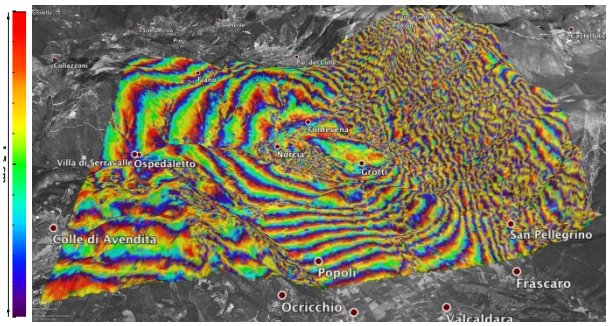

Figure 4. In the framework of ASI and Italian Civil Protection (DPC) agreement, earthquake mapping (Norcia-Italy). InSAR processing based on CSK images collected in October 2016, pre and post earthquake events [COSMO-SkyMed© ASI, processed by IREA-CNR/DPC].

7. CSK CONTRIBUTION IN LANDSLIDES EMERGENCIES.

Landslides represent one of the natural hazards that occur most frequently worldwide. The occurrence of landslides depends on complex interactions among a large number of interrelated factors, such as geologic setting, seismicity, and the impacts of anthropogenic changes to the landscape.

Every year, large landslides causes damage and casualties, affecting urban areas, roads, rails and causing emergencies. In such scenarios, rapid mapping of the location and extent of the surface deformation caused by landslides can provide significant indications of the civil protection response to recovery operations. Where the ground displacements are too massive, accessing to the landslide area may be difficult, impossible or too dangerous to acquire in situ information. In these circumstances, remote sensing techniques provide an effective alternative to perform assessments of the ground deformations (Madry, 2015).

CSK mission are well suited to supporting both operational and scientific users on landslide identification, mapping and monitoring. In fact, using CSK data at weekly repeat cycles have shown the unmatched precision and level of details achievable, a crucial requirement for monitoring and early-warning practices. The constellation provides continuity and consistency of acquisition of radar data, to guarantee availability of image stacks

and archives in the coming years, allowing the comparison of recent and past scenarios of landslide evolution and consequences (Koishi et al., 2018). In addition, the availability of CSK dual-mode datasets (i.e. ascending and descending) for hilly and mountainous areas, allows to better constraints landslide motions increasing the number of slopes monitored within the observed areas.

Year	Country
2010	Vibo Valentia - Italy
2013	Monte Scaglioso- Italy
2014	Liguria - Italy
2014	Washington State - USA
2015	Puglia - Italy
2017	Stigliano - Italy

Table 6. Some examples of COSMO-SkyMed contribution in landslide emergency events.

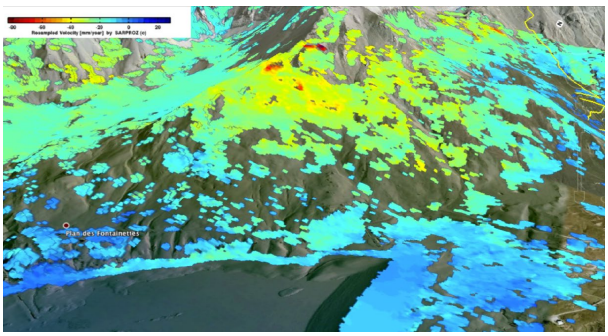

Figure 5. In the framework of ASI-Sapienza agreement, landslide mapping (Moncenisio Dam-Italy): based on InSAR processing using CSK images of 2011 and 2012. [COSMO-SkyMed© ASI, processed by NAZCHA/Sapienza-Università di Roma]

8. CONCLUSIONS

The COSMO-SkyMed constellation represents a powerful instrument in supporting DRR. Since the launch of the first satellite in 2007, CSK mission has provided a concrete contributions to manage and to prevention of natural or man-made disasters. In this context, CSK represents one of the most exploited SAR system during disaster events thanks to a unique characteristic that allows a superior performance for emergency applications: the revisit time.

In fact, CSK constellation enables its users to collect multiple images daily over any area worldwide. This is a key feature for emergency response, as by definition, in most cases it is not possible to predict where a relevant event will strike. In case of earthquakes, volcano eruptions, floods, landslides and oil spills the most tight requirement from emergency responders is timeliness of information delivery to build up rapid mapping providing damage assessment of affected area. In this context, InSAR techniques, integrated with other sources as in situ information, allow useful products such as landslide inventories, hazard zoning, floods susceptibility maps, forecasting and monitoring of slow moving landslides, subsidence mapping and volcanos monitoring.

Furthermore, damages prevention and assessment can be carried out using CSK data archive (Background Mission). In this context, the importance of a low priority acquisition plan is to generate an historical image archive data set that could be used to manage future emergencies. To conclude, thanks of its observation capabilities of high revisit time, high spatial resolution and accuracy, acquiring data in every atmospheric condition and during night and day, CSK constellation is currently involved in several cooperation and agreements, with national and international institutions, to improve DRR.

ACKNOWLEDGEMENTS

The authors wish to thanks the e-Geos Technical Support Team, Customer Service and operators that constantly provide their contribution to the ASI's activities.

REFERENCES

Bamler, R., Hartl, P., 1998. Synthetic aperture radar interferometry. In *Inverse Problems*, Vol.14 (4), R1-R54.

Battagliere, M.L., Virelli, M., Lenti, F., Coletta, A., 2017. COSMO-SkyMed Data Exploitation: Global Trend, Perspectives and Lessons Learnt. In *68th International Astronautical Congress*, Adelaide, Australia.

European Commission, 2017. Disaster Risk Reduction in *European Civil Protection and Humanitarian Aid Operations*-ECHO Factsheet, pp.1-2.

Chan, Y. K., Koo, V. C., 2008. An Introduction to Synthetic Aperture Radar (SAR). In *Progress In Electromagnetics Research B*, Vol. 2, pp. 27–60.

Cheng, Y., Liu, B., Li, X., Nunziata, F., Xue, Q., Ding, X., Migliaccio, M., Pichel, W. G., 2014. Monitoring of oil spill trajectories with COSMO–SkyMed X–band SAR images and model simulation. In *IEEE Applied Earth Observations and Remote Sensing* Vol 7, N°3.

Koishi, T., Suga, Y., 2018. Landslide detection using COSMO-SkyMed images:a case study of a landslide event on Kii Peninsula, Japan. In *European Journal of Remote Sensing* VOL. 51, NO. 1, pp.205–221.

Madry, S., 2015. Space Systems for Disaster Warning, Response, and Recovery. Springer Publishing, New York, USA, pp. 67-91.

Massonnet, D., Feigl, K. L., 1998. Radar interferometry and its application to changes in the earth's surface. In *Reviews Geophysics*, Vol 36 (4), pp. 441–500.

Milillo, P., Riel, B., Minchew, B., Yun,S., Simons, M., Lundgren, P., 2016. On the Synergistic Use of SAR Constellations' Data Exploitation for Earth Science and Natural Hazard Response. In *IEEE Applied Earth Observations and Remote Sensing*, VOL. 9, N°3.

Pulvirenti, L., Pierdicca, N., Boni, G., Rudari, R., 2014. Flood Damage Assessment through Multitemporal COSMO-SkyMed Data and Hydrodynamic Models: The Albania 2010 Case Study. In *IEEE Applied Earth Observations and Remote Sensing*, Vol.7, n°7.

Sacco, P., Daraio, M., G., Battagliere, M. L., Coletta, A., 2015. Mitigation of Volcanic risk: the COSMO-SkyMed contribution. In *FRINGE 2015*, pp168-174.

Teodorescu, H.N., Kirschenbaum, A., Cojocaru, S., Bruderlein, C., 2014. Improving Disaster Resilience and Mitigation - IT Means and Tools. Springer Publishing, New York, USA, pp. 24-25.

Virelli, M., Battagliere, M.L., Coletta, A., 2014. ASI COSMO-SkyMed: Mission overview and data exploitation. In *IEEE Geoscience Remote Sensing Magazine*, VOL 2, pp. 64–66.

THE USE OF REMOTE SENSING FOR WATER PROTECTION IN THE KARST ENVIRONMENT OF THE TABULAR MIDDLE ATLAS / THE CAUSSE OF EL HAJEB/ MOROCCO

A. Muzirafuti[1]*, M. Boualoul[1], G. Randazzo [2], S. Lanza[2], A. Allaoui[1], H. El Ouardi[3], H. Habibi[3], H. Ouhaddach[3]

[1] Team of applied geophysics, Nat Ress. and Heritage, Dept. of Geology, Fac. of Sciences, University of Moualy Ismail, BP. 11201 Zitoune, Meknes, Morocco – (muzansel, abdelhamid.gaig11)@gmail.com, boualoul@yahoo.fr

[2] Section of Earth Sciences, Dept. of Math and Computer Science, Physical Sciences and Earth Sciences, Univ. of Messina.Via F. Stagno d'Alcontres, 31 98166 - Sant'Agata di Messina, Messina, Italy – (grandazzo, lanzas)@unime.it

[3] Team of tec mapping, Dept. of Geology, Fac. of Sciences, University of Moualy Ismail, BP. 11201 Zitoune, Meknes, Morocco - h.elouardi@fsumi.ac.ma, (habibim58, hafida.ouhaddach)@gmail.com

KEY WORDS: Causse of El Hajeb, Water protection, Turbidity, Remote sensing, Karst environment

ABSTRACT:

Deep water bodies constitute the strategic water reserves of Morocco. These natural resources are used in many activities such as irrigation in agriculture, and, more importantly, they are the source of fresh drinking water for the local population. However, these resources are vulnerable to anthropogenic and natural phenomena due to ongoing climate change and the increase in population growth. To contribute to the recent initiative for the protection of the karstic environment of water springs in the Tabular Middle Atlas of El Hajeb, the present research work aims to characterize different karst landforms in Liassic carbonate rocks of the Tabular Middle Atlas in the Causse of El Hajeb, where pollution identified in water samples in this region originates. Satellite imagery (Sentinel-2, Landsat, Terra-ASTER, ASTER-GDEM) and GIS tools were used. Based on surface reflectance of dolomite and limestone, especially in shortwave infrared, we delineated the extent of carbonate rocks and areas with intense human activities. Fractures affecting these Liassic rocks were extracted mechanically and manually after the application of Sobel operator filter in N, S, NE and SW main directions. The results show an improvement and a better understanding of the hydrogeological system of this karst environment, in particular the location of new faults identified in NE-SW and NW-SE fault systems which involve infiltration of surface water and groundwater drainage respectively. The percolation of slightly acidic water through these fractures has gradually created cavities and sinkholes which are believed to be the origin of turbidity observed during the analysis of the water springs.

1. INTRODUCTION

Remote sensing has been used in many environmental studies (Julien, 2018) because of its capacity to provide information rapidly on large and hard-to-reach areas. Recently, many programmes such as ASTER, Landsat and Copernicus Sentinels have provided satellite imagery of both high temporal and spatial resolutions free of charge. These data, combined with ground measurements, can lead to solutions for modern challenges such as climate change, natural hazards and increasing population growth. We used this technology in a region which is both sensitive and vulnerable to these phenomena, the karst environment of the Tabular Middle Atlas (TMA) of Morocco, in order to identify its different surface karst landforms.

The TMA of Morocco contains an important water reservoir, located in Liassic carbonate rocks (dolomite and limestone), used for everyday activities by 4236892 population living in Fez-Meknes region, according to 2014 national census of population in Morocco. Because of its importance and the value it holds in the economy of the region, it has been described as château d'eau (SRAT de la Région Fès Boulemane, 2013). Recent studies conducted in this region (Howell, 2016) show that water quality is deteriorating due to anthropologic activities and natural processes. The present study proposes the use of earth observation and free available data to map various forms of karst (avens, dolines, poljes...) and fault systems; these are the most fragile hotspots where water from the ground surface charged with with pollutants can easily infiltrate and reach under groundwater bodies. We intend to answer the question related to the part played by each fault system, in order to find out which one is responsible for the infiltration of surface water and consequently is contributing to the development of sinkholes, shown in figure 3. At the time we want to identify which fault system drains water from the Causse to the basin.

The aim of this study is to enhance the understanding of the hydrogeological system of the TMA by adopting a methodology combining space technology and ground-based field work, in order to identify : (1) the direction of the fault systems involved in water infiltration and in development of different karst landforms, (2) the predominant location of karst landforms responsible for the turbidity and chemicals observed in water springs, and (3) human activities contributing to the degradation of water reservoirs.

2. METHODS AND MATERIALS

2.1 Area of study

The TMA of Morocco is located in the northwest of Morocco, bordered to the north by the Saiss basin, to the southwest by the Hercynian Massif Central and to the west by the pleated Middle Atlas shown in figure 1. It holds an important water reservoir, located in Liassic carbonate rocks (dolomite and limestone). It is characterized by a Mediterranean climate with annual

* Corresponding author

precipitation (rain and snow), varying between 700 mm and 900 mm for the period from 1973 to 2008 at Ifrane. The region is occupied by a large number of water springs, such as Ain Aguemguem, Ain Bittit, Ain Boujaoui, Ain Ribaa, Ain Marrouf, Ain Amjrar, Ain Kadhem, ain Zerouka, and lakes called dayets; these are the easily observable karst landforms created by progressive erosion of limestone by water infiltration along faults.

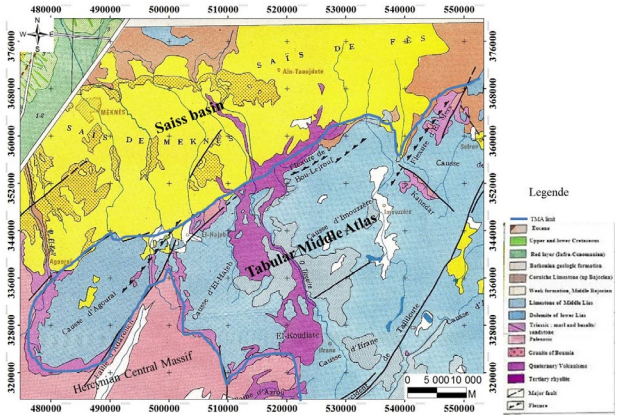

Figure 1: Modified geological stretch map of the TMA

Spectral signatures, shown in figure 2, extracted from Copernicus Sentinel-2 images, show dolomite and limestone with high reflectance in shortwave infrared, vegetation in near infrared and water in blue. Visual interpretation of RGB Sentinel-2 Shortwave Infrared (Band 12,8,4) false color composite image acquired on 10 December 2016 revealed the locations of different geological formations especially carbonate rocks. While principle component analysis was applied to maximize information from a small number of bands (components). In ArcGIS software the high percentage of information observed in response was compared with regional geologic information in order to digitalize linear and curvilinear structures corresponding to lineaments related to both major faults and newly identified fractures . Using Arc Hydro Tool, surface water pathways were extracted on ASTER-DEM; these drainage lines correct precipitations (rain water and snow) from the Causse to the basin and in some cases infiltrate into the ground through fractures.

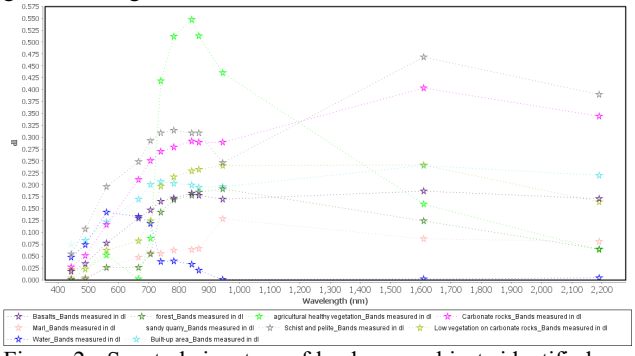

Figure 2 : Spectral signature of land cover objects identified on Sentinel-2 image acquired on 10 December 2016 in TMA

Karst landforms were extracted by subtracting sink-filled and unfilled ASTER-DEM images; we noticed that they are located both on main faults and localized fractures. Agriculture is the most dominant activity in the TMA, mainly in areas occupied by Plio-quaternary geological formations, in some cases in fractured and weathered carbonate rocks.

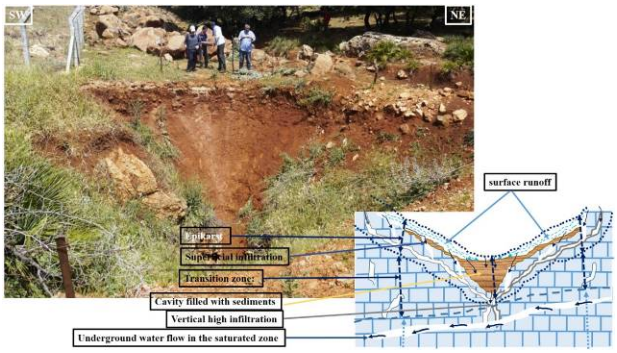

Figure 3: photo of sinkhole taken in the Causse of El Hajeb-Morocco, photograph © 04/05/017.

2.2 Data and software used

In this study we used multi-source satellite images shown in table 1, with Landsat, Terra-ASTER and ASTER-GDEM images downloaded from https://earthexplorer.usgs.gov while sentinel-2A images were downloaded from https://scihub.copernicus.eu).

Table 1 : Satellite images used

Landsat image			
Acquisition date	Acquisition time	Sensor	Path / Row
22 May 2016	10 h 57 min 10 sec	L8 (OLI) Level-2	201/37
Copernicus Sentinel-2A image			
Aquisition date	Acquisition time	Processing level	File Format
10 December 2016	11h 04min 42sec	Level-1C	JPEG2000, HTML, XML
Terra-ASTER images			
Aquisition date	Acquisition time	Processing level	Path / Row
06 August 2000	11h 29min 17sec	Level-1T	201/37
16 October 2005	11h 07min 47se		201/37
ASTER-GDEM			
Aquisition date	Entity ID	Spatial Resolution	Map projection
17 October 2011	ASTERGDEMV2_ 0N33W006	1 ARC-SECOND	Geographic

These are free satellite images with high and middle spatial resolution (from 10 to 60 m). Geological maps with a 1:10,000 scale and a 1:50,000 scale, and topographic maps with a 1:50,000 scale were used to calibrate and enhance the classification of satellite images. Free open source software QGIS was used for atmospheric correction, band combination of Landsat 8 and Terra-ASTER while SNAP Desktop was used for atmospheric correction, band combination and image principale component analysis for Sentiel-2A. This Sentinel-2A was further processed and its final results were introduced into ArcGIS 10.3 for layout.

We conducted field work to take structural measurements on basalts and fractured carbonate rocks in order to validate the classification and the location of different karst landforms and fault systems extracted by remote sensing data.

2.3 Data processing and analysis

We adopted a multidisciplinary approach combining multiple sources of data so that we could have sufficient information in our database. We started by geo-referencing topographic and geological maps which gave us a general idea of the area of study. These maps were later compared to satellite images for pixel-based classification.

2.3.1 Satellite imagery pre-processing:

2.3.1.1. Pre-processing and geo-coding:

Our area of study covers a very large surface area which implies utilization of the moisics of two scences for Sentinel-2 and one scence for Landsat 8. For Terra-ASTER we used two scenes covering Agourai and El hajeb Causses and Saiss basin. During geo-coding processing the verification of spatial resolution and geometric quality were perfomed in order to ensure the quality of our database. In the case of geometrical differences between images and maps, control ground points data acquired by Garmin GPS were used to enhance the precision.

2.3.1.2 Pre-processing and geometric adaptation of archive data:

Satellite images, geological and topographic maps were used as reference for calibration and interpretation of archive data such as google images, photographs and open street maps.

2.3.1.3 Pre-processing and atmospheric correction:

Due to the atmospheric conditions and scattered radiance saved by satellite, Dark object substraction atmospheric correction was perfomed in QGIS for Landsat 8 OLI and Terra-ASTER images while Sentinel-2 images were atmospherically corrected using Sen2Cor plugin installed in SNAP desktop.

2.3.2. Processing and land cover features extraction:

After the creation of a reliable dataset, optical and RADAR satellite images have been processed in order extract geologic and land cover information.

2.3.2.1. Processing of optical images:

We limited the processing of Landsat 8 OLI and Terra-ASTER images on band combination, shown in table 2, technique for identification of geological formation, Rockwell, 2015, and qualitative landscape interpretation. With spatial resolution of 10 m, 20m and 60 m and spectral resolution of 13 bands, Sentinel-2A images were chosen for geologic and land cover mapping.

Table 2 : RGB band combination used

Satellite	Color affected to the band			RGB image visual interpretation
	Red	Green	Blue	
S-2A	SWIR Band 12	NIR Band 8	Red Band 4	Carbonate rocks appear in pink, Vegetation appears in green, basalts appear in pulpe and water appears in dark blue
L8 (OLI)	SWIR 2 Band 7	NIR Band 5	Red Band 4	Carbonate rocks in appear pink, Vegetation appears in green, basalts appear in dark blue and water appears in blue
Terra - ASTER	VNIR Band 3N	VNIR Band 2	VNIR Band 1	Carbonate rocks in appear pink, Vegetation appears in red, basalts appear in dark green and water appears in blue

Object and pixel-based minimum distance supervised classification technique was applied to identify and locate dolomite, limestone, clay and quaternary basalts, agricultural areas, forests, built-up areas, sand quarries, and Paleozoic geological formations with overall accuracy of 96 % and kappa coefficient of 0.86. Normalized difference vegetation index , NDVI=(ρNIR-ρRED/ρNIR+ρRED) was computed to provide information on areas occupied by forest, grass, cultivated and uncultivated fields.

In SNAP desktop software, principal component analysis technique, (Loughlin, 1991), was applied on SWIR, NIR and Red bands of Sentinel-2 in order to maximize information in one band. Maximum information was observed in response band resulting from this process. Spatial profile extracted on this response band along the line interpolated on carbonate rocks showed the fluctuation of pixel values with low values on areas of eroded carbonate rocks due to the presence of gradual erosional clays (Terra-rossa) and values were observed on unaltered dolomite. Based on geologic and topographic maps, photointerpretation of changes in these values helped us to identify the continuity of curvilinear or linear structures, such as cracks, faults, fissures and fractures in dolomite and limestone. We also applied direction filter Sobel operator (with 5×5 kernel) on this response band in order to enhance the appeance of curvilinear and linear structures in Nord, South, West,and East directions. Manual digitization and classification of these structures were conducted in ArcGIS to map various fractures of fault systems identified in geological formations.

2.3.2.2. Processing of RADAR (ASTER-GDEM) images:

Advanced Spaceborne thermal Emission and Reflection Radiometer Global Digital Elevation Models (ASTER-GDEM) version 2 with 30 m spatial resolution, acquired on 17 October 2011 was processed in ArcGIS software. We started by extraction elevation information which was later compared to topographic maps to identify depressions, cliffs, valleys, volcanoes, and quarries and slope variation. Like other automatic operators, a photo-interpretation technique was used to identify and locate probable carbonate depressions.

3. RESULTS AND DISCUSSION

Lineaments extracted via satellite images revealed two main fault systems in NW-SE and NS-SW directions shown in table 3. These fractures mainly affect carbonate rocks and play an important role in the hydrogeology system of the region, where they contribute to the infiltration of surface water through the aquifer and also facilitate its movement insider the aquifer.

Table 3 : Direction of main fault systems in TMA

Direction	N-S	E-W	NE-SW	NW-SE
Percentage	20 %	14 %	32 %	27 %

Over one thousand karst landforms, including collapsing and subsidence sinkholes, karst depressions, lakes, pond landscapes, water springs and surface water stream flows, were identified in TMA as shown in figure 4. Their locations on main fault system affecting dolomite and limestone showed that their development is driven by tectonic processes affecting this area.

In order to validate the results obtained from satellite image processing, we conducted field works to take ground-based measurements of fractures and take GPS coordinates of some sinkholes. We took measurements on carbonate rocks and also measurements alongside water springs located in the Tabular Middle Atlas and in its area of contact with the Saiss basin. We found that a large number of sinkholes are located on the NE-

SW fault system, as shown in figure 4, forming a semi-circular axis, while water springs are located on the NW-SE fault system mainly in the area of contact of the TMA and Saiss basin where they are used in irrigation and for drinking water by people living in the Meknes-Fez region. Land cover information obtained from NDVI, shownin table 4, and supervised classification on sentinel-2 shows that in TMA 55 % is occupied by carbonate rocks, 25 % occupied by forest and agricultural areas, while 8 % occupied by basalts and clays.

Table 4 : NDVI and land cover classification

NDVI value	Land cover classification
0.25 <	Carbonate rocks, schists, pelite, basalts and water
0.25 to 0.45	Vegetation spreads on carbonate and schists
0.45 to 0.7	Agriculture vegetation
> 0.7	Dense forest and good healthy vegetation

Agriculture activities conducted on altered and fractured rocks especialy basalts and carbonate rocks are believed to be the origin of chemicals products observed in water springs located in the contact of TMA and Saiss basin. In addition the use of fertilizers, pesticides and herbicides for agricultural crops growth modified surface water composition and contribute to dissolution of carbonate rocks.

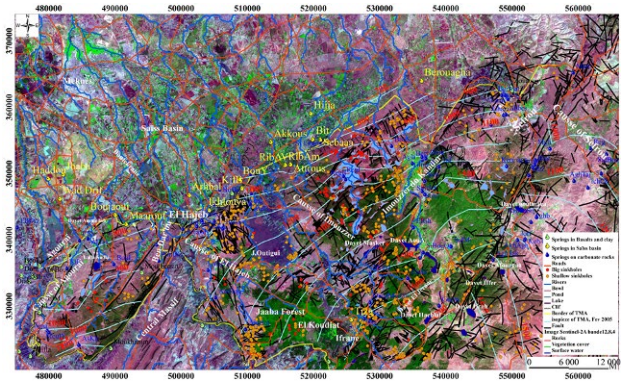

Figure 4: Various karst landforms in Tabular Middle Atlas.

4. CONCLUSION

This study shows the importance of remote sensing and GIS tools. The combination of satellite images and ground-based measurements provides useful information for studies conducted both in large and hard-to-reach areas. We analyzed changes in vegetation using NDVI, changes in surface water, changes in soil minerals and built-up areas using band combinations, and lineament fractures were extracted based on the variation of pixels values on the response of principal component analysis. Karst depressions were extracted manually digitized on ASTER GDEM images.

-Analysis of fractures extracted on satellite images revealed that the NE-SW fault system plays an important role in recharging TMA groundwater aquifers by facilitating the infiltration of surface water from precipitation and melting snow. Many sinkholes and karst depressions are also located along this fault system.

-NDVI and supervised classification results were validated by ground-based measurements taken during our field works and confermed the location of some collapsing and subsidence sinkholes located near agricultural areas, we also identify geological processes such as dissolution, erosion, and mylonitization affecting fractured carbonate rocks. The dissolution of dolomite and limestone has created cavities and channels inside these rocks; these channels are the pathway for the movement of groundwater from the TMA to the Saiss basin through NW-SE fault system and can carry with this water erosion products. These products originated either from inside the rocks or from water which has infiltrated from ground surface through sinkholes located on NE-SW faults system.

-The TMA is slightly pleated, creating lowlands and large depressions which people are using for farming activities. The products used to enhance the farming yield, such as fertilizers, pesticides and herbicides, can be mixed with water and change its chemistry, and when they percolate through fissures they have an effect on carbonate rocks because they dissolve them at a fast rate and gradually create underground cavities and sinkholes. In addition, during the period of high precipitation the quantity of water infiltrated becomes high and brings with it more material, leading to the change of water colour mostly observed in water springs. This turbidity affected the health of people using this water.

Human activities are having an impact on the structuration of this karst environment where the quantity of groundwater extracted for irrigation is estimated to be 25 Mm3 per year. On the other hand, ongoing climate change and over-exploitation of water have an impact on aquifer recharge zones by reducing the quantity of precipitation for infiltration and enhancing the evapotranspiration process on the surface, this has contributed to a water loss of 10 Mm3 per year, SRAT de la Région Fès Boulemane, 2013. A protection perimeter around sinkholes identified in agricultural areas is needed in order to reduce human impact on water quality at the same time taking advantage of economic activities conducted in this area.

REFERENCES

Howell, Brett A., 2016. Spring Responses to Storms and Seasonal Variations in Recharge in the Middle Atlas Region of Morocco. Theses and Dissertations—Earth and Environmental Sciences. P41, http:// Uknowledge.uky.edu/ees_etds/41

Julien Andrieu, 2018. Land cover changes on the West-African coastline from the saloum Delta (Senegal) to Rio Geba (Guinea-Bissau) between 1979 and 2015. European Journal of Remote sensing, 51:1, 314-325

Loughlin W.P., 1991. Principal component analysis for alteration mapping. Photogrametric Engineering & Remote Sensing, Vol.57, N°9, Sept 1991, pp.1163-1169.

Rockwell, B.W., Knepper, D.H., Jr., and Hothon, J.D., 2015. Landsat maps (Phase V, deliverable 60), ASTER maps (Phase V, deliverable 62), ASTER_DEM maps (Phase V, deliverable 63), and spectral remote sensing in support of PRISM-II mineral resource assessment project, Islamic republic of Mauritania (Phase V, deliverable 61 and 64).

Schéma Régional d'Aménagement du Territoire (SRAT) de la Région Fès Boulemane ,2013. Phase 1 : Diagnostic Territorial Stratégique-Etape 1 : Rapports Sectoriels, p29.

ANALYSIS OF FLOODS, URBANIZATION AND MORPHOMETRY OF WATERSHEDS IN SANTO ANDRÉ-BRAZIL

J. Gueiros Fusato[1]*, M.C. Valverde[2]

[1] Geologist, MSc in Environmental Science and Technology – fusatojuliana@gmail.com
[2] Dept. of Engineering, Modelling and Applied Social Sciences (CECS), Federal University of ABC, 5001 Av. Dos Estados, Santo André, 09210-580 BR – maria.brambila@ufabc.edu.br

KEY WORDS: Floods, Santo André, Morphometry

ABSTRACT:

The city of Santo André, located in the Metropolitan Region of the State of São Paulo – Brazil, constantly suffers from floods. This research has the aim to study the floods that occur in Santo André focusing on the morphometric analysis of the urban drainage subbasins of the Tamanduateí river that drain the city: Tamanduateí Médio I and Guarará, which are the most affected according to the inventory of flood occurrences from 2001 to 2016. 12 morphometric parameters were analysed regarding the geometry, drainage system, and relief using georeferenced files in the Geographic Information System: drainage system in scale 1:10.000, the slope maps and contour lines in scale 1:25.000. The results found indicate that the flood problems in the urban area of Santo André are not related strictly to the morphometry of the basins, since the two of them that were analysed have different features, mainly related to the shape, relief and lithology. According to the results the Guarará subbasin is more susceptible to floods regarding its relief, which is not true for Tamanduateí Médio I, whose geometry would make it more prone to floods. It is possible to infer that the anthropization plays the fundamental role in the occurrence of floods in Santo André, since different watersheds are equally affected. This could be due to inadequate drainage projects and structural measures that are not capable to deal with the surface runoff that comes from the rainfall in the summer months, magnifying the occurrence of floods.

INTRODUCTION

Floods are mainly caused by intense rainfall and are related to the morphometric features of a watershed and can be magnified by inadequate urban infrastructure. It is normal for a river to invade its marginal areas when there is an intense pluviosity and therefore a flood is only considered a natural disaster if it affects the population living nearby. Because of this, it is important to calculate specific parameters related to the morphometry of the watersheds to comprehend the factors that lead to the occurrence of this type of disaster or if the urbanization played the fundamental role. This helps understand how the land use influences the occurrence of floods and therefore what could be done to improve the urban infrastructure to prevent this type of event.

Hydrographic basins are special units of varied dimension where superficial water resources are organized in function of the relations between the geological-geomorphological structures and the climatic conditions (MAGALHÃES JR., 2007). It is the fundamental element of analysis within the hydrologic cycle (COLLISCHON; TASSI, 2008). The knowledge of the physical features of a hydrographic basin is extremely important to comprehend its hydrological behaviour and the availability of water resources (FREITAS, 2006).

Urbanization affects the processes of runoff produced by floods, reducing hydrological response of the watershed due to impermeabilization of the surface, channel rectification and built drainage system (WRIGHT et al., 2012).

The purpose of this paper is to analyse the morphometric features of the two most affected urban watersheds in the city of Santo André: Tamanduateí Médio I and Guarará. These urban subbasins suffer every year from floods but there are no current studies that analyse their morphometry in order to understand if the urbanization plays the main role regarding the flood occurrences. Therefore, the main goal of this study is to characterize the watersheds mentioned through morphometric features along with the inventory of floods in the area to comprehend the water bodies that influence the occurrence of the cases.

2. DATA AND METHODS

2.1 Study area

The city of Santo André is located within the metropolitan area of São Paulo, 760 meters above sea level, with 175 km² of area. Its geographic coordinates are 23° 39' 50" S and 46° 32' 16" W (Figure 1). The city is inserted into the High Tietê Hydrographic Area, subarea Billings/Tamanduateí and is divided into two zones: Urban and Ambiental Protection. The two subbasins studied are both inserted into the urban zone. The north portion of Santo André is totally urbanized and it also has many industries nearby. Green areas are scarce.

2.2 Methods

The methods used for this research was firstly the inventory of flood events provided by the municipality of the city of Santo André (SEMASA). 16 years of record of flood events were analysed, from 2001 to 2016. All the events were separated by location and it was possible to carry out a temporal and spatial analysis of the occurrences. Therefore, it was possible to comprehend which watershed was the most affected by floods and during which period of the year. This initial step helped the decision of which subbasins should be studied.

* Corresponding author

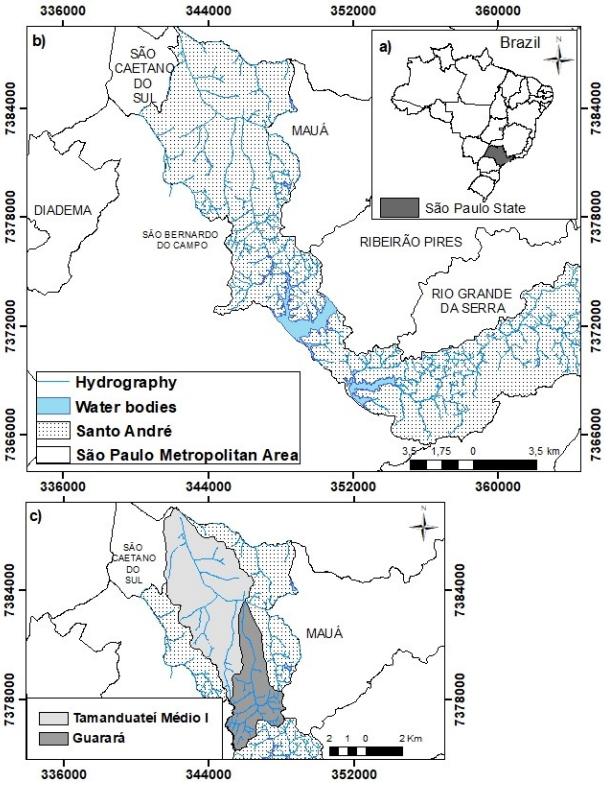

Figure 1 – Location of the study area. a) Location of São Paulo in Brazil; b) location of Santo André in the Metropolitan Area of São Paulo; c) Location of the two subbasins studied in the north portion of Santo andré.

After this initial statistical analysis, the morphometry of the watersheds was analysed. There are many parameters that could be used to characterize a watershed. In this study, the most important parameters chosen were divided into geometry: elongation ratio (Equation 1) form factor (Equation 2), circularity ratio (Equation 3) and; drainage system: drainage density (Equation 4), first order stream frequency (Equation 7), sinuosity of the main river (Equation 6); and relief: relief ratio (Equation 5), topographic factor (circulation ratio + first order stream frequency + relief ratio), amplitude (Equation 9), main stream slope (Equation 10) and concentration time (Equations 11, 12).

Regarding the basin analysis, form factor is defined as the ratio of basin area to square of the basin length and is a dimensionless number varying from 0 to 1. The higher the value, the higher the tendency to floods. The circularity ratio is the relation between the total area of the basin and the area of a circle with the same perimeter. Values over 0,51 indicate a circular shape and higher susceptibility to floods (VILLELA; MATTOS, 1975).

Re (elongation Ratio)	$(0{,}28)\frac{P}{\sqrt{A}}$	(1)
Rf (form factor)	$\frac{A}{L^2}$	(2)
Rc(circularity ratio)	$\frac{4\pi A}{p^2}$	(3)
Dd (drainage density	$\frac{Lt}{A}$	(4)
Rh (relief ratio)	$\frac{Aa}{Mc}$	(5)
Is (sinuosity of the main river)	$\frac{L}{L_t}$	(6)
Fs (stream frequency	$\frac{N_1}{A}$	(7)
Tf (topographic factor	Fs + Rh+ Rc	(8)
Aa (amplitude)	$A_{max} - A_{min}$	(9)
Dm (main stream slope)	$\frac{Aa_{ups} - Aa_{dov}}{L}$	(10)

where A = area
L = length of the main channel
P = Perimeter
Mc = straight distance from river mouth until the most extreme point of the basin.
N_1 = number of first order rivers
Lt = straight total length of the main channel
Aa = amplitude

The relief ratio expresses the relation between the amplitude and the length of the main channel, measuring the global slope of the basin (SCHUMM, 1956). The higher the value, the greater will be the erosion processes within the basin. The topographic factor is proportional to the potential to flood at the mouth of the river, the higher the value, the higher the potential (MORISAWA, 1962).

The slope of the main river indicates the flux velocity. The bigger the value, the steeper will be the hydrograms, showing higher energy associated to flux, magnifying the flood events (VILLELA; MATOS 1975).

Areas with high drainage density answer faster to precipitaion, whereas the hydrologic responde is slower in basins with slower drainage densities (SCHUMM, 1956).

The concentration time is an important parameter for basin analysis and represents the time needed for the whole basin to contribute to the surface runoff in a considered area, which is in this case, the river mouth. The lower the value, represented in hours, the faster will be the flood waves (TOMAZ, 2005). Given that the studied watersheds are urban basins, the concentration time developed by Tsuchya (1978) was used because it takes into consideration the parameters related to urbanization (Equation 11).

$$CT = 0,36 \times L / Ieq^{0,5} \quad (11)$$

$$57x\,(L^3/Aa)^{0,385} \quad (12)$$

where Ieq: equivalent slope

A general equation created by Kirpich (apud Tomaz, 2005) that does not take into consideration urbanization was used for means of comparison of values (Equation 12). In order to do this, the georeferenced files of the watersheds supplied by the municipality were opened in the Geographic Information System environment. This files include the basin limits, drainage system in scale 1:10.000, the slope maps and contour lines in scale 1:25.000. The relief data was provided by CPRM (Brazilian Geological Service).

3. RESULTS

The analisys of the occurrence of floods events in the city shows that they are more frequent during the summer e more scarse during the winter. The results showed a total of 273 flood events

during the 16 years mentioned, 146 only in the Guarará sub-basin, the most affected during the period.

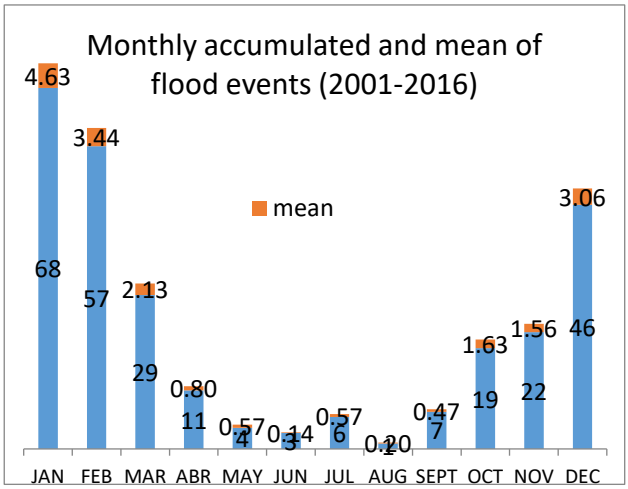

Figure 2 – Total of flood events by month registered by the Civil Defence in the city of Santo André from 2001 to 2016.

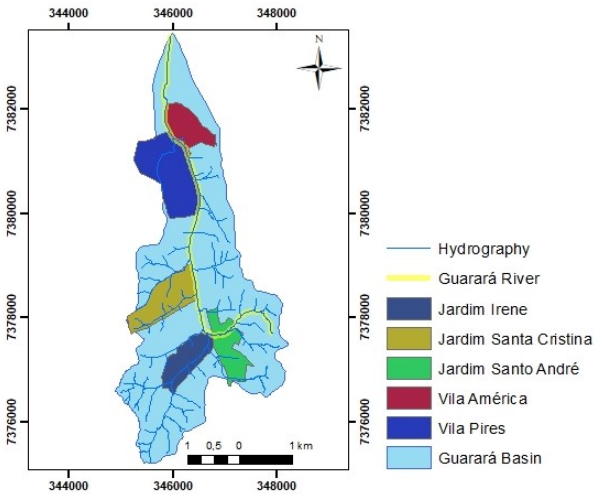

Figure 3 – Guarará subbasin and the most affected neighboorhoods

The second most affected watershed in Santo André was the Tamanduateí Médio I, with 64 cases. A study developed by Neves (2017) regarding the seasonal precipitation cycle in Santo André indicates that the flood events follow the rain seasonality. As it is possible to see in Figure 2, the major part of events is distributed within the summer (December, January and February) which is the rainiest season. The winter months, which are the driest ones (June, July and August), have much less occurences registered by the Civil Defense.

Regarding the physical features of the basins, the Guarará subbasin is located on the Complex of Embu, that comprehends micaschists and also migmatites. This leads to higher erosion and therefore greater siltation, supporting a steeper relief, which also makes the flux velocity faster.

The Tamanduateí Médio I is located on the Tertiary Basin of São Paulo, supported by sedimentary rocks, mainly conglomerates, sandstones and siltstones as well as the Quaternary deposits, that form alluvial plains. This lithology is realated to a flatter relief, and smaller flux velocity and therefore less erosion of the terrain.

The Guarará subbasin has an area of 13,46 km^2 and there are four neighborhoods that were most affected: two of them downstream (Vila America e Vila Pires) and the other two upstream (Jardim Santo André e Jardim Irene) (Figure 3). These areas are economicaly diverse and have different types of land uses, being the one upstream more permeable, with the the level of urbanization lower than the first. If analyzed only the parameters related to the shape of this sub-sin, such as form factor (0.20) and circularity ratio (0.38), it would not be naturally prone to floods.

The Tamanduateí Médio I has an area of 27.76 km^2, with two neighborhoods most affected: Vila Alzira and Bairro Silveira, both of them upstream and totally urbanized (Figure 4). In fact, this areas are closer to the Guarará river than the Tamanduateí river itself. The circularity ratio for this basin is 0.47 and according to Miller (1953) this basin would have a higher tendency to flooding occurrence in terms of geometry. The value of the form factor is 0.23. The amplitude of the Tamanduateí sub-basin is 98, whereas the Guarará is 202 meters, indicating a steeper relief, since the area of the second is smaller.

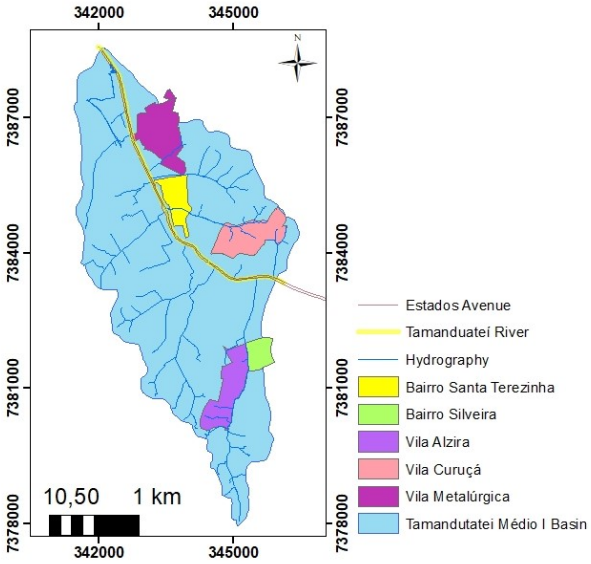

Figure 4- Tamanduateí Médio I subbasin and the most affected neighboorhoods

The Tamanduteí Médio I subbasin has a lower drainage density: 2,07 m/km^2. Lower drainage densities are often observed in flatter reliefs in sedimentary terrains (HIRUMA; PONÇANO, 1994). The Guarará subbasin has a drainage density of 3,46 m/km^2. The slope of the Guarará river is much higher than the Tamanduateí river, being 0.0177 for Guarará and 0.0018 for the second, which demonstrates that Tamanduateí river is not as steep. This means that the Guarará subbasin has higher energy associated to the water flux of the rain when compared to the Tamanduateí Médio I, even though the Tamanduateí river is less sinuous, which increases the flux velocity.

The topographic factor, which is directly proportional to the flood potential in the main river mouth (MORISAWA, 1962), is 11,13 for Tamanduateí Médio I and 30,35 for Guarará, which corroborates the relief ratio: 24.7 for Guarará and 9 for Tamanduateí, which indicates higher tendency to erosion regarding the first. This means that the Guarará subbasin has a

higher potential to accumulate sediments at its mouth and therefore magnify the floods events due to siltation.

Parameter	Subbasin	
	Guarará	Tamanduateí Médio I
A	13.46	27.76
Re	1.63	1.45
Rf	0.199	0.3
Dd	3.46	2,07
Is	1.28	1,10
L	7.8	7.4
Rh	24.7	9
Rc	0.371	0,47
Fs	5,35	1,76
Tf	30,35	11,13
Aa	202	98
Dm	0,0177	0,0018
Ct*	1,32	1,64
Ct**	1,14	1,99

Table 1. Results of the morphometric parameters.

For the concentration time, the value for the Guarará subbasin was 1,32 hours when using the equation elaborated by Kirpirch. Using the formula created by Tsuchiya (1978), the value decreases to 1,14 hours, which was already expected due to the fact that anthropization changes the hydrological response of the basin, making it faster. For the Tamanduateí Médio I, the concentration time found is 1,64 not taking into consideration urbanization and 2 hours when using the formula developed by Tsuchiya (1978), which was not expected since it means that in this case the urbanization positively influences the concentration time. This shows that these formulas might not be accurate.

According to geometric parameters, the Guarará subbasin would not be prone to floods, but the relief parameters indicate a higher potential. This is not true for the Tamanduateí subbasin: according to the geometry, it would be more similar to a circular shape, which indicates propension to floods, but its relief does not classify it as prone to such occurrence. Its amplitude is low as well as the slope of the main river Tamanduateí, which is totally channelized, surrounded by big avenues, with almost no vegetation. This could be also an explanation for the low drainage density: the urbanization tends to lower this parameter, since it is common to find buried rivers in such urban areas. On the other hand, a lower drainage density would make the area less prone to floods since the hydrological response in such areas is slower.

4. CONCLUSIONS

The results found indicate that the flood problems in the urban area of Santo André are not related strictly to the morphometry of the basins, since the two of them that were analyzed have different features, mainly related to the shape, relief and lithology. These natural disasters affect also places with different land uses, shown by the most affected neighborhoods. It is possible to infer that the Guarará subbasin is more susceptible to floods regarding its relief, which is not true if only the geometric parameters are analyzed.

Regarding the Tamanduateí Médio I, it would be slightly more susceptible to floods according to its geometric features but when it comes to its relief, this basin would not have a lower tendency to floods. This means that even though these basins are different from each other regarding lithology and morphology, both are affected by floods with basically the same intensity. Besides, the location of the subbasins in the central, totaly urbanized portion of Santo André, inadequate drainage projects and structural measures that are not capable to deal with the surface runoff that comes from the rainfall in the summer months, magnifies the occurrence of floods. Therefore, it seems that the anthropization plays the fundamental role in the ocurrence of floods in Santo André, since different watersheds, with different features are affected.

Further studies regarding the rainfall upstream and downstream the basins have to be carried out in order to better understand the ocurrences of floods in Santo André, as well as the study of the basins nearby.

REFERENCES

Collischonn, W., Tassi, R., 2008 *Introduzindo Hidrologia***.** 5. ed. Porto Alegre: Iph Ufrgs, 2008. 149 p.

Freitas, G. V., 2006. A bacia hidrográfica como unidade territorial para o planejamento e gestão ambiental: estudo da bacia hidrográfica do Ribeirão Preto no município de Ribeirão Preto-SP. *Dialogus. Ribeirão Preto*, v. 1, n. 2, p. 65-84.

Hiruma, S. T., Ponçano, W. L., 1994. Densidade de drenagem e sua relação com fatores geomorfopedológicos na área do alto Rio Pardo-SP e MG. *Revista do Instituto Geológico*, v. 15, n. 1/2, p. 49-57.

Magalhães Júnior, A. P., 2007. Indicadores ambientais e recursos hídricos: realidade e perspectivas para o Brasil a partir da experiência francesa. Rio de Janeiro: *Bertrand Brasil*, 688p.

Morisawa, M. E., 1962. Quantitative Geomorphology of Some Watersheds in the Appalachian Plateau. *Geological Society of America Bulletin,* vol. 73, issue 9, p. 1025.

Neves, B. F., 2017. Estudo das inundações no município de Santo André e sua relação com as chuvas intensas. 2016. 99 f. Monografia - Curso de Eng. Ambiental e Urbana, Universidade Federal do Abc, Santo André.

Schumm, S.A., 1956. The evolution of drainage systems and slopes in bad lands at Perth, Amboi, New Jersey. *Geol. Soc. Ame. Bull.* 67 (5), pp. 597-646.

Tomaz. P., 2009. Curso de manejo de águas pluviais. *Guarulhos: Plínio Tomaz*.

TSUCHIYA, A., 1978. Evaluation of on-site stormwater detention methods in urbanized area. In: HELLIWELL P.R. (editor*).* Urban storm drainage. London – England: *Centech Press,* p.470-478.

Villela, S., Mattos, A., 1975. *Hidrologia Aplicada***.** São Paulo: Mcgraw-hill,, 1975. 245 p.

Wright, D., Smith, J., Villarini, G., Lynn Baeck, M., 2012. The Hydroclimatology of flash flooding in Atlanta. *Water Resources Research,* v. 48, n. 4.

DETECTION OF WATER BODIES USING OPEN ACCESS SATELLITE DATA: THE CASE STUDY OF KASTORIA LAKE IN NORTH-WESTERN GREECE

A. Karagianni*

Aristotle University of Thessaloniki, Faculty of Engineering, School of Civil Engineering, Lab. of Photogrammetry - Remote Sensing, Thessaloniki, Greece – aikateck@civil.auth.gr

KEY WORDS: Remote Sensing, Digital Image Processing, Image Interpretation, Water Body Detection, Optical Satellite Data

ABSTRACT:

Water bodies play an important role in the environment as their variations impact other natural resources and human assets. Particularly the study of inland lakes is a challenging task since it requires the involvement of various scientific principles. Remote sensing techniques and satellite data could provide valuable information regarding detection and monitoring of water bodies in the study of lakes and their surroundings, contributing to environmental and development issues. This paper concerns the wide area of Kastoria Lake (Lake Orestiada) in north-western Greece, an area of particular interest as the lake is included in the Natura 2000 network and is surrounded by diverse landcovers. Optical, open access satellite data derived from Sentinel-2 are being used and digital image processing techniques are applied in order to detect the water surface. The data are initially resampled to an identical resolution. Two water indices are calculated in order to delineate open water features eliminating the presence of soil and vegetation, as well as to enhance their presence in the optical imagery highlighting the water surfaces (even those of smaller size). Further digital processing concerns the creation of a water mask to extract the water information. Visual interpretation of the area using various band combinations and applying enhancement techniques is also being done, contributing to the detection study. Due to the spatial resolution of Sentinel-2 data, the water surfaces are discernible and the coastal areas around the water body are well delineated. Open access satellite data offer the ability to detect and map water surfaces effectively, which may be essential to a variety of scientific and civil applications. In general, the results are satisfactory at this stage and can be used for further monitoring of the lake with possible extensions to a wider region.

1. INTRODUCTION

Water bodies play an important role in the environment as a part of the hydrological cycle. Especially inland lakes (enclosed water bodies surrounded by land with no direct access to the sea) are particularly important for environmental and development issues (Thomas et al., 1996), as they are complex systems presenting an interaction of various processes (hydrological, geological, physical, chemical and biological).

Lakes are closely linked to their surroundings forming a unique system and their study requires the involvement of various scientific principles offering multiple information in fields such as lake and coastal zone management, watershed definition, erosion and contamination monitoring, evaluation of water resources, etc. (Kondratyev and Filatov, 1999; Ouma and Tateishi, 2006). Among the scientific disciplines that are involved in the study of lakes and their surroundings, remote sensing techniques and satellite data could provide valuable information regarding detection and monitoring of water bodies. Wide coverage, multitemporal and repetitive information, as well as continuous monitoring are some of the advantages that satellite data can offer.

This paper concerns the wide area of Kastoria Lake (Lake Orestiada) in north-western Greece, an area of particular interest as the lake is included in the Natura 2000 network and is surrounded by diverse landcovers (built up areas, agricultural land, etc.). Optical, open access satellite data derived from Sentinel-2 are being used and digital image processing techniques are applied (including resampling, water indices calculation and water mask extraction) in order to detect/delineate the water surface and enhance its presence in the optical imagery. Visual interpretation of the area using various band combinations and applying enhancement techniques is also being done, contributing to the detection study.

2. STUDY AREA AND SATELLITE DATA

2.1 Study area

Study area is located in medium-high altitude (630 m) in the north western part of Greece, region of Western Macedonia (Figure 1) and concerns the wide area of Kastoria Lake (Lake Orestiada). The city of Kastoria is located at the western shore of the lake and the area is surrounded by mountains.

The lake has tectonic origin with karstic nature, and is characterized by an average depth of 4 m and a maximum depth of 8 m (Kousouris, 2014). It is an open lake that is discharged through a natural canal to a stream which contributes to Aliakmon River at a southern point and had been receiving sewage effluents for years until 1994, presenting several times eutrophication problems (Moustaka-Gouni et al., 2006). Lake Orestiada is included in the Natura 2000 network.

* Corresponding author

Figure 1. Study area in the north western part of Greece

2.2 Satellite Data

The data employed for this study concern Sentinel-2A satellite imagery. Sentinel-2 is a European wide-swath, high-resolution, multispectral imaging mission and consists of two polar-orbiting satellites (Sentinel-2A & Sentinel-2B) providing high-resolution optical imagery for land monitoring.

Sentinel-2A was launched on June 23, 2015 while Sentinel-2B on March 07, 2017. Both satellites are equipped with the MSI (Multispectral Imager) instrument that offers high-resolution optical-multispectral images. The sensor covers 13 different spectral bands: four visible and near-infrared bands with a spatial resolution of 10 m (bands 2, 3, 4, 8), six red edge and shortwave infrared bands with a spatial resolution of 20 m (bands 5, 6, 7, 8A, 11, 12) and three atmospheric correction bands with a spatial resolution of 60 m (bands 1, 9, 10). The orbital swath width is 290 km (https://sentinel.esa.int/web/ sentinel/missions/sentinel-2).

Sentinel data products are available to all users and can be accessed free of charge (free, full and open data policy adopted for the Copernicus programme) through the Copernicus Open Access Hub (https://scihub.copernicus.eu).

The image data that have been used in this study derive from Sentinel-2A (S2A_MSIL2A) and were acquired at 16-10-2017 with level processing 2A. The Level-2A products provide Bottom of Atmosphere (BOA) reflectance images derived from the associated Level-1C products. Each Level-2A product is composed of 100x100 km^2 tiles in cartographic geometry (UTM/WGS84 projection).

3. DIGITAL IMAGE PROCESSING AND VISUAL INTERPRETATION

To detect and delineate the water body in the study area, several methods can be applied. Digital processing of Sentinel-2A data included resampling at 10 m, layerstacking of the downloaded data, subsetting the scene to the study area, enhancement techniques implementation, water indices calculation and water mask extraction. The software that was used for the digital processing of the satellite imagery is ERDAS Imagine 2011 and SNAP (Sentinel Application Platform) freely distributed by ESA. Visual interpretation was performed in every stage, contributing to the water body detection.

Initially, different color composites can be used to highlight several features in the landscape, as the water surface and its wider area in this study. Using different band combinations certain features will contrast greatly with their surroundings, enabling better delineation as spectral bands capture energy in different parts of the electromagnetic spectrum.

In this study, among various possible combinations, the color composites that were considered the most effective for a qualitative approach of water body detection were the natural color composite R:4-G:3-B:2 (Figure 2) and the color composite R:8-G:11-B:4 (Figure 3).

Figure 2. Study area in natural color composite (RGB-4,3,2)

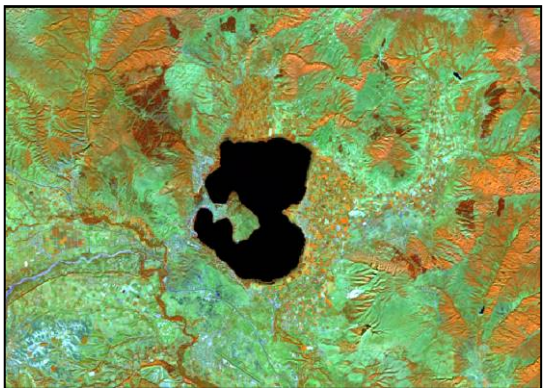

Figure 3. Study area in color composite (RGB-8,11,4)

In the natural color composite (Figure 2) the water body is easily discerned in the center of the image, as all the features appear in colors similar to their appearance to the human visual system. In the second band combination (Figure 3) water features are clearly highlighted and stand out even more (black color) in relation to land features (green to light brown colors). This combination is also proposed as a combination for Land/Water delineation through SNAP.

Subsequently, an Intensity-Hue-Saturation (IHS) transformation was implemented to exploit the digital processing capabilities of the multispectral optical data. IHS transformation is a spectral enhancement technique which alters the image colors based on brightness, dominant wavelength and spectral purity of a pixel across different bands. Following this algorithm, an alternate color space is defined which uses intensity (I), hue (H) and saturation (S) as the three positioned parameters (instead of R, G, B). This system is advantageous as it presents colors more nearly as perceived by the human eye (ERDAS Field Guide, 2013). Figure 4 presents the study area after IHS transformation where the water surface and its boundaries are clearly highlighted. In addition, some color changes on the water body surface are noticeable.

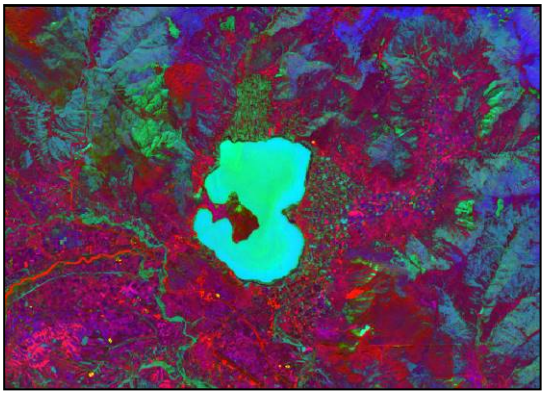

Figure 4. Study area after IHS transformation

To exploit further the high spatial resolution that Sentinel-2 offers (10 m after resampling), as well as the processing level of the data (L2A data are atmospherically corrected) relevant water indices were calculated.

Water bodies have strong absorbability and low radiation in the range from visible to infrared wavelengths. The Normalized Difference Water Index (NDWI) index uses the green and near infrared bands of remote sensing images based on this phenomenon, detecting surface waters in wetland environments (McFeeters, 1996). The index can enhance the water body information effectively and separates water from non-water objects. The index formula is presented in Equation 1. For Sentinel-2A the Green band is band 3 and the NIR band is band 8. The result is a single band gray-scale image (Figure 5).

$$NDWI = \left(\frac{Green - NIR}{Green + NIR} \right) \quad (1)$$

where

Green = the green band value for a cell
NIR = the near infrared band value for a cell

According to McFeeters (1996), values of NDWI greater than zero represent water features, while values less than or equal to zero represent non-water features, as vegetation and soil features (Land < 0 < Water). In Figure 5 water surfaces are detected in white color. The main water body (Kastoria Lake) is observed in the center of the image. Furthermore, water surfaces of smaller size are also highlighted with white color (red circles in Figure 5 - positions of two small dams).

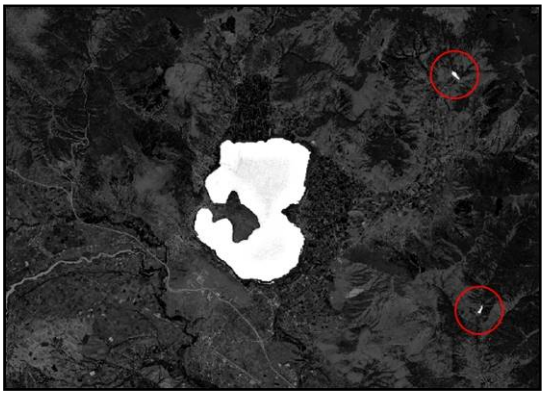

Figure 5. Normalized Difference Water Index (NDWI)

NDWI index is widely used due to its simplicity along with a clear physical meaning. However, although the index can enhance information about water bodies restricting information about vegetation and soil features, there still exist several limitations. According to Xu (2006) and Li et al. (2013), it is sensitive to built-up land and can result in over-estimated water bodies.

A more accurate delineation of the water surface is achieved in this case study calculating the Modified Normalized Difference Water Index (MNDWI) proposed by Xu (2006). This index can be applied due to its superiority in urban surface water extraction (Du et al., 2016; Yang et al., 2017) and can enhance open water features while efficiently suppressing or even removing built-up features as well as vegetation and soil features (Li et al., 2013). The formula for MNDWI index is presented in Equation 2. For Sentinel-2A the Green band is replaced by band 3 and the SWIR band by band 11 in the equation.

$$MNDWI = \left(\frac{Green - SWIR}{Green + SWIR} \right) \quad (2)$$

where

Green = the green band value for a cell
SWIR = the shortwave infrared band value for a cell

The resulting values representing the water features are positive and those representing non-water features are negative. In general, water bodies have larger positive values in MNDWI compared with NDWI because they generally absorb more SWIR light than NIR light. On the contrary, soil, vegetation and built-up features have smaller negative values because they reflect more SWIR light than green light (Yang et al., 2017). The result after the second index calculation is also a single band gray-scale image (Figure 6).

In Figure 6, the main water body is observed in the center of the image in white color, while the surfaces of smaller size water bodies derived after MNDWI calculation are also noticeable in white color (red circles in Figure 6 - positions of two small dams).

Figure 6. Modified Normalized Difference Water Index (MNDWI)

A threshold value for MNDWI image (threshold of zero) can be set to classify the results into two classes, water and non-water features (Xu, 2006; Du et al., 2016), leading to a water mask image which can contribute further to visual interpretation (Figure 7). The mask can be colored accordingly and superimposed on a base of natural color image.

Figure 7. Water mask derived from MNDWI

4. SUMMARY – CONCLUSIONS

Water bodies are particularly important for environmental and development issues hence, their study requires multiple information. Especially the study of lakes as complex water bodies, due to the interaction of different processes, requires the involvement of various scientific principles. Remote Sensing is among the scientific disciplines that can contribute to the acquisition of suitable information, offering valuable tools.

This paper concerns the wide area of Kastoria Lake (Lake Orestiada) in north-western Greece. Optical, open access satellite data derived from Sentinel-2 are being used and digital image processing techniques are applied in order to detect the water surface. Sentinel-2 mission offers long-term time series of images with high temporal resolution, suitable for monitoring purposed of water bodies (water surface boundaries and coastlines, water quality and floating vegetation, flood phenomena and environmental or biodiversity issues, etc.). Due to the spatial resolution of Sentinel-2 data, the water surfaces are discernible and the coastal areas around the water body are well delineated.

Digital processing of the multispectral data included resampling, spectral enhancement techniques implementation, water indices calculation and water mask extraction. In addition, visual interpretation of the area was done (using various band combinations, as well as after image processing), contributing to the detection study.

The Normalized Difference Water Index (NDWI) that was applied to detect surface waters eliminates the presence of soil and vegetation features, highlighting the water surfaces and allowing for possible future measurements of the surface extent. The infrared wavelengths that are used give useful information for water mapping, as the strong absorption of infrared light by water bodies gives them a distinctively low spectral response in this range. In addition, index calculation presents further utility in land cover classification, water content evaluation, etc., by exploiting suitable spectral bands of satellites.

While NDWI index can enhance information about water bodies, restricting information about vegetation and soil features, it presents relevant weaknesses in distinguishing built-up features from water bodies. The build-up noise can affect the index causing some misclassifications in built-up areas with a ratio similar to the ratio that water surfaces present. A more accurate delineation of the water surface is achieved in this case study calculating the Modified Normalized Difference Water Index (MNDWI). This index, which has demonstrated its superiority in many applications related to water bodies, including urban surface water extraction, can be calculated when a SWIR band is available giving satisfactory results.

In both cases, application of water indices delineates boundary information and water surfaces of smaller size are also highlighted. The results can be used for further monitoring of the lake with possible extensions to a wider region. The ability to detect and map water surfaces effectively (which is offered from open access satellite data) may be essential to a variety of scientific and civil applications.

REFERENCES

Du, Y., Zhang, Y., Ling, F., Wang, Q., Li, W., Li, X., 2016. Mapping from Sentinel-2 Imagery with Modified Normalized Difference Water Index at 10-m Spatial Resolution Produced by Sharpening the SWIR Band. *Remote Sensing*, 8(4), pp. 1-19.

ERDAS Field Guide™, Intergraph Corporation, Erdas Inc., U.S.A, 2013, pp. 447-449.

Kondratyev, K. Y. and Filatov, N. N., 1999. *Limnology and Remote Sensing: A Contemporary Approach*. Springer – Praxis Series in Remote Sensing, pp. 374-376.

Kousouris, Th., 2014. *The Lakes in Greece: 3/6 Macedonia*. EKKE, Athens, pp. 62-64.

Li, W., Du, Z., Ling, F., Zhou, D., Wang, H., Gui, Y., Sun, B., Zhang, X., 2013. A Comparison of Land Surface Water Mapping Using the Normalized Difference Water Index from TM, ETM+ and ALI. *Remote Sensing*, 5(11), pp. 5530-5549.

McFeeters, S.K., 1996. The use of the Normalized Difference Water Index (NDWI) in the delineation of open water features. *International Journal of Remote Sensing*, 17(7), pp. 1425-1432.

Moustaka-Gouni, M., Vardaka, E., Michaloudi, E., Kormas, K. A., Tryfon, E., Mihalatou, H., Gkelis, S., Lanaras, T., 2006. Plankton food web structure in a eutrophic polymictic lake with a history of toxic cyanobacterial blooms. *Limnology and Oceanography*, 51(1, part 2), pp. 715-727.

Ouma, Y., Tateishi, R., 2006. A water index for rapid mapping of shoreline changes of five East African Rift Valley lakes: An empirical analysis using Landsat TM and ETM+ data. *International Journal of Remote Sensing*, 27(15),pp.3153-3181.

Thomas, R., Meybeck, M., Beim, A., 1996. Lakes. In: *Water Quality Assessments-A Guide to Use of Biota, Sediments and Water in Environmental Monitoring*, ed. by Deborah Chapman, 2nd ed. (E&FN Spon, Great Britain, 1996), pp. 325-370.

Xu, H., 2006. Modification of normalized difference water index (NDWI) to enhance open water features in remotely sensed imagery. *International Journal of Remote Sensing*, 27(14), pp. 3025-3033.

Yang, X., Zhao, S., Qin, X., Zhao, N., Liang, L., 2017. Mapping of Urban Surface Water Bodies from Sentinel-2 MSI Imagery at 10 m Resolution via NDWI-Based Image Sharpening, *Remote Sensing*, 9(6), pp. 1-19.

Websites: https://sentinel.esa.int/web/sentinel/missions/sentinel-2 & https://scihub.copernicus.eu (last retrieved Sept. 2018).

A COMPARISON BETWEEN UAV AND HIGH-RESOLUTION MULTISPECTRAL SATELLITE IMAGES FOR BATHYMETRY ESTIMATION

L. Rossi[1,2]*, I. Mammi[1], E. Pranzini[1]

[1] Dept. of Earth Science, University of Florence, Italy - epranzini@unifi.it
[2] GeoCoste snc, Florence, Italy- lrossi@geocoste.com

KEY WORDS: Coastal monitoring, Bathymetry, High resolution satellite images, UAV, Drone, Multispectral camera.

ABSTRACT:

Shallow water bathymetric surveys support Integrated Coastal Zone Management and Maritime Spatial Planning, e.g. in coastal erosion monitoring, shore protection design and landfall projects oil and gas pipelines. High-resolution multispectral satellite imagery, such as Quick Bird and Worldview, are increasingly used for this purpose. The present study shows the results of a comparison between high resolution satellite and Unmanned Aerial Vehicle (UAV) derived bathymetry. Accuracy was validated through an hydrographic survey performed with a Multibeam Echosounder (MbEs) at the same time of UAV acquisition. The drone was equipped with a small and light multispectral camera, acquiring in the same WorldView-2 sensors spectral bands. The study area, located in the central Tuscany coast (Italy), is approximately 0.5 km^2. Because of the high percentage of water present in UAV images, a new method was implemented to produce a georeferenced orthophoto mosaic. Multispectral images were processed to retrieve bathymetric data with Stumpf's algorithm. Different pairs of bands were tested to determine the best fit for real water depth data. The influence of sea bottom control points density on data accuracy was also analyzed. Results show the possibility to produce accurate remote sensing bathymetric maps with low operational costs and easy data processing, giving the chance to set up shallow water monitoring programs based on UAV surveys. A further advantage of this method is the capability to produce a full sea-floor coverage bathymetry in very shallow water areas, were MbEs is usually unable to work properly and to represent the aerial option to survey very shallow waters alternatively to Unmanned Surface Vehicles (USV) a.k.a. ASV (autonomous surface vehicles).

1. INTRODUCTION

Coastal environments are dynamic areas affected by long-term and short-term evolution. Nearshore hydrodynamic processes such as waves, tides, currents and fluvial discharges play significant roles in forcing short-term coastal morphological change.

The growing demand of bathymetric information is ascribed to marine navigation, environmental protection, exploration and exploitation of marine resources, fisheries, coastal defence, tourism and recreation.

Bathymetric data are usually acquired with Singlebeam Echo sounders system (SbEs) and lately also with Multibeam Echosounder system (MbEs). Such approaches require hard fieldwork and are extremely time-consuming, especially if wide areas have to be surveyed. In very shallow water, shipborne soundings regularly use a SbEs which is only capable to produce low spatial resolution data (Said et al., 2017).

Although the traditional hydrographic survey is still the first option to provide accurate bathymetric data, high resolution satellite images have been increasingly used for coastal monitoring and bathymetric mapping, particularly in shallow water areas. In the last years, satellite remote sensing have provided a cost and time-effective solution to gather bathymetric data in shallow water.

Bathymetric mapping is carried out through high-resolution multispectral satellite image processing, such as WorldView-2 and 3, Quick Bird etc. (Said et al., 2017). Multispectral imagery derived bathymetry is based on the principle that electromagnetic radiation at different wavelengths can penetrate the water column to different depths.

Various methods have been proposed by several authors e.g. Lyzenga (1978), Jupp (1989), and Stumpf et al. (2003). The latter, using a simple ratio of reflectance at different wavelengths, may be suitable for implementation in a procedure for regular monitoring programs of sensitive coastal areas.

For bathymetric mapping purposes the most accurate result reported so far using satellite multispectral approaches has a relative depth error of approximately 10% in water depths lower than 15 m (Panchang and Kaihatu, 2018).

Currently, UAVs (Unmanned Aerial Vehicles) are the fastest monitoring systems for coastal area and the processing of ortho-images provides a powerful tool for coastal and marine areas monitoring.

UAV technology has inherent advantages, such as full coverage of areas of interest with very high accuracy and the ability to quickly produce images with high spatiotemporal resolution.

This paper presents a methodology for remote sensing derivation of bathymetric data using a small and light multispectral camera mounted on a UAV. A comparison between bathymetric maps derived from multispectral UAV and Worldview2 images, using the Stumpf's algorithm, is

* Corresponding author

also provided and their accuracy verified with a MbEs bathymetric survey.

2. LOCATION

The test area (Fig.1) is located on the central Tuscany coast at San Vincenzo (LI) in Italy. The area is approximately 300x400 m^2 and is characterized by a sandy beach with very shallow water and sandbars. Investigated depth was from the shoreline down to the inner edge of *Posidonia oceanica* prairie, at about 10 m depth. The coordinate reference system used for all the applied surveys was EPSG 32632 (WGS84/UTM 32 North) and national vertical datum referred to mean sea level recorded at Genova Tide Gauge in 1942.

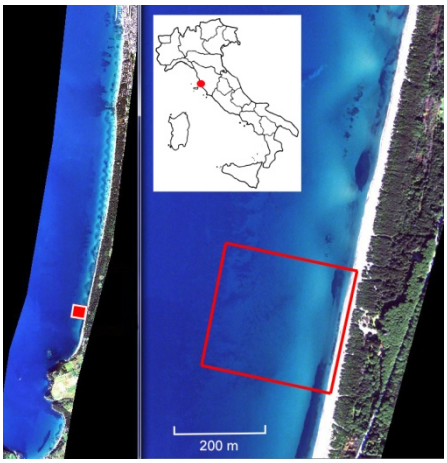

Figure 1. Location map on WV2 satellite image in true colours. In the red square the study area.

3. METHODOLOGY

Bathymetry was obtained by applying Stumpf et al. (2003) ratio transform algorithm on different band combination of WV2 and UAV multispectral imagery. Stumpf's Relative Water Depth (RWD) algorithm uses a log-transformation to linearize the relationship between band spectral value and depth.

The algorithm uses a pair of bands in order to reduce the number of parameters and determine the depths. Because both bands are equally distributed, the error due to the varying radiation in the atmosphere, water column, and seafloor is reduced (Pushparaj and Hegde, 2017).

Equation (1) is used to estimate the depth in shallow water:

$$Z = m_1 \frac{\ln(nR_w(\lambda_i))}{\ln(nR_w(\lambda_j))} - m_0 \quad (1)$$

where, Z= derived relative depth
m_1, m_0= constants
R_w= observed radiance
$\lambda_{i,j}$ = bands
n is a constant chosen to keep the ratio positive for any reflectance value

Relative Water Depth was computed with ENVI™ 5 suite for different combination of band pairs (Coastal Blue-Green; Yellow-Green; Blue-Green) in order to estimate their influence in the accuracy of resulting RWD.

Input data for the production of satellite-derived bathymetry map has been a WV2 image acquired on 13-12-2016 (panchromatic 50 cm res. + 8 multispectral bands 2 m res.). This was the most recent and good quality image available for the study area in terms of cloud coverage and sea waves conditions.

The Rational Polynomial Functions model has been used for the Ortho-rectification process using Ground Control Points (GCPs), taken from reference cartography. Nearest neighbour re-sampling technique has been used in order to preserve the original radiometric data. Radiance and reflectance conversion have been also applied. Finally, thresholding on band 7 (Near-infrared 1) was performed to mask out the emerged portion of the beach.

The UAV used for this study was a hexacopter equipped with MAIA WV (Fig. 2), a multispectral camera specifically designed to be employed on board of drones. MAIA WV has a 9 sensors array with 1.2 Mpixel (8 multispectral + 1 RGB) acquiring in the VIS-NIR spectrum. It acquires on the same wavelength intervals of WV2 satellite, from 433 to 875 nm. CMOS sensors settled in MAIA have 1280x960 pixels and the dimension of each pixel is 3.75 x 3.75 µm. Each sensor is global shutter and they shoot simultaneously: it follows that it is not necessary to stabilize acquisition with gimbal, which is indispensable with rolling shutter sensors to avoid distortion, crawling and blurring pixels in the images. Images pre-processing software allows to correct raw image geometrical distortion and radial distortion; it also allows to stitch the images of each single band into one multispectral image with the pixel-pixel convergence.

Figure 2. UAV equipped with MAIA multispectral camera used for the survey

Nine multispectral images were acquired on April 2018 at 150 m flight height (Fig. 3) with fair weather conditions and in the morning with the sun low on the horizon (Fig. 2) for sun glint reduction. Sun-glint patterns produce, especially for UAV surveys, an irregular noise in the water reflectance difficult to be completely removed. Hedley et al. (2005) method was applied for this correction.

Given the impossibility of applying a SfM (Structure for Motion) 3d model and a bundle adjustment to generate the

orthophoto due to an almost complete presence of water in the images, a new technique has been tested.
Images were georeferenced using the UAV control-unit flight parameters as GPS position, heading, picth & roll and knowing the camera ground footprint for that elevation (96x72 m) and also verified with an RTK GPS survey. Furthermore, two buoys equipped with a GPS, recording in real time their position, have been used as sea control points. Finally, a GeoTIFF image mosaic has been produced.

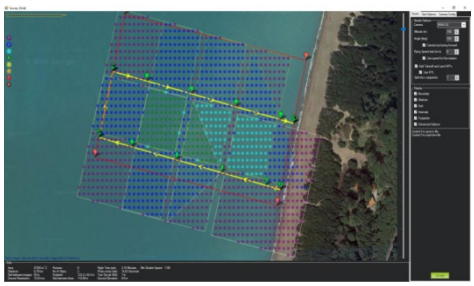

Figure 3. UAV flight plan

A SbEs, up to 2 m depth, and MbEs bathymetric survey down to 12 m were carried out on the same day on the study area (Fig. 4). These measurements have been converted into elevations relative to national vertical datum, and averaged at 5x5 m grid for noise reduction. A certain number of SBCPs (Sea Bottom Control Points) have been used for RWD output calibration (50, 200, 500 Pts). The remaining points were used for method validation and a verification of the goodness of the result.

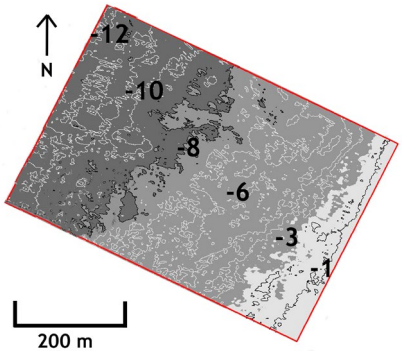

Figure 4. 2018 bathymetric survey

Significant morphological variations are present from the shoreline to the external side of the bar system (approx. 4 m depth), whereas offshore this limit minor changes occur.

Images processing sequence (SAT and UAV):

- Ortho-rectification – mosaic;
- Radiance and reflectance conversion;
- Land mask;
- Sun glint correction;
- Stumpf Relative Water Depth (RWD) testing different pairs of bands;
- Density slice at spectral reflectance intervals;
- Density slice calibration with real survey depths testing different number of SBCPs;
- Bathymetric map and DTM (Digital Terrain Model) at different scale resolution.

Figure 5 shows a UAV RGB image (left) and the Relative Water Depth image (right) derived by applying the equation (1). Warm colours indicate shallow water (S) and cold ones for deeper waters (D).

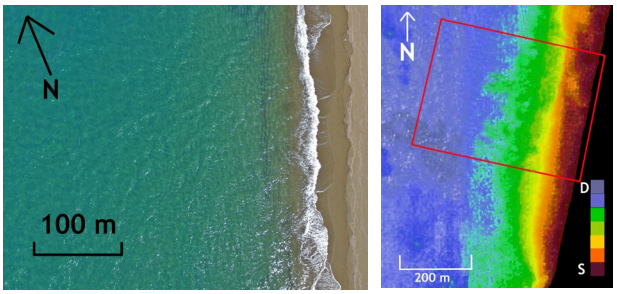

Figure 5. UAV RGB image (left) and Relative Water Depth image (right)

4. RESULTS

Depth values retrieved from UAV and from SAT images have been compared with measured depth in 28.000 points.
Scatter plot of Surveyed bathymetry *vs.* SAT RWD (Fig. 6) shows a points dispersion growing with the depth and in the bars area.
Poor correlation near the depth of closure, better with AUV RWD, where morphological changes are minor, are very likely due to accuracy reduction where light penetration is low, whereas point dispersion in the nearshore is mostly the result of morphological variation of the system in the time passed between the bathymetric survey and satellite image acquisition. Satellite data fairly average water depth between the bars and approximately 7 m depth; under-estimate depth in the bar area and in the very offshore part of the profile, whereas over-estimation is between -7 and -9 m.

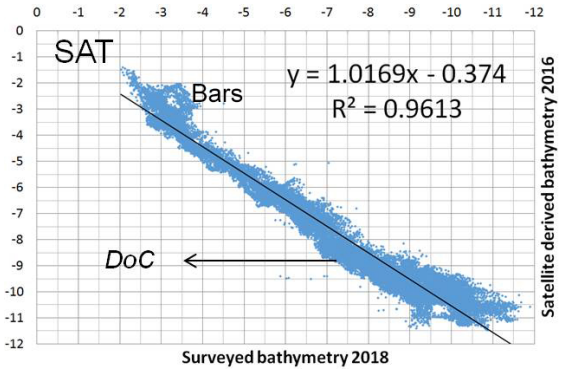

Figure 6. SAT RWD and measured bathymetry plot

In Surveyed bathymetry *vs* UAV-RWD graph (Fig. 7) points dispersion is lower and correlation higher. Under-estimation is in shallower and deeper water, whereas in intermediate water over-estimation is present. The same is significantly increasing approximately below 10 m depth.

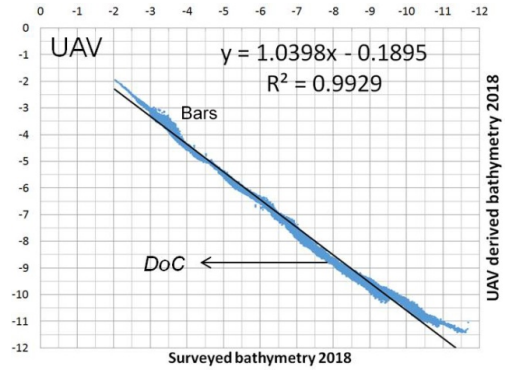

Figure 7. UAV RWD and measured bathymetry plot

A comparison between surveyed and estimated bathymetric profiles, located at the centre of the study area, is reported in Figure 8, where a larger deviation for satellite than UAV estimated bathymetry from measured data is evident.

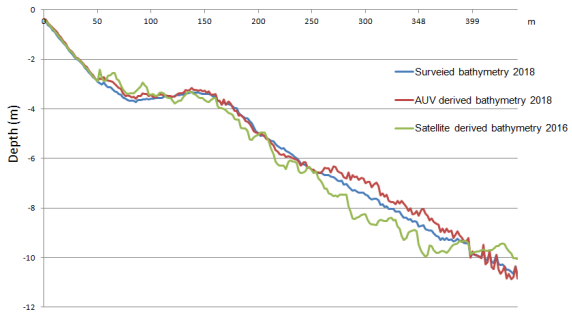

Figure 8. SAT-UAV RWD and surveyed profile

A verification of the goodness of the results was made also with the Mean Absolute Deviation (MAD) between measured and estimated values (m) at different depth ranges for the considered 28.000 points (Table 1).

Blue - Green		
Depth	**SAT**	**UAV**
0-5	0.43	0.21
0-11	0.59	0.47

Coastal Blue - Green		
Depth	**SAT**	**UAV**
0-5	0.49	0.29
0-11	0.71	0.60

Table 1. MAD for different depth and bands combination.

For both the methodologies best band combination in our test area and condition is Blue (440–510 nm) - Green (520–590 nm). On the contrary MAD using Coastal Blue – Green bands at 5 m depth was 0.29 cm.
Moreover, not many calibration points are necessary to obtain the most accurate bathymetry. Using 50, 200 or 500 calibration points the difference in terms of accuracy is less than 1 % of the depth down to -5 m.

5. CONCLUSION

In the study area Stumpf et al. (2003) log-ratio model demonstrated to accurately estimate water depth in shallow water and homogeneous sea bottom. UAV derived bathymetry accuracy showed to be higher compared to what present in literature for satellite derived depth (Panchang and Kaihatu, 2018) and also confirmed in this research. This is more evident close to the depth of closure where morphological changes are minor reducing the possible error due to the two years before satellite data.
Furthermore, a disadvantage in using satellite images for any beach monitoring is the availability of data acquired in the requested period. Clouds presence and sea conditions can also limit images availability. On the contrary, UAV surveys can guarantee low cost and easily acquired images for coastal monitoring on small to medium size areas.
Data availability with UAV survey is more immediate than with satellite and this is useful when other field activities must be carried out immediately after the survey and based on acquired data (e.g. sediment or water sapling) or in case of an urgent coastal monitoring. Moreover, it can be combined with the 3D survey of the emerged coast and is not necessary to perform any atmospheric correction.
With an accuracy of *circa* 20 cm (down to 5 m depth) it allows to connect the dry beach topography to the single- or MbEs survey, at depth where the latter cannot operate.
Further tests are necessary to better understand the real potential and limits of this methodology in order arrive to a standardization of the process and make it an useful tool for shallow water bathymetry.

AKNOWLEDGEMENTS

This research was developed within Interreg Marittimo IT-FR MAREGOT cooperation and in collaboration with Geocoste snc.

REFERENCES

Hedley, J.D., Harborne, A.R. and Mumby, P.J. (2005). Simple and robust removal of sun glint for mapping shallow-water benthos *Int. J. Remote Sensing,* 26 (10), 2107-2112.

Jupp, D. L. B. (1988). Background and extensions to depth of penetration (DOP) mapping in shallow coastal waters. In Proceedings of the Symposium on Remote Sensing of the Coastal Zone (p. IV-2).

Lyzenga, D.R. (1978). Passive remote sensing techniques for mapping water depth and bottom features. *Appl. Opt.* 17, 379–383.

Panchang, V. and Kaihatu, J.M. (2018). Advances In Coastal Hydraulics. World Scientific, Singapore, 502 pp.

Pushparaj, J. and Hegde, A.V. (2017). Estimation of bathymetry along the coast of Mangaluru using Landsat-8 imagery. *Journal of Ocean and Climate: Science, Technology and Impacts.* 8, (2), 71-83.

Said, M., Mahmud, M. and Hasan, C. (2017). Satellite-derived bathymetry: accuracy assessment on depths derivation algorithm for shallow water area.
The International Archives of the Photogrammetry. Remote Sensing and Spatial Information Sciences, Vol. XLII-4/W5.

Stumpf, R.P., Holderied, K. and Sinclair, M. (2003). Determination of water depth with high-resolution satellite imagery over variable bottom types. *Limnol. Oceanogr.*, 48, 547–556.

ANALYSIS OF WATER BODIES UNDER PARTIAL CLOUD CONDITIONS USING SATELLITE IMAGES

R. Neware[1]*, M. Thakare[1], U. Shrawankar[2]

[1] PG Scholar, Dept. of Computer Science and Engineering, G.H. Raisoni college of Engineering Nagpur, Maharashtra, India – (neware_rahul.ghrcemtechcse, mansi.thakare.ghrcemtechce)@raisoni.net

[2] Sr. Member, IEEE, Dept. of Computer Science and Engineering, G.H. Raisoni college of Engineering Nagpur, Maharashtra, India – urmila@ieee.org

KEY WORDS: Water Bodies, Satellite Images, Vector Data, SVM, Positive and Negative Buffering, Polygons.

ABSTRACT:

The technique of obtaining information or data about any feature or object from afar, called in technical parlance as remote sensing, has proven extremely useful in diverse fields. In the ecological sphere, especially, remote sensing has enabled collection of data or information about large swaths of areas or landscapes. Even then, in remote sensing the task of identifying and monitoring of different water reservoirs has proved a tough one. This is mainly because getting correct appraisals about the spread and boundaries of the area under study and the contours of any water surfaces lodged therein becomes a factor of utmost importance. Identification of water reservoirs is rendered even tougher because of presence of cloud in satellite images, which becomes the largest source of error in identification of water surfaces. To overcome this glitch, the method of the shape matching approach for analysis of cloudy images in reference to cloud-free images of water surfaces with the help of vector data processing, is recommended. It includes the database of water bodies in vector format, which is a complex polygon structure. This analysis highlights three steps: First, the creation of vector database for the analysis; second, simplification of multi-scale vector polygon features; and third, the matching of reference and target water bodies database within defined distance tolerance. This feature matching approach provides matching of one to many and many to many features. It also gives the corrected images that are free of clouds.

1. INTRODUCTION

Satellite images are known as remotely detected images, which enables precise mapping of land cover and highlights scenes that are justifiable on local, mainland and even worldwide scales. Normally, governments and big corporate houses across the world launch and operate their own imaging satellites, which record and collect images of our planet and other different planets in the galaxy. Satellite images are extremely efficient in mapping expanded regions (Neware and Khan, 2018).

In India, the Hyderabad-based National Remote Sensing Centre (NRSC) ISRO, is at the forefront of keeping track, through satellite images, on the relative standing and position of all water surfaces in the country. It also issues a fortnightly publication giving information about water spread areas. Thus, since 2012 the Centre has been collecting time-segmented information about water surfaces. This has been organised in a geo-spatial database under the classification of water reservoirs. Listed as Water Body Information System (WBIS), this data is published on Bhuvan Geo-platform, for observation and queries relating to areas of water spread. It provides integrated view of water-spread dynamic for over 12,500 water reservoirs in the nation. But the appearance of cloud can lead to errors or underestimation of the spread in a few areas, as optical images cannot penetrate cloud cover (Bhuvan Water Body Information System, 2018; Neware and Khan, 2018).

Several methods were tried and used to restore the cloud affected areas, but most of them are used now for removing thin clouds (Chanda & Majumder, 1991). To remove cloud and shadow defects Abd-Elrahman et al. used fusion techniques. Which is also used by have Borchartt et al. and suggested a new method that works well, but the algorithm fails to compensate cloud-shadow, so the scaling factor, for each segment of the image, has be secured experimentally (Abd-Elrahman et al., 2008; Borchartt et al., 2011).

This paper advances a new approach to obtain cloud-free satellite images by comparing cloudy target images with cloud-free reference images with the help of vector data processing. The samples used in this study include the water reservoirs of Maharashtra, comprising areas greater than 3000 m. This database is in vector form represented by complex polygons. Each polygon shows a particular water body in Maharashtra state. For this analysis Quantum Geographical Information System (QGIS) is used. QGIS is open source software used for the different GIS operations (QGIS-2.8-UserGuide, 2018).

2. LITERATURE REVIEW

Taking a look at the relevant literature, we find that in their study Abraham and Sasikumar analysed together with visible and infrared satellite images, remotely sensed RGB and monochrome images, using adaptive segmentation algorithm to detect the cloud in cloudy regions. First, they converted RGB images into YIQ and then measured average intensity. Variation in window size indicated the cloud present in an image. Then, applying threshold to images, they extracted the cloud (Abraham & Sasikumar, 2013). Meanwhile, to extract cloud Yuan and Hu advanced the segmentation strategy, which employs the Bag-of-Words (BoW) model to divide image into super-pixels to extract its features. Then Simple Vector Machine (SVM) is applied to separate cloud and cloud-free areas in a training data sample (Yuan & Hu, 2015). Finally, GrabCut algorithm, which delineates the foreground and background parts of an image correctly, is employed get better cloud region. But on their part Bai et al. have focused on the smart information reconstruction (SMIR) technique to restore cloud-contaminated images through use of Extreme Learning Machine-ELM (Bai et al., 2016). For instance, on an image of a lake captured by Moderate Resolution Imaging Spectroradiometer (MODIS), SMIR is applied to get the loss value of reflectance, resulting from cloud, in the image. Then, application of Back

* Corresponding author

prorogation (BP) neural network algorithm gives a comparison between cloudy and non-cloudy pixels in the image. Finally, a thorough analysis creates cloud-free images in time series.

In their study, to interpret cloud coverage in satellite images Ik-Hyun & Mahmood categorized cloud as thick cloud, thin cloud and ground cloud, using local and global threshold, the latter of which determines presence of cloud in an image (Ik-Hyun & Mahmood, 2015). This approach involves feature extraction and feature matching, outlier removal, re-sampling process. It uses uniform feature scale invariant feature transform (UF-SIFT) to obtain more correct image classification. However, to create cloud-free satellite images, Chen et al. execute spatially and temporally weighted regression (STWR) model. This model involves choice of spatial and temporal pixels, interpretation of target and reference images, analysis of cloud-affected area through use of spatially and temporally weighted regression (STWR), removal of similar pixels in images through use of inverse distance weighted (IDW) and finally, creation of repetitive cloud-free images by processing cloudy images (Chen et al., 2017). Meanwhile Machiwal et al. present an extensive survey of water management techniques available in remote sensing area, the remote sensing and GIS applications for monitoring the surface water bodies and the pre-processing stages for data extraction and analysis in remote sensing area. Expounding the fundamental concept of GIS in water bodies' data monitoring, it also highlights its limitation areas (Machiwal et al., 2010).

On the other hand, the study of Hargrove et al. puts forth the Goodness-of-Fit (GoF) approach to calculate degree of sameness in two or more than two spatial datasets. This method interprets the degree of best among different datasets that are in polygon form and can be applied to the entire satellite map (Hargrove et al., 2006). For comparing two datasets, this approach uses GoF algorithm, which marks the intersection between two polygonal data that assigns the values of insideness and area weighting term. Meanwhile, the research paper of Huh focuses on the matching technique for spatial data sets' boundary edges, which uses the string-matching algorithm. In this, spatial data sets' boundary points are culled in pre-processing stage. Then, polygon objects are separated in the form of string for further interpretation (Huh, 2015). To ensure correctness of string matching, buffering is executed. Finally, the study of Martínez et al. advocates executing Boolean operations on polygons. The stated algorithm is effective for concave polygons, several contour and intersecting edges. It creates the resulting contour as common intersecting area between two polygons. Then, the polygons' edges are subdivided and those that lie inside or outside of another polygon are chosen. When the common edges of two intersecting polygons are joined, the contour is created (Martínez et al., 2009).

From the above literature review it is evident that researchers have used satellite image datasets in diverse areas of study. It also transpires that water management has also emerged as a crucial field in today's world and the fact that remote sensing can facilitate its study. Particularly, the analysis of water bodies needs to be focused on and improved, with special emphasis on proper analysis of features of surface water bodies.

3. VECTOR DATA ANALYSIS IN SATELLITE IMAGES

The structure of a vector data model is far removed from the structure of a raster data model. A vector model stores all spatial data as a line, point or polygon. On the other hand, a raster data model uses sets of grid cells to record all data. In remote sensing, vector data is referred to as coverage. In this paper, vector data is represented as coverage. The three types of spatial data - a point, line or polygon - are referred to as features, and a vector GIS can be termed a feature-based technology (Qingxiang et al., 2012). The shape of the spatial entity is stored using two-dimensional (x, y) coordinate system.

In this study, polygon feature represents water bodies in vector data format. Polygon encloses a homogeneous area which is a set of (x, y) coordinate pairs. Figure 1 shows a water body at Nizamabad and Adilabad through a complex polygon structure.

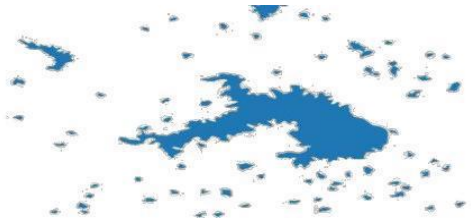

Figure 1. Polygon Representing Water Body at Nizamabad and Adilabad

4. METHODOLOGY

4.1 Creation of Database for Vector Analysis

Creation of Database for Vector Analysis Database for the vector data processing is done in QGIS framework which includes the coverage of Maharashtra water bodies whose area is greater than 3000 m. Figure 2 shows workflow of this study. Figure 3 (a) and (b) display the water bodies listed in Bhuvan Geo-platform's Water Body Information System (WBIS), representing Maharashtra state and Jayakwadi respectively.

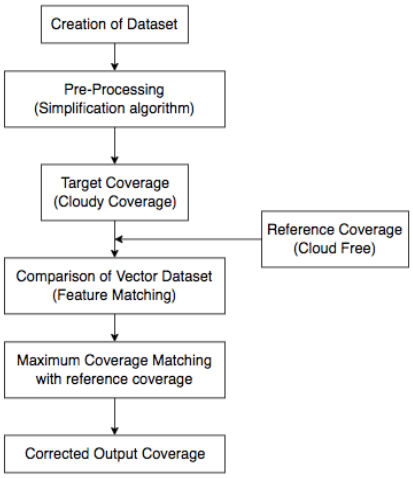

Figure 2. Study Workflow

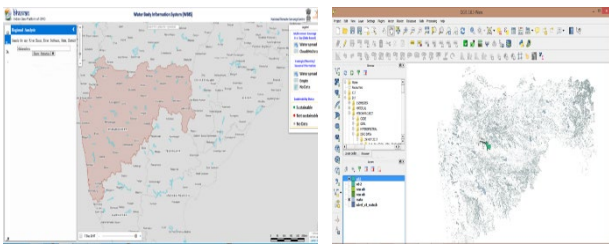

(a) (b)

Figure 3. (a) Showing different water bodies from Maharashtra State in Bhuvan portal, (b) Selection Specific District (Maharashtra) to create a particular Subset of Database

4.2 Simplification of Multi-Scale Vector Polygon Features

For comparing the two polygon vector data sets for the feature matching purpose, geometric characteristics of polygon play an important role. Some nodes of polygon feature also play a significant role. And among the outline feature point of the polygon, some decisive points can be extracted to recognize shapes. The specific points (shown in Figure 4) are the articulation points of the polygon (Shao and Tong, 2010). During the process of gradual change of gradient, theses points can decide the geometric shape of elements, known as the principle points. The rest of the point also characteristics point, less important than the principal points (Xie et al., 2010). In order to meet the actual requirement for GIS data producing, an adaptively improved algorithm based on Douglas-Peucker is used, which simplifies the vertices of polygon without changing its actual features. It also uses a parameter, which is distance threshold-T, to increase the matching accuracy.

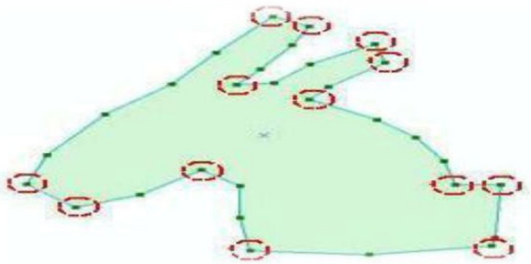

Figure 4. Principal Points in Polygon Features

The delineated method is implemented in the QGIS framework through visual inspection, quantitative measures and applications in water body contours. QGIS speeds up the data processing workflow with acceptable results as shown in Figure 5 (QGIS-2.8-UserGuide, 2018).

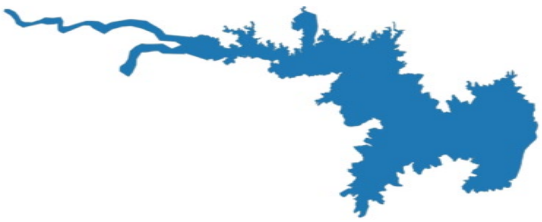

Figure 5. Polygon Edges Simplification

4.3 Providing the Distance Tolerance

In GIS, distance tolerance is called as buffer. Buffering is the process of creating one or more zones around selected features, within a pre-specified distance from these features (smith et al., 2015). Buffering usually creates two areas, positive (outward) and negative (inward) buffers as shown in Figure 7. Here, positive and negative buffering operations are performed to create two polygons, external and internal to the original geometry as shown in Figure 6. The distance tolerance used during this study is 70 meters. This method allows the comparison between two datasets with specified distance tolerance, which can be deemed also as buffering zone.

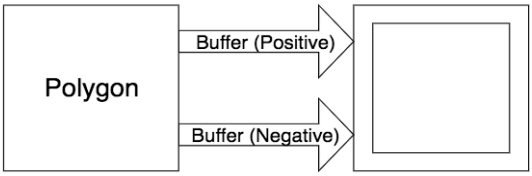

Figure 6. Demonstrates the effect of positive and negative buffering operations carried out on a simple polygon.

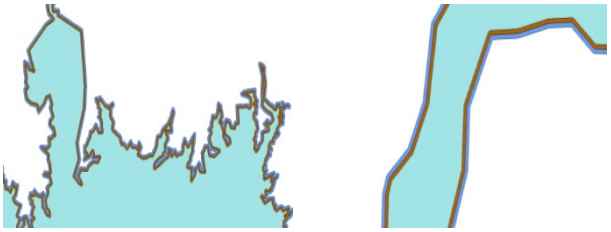

(a) (b)

Figure 7. (a) Buffer Polygon, (b) Positive and Negative buffer to the original Water body (Shown in Brown Color)

4.4 Feature Matching

Feature matching means to identify identical features or entities in different sources through some similarity measures, which is a process of establishing correspondence between spatial features. The existing matching algorithms can be divided into geometric matching, topological matching, and semantic matching (Chan-Hee & Yun-Ho, 2011). During this study, the feature matching method implemented uses positive and negative buffering operations to blend with the basic topological test's setup, if the geometries match. Figure 8. represents the cloud-free reference coverage of a water body at Aurangabad district. Figure 9. represents the cloudy coverage of the same location. After the feature matching, corrected coverage is obtained of the same location as shown in Figure 10.

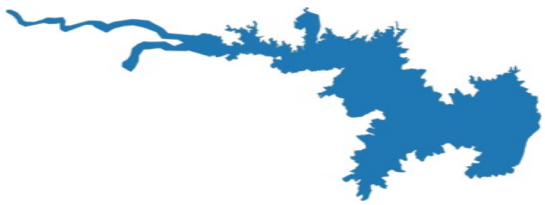

Figure 8. Water Body Coverage at Aurangabad-Cloud Free

Figure 9. Water Body Coverage at Aurangabad Cloud

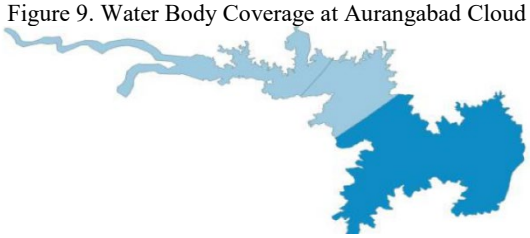

Figure 10. Corrected Water Body Coverage at Aurangabad

5. CONCLUSION

This study paper provides the analysis to obtain cloud-free satellite images of water bodies. Feature matching of water bodies, in the form of spatial vector data, gives simplified workflow to retrieve cloud-free images. Furthermore, the algorithm that simplifies the complex polygonal structure of water bodies also removes the noise in original datasets and improves stability. This study is based on spatial vector data matching, which helps in updating more efficiently datasets of cloud-free water bodies.

The results of this study can be implemented on a large number of datasets in various remote sensing applications. This suggests that matching vector objects within a buffering zone is the proper method of relating pixel locations to geographical coordinates for the purpose of automatic recording of cloud free satellite images.

REFERENCES

Abd-Elrahman, A., Shaker, I.F., Abdel-Gawad, A.K., Abdel-Wahab, A., 2008. Enhancement of Cloud-Associated Shadow Areas in Satellite Images Using Wavelet Image Fusion. World Applied Sciences Journal 4(3), 363–370.

Abraham, L., & Sasikumar, M., 2013. Cloud Extraction and Removal in Aerial and Satellite Images. Intelligent Informatics, 341–347. doi:10.1007/978-3-642- 32063-7_36.

Bai, K., Chang, N.-B., & Chen, C.-F., 2016. Spectral Information Adaptation and Synthesis Scheme for Merging Cross-Mission Ocean Colour Reflectance Observations from MODIS and VIIRS. IEEE Transactions on Geoscience and Remote Sensing, 54(1), 311–329. doi:10.1109/tgrs.2015.2456906.

Bhuvan | Water Body Information System 2018. Bhuvan.nrsc.gov.in, http://bhuvan .nrsc.gov.in/gis/thematic/wbis/#!/map. (20 March 2018).

Borchartt, T.B., de Melo, R.H.C., Gazolla, J.G.F.M., Resmini, R., Conci, A., Sanchez, A., de A. Vieira, E. (2011). On the reduction of cloud influence in natural and aerial images. In: 18th International Conference on Systems, Signals and Image Processing, pp. 1–4.

Chan-Hee H, Yun-Ho K, 2011. Fast Shape Matching Using Statistical Features of Shape Contexts. IEICE Transactions on Information and Systems, pp. 2056-2058.

Chanda, B., & Majumder, D. D., 1991. An iterative algorithm for removing the effect of thin cloud cover from LANDSAT imagery. Mathematical Geology, 23(6), 853– 860. doi:10.1007/bf02068780.

Chen, B., Huang, B., Chen, L., & Xu, B., 2017. Spatially and Temporally Weighted Regression: A Novel Method to Produce Continuous Cloud-Free Landsat Imagery. IEEE Transactions on Geoscience and Remote Sensing, 55(1), 27–37. doi:10.1109/tgrs.2016.2580576.

Hargrove, W. W., Hoffman, F. M., & Hessburg, P. F., 2006. Mapcurves: a quantitative method for comparing categorical maps. Journal of Geographical Systems, 8(2), 187–208. doi:10.1007/s10109-006-0025-x

Huh, Y., 2015. Local edge matching for seamless adjacent datasets with sequence alignment. ISPRS International Journal of Geo-Information 4: 2061–2077. Doi:10.3390/ijgi4042061.

Ik-Hyun Lee, & Mahmood, M. T., 2015. Robust Registration of Cloudy Satellite Images Using Two-Step Segmentation. IEEE Geoscience and Remote Sensing Letters, 12(5), 1121–1125. doi:10.1109/lgrs.2014.2385691.

Machiwal, D., Jha, M.K., & Mal, B.C., 2010. Assessment of Groundwater Potential in a Semi-Arid Region of India Using Remote Sensing, GIS and MCDM Techniques. Water Resources Management, 25(5), 1359-1386. doi:10.1007/s11269-010-9749-y.

Martínez, F., Rueda, A. J., & Feito, F. R., 2009. A new algorithm for computing Boolean operations on polygons. Computers & Geosciences, 35(6), 1177–1185. doi:10.1016/j.cageo.2008.08.009.

Meng Qingxiang, Fu a Zhongliang, Huang b Yan and Shen Meicen, 2012. A fast matching approach of polygon features, *ISPRS Journal of the Photogrammetry, Remote Sensing and Spatial Information Sciences*, Volume I-2, pp.45-49.

Neware R., and Khan A., 2018. Survey on Classification techniques used in remote sensing for Satellite Images', in 2nd International conference on Electronics, Communication and Aerospace Technology (ICECA 2018), pp.1860-1863.

Neware, R. and Khan, A., 2018. "identification of agriculture areas in satellite images using supervised classification technique," international journal of creative research thoughts (IJCRT), 6(2), pp.682-688, 2018.

QGIS-2.8-UserGuide-en.pdf | Geographic Information System | Command Line Interface. Scribd. https://www.scribd.com/document/353653928/QGIS-2-8-UserGuide-en-pdf. (10 February 12, 2018).

QGIS-2.8-UserGuide-en.pdf | Geographic Information System | Command Line Interface. Scribd. https://www.scribd.com/document/353653928/QGIS-2-8-UserGuide-en-pdf. (February 12, 2018).

Shao S, Tong C, 2010. A matching method for multi-characteristic vector elements of complex polygon. 2010 International Conference on Multimedia Technology (ICMT), pp. 1-4.

Smith, Goodchild, Longley, 2015. Geospatial Analysis – 5th Edition, 2015. http://www.spatialanalysisonline.com/HTML/index.html?simple_regression_and_trend_su.html

Xie J, Xu G, Zhang F, et al., 2010. A local tangent space-based approach for single-trial representation of event-related potentials. 5th Cairo International Biomedical Engineering Conference, CIBEC2010, pp.184-187.

Yuan, Y., & Hu, X., 2015. Bag-of-Words and Object-Based Classification for Cloud Extraction from Satellite Imagery. IEEE Journal of Selected Topics in Applied Earth Observations and Remote Sensing, 8(8), 4197–4205. doi:10.1109/jstars.2015.2431676.

ESTIMATING VULNERABILITY OF WATER BODY USING SENTINEL-2 IMAGES AND PREDICTIVE EUTROPHICATION MODELS: the STUDY CASE OF BRACCIANO LAKE (Italy)

C. Giuliani[1]*, M. Piccinno[1], A. Veisz[1], F. Recanatesi[2]

[1] DIAP, Department of Architecture and Design, Sapienza, University of Rome, Borghese Square 9, 00186, Rome, Italy – (chia.giuliani, matteo.piccino, adrienn.veisz)@uniroma1.it

[2] DAFNE, Department of Agriculture and Forest Sciences, Tuscia University, Viterbo, San Camillo de Lellis snc Road, 01100, Viterbo, Italy – fabio.rec@unitus.it

KEY WORDS: Bracciano Lake, Multispectral images Sentinel-2, Supervised classification, Vulnerability, Eutrophication status, monitoring

ABSTRACT:

Due to the concomitance of several factors related to progressive climate changes and to increased water management for anthropogenic usage, drastic fall in level of Bracciano Lake was reported in the summer of 2017. By November 2017, the water level decreased 0,198 meters below the hydrometric zero established at 163.04 meters s.l.m. Such alarming rate has not been detected in the last seventeen years. The consistent change in water level causes modifications in its environment, on the edge of the coasts and specifically, brings about an increase in the rate of eutrophication (trophic enrichment phenomenon).
The determination of the volume of water contained in the lake basin was estimated with GIS tools modeling, by analysing the bathymetry of the water body and applying the supervised classification of Sentinel-2 images; this allowed to identify the reservoir and consequently to reconstruct the course of the coastline. Once defined the hydrometric reduction in the water body for the observed period, the Vollenweider model, that calculates the trophic state of a lake, was used to quantify nutrients concentration and relative increase of eutrophication status as a consequence of the anthropic activities practiced in the belonging basin.
The quantification of the water level changes of Bracciano Lake, before and after the hydrometric crisis, occurred in 2017, related to the estimate of the level of eutrophication, allows us to define the degree of vulnerability of the lake ecosystem. The proposed methodology represents an efficient monitoring tool for assessing the vulnerability of water bodies influenced by eutrophication.

1. INTRODUCTION

The Italian Ministry of the Environment and Protection of Land and Sea with the Water Framework Directive (WFD) 2000/60/CE (European Commission, 2000) aims to achieve ambitious goals: avoiding deterioration of freshwater quality and quantity, improving water quality and promoting sustainable water use based on a long-term protection of available water resource.
The eutrophication of the drainage basins is a leading cause of impairment of many freshwater and coastal marine ecosystems (Chislock et al, 2013). Eutrophication is now a problem on a world scale (Olem and Simpson, 1994; Chebud et al, 2011).
The eutrophication occurs, when the surface runoff and the resulting erosional processes can transport the nutrients, mainly phosphorus (P) and nitrogen (N), from human activities or industrial waste products, to the water basins. The surface water becomes overly enriched with minerals and nutrients that induce excessive growth of aquatic species and phytoplankton, that generate oxygen depletion. This process is defined as the phenomenon of trophic enrichment of the water bodies characterized by a slow turnover, which causes a degenerative state of water quality. This phenomenon motives the phytoplankton blooms that, by lowering the rate of oxygen, makes the environment unsuitable for other species. River basins, such as lakes, are very vulnerable with very long lake retention times (Wang and Pant, 2011). In fact, they receive oxygen in small quantities thanks to the mixing of the water due to winds and thermal gradients. If the plant biomass in the basins remain low, it can be degraded by aerobic route. When there is an increase in plant biomass, oxygen is no sufficient and, once it is over, anaerobic degradation processes are established, with the collapse of the system quality.
For instance, on the case of the Black Sea, since the Seventies, occurs this phenomenon due to the increase of phosphorus and nitrogen caused by human activities, in particular by the use of fertilizers. The inputs in the Nineties in the northern part of the Black Sea were six times higher than those in the Baltic Sea. The effects of eutrophication became evident in 2000 when on 14000 km2 of the total surface of the Black Sea, brown algae were supplanted by green and red algae controlled by cyanobacteria, that produces potent toxins also to humans. In 1992, the Convention for the Protection of the Black Sea from Pollution has been signed by the six bordering countries (Ukraine, Russia, Turkey, Georgia, Romania and Bulgaria) to develop strategic action plans. Another example is the Lake Okeechobee, in south-central Florida, which is also significantly damaged by the increasing levels of nutrients, come from anthropogenic activities, that lead to eutrophication. (Chebud et al, 2011).

Bracciano Lake is a lake of volcanic origin, part of the Regional Natural Park complex of Bracciano-Martignano lake, located in the Italian region of Lazio, 32 km northwest of Rome. The watershed is characterized mainly by natural and agricultural land uses, while the anthropic settlements represent a small area. During the summer of 2017, as result of water supply, evaporation and the lack of rainfall, Bracciano Lake experienced serious water deficits with water decrease of 0.181 meters below the hydrometric zero. The water level has continued to decline in November 2017 with a decrease of 0.198 m a.s.l. Such a fall in water level has serious consequences for its ecosystem,

* Corresponding author

biodiversity, tourism, while the lake's self-purifying capacities and its degree of eutrophication have also been affected.

1.1 Aim of the study

The present study, carried out within the catchment area of Lake Bracciano, aims to quantify the reduction of the water body for the observed period (between 2015 and 2017), to quantify nutrients concentration and the relative increase of eutrophication status, that allows us to define the degree of vulnerability of the lake ecosystem. Another purpose of this study is to arrange a monitoring tool useful for assessing the vulnerability of water bodies exploited for water supply.
The study required to proceed by steps as follows:
1. Creation of an LCM (Land Cover Map) with the help of supervised classification of Sentinel-2 images, accomplished in QGIS with Semi-automatic classification plugin (Congedo, 2016), determination of the diffused structure (Sprawl);
2. Digitization and modeling of bathymetric Map; The model was done by using the "Topo to raster" tool in ArcGIS which allows creation of hydrologically correct digital elevation models (DEMs). As such, it is the only ArcGIS interpolator specifically designed to work intelligently with contour inputs. The "Surface Volume" tool by ArcGIS allows you to calculate the area and volume of a specific region between a surface and a reference plane.
3. Determination of the phosphorus (P) load at the basin scale with the application of the GLEAMS (Ground water Leaching Effects of Agricultural Management Systems) model to quantify phosphorus load for the considered scenarious (kg / ha / year) from each land use class (Sarmah A. K. et al., 2005; Leone et al., 2009; Reyes M.R. et al., 2004; Garnier M. et al., 1998; De Paz J. M. et al., 2002; Knisel W. G. et al., 1991, 1993; Stallings C. et al., 1992), and estimation of the total load at crisis (2017) and before crisis (2015), with Vollenweider model.

2. MATERIALS AND METHODS

In order to reach our goals, we applied remote sensing of satellite images and predictive eutrophication models. The analysis was conducted in two scenarious (2015, 2017) to compare the pre-crisis scenario with the critical one occurred in 2017.
The research process can be overviewed in Figure 1, at the workflow chart, that shows the progress of the data collection, data analysis and the outputs.

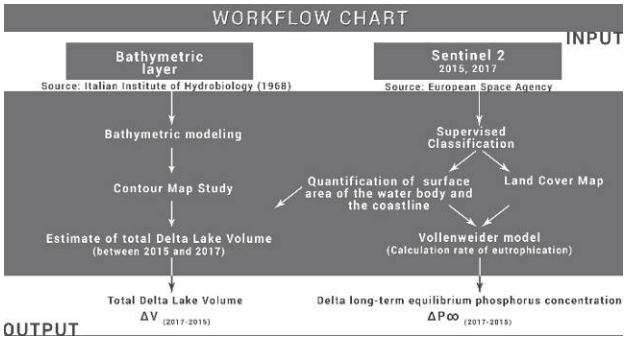

Figure 1. Workflow of the proposed methodology

Open access data were collected and analysed with two different types of Geographic Information System (GIS): ESRI's ArcGIS for bathymetric modelling and Quantum GIS for the production of supervised classifications. The Bathimetric layer, collected from the Italian Institute of Hydrobyology (1968), were used to model the water body and to estimate the change of the Lake volume between 2015 and 2017. Supervised Classification were conducted in Quantum GIS (open-source software), with Sentinel-2 satellite images (open access European Space Agency; https://scihub.copernicus.eu/; period December 2015 and November 2017) in order to quantify the surface area of the water body, the coastline, and to create the land cover map.
The phosphorus export coefficients were determined using the GLEAMS simulation model, Ground water Loading Effects of Agricultural Management Systems. GLEAMS is a simulation model of the field hydrological balance. It allows to simulate and then evaluate the effects of agricultural practices on the chemical compounds movement in the root zone, the leaching of the same, the percolation and the soil erosion determined by the various cultivation techniques.
The final step was the Vollenweider model, applied to calculate the degree of eutrophication and, in this way, calculate the vulnerability of the lake ecosystem (Rana Magar and Khatry, 2017; Milstead et al., 2013). This model, proposed by the Austrian limnologist in 1976, is very useful for territorial analysis, as it correlates, with considerable simplicity, the P export from a lake basin caused by land use and the lake trophic state.

2.1 Bathymetry and Edge of Bracciano Lake in GIS environment.

The official Bathymetric Layer of Bracciano-, Martignano- and Monterosi Lake, belongs to the Italian Institute of Hydrobiology, published in 1968, was instantly obtained at scale 1: 25.000. In order to quantify the volume of the water body, bathymetry and edge map study was conducted in geographic information system (GIS) environment. The scanned Bathymetric map (600 dpi) was georeferenced in WGS 84 coordinate system, and all lake depicted were digitized and translated in intelligent contour polygons with quotas above sea level and above the hydrometric zero of Bracciano´s water body (Figure 2). The GIS software has allowed us to gain a model with the bottom of the water body.

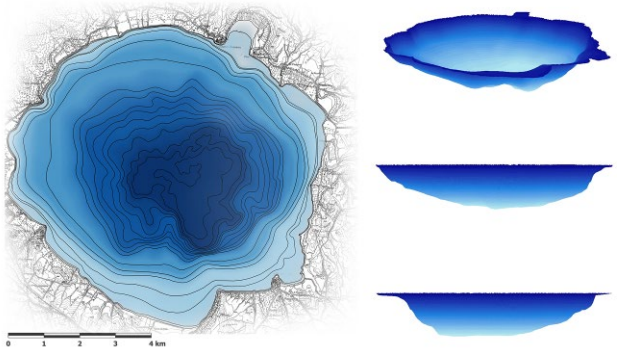

Figure 2. Bathymetry and Edge Map Study, GIS model of the water body

Having a detailed bathymetric map and the lake surfaces in the two years, the volume of water (3) was calculated for the two scenarios (2015, 2017). The calculation was done by using the *surface volume routine* within ArcMap, which calculates the area and volume of a raster or tin surface above or below a given reference plane, using the bathymetric map of the water body and its shoreline as input.
The GIS software has allowed us to gain a model with the bottom of the water body. The model was done by using the "Topo to raster" tool in ArcGIS 10.3, which allows the creation of hydrologically correct digital elevation models (DEMs). As such, it is the only ArcGIS interpolator specifically designed to work intelligently with edge inputs.

The informative digital elevation model (DEM) layer was implemented with a spatial resolution of 10 meters (Figure 3), better than the one usually used by the sen2core tool.

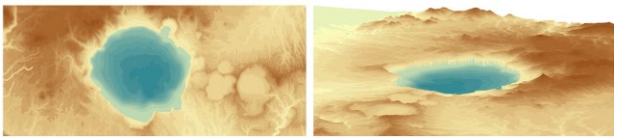

Figure 3. Digital Elevation Model of Bracciano basin

2.2 Supervised Classification of Sentinel-2 Multi Spectral Images (2015, 2017)

To investigate the quantitative and spatial variation of the hydrometric level of Bracciano lake, we used Sentinel-2 multispectral images, which were processed through the Sen2core program. Sen2Cor is a processor for Sentinel-2 Level 2A product generation and formatting; it performs the atmospheric-, terrain and cirrus correction of Top-Of-Atmosphere Level 1C input data. Sen2Cor creates Bottom-Of-Atmosphere, optionally terrain- and cirrus corrected reflectance images; additional, Aerosol Optical Thickness-, Water Vapor-, Scene Classification Maps and Quality Indicators for cloud and snow probabilities.

The multi-temporal image datasets, selected for the study area through Sentinel-2 Multi Spectral Instrument (MSI), report a pre-crisis situation referred to December 2015 and a crisis scenario referred to November 2017. Both image datasets were processed by Supervised Classification (Semi-Automatic Classification plugin by Luca Congedo in the Quantum GIS software was used), that allowed us to produce a Land Cover Map (LCM) and to isolate the water body from the rest of the basin area and to quantify the surface and the perimeter of the coast (Figure 4).

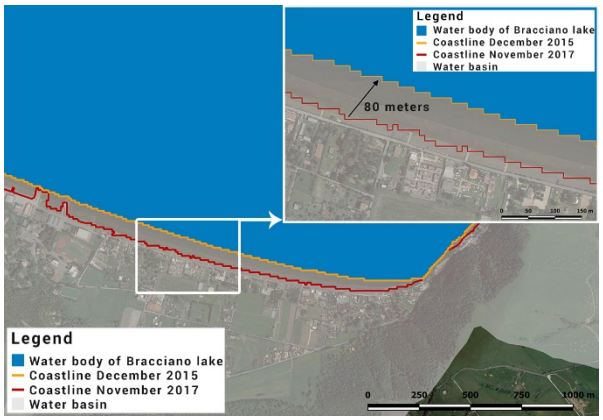

Figure 4. Coastline and the surface area determination

The Supervised Classification of Sentinel-2 Multi Spectral Images (2015, 2017) was significant also for the discrimination of the territory included in Bracciano basin in four main classes: the anthropic area consisting of the whole impermeable surfaces, the agricultural, the water body, forests and uncultivated areas.
The algorithm used for supervised classification is Spectral Angle Mapping, that calculates the spectral angle between spectral signatures of image pixels and training spectral signatures.
The validation process was based on the random distribution (for each land cover card) of 50 control points for each identified land cover class if the cover card reports less than twelve classes of coverage (Congalton, 1991). The control points were checked with information layers with higher spatial resolution and a confusing matrix was constructed. The results of the matrix return an overall accuracy close to 100% for the definition of the lake surface and 91% for the land cover map referred to 2018.
The realization of the land cover map updated to 2018 (Figure 5), correlated with GLEAMS phosphorus export coefficients allowed us to estimate the phosphorus and potassium concentrations that contribute to the eutrophication of the water body.

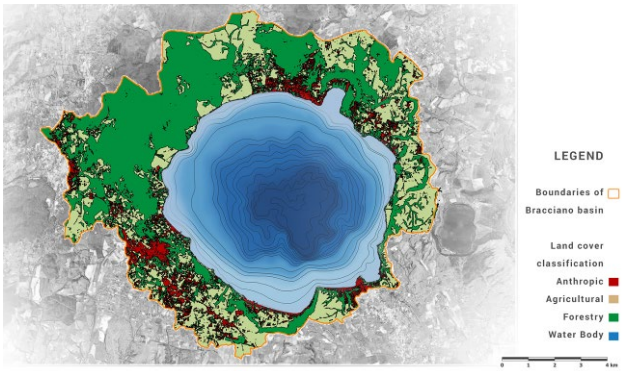

Figure 5. Supervised classification, LCM of Bracciano basin

2.3 Calculation of Phosphorus Concentration with Vollenweider model

The Vollenweider model (1) correlates the trophic state of a lake with the long-term equilibrium phosphorus [P] concentration, [µg / l] (2) with anthropic activity and with the morphology of the relevant catchment basin.

$$[P]\infty = \frac{L(P)\, t_w}{Z\,(1+t_w)} \qquad (1)$$

where
[P]= long-term equilibrium phosphorus [P] concentration, [µg/l];
Z = average depth of the lake, [m];
t_w = theoretical renewal time of lake water, [years].
L(P)= specific surface load, [Kg/Km^2]

$$L(P)=CfAf+CagAag+CuAu+CaA0+Cst*Na*(1-SR) \qquad (2)$$

where
Cf = export coefficient for the forest territory;
Cag = export coefficient for the agricultural territory;
Cu = export coefficient for urbanized areas;
Ca = export coefficient from atmospheric contributions
Cst = export coefficient related to the impact on the lake of the urban waste system;
Af = forest area (ha);
Aag = agricultural area (ha);
Au = urbanized area (ha);
Ao = area of the lake (ha);
Na = number of inhabitants served by septic tanks (leaking).
SR = coefficient linked to soil retention factors

The phosphorus export coefficients were determined using the GLEAMS simulation model, *Ground water Loading Effects of Agricultural Management Systems*.
The SR coefficient, linked to soil retention factors, has been defined equal to 0, assuming that all the nutrient produced arrives in the long term in the lake because of the morphology of the river basin and the shape of a volcanic caldera.
We obtained the land use areas considered in the Vollenweider model with the Supervised Classification of the land cover map. The total surface of the Urban Area (697.76 ha) was divided

between the surface of the building served by the sewerage service and the sprawl that could leak nutrients by the septic tanks. In the model only the sprawl area was considered.
The Na parameter, "number of inhabitants served by septic tanks", was obtained, photo-interpreting Google Earth aerial images of the year 2018, 8763 sprawl units and considering an average of 2 residents per unit.

3. RESULTS

The surface of the water body in the two selected temporal scenarios (December 2015 and November 2017) was determined as a result of the supervised classification process that allowed to quantify the surface of the water mirror and therefore the variation of the coastline.

ΔWATER BODY SURFACE (2015-2017) = 88.44 ha

The data modeling, related to the bathymetry of Bracciano Lake´s water body, allows to provide high quality information to evaluate the volume of water resources. The coastline and the surface area determination, correlated to the modelled bathymetry data, helped us to assess the volume of the water resources and its delta between the two periods (1).

2015: $V = 4194356497{,}95\ m^3 = 4194356497949\ l$ (3)
2017: $V = 4054711145{,}44\ m^3 = 4054711145440\ l$
$\Delta V = 139645352{,}51\ m^3 = 139645352510\ l$

where V = volume of water

Considering the surface, obtained with the land cover analysis (Table 1), we achieve the phosphorus amount stem from land use infiltration and urban system (Table 2).

Land Cover Surfaces	(ha)
Sprawl	219.08
Urban Area	697.76
Agricultural area	8596.24
Forest/uncultivated	4109.69
Total Basin Area	**13403.69**

Table 1. The measurement of Land Cover

P origin	P kg/year 2015	P kg/year 2017
Forest/uncultivated	410.97	410.97
Agricultural area	5157.74	5157.74
Sprawl	59.15	59.15
Atmospheric contributions	285.12	280.69
Urban waste system	2891.79	2891.79
Total $L_{(P)}$	8804.77	8800.34

Table 2. The influence of land use on the Phosphorus level

Using the Vollenweider model considering the phosphorus load $L_{(P)}$ of 2015 (same basin area) for both scenarios and depth of the lake for the two years (88.6 m in the 2015; 86.6 m in the 2017) we obtained the P concentration:

$P\infty_{2015} = 98.66\ \mu g/L$ $P\infty_{2017} = 100.93\ \mu g/L$ $\Delta P\infty = +2.28\ \mu g/L$

If we consider the volume of water that has been lost (ΔV) and the P concentration that we had in 2015 (98.66 µg/L), we can estimate the amount of P that was dissolved in the water and which contributing the increase of the total trophic level in 2017 equal to 13.78 tons.

4 CONCLUSIONS AND DISCUSSION

The application of Remote Sensing and the Vollenweider model have allowed us to estimate the critical nutrient load that affects Bracciano Lake and to define its trophic state according to the trophic classification scheme for lake waters proposed by the O.E.C.D. (Organization for Economic Co-Operation and Development - 1982 Eutrophication of waters, monitoring, assessment and control). The results of this study show the eutrophic state of the water basin in 2015 that recorded a deterioration in the scenario referred to November 2017, motivated by the reduction of the water volume. There was a reduction of 3.33% of the water volume, with an increase in the amount of phosphorus of 2.3% per liter. The increased eutrophication level can be justified also by the reduction of the surface in the first part of the coast where the major phytodepuration processes take place.
According to the lake water quality classification proposed by the OECD (O.E.C.D, 1982), currently the lake is classifiable as a very eutrophic lake that has reached a slightly hypertrophic level in the period of water crisis.
Both researchers and managers are seeking new applicable, effective way to understand freshwater ecosystem vulnerability to environmental change. the present case study research was carried out with mixed method analysis to develop an effective and reliable conceptual model for long term monitoring of freshwater ecosystems. The proposed methodology represents an efficient monitoring tool for assessing the vulnerability of water bodies influenced by eutrophication.

REFERENCES

Chebud, Y., Naja, G.M., and Rivero, R. (2011). Phosphorus run-off assessment in a watershed, Journal of Environmental Monitoring. 13(1), 66–73.

Chislock, M.F., Doster, E., Zitomer, R.A., and Wilson, A.E. (2013). Eutrophication: Causes, Consequences, and Controls in Aquatic Ecosystems. Nature Education Knowledge 4(4):10.

Congalton, R.G. (1991). A review of assessing the accuracy of classifications of remotely sensed data. Remote sensing of Environment. 37(1), 35-46.

Congedo, L. (2016). Semi-Automatic Classification Plugin Documentation..Release 6.0.1.1. DOI: 10.13140/RG.2.2.29474.02242/1.

De Paz, J.M., and Ramos, C. (2002). Linkage of a geographical information system with the gleams model to assess nitrate leaching in agricultural areas. Environmental Pollution. 118(2), 249-258.

European Commission (2000). Water Framework Directive (WFD) 2000/60/CE. Official Journal (OJ L 327), 22 December 2000.

Garnier, M., Porto, A.L., Marini, R., and Leone. A. (1998). Integrated use of GLEAMS and GIS to prevent groundwater pollution caused by agricultural disposal of animal waste. Environmental management. 22(5), 747-756.

Leone, A., Ripa, M.N., Uricchio, V., Deak, J., and Vargay, Z. (2009). Vulnerability and risk evaluation of agricultural nitrogen pollution for Hungary's main aquifer using DRASTIC and GLEAMS models. Journal of Environmental Management. 90(10), 2969-2978.

Milstead, W.B, Hollister, J.W., Moore, R.B., and Walker, H.A. (2013). Estimating summer nutrient concentrations in Northeastern lakes from SPARROW load predictions and modeled lake depth and volume. PLoS ONE, 8(11), Article number: e81457.

Olem, H. and Simpson, J. (1994). Lake and reservoir management. Water Environment Research, vol. 66, numero 4: 489-496.

Rana Magar, M. S., and Khatry, S.B. (2017). Vollenweider Model for Temporal Eutrophication Characteristics of Naghada Lake, Nepal. Asian Journal of Water, Environment and Pollution, 14(1), 29–39.

Wang, J,and Pant, H. (2011). Land Use Impact on Bioavailable Phosphorus in the Bronx River, New York, Journal of Environmental Protection, 2011, 2, 342-358.

Coastal monitoring by remote sensing

PRONENESS TO FUTURE MARINE INUNDATION OF CAMPANIA COASTAL PLAINS (SOUTHERN ITALY) IN RELATION TO THEIR SUBSIDENCE TRENDS ASSESSED BY INTERFEROMETRIC SAR TECHNIQUES

G. Di Paola[1]*, P.P.C. Aucelli[2], F. Matano[3], A. Rizzo[2]

[1] Department of Biosciences and Territory, University of Molise, Pesche, Isernia, Italy - gianluigi.dipaola@unimol.it
[2] Department of Science and Technology, University of Naples "Parthenope", Naples, Italy – (pietro.aucelli, angela.rizzo)@uniparthenope.it
[3] Consiglio Nazionale delle Ricerche, Istituto di Scienze del Mare (ISMAR), Naples, Italy – fabio.matano@cnr.it

KEY WORDS: Coastal subsidence; InSAR; Relative sea level rise; Coastal hazard mapping; Climate Change

ABSTRACT:

In Campania Region there are several coastal areas considered to be particularly prone to inundation hazards due to their geomorphologic and topographic features, being characterized by low-lying areas and relevant ground vertical displacements. Furthermore, these zones can be affected by the negative impacts of the ongoing eustatic Sea Level Rise (SLR), in terms of both erosion and flooding processes. SLR is locally enhanced by high subsidence trends. In this study, an evaluation of the current subsidence rates is provided, derived by the analysis of Synthetic Aperture Radar interferometry (InSAR) datasets acquired over the Campania coastal sectors from June 1992 to July 2010. The vertical ground displacements have been coupled with future SLR scenarios, in order to obtain the local Relative Sea Level Rise (RSLR) and identify the most critical areas along the Volturno, Sarno, Sele and Alento plains. The results highlight with a high resolution the importance of the InSAR data for the spatial hazard assessment to the coastal areas flooding. RSLR scenarios suggest that in the near future natural areas, beaches, human infrastructures, and wide portions of agricultural areas located in the plain will be potentially affected by marine flooding, with several zones located below the projected sea levels.

1. INTRODUCTION

The low coasts of Campania Region (southern Italy) are generally located along the main alluvial plains. During the Late Holocene, these coasts were subjected to progradation thanks to river sediment supplies and locally to volcanic deposit inputs. More recently, erosion and episodic flooding expose natural and anthropic assets to permanent damages. In general, these phenomena can be amplified by ground subsidence that may enhance marine inundation and irreversible coastal erosion processes (Wright et al., 2019; Shirzaei and Bürgmann 2018; IPCC, 2014; Pappone et al., 2012; Schaeffer et al., 2012; Teatini et al., 2012; Brambati et al., 2003).

The analysis of InSAR (Synthetic Aperture Radar Interferometry) data referred to the low coast sectors of the Campania Region (Volturno, Sarno, Sele and Alento alluvial coastal plains; Figure 1) highlights the presence of wide coastal sectors characterized by different Vertical Ground Displacements (VGD) (Vilardo et al., 2009). These phenomena are currently contributing to increase the exposure of these coastal areas to the negative impacts of marine processes, such as inundation and erosion. Several recent studies, such as Antonioli at al. (2017) underline the importance of a detailed estimate of subsidence rate in order to understand its causes and provide a more adequate management of the territory.

Based on both new and published data (Di Paola et al., 2018; Matano et al., 2018; Aucelli et al., 2017), this research provides a detailed evaluation of the subsidence rates in in the main coastal plains of Campania region, which are considered to be particularly prone to be inundated due to their low topography. In this study, the analysis and interpretation of interferometric SAR datasets acquired by three satellite (ERS, RADARSAT and ENVISAT) over the Campania coastal sectors (Figure 1) from June 1992 to July 2010 are shown. InSAR data provide new insights into the spatial variability of VGD (subsidence/uplift) which influences on the future marine inundation due to Relative Sea Level Rise (RSLR).

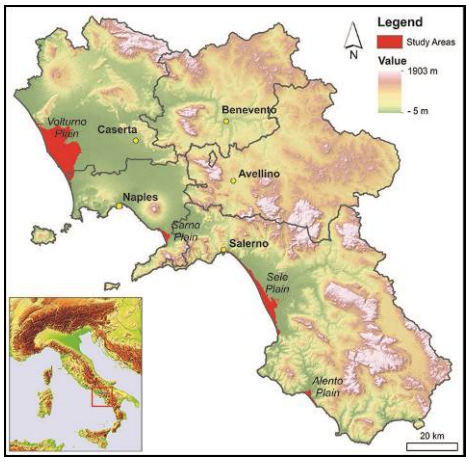

Figure 1. Location Map of the study areas in the Campanian Region

Campanian coast is about 450 km long and made of alternating high carbonatic rocky coasts (Sorrento peninsula and Cilento promontory), volcanic coastal sectors (Phlegrean Fields and Vesuvius) and low sandy coasts, including Volturno, Sele, Sarno and Alento Rivers alluvial coastal plains. These coastal plains, here investigated, are the terminal point of the major rivers in the region and their catchment areas comprising almost the whole territory of Campania, especially the ones of the Volturno and Sele Rivers. During the Early Holocene, these areas were affected by marine transgression caused by post-glacial sea level rise. Starting from 6.0 ky BP, and especially during the Greek-Roman and Late Roman periods, the shorelines prograded several hundred meters mainly due to the

* Corresponding author

decrease of the rate of late Holocene sea level rise, the increase of fluvial inputs due to climatic and land-use changes, and the deposition of the pyroclastic sediments of the 79 AD Vesuvius eruption (Cinque et al., 1996; Pappone et al., 2011).
The investigated plains have high social and economic value due to the presence of touristic activities that provide a high employment ratio, especially during the summer season. Moreover, in these areas agricultural and zootechnical activities, which are the main economic activities even associated with PDO (Protected Designation of Origin) dairy production, also take place. Finally, the high environmental value is due to the presence of several wide protected areas, protected also by UNESCO.

2. METHODS

2.1 InSAR Analysis

Italian national and regional remote sensing projects (Regione Campania, 2009; EPRS, 2015) have processed with different Persistent Scatterer Interferometry (PSI) techniques the available satellite radar interferometry data referred to a relatively long time period (1992-2010). These datasets have been implemented with different processing techniques, such as Permanent Scatterers (PS-InSAR) (Ferretti et al., 2001) and Persistent Scatterers Pairs (PSP) (Costantini et al., 2009), related to interferometric dataset acquired by C-band sensors onboard ERS-1/2, ENVISAT and RADARSAT satellites.
The post-processing and analysis of the available PSI datasets, related to Campania coastal plain sectors, allowed us to obtain a retrospective view on the spatial and temporal distribution of ground deformation for the studied alluvial coastal plains at a decennial scale.
For those areas common to both acquisition satellite geometries (ascending and descending orbits), the availability of coeval datasets from different point of view allows for the evaluation of the vertical components of the deformation, based on the interpolation of PS point data and some trigonometric calculations (Vilardo et al., 2009; Matano et al., 2018).
The obtained 50-m spaced grid maps show the distribution of the vertical components of ground deformation velocity in the coastal plains for the used datasets related to 1992–2000 (ERS-1/2), 2003–2007 (RADARSAT) and 2003–2010 (ENVISAT). In order to obtain a quantitative assessment of the subsidence process referred to the analysed period, the rates of Vertical Ground Deformation (expressed in mm/year) for the period 1992-2010 was calculated.

2.2 Coastal Inundation Analysis

To assess the potential coastal inundation, an initial requirement is the development the digital elevation models of the investigated areas. They have been defined by using LiDAR data of the Italian Environmental Ministry, which have 2 m cell resolution along the coastal stretch (800 m from the shoreline) and 1 m cell resolution within the coastal plains. In this study, both datasets have been taken into account, summing them using the tool Map Algebra in ArcGIS (ESRI©), in order to obtain a complete raster model with a 2 m cell size.
Based on the assumption that the subsidence trend will be kept constant for the near future, the VGD rates, detected by the PSI-based technique, have been used to obtain the future topography of the investigated coastal plains.
In details, VGD rates have been first projected to 2065 and 2100 then the grids of the predicted total amount of VGD in 2065 and 2100 have been added to the present day DEM obtaining the raster models of the 2065 and 2100 topographies.
Based on the criteria that the areas potentially prone to be inundated are those areas lying either below sea level or less elevated above it, the inundation maps for each projected sea level scenario have been defined for the investigated plains. As suggested by EUROSION (2004), the inland limit for the inundation analysis has been set at 5 m above sea level, including in this way the most susceptible coastal areas.

3. RESULTS

The PSI-derived VGD rates show that during the 1992 to 2010 time interval the coastal sector of the Volturno, Sarno, Sele and Alento alluvial coastal plains are characterized by different and complex vertical velocity patterns.
The coastal sector close to the Volturno River mouth is characterized by cumulate subsidence values between -50 to -150 mm during 1992-2010, whereas the dune ridge system shows low subsidence or stability (0 to -50 mm). Conversely, higher subsidence values (-50 to -200 mm) are found in the back-dune depressions, near Lake Patria and Villa Literno. The central part of the Volturno Plain displays subsidence values ranging from -50 to -400 mm with the highest negative values along the course of the Volturno River around the city of Cancello ed Arnone (Aucelli et al., 2017; Matano et al., 2018).
The Sarno River coastal plain is characterized by localized subsidence ranging between -5 to -20 mm during 1992-2010 near Castellammare di Stabia and higher values (-20 to -100 mm) near the river mouth. In the strip between 1 to 2 km inland the coastline, the ground shows stability trend (-5 to +5 mm), while along the inner alluvial plain strong subsidence affects the area close to the Sarno River around the city of Pompei.
Sele River coastal plain shows different subsidence pattern between northern and southern sectors (Di Paola et al., 2018). In northern sector of the plain, a continuous coastal strip, up to 18 km long, is characterized by cumulate subsidence values ranging between -50 to -200 mm during 1992-2010; the hilly area towards the east is characterized by stability or discontinuous uplift values (+10 to +50 mm). At the Sele River mouth area, a hot spot of subsidence, developing 5 km inland, is very evident (-50 to -150 mm), while the southern sector to the Sele River shows a general condition of stability with small subsiding areas (-25 to -50 mm).
Alento River coastal plain shows a moderate pattern of vertical ground deformation. While the northern sector shows subsidence between -5 and -30 mm during 1992-2007, the coastal narrow strip among Foce, Velia and Marina di Ascea displays stability or fair uplift (-5 to + 10 mm). Along the Alento River course, a hot spot of subsidence, developing 1-2 km inland, is evident (up to than -50 mm).
The coastal inundation maps obtained taking into account IPCC sea level rise scenarios predicted for the years 2065 and 2100 coupled with VGD (Figure 2, 3, 4 and 5) show that Campania plains exhibit different degree of marine inundation hazard, especially due to the various subsidence rates that characterize the investigated areas.
The InSAR analysis underlines that the plains are characterized by different VGD: they influence in different way the future topography of the plains increasing the RSL rates, as in the case of Volturno and Sele plains. RSLR will enhance the extension of the areas below the projected sea level, which represent the most susceptible zones to marine inundation. In 2100 scenario, they occupy a surface of 63.2 km^2 in the Volturno area, 9 km^2 in the Sele area, 0.3 km^2 in Sarno area and 0.2 km^2 in Alento area.

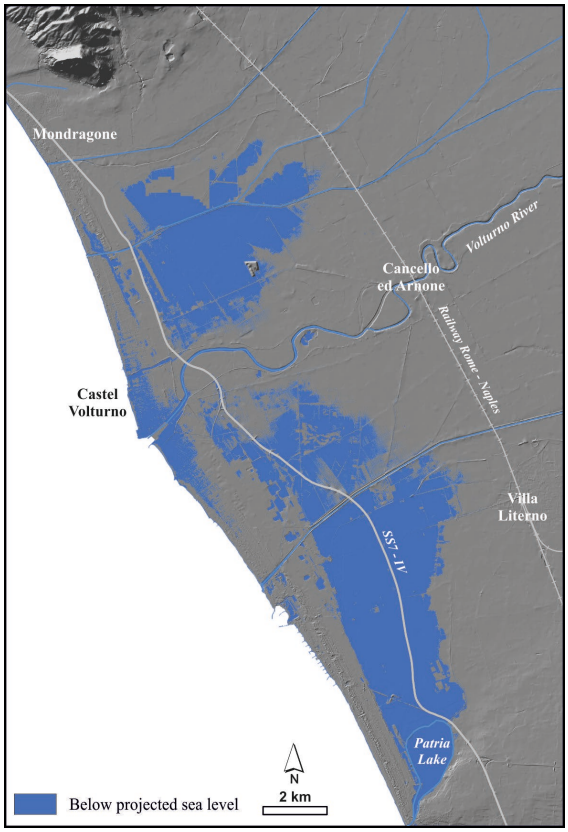

Figure 2. Area below the projected sea level in 2100 for the RCP8.5 scenario (Volturno coastal plain).

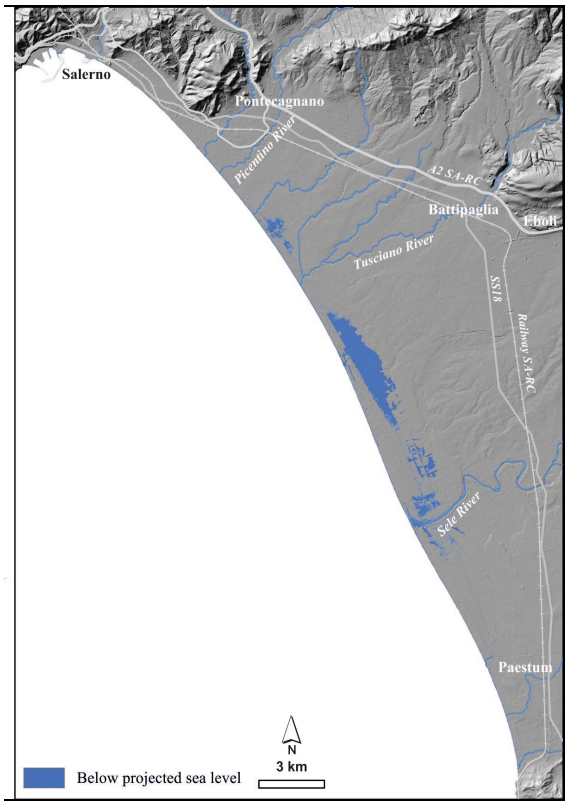

Figure 3. Area below the projected sea level in 2100 for the RCP8.5 scenario (Sele coastal plain).

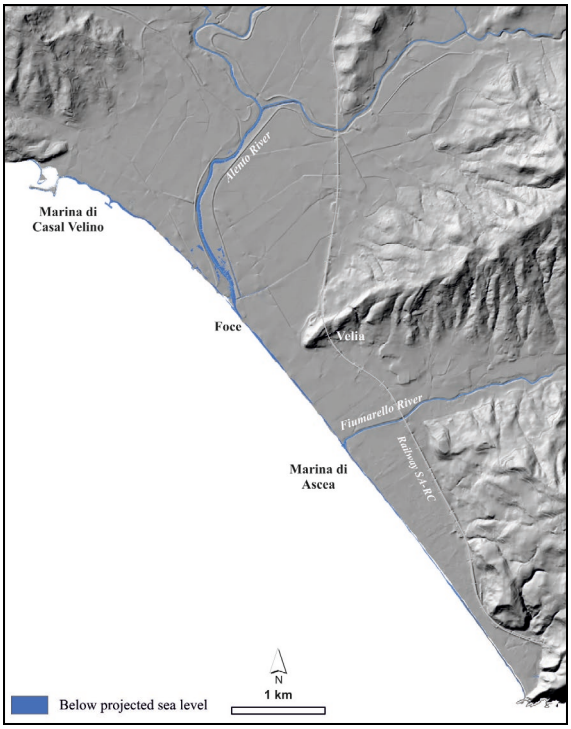

Figure 4. Area below the projected sea level in 2100 for the RCP8.5 scenario (Sarno coastal plain).

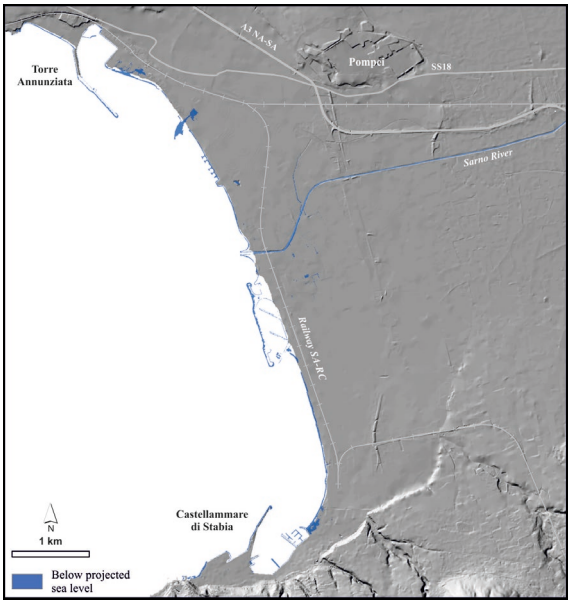

Figure 5. Area below the projected sea level in 2100 for the RCP8.5 scenario (Alento coastal plain).

The high resolution of the obtained results highlights the importance of the PSI datasets for the spatial susceptibility assessment to the inundation of the coastal areas. RSLR scenarios suggest that in the near future natural areas, beaches, human infrastructures, and wide portions of agricultural areas located in the investigated plains will be affected by potential marine inundation, with several zones in high hazard inundation level (Table 1).

	Volturno Plain		Sarno Plain		Sele Plain		Alento Plain	
	km^2	%	km^2	%	km^2	%	km^2	%
Present day	26.2	14.0	0.1	1.1	1.3	2.0	0.0	0.4
2065 RCP 2.6	37.5	20.1	0.1	1.2	3.8	5.7	0.1	0.7
2100 RCP 2.6	39.1	21.0	0.2	1.7	4.2	6.4	0.1	0.9
2065 RCP 8.5	49.2	26.4	0.2	1.9	6.2	9.4	0.1	1.6
2100 RCP 8.5	63.2	33.9	0.3	2.8	9.0	13.8	0.2	3.0

Table 1. Extend of the areas below the projected sea level in 2065 and 2100 expressed in km^2 and in percentage of each coastal plain.

4. DISCUSSION AND CONCLUSION

The analysis of the Campania coastal plains performed in this study highlights that all the investigated areas are characterized by negative vertical ground movements, with different areal distribution and rates, ranging from -1 to -25 mm/yr.

The subsidence of the Campania coastal plains can be considered as a natural process mainly due to the compaction of the alluvial sediments fill under the lithostatic load. Conversely, anthropic influences (e.g., water pumping and urbanization) are considered as an additional factor that locally enhances the subsidence processes.

The results here obtained confirm the fundamental importance of InSAR data analysis that, combined with other coastal trends indicators, enhances the hazard coastal inundation assessment due to SLR. In fact, the subsidence rates here evaluated can determinate an increase in future sea level rates at local scale, which could even became higher than the rates proposed by IPCC (2014) at global scale. Therefore, the proposed sea level hazard inundation maps represent a valuable tool for effective territorial management aimed to future coastal risk assessment and mitigation. To date, the management plans provided by the regional Authorities are drawn up according to the national regulations, which suggest taking into account only the impact of storm surges with different return periods in order to provide coastal flood risk maps. This study highlight the importance of introduce a dynamic component associated with the local VGD and future SLR projections for providing more detailed data on future RSLR hazard scenarios required for detailed coastal risk evaluation.

REFERENCES

Antonioli, F., Anzidei, M., Amorosi, A., Lo Presti, V., Mastronuzzi, G., Deiana, G., De Falco, G., Fontana, A., Fontolan, G., Lisco, S., Marsico, A., Moretti, M., Orrù, P.E., Sannino, G.M., Serpelloni, E. and Vecchio, A., 2017. Sea-level rise and potential drowning of the Italian coastal plains: Flooding risk scenarios for 2100. *Quaternary Science Reviews*, 158, pp. 29-43 https://doi.org/10.1016/j.quascirev.2016.12.021.

Aucelli, P.P.C., Di Paola, G., Incontri, P., Rizzo, A., Vilardo, G., Benassai, G., Buonocore, B. and Pappone, G., 2017. Coastal inundation risk assessment due to subsidence and sea level rise in a Mediterranean alluvial plain (Volturno coastal plain-southern Italy). *Estuarine, Coastal and Shelf Science*. 198, pp. 597–609 https://doi.org/10.1016/j.ecss.2016.06.017.

Brambati, A., Carbognin, L., Quaia, T., Teatini, P., Tosi, L., 2003. The Lagoon of Venice: geological setting, evolution and land subsidence. *Episodes* 26, pp. 264-268.

Cinque, A., Rosskopf, C., Barra, D., Campajola, L., Paolillo, G. and Romano, M., 1995. Nuovi dati stratigrafici e cronologici sull'evoluzione recente della Piana del Fiume Alento (Cilento, Campania). *Il Quaternario*, 8(2), pp. 323-338.

Costantini, M.; Falco, S.; Malvarosa, F.; Minati, F.; Trillo, F. Method of Persistent Scatterer Pairs (PSP) and high resolution SAR interferometry. In Proceedings of the 2009 IEEE International Geoscience and Remote Sensing Symposium (IGARSS), Cape Town, South Africa, 12–17 July 2009; Volume 3, pp. 904–907.

Di Paola, G., Alberico, I., Aucelli, P.P.C., Matano, F., Rizzo, A. and Vilardo, G., 2018. Coastal subsidence detected by Synthetic Aperture Radar interferometry and its effects coupled with future sea-level rise: the case of the Sele Plain (Southern Italy). *Journal of Flood Risk Management* 11(2), pp. 191-206 https://doi.org/10.1111/jfr3.12308.

EPRS-E. 2015. Not-Ordinary Plan of Environmental Remote SensingWeb Page. National Geoportal (NG) of the Italian Ministry of Environment and of Protection of Territory and Sea. http://www.pcn.minambiente.it/GN/en/projects/not-ordinary-plan-of-remote-sensing

EUROSION. 2004. Living with coastal erosion in Europe: sediment and space for sustainability. Reports on-line. http://www.eurosion.org

Ferretti, A., Savio, G., Barzaghi, R., Borghi, A., Musazzi, S., Novali, F., Prati, C. and Rocca, F., 2007. Sub-millimeter accuracy of InSAR time series: experimental validation. *IEEE Transactions on Geoscience Remote Sensing*. 45(5), pp. 1142-1153 https://doi.org/10.1109/TGRS.2007.894440.

IPCC, 2014. Fifth assessment report—climate change 2014. Impacts, adaptation and vulnerability: regional aspects. Cambridge University Press, Cambridge

Matano F., Sacchi M., Vigliotti M. and Ruberti D., 2018. Subsidence Trends of Volturno River Coastal Plain (Northern Campania, Southern Italy) Inferred by SAR Interferometry Data. *Geosciences*. 8, 8 https://doi.org/10.3390/geosciences8010008.

Pappone, G., Alberico, I., Amato, V., Aucelli, P.P.C., Di Paola, G., 2011. Recent evolution and the present-day conditions of the Campanian Coastal plains (South Italy): the case history of the Sele River Coastal plain. *WIT Trans. Ecol. Environ.* 149, pp. 15-27 http://dx.doi.org/10.2495/CP110021.

Pappone, G., Aucelli, P.P.C., Alberico, I., Amato, V., Antonioli, F., Cesarano, M., Di Paola, G. and Pelosi, N., 2012. Relative sea-level rise and marine erosion and inundation in the Sele River coastal plain (Southern Italy): scenarios for the next century. *Rendiconti Lincei* 23, pp. 121-129 https://doi.org/10.1007/s12210-012-0166-4.

Regione Campania. 2009. Progetto TELLUS web page. http://www.difesa.suolo.regione.campania.it/content/category/4/64/92/

Schaeffer, M., Hare, W., Rahmstorf, S. and Vermeer M., 2012. Long-term sea-level rise implied by 1.5 °C and 2 °C warming levels. *Nature Climate Change*. 2(12), pp. 867–870 https://doi.org/10.1038/nclimate1584.

Shirzaei, M., and Bürgmann, R. 2018. Global climate change and local land subsidence exacerbate inundation risk to the San Francisco Bay Area. *Science Advances*. 4(3), eaap9234.

Teatini, P., Tosi, L., Strozzi, T., Carbognin, L., Cecconi, G., Rosselli, R. and Libardo, S., 2012. Resolving land subsidence within the Venice Lagoon by persistent scatterer SAR interferometry. *Physics and Chemistry of the Earth*, 40-41, pp. 72-79 https://doi.org/10.1016/j.pce.2010.01.002.

Vilardo, G., Ventura, G., Terranova, C., Matano, F., Nardo, S., 2009. Ground deformation due to tectonic, hydrothermal, gravity, hydrogeological, and anthropic processes in the Campania region (southern Italy) from permanent scatterers synthetic aperture radar interferometry. *Remote Sensing of Environment* 113, pp. 197-212 https://doi.org/10.1016/j.rse.2008.09.007.

Wright, L.D., Syvitski, J.P.M. and Nichols, C.R. 2019. Sea Level Rise: Recent Trends and Future Projections. In: Wright L., Nichols C. (eds) Tomorrow's Coasts: Complex and Impermanent. Coastal Research Library, vol 27. https://doi.org/10.1007/978-3-319-75453-6_3.

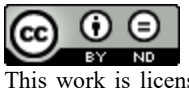

LASER SCANNER AND MULTIBEAM INTEGRATED SURVEY FOR THE ASSESMENT OF ROCKY SEA CLIFF GEOMORPHOLOGICAL HAZARD

S. Guida[1], N. Corradi[1], B. Federici[2], A. Lucarelli[3], P. Brandolini[1]*

[1] DISTAV, Dipartimento di Scienze della Terra, dell'Ambiente e della Vita, University of Genoa, 16132 Genoa,, Italy - geosaraguida@libero.it, corradi@dipteris.unige.it, brando@unige.it

[2] DICCA, Dipartimento di Ingegneria Civile, Chimica e Ambientale, University of Geonoa, 16145 Genoa, Italy, - bianca.federici@unige.it

[3] DSS, Drafin Sub Survey, Genoa, Italy - alucarelli@dssurvey.com

KEY WORDS: Laser scanner, Multibeam echosounder, Rocky coast, Geomorphologic hazard, Gallinara island, NW Italy

ABSTRACT:
Within land management of coastal zone, considering both emerged and submerged areas, a large amount of high resolution georeferenced spatial data is required. Remote sensing techniques fully satisfy these needs and allow to obtain all information in a single survey campaign. An integrated survey of laser scanner and multibeam techniques has been experienced along the rocky cliffs of the Gallinara Island (Western Liguria, Italy), in order to produce a geomorphological map addressed to hazard evaluation. The resulting data allowed obtaining significative geo-structural and morphological information to evaluate the quality of the sea cliffs and the definition of their susceptibility to instability.

1. INTRODUCTION

The rapid technological evolution of the survey techniques has led many researches to focus on their integration and on the management and elaboration of the huge amount of data produced (point clouds and digital terrain/surface models), paying attention to reach the necessary precision and resolution (Nex et al., 2014; Gagliolo et al., 2018; Passoni et al., 2018), in various application fields, from the analysis of the territory to the cultural heritage.
Within land planning and management strategies in coastal areas, the application of remote sensing techniques, such as multibeam, laser scanner and terrestrial or UAV photogrammetry, in support of geomorphological hazard assessment is of great interest and relevance (Faccini et al., 2005; Mills et al., 2005; Rosser et al., 2005; Brandolini et al., 2007a; 2009; 2013; 2015; 2017; 2018; Naylor et al., 2010; Mancini et al., 2013; Del Monte et al., 2015; Monteys et al., 2015; Troisi et al., 2015; Aguilar et al., 2016; Raso et al., 2016; 2017; Capra et al., 2017). In the framework of rocky coastal environment, where it is necessary to get detailed georeferenced data both at sea and inland, remote sensing techniques allow the acquisition of the whole information in a single and integrated survey campaign.
In the context of this topical issue, a survey of rocky coast and seabottom of Gallinara Island (Western Liguria, Italy; Fig. 1) was carried out with the aim to produce a geomorphological map of the emerged and submerged coastal zone (Brandolini et al., 2007b; Cevasco et al., 2013; Scarpati et al., 2013; Lucchetti et al., 2013; Brandolini et al., 2018). Gallinara, included in a regional park since 1989, is a small island with an extent of 0,11 km^2 and a maximum elevation of 87 m a.s.l. The island is mainly featured by the cropping out of quartzites and secondly by conglomerates belonging to "Quarziti of Monte Bignone" Formation (Upper Cretaceous).
The small extent of Gallinara, together with its particular meteomarine climate conditions, makes the island a large scale significative laboratory for testing the application of remote sensing technologies within coastal geomorphological investigations and management. Hence the final aim of this study is the production of a susceptibility map to rock coast instability.

Figure 1. Location of the study area and north-west view of Gallinara Island.

2. METHODS

2.1 Integrated survey

The integrated coastal survey has been performed using a Laser Scanner (LS) RIEGL mod. LMS-Z420i, a MultiBeam EchoSounder (MBES) R2Sonic 2024, two GPS 5700 TRIMBLE in RTK (Real Time Kinematic) base-rover configuration and an IMU IXBLUE mod. HYDRINS III.
The survey has been carried out in only two days, mainly from the seaside, not having access to the island, because private, except for the refuge port of public property. A boat properly equipped by the Teledyne Reson PDS2000 platform for the simultaneous acquisition of MBES and LS in profiler mode data (Fig. 2), circumnavigated the island. In the refuge port a static LS survey from the protective piers, integrated with RTK GPS positioning along transects in the area characterized by low water depth, where the boat was not able to enter, has been performed too. GPS positioning was also necessary to georeference both the cornerstones (four on the coast and one in the refuge port of the island) by means of a static survey, and the boat by placing the base receiver on the island's cornerstones and the rover on the boat, connected to the acquisition platform.
The RIEGL instrument, characterized by 1 km maximum range and a repeatability of 8 mm on a single measurement and 4 mm on average, allowed reaching precisions of the order of 1 cm

* Corresponding author

during the static survey. The static LS survey has been performed in three different positions and three cylindrical targets reflectors were used, in addition to natural or anthropogenic targets, to improve the accuracy of the cloud registration phase. In profiler mode precision varies between 3 and 5 cm, depending on the angular precision of IMU and the distance from the cliff.
LS was also integrated with a camera so to associate the color to the resulting point cloud
The MBES instrument is characterized by a 256 beams of 0,5° x 1° beamwidth across and along track at 450 kHz. In order to investigate the portions of the bottom close to the free surface, the Multibeam was mounted on a joint angled at 30°, thus physically tilting the transducer to exploit the entire swath of the MBES.
The MBES system requires a preventive calibration phase both for the synchronization of the time scale of each instrument (IMU, MBES, LS) with respect to the GPS time and for the compensation of the Roll, Pitch and Yaw rotations due to the mechanical assembly of the system with respect to the ideal configuration. An analogous manual calibration procedure is necessary for the correction of the Roll, Pitch and Yaw parameters of the Laser Scanner Profiler.
The MBES control interface allows data filtering, which is essential both for the automatic removal of most noise in water often caused by navigation motion. Sound Velocity Probe (SVP) allow to reduce the depth measurement error. Despiking is recommended to be performed manually by an experienced operator, especially in presence of articulated geological structures.
Seabottom MBES, processed by the platform Teledyne Reson PDS2000, allowed to obtain a detailed submerged Digital Terrain Model (DTM) of 0,25x0,25 m resolution. The static LS data, processed with the software Riscan Pro by Riegl, and the profiles LS data, processed by the platform Teledyne Reson PDS2000, allowed to describe the emerged rocky coast at 2-4 cm resolution. The final result was the reconstruction of a continuous 3D model both for emerged and submerged coastal zone (Figs. 3, 4), that allows to extract information on site geology and geomorphology.

Figure 2. On board technical equipment for the integrated survey: 1) GPS-RTK; 2) IMU; 3) SVP; 4) MBES; 5) LS.

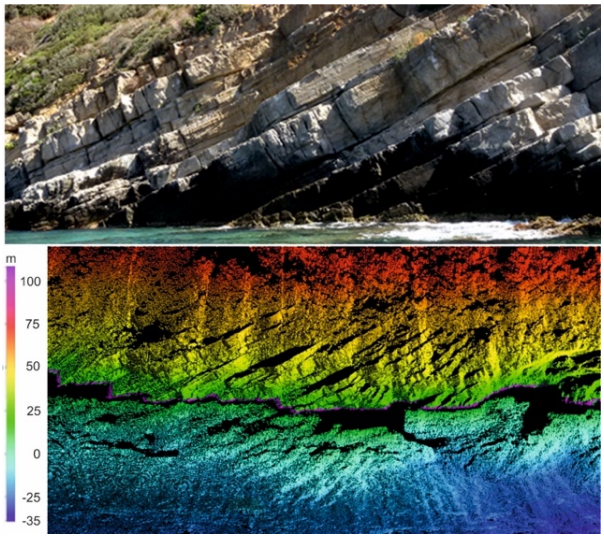

Figure 3. Example of clouds points continuity between Multibeam and Laser Scanner acquisition: comparison a current photo (A) and integrated survey (B).

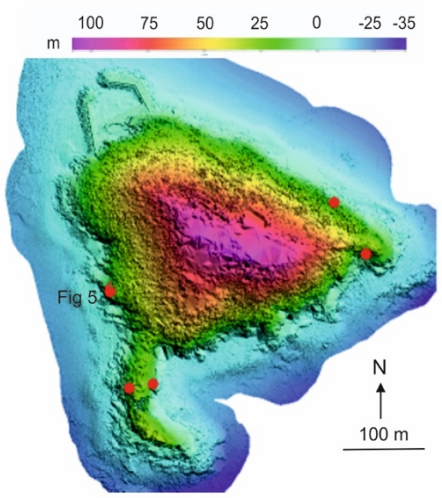

Figure 4. Gallinara Island DTM. The red dots indicate the SCMR test areas.

2.2 Geomorphological hazard mapping

The obtained data, checked and integrated with field observations and aerial photo interpretation, allowed to produce a geomorphological map following the guidelines of the new legend of the Italian Geomorphological Map proposed by AIGEO, the Italian Association of Physical Geography and Geomorphology (Mastronuzzi et al., 2017; Chelli et al., 2018).
Moreover, the processing of the collected data (e.g. characteristics of the outcrops and the joints) allowed the application of the "Sea Cliff Mass Rating" (SCMR) method for the evaluation of the quality and state of stability of sea cliffs (Lucchetti et al., 2013). SCMR partly takes in account the index Slope Mass Rating (SMR) by Romana (1993), introducing some new parameters related to the interaction of sea wave with cliff and seabottom (e.g. slope angle of the cliff; angle between the sea waves direction and the coast line; broken or breaking waves and the sea wave energy).
Finally, a susceptibility map of coastal instability, based on the correlation between SCMR and geomorphological data, has been produced according to the methods proposed by Lucchetti et al. (2014). Five classes of susceptibility of coastal instability (SCI) have been identified according to their quality and state of

stability. Moreover a sixth class, defined as “techno-coast", has been added to represent the harbor works and others man made interventions that have completely obliterated the sea cliff.

3. RESULTS AND FINAL REMARKS

Thanks to the effectiveness of the configuration adopted during the acquisition, MBES and LS have been correctly aligned and integrated in order to reconstruct in great detail the morphology of the Gallinara Island. Seabottom multibeam data allowed to obtain a detailed grid of 0,25x0,25 m of the submerged area, while emerged rocky coast were described at a 2-4 cm resolution by laser scanner data.

The 3D digital model of both emerged and submerged areas was reliable and useful for geomorphological and structural analysis of the entire island. Based on DTM data, together with field survey and aerial photo interpretation, geomorphological features of the island have been outlined: the whole perimeter of the island is mainly characterized by active rocky cliff with height up to about 30 m; an active coastal rock fall landslide is located in the southern sector affect by the main wave from SW (dominant) and SE; two flat surfaces, identifiable as quaternary marine terraces, are observable on the eastern and western promontories at an elevation of about 30-32 m.

The high resolution of DTM allowed to measure the attitude of the layers and the main discontinuities features of the bedrock (Fig. 5) used for the application of SCMR classification.

The application of SCMR classification was carried out in 5 representative areas of the island, identified as red dots in figure 4. Measurements, made on approximately 50 m for each area, highlighted the quality of the sea cliff in relation to bedrock condition and sea wave action.

The correlation between SCMR and geomorphological data allowed to produce the susceptibility map of coastal instability of the island perimeter. Very high susceptibility (SCI-4) has been found in the southern sector of the island within a wider sector with medium susceptibility (SCI-2). The remaining sea cliff are classified between low (SCI-1) and very low (SCI-0), except for a small sector identified with high susceptibility (SCI-3), affected by an active rock fall (Fig. 6)

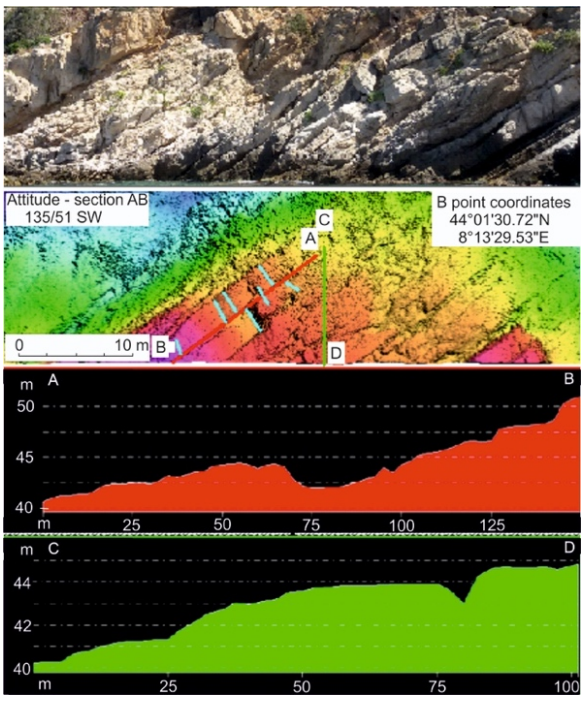

Figure 5. Example of attitude and joints measurement

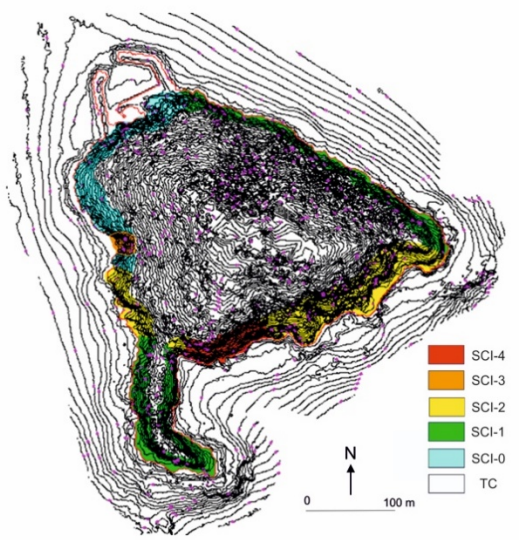

Figure 6. Susceptibility coastal instability (SCI) map: SCI-4 - very high susceptibility - active landslides and sea cliffs with SCMR = 0-20; SCI-3 - high susceptibility - deep seated gravitational slope deformation (D.S.G.S.D.) and sea cliffs with SCMR = 21-40; SCI-2 - medium susceptibility - sea cliffs with SCMR = 41-60; SCI-1 - low susceptibility - sea cliffs with SCMR = 61-80; SCI-0 - very low susceptibility - beaches and sea cliffs with SCMR = 81-100; TC - techno-coast.

In conclusion, the integrated remote sensing technologies showed to be very effective both in term of time, cost and accuracy of the result.

The application of an integrated survey based on MBES and LS techniques allowed detecting a large amount of high-accuracy and significant data in a single survey campaign, even in areas difficult to detect with direct traditional techniques. The results allowed assessing consistently the stability conditions of rocky coast, according to Lucchetti et al., highlighting the most hazardous areas along the south western sectors of Gallinara Island, which are exposed to dominant waves.

REFERENCES

Aguilar, F.J., Fernandez, I., Casanova, J.A., Ramos, F.J., Aguilar, M.A., Blanco, J.L., and Moreno, J.C., 2016. 3D Coastal Monitoring from very dense UAV-Based Photogrammetric Point Clouds, Advances on Mechanics, *Design Engineering and Manufacturing*, DOI: 10.1007/978-3-319-45781-9_88, (879-887).

Brandolini, P., Canepa, G., Faccini, F., Robbiano, A., and Terranova R., 2007a. Geomorphological and geo-environmental features of the Graveglia Valley (Ligurian apennines, Italy). *Geografia Fisica e Dinamica Quaternaria*, vol. 30, pp. 99-116, ISSN: 0391-9838

Brandolini, P., Faccini, F., Robbiano, A, and Terranova, R., 2007b. Geomorphological hazard and monitoring activity in the western rocky coast of the Portofino Promontory (Italy). *Quaternary International*, vol. 171-172, pp. 131-142, DOI: 10.1016/j.quaint.2006.11.006

Brandolini, P., Faccini, F., Robbiano, A., and Terranova, R., 2009. Slope instability on rocky coast: a case study of Le Grazie landslides (Eastern Liguria, Italy). In: Violante, C. (ed.) *Geohazard in Rocky Coastal Areas*. vol. 322, pp. 143-154, London, Geological Society, DOI: 10.1144/SP322.6

Brandolini, P., Faccini, F., Pelfini, M., and Firpo M., 2013. A complex landslide along the Eastern Liguria rocky coast (Italy). *Rendiconti Online Società Geologica Italiana*, vol. 28, pp. 28-31, ISSN: 2035-8008

Brandolini, P., Cevasco, A., 2015. Geo-hydrological risk mitigation measures and land-management in a highly vulnerable small coastal catchment. In *Engineering Geology for Society and Territory - Urban Geology, Sustainable Planning and Landscape Exploitation*. vol. 5, pp. 759-762, Springer International Publishing. DOI: 10.1007/978-3-319-09048-1_147

Brandolini, P., Faccini, F., Paliaga, G., Piana, P., 2017. Urban geomorphology in coastal environment: man-made morphological changes in a seaside tourist resort (Rapallo, Eastern Liguria, Italy). *Quaestiones Geographicae*, 36 (3), pp. 97-110. DOI: 10.1515/quageo–2017–0027 ISSN 0137–477X

Brandolini, P., Cevasco, A., Capolongo, D., Pepe, G., Lovergine, F., and Del Monte M., 2018. Response of terraced slopes to a very intense rainfall event and relationships with land abandonment: a case study from Cinque Terre (Italy). *Land Degradation & Development*, pp. 630-642, ISSN: 1099-145X, DOI: 10.1002/ldr.2672

Brandolini, P., Pepe, G., Capolongo, D., Cappadonia, C., Cevasco, A., Conoscenti, C., Marsico, A., Vergari, F., and Del Monte, M., 2018. Hillslope degradation in representative italian areas: just soil erosion risk or opportunity of development? *Land Degradation & Development*, Vol. 29, pp. 3050-3068. DOI: 10.1002/ldr.2999

Capra, A., Castagnetti, C., Dubbini, M., Gruen, A., Guo, T., Mancini, F., Neyer, F., Rossi, P., Troyer, M., 2017. High accuracy underwater photogrammetric surveying. In: Proceedings of 3rd IMEKO International Conference on Metrology for Archeology and Cultural Heritage. P. 696-701, ISBN: 978-92-990084-0-9, Lecce, Italy, 23-25 October 2017.

Cevasco, A., Pepe, G., and Brandolini P., 2013. Geotechnical and stratigraphic aspects of shallow landslides at Cinque Terre (Liguria, Italy). *Rendiconti Online Società Geologica Italiana*, vol. 24, pp. 52-54, ISSN: 2035-8008

Chelli, A., Aringoli, D., Aucelli, P.P.C., Baldassarre, M.A., Bellotti, P., Bini, M., Biolchi, S., Bontempi, S., Brandolini, P., Davoli, L., Deiana, G., et al., 2018. Morphodynamics of coastal areas represented in the new geomorphologic map of Italy: Draw the landforms of the past to outline the future. *Alpine and Mediterranean Quaternary*, vol. 31(1), pp. 17-21., ISSN (print): 2279-7327, ISSN (online): 2279-7335

Colbo, K., Ross, T., Brown C., and Weber, T., 2014. A review of oceanographic applications of water column data from multibeam echosounders. *Estuarine, coastal and shelf scien*ce, Elsevier, Vol. 145, 41-56.

Del Monte M., Vergari F., Brandolini P., Capolongo D., Cevasco A., Ciccacci S., Conoscenti C., Fredi P., Melelli L., Rotigliano E., and Zucca, F., 2015. Multi-method evaluation of denudation rates in small mediterranean catchments. In *Engineering Geology for Society and Territory, Climate Change and Engineering Geology*. vol. 1, pp. 563-567, Springer International Publishing, DOI: 10.1007/978-3-319-09300-0_105

Faccini, F., Brandolini, P., Robbiano, A., Perasso, L., and Sola, A., 2005. Instability, precipitation phenomena and land planning: The flood of 2002 in lower Lavagna valley (Eastern Liguria, Italy). *Geografia Fisica e Dinamica Quaternaria*, vol. suppl. VII, pp. 145-153, ISSN: 0391-9838

Gagliolo S., Fagandini R., Passoni D., Federici B., Ferrando I., Pagliari D., Pinto L., and Sguerso, D., 2018. Parameter optimization for creating reliable photogrammetric models in emergency scenarios. *Applied Geomatics*, pp. 1-14, Springer Berlin Heidelberg, ISSN 1866-9298, https://doi.org/10.1007/s12518-018-0224-4

Lucchetti, A., Brandolini, P., Robbiano, A., Firpo, M., and Faccini F., 2013. The Sea Cliff Mass Rating geomechanical classification for the rocky coastal management plan. In: Proceedings of the 12th European Geoparks Conference. pp. 158-161, ISBN: 9788890728105

Lucchetti, A., Brandolini, P., Faccini, F., and Firpo M., 2014. Proposta di valutazione della stabilità delle coste rocciose (SCMR – Sea Cliff Mass Rating): il caso studio delle falesie tra Genova e Camogli (Liguria orientale). *Studi Costieri*, vol. 22, p. 137-149, ISSN: 1129-8588

Mastronuzzi, G., Aringoli, D., Aucelli, P.P.C., Baldassarre, M.A., Bellotti, P., Bini, M., Biolchi, S., Bontempi, S., Brandolini, P., Chelli, A., Davoli, L., et al., 2017. Geomorphological map of the Italian coast: from a descriptive to a morphodynamic approach. *Geografia Fisica e Dinamica Quaternaria*, vol. 40 (2), pp. 161-196, DOI 10.4461/ GFDQ 2017.40.11

Mancini, F., Dubbini, M., Gattelli, M., Stecchi, F., Fabbri, S., Gabbianelli, G., 2013. Using Unmanned Aerial Vehicles (UAV) for High-Resolution Reconstruction of Topography: The Structure from Motion Approach on Coastal Environments. *Remote Sensing*, 5(12), 6880-6898; DOI:10.3390/rs5126880

Monteys, X., Harris, P., Caloca, S., and Cahalane, C., 2015. Spatial Prediction of Coastal Bathymetry Based on Multispectral Satellite Imagery and Multibeam Data. *Remote Sens.*, 7(10), 13782-13806; doi:10.3390/rs71013782

Nayor, L.A., Stephenson, W.J., and Trenhaile, A.S., 2010. Rock coast geomorphology: recent advances and future research directions. *Geomorphology*, 114 (1–2), pp. 3-11. DOI: 10.1016/j.geomorph.2009.02.004

Nex, F., and Remondino, F., 2014. UAV for 3D mapping applications: a review. *Applied Geomatics*, Vol.6(1), pp. 1-15; DOI: 10.1007/s12518-013-0120-x

Passoni, D., Federici, B., Ferrando, I., Gagliolo, S., and Sguerso, D., 2018. The estimation of precision in the planning of UAS photogrammetric surveys. *International Archives of the Photogrammetry, Remote Sensing and Spatial Information Sciences - ISPRS Archives*, pp. 1-7.

Raso, E., Brandolini, P., Faccini, and F., Firpo ,M. 2016. The Guvano complex landslide in the Cinque Terre National Park, Italy: geomorphological characterization, GNSS monitoring and risk management. In: *Eurock 2016, Rock Mechanics and Rock Engineering: From the Past to the Future*. Taylor & Francis, London, pp. 1287-1291, ISBN: 978-1-138-03265-1

Raso, E., Brandolini, P., Faccini, F., Realini, E., Caldera, C., and Firpo, M., 2017. Geomorphological evolution and monitoring of San Bernardino-Guvano coastal landslide (eastern Liguria, Italy).

Geografia Fisica e Dinamica Quaternaria, vol. 40 (2), pp. 197-210, IT ISSN 0391-9838, 2017. DOI 10.4461/ GFDQ 2017.40.12

Romana, M., 1993. A geomechanics classification for slopes: Slope Mass Rating. Hudson, J. Ed., Comprehensive Rock Engineering, Pergamon, 3, 575-600.

Rosser, N.J., Petley, D.N., Lim, M., Dunning, S.A., and Allison, R.J., 2005. Terrestrial laser scanning for monitoring the process of hard rock coastal cliff erosion. *Quarterly Journal of Engineering Geology and Hydrogeology*; 38 (4): 363–375. DOI: 10.1144/1470-9236/05-008

Scarpati, A., Pepe, G., Mucerino, L., Brandolini, P., and Firpo, M., 2013. Rocky cliff landslide hazard: the Capo Noli Promontory case study (western Liguria, NW Mediterranean Sea). *Rendiconti Online Società Geologica Italiana*, vol. 28, pp. 137-141, ISSN: 2035-8008

Troisi, S., Del Pizzo, S., Gaglione, S., Miccio, A., Testa, R.L., 2015. 3D models comparison of complex shell in underwater and dry environments. International Archives of the Photogrammetry, Remote Sensing and Spatial Information Sciences – ISPRS Archives, 40(5W5), 215-222.

SHORELINE CHANGES AT SANT'AGATA RIVER MOUTH (REGGIO CALABRIA, ITALY)

G. Barbaro[1]*, G. Bombino[2], V. Fiamma[1], G. Foti[1], P. Puntorieri[1], F. Minniti[1] C. Pezzimenti[3]

[1] DICEAM Department, Mediterranea University of Reggio Calabria, 89122 Reggio Calabria, Italy - (giuseppe.barbaro, vincenzo.fiamma, giandomenico.foti, pierfabrizio.puntorieri, francesca.minniti)@unirc.it

[2] Agriculture Department, Mediterranea University of Reggio Calabria, 89122 Reggio Calabria, Italy – giuseppe.bombino@unirc.it [3] DICEAM Department, Mediterranea University of Reggio Calabria, 89122 Reggio Calabria, Italy – pezzimenti.carmen@gmail.com

KEY WORDS: Shoreline changes, Shoreline position, Remote sensing, EPR, NSM, Longshore transport, River transport

ABSTRACT:

The analysis of shoreline changes is very important for coastal planning and management. In territories such as Calabria (Italy), characterized by significant anthropogenic pressures and various eroded coasts, the knowledge of the shoreline changes, and the factors that influence them, is necessary for management and planning of coastal areas. In fact, shoreline position is one of the most important indicators of coastal dynamics and undergoes both instantaneous and seasonal variations that may have natural or anthropogenic causes. From this point of view recent advances in remote sensing and GIS techniques allow to estimate with great precision the shoreline changes over the years. The use of any particular method of analysis being influenced by the data sources and resources available. The paper analyzes the shoreline changes near the mouth of the Sant'Agata River (Reggio Calabria, Italy), carried out through the comparison of cartography data of the last 60 years. Furthermore, the paper analyzes the main factors influencing the coastal dynamics, in particular longshore and river transport and rainfall, in order to identify possible correlation between these factors and the shoreline changes.

1. INTRODUCTION

Coastal areas represent the transition zone between sea and land (Boak and Turner, 2005) and are of particular importance for the presence of housing settlements. In fact over 30% of the world (Syvitski et al., 2005) and the Mediterranean (European Union, 2012) population live a short distance from the coastline. Coastal areas are very vulnerable under the action of both natural and anthropic factors which influence the shoreline position and coastal dynamics in general (Komar, 2000; Pilkey and Hume, 2011; Yang et al., 2015).

In the last 50 years, the anthropic factors, such as the construction of buildings, infrastructures, ports and coastal defence works, have increased the vulnerability of coastal areas to natural events such as floods, storms, coastal erosion, or a combination of these (Fiori et al., 2014; Barbaro et al., 2018; Li et al., 2018; Scionti et al., 2018). Amongst the natural factors, wave action and longshore and river transport are of particular importance (Barbaro et al., 2011; Rahman et al., 2011; Barbaro et al., 2012; Sicilia et al., 2013; Li et al., 2014; Tomasicchio et al., 2015; Borrello et al., 2017; Geria et al., 2018). Misdiagnosis of these factors can lead to environmental disasters as in the case of Saline Joniche, near the Messina Strait (Barbaro, 2013), or in the case of Badolato, in the Calabrian Ionian coast (Miduri et al., 2017). So, for effective management of coastal areas it is of fundamental importance to know all the factors which influence the coastal dynamics (Barbaro, 2016).

The paper describes a case study related to the Sant'Agata river mouth, where the analysis of the shoreline changes was carried out through the comparison of cartography data of the last 60 years. Furthermore, the paper analyzes the main factors influencing the coastal dynamics in order to identify possible correlation between these factors and the shoreline changes.

2. SITE DESCRIPTION

The study area is located in the Southern part of the Reggio Calabria city (Italy) and it is characterized by the presence of sea and mountains very close to each other and by the presence of "*fiumare*". These are typical rivers of southern Italy with torrential and irregular regime, characterized by extensive dry periods and with frequent events of sudden flood, generated by short and intense rainfall (Terranova et al., 2009). In Reggio Calabria there are more than 10 fiumare and, not far from the Sant'Agata, there are other three rivers, all enclosed in a few kilometers. The final part of the Sant'Agata river is heavily anthropized due to the presence, especially, of the airport situated between Sant'Agata and Armo rivers, a sport center and various industrial activities (Figure 1) (Versaci et al., 2018).

Figure 1. Detail of the final part of Sant'Agata river, it is possible to observe the airport, a sport center and industrial activities

* Corresponding author

3. SHORELINE CHANGES

The analysis of the shoreline changes was carried out through the comparison of cartography data of the last 60 years, which consists of: aerophotogrammetry provided by Italian Military Geographic Institute, orthophotos taken from the Open Data section of the National Geoportal, and satellite imagery provided by Google Earth Pro.

The analysis was divided into three phases as follows. The first phase concerned the manual digitization of the shoreline, for each cartography data and using QGIS for aerophotogrammetry and orthophotos and using the spatial analysis tools of Google Earth Pro for satellite imagery. The second phase concerned the evaluation of the beach width at a transept positioned at the mouth of the Sant'Agata river (Figure 2). Finally, the last phase concerned the determination of shoreline rates of change using end point rate (EPR) and net shoreline movement (NSM) statistics (Table 1).

The shoreline position is the most important geoindicator of coastal evolution (Boak and Turner, 2005). Recent advances in remote sensing and geographical information system (GIS) techniques allow us to estimate with great precision the shoreline changes over the years (Moore, 2000; Alesheiikh et al., 2007; Maiti and Bhattacharya, 2009; Pardo-Pascual et al., 2012; Ayadi et al., 2015; Natesan et al., 2015).

Regarding the identification of the correct shoreline position, due to the varying oceanographic conditions among the different cartographies, the reference line chosen was the wet/dry line. Furthermore, in the study area the tidal excursion is of the order of tens of centimeters (Sannino et al., 2015) so the effects on the variation of the shoreline position are negligible. The digitalization of the shoreline was carried out on a scale of 1:1000 on QGIS and on a higher scale on Google Earth Pro. Therefore, the shoreline position has precision of the order of the meter and the shoreline changes have been approximated to the meter. This accuracy is in agreement with the aims of the paper, which concern the evaluate of the erosion and advancement trends, and not their precise quantification.

Figure 2. Shorelines and transept digitized using QGIS (scale 1:1000). Legend: dark blue = 2012, light green = 2006, violet = 1998, yellow = 1996, brown = 1985, dark green = 1954. The transept is shown in red

Figure 3. Maximum (to the left, in 2015) and minimum (to the right, in 2002) beach width. Legend: yellow = shoreline, red = transept. (source: satellite imagery of Google Earth Pro)

Date	Source	Beach width [m]	NSM [m]	EPR [m/year]
2017 (September)	Satellite	81	-1	-0.5
2015 (March)	Satellite	82	0	0
2012 (June)	Orthoph.	82	36	7.2
2007 (July)	Satellite	46	-30	-30
2006 (May)	Orthoph	76	44	11
2002 (July)	Satellite.	32	-33	-8.3
1998 (May)	Orthoph	65	7	3.5
1996 (August)	Orthoph.	58	5	0.5
1985	Aeroph.	53	-18	-1
1954	Aeroph.	71		

Table 1. Beach width at a transept positioned at river mouth, and NSM and EPR statistics

From the analysis of the results shown in Table 1 it is possible to observe how advancement and erosion phases alternated from 1954 to today, from these data it is clear that: minimum width was observed in 2002 (32 m) while the maximum width was observed in 2015 (82 m) (Figure 3). The maximum negative EPR was observed in the period 2006 - 2007 (30 m/year) while the maximum positive EPR was observed in the period 2002-2006 (11 m/year). Other significant changes are those observed between 1998 and 2002 (erosion of more than 8 m/year) and between 2007 and 2012 (advancement of about 7 m/year).

4. LONGSHORE AND RIVER TRANSPORT

Longshore transport was estimated using the Tomasicchio et al. (2013) model, starting from the wave data provided by the ABRC-MaCRO software. The time series obtained extends from October 16, 1986 to March 31, 2006 and consists of 147467 sea states, for each of which significant height, mean and peak periods and direction are available. These data were grouped in sectors of 10° each and in classes with a significant height H_s of 0.5 m each and, beyond the solid transport, it was possible to calculate frequency and mean energy flux from them. A further grouping was made in time intervals that were in agreement with what emerged from the analysis of the shoreline changes (Table 2).

H_s [m] / Recorded	1986-2006	1986-1996	1996-1998	1998-2002	2002-2006
0.0 – 0.5	125595	62953	12449	29430	20763
0.5 – 1.0	19240	12885	768	3632	1955
1.0 – 1.5	1777	1695	1	64	17
1.5 – 2.0	732	709	0	0	23
2.0 – 2.5	113	113	0	0	0
2.5 – 3.0	10	10	0	0	0
Total	147467	78365	13218	33126	22758

Table 2. Wave data, grouped in classes of H_s and in time intervals

From the analysis of these data it is possible to observe that the study area is characterized by modest wave motion (less than 1% of the recorded sea states exceeds the threshold of 1.5 m and no sea level exceeds the threshold of 3 m) and most of the intense wave motion is concentrated in the interval 1986-1996 (after 1996 the threshold of 2 m is never exceeded while from 1996 to 2002 the threshold of 1.5 m is never exceeded). The frequency is concentrated in two main directions: one from the North-West and one from the South. Regarding the first direction, it is associated with a high frequency (more than 15% in the sector centered on 340° compared to the North) but has a

low energy content due to the small fetches (of the order of ten km, because the study area is located within the Strait of Messina). Regarding the second direction, it is characterized by a lower frequency than the first (about 7% in the sectors centered on 180 and 190° compared to the North) but has much higher energy content due to exposure to the wave coming from the southern mouth of the Strait. For the evaluation of longshore transport, the study area was divided into two sections (one to the north and one to the south of the mouth) due to the different exposure to wave motion: in the northern section the average value is about 11000 m3/year while in the southern section the average value is about 20000 m3/year, in both cases it is directed from South to North.

Regarding the river transport, in the fiumare most of the solid transport is related to soil erosion triggered by rainfall for which this parameter was estimated using the Gavrilovic model (1959). Preliminarily it was necessary to analyze the rain and temperature data of the internal stations or near the basin (Reggio Calabria and Cardeto, whose areas of influence were assessed using the Thiessen polygon method).

Gauge	Period	Elev. [m]	Weight [%]	Av. rainfall [mm]	Av. rain. 1998-2002 [mm]	Av. rain. 2002-2006 [mm]
Reggio Calabria	1917-2017	10	20	594.4	542.8	614.3
Cardeto	1999-2017	690	80	1300.6	1200.9	1352.3

Table 3. Hydrological characteristics of Reggio Calabria and Cardeto gauges

Moreover, it was necessary to perimeter and morphometrically characterize the river basin, starting from the data available in the Open Data section of the Geoportal of the Calabria Region (http://geoportale.regione.calabria.it/) and using the GIS Map Window and its Watershed Delineation plugin. The results are shown in Figure 4 and Table 4. Finally, from the application of Gavrilovic's model an average value of about 20000 m^3/year of solid transport was obtained.

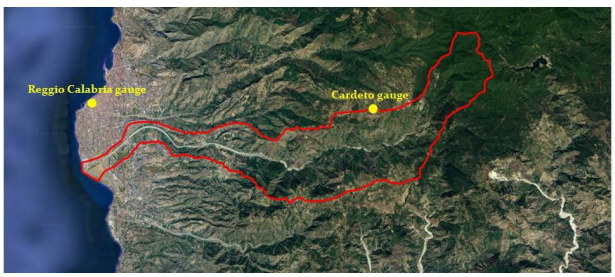

Figure 4. Sant'Agata river basin and Reggio Calabria and Cardeto gauges

Parameter	Value
Area	52.3 km^2
Perimeter	54.3 km
Main stream lenght	26.2 km
Maximum height	1665 m
Minimum height	0 m
Average height	865.6 m
Average slope	37.4 %
Horton order	5
Run-off time	2.9 hour
Gravelius index	2

Table 4. Morphometric characteristics of Sant'Agata river basin

5. DISCUSSION AND CONCLUSIONS

The paper describes the shoreline changes which occurred near the Sant'Agata river mouth over the last 60 years, using End Point Rate (EPR) and Net Shoreline Movement (NSM) statistics, in order to identify possible correlation between the factors that influence coastal dynamics and the shoreline transformation.

Due the morphology of the territory (the area under study is located within the Strait of Messina), both the wave motion and, consequently, the longshore transport are modest. In the period 1998-2002 (in which the shoreline eroded with a speed of more than 8 m/year), longshore transport assumed values lower than average. In the period 2002-2006 (in which the shoreline advanced with a speed of 11 m/year), on the other hand, longshore transport assumed values higher than the previous interval, but still below the average values. Therefore, there seems to be no correlation between these parameters.

River contribution is mainly related to soil erosion triggered by precipitation because the studied river has torrential regime. River transport is, on average, of the same amount of longshore transport to the south of the mouth (in this section the beach is few meters wide) while to the north of the mouth it is greater (in this section the beach is between 20 and 30 m wide).

In the period 1998-2002 the rainfall was lower than the average value, while in the period 2002-2006 it was higher, so in this case study there seems to be a direct correlation between rainfall (and, therefore, river transport) and the shoreline changes. The lack of meteorological data after 2006 and of rainfall data from the Cardeto station (which has the largest area of influence) before to 1999 did not allow to investigate the other time periods.

The methodology for analyzing the shoreline changes, as described in this paper, is particularly useful for better understanding the factors that most influence the coastal balance and, therefore, is applicable to many contexts which are similar to the Sant'Agata river mouth.

REFERENCES

Alesheikh, A.A., Ghorbanali, A., Nouri, N., 2007. Coastline change detection using remote sensing. International Journal of Environmental Science and Technology, 4 (1), 61–66.

Ayadi, K., Boutiba, M., Sabatier, F., Guettouche, M.S., 2015. Detection and analysis of historical variations in the shoreline, using digital aerial photos, satellite images, and topographic surveys DGPS: case of the Bejaia bay (East Algeria). Arabian Journal of Geosciences, 9, 1–18.

Barbaro, G., 2013. Saline Joniche: a predicted disaster. Disaster Advances, 6, pp. 1-3.

Barbaro, G., 2016. Master Plan of solutions to mitigate the risk of coastal erosion in Calabria (Italy), a case study. Ocean & Coastal Management, 132, pp. 24-35.

Barbaro, G., Foti, G., Malara, G., 2011. Set-up due to random waves: influence of the directional spectrum. In: Proceedings of the 30th International Conference on Ocean, Offshore and Artic Engineering OMAE (Rotterdam, The Netherlands), 2011.

Barbaro, G., Foti, G., Mandaglio G., Mandaglio, M., Sicilia, C. L., 2012. Estimate of sediment transport capacity in the basin of the Fiumara Annunziata (RC). Rendiconti Online Società Geologica Italiana, 21(1), pp. 696-697.

Barbaro G., Petrucci O., Canale C., Foti G., Mancuso P., Puntorieri P., 2018. Contemporaneity of floods and storms. A case study of Metropolitan Area of Reggio Calabria in Southern Italy. In: *Prooceedings of New Metropolitan Perspectives (NMP)*, Reggio Calabria, Italy.

Boak, E.H., Turner, I.L., 2005. Shoreline definition and detection: a review. Journal of Coastal Research, 21(4), pp. 688-703.

Borrello, M.M., Foti G., Puntorieri P., 2017. Shoreline evolution near the mouth of the Petrace River (Reggio Calabria, Italy). In: Proceedings of the 9th International Conference on River Basin Management (Prague, Czech Republic).
European Union, Sustainable tourism in the Mediterranean. Report, 2012.

Fiori, E., Comellas, A., Molini, L., Rebora, N., Siccardi, F., Gochis, D.J., Tanelli, S., Parodi, A., 2014. Analysis and hindcast simulations of an extreme rainfall event in the Mediterranean area: The Genoa 2011 case. Atmospheric Research, 138, pp. 13-29.

Gavrilovic, S., 1959. Méthode de la classification des bassins torrentiels et équations nouvelles pour le calcul des hautes eaux et du débit solide, Vadoprivreda, Belgrado, Serbia. (in French)

Geria, P.F., Foti, G., Puntorieri, P., 2018. Morphodynamic analysis of Tuccio River (South Calabria, Italy). In: Proceedings of 6th International Conference on Flood and Urban Water Management, A Coruna, Spain.

Komar, P.D., 2000. Coastal erosion–underlying factors and human impacts. Shore & Beach, 68(1), pp. 3-16.

Li, N., Yamazaki, Y., Roeber, V., Cheung, K.F., Chock, G., 2018. Probabilistic mapping of storm-induced coastal inundation for climate change adaption. Coastal Engineering, 133, pp. 126-141.

Li, X., Zhou, Y., Zhang, L., Kuang, R., 2014. Shoreline change of Chongming Dongtan and response to river sediment load: a remote sensing assessment. Journal of Hydrology, 511, pp., 432-442.

Maiti, S., Bhattacharya, A.K., 2009. Shoreline change analysis and its application to prediction: A remote sensing and statistics based approach. Marine Geology, 257(1-4), pp. 11-23.

Miduri, M., Foti G., Puntorieri P., 2017. Impact generated by Marina of Badolato (Italy) on adjacent coast. In: Proceeding of the 13th International Congress on Coastal and Marine Sciences, Engineering, Management and Conservation MEDCOAST (Mellieha, Malta).

Moore, L.J., 2000, Shoreline mapping techniques: Journal of Coastal Research, 16, 111–124.

Natesan, U., Parthasarathy, A., Vishnunath, R., Kumar, G.E.J., Ferrer, V.A., 2015. Monitoring longterm shoreline changes along Tamil Nadu, India using geospatial techniques. Aquatic Procedia, 4, 325–332.

Pardo-Pascual, J.E., Almonacid-Caballer, J., Ruiz, L.A., Palomar-Vázquez, J., 2012. Automatic extraction of shorelines from Landsat TM and ETM+ multi-temporal images with subpixel precision. Remote Sensing of Environment, 123, 1–11.

Pilkey, O.H., Hume, T., 2011. The shoreline erosion problem: lessons from the past. Water & Atmosphere, 9(2), pp. 22-23.

Pranzini, E., Williams, A., 2013. Coastal erosion and protection in Europe. Routledge, Oxon.

Rahman, A.F., Dragoni, D., El-Masri, B., 2011. Response of the Sundarbans coastline to sea level rise and decreased sediment flow: a remote sensing assessment. Remote Sensing of Environment, 115(12), pp. 3121-3128.

Sannino, G., Carillo, A., Pisacane, G., Naranjo, C., 2015. On the relevance of tidal forcing in modeling the Mediterranean thermohailine circulation. Progress in Oceanography, 134, 304–329.

Scionti, F., Miguez, M.G., Barbaro, G., De Sousa, M.M., Foti, G., Canale, C., 2018. An integrated methodology for urban flood risk mitigation: the case study of Cittanova (Italy).
Journal of Water Resources Planning and Management, 144(10).

Sicilia, C.L., Foti, G., Campolo, A., 2013. Protection and management of the Annunziata river mouth area (Italy). Air, Soil and Water Research, 6, pp. 107-113.

Syvitski, J.P.M., Vorosmarty, C.J., Kettner, A.J., Green, P., 2005. Impact of humans on the flux of terrestrial sediment to the global coastal ocean. Science, 308(5720), pp. 376-380.

Terranova, O., Antronico, L., Coscarelli, R., Iaquinta, P., 2009. Soil erosion risk scenarios in the Mediterranean environment using RUSLE and GIS: An application model for Calabria (southern Italy). Geomorphology, 112(3-4), pp. 228-245.

Tomasicchio, G.R., D'Alessandro, F., Barbaro, G., Malara, G., 2013. General longshore transport model. Coastal Engineering, 71, pp. 28-36.

Tomasicchio, G.R., D'Alessandro, F., Barbaro, G., Musci, E., De Giosa, T.M., 2015. Longshore transport at shingle beaches: an independent verification of the general model. Coastal Engineering, 104, pp. 69-75.

Versaci, R., Minniti, F., Foti, G., Canale, C., Barillà, G.C., 2018. River anthropization: case studies in Reggio Calabria (Italy). In: Proceedings of 10th International Conference on Sustainable development and Planning, Siena, Italy.

Yang, Z., Wang, T., Voisin, N., Copping, A., 2015. Estuarine response to river flow and sea-level rise under future climate change and human development. Estuarine, Coastal and Shelf Science, 156, pp. 19-30.

EARTH OBSERVATION AS AN AID TO COASTAL WATER MONITORING: POTENTIAL APPLICATION TO HARMFUL ALGAL BLOOM DETECTION

C. Lapucci[1,2*], S. Taddei[2], B. Doronzo[1,2], M. Fattorini[1,2], S. Melani[1,2], G. Betti[1,2], F. Maselli[1], A. Ortolani[1,2], B. Gozzini[2], C. Brandini[1,2]

[1] IBIMET-CNR (Institute of BioMeteorology, National Council of Research), Via Madonna del Piano 10, 50019 Sesto Fiorentino, Firenze, Italy - (lapucci, doronzo, fattorini, melani, betti, ortolani, gozzini, brandini)@lamma.rete.toscana.it, maselli@ibimet.cnr.it
[2] LaMMA Consortium (Environmental Modelling and Monitoring Laboratory for Sustainable Development), Via Madonna del Piano 10, 50019 Sesto Fiorentino, Firenze, Italy, (taddei, gozzini)@lamma.rete.toscana.it

KEY WORDS: Earth Observation, Harmful Algal Blooms, Chlorophyll, O. ovata

ABSTRACT:

In this work we show the application and prospects of the combined use of satellite and in-situ measurements for the monitoring of vulnerable coastal zones. The focus is on areas of outstanding environmental value but subject to strong anthropogenic pressures and recurrent issues like harmful algal blooms (HAB), such as Marine Protected Areas. Given the highly dynamic variability of marine systems, a comprehensive monitoring method needs to combine multiple sources of information. The biogeochemical and physical data of a specific area derived from in situ and satellite sources – MODIS Aqua and OLCI Sentinel 3 - are here compared with specific thresholds, in order to detect the conditions under which a potential damaging event for the environment is likely to occur. This study describes, as an application of the method, an exploratory analysis conducted in an area of Tuscany coast known to be particularly vulnerable to HAB, Ostreopsis ovata (O. ovata). In spite of the discontinuous temporal frequency of the available O. ovata monitoring data, bloom favourable conditions concerning sea state and water temperature were identified from weather stations and buoys data, as well as from satellite data. This monitoring method, together with high resolution hydrodynamic modelling, was originally developed within the ESA Sympa (Satellite assets Integration for Marine Protected Areas) demonstration project.

1. INTRODUCTION

1.1 Aim of the work

Coastal zones of outstanding environmental value, like Marine Protected Areas, can be subject to strong anthropogenic pressures, connected to events such as harmful algal blooms (HAB), and therefore need accurate monitoring. The Sympa (Satellite assets Integration for Marine Protected Areas) demonstration project, co-funded in the framework of ESA Integrated Application Promotion (IAP) programme proposed a support to the monitoring of vulnerable areas, developing a set of software applications for observation based on Earth Observation (EO) data, in situ measurements and modelling. In this work we present a procedure, implemented during the project on selected areas of Mediterranean basin, which is based on satellite monitoring and combined with in situ observations. As for the remote sensing component of the method, the Earth Observation algorithm, which monitors parameters involved in algal bloom triggering is here described. Satellite physical and biogeochemical monitoring is in fact very advantageous, although not as accurate as in situ measurements. In fact it is much less time consuming, and it allows to perform observations with high spatial and temporal coverage at synoptic scale.
In order to test the method, an exploratory analysis concerning a coastal area particularly vulnerable to Ostreopsis ovata (O. ovata) in Tuscany (Italy) is here shown.
This work also shows a first application of OLCI (Ocean and Land Colour Instrument) Sentinel 3 data to coastal monitoring, compared with MODIS (Moderate-resolution Imaging Spectroradiometer) Aqua data, in view of the development of a combined use of all those techniques, including the modelling component of Sympa project.

1.2 Ocean color remote sensing in coastal areas and application to HAB detection

Coastal remote sensing, dealing with optically complex waters shows some issues such as satellite low spatial resolution, coastal atmospheric correction (Sathyendranath et al., 1983) and adjacency effects (Santer at al., 2000; Lee, 2006). In spite of that, remote sensing has been proposed as a monitoring instrument of surface Chlorophyll *a* concentration for the UE Marine Strategy implementation (Cristina et al., 2015). The new ESA satellite Sentinel 3 OLCI is designed to overcome many of the issues here described.
The potential use of remote sensing for HAB detection was first demonstrated by Mueller (1979). The application of remote sensing to the monitoring of various HAB-causing organisms can have different approaches. Detection using purely optical methods can be useful for massive HAB phenomena (Stumpf et al., 2005; Tester et al., 1998). When the HAB is limited to small areas very close to the coasts, as in the case of O. ovata, the event cannot be directly detected via direct optical observation. An indirect detection of HAB is here proposed, monitoring the variations of physical and ecological characteristics of a larger area including the target one.

2. DATA & METHODS

2.1 Satellite data and relative products

EO data obtained from OLCI, are particularly suitable for coastal area studies because of instrument high spatial

* Corresponding author

resolution (300 m) and characteristics. Because of OLCI discontinuous time coverage (<2.8 days with 1 satellite, <1.4 days 2 satellites), MODIS data were also used in this study as their overpass is almost daily, in spite of its spatial resolution too low for coastal observations (1 km). Despite this, after a strict level 2 Flags masking applied, MODIS provided reliable observations, in terms of the observed space and time dynamics.
Three EO products were selected to assess the biogeochemical and physical environmental conditions of the target area.
Phytoplankton growth imbalance such as eutrophication, can be indirectly estimated by satellite surface chlorophyll a concentration (Chl *a)* as an index of ecological status of the sea. Chl *a* assessment is an instrument of the Marine Strategy Directive (2008/56/EC) and many environmental directives (Colella et al., 2016). Standard Chl *a* L2 algorithms were here used, known to perform well in the area (Lapucci et al., 2012) – OCx family for MODIS, together with OC4Me for OLCI (as it is designed in continuity with MERIS).
Water clarity is directly related to turbidity, which can affect the rates of photosynthesis, negatively influencing primary productivity and dissolved oxygen availability to support other organisms. Water clarity can be observed by KD490, the diffuse attenuation coefficient at 490 nm (Saulquin, 2013). Many water quality monitoring programs include turbidity, defined in the standard ISO7027, as a parameter routinely measured. Standard L2 MODIS and OLCI products were here used.
As for SST, in water quality assessment water temperature is a very important factor as it affects nearly every other water quality parameter. Water temperature can for instance affect metabolic rates and photosynthesis production, compound toxicity, and dissolved oxygen. Standard MODIS SST product was here used.
As in coastal areas the bottom effect is too strong to allow a direct satellite detection of the studied bloom, which occurs within a few meters from the sea shore, observations were made on a larger area including the one where the bloom occurs. The three parameters are here used therefore as an indirect index of their dynamics in the target area. Trophic state was evaluated as Chl *a*, water temperature was evaluated as Sea Surface Temperature (SST), and Water Clarity was evaluated as diffusion attenuation coefficient at 490 nm (KD490).

2.2 Data from weather stations and marine buoys

Data from weather stations and marine buoys used here are: significant wave height, wave peak period, average sea surface temperature (SeaST), main wind direction, cumulated precipitation, average wind speed, average air temperature. They were measured by Gorgona Buoy and by Bocca d'Arno weather station, both located in the proximity of the O. ovata monitoring stations and owned by Tuscan Regional Government
(http://www.cfr.toscana.it/index.php?IDS=4&IDSS=37).

2.3 O. ovata monitoring data distributed by ARPAT

Dinoflagellate O. ovata lives on the surface of macroalgae and rocks. O. ovata has recently found optimal climatic conditions in the Mediterranean Sea. In fact, during the last 15 years, it was found in high concentrations during the summer (Mangialajo et al., 2008). The blooms can be harmful both for the ecology of an area and for human health (Accoroni, 2016). Peculiar climatic and meteorological conditions, areas affected by coastal eutrophication with reduced water exchange, and high SeaST favor the O. ovata growth in the study area (Sansoni et al., 2003). O. ovata cell concentration data in water column (as blooms occur after cells resuspension in water column following wave motion) were obtained from ARPAT (Agency for Environmental Protection of Tuscany) (http://www.arpat.toscana.it/temi-ambientali/acqua/balneazione/ostreopsis-ovata/dati-monitoraggio/ostreopsis-ovata), as they are monitored within the national coastal marine monitoring program (2006/7/EC). Sampling of water and analyses are performed monthly in June and September and every 10-15 days in July and August (intensified in case of bloom).

2.4 Earth Observation algorithm

The Earth Observation algorithm estimates conditions of potential environmental alert for Chl *a,* KD490 and SST, computing the spatial average of the parameter in a target area, and compared to specific thresholds. The definition of the threshold is crucial: critical values for high standard water condition are tailored on the study area specific features affecting O. ovata bloom. The latest European Directives on the protection of marine and coastal environment (2000/60/EC, 2008/56/EC), scientific literature concerning environmental and ecosystem characteristics, and satellite data climatologies were used to define thresholds. For the study area (Figure 1), MODIS monthly climatologies of Chl *a,* KD490 and SST were computed for the period June to September of the years 2007 to 2015. As for OLCI, MERIS monthly climatologies of the years 2007 to 2011 (MERIS mission ended in May 2012) were computed, as OLCI instrument is continuity of the ENVISAT MERIS instrument capability.

3. EXPLORATORY ANALYSIS: O. OVATA

As for O. ovata bloom occurrence, specific environmental conditions appear to be crucial factors determining the proliferation of these species, when associated with the presence of docks and marinas (Pistocchi, 2011).
In Tyrrhenian and Ligurian seas, the main drivers of O. ovata bloom during the summer months are: closed gulfs, low water depth, presence of rocky substrates/macroalgae, poor hydrodynamism due to the natural morphology of the coast or the presence of brushes or artificial reefs for the containment of coastal erosion, absence of thermocline, SeaST above 25 °C (ISPRA, 2011).

3.1 Study area: coastal area near Pisa

The study area is located south the Arno river mouth, in Marina di Pisa; it was chosen for its environmental value, and also because it is subject to strong anthropogenic pressures (Cipriani et al., 2010), as well as to O. ovata blooms. The area is in fact characterized by the geomorphological characteristics suitable for O. ovata growth, the presence of coastal defences (ISPRA 2017). There are three ARPAT O. ovata sampling stations located in Marina di Pisa. For satellite data elaboration, a 10 km x 10 km area (black square in Figure 1) containing the three ARPAT sampling stations (black triangles within black square in Figure 1) was defined.

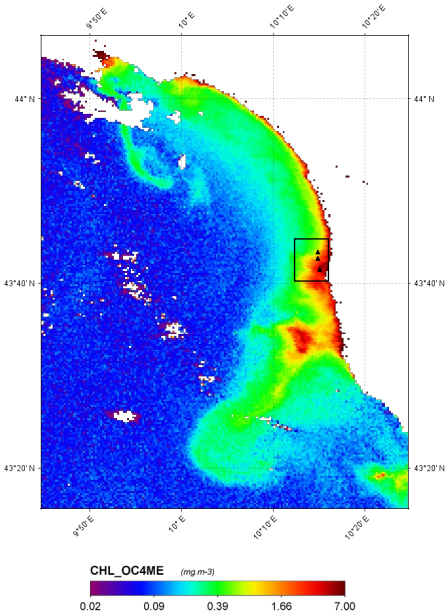

Figure 1. Sentinel 3A FR Chl *a* OC4ME, (31/7/2017). Black square shows the area of satellite observations. Black triangles are O. ovata monitoring stations.

3.2 Analysis of O. ovata bloom, meteo-marine and satellite data

Among all the meteo-marine data examined (paragraph 2.2) comparing their trends with O. ovata bloom trends in the years 2010 – 2015 the favourable conditions for bloom onset (paragraph 3) appear to be: days of appropriate water motion causing cell resuspension, followed by days of calm sea conditions and SeaST equal or higher than 25°C. Years 2014 and 2015 are here taken as example of meteo-marine and O. ovata bloom dynamics observed during the whole period. As for satellite monitoring in the study area, years 2016 and 2017 were used, as OLCI data are available since February 2016. Satellite versus satellite comparison was performed for OLCI vs MODIS.

3.2.1 OLCI validation vs MODIS in the study area: Chl *a* and KD490

The coefficient of determination (R^2), the intercept and the slope of the linear regression between Chl *a* estimated by the two sensors were computed together with the root mean square error (RMSE) and the mean bias error (MBE) for the simultaneous days of overpass (21 days in 2016, 24 days in 2017, table 1 and 2). The statistics that summarize the results are shown in Table 1 and 2. Determination coefficient is similar for all the products and years, showing an average of 0.82 for Chl *a* and 0.83 for KD490 in the two years. RMSE shows a better agreement between the two satellites for KD490 than for Chl *a*. MBE% shows a general overestimation of OLCI compared to MODIS: 31,08 % for Chl *a* and 17.31 % for KD490 averaged in the two years. The area covered in terms of valid pixels after atmospheric correction is higher for OLCI (19.46 km^2) than for MODIS (11.22 km^2), confirming better performances of OLCI in coastal areas.

21 matchups 2016	Chl *a*	KD490
Determination coefficient	0.84	0.83
RMSE	7.03	0.55
MBE%	50.56	26.25

Table 1. Determination coefficients, RMSE and MBE% related to the MODIS and OLCI matchup days, 2016

24 matchups 2017	Chl *a*	KD490
Determination coefficient	0.80	0.84
RMSE	2.24	0.12
MBE%	11.60	8.38

Table 2. Determination coefficients, RMSE and MBE% related to the MODIS and OLCI matchup days, 2017

3.2.2 O. ovata bloom drivers – meteo-marine data

Significant wave height, wave peak period, average SeaST, main wind direction, cumulated precipitation, average wind speed, average air temperature (paragraph 2.2) were analysed in relation to O. ovata monitoring data for the 2010 – 2015 years. The conditions favouring HAB related to the years 2010 – 2015 in the study area can be summarized observing the 2014 and 2015 years plots (figure 2 and 3). In 2014 (figure 2) SeaST is mostly below 25°C; only when it reaches 25°C and after a period of wave motion there is small O. ovata growth. In 2015 (figure 3) an initial period of SeaST below 25°C seems to inhibit O. ovata growth, in spite of wave motion. This is followed by anomalously high SeaST, which apparently inhibit O. ovata growth (although in presence of wave motion). Only when SeaST reaches 25°C wave motion seems to be able to cause a bloom. Therefore, an interplay between SeaST favouring the bloom (25°C) preceded by days of appropriate wave motion to favour cells resuspension in the water column and followed by days of calm sea, seems to create the conditions that can trigger a bloom in the study area. Satellite data were not taken into consideration for those years because Sentinel 3 data are available since 2016.

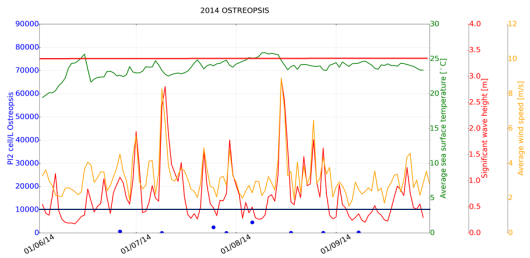

Figure 2. Meteomarine, and O. ovata data, June to September 2014

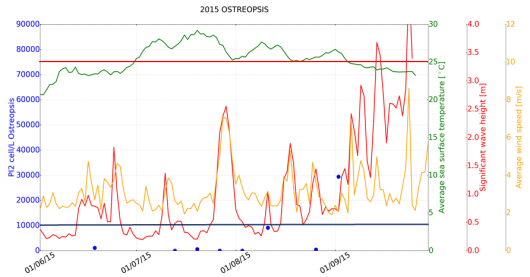

Figure 3. Meteomarine and O. ovata data, June to September 2015

3.2.3 O. ovata bloom drivers, meteomarine and satellite data

After having identified the meteomarine conditions favouring O. ovata bloom, the Earth Observation algorithm was applied.

For the year 2016 (Figure 4), SeaST was below 25°C until the 7/7, apparently not allowing bloom to occur. An high O. ovata cell concentration - 8960 cell/L, just below bloom cell number threshold (10000 cell/L) - was found on the 27/7, and a bloom on the 1/8 (14360 cell/L). This occurred after 3 days of moderate to rough sea (14/7 to 17/7) followed by 5 days of SeaST above 25°C (27/7 to 31/7). OLCI and MODIS Chl *a*, KD490 and SeaST were always above threshold during those 2 days (Table 3 and 4).

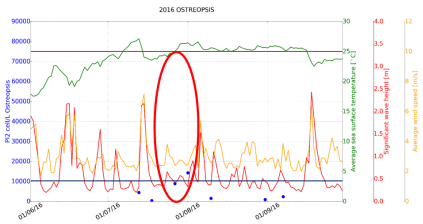

Figure 4. Satellite, meteomarine, and O. ovata data June to September 2016

Bloom 27/07/2016	Data	Threshold
OLCI Chl *a* (mg/m^3)	0.499	0.3
MODIS Chl *a* (mg/m3)	0.281	0.3
OLCI KD490 (m^{-1})	0.063	0.04
MODIS KD490 (m^{-1})	0.048	0.04
MODIS SST (°C)	26.22	25
O. ovata (cell/L)	8960	10000

Table 3. Satellite and O. ovata data of the 27/07/2016

Bloom 01/08/2016	Data	Threshold
OLCI Chl *a* (mg/m^3)	0.970	0.3
MODIS Chl *a* (mg/m3)	0.404	0.3
OLCI KD490 (m^{-1})	0.085	0.04
MODIS KD490 (m^{-1})	0.060	0.04
MODIS SST (°C)	27.62	25
O. ovata (cell/L)	14360	10000

Table 4. Satellite and O. ovata data of the 01/08/2016

For the year 2017 (Figure 5), SeaST was below 25°C until the 17/6, apparently not allowing bloom to occur. A high O. ovata cell concentration - 9560 cell/L, just below bloom threshold - was found on the 20/7, after 5 days of moderate to rough sea (5/7 to 9/7) followed by 3 days of SeaST above 25°C (17/7 to 19/7). A long lasting bloom (29806 cell/L) was found on the 5/7, also detected after 5 days (10/07, 60480 cell/L), following a period of 15 days of SeaST above 25°C (15/6 to 29/6), and moderate to rough sea conditions (30/6 to 4/8), thus creating the right conditions for a bloom. As for satellite data, on the 20/06 and 10/07 blooms, OLCI and MODIS Chl *a*, KD490 and SST were above thresholds (Table 5, and 7). Satellite data of the 05/07 bloom were not available because of the presence of clouds, so MODIS and OLCI data of the following day were taken (06/07): in this case also, Chl *a*, KD490 and SST were above threshold (table 6).

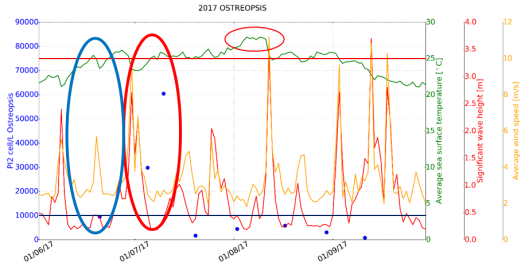

Figure 5. Meteomarine and O. ovata data, June to September 2017

Bloom 20/06/2017	Data	Threshold
OLCI Chl *a* (mg/m^3)	0.869	0.3
MODIS Chl *a* (mg/m3)	0.322	0.3
OLCI KD490 (m^{-1})	0.086	0.04
MODIS KD490 (m^{-1})	0.053	0.04
MODIS SST (°C)	25.8	25
O. ovata (cell/L)	9560	10000

Table 5. Satellite and O. ovata monitoring data of the 20/06/2017

Bloom 05/07/2017, satellite data of 06/07/2017	Data	Threshold
OLCI Chl *a* (mg/m^3)	0.539	0.3
MODIS Chl *a* (mg/m3)	0.352	0.3
OLCI KD490 (m^{-1})	0.044	0.04
MODIS KD490 (m^{-1})	0.056	0.04
MODIS SST (°C)	26.3	25
O. ovata (cell/L)	29800	10000

Table 6. Satellite and O. ovata data of the 06/07/2017

Bloom 10/07/2017	Data	Threshold
OLCI Chl *a* (mg/m^3)	0.472	0.3
MODIS Chl *a* (mg/m3)	-	0.3
OLCI KD490 (m^{-1})	0.060	0.04
MODIS KD490 (m^{-1})	-	0.04
MODIS SST (°C)	25.9	25
O. ovata (cell/L)	60480	10000

Table 7. Satellite and O. ovata data of the 10/07/2017

4. DISCUSSION AND CONCLUSIONS

As we could not rely on specific campaigns for O. ovata monitoring, we performed an exploratory analysis limited to the ARPAT days of sampling, as those data were not sufficient to fully investigate the algal behaviour. In spite of that, this method was able to detect bloom favourable conditions limited to the days of O. ovata monitoring, merging weather stations and buoy data regarding sea state and SeaST, with satellite observations of biogeochemical and physical parameters.

The data of significant wave height, wave peak period, SeaST ,wind direction, cumulated precipitation, wind speed, air temperature (paragraph 2.2) in relation to O. ovata monitoring for the years 2010 – 2015 suggest that an interplay between SeaST favouring the bloom (25°C) preceded by wave motion seems to create the conditions favourable for an O. ovata bloom.

Bloom occurrence seems to be bound to SeaST reaching 25°C but not near or over 27°C. SeaST is confirmed as being a critical factor in this area, as water motion *per se* is not able to trigger a bloom if it is not supported by days of SeaST equal or above 25°C (as shown in Figure 2).
We could observe that in the summer months of the years 2016 and 2017, during the bloom days the remote sensed Chl *a*, KD490 and SST were always above selected thresholds both for MODIS and OLCI. This analysis does not allow us to draw final conclusions, as is representative of a limited set of O. ovata monitoring data that are related to water sampling and analyses performed monthly in June and September and every 10-15 days in July and August (intensified in case of bloom). In spite of that, those results give precious information that are promising for future studies concerning a larger number of observations and appropriate O. ovata monitoring campaigns.
As for OLCI, this study confirms the good performances of this satellite in coastal areas, as the study area covered in the days of simultaneous satellites overpass in terms of valid pixels after atmospheric correction is higher for OLCI than for MODIS. Moreover, in terms of a possible future development, Sentinel 2 data could be used together with Sentinel 3: in spite of having been designed for land remote sensing, Sentinel 2 is giving promising results on ocean color coastal areas observations as well.
Indeed, the issues connected to satellite revisiting time and cloud coverage can be dealt with by modelling: hydrodynamic and biogeochemical data from high-resolution models provide dynamic maps of physical and biogeochemical parameters. A combined use of all those techniques will be developed and described in a further work, including the modelling component of Sympa project constituted by a chain of very high-resolution nested models, whose boundary and initial conditions are extracted from Copernicus Marine Service.

REFERENCES

Accoroni S., Totti C., The toxic benthic dinoflagellates of the genus Ostreopsis in temperate areas: a review, Advances in Oceanography and Limnology, 2016; 7(1): 1-15, DOI: 10.4081/aiol.2016.5591

Colella S, Falcini F, Rinaldi E, Sammartino M, Santoleri R (2016) Mediterranean Ocean Colour Chlorophyll Trends. PLoS ONE 11(6): e0155756. doi:10.1371/journal.pone.0155756.

Cristina S. Icely J., Goela P. C., Del Valls T. A., Newton A., Using remote sensing as a support to the implementation of the European Marine Strategy Framework Directive in SW Portugal, Continental Shelf Research 108(2015) 169–177.

Directive 2000/60/EC of the European Parliament and of the Council of 23 October 2000, OJ L 327, 22.12.2000, p. 1–73

Directive 2008/56/EC of the European Parliament and of the Council of 17 June 2008, OJ L 164, 25.6.2008, p. 19–40

Directive 2006/7/EC of the European Parliament and of the Council of 15 February 2006 OJ L 64, 4.3.2006, p. 37–51

ISPRA, 2012 - Monitoraggio di Ostreopsis ovata e Ostreopsis spp.: Protocolli Operativi. Quaderni Ricerca Marina n.5, www.isprambiente.gov.it. pp. 29.

Lapucci C., Ampolo Rella M., Brandini C., Ganzin N., Gozzini B., Maselli F., Massi L., Nuccio C., Ortolani A., Trees C., Evaluation of empirical and semi-analytical chlorophyll algorithms in the Ligurian and North Tyrrhenian Seas, J. Appl. Remote Sens. 6 (1), 063565 (September 21, 2012); doi: 10.1117/1.JRS.6.063565

Lee Z-P., editor. Remote Sensing of Inherent Optical Properties: Fundamentals, Tests of Algorithms and Applications. International Ocean Color Coordinating Group; 2006

Mangialajo L., Bertolotto R., Cattaneo-Vietti R., Chiantore M., Grillo C., Lemee R., Melchiorre N., Moretto P., Povero P., Ruggieri N., The toxic benthic dinoflagellate Ostreopsis ovata: Quantification of proliferation along the coastline of Genoa, Italy, Marine Pollution Bulletin 56 (2008) 1209–1214

Rapporto ISPRA n. 148/2011 e 275/2017., "Monitoraggio di Ostreopsis ovata e altre alghe potenzialmente tossiche lungo le aree marino costiere italiane. Anno 2010 e Anno 2016.

Sansoni G., Borghini B., Camici G., Casotti M., Righini P., Rustighi C., Fioriture algali di Ostreopsis ovata (Gonyaulacales:Dinophyceae): un problema emergente, Biologia Ambientale, 17 (1): 17-23, 2003

Santer R., and Schmechtig C., "Adjacency effects on water surfaces: primary scattering approximation and sensitivity study," Appl. Optics 39, 361–375 (2000).

Cipriani L. E., Perfetti A., Pranzini E., Vitale G.: Azioni di tutela delle dune costiere del Parco Regionale Migliarino San Rossore Massaciuccoli (Toscana settentrionale), Studi costieri 2010 - 17: 165-179).

Mueller, J.L. 1979. Prospects for measuring phytoplankton bloom extent and patchiness using remotely sensed ocean color images: an example. In: Toxic Dinoflagellate Blooms, Elsevier, North Holland, Inc., New York. Pp. 303-308.

Pistocchi R., A review on the effects of environmental conditions on growth and toxin production of Ostreopsis ovata, Toxicon 57 (2011) 421–428

Sathyendranath S. and Morel A., "Light emerging from the sea-interpretation and uses in remote sensing,", in Remote Sensing Applications in Marine Science and Technology, A. P.Cracknell, Ed., pp. 323–357, D Reidel Publishing Company, Dordrecht, The Netherlands (1983).

Saulquin B., Hamdi A., Gohin F., Populus J., Mangin A., d'Andon O. F., Estimation of the diffuse attenuation coefficient KdPAR using MERIS and application to seabed habitat mapping, Remote Sensing of Environment January 2013, Volume 128, Pages 224 – 233.

Stumpf R. P, and Tomlinson M. C., Remote sensing of harmful algal blooms, in: R.L. Miller et al. (eds.), Remote Sensing of Coastal Aquatic Environments, Chapter 12, 277–296. Springer 2005)

Tester, P.A., R.P. Stumpf, and K. Steidinger. Ocean color imagery: What is the minimum detection level for Gymnodinium breve blooms? In: Harmful Algae. Reguera. B, J. Blanco., M.L. Fernandez and T. Wyatt (Eds). Xunta de Galacia and Intergovernmental Oceanographic Commission of UNESCO, 1998.

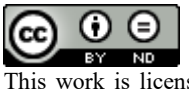

INTEGRATING REMOTE SENSING DATA FOR THE ASSESSMENTS OF COASTAL CLIFFS HAZARD: MAREGOT PROJECT

G. Deiana[1], M. T. Melis[1]*, A. Funedda[1], S. Da Pelo[1], M. Meloni[1], L. Naitza[1], P. Orrù[1], R. Salvini[2], A. Sulis[1]

[1] Department of Chemical and Geological Sciences, Università degli Studi di Cagliari, Cittadella Universitaria – S.S. 554 bivio per Sestu I-09042 Monserrato (CA), Italy – (titimelis, afunedda, sdapelo, orrup, asulis)@unica.it – (gdeiana80, lnaitza)@gmail.com – melonimattiaalessio@tiscali.it

[2] Department of Environment, Earth and Physical Sciences and Centre of GeoTechnologies, University of Siena, San Giovanni Valdarno, Arezzo, Italy – riccardo.salvini@unisi.it

KEY WORDS: Geology, Landslides, Coastal Erosion, Geomorphology, Sardinia

ABSTRACT:

The assessment of cliffs instability to understand the dynamics of erosive phenomena and the dynamics of coastlines, in relation to the geomorphological and hydrodynamic characteristics of the coast is an important challenge worldwide, mainly where coastal retreat imply an economic impact. The MAREGOT Project (MAnagement des Risques de l'Erosion cotière et actions de GOuvernance Transfrontalière – "Managing the Risks of Coastal Erosion and Cross-border Governance Actions), funded under the Programme: 2014 - 2020 INTERREG V-A Italy - France (Maritime), aims at the joint prevention and management of the risks arising from coastal erosion in the cooperation area. In this context, a methodology consisting in the characterization of morphological and geological features collecting data from remote and proximal sensing sensors either on the sub-aerial or in the submerged cliff has been proposed. These data will be integrated by direct observation and surveys of the different geological features and with laboratory analysis of the geotechnical properties of sampled rocks and terrains. The main aim of this study is to integrate data acquired by different sensors as optical and Lidar data, side scan sonar and multibeam information to propose methodologies to assess and monitor coastal cliff landslide susceptibility.

1. INTRODUCTION

1.1 Coastal erosion

Coastal morphology is generally related to the interaction of marine and gravitational processes that act on outcropping lithologies, but it is impossible to define with certainty the extent to which the triggers affect the system. The collapses that occur along the cliff are episodic, discontinuous in time and in space, and occur mainly in very fractured rock masses in correspondence of large storms (Andriani & Walsh, 2007, Paronuzzi, 2010, Budetta & Nappi, 2011; Martino & Mazzanti, 2014). The vulnerability of coastal cliffs is a very important issue as sea cliffs occur along about 80% of the world's shorelines (Emery & Kuhn, 1982).

The coastal retreat of rocky cliffs is influenced by the geology, particularly by the structure and lithology of rock formations that crop out on the coast and their response to local weathering. Geological setting with its complete characterization has to be analysed with different techniques aiming to reconstruct the past evolution and future dynamics that will affect the coasts, considering the environments emerged and submerged as a single evolutionary system.

In recent years, investigative techniques on coastal landslides have been developed with the contribution of new Remote Sensing tools (Budetta et al., 2000; Fall et al., 2006; De Blasio & Mazzanti, 2010; De Vita et al., 2012; Budetta & De Luca, 2015; Ružić, et al., 2015; Budetta et al., 2016). However, currently there are no well-defined investigative protocols. Existing studies often do not follow uniform methodologies, mainly due to lack of knowledge and complexity in collecting data on the processes that generate coastal erosion (Sunamura, 1977; 1983; 1992).

The proposal of a methodology for the characterization of geological features, collecting data from remote and proximal sensing sensors, either on the sub-aerial or in the submerged cliff is part of MAREGOT Project (Managing the Risks of Coastal Erosion and Cross-border Governance Actions). This project aims at the joint prevention and management of the risks arising from coastal erosion in the cooperation area. Five pilot sites were chosen to test the methodology. In this paper, the study carried out in the area of "Sella del Diavolo" on the South coast of Sardinia (Italy) is presented.

2. STUDY AREA

Sardinia is the second largest island of the Mediterranean area, but holds the record of having the longest coastline perimeters. Rocky coasts, cliffs or slopes, represent more than 68% of the coastal areas (ISPRA, 2016). Moreover, the geological complexity of Sardinia makes it suitable to represent most of the cliff environments present in the Mediterranean area (Carmignani et al., 2016). Therefore, sites from the North-west to the Southeast, along the coast of Sardinia, have been chosen to test the proposed methodologies (Figure 1).

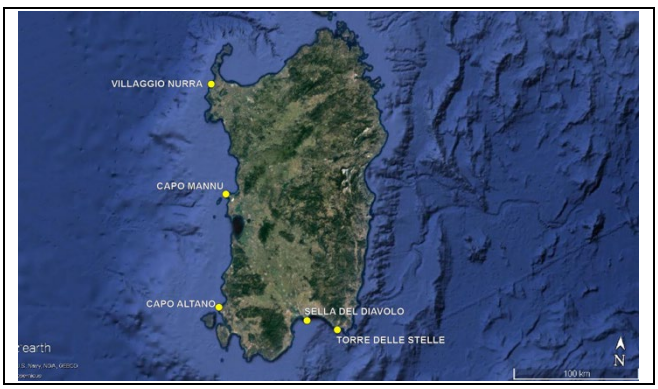

Figure 1. Study sites along the coast of Sardinia

* Corresponding author

They are representative of sites where different lithology, coastal dynamic, and landslides occur. Lithology ranges from metamorphic rocks of the Palaeozoic Basement (Villaggio Nurra, Figura 2), where landslides phenomena occur mainly as rock slide, to the aeolian succession, made up from Upper Pliocene-Lower Pleistocene sandstones (Capo Mannu) where rockfalls, topples and slumping are more frequent.

Figure 2. Study site: Villaggio Nurra

In the Oligo-Miocene volcano-sedimentary succession (Capo Altano) and in the Upper Carboniferous-Permian plutonic complex mainly made up by granodiorites, tonalites, gabbro and intrusive dikes (Torre delle Stelle, Figura 3), a gradual retrograde erosion of the cliffs due to gravitational processes as rockfall, topples and wedges failure develops.

Figure 3. Study site: Capo Mannu

The pilot site of "Sella del Diavolo", presented in this paper (Figura 4), is located on the southern coast of Sardinia, where Upper Miocene sedimentary rocks and Quaternary deposits crop out. Miocene succession mainly consists of sandstones at the base, overlie by bioclastic limestones and ancient landslide deposits.

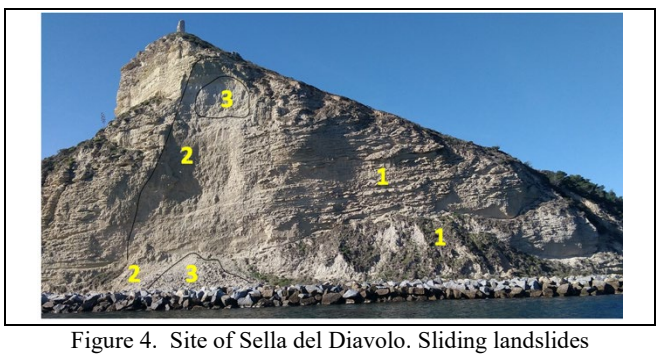

Figure 4. Site of Sella del Diavolo. Sliding landslides developed along sub-planar surfaces of fracturing and collapses have thirty-year recurrence time. Collapsed landslide deposits: 1) altered main scarp and the deposit colonized by vegetation evolved between 1940 and 1950; 2) main scarp and deposit at the foot of the landslide of July 2, 1987; 3) main scarp and deposit of 21 February 2017. In the foreground the protective breakwater, put in place after the event of 1987.

The Pleistocene deposits consist of littoral conglomerates and sandstones. The Holocene deposits are mainly gravitational sediments originating from the dismantling and erosion of nearby outcropping formations. The study area is affected by rockfalls, topples, debris flows and slides, which in the past caused damage to people.

3. METHODOLOGY

The methodological approach aiming to define the morphological model is discussed. This model will be used for the definition of the potential instability model of the coastal cliffs, starting from a deep knowledge of the geological processes occurring at the slopes. The processing of the data and the proposed protocol as based on an integrated multidisciplinary survey considering the emerged and submerged areas as a single system of evolutionary dynamics.

Vertical surfaces, sloping or very steep slope, are not visible from the maps returned by zenith acquisitions and therefore must be detected with specifically positioned measuring systems. Moreover, as these areas are often not accessible, surveys require remote sensing systems to build a DEM. This is a widely diffused tool for geomorphological mapping and landslide susceptibility/hazard assessment, mainly because it provide the foundation for deriving surface morphological parameters such as slope aspect, curvature, slope profile and catchment areas (Calligaris et al., 2013).

Boat and unmanned aerial vehicle (UAV) digital photogrammetric surveys have been proposed as a new approaches to extract 3D point clouds of coastal cliffs (Esposito et al., 2017; Salvini et al., 2011). Observations could be conditioned by the visibility cones, thus data acquisition has to be plan carefully. According to these methods, an acquisition campaign has been carried out in the Sella del Diavolo study site. The survey provided cliff surface data capture using both photogrammetry from boat and Terrestrial Laser Scanner (TLS) systems. Geo-referencing target points using GNSS and total station instruments (for TLS) ensured survey geometry and position accuracy. Collected data have been then processed using commercial and free 3D data computing software, obtaining dense point clouds as surfaces models of the cliffs. For the site of Sella del Diavolo, a TLS data subset containing around 23.5 M points has been chosen for the cliff geometric characterization. Applying the kd-tree algorithm of the free 3D data software "CloudCompare v2.9.1", 9,355 facets in the cliff have been detected setting 20 degrees of maximum variation. Thirty-six main sets of surfaces with dip and dip direction ranging in a neighbourhood of 30 degrees were identified. Resulting surfaces have been statistically analysed, providing the main orientations occurring on the cliff.

In the submerged sector of the Sella del Diavolo, a Single Beam (HYDROTRAC ™ II - 200 Khz) and Side Scan Sonar (StarFisch 990F - 1 Mhz) data surveys with total coverage were carried out. The correct positioning was guaranteed by the GPS system. The Single Beam data covered an area of 3560 km^2 with tracklines orthogonal to the coast. Cleaning and filtering of Single Beam data were performed by PDS2000 software, and Global Mapper was used to provide the bathymetric map. The bathymetry was plotted on a grid data of 0.5 m node spacing as contour plot to display detailed bathymetric information, as slope value and as illuminated 3D perspective view to visualize prominent features along sea floor.

4. PRELIMINARY RESULTS

The analysis of the facets of the Sella del Diavolo site derived from TSL point clouds leaded to the detection of surfaces

characterizing the cliff geometry. Facets discriminated homogeneous surface zones, located on the centre of the cliff wall, from those more heterogeneous on the cliff foot and on the most peripheral areas. The homogeneous surfaces (in yellow and in blue in Figure 6) represent the most frequent dip directions, counting around 5,450 facets over 9,355 and covering an overall surface of about 3,505 m^2 over 19,559 m^2 of the cliff.
These sets mainly occur in correspondence of the collapse areas of the landslides fallen in 1987 and 2017 (Figure 5).

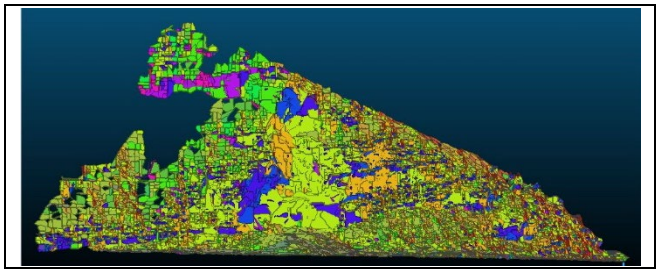

Figure 5. Facets extracted by CloudCompare from Terrestrial Laser Scanner (TLS) point cloud of the "Sella del Diavolo" site

The stereographic projection of poles diagram in Figure 6 shows the spatial distribution of the poles of the facets according to the dip direction. The bar histogram shows that the dominant dip direction distribution includes values between 35.9 and 71.8 degrees, and then from 71.8 to 107.7 degrees.

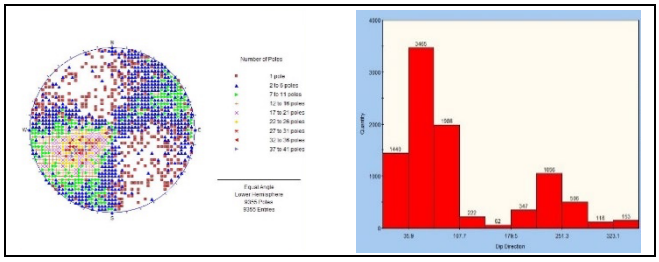

Figure 6. Stereographic projection of poles diagram (equiangular projection on lower hemisphere) and bar histogram of facet distribution of "Sella del Diavolo" site

The analysis of data in the submerged sector allowed to define detailed distribution of incoherent sediments, the landslide deposits at the base of the cliffs, rock outcrops and the main morphologies of the seabed (Figure 7).
In the western sector, a subvertical cliff exposed to east has been detected. In this area, the submerged part of the cliff is sub-vertical and reaches the maximum depth of -8 ÷ -9 m. Fall and toppling deposits, characterized by blocks with dimensions between few decimeters and 1÷2 meters, occur at the base of the cliff.
The morphometric survey of tidal notches detectable in this area confirms that the amplitude is proportional with the magnitude of tidal oscillation, that the point of maximum depth of incision corresponds to the middle sea level, and that greater incisions are located close at submarine resurgences of fresh water (Antonioli el al., 2015). The upper limit of the prairies of Posidonia oceanica is about 35 meters from the coast and detectable at -10.5 meters depth. Large areas with coarse and medium sands with predominant lithoclastic composition occur in the central sector, dominated by a low slope area, at a depth between -1 m and -8 meters. This characteristic can be correlated with the cliff exposure to the maximum wave energy that reworks quickly the landslide deposits at the base of the rocky slopes. In fact, in the emerged part, evidences of accelerated erosion processes (gullies) have been detected, also typical of weakly cemented and medium-low permeable soils. The presence of large blocks, located at depths between -2 and -5 meters, which rise up to 3 meters above sea level can be related to paleo-rockfall deposits. The elaboration of rockfall deposits deriving from Miocene sandstone (Arenarie di Pirri Fm.) and the dynamic of currents formed megaripples with a wavelength of 0.5 ÷ 1 m (Figure 8).

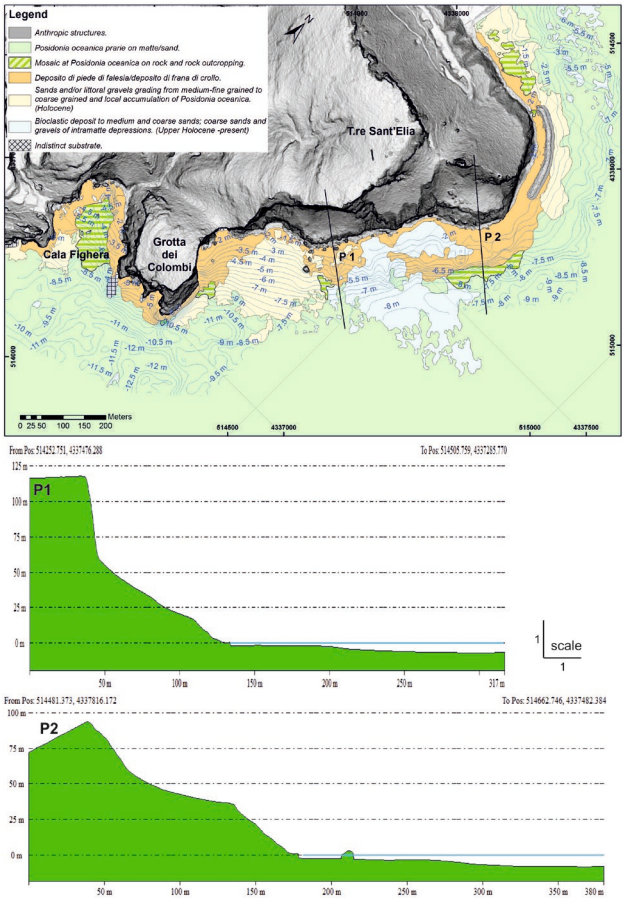

Figure 7 – Sea bad map of Sella del Diavolo

In the north-eastern sector of the surveyed area, the sea beds in front of the cliff are characterized by the presence of an abrasion platform detectable at a depth of -2.5 m and 4 m. It is a morphology engraved on the rocky substrate and with a polycyclic evolution starting from the last sea-level rise - Stage 5.

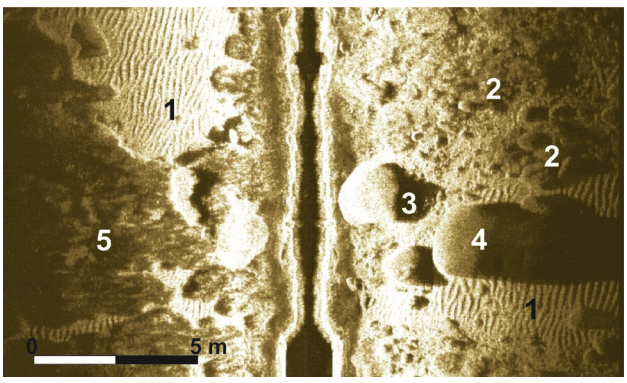

Figure 8 - Side Scan Sonar image (1MHz – 8 meter depth) – Sella del Diavolo cliff. 1) Megaripples structures on Silicoclastic sediments (λ= 0.5÷1 m); 2) elaborated landslide deposits; 3) Block fall (d=4 m h= 3m); 4) Block fall (d=6 m h= 5m); 5) Posidonia oceanica on wave-cut platform.

A strong correlation between the evolution of the perilitorial rock platforms (elevation, slope, continuity, integrity, height and rate of inner margin retreat) with exposure to extreme event has been observed, according to what described by Chelli et al. (2010) and Pappalardo et al. (2016).
On the summit surface of the abrasion platform, erosion pits and canals morphologies occur, which are linked to the movement of deposits at the base of the cliff. Instead, on the sub-horizontal rocky surfaces at the intertidal and supralitoral band, the bio-modeling and bio-demolition processes interact each other (Pappalardo et al., 2017).

5. CONCLUSIONS

Different techniques aiming to reconstruct the past evolution and future dynamics that will affect the rocky coasts have been applied in a pilot sites in the south of Sardinia, considering the emerged and submerged coastal cliff in a single system of evolutionary dynamics.
Reconstruction of the geometry and morphologies of cliff surfaces using digital photogrammetry and TLS demonstrates that 3D models of the surface can be obtained with a good accuracy. Moreover, once the GPS points are fixed and known, it can be proposed as a monitoring system for large areas as the acquisition and processing of data is quite simple.
The comparison of point clouds derived from photogrammetry and terrestrial laser scanner is ongoing. For areas that are not completely accessible, the acquisition by UAV will be mandatary to obtain the complete point clouds without blank points, as planned in the next steps of the MAREGOT project.
Single Beam and Side Scan Sonar surveys allowed mapping submerged area close to the cliff and recognizing main morphological features. Main identified morphologies are coherent with processes observed in the exposed cliff, pointing out a strong correlation between the evolution of the perilitorial areas exposure to extreme events.

ACKNOWLEDGEMENTS

MAREGOT is a strategic project of INTERREG Italy-France Maritime 2014.2020, Cross-border Program co-financed by the European Regional Development Fund (ERDF) under the European Territorial Cooperation (ETC) objective.

REFERENCES

Andriani GF, Walsh N., 2007. Rocky coast geomorphology and erosional processes: a case study along the Murgia coastline south of Bari, Apulia- SE Italy. Geomorphology 87(3): 224–238.

Antonioli F., Lo Presti V., Rovere A., Ferranti L., Anzidei M., Furlani S., Mastronuzzi G., Orru P.E., Scicchitano G., Sannino G.M., Spampinato C.R., Pagliarulo R., Deiana G., De Sabata E., Sanso P., Vacchi M., Vecchio A., 2015. Tidal notches in Mediterranean Sea: a comprehensive analysis. Quaternary Science Reviews, 119: 1-19.

Budetta, P., G. Galietta, and A. Santo, 2000. A methodology for the study of the relation between coastal cliff erosion and the mechanical strength of soils and rock masses. Engineering Geology 56.3-4: 243-256.

Budetta P, Nappi M., 2011. Heterogeneous rock mass classification by means of the geological strength index: The San Mauro formation (Cilento, Italy). Bull Eng Geol Environ 70:585–593. doi:10.1007/ s10064-011-0351-1

Budetta, P., & De Luca C., 2015. Wedge failure hazard assessment by means of a probabilistic approach for an unstable sea-cliff. Natural Hazards 76.2: 1219-1239.

Calligaris C., Poretti G., Tariq S., Melis M.T., 2013. First steps towards a landslide inventory map of the Central Karakoram National Park. European Journal of Remote Sensing, 46: 272-287.

Carmignani L., Oggiano G., Funedda A., Conti P., Pasci S., 2016 The geological map of Sardinia (Italy) at 1:250,000 scale. Journal of Maps, 12, 5: 826–835. http://dx.doi.org/10.1080/17445647.2015.1084544

Chelli A., Pappalardo M., Arozarena Liopis I., Federici P.R. 2010. The relative influence of lithology and weathering in shaping shore platforms along the coastline of the Gulf of La Spezia (NW Italy) as revealed by rock strength. Geomorphology 118: 93–104.

De Blasio F.V. & Mazzanti P., 2010. Subaerial and subaqueous dynamics of coastal rockfalls. Geomorphology, 115: 188-193.

De Vita P., Cevasco A., Cavallo C., 2012. Detailed rock-failure susceptibility mapping in steep rocky coasts by means of non-contact geostructural surveys: the case study of the Tigullio Gulf (Eastern Liguria, Northern Italy). Natural Hazards and Earth System Sciences, 12, 867–880. www.nat-hazards-earth-syst-sci.net/12/867/2012/.

Emery, K. O. and Kuhn, G. G., 1982. Sea cliffs: Their processes, profiles, and classification, GSA Bulletin, 93, 644–654.

Esposito G., Salvini R., Matano F., Sacchi M., Danzi M., Somma R., Troise C., 2017. The Photogrammetric Record 32(160): 459–479. doi: 10.1111/phor.12218

Fall, M., R. Azzam, and Noubactep C., 2006. A multi-method approach to study the stability of natural slopes and landslide susceptibility mapping. Engineering geology 82.4: 241-263.

ISPRA, 2017. Linee Guida Nazionali per la difesa della costa dai fenomeni di erosione e dagli effetti dei cambiamenti climatici. Tavolo Nazionale sull'erosione costiera MATTM-Regioni: 312 http://www.erosionecostiera.isprambiente.it/files/linee-guida-nazionali/TNECLLGGNazionaliDifesadellaCostadallErosione_mar2017.pdfclimatici. Last view 01/04/2019 *in italian*

Martino, S., and Mazzanti P., 2014. Integrating geomechanical surveys and remote sensing for sea cliff slope stability analysis: the Mt. Pucci case study (Italy). Natural Hazards and Earth System Sciences 14.4: 831.

Pappalardo M., Buehler M., Chelli A., Cironi L., Pannacciulli F. & Qin Z. 2016. Quantitative Estimate sof Bio-Remodeling on Coastal Rock Surfaces. J. Mar. Sci. Eng., 4(2): 37.

Pappalardo M., Cappietti L., Arozarena Llopis I., Chelli A. & De Fabritiis L., 2017. Development of Shore Platforms along the NW Coast of Italy: The Role of Wind Waves. Journal of Coastal Research: 33, 5: 1102-1112.

Paronuzzi P., 2010. Flexural failure phenomena affecting continental Pleistocene deposits along coastal cliffs (Croatia). Ital J Eng Geol Environ 1: 93–106.

Ružić, Igor & Marović, Ivan & Benac, Čedomir & Suzana, Ilic., 2015. A stability assessment of coastal cliffs using digital imagery. Acta geotechnica Slovenica, 12: 25-35.

Salvini, R., Francioni, M., Riccucci, S., Fantozzi, P. L., Bonciani, F. and Mancini, S., 2011. Stability analysis of "Grotta delle Felci" cliff (Capri Island, Italy): structural, engineering–geological, photogrammetric surveys and laser scanning. Bulletin of Engineering Geology and the Environment, 70(4): 549–557.

Sunamura, T., 1977. A relationship between wave-induced cliff erosion and erosive force of waves. J. Geol. 85: 613–618.

Sunamura, T., 1983. Processes of sea cliff and platform erosion. In: Komar, P.D. (Ed.), CRC Handbook of Coastal Processes and Erosion. CRC Press, Boca Raton, FL: 233–265.

Sunamura, T., 1992. The Geomorphology of Rocky Coasts. Wiley, Chichester.

COASTAL MONITORING THROUGH FIELD AND SATELLITE DATA

M. Perna[1]*, G. Vitale[2], C. Brandini[2], E. Pranzini[3], B. Gozzini[1]

[1] Consorzio LaMMA, Via Madonna del Piano 10, Sesto Fiorentino (FI) – (perna, gozzini)@lamma.rete.toscana.it
[2] CNR Ibimet, Via Caproni 8, Firenze – Consorzio LaMMA, Via Madonna del Piano 10, Sesto Fiorentino (FI) – carlo.brandini,@cnr.it, vitale@lamma.rete.toscana.it
[3] Dipartimento di Scienze della Terra, Università di Firenze, Via Micheli 6, Firenze - enzo.pranzini@unifi.it

KEY WORDS: Remote sensing, Shoreline, Coastal dunes, Beach monitoring, GPS.

ABSTRACT:

Several different indicators have been adopted to map shoreline evolution from remotely-sensed images, some of them are based on the identification of specific features (shoreline, dune foot, etc.), others concern specific vertical datum related to a given sea level.
Tuscany Region adopted the 0 m elevation contour as proxy to monitor coastal evolution and surveys with traditional topographic instruments, at first, and with dGPS/GNSS, later, have been carried out since the mid 1980s.
The need to frequently update this dataset and have synchronous measurements along the whole regional coast found answer in the methodology presented in this paper, which is based on the Pleiades images processing for a semiautomatic shoreline extraction.
The 0 m elevation contour is postulated to be midway between the run-up and the run-down; the formers to be located at the contact between dry and wet sand, the latter where foam borders the beach under fair sea state.
For the regional coast, where tidal range is within few decimetres, and for images acquired after several days from a storm, this indicator, easily retrieved from ad hoc processed satellite images, proved to be reliable.
A comparison between manually drawn and semi-automatically extracted shorelines gave an accuracy of 0.14 m.
Being the position of the so acquired shoreline affected by errors (e.g. pixel size, threshold identification, etc.) and influenced by physical factors (e.g. tide and swash zone slope) error analysis for the beach at Marina di Cecina was performed, giving a maximum value of ± 1.8 m, which is considered acceptable for a regional monitoring.
Dune foot position, which is less sensitive to short term beach variability, was retrieved as well and showed the same accuracy.
Considering that, where tidal range is within few decimetres and under fair sea, 0 m elevation contour (which is the common reference for shoreline field detection through dGPS/GNSS) can be approximately set between the run up limit (wet/dry sand limit) and the run-down limit (approx. upper side of the beach step), we used the strip delimited by these two limits as the proxy for our shoreline, and defined it as a first approximation as the midline of this strip. A method in which the different data (in-situ, satellites) are processed as well as a quantitative validation of this method is presented. Errors that can occur derive from manual digitation, pixel error related to the image spatial resolution, and geometric error due to the orthorectification process. Nevertheless, results show average differences between EO data and survey data far below 1m, which is a good result in for regional scale monitoring purpose. The same analysis has been performed on coastal dunes proxy, using existing multi-temporal datasets.

1. INTRODUCTION

Shoreline position monitoring is a crucial activity in a wide range of studies related to coastal management and mostly in evaluating coastal erosion.
This work addresses the criticalities associated with the monitoring of the shoreline position (proxy definition, error evaluation, etc.) (Boak & Turner, 2005), with the aim of minimizing the scatter between the ground observations and the EO data. A quantitative validation of this method is presented, as well as the ways in which the different data (in-situ, satellites) have been processed and compared. Also, by means of the same EO data, coastal dunes have been measured and monitored through multi-temporal analysis, using existing datasets. The definition of a proxy is necessary both for shoreline and dune semi-automatic extraction and for the digitizing activity (Boak & Turner, ibid.). In order to perform a correct coastal monitoring, the proxies should allow the comparison of final results with existing dataset available in the area (Cenci et al. 2018).
For the shoreline, which is intrinsically highly instable, and also for coastal features many indicators (proxies) have been proposed in the literature (Fletcher et al., 2003; Carli et al., 2008; El Banna and Hereher, 2009; Kumar, Narayana, and Jayappa, 2010). Anyway, in a monitoring activity of morphological evolution, one of the most important goal is to produce (field and/or remotely-sensed) data which is possible to compare with existing datasets, that is data detected using the same proxy; the proxies chosen for this work try to respond to these needs.

2. MATERIALS AND METHODS

With the Law 80/2015, Regione Toscana established "Rules on soil protection, protection of water resources and protection of the coast and coastal habitats" confirming the need to monitor coastal areas at regional scale.
Regione Toscana and LaMMA Consortium have started a regional scale coastal monitoring activity, with particular reference to annual monitoring of the shoreline and, through the use of satellite optical images, taking advantage of the availability of remotely sensed data at higher resolution than in the past (less than 1 m), and at sustainable costs. In this work we focus on the coast-south of Marina di Cecina (tidal range 0.3 m), which is being affected in these years by a severe erosion.

* Corresponding author

The analysis was conducted on an image acquired on August, 3rd 2017 when significant wave height (Hm0) was 0.2 m.

2.1 Pre-processing of satellite images

Subsets of Pléiades satellite scenes have been acquired for the whole regional coast with 4 Multispectral bands (Spatial resolution: 2 m) and 1 Panchromatic band (Spatial resolution: 0.5 m). Images consists in a 6 km strips (about 5 km on land and 1 on the sea) to allow the complete analysis of coastal areas processes.
Images has been pre-processed: at first pan-sharpening has been applied, which consists in merging the multispectral image with the panchromatic one to obtain a set of high resolution multiband data.
Than topographic correction has been applied (orthorectification) using the RPC models in bundle with the image. The rational polynomial coefficients can replace the rigorous imaging model, in addiction with a few control points per image (RMS = 0.49).
In order to perform the shoreline detection, image has then been subsected to extract only the subaerial and the nearshore area.

2.2 Proxy definition for shoreline and dune semi-automatic extraction

Available shoreline datasets of the study area, had been acquired through dGPS/GNSS (detecting 0 elevation contour). The remotely-sensed data proxy should allow to acquire shoreline and dune foot data comparable with these measures. So, for the shoreline detection, a "double" proxy has been chosen: the run-up limit and the step line. This because in a beach profile, in micro tidal coasts, this range normally comprehend the 0 m elevation. So, as reference for the shoreline, its approximated midline has been considered.
While is relatively easy to identify the run-up upper limit in the image, the lower limit (upper beach-step) can be identified directly in the image (in clear water and calm conditions) or detecting the position of the last breaker towards the beach in smooth sea conditions.
As proxy of the dune foot, the main scarp in the eroded foredune, which, in this case, is consistent with the limit of continuous vegetation, has been considered.
All the methods for the semi-automatic extraction of both shoreline and dune foot have been exploited by open source codes and software (R, GDAL, QGis, Orfeo Toolbox - OTB) (R Core Team, 2017; GDAL/OGR contributors, 2018; QGIS Development Team, 2009; Inglada J. and Christophe E., 2009).

2.3 Semi-automatic extraction of the shoreline

For the semi-automatic extraction of the shoreline, the NIR (near infrared) band has been used because in this wavelength we have the maximum difference in reflectivity between water and land pixel values (Sabins, 2007).
Different steps have been followed to accomplish this task: first of all, image have been slightly smoothed with a Gaussian filter (isoblurring; sigma = 1), to eliminate the high frequency noise in the image which may create problems in the semi-authomatic extraction of the features; tests with and without this filter showed there are no significant differences in the results.
An edge detection algorithm (canny) has been applied in R (Barthelme, 2018). This algorithm produced inaccurate limits between wet and dry sand (run-up limit) and in correspondence of last breaker towards the beach. This step is the most important and it must be accurately accomplished with a try and error procedure, which can be high time consuming, depending on the quality of the image and the sea conditions at acquisition time. That's why it's important to acquire the image after a period of quite stable sea conditions.

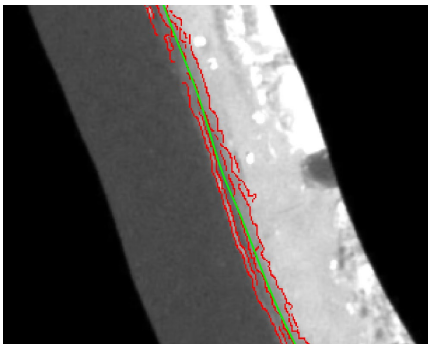

Figure 1. Spline interpolation of edge detection results, to perform the semi-automatic extraction of the shoreline

Finally, these limits were interpolated with a spline to extract the shoreline position.
The described method, consists in a simple and repeatable procedure which is normally very fast, compared with the manual digitation in GIS, and it's only slightly affected by the operator's choices.

2.3.1 Comparison between manual digitizing and semi-automatic extraction of shoreline

The comparison has been realized analyzing the average differences between the datasets produced along sectors of coast of about 50 m.
Average difference between manual digitizing and semi-automatic extraction of shoreline is 0.55 m. It shows a good accordance between the two datasets, confirming the confidence of this semi-automatic method, especially at a regional monitoring scale; we define a monitoring regional scale data referring to a few hundreds of kilometers area, with a spatial accuracy of about 1 meter.

2.4 Semi-automatic extraction of the dune-foot limit

The strong erosion affecting this area is evident in the beach profile, so instead of the incipient dune areas, an almost vertical scarp in the foredune has developed (Fig.2). This scarp is not continuous along the beach and sometimes switch to a gentler slope degrading to the flattened beach. Anyway, this limit is quite visible in the image also because it usually represents the limit of continuous vegetation.

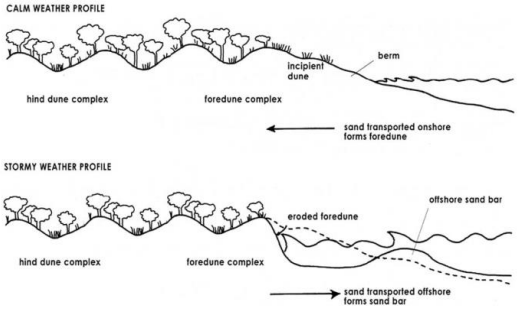

Figure 2. Profile scheme of a beach-dune system. Top: calm conditions; Bottom: stormy conditions

Different techniques have been tested for the semi-automatic mapping of coastal landforms to evaluate this limit in the image:

1. Unsupervised (KMeans) (Grizonnet et al., 2017)
2. Supervised (Random forest) (Liaw & Wiener, 2002)
3. Segmentation (Mean shift) (Grizonnet et al., ibid.)

All the bands have been used to perform these classifications.
At the end, a comparison between the position of extracted dune-foot and the position of the digitized one has been conducted.

2.4.1 Unsupervised extraction of coastal landforms

This method performs an unsupervised K-Means image classification implemented in OTB. K-Means Classification is a composite application, using an existing training and classification application.
The algorithm automation perform an image classification through a number of steps:

1) ImageEnveloppe: create a shapefile (1 polygon),
2) PolygonClassStatistics: compute the statistics,
3) SampleSelection: select the samples by constant strategy in the shapefile (1000000 samples max),
4) SamplesExtraction: extract the samples descriptors (update of SampleSelection output file),
5) ComputeImagesStatistics: compute images second order statistics,
6) TrainVectorClassifier: train the model,
7) ImageClassifier: performs the classification of the input image according to a model file.

The following parameters have been selected for this procedure:

- Number of classes (nc): 15 (Number of modes, which will be used to generate class membership). This value derived from considering about 3 times the number of different features to extract (sea, dry sand, wet sand, incipiently vegetated dune, forested dune).
- Training set size (ts): 1000 (Size of the training set, in pixels).
- Maximum number of iterations (maxit):1000 (Maximum number of iterations for the learning step).

Than morphological operators were used to eliminate the typical noise of raster classification outputs.

2.4.2 Supervised extraction of coastal landforms

Supervised classification was exploited using Random forests (RF) algorithm implemented in R.
RF is a peculiar machine learning algorithm which uses randomness at 2 levels:

1) Data selection (n random subset of data - bootstrapping)
2) Attribute selection (m random attributes –in this case: image bands' values).

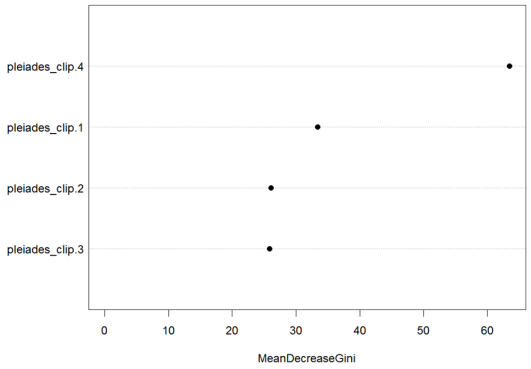

Figure 3. Plot of mean decrease in Gini coefficient for the 4 bands of the image used (band1 = Blue, band2 = Green, band3 = Red, band4 = NIR). The mean decrease in Gini coefficient is a measure of how each variable contributes to the homogeneity of the nodes and leaves in the resulting random forest.

A set of training points has been chosen to extract raster bands data and perform the supervised classification.
The RF importance plot (Figure 3) confirms that band 4 (NIR) of the image is by far the most effective one to discriminate the classes of landforms, and in particular the dune foot limit.

2.4.3 Segmentation procedure to extract coastal landforms

The segmentation was produced using mean shift algorithm from OTB (Grizonnet et al., ibid.). The output is a classical image of unique labels identifying the segmented regions.
This algorithm has a high parametrization level. filter.meanshift.thres = 0.1 (Algorithm iterative scheme will stop if mean-shift vector is below this threshold or if iteration number reached maximum number of iterations).
A set of parameters of software called Vector Parameters, in particular, allow to obtain very different results and can be modulated according to the scale of work and the resolution needed for the output features.

2.4.4 Comparison between manual digitizing and semi-automatic extraction of dune foot

In the following table the results of the comparison, conducted as described in 2.3.1, show that supervised classification gave a better accordance with the digitized data. The highest differences are in sectors where the dune foot is not so evident, that is where, as discussed before, the scarp in the foredune was not developed (Table 1).

	Unsup.	Sup.	Segm.
Avg. diff. with manual digitizing	2,0 m	1,60 m	2,1 m

Table 1. Average shift between digitized and semi-automatic extracted dataset of dune foot.

2.4.5 Analysis of the uncertainty of the measurements

Trends and rates of shoreline and of dune foot variation are as reliable as the measurement error that determines the accuracy of each position (Hapke et al., 2006). For this activity, 4 sources of uncertainty were considered:

- Pixel Error (PE) related to image resolution (Virdis et al., 2012).

- Geometric Error (GE), relative to the geo-referencing of the image.
- Digitization Error (DE), related to the uncertainty in the proxy digitization.

And specifically for shorelines:

- Correction with the estimate of the MSL near the coast (ME). This value was estimated using the one recorded at the closest tide gauge and, in particular, at mareographic station in Livorno. For example, a recorded variation of mean sea level of 0.1 m corresponds, on a 7.7° avg. slope shore such as Marina di Cecina, to 0.74 m horizontal displacement of shoreline. Of course, this correspondence doesn't take into account the different amplitude and phase of tide due to the distance between Cecina and Livorno (~ 40 km) and also the differences in atmospheric pressure conditions.
- All of these sources of uncertainty make it possible to first have an estimate of the maximum deviation from the dGPS/GNSS measures (SE), net of the above errors.

Finally, it is possible to estimate the maximum deviation of the limits extracted from the dGPS/GNSS.

$$ETM = \sqrt{PE^2 + GE^2 + DE^2 + SE^2 + ME^2}$$

These are the values for the specific image considered in this work.
Pixel error (PE) ± 0.5 m
Geometric Error (GE) ± 0.4 m
Digitization error (DE) ± 1.0 m
Maximum threshold detection error (SE) ± 1.4 m
Correction with the estimate of the MSL near the coast (ME) ± 0 m (recorded at the same time of the image acquisition)
Estimation of Total Maximum deviation of the limits extracted from the dGPS/GNSS (*ETM*) ± 1.8 m

2.5 Shoreline/dune co-evolution

Using the dataset described above, an analysis on trends and rates of shore/dune system was performed. Five existing datasets acquired in eleven years (2008-2018) had been analysed (Figure 4).

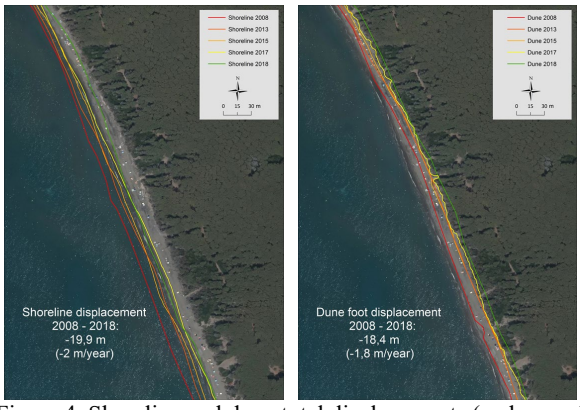

Figure 4. Shoreline and dune total displacements (and annual rate) evaluated with 5 datasets between 2008 and 2018.

Rates of both shoreline and dune foot displacement are quite similar (2 m/yr and 1,8 m/yr respectively).

So, a severe erosion occurred to this beach/dune system, nevertheless the natural conditions backward this system have allowed the beach width, which is a high valuable natural asset, to remain constant during these years.

3. CONCLUSIONS

The comparison between the shorelines obtained through manual digitization and from semi-automatic extraction from satellite image and the relative dGPS/GNSS surveys was assessed as described in 2.3.1 (Table 2).

Platform	Avg. distance to 0 contour line (dGPS/GNSS)/Manual digitizing	Average distance to 0 contour line (dGPS/GNSS)/Semi-automatic extraction
Pleiades 1A	0,43 m	0,57 m

Table 2. Average shift between dGPS/GNSS and digitized shoreline and between dGPS/GNSS and semi-automatic shoreline (Aug. 2017).

The manual digitization method is preferred for the best alignment results with the dGPS/GNSS data, although it is more laborious (and longer to perform) than the data obtained through semi-automatic extraction. On the other hand, semi-automatic methods have the advantage not to depending on the experience of the operator. From the tests performed, however, it can be stated that today it is possible to obtain results from satellite data that on average have a distance with respect to the measured data on the ground that is significantly lower than 1 meter. Besides, accurate analysis of trends/rates of shoreline and dune foot displacements help to monitor coastal condition in order to assess the presence and the intensity of erosion processes. As shown in this work, these tasks can be performed, at least at a regional scale, using very high resolution optical satellite images, both through manual digitizing directly from the image, which is a relatively time consuming process, and from semi-automatic acquisition, with a faster, repeatable and still reliable methodology.

REFERENCES

Barthelme S., 2018. imager: Image Processing Library Based on 'CImg'. R package version 0.41.1. https://CRAN.R-project.org/package=imager

Boak E, H., and Turner I. L., 2005. Shoreline Definition and Detection: A Review. Journal of Coastal Research: Volume 21, Issue 4: pp. 688 – 703.

Carli S., Iandelli N., Pranzini E., Salvatori R., 2008. L'utilizzazione di immagini telerilevate ad alta risoluzione per lo studio dell'erosione costiera: estrazione della linea d'acqua e valutazione della sua accuratezza. Studi Costieri, 14, pp. 43-54.

Cenci L., Disperati L., Persichillo M. G:, Oliveira E. R:, Alves Fàtima L. & Phillips M., 2018 Integrating remote sensing and GIS techniques for monitoring and modeling shoreline evolution to support coastal risk management, GIScience & Remote Sensing, 55:3, 355-375, DOI: 10.1080/15481603.2017.1376370

Fletcher C., Roone, J., Barbee M., Lim S.C. & Richmond, B., 2003. Mapping shoreline change using digital ortho-

photogrammetry on Maui, Hawaii. *Journal of Coastal Research Special Issue,* N° 38, 106–124.

GDAL/OGR contributors, 2018. GDAL/OGR Geospatial Data Abstraction software Library. Open Source Geospatial Foundation. URL http://gdal.org (27 September 2018).

Grizonnet, M.; Michel, J.; Poughon, V.; Inglada, J.; Savinaud, M.; Cresson, R., 201. Orfeo ToolBox: Open Source Processing of Remote Sensing Images. Open Geospatial Data, Software and Standards 2017, 2. doi:10.1186/s40965-017-0031-6.

Hapke C.J., Reid D., Richmond B.M., Ruggiero P. and List J., 2006. National Assessment of Shoreline Change part 3— Historical shoreline change and associated coastal land loss along sandy shorelines of the California coast. U.S. Geological Survey, Open-File Report 2006-1219, http://pubs.usgs.gov/of/2006/1219.

Inglada J. and Christophe E. 2009, The Orfeo Toolbox remote sensing image processing software. *2009 IEEE International Geoscience and Remote Sensing Symposium*, Vol. IV, pp. 733-736. doi: 10.1109/IGARSS.2009.5417481

Liaw A. and Wiener M., 2002. Classification and Regression by randomForest. R News 2(3), 18--22.

QGIS Development Team, 2009. QGIS Geographic Information System. Open Source Geospatial Foundation. Open Source Geospatial Foundation. https://www.qgis.org/en/site/ 21 September 2018.

R Core Team, 2017. R: A language and environment for statistical computing. R Foundation for Statistical Computing, Vienna, Austria. URL https://www.R-project.org/ 21 September 2018.

Sabins F. F., 2007. Remote Sensing: Principles and Applications, Third Edition. Waveland Press, 2007
(SPOSTATA PIU' IN ALTO)

Virdis S.G.P., Oggiano G. & Disperati, L., 2012. A Geomatics Approach to Multitemporal Shoreline Analysis in Western Mediterranean: The Case of Platamona-Maritza Beach (Northwest Sardinia, Italy). *Journal of Coastal Research*, 28(3), 624 – 640.

Application of remote sensing in urban environments

REMOTE SENSING AND URBAN METRICS: AN AUTOMATIC CLASSIFICATION OF SPATIAL CONFIGURATIONS TO SUPPORT URBAN POLICIES

E. Barbierato[1]*, I. Bernetti[1], I. Capecchi[1], C. Saragosa[2]

[1] DAGRI, Department of Agricultural, Food, and Forestry, 50144 Piazzale delle Cascine Florence, Italy - (elena.barbierato, iacopo.bernetti, irene.capecchi)@unifi.it

[2] DIDA, Architecture School, 50053 Empoli Florence, Italy – claudio.saragosa@unifi.it

KEY WORDS: Urban green; Urban ecology; Urban quality; LiDAR; Remote sensing; Urban configurations; Urban policies

ABSTRACT:

The main aim of the research has been to create a classification system to evaluate the ecological characteristics of urban green spaces. From the current literature, we know that urban green allows us both to solve some problems such as air pollution, noise pollution and urban heat island, and to improve the aesthetic perception of urban quality. For this reason, in this paper the attention has been focused on the classification of urban green, and has been proposed an automatized methodology based on landscape metrics and remote sensing data, which have been distinguished homogeneous areas with the same structural and morphological characteristics of the vegetation. The innovative aspects of the method has been mainly three: the use of the coverage and height of the urban green from multispectral images and LiDAR data, the spatialization of this data on a central element of urban planning, namely city block, and, lastly, the use of a spatially bound geographic clustering procedure to identify both homogeneous and neighboring areas. The results have been shown the city of Livorno divided into different clusters, which have been highlighted the characteristics of the urban green. Each group has been characterized by city blocks that differ according to the shape and distribution of vegetation. The method permitted to differentiate the historical center from the suburbs and in according to this results we are able to determine guidelines useful for urban and landscape planning to regenerate and plan new urban spaces.

1. INTRODUCTION

1.1 Literature references and aim

One of the major problems in the 21st century are urbanization and industrialization processes, because these have brought about several undesirable environmental changes (Rakhshandehroo, Mohdyusof, Tahirholder &Yunos, 2015).
The cities are affected by some problems such as the poor air quality, the noise pollution and the effects of the heat island caused above all by the gradual replacement of urban green spaces with the urban fabric (Zhou & Rana, 2012; Song & Park, 2014). In addition to these environmental problems, the replacement of urban green has also entailed social problems. In fact, the visual perception of vegetation plays an important role in urban planning, and it contributes to the quality of residents' lives. (Cheng, Chu, Zong, Li, Wu & Li, 2017).
Therefore, it is important to study these problems to identify effective measures in order to improve the cities. Since many studies have shown that the green spaces can greatly affect the quality of the environment and life in the city (ISPRA, 2009), the research has been focused on the classification of the urban green. The main aim of the study has been to create a classification system that would be useful for analysis method urban quality and urban ecology. For this reason we proposed an automatized methodology based on landscape metrics and remote sensing data, which distinguished homogeneous areas with the same structural and morphological characteristics of the vegetation. These areas can be traced back to urban green patterns, on which it is possible to determine guidelines useful for urban and landscape planning to regenerate and plan new urban spaces.

2. MATERIALS AND METHOD

2.1 Study area

Livorno is a municipality of Central Italy located on the Tuscan coast and overlooking the Ligurian Sea. Since the topic of the paper focuses on urban green, the perimeter of the study area only includes the urbanized territory of the city.
Thus, industrial areas to the north of the city, rural districts and hamlets that are too far from the city centre have been excluded from the municipal territory.

2.2 Data

The input data have been cartographic information and remote sensing data, both downloaded by database of Tuscan region. The vegetation cover was obtained by the photogrammetric processing of 14 aerial multispectral frames (four bands: red, green and blue + near infrared regions (NIR)) acquired in December 2012 by means of an UltraCam Xp (Vexcel) digital metric camera, resolution was 0,2x0,2m.
The height of vegetation derived from 18 LiDAR images on 2008 with resolution 1x1m. In the end, the city blocks derives from topographic database on 2002-2004 with a detail of scale 1:2.000. All the input raster - multispectral images and city blocks raster - have been aligned at 1 x 1 m resolution using the nearest neighbour algorithm.

2.3 Method

The method used was divided into 4 steps:
The first allowed us to obtain the coverage and height of the vegetation. The second ensured to spatialize this data on the city blocks. In the third it was calculated landscape metrics, and,

* Corresponding author

lastly, in the last one the results were analyzed using the skater method to obtain homogeneous clusters.

2.3.1 Step 1 - Remote sensing data

The urban vegetation coverage was identified through the analysis of the Normalized difference vegetation index (NDVI). As reported in the literature (Rodgers III, Murrah & Cooke, 2009; Bhandari, Kumar, Singh, 2012), since only healthy vegetation was needed for the study, it was extracted only the NDVI with a value greater than or equal to 0.2. The result is a boolean map, in which the value 0 indicates the absence of vegetation, while the value 1 the presence of vegetation, with a resolution of 1 meter similar to that of the LiDAR data.
Since the urban green is characterized by various types, that have a different ecologic and perceptive function, we distinguished these types according to height value.
To obtain the height of the vegetation we made an overlay operation between the NDVI binary and Normalized Digital Surface Model (nDSM), generated from LIDAR data. The result of this operation was a raster map divided into 3 height classes. The first class from 0 to 0.40 m represented grass, the second from 0.40 to 3 m was classified as hedges and the third greater than 3 m was classified as trees.

2.3.2 Step 2 - Spatial data of the city blocks

We analyzed the vegetation inside city blocks, because these are a central elements of urban planning and urban design, and they are basic building blocks in urban city.
In according to the definition of Oxford Dictionary, a city block is the smallest area that is surrounded by four streets, usually containing several buildings and vegetation. In this paper the city blocks were obtained by clipping roads, railways and waterways from the study area.
Next, we rasterized the city blocks vector, maintaining the same resolution of the other data.

2.3.3 Step 3 - Landscape metrics

We started from the concept that, as it happens in enclosed spaces, the ecological characteristics of urban green depend not only on the overall surface, but also on the shape and distribution of vegetation within city blocks. For this reason we identified homogeneous city blocks through the use of landscape metrics. Using the Fragstats 4.2 software (McGarigal, Cushman & Ene, 2012), we used the class level among the various levels of landscape analysis, because it allowed us to calculate for each singular geometry the metrics of each type of green. The metrics we used were: Percentage of Landscape and Edge density, both normalized on the area. The former allowed us to understand the percentage of plant cover of each city block; the operation is as follows:

$$PLAND = P_i = \frac{\sum_{j=1}^{n} a_{ij}}{A}(100) \qquad (1)$$

where P_i = proportion of the landscape occupied by patch type (class) i.
a_{ij} = area (m^2) of patch ij.
A = total landscape area (m^2).

The latter allowed us to understand the compactness and distribution of the vegetation of each block. The calculation is as follows:

$$ED = \frac{\sum_{k=1}^{m} e_{ik}}{A}(10{,}000) \qquad (2)$$

where e_{ik} = total length (m) of edge in landscape involving patch type (class) i; includes landscape boundary and background segments involving patch type i.
A = total landscape area (m^2).

We chose the Percentage of Landscape because the urban blocks had different dimension; while the Edge density represented an important ecological parameter, since many benefits of urban green (e.g. pollution abatement, acoustic barrier, aesthetic appreciation) depend on the linear development of vegetation rather than on the surface (Maimaitiyiming, Ghulam, Tiyip, Pla, Latorre-Carmona, Halik, Sawut, Caetano, 2014; Tian, Jim & Wang, 2014; Cho, Poudyal & Roberts, 2008). The results represented through three maps showing the quantile distribution of the different types of vegetation: grass, hedge and tree (Figure 1,2,3).

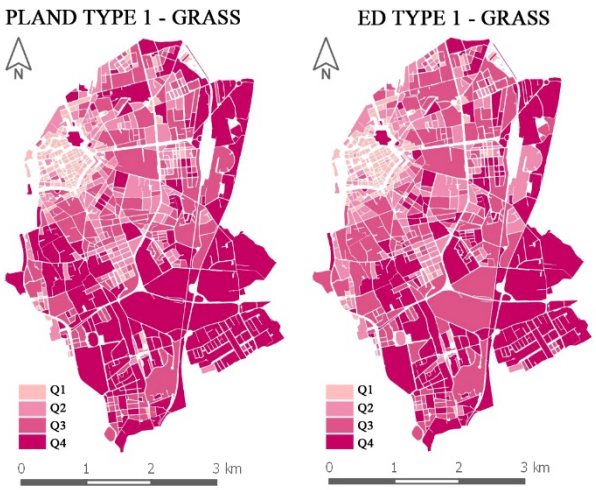

Figure 1. Quantile distribution of grass

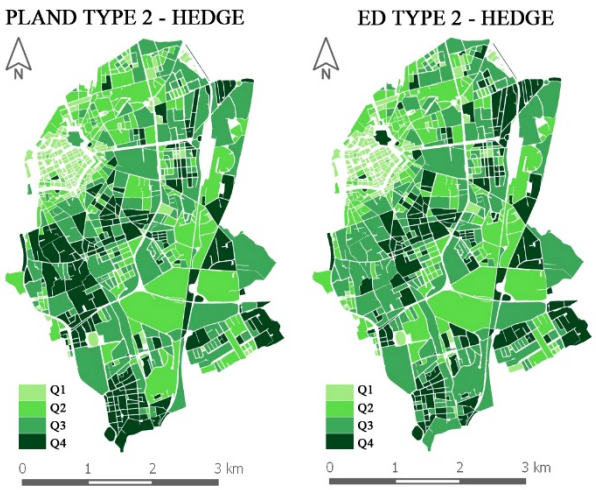

Figure 2. Quantile distribution of hedge

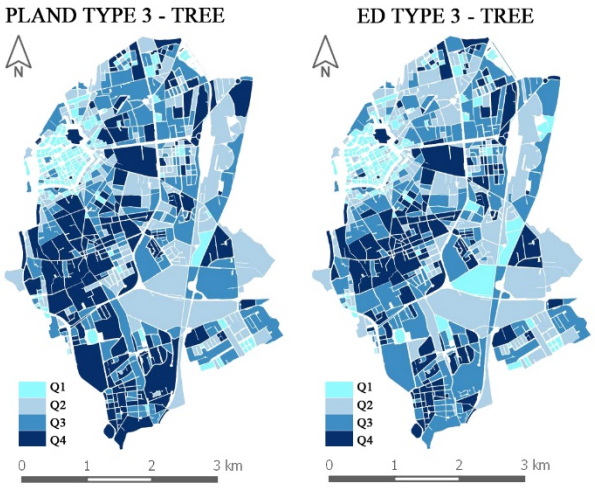

Figure 3. Quantile distribution of tree

2.3.4 Step 4 - Clustering

Since the ecological and visual characteristics of the city can not be reduced to the analysis of the single city block, it was necessary create homogeneous areas based on the similar characteristics of the urban green through a Cluster Analysis of the city. Considering that the traditional clustering procedures do not take account the spatial relation among the geometries (MacQueen, 1967), we used a spatially bound geographic clustering procedure, that groups the territorial area objects into homogeneous contiguous regions (Haining, 2003). The most effective method for regionalization is the SKATER procedure (Assunção, Neves, Câmara & Da Costa Freitas, 2006).
This procedure is divided into 4 steps:

1. The calculation of a connectivity graph that captures adjacency relations among the objects.
2. The association to the connectivity graph of similarity/dissimilarity index based on the concept of weighted multidimensional distance.
3. The progressive elimination of the connections among the objects with greater dissimilarity, the "minimum spanning tree" (MST)
4. The progressive cut of MST that eliminates the residual branches with higher dissimilarity to obtain objects characterized by high internal homogeneity and a heterogeneity among the other groups.

In this research the results of the landscape metrics were analyzed using this method. To calculate a connectivity graph we defined a distance weight based on 12 as number of neighbours, because it was the smaller value that allowed the complete connection of all city blocks.
Then, the analysis of the standard deviation showed that the number of the clusters was 12. Each clusters had a minimum bound of 10 geometry, because it was the minimum number that must had to have a cluster to be relevant. In fact, after several tests we saw that this number was the only one that allowed us to have sufficient and efficient macro-areas for landscape and urban planning, reducing to a minimum the fragmentation of the city.The clusters are shown in Figure 4.

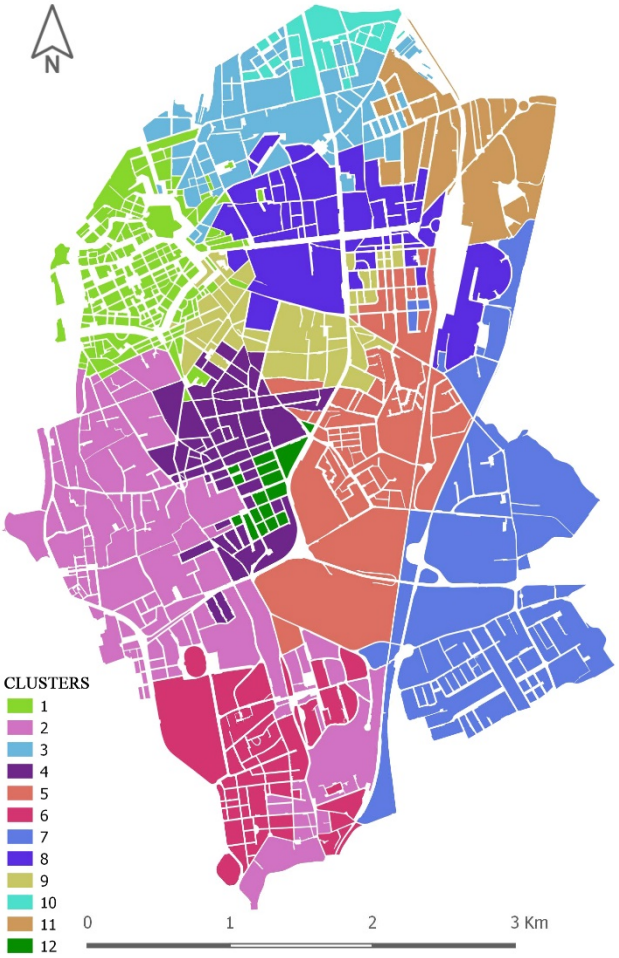

Figure 4. The clusters

3. DISCUSSION AND CONCLUSIONS

The clusters were analyzed through box plots, that allowed us to understand how the distribution of the vegetation characterized the various clusters (Figures 5 and 6).

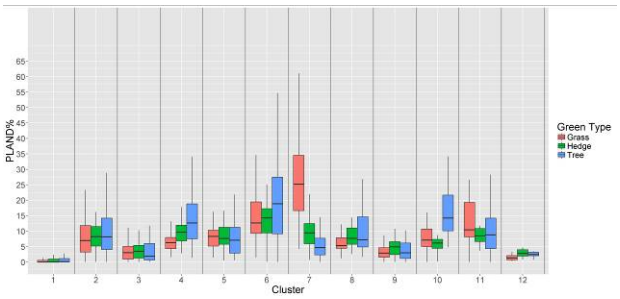

Figure 5. Boxplot of PLAND

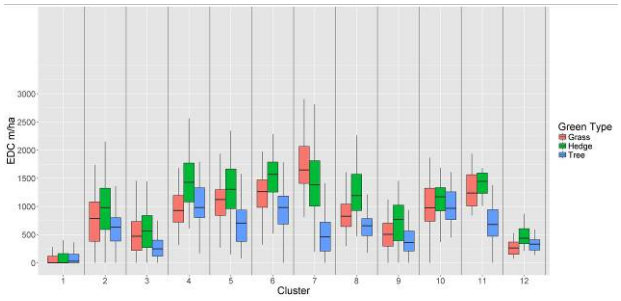

Figure 6. Boxplot of ED

The results of PLAND (Figure 5) show the percentage of the vegetation cover. The clusters number 1 and 12 are composed of city blocks that have less green, in fact the former has a median value of 0% for each green type, the latter has 1% of grass, 3% of hedge, 2% of tree. Instead the clusters number 6 and 7 have the highest percentage value of vegetation cover. The cluster 6 has a median value 13% of grass, 14% of hedge, 19% of tree, while the 7 has 25% of grass, 9% of hedge, 5% of tree.

The results of ED (Figure 6) show the values of no-compactness of the vegetation, it is negatively related to the compactness of urban green. Analyzing the boxplot, it is possible observe that the cluster number 1 has the lowest values, while the cluster number 7 has the highest. In fact the former has a median value of 0 m/ha of grass and hedge, 29 m/ha of tree; the latter has a median value of 1647 m/ha of grass, 1569 m/ha of hedge, 980 m/ha of tree.

To examining the results, we have taken into account the cluster number 2, as this with the major area (19%), and the cluster number 7, as the cluster with a more different composition of vegetation, to determine guidelines useful for the management and maintenance of green areas. The former is composed of a homogeneous green that is either in the inner area of city blocks or as linear element to separate the buildings; the latter is characterized by linear green as linker areas among the houses.

It is important to underline that the method is a first step of the research, but it is able to analyze urban quality and urban ecology.

In conclusion, the future developments of the research are mainly on three issues:

1. To expanding the survey to other urban elements, in particular buildings and roads
2. To verify the relationships among the homogeneous clusters for characteristics of landscape ecology with: visual quality of the city, climatic well-being pollution reduction, etc..
3. To try different and more complex landscape metrics.

REFERENCES

Assunção, R.M., Neves, M.C, Câmara, G., & Da Costa Freitas, C., 2006. Efficient regionalisation techniques for socio-economic geographical units using minimum spanning trees. International Journal of Geographical Information Science, 20(7), 797-811. https://doi.org/10.1080/13658810600665111

Bhandari, A. K., Kumar, A., & Singh, G. K., 2012. Feature extraction using Normalized Difference Vegetation Index (NDVI): A case study of Jabalpur city. Procedia technology, 6, 612-621. https://doi.org/10.1016/j.protcy.2012.10.074

Cheng, L., Chu, S., Zong, W., Li, S., Wu, J., & Li, M., 2017. Use of Tencent Street View Imagery for Visual Perception of Streets. ISPRS International Journal of Geo-Information, 6(9), 265. http://doi:10.3390/ijgi6090265

Cho, S. H., Poudyal, N. C., & Roberts, R.K., 2008. Spatial analysis of the amenity value of green open space. Ecological economics, 66(2-3), 403-416. https://doi.org/10.1016/j.ecolecon.2007.10.012

Haining, R., 2003. Spatial Data Analysis: Theory and Practice Cambridge University Press. https://doi.org/10.1017/CBO9780511754944

ISPRA, 2009. Report 96/2009. Classificazione del verde urbano: una proposta metodologica. ISBN 978-88-448-0303-2

MacQueen, J., 1967. Some methods for classification and analysis of multivariate observations. Proceedings of the Fifth Berkeley Symposium on Mathematical Statistics and Probability, Volume 1: Statistics, 281-297, University of California Press, Berkeley, Calif. https://projecteuclid.org/euclid.bsmsp/1200512992

Maimaitiyiming, M., Ghulam, A., Tiyip, T., Pla, F., Latorre-Carmona, P., Halik, Ü., Sawut, M., & Caetano, M., 2014. Effects of green space spatial pattern on land surface temperature: Implications for sustainable urban planning and climate change adaptation. ISPRS Journal of Photogrammetry and Remote Sensing, 89, 59-66. https://doi.org/10.1016/j.isprsjprs.2013.12.010

McGarigal, K., Cushman, S.A, & Ene, E., 2012. FRAGSTATS v4: Spatial Pattern Analysis Program for Categorical and Continuous Maps. Computer software program produced by the authors at the University of Massachusetts, Amherst. Available at the following web site: http://www.umass.edu/landeco/research/fragstats/fragstats.html

Rakhshandehroo, M., Mohdyusof, M. J., Tahirholder, O. M., & Yunos, M. Y. M., 2015. The socialbenefits of urban open green spaces: a literature review. Management Research and Practice. Vol. 7, issue 4, 60-71. Available at the following web site: https://www.researchgate.net/publication/285596013

Rodgers III, J.C., Murrah, A.W., & Cooke, W.H., 2009. The Impact of Hurricane Katrina on the Coastal Vegetation of the Weeks Bay Reserve, Alabama from NDVI Data. Estuaries and Coasts, 32(3), 496-507. https://doi.org/10.1007/s12237-009-9138-z

Song, B., & Park, K., 2014. Validation of ASTER Surface Temperature Data with In Situ Measurements to Evaluate Heat Islands in Complex Urban Areas. Advances in Meteorology. http://dx.doi.org/10.1155/2014/620410

Tian, Y., Jim, C. Y., & Wang, H., 2014. Assessing the landscape and ecological quality of urban green spaces in a compact city. Landscape and urban planning, 121, 97-108. http://dx.doi.org/10.1016/j.landurbplan.2013.10.001

Zhou, X., Rana, Md. M. P., 2012. Social benefits of urban green space: A conceptual framework of valuation and accessibility measurements. Management of Environmental Quality: An International Journal, Vol. 23, Issue: 2, pp.173-189. https://doi.org/10.1108/14777831211204921

REMOTE SENSING OF THE URBAN HEAT ISLAND WITH DIFFERENT SPATIAL AND TEMPORAL RESOLUTIONS: ANALYSIS BY MODIS AND LANDSAT IMAGERY

S.Bonafoni[1]*, C. Keeratikasikorn[2]

[1] Dept. of Engineering, University of Perugia, via Duranti 93, 06125 Perugia, Italy - stefania.bonafoni@itu.edu.tr
[2] Dept. of Computer Science, Khon Kaen University, Khon Kaen, 40002 Thailand - chaiyapon@kku.ac.th

KEY WORDS: Urban Heat Island, Land Surface Temperature, Bangkok, MODIS, Landsat, Gaussian fitting, Zoning plan.

ABSTRACT:

In this study, we propose the SUHI analysis of the Bangkok megacity, Thailand, from two standpoints: exploiting satellite thermal data at lower spatial resolution (from MODIS, 1-km pixel size) and at higher spatial resolution (from Landsat 8, 100-m pixel size). First, Bangkok was monitored during a long-time interval (2003-2016), both daytime and nighttime, using 728 MODIS scenes. To analyze the SUHI patterns in terms of temporal and spatial trends, a two-dimensional Gaussian fitting technique was applied to quantify the phenomenon. Results highlight that SUHI in the daytime is more evident with respect to nighttime, mainly due to the solar forcing and to the intense traffic and human activities. The SUHI maximum intensities are during daytime, with values reaching 6°C; during nighttime, they are around 1-2 °C. Then, by means of seven Landsat 8 images in the time interval 2014-2016, the SUHI pattern analysis within the land use categories of the Bangkok zoning plan was performed. This monitoring not only describes the current situation, but also provides a perspective insight of the municipal urban plan policy. Overall, the analysis shows that the classes in the city center area, i.e. high-density residential, commercial, historical and military categories, exhibit the highest mean SUHI intensities. The vegetated pixels of these classes exert a less cool effect with respect to the ones placed far from the city core.

1. INTRODUCTION

The urban heat island (UHI) is a well-known anthropogenic thermal modification having implications for human comfort and health, local weather, ecosystem function, urban planning and energy management (Chen et al., 2017; Bhargava et al., 2017; Liao et al., 2017). The UHI phenomenon is due to urban land transformations, especially when vegetated and rural zones are substituted by impervious surfaces absorbing solar radiation (Memon et al., 2007). Therefore, a difference in air and surface temperature between urban area and rural surroundings arises, quantified as UHI intensity. Many studies estimated the UHI pattern by using air temperature from ground-based weather stations, but their uneven distribution does not allow a global analysis over the urban area. Advances in satellite remote sensing and data availability contribute to the surface urban heat island (SUHI) studies in several cities around the world, exploiting the spatial and temporal coverage of spaceborne remote sensing missions (Zhou et al., 2019). The SUHI mapping and analysis can also fulfill the growing demand for sustainable urban planning, providing a scientific support for urban development policies (Bonafoni et al., 2017).

In this study, the SUHI analysis of the Bangkok megacity, Thailand, was carried out from exploiting the different spatial and temporal resolution of MODIS and Landsat 8 data. Specifically, MODIS products provide images at lower spatial resolution (1-km pixel size) but with higher temporal resolution (four passes a day), whilst Landsat data have a higher spatial resolution (100-m pixel size for thermal band) but providing images over the same area every 16 days. Such difference will allow us to perform two different quantitative investigations over the Bangkok city area. In the first analysis, Bangkok was monitored during the period 2003-2016 using 728 MODIS scenes, with daytime and nighttime images. The study provides an extensive spatio-temporal investigation: to analyze the SUHI patterns and its relevance in terms of temporal and spatial trends, a two-dimensional least-square Gaussian fitting technique has been applied to quantify the phenomenon. Such approach represents an efficient quantitative tool to perform comparisons that a visual inspection of several maps would not allow, suitable in the case of large areas and large pixel size.

The second analysis with Landsat 8 data (7 images in the period 2014-2016) allows an insight over the different land use categories of the last comprehensive zoning plan. Since the insight was performed over the government land use plan, it describes the current situation but also can help to verify if the proposed urban plan requires specific future actions for the SUHI mitigation, or if the maintenance of the current municipal development model is in line with the environmental sustainability.

2. STUDY AREA AND DATA SETS

2.1 Bangkok area

The investigated area is Bangkok (Figure 1), the capital and biggest city of Thailand, with a population of over 8 million. The urban area is mainly constituted by Residential and Commercial areas, Military and Public Utilities zones, and with the presence of some parks in the city center (Keeratikasikorn et al., 2018a). Bangkok has been exhibited an evident urban expansion in the last 15 years: the urban density, higher in the city core and decreasing toward the hinterland, was previously modelled and related to the land surface temperature (LST) using a ring-based approach (Bonafoni et al., 2018).

Bangkok has a tropical climate, characterized by monsoons occurring from October to February and by three seasons: winter (from November to mid-February), summer (from mid-February to mid-May) and rainy season (from mid-May to October). The average air temperature ranges from 22 °C in December to 35 °C in April

* Corresponding author

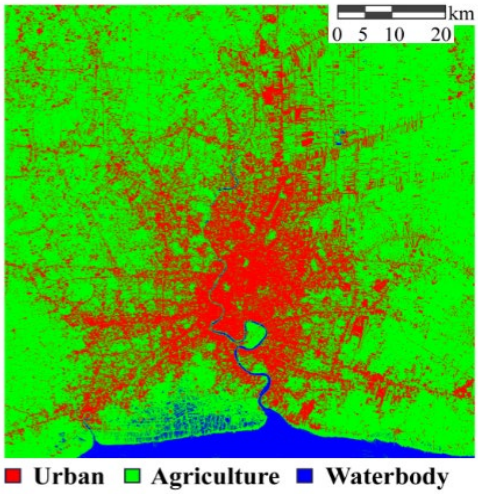

Figure 1. Land cover of Bangkok area (map centre: Lat 13.83° N, Lon 100.54° E) in 2016 from Landsat 8 (see Section 2.3)

2.2 MODIS data

LST images from MODIS sensor on board Terra and Aqua satellite platforms were obtained from the Distributed Active Archive Center (DAAC ORNL, 2017), downloading MOD/MYD11A2 eight-day LST products having a 1-km spatial resolution; cloudy pixels were masked out. In this work MODIS LST maps during winter and summer were considered, for a total of 728 images. This wide dataset was analyzed at three timescales: diurnal (daytime: 10:00 and 14:00; nighttime: 22:00 and 02:00), seasonal (summer and winter), multiyear (interval 2003-2016). Overall, the images were averaged to obtain seasonal mean LST values at the four diurnal times, for each year. For the SUHI computation (see Section 3), the yearly MODIS Land Cover Type Product (MCD12Q1) was used to identify urban and rural pixels

2.3 Landsat 8 data

SUHI maps were retrieved also using Landsat 8 data. This satellite has two sensors, the Operational Land Imager (OLI), with seven reflective band (30 m pixel size), and the Thermal Infrared Sensor (TIRS), with two thermal channels of 100 m pixel size. TIRS bands are also provided resampled at 30 m by the US Geological Survey archive (USGS, 2017).

LST from TIRS Band 10 (10.60 μm – 11.19 μm) (Yu et al., 2014) was obtained by inverting the radiative transfer equation, applying the atmospheric correction and estimating the surface emissivity from reflective bands (Bonafoni, 2016). Seven clear-sky images were processed for LST/SUHI retrieval (17 November 2014, 04 January 2015, 20 January 2015, 05 February 2015, 06 December 2015, 12 April 2016).

To compute the SUHI pattern, the identification of urban and rural pixels in the study area (Figure 1) is performed deriving the Land Use and Land Cover (LULC) map to each of the seven images. The land covers were classified into three types (water, cropland, built-up) applying a supervised maximum likelihood classification technique (Bolstad et al., 1991; Phiri et al., 2017) to OLI data. The LULC map accuracy, evaluated by selected sites in GoogleEarth Pro high-resolution images, exhibited a Kappa coefficient larger than 0.8 for each image.

Concerning the SUHI pattern, to have an average insight of the heating dynamics within the urban area, dampening the seasonal effects of each scene, the mean SUHI map of the seven Landsat scenes will be used in the comparison with the Bangkok land use zoning plan.

3. METHOD

The SUHI intensity in each satellite scene is computed as the difference between the LST of urban pixels and the reference rural LST value. This rural temperature is a bias value computed as the mean LST of the rural pixels in a buffer area of few kilometers surrounding the urban area. Water pixels were discarded from the rural buffer (Zhou et al., 2018).

For the MODIS maps, a method based on a Gaussian surface fitting is used to describe the spatially distributed SUHI pattern at (x,y) pixel location as follows (Streutker, 2003):

$$SUHI(x,y) = a_0 \cdot \exp\left[-\frac{((x-x_0)\cos\phi+(y-y_0)\sin\phi)^2}{0.5a_x^2} - \frac{((y-y_0)\cos\phi-(x-x_0)\sin\phi)^2}{0.5a_y^2}\right] \quad (1)$$

This least-square fit allows to estimate the magnitude (a_0) of the SUHI maximum intensity, its spatial extent (a_x and a_y), orientation (ϕ), and central location (x_0 and y_0) (Streutker, 2003). The parameters a_x and a_y were used to determine the overall area or footprint of the SUHI: it is an ellipse with orientation ϕ (major axis direction). The footprint where the SUHI intensity decreases from the maximum value in the centre up to a level of $e^{-1/2}$, or 61%, will be named A61%. Therefore, each SUHI(x,y) image from MODIS data is fitted to a Gaussian surface using (1), determining the above parameters to quantitatively describe the spatial pattern. This fitting method is suitable for satellite data of low spatial resolution, like MODIS. Since the fitting produces a smoothed surface, the greater variability of higher spatial resolution maps (e.g. Landsat images) reduces the representativeness of the Gaussian surfaces in describing heat island patterns (Anniballe et al., 2014).

4. RESULTS AND DISCUSSION

4.1 Gaussian parameterization of MODIS maps

The Gaussian fitting provides a useful representation of a SUHI pattern having a decreasing trend towards the rural area. This empirical metrics have been applied to quantify the SUHI of a great number of maps and to perform comparative analyses in Thailand (Keeratikasikorn et al., 2018b). Figure 2 show the SUHI pattern and the correspondent Gaussian fitting during summer 2004 and 2012, both for daytime (14:00) and nighttime (02:00). Each SUHI(x,y) maps from MODIS, with x and y standing for latitude and longitude, were fitted with a Gaussian surface: in Figure 2 the black continuous ellipse represents the footprint area A61%. The dashed ellipse, instead, is the fitting area of the UHI for which the temperature is greater than 1.0 K. The red and green lines represent the ellipse major and minor axis directions, the former defining the orientation angle ϕ. The ellipse center is the central location (x_0, y_0). For each map, the magnitude a_0 is also estimated.

The daytime footprint orientation is along the NE-SW quarters and follows the urban land use constituted by commercial and residential zones, mainly deployed in the NE-SW quarters. During nighttime, the absence of solar forcing and the reduced working activities clearly mitigate the heating intensity and modify the SUHI shape and orientation, as evident in Figure 2. In daytime, the footprint central location moves towards the core of the commercial and high-density residential areas. At nighttime, the SUHI footprint is more evident in the south of the city, towards the coastal zone.

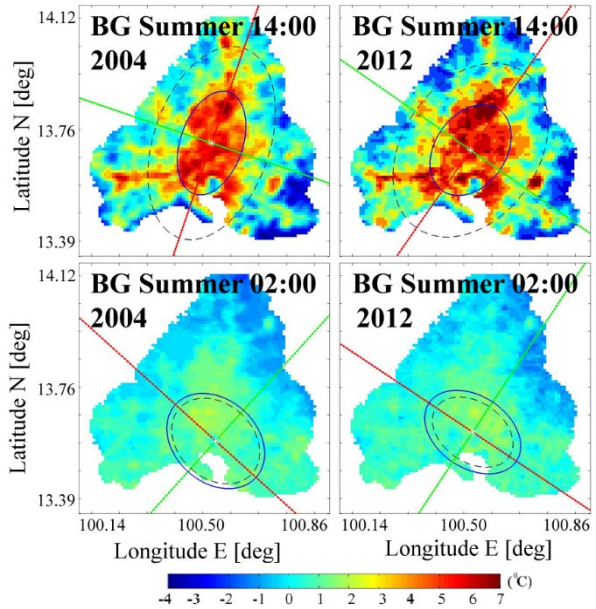

Figure 2. Summer 2004 and 2012: SUHI from MODIS data and Gaussian fitting for daytime (14:00) and nighttime (02:00)

Figure 3 and Figure 4 show the magnitude a_0 and the footprint area A61%, respectively, as mean value and standard deviation (std) computed over the years 2003-2016. Also, in these figures the seasonal behaviour (summer/winter) and the diurnal variation (10:00, 14:00, 22:00 and 02:00) are displayed.

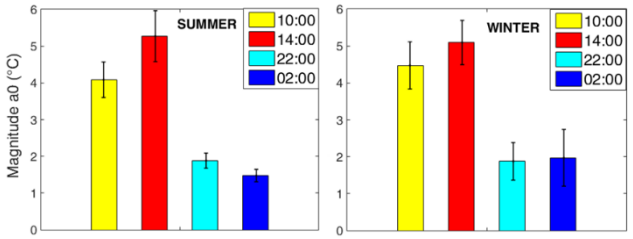

Figure 3. Magnitude a_0 (°C) averaged over the 14 years during summer (left panel) and winter (right panel). The diurnal variation (10:00, 14:00, 22:00 and 02:00) is also reported. The black bar is the standard deviation across the years

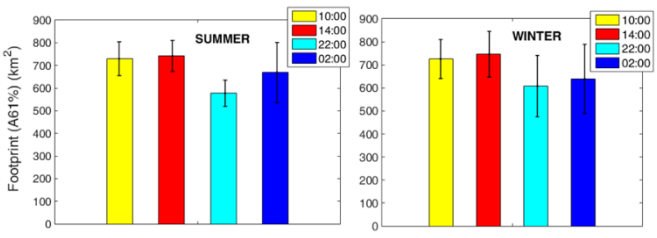

Figure 4. Footprint area A61% averaged over the 14 years in summer (left panel) and winter (right panel), reporting also the diurnal trend (10:00, 14:00, 22:00 and 02:00). The black bar is the standard deviation across the years

Overall, the results of the 14-year interval point out that SUHI does not exhibit significant seasonal differences, with SUHI in the daytime more evident with respect to nighttime, mainly due to the solar forcing and to the intense traffic and human activities. The SUHI maximum intensities during daytime reach 5-6°C; during nighttime they are around 1-2 °C.

4.2 Zoning plan analysis by Landsat 8 data

The MODIS LST maps analyzed in the subsection 4.1 have the main limit in the spatial resolution, hindering more detailed SUHI investigations at finer spatial scale and smoothing warming/cooling sharp peaks.
Therefore, Landsat 8 thermal channel data (with native 100 m pixel size resampled at 30 m) can be used to single out the SUHI pattern within the different land use classes of the zoning plan of Bangkok (Keeratikasikorn et al., 2018a), assessing the surface warming dynamics. Figure 5 reports the last comprehensive land use zoning plan regulating the Bangkok urban area, where ten land categories are present: three Residential zones (with Low/Medium/High-density), Industrial and Commercial zones, Military zone, Historical Protection zone, Public Utilities zone, Agricultural and Rural Conservation zones.
However, the typical SUHI pattern variability obtained using Landsat thermal images is not suitable for a Gaussian fitting, as in the previous investigations with MODIS data. Therefore, in this analysis the mean SUHI map obtained from the seven Landsat scenes in the period 2014-2016 was straightforwardly used to extract the heating pattern of each category of the land use zoning plan.

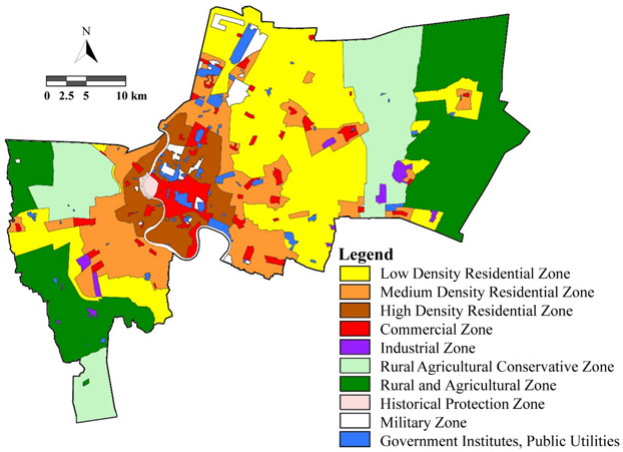

Figure 5. The last land use zoning plan of Bangkok, effective from 2013, released by the City Planning Department of the Bangkok Metropolitan Administration.

This procedure allows to identify if some classes of the zoning plan require specific actions for the SUHI mitigation, or if the adopted urban policy moves towards a sustainable development. In fact, this study assesses the current heating situation and also provides a perspective insight.
Figure 6 shows the main statistics of the SUHI intensity within the 10 categories processing the Landsat SUHI mean map. From the visual analysis of the SUHI pattern within each class, the negative minimum values reported in Figure 6 are ascribed to vegetation pixels, whilst the maximum values are due to the presence of hot spot zones. The average SUHI intensity grows from the Low-density to the High-density Residential class, the latter mainly placed in the city core having more traffic congestion and human activities. Also, Commercial, Historical and Military zones have a high mean SUHI (around 4 °C), whilst the Industrial category, placed in the Bangkok outskirts, has a lower mean intensity (2.7 °C).
Generally, the minimum intensity of greenery pixels is less cool when they are placed in the urban core (Military, Commercial, High-density Residential, and Historical classes). The maximum intensity is independent from the class, since it is due to isolate pixels independent from the average heating pattern dynamic.

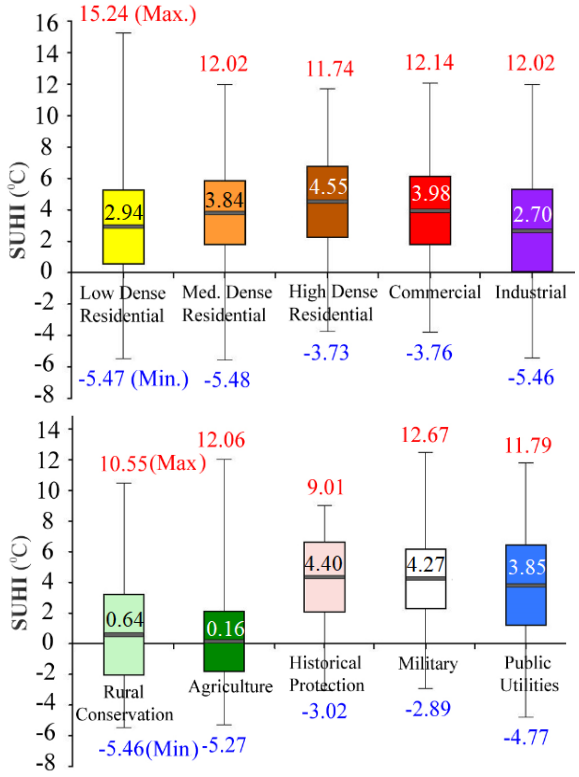

Figure 6. SUHI statistics of the 10 classes: mean (black horizontal line with value), standard deviation (± std, length of the bar), maximum (red) and minimum (blue). Period: 2014-2016

5. CONCLUSIONS

The SUHI monitoring of Bangkok area points out how the different spatial and temporal resolution of the selected satellite sensors provides a SUHI analysis from two different standpoints. The MODIS data allow a trend study at seasonal and diurnal timescale, though the 1-km pixel size hinders a district level analysis and smooths warm/cold peak. Landsat thermal images fill this gap, even is the data availability is every 16 days. However, both studies highlighted a more intense daytime SUHI effect in the city core, where commercial activities and high-density built-up areas are present. Different factors linked to the urban texture and construction materials affect the SUHI intensity in terms of heat absorption and release. Fundamental strategies to mitigate the SUHI phenomenon, to take into account in the urban development design, rely on vegetation and green spaces increase, surface albedo reduction, anthropogenic heat release reduction with more energy efficient buildings, optimized design of building layout, slope and height.

REFERENCES

Anniballe, R., Bonafoni, S., and Pichierri, M., 2014. Spatial and Temporal Trends of the Surface and Air Heat Island over Milan Using MODIS Data. *Remote Sens. Environ.*, 150, pp. 163–171.

Bhargava, A., Lakmini, S., and Bhargava, S., 2017. Urban Heat Island Effect: It's Relevance in Urban Planning. *J. Biodivers. Endanger. Species.*, 5, pp. 1-4.

Bolstad, P. V., and Lillesand, T. M., 1991. Rapid Maximum Likelihood Classification. *Photogramm. Eng. Remote Sensing.*, 57(1), pp. 67–74.

Bonafoni, S., 2016. Downscaling of Landsat and MODIS Land Surface Temperature Over the Heterogeneous Urban Area of Milan. *IEEE J. Sel. Top. Appl. Earth Obs. Remote Sens.*, 9(5), pp. 2019–2027.

Bonafoni, S., Baldinelli, G., and Verducci, P., 2017. Sustainable strategies for smart cities: analysis of the town development effect on surface urban heat island through remote sensing methodologies. *Sust. Cities Soc.*, 29, pp. 211-218.

Bonafoni, S., and Keeratikasikorn, C., 2018. Land Surface Temperature and Urban Density: Multiyear Modeling and Relationship Analysis Using MODIS and Landsat Data. *Remote Sens.*, 10(9), 1471.

Chen, W., et al., 2017. Evaluation of Urbanization Dynamics and Its Impacts on Surface Heat Islands: A Case Study of Beijing, China. *Remote Sens.*, 9(5), 453.

DAAC ORNL (Distributed Active Archive Center), https://daac.ornl.gov/get_data/ (1 September 2017).

Keeratikasikorn, C., and Bonafoni, S., 2018a. Urban Heat Island Analysis over the Land Use Zoning Plan of Bangkok by Means of Landsat 8 Imagery. *Remote Sens.*, 10(3), 440.

Keeratikasikorn, C., and Bonafoni, S., 2018b. Satellite Images and Gaussian Parameterization for an Extensive Analysis of Urban Heat Islands in Thailand. *Remote Sens.*, 10(5), 665.

Liao, W., Liu, X., Wang, D., and Sheng, Y., 2017. The Impact of Energy Consumption on the Surface Urban Heat Island in China's 32 Major Cities. *Remote Sens.*, 9(3), 250.

Memon, R. A., Leung, D. Y. C., and Chunho, L. 2008. A Review on the Generation, Determination and Mitigation of Urban Heat Island. *J. Environ. Sci.*, 20(1), pp. 120–128.

Phiri, D., and Morgenroth, J., 2017. Developments in Landsat Land Cover Classification Methods: A Review. *Remote Sens.*, 9 (9), 967.

Streutker, D., 2003. Satellite-Measured Growth of the Urban Heat Island of Houston, Texas. *Remote Sens. Environ.*, 85, pp. 282–289.

USGS (US Geological Survey), http://earthexplorer.usgs.gov.

Yu, X., Guo, X., and Wu, Z., 2014. Land Surface Temperature Retrieval from Landsat 8 TIRS—Comparison between Radiative Transfer Equation-Based Method, Split Window Algorithm and Single Channel Method. *Remote Sens.*, 6(10), pp. 9829–9852.

Zhou, D., et al., 2018. Remote sensing of the urban heat island effect in a highly populated urban agglomeration area in East China. *Sci. Total Environ.*, 628-629, pp. 415-42

Zhou, D., et al., 2019. Satellite Remote Sensing of surface Urban Heat Island: Progress, Challenges and Perspectives. *Remote Sens.*, 11(1), 48.

BUILDING FOOTPRINT EXTRACTION FROM VHR SATELLITE IMAGERY USING A DEEP LEARNING APPROACH

C. Sandu[1] *, S. Ghassemi [2], A. Fiandrotti[2], F. Giulio Tonolo[3], P. Boccardo[4], G. Francini[5], E. Magli[2]

[1] ITHACA, Information Technology for Humanitarian Assistance, Cooperation and Action, Turin, Italy - constantin.sandu@ithaca.polito.it
[2] Dept. of Electronics and Telecommunications, Politecnico di Torino, Turin, Italy - (sina.ghassemi, attilio.fiandrotti, enrico.magli)@polito.it
[3] Dept. of Architecture and Design, Politecnico di Torino, Turin, Italy, - fabio.giuliotolo@polito.it
[4] Dept. of Regional and Urban Studies and Planning, Politecnico di Torino, Turin, Italy, - piero.boccardo@polito.it
[5] Telecom Italia S.p.A., Torino, Italy, - gianluca.francini@telecomitalia.it

KEY WORDS: Building, VHR, Satellite imagery, Deep Learning

ABSTRACT:

Updated reference cartographic datasets are one of the main input data sources in several application domains requiring spatial modelling. The aim of this work is to semi-automatically extract building footprints from very high-resolution satellite images to update already existing cartographic datasets or generate them if missing over the target area.
The proposed approach for building footprint detection takes advantage of a convolutional neural network for segmenting VHR satellite images. The images from which the building footprints are extracted are different from the images used to train the network. The adopted architecture enables to generalize the learning features from images that have different statistics from the segmented image.
One application domain where this feature is critical is emergency mapping since it enables to rapidly extract reference information over the area of interest. Such reference data allows possible damages to infrastructures to be assessed and delineated. The results indicate that the procedure can be adopted for purposes that range from urban sprawl monitoring to rapid mapping activities using a different approach in comparison to classic image segmentation methods. For example, in emergency mapping activities, if no reference data is available (either from authoritative or open data sources) building footprints must be manually extracted by means of visual interpretation. The proposed procedure enables a faster reference data extraction, limiting the human intervention.

1. INTRODUCTION

Thanks to the diffusion of very high-resolution (VHR) satellite imagery it is possible to extract information with a high level of detail useful for different application domains (mapping, environmental analysis, rapid-mapping, web-maps, etc.). Building footprint extraction from satellite orthoimagery is generally carried out manually and represents one of the most time consuming activity in the case of satellite-based emergency mapping (Voight et al., 2016). Therefore, the development of automatic or semi-automatic feature extraction algorithms aimed at speeding up this process are considered a priority.

In recent years, Convolutional Neural Networks (CNN) (LeCun, 1998) have found application in different image processing tasks (Szegedy et al, 2015), (He et al, 2016). In the present work we propose an encoder-decoder CNN architecture with a residual encoder and deconvolutional decoder that can be trained to fully classify satellite images in a supervised manner (Ghassemi et al, 2018). The neural network has been trained over images covering completely different geographic locations from the ones used for testing. The proposed architecture permits to vastly reduce the amount of time necessary for the extraction of features of interest from the satellite orthoimagery, limiting the intervention of operators. Specifically, this work address the building footprint extraction task, which is one of the most time-consuming activities during satellite emergency mapping.

The paper is structured as follows. Sec. 2 provides the necessary background useful to understand the underlying approach. Sec. 3 describes the proposed network architecture and its relative training procedures. Sec. 4 describes the experimental methodology, the results and a comparison with existing algorithms available in commercial software. Conclusions are drawn in Sec. 5.

2. BACKGROUND

2.1 Residual Networks

Residual networks (ResNets) (He et al, 2016) have been proposed to address the problem of vanishing/exploding gradients in very deep CNNs. By increasing the number of layers within a plain CNN, training and gradients back-propagation throughout the network become challenging. ResNets address this problem by introducing skip connections between convolutional layers enabling learning residual functions and allowing much deeper networks (up to 200 layers) with respect to plain counterparts. ResNets are made up of building blocks to which we refer as units in this text. Each unit includes two or three convolutional layers each followed by ReLU activations functions as illustrated in Figure 1. These residual units are stacked in a sequential manner to form a residual block and five of these blocks form the convolutional part of ResNets. The first unit in each block includes a convolutional layer with stride of 2 pixels which results in down-sampling the input by a factor of two while the number of feature maps increase from one block to the subsequent one. At the end, the generated feature maps at the last block are processed through an average pooling layer then vectorized and input to fully connected layers where the classification is performed.

2.2 Deconvolutional Networks

Deconvolutional networks were proposed to address the loss of mid-level cues (Zeiler et al, 2010) inside CNNs and due to

* Corresponding author

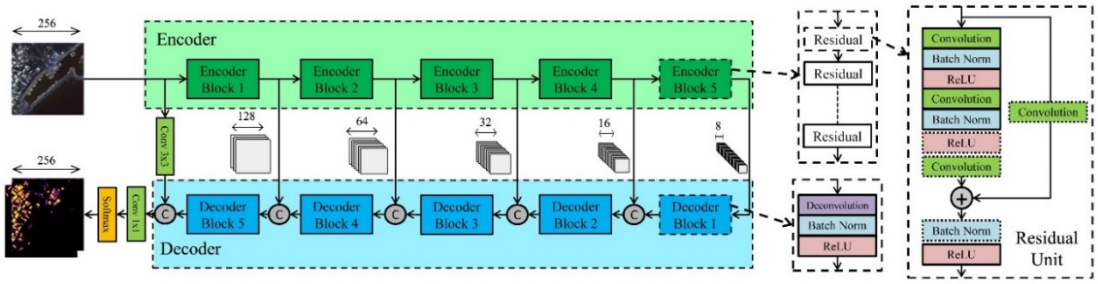

Figure 1. Proposed Network include encoder (top) and decoder (bottom) modules, an encoder and a decoder block are detailed in dashed boxes

pooling layers. In most CNN-based architectures employed for semantic segmentation, firstly a convolutional part which include a number of consecutive convolutional layers extracts visual representations, namely feature maps, from the input image. These feature maps are down-sampled by the pooling layers interleaved in the network which contribute to translation invariance property of the network. Accordingly, many CNNs which are designed for semantic segmentation, employ deconvolutional layers enabling the spatial resolution retrieval of feature maps which has been degraded in pooling operation. Deconvolutional layers include up-sampling filters able to scale up the input with the weights that are learned during the training. Many CNNs, particularly the networks designed for semantic segmentation, employ deconvolutional layer enabling the spatial resolution retrieval of feature maps which have been degraded in pooling operation. The deconvolution operation is performed in two stages: first the input pixels are interleaved with zeros resulting in a sparse output. Then a convolution operation with learnable filters is applied over the sparse input and generates dense output. In our proposed methodology, the deconvolutional layers are employed enabling feature map up-sampling within the networks.

3. METHODOLOGY

3.1 Adopted network architecture

The proposed network architecture (shown in figure 1) consists of *encoder* and *decoder* modules which process the input image with a bottom-up (encoder) and top-down (decoder) approach. Firstly, encoder module extracts high level visual representations namely feature maps from an input image. Secondly, decoder module takes as input the generated feature maps and predicts the corresponding segmentation score maps over several predefined classes. In the following the structure and function of each module is described in detail.

3.1.1 Encoder: The proposed encoder module is arranged into five subsequent blocks and based on residual units. The residual encoder enables very deep architectures (up to 200 layers) while the training process remains feasible. We argue that deeper residual encoder enables learning high level visual features and results in better generalizations across samples with various semantic characteristics.

The encoder module takes as input an image sized 256 x 256 composed of 4 spectral channels and through five subsequent blocks the corresponding feature maps are extracted using residual units. The first layer of each block is a convolutional layer with stride of 2 pixels in which the generated feature maps are halved in spatial size while the number of feature maps increases with a specific factor depending on the encoder depth. The number of feature maps and convolutional layers for six different depths of encoder are provided in table 1. For instance, considering an encoder with depth of 18 layers, the first block takes as input 256 by 256 pixels input image, then the first block produces 64 feature maps of 128 by 128 pixels. Next, these feature maps are input to the subsequent block where 128 feature maps of 64 by 64 pixels are generated. This process continues at the next three blocks and in the end, the fifth block outputs 512 feature maps sized 8 by 8 pixels. That is, by proceeding to deeper layers in the encoder, higher level semantic patterns are extracted from the input and each block outputs increasing number of feature maps with decreasing resolutions. In addition, by proceeding to deeper blocks, the field of view of convolutional layers is expanding which results in learning visual representations in wider range.

3.1.2 Decoder: The decoder module is organized in five blocks symmetrical to the encoder and based on deconvolutional layers. Decoder takes as input the generated feature maps by encoder and predicts the segmentation score maps over land-use classes. Each decoder block is made up of a deconvolutional ReLU and a batch normalization layer in which the feature maps are scaled up by factor of two while the feature maps number decreases. Let us consider the case of encoder with depth of 18 layers which detailed in previous section. The first decoder block takes as input 512 feature maps sized 8 by 8 pixels and generated by the last encoder block. Then, these feature maps are scaled up by factor of two while their number decreases resulting in 16 by 16 pixels of 256 feature maps. Next, through skip connection which are provided between each encoder block output and each decoder block input, these feature maps are concatenated with the feature maps with identical size generated by forth encoder block and then are input to second decoder block. These skip connections which provide the spatial information of higher resolution encoder feature maps in the decoder, are necessary to produce finer segmentation score maps. This process continues for the next three decoder blocks and the last block outputs 64 feature maps of 256 by 256 pixels matching the input size. The last convolutional layer is employed to perform a 1 by 1 convolution on the 64 feature maps and predicts the related confidence scores over each land-use class. Finally, since we are interested in class probabilities, a spatial SoftMax layer (Bridle J.S., 1990) utilized to outputs the class score maps.

Depth	Block 1	Block 2	Block 3	Block 4	Block 5
18	(64, 1)	(64, 4)	(128, 4)	(256, 4)	(512, 4)
34	,,	(64, 6)	(128, 8)	(256, 12)	(512, 6)
50	,,	(256, 9)	(512, 12)	(1024, 18)	(2048, 9)
101	,,		,,	(1024, 69)	,,
152	,,		(512, 24)	(1024,108)	,,
200	,,		(512, 72)	,,	,,

Table 1 The number of (feature maps, convolutional layers) for each block in encoder module for different depth.

3.2 Network Training

After defining the network architecture, we detail the process used for training the network.

Firstly, the images in the dataset are divide into two sets: one set is used to generate training and validation samples while the other set is used for testing the trained network. Therefore, the train and test samples are extracted from different images indicating a statistically large difference between train and test samples. This difference stresses the proposed methodology and enables measuring the generalization capability of the network in a more practical condition in which the trained network expected to be applied over an image with no similarity with the training images. Next, to produce training samples, about 80% of each image in the first set is subdivided into 364 by 364 tiles by a translation of 120 pixels while the rest 20 % are used to extracted 256 by 256 validation samples with no translation. While the network input size is 256 by 256, the larger tiles used for training enables several label-preserving transformations during training such as random rotation and cropping. These transformations allow data augmentation improving the generalization capability of the network. Finally, the test tiles are extracted out of the second set of images and with the size of 512 by 512 which is the maximum size allowed by the GPU memory (NVIDIA Titan X Pascal GPU 12 GB of RAM). Overlapping tiles are deployed to prevent the artifacts around tile boundaries.

Next, after generating the training samples, we proceed training the network by minimizing the following loss function:

$$L(w,y,t) = \sum_{i=1}^{HxW} \sum_{k=1}^{C} t_{i,k}\, log\left(y_{i,k}\right)$$

where y and w is the network output and parameters respectively, t is the expected output and H, W and C are height, width and the number of classes respectively. In addition, to prevent overfitting and help generalization, we optimize the following function at training time:

$$J(w,y,t) = \eta L(w,y,t) + \lambda R(w)$$

where η and λ are learning rate and regularization parameters and R(w) is the L2 norm of all network parameters. The training is performed using Stochastic Gradient Descent with momentum of 0.9 and over mini-batches of 8 samples. The initial learning is 0.005 and divided by 5 every 30 epochs.

4. RESULTS

4.1 Dataset

The dataset used for our experiments includes 9 VHR satellite images acquired over 9 different areas of interest worldwide by three different Earth Observation (EO) satellites (Pleiades-1A, Pleiades-1Band WorldView-2), permitting a better generalization of the CNN proposed method The images are characterized by 4 spectral bands (blue, green, red and near infrared), a nominal spatial resolution of 0.5 m and different off-nadir angles: they have been delivered as pansharpened data by the data providers. The selection criteria were based mainly on the presence of urban areas and the lack of cloud coverage. As it is described in Section 3, dataset must be subdivided into two sets: one set is used to generate training and validation samples and the other set of images is reserved to test the trained network. Therefore, 6 out of 9 images are considered for training and validation (D5, D13, D16, D17, D18 and D20), while the other 3 images (D12, D19 and D22) is regarded as test set. Training samples are extracted from the first set of images and covering 80 percent of each image while the validation samples are generated from the other 20 percent of each image. To measure the proposed network performance and to be able to compare it with existing classification algorithms available in commercial software, the test set is used. The ground truth is generated using the building footprints extracted from Open Street Map that are manually refined and integrated in case of missing data. Figure 2 provides 3 test images (D12, D19 and D22) each sized 6000 x 4500, 3700 x 2100 and 8700 x 6600 respectively.

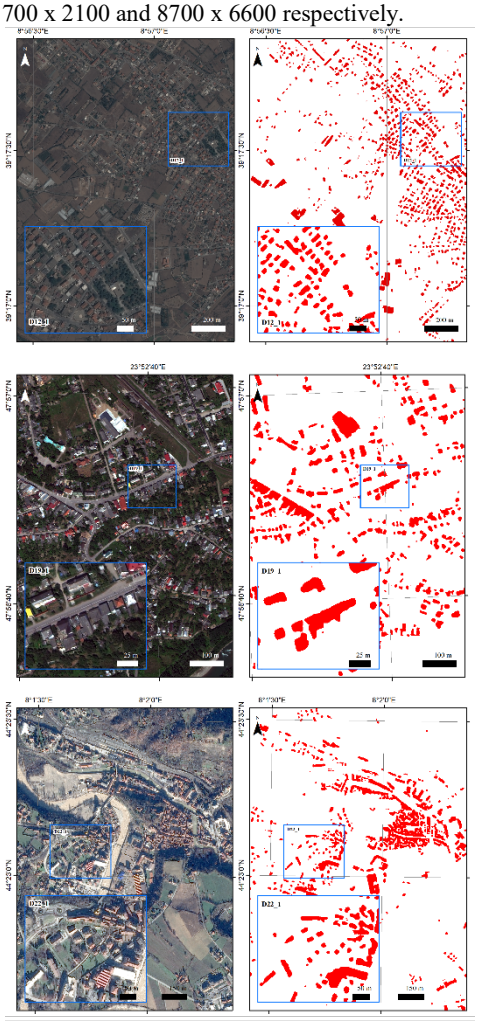

Figure 2. From top to bottom test images D12, D19 and D22 on the left the true colour composite, on the right the segmentation image with probability >50% and in the blue boxes the detail of the segmentation (Datum: WGS84)

4.2 Results

As described in (Ghassemi et al., 2018) it has been observed that depth of encoder plays a crucial rule in generalization of the network through learning visual representations of high semantic level which are not limited to training images. Authors showed that the network with the encoder including 152 layers obtains the best results. Moreover, this type of encoder outperforms existing neural networks like the standard U-Net with 19 and 35 layers. In this section, the results of the proposed method are compared to the outputs of a supervised Mahalanobis distance (MDist) classification based on region of interest (ROI) extracted from each training dataset. The classification was performed in Envi 5.4. For the MDist classification the ROIs

were manually extracted and used as training samples from each satellite image. The samples consisted in: i) footprints of buildings characterised by different type of roofs and tile colours (red and grey), ii) vegetation, iii) agricultural fields, iv) roads.
The classification was performed for each testing dataset and was then evaluated computing the respective Producer Accuracy (P.A.) and User Accuracy (U.A.) and compared to the P.A and U.A. of the results obtained with our proposed approach. The results are visible in Table 2.Moreover, Omission Errors (O.E.) and Commission Errors (C.E.) have been also evaluated, as shown in Table 3. The results in Table 2 and 3 are related to a subset of the total building area of each image, specifically: 69,8% for D12, 53% for D19 and 30,9% for D22.

	P.A. CNN	P.A. MDist	U.A. CNN	U.A. MDist
D12	54,98	87,30	76,07	96,80
D19	58,90	52,36	71,90	61,80
D22	69,38	34,43	75,01	22,49

Table 2 Comparison of Producer and User Accuracy of the proposed method (CNN) vs a Mahalanobis distance supervised classification (MDist)

	O.E. CNN	O.E. MDist	C.E. CNN	C.E. MDist
D12	45,02	12,70	23,93	3,20
D19	41,10	47,64	28,10	38,20
D22	30,62	65,57	24,99	77,51

Table 3 Comparison between Omission and Commission errors of the proposed method (CNN) vs a Mahalanobis distance supervised classification (MDist)

The results show that the proposed implementation outperforms the MDist algorithm in D19 and D22. For D12 the user and the producer accuracies are noticeably higher, mainly due to the characteristics of the satellite image. In fact, the image has a low off-nadir angle and the shape of the buildings can be easily detected by the MDist process. Figure 3 shows how the proposed CNN architecture outperforms the MDist algorithm especially in the densely built area in the north-eastern part of the image. It has to be highlighted that the CNN approach is characterised by commission errors in dense built-up areas and omission errors related to the edges of building footprints. Generally, the algorithm performs better with regularly shaped features.
Concerning time constraints, the processing and the segmentation of the three test images took 110, 55 and 200 seconds for images D12, D19 and D22 respectively. The process is by far faster than: i) the manual digitalization of features from the orthoimagery (that took about 10 hours for each dataset), ii) the MDist classification (that took about 2 hours for each dataset using a desktop pc with the following specifications: Intel(R) Core(TM) i7-7700 CPU @ 3.60GHz, 16GB of RAM, NVIDIA GeForce GT 710).

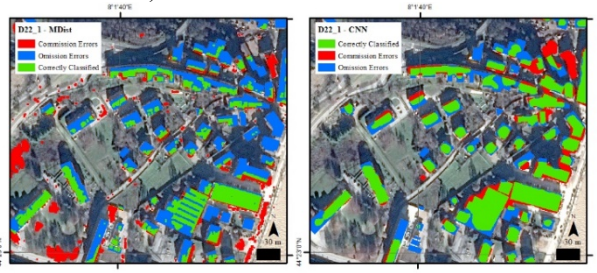

Figure 3. Comparison between the outputs generated by Mahalanobis distance (MDist, left) and proposed CNN (right) of dataset D22 (Datum: WGS84)

5. CONCLUSIONS

In this work the CNN segmentation procedure proposed in (Ghassemi et al., 2018) is described and validated. The process is based on deep CNN and enables to segment satellite images in order to extract building footprints. Due to its accuracy and generalization ability, the proposed approach can be potentially applied worldwide and is capable to provide rapidly reference data where no data is available. From our experiments it is notable that the proposed CNN outperforms in most cases a common pixel-based supervised classification algorithm (Mahalanobis distance). A future test will compare the proposed method with other algorithms available in commercial software. This will allow the robustness of the segmentation process to be thoroughly assessed. Finally, the procedure will get as input more sample categories (e.g. features that represent water, vegetation and clouds) to test the impact of a larger number of sample categories on the feature extraction thematic accuracy.

REFERENCES

Bridle J.S. (1990) Probabilistic Interpretation of Feedforward Classification Network Outputs, with Relationships to Statistical Pattern Recognition. In: Soulié F.F., Hérault J. (eds) Neurocomputing. NATO ASI Series (Series F: Computer and Systems Sciences), vol 68. *Springer*, Berlin, Heidelberg

Christian Szegedy, Wei Liu, Yangqing Jia, Pierre Sermanet, Scott Reed, Dragomir Anguelov, Dumitru Erhan, Vincent Vanhoucke, Andrew Rabinovich, et al., "Going deeper with convolutions," Cvpr, 2015.

Kaiming He, Xiangyu Zhang, Shaoqing Ren, and Jian Sun, "Deep residual learning for image recognition," in *Proceedings of the IEEE conference on computer vision and pattern recognition*, 2016, pp. 770–778.

Matthew D Zeiler, Dilip Krishnan, Graham W Taylor, and Rob Fergus, "Deconvolutional networks," in *Computer Vision and Pattern Recognition (CVPR), 2010 IEEE Conference on*. IEEE, 2010, pp. 2528–2535.

Sina Ghassemi, Attilio Fiandrotti, Constantin Sandu, Fabio Giulio Tonolo, Piero Boccardo, Enrico Magli, and Gianluca Francini, "Satellite image segmentation with deep residual architectures for time-critical applications," in *European Signal Processing Conference (EUSIPCO), 2018 IEEE The 26th*. IEEE, 2018, pp. 1–6

Stefan Voigt, Fabio Giulio-Tonolo, Josh Lyons, Jan Ku˘cera, Brenda Jones, Tobias Schneiderhan, Gabriel Platzeck, Kazuya Kaku, Manzul Kumar Hazarika, Lorant Czaran, et al., "Global trends in satellite-based emergency mapping," *Science*, vol. 353, no. 6296, pp. 247–252, 2016.

Yann LeCun, L´eon Bottou, Yoshua Bengio, and Patrick Haffner, "Gradient-based learning applied to document recognition," *Proceedings of the IEEE*, vol. 86, no. 11, pp. 2278–2324, 1998.

AN INTEGRATION OF VHR OPTICAL AND RADAR MULTISCALE IMAGES PROCESSING DATA AND GEOGRAPHICAL INFORMATION SYSTEM APPLIED TO A GEO-ARCHEOLOGICAL RECONSTRUCTION IN THE FERRARA AREA

L. Damiani[1]*, F. Immordino[2], E. Candigliota[2]

[1]Archeology Student, University of Perugia and Siena, Italy - linda.damiani@outlook.it.
[2]ENEA, Italian National Agency for New Technologies, Energy and Sustainable Economic Development, - (francesco.immordino, elena.candigliota)@enea.it
Via Martiri di Monte Sole 4 - 40129 Bologna, Italy.

KEY WORDS: Landsat-8, Pleiades, Sentinel-1, Ferrara, Geoarcheology, Bronze Age

ABSTRACT:

A preliminary tool for the identification of palaeoforms and forms attributable to archaeological emergencies in environmental context with high hydrogeological risk is proposed; in particular the study area represents one of the most characteristic phases of the Average Bronze Age (2000-1550 B.C.) in the Po fluvial plain: the "terramaricola" culture. The historical reconstruction and the geomorphological structure analysis took place using a methodological approach based on the analysis of optical and radar satellite data, in order to better understand the landscape forms and development. The methods utilized are photointerpretation and image processing of satellite data, with the aim of promoting the preservation and protection of cultural, historical and archaeological heritage. This methodological approach allows to produce useful data from a geo-archaeological reconstruction of the study area, which can assist the most traditional methods of research, such as archival documentation and cartography (historical and archaeological map). Moreover, the possibility to favor the communication with the public administrations to assist the land management in environmental monitoring and prevention of geological risk is added to the scientific interest.

1. INTRODUCTION

The investigated site is located to South of the Po river, between the Modena and Ferrara cities, an area characterized throughout history by geomorphological processes, still visible in the current landscape. (**fig. 1**)
Furthermore, most of archaeological evidences have been discovered in this area, proving a dense human presence. The region has also been vastly transformed by the anthropization of agricultural settlements, the urban expansion and the development of a dense road network.
For these reasons, the geomorphological interpretation of the current territory is very difficult, but it is interesting from the geoarcheological point of view.

Figure 1. Investigated area: between Modena and Ferrara cities, Emilia Romagna, Italy (Google Earth).

Figure 2. Paleoforms on subset Pléiades image (ASTRIUM). Acquisition: February 14, 2013.

2. AIMS OF THE RESEARCH

This project is a preliminary study for the identification of ancient geomorphological structures related to archaeological sites in an environment with a high landslide hazard.
The research purpose is the historical and geomorphological reconstruction of the territory (**fig. 2**), during the Bronze Age, when the well-known culture of the *Terramare* became diffuse in the Po Valley area, producing a risk assessment and

* Corresponding author

archeological map of the investigated area. Also, this study aims to test a methodology to support the understanding of the landscape evolution and to integrate with other sources such as document archives, historical cartography and archeological mapping.
In addition to the scientific interest, there is a possibility that such knowledge could support to local administration with landscape management. The historical and geomorphological reconstruction has been conducted through the aerial photography interpretation and the satellite images (optical and radar) processing.

3. METHODS

Optical satellite imagery at high (Landsat-8, **fig. 3**) and very high resolution (Pleiades, **fig. 4**) and radar images (Sentinel-1) have been used to carry out the historical and geomorphological reconstruction.

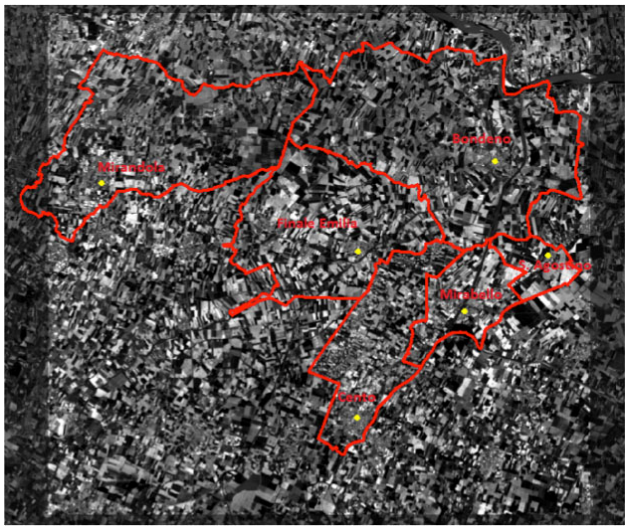

Figure 3. Subset image Landsat-8 panchromatic band (USGS). Acquisition: May 28, 2014. In red the municipal boundaries.

Considering the morphological complexity of the investigated area, a multiscale approach has been adopted in order to allow a progressive identification and interpretation of the territory forms. At first, Landsat-8 image has been useful for the anomalies individuation connected to the road and the agricolural patterns, especially used in the panchromatic band (15 m of resolution). Pléiades images with very high resolution (0.50 m), instead, allowed to highlight every particular sign, to add more information. The anomalies have been focused on through the satellite imagery interpretation, which is based on three key factors: tone changes, agricultural patterns and the development of road networks. These key factors have been identified through the satellite image processing: for optical images (L8 and Pléiades), have been utilized the techniques of radiometric, spatial and spectral enhanced, such as contrast stretching (**figg. 5-6**), directional filters (edge detection, **fig. 7**) and Principal Component Analysis (PCA). These techniques allowed to find signs of changes in tone linked to archeological evidences and ancient geological traces, because the *contrast stretching* is a technique that maximizes the contrast of the data and redistributes pixel values, so it allows to make brighter the objects to better identify them from neighbouring elements.

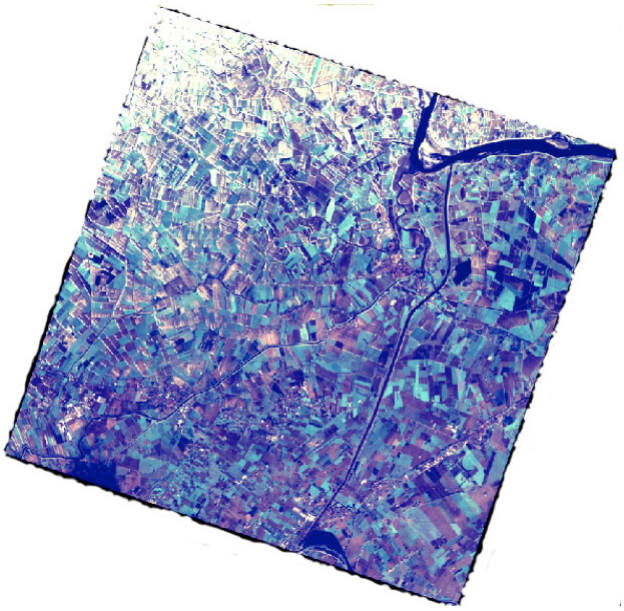

Figure 4. Pléiades pansharpened, *colour composite* 321. Acquisition date: February 14, 2013 (ASTRIUM).

Figure 5. Radiometric enhance example: No Filter (colour composite 432) on Pléiades image (ASTRIUM).

Figure 6. Radiometric enhance example. Contrast Stretching – Histogram Equalization on Pléiades image (ASTRIUM).

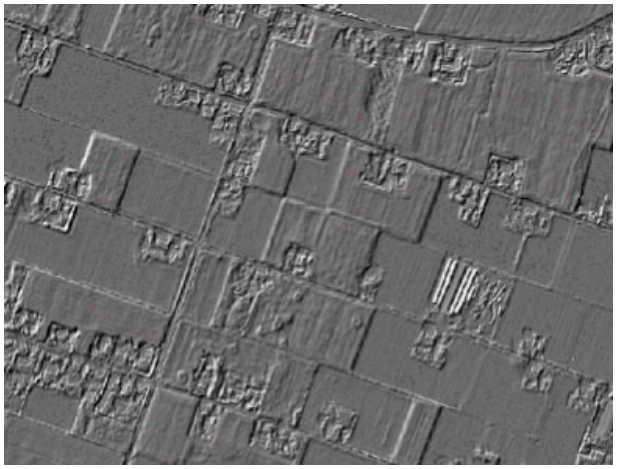

Figure 7. Spatial enhance example. Directional Filter 45° on Pléiades image.

Whereas *directional filters* are spatial enhance technique that allows to change the Digital Number of adjacent pixels as regard to specific direction definited by the user. At last, the PCA is a method of data compression: it allows redundat data to be compacted into fewer bands that is the dimensionality of the data is reduced.

The radar sensor is different, because it is an active system, which means that it illuminates the Earth's surface with electromagnetic signals of a specific microwave wavelenght and measures the reflected signal. Microwave images provide information about the geometric and dielectric properties of the surface or the volume of the objects, that depends on roughness of surface, kind of material and moisture content. Furthermore radar images are black and white, so in this work, radar data interpretation has been improved producing a colour radar image by combing three single images from different dates to produce a multi-temporal composite, through the layer stacking technique (**fig. 8**). The radar images utilized are three and they have been acquired on three different periods of the year: 28 january 2015, 9 august 2015 and 1 november 2015. Each individual image is displayed in one of the three colours used to form any colour picture: red, green and blue, that are combined to produce other colours that can be interpreted by image processors.

Every kind of data processed have been compared with each other through ovarlay of the images with the aim to integrate all elements: every information has been put into a geodatabase realized with GIS technology (**fig. 9**).

The principal product of this research is an archeological risk map based on the archeological evidences and the possible archeological traces highlighted from the satellite image processing.

The interpretation of the traces identified until now partially coincide with previous historical and geological studies, but should be verified with archeological surveys.

The paleoforms due to ancients river beds, identified between Modena and Ferrara cities, which are connected to the archeological finds discovered in this area over the years, shows when the ancients river beds were worked and their valleys were populated by the ancient colture of "Terramare". This information about the paleoforms localized through the image processing and photointerpration, could be also used to support decisions concerning the environmental monitoring and prevention of a high-hydrogeological risk area, because they are proof of the hydrogeological development of the investigated site throughout the centuries, they are therefore

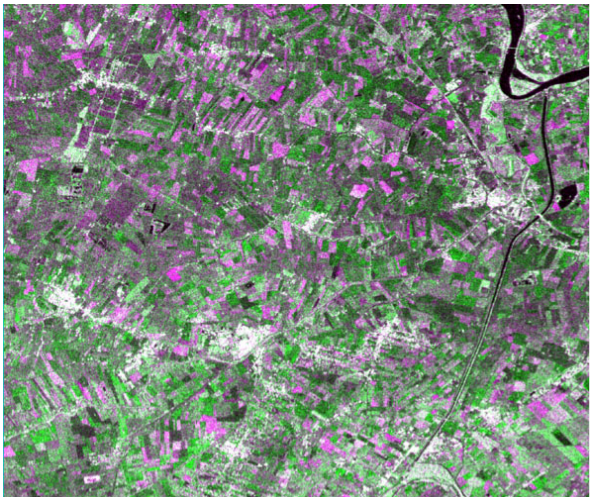

Figure 8. Colour radar image created by combing three single images from different dates to produce a multi-temporal composite

an appropriate tool could be used to assist a coherent programme for flood risk prevention and nature protection.

This preliminary work shows a good reliability of the results that can be obtained with this method and it can be a starting point of future possible researches.

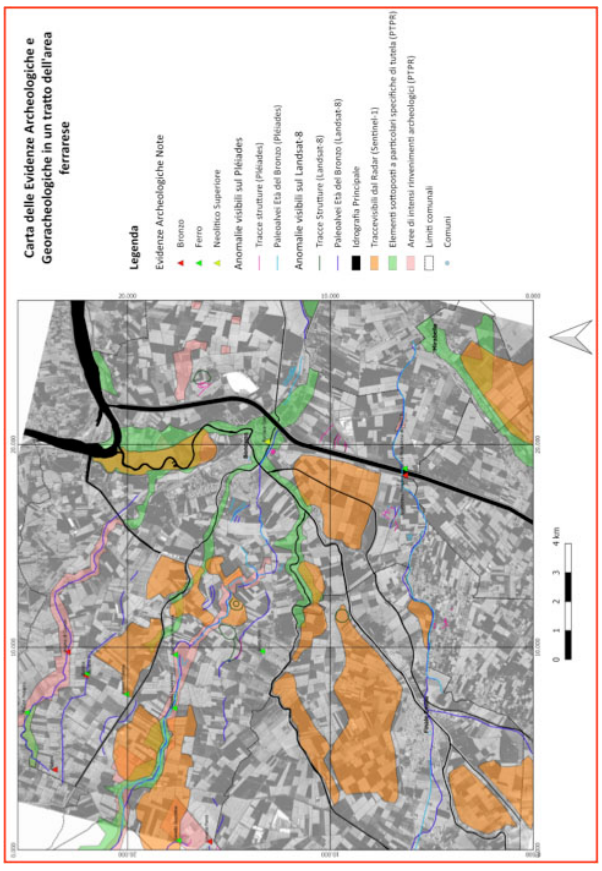

Figure 9. Archeological risk map based on archeological evidences and possible archeological traces highlighted from the satellite image processing. The features detected from radar in orange, the protected areas in green, the archeological areas in pink. The points elements represent the archeological finds in the area.

REFERENCES

Bernabò Brea M., Cardarelli A., Cremaschi M. (a cura di), *Le terramare. La più antica civiltà padana*. Electa Ed., Milano 1997.

Bernabò Brea M., Cardarelli A., *Terramare. Cinque secoli di vita nella grande pianura*, p. 24 in Bernabò Brea M., Cardarelli A., Cremaschi M. (a cura di), Le terramare. La più antica civiltà padana. Electa Ed., Milano 1997.

Barnabò Brea M., *Il territorio di Bondeno nel quadro dell'età del Bronzo* Emiliana, in BERTI F., GELICHI S., STEFFE G. (a cura di), *Bondeno e il suo territorio, dalle origini al Rinascimento*, Grafis Edizioni, Bologna 1988.

Biancardi D., *Carta archeologica del territorio di Bondeno (Ferrara) dalla Preistoria all'Età moderna.* Tesi di laurea in Quaternario, Preistoria e Archeologia, relatori Zerbini L., Calzolari M. Università degli studi di Ferrara, 2013.

Bondesan M., *L'area deltizia del Po: evoluzione e problemi territoriali,* in Ferrari C, Gambi L. (a cura di), *Un Po di terra. Guida all'ambiente della bassa pianura padana e alla sua storia*, Reggio Emilia: Diabasis.

Brivio P. A., Lechi G., & Zilioli E., *Principi e metodi e Telerilevamento*, Milano: Città Studi, 2006.

Calzolari M., *Gli insediamenti terramaricoli della bassa pianura tra Po, Secchia e Panaro. Aspetti topografici*, in Desantis P., Steffe' G. (a cura di), *L'insediamento terramaricolo di Pilastri (Bondeno-Ferrara). Prime fasi di una ricerca. Catalogo della mostra*, All'insegna del Giglio Ed., Firenze 1997.

Castiglioni G. B., *Geomorfologia*, UTET, Torino 1982.

Cremaschi M., *Terramare e paesaggio padano*, in Bernabo' Brea M., Cardarelli A., Cremaschi M. (a cura di), *Le terramare. La più antica civiltà padana*. Electa Ed., Milano 1997.

Dainelli N., *Fotointerpretazione. L'osservazione della Terra,* Flaccovino Dario Editore, Palermo 2011.

Dainelli N., *Telerilevamento. L'osservazione della Terra,* Flaccovino Dario Editore, Palermo 2011.

Desantis P., Steffè G. (a cura di), *L'insediamento terramaricolo di Pilastri (Bondeno-Ferrara). Prime fasi di una ricerca*. *Catalogo della Mostra*, All'insegna del Giglio Ed., Firenze 1997.

Francovich R., Manacorda D. (a cura di), *Dizionario di Archeologia*, Editori Laterza, Bari 2009.

Gomarasca M. A, *Elementi di geomatica*, Associazione Italiana di Telerilevamento, 2004.

Lasaponara R., Fulong C., Masini N., *An overview of satellite Syntetic Aperture Radar remote sensing in archeology: from site detection to monitoring,* in Journal of Cultural Heritage, Elsevier, 2015.

Marcolongo B., Simone M., *Strategie di ricerca e modelli d'insediamento tra V e II millennio a. C. nell'alta valle dell'Eufrate. Il contesto fisico ambientale dell'area di Malatya-Turchia ricostruito attraverso interpretazione di dati telerilevati e ricognizioni dirette.,* Atti del 5° Workshop tematico "Telerilevamento e le nuove scienze della terra", ENEA, Bologna 2011.

Pellegrini & Tellini, *L'origine della pianura padana*, in Ferrari C., Gambi L. (a cura di), *Un PO di terra. Guida all'ambiente della bassa pianura padana e alla sua storia*, Diabasis, Reggio Emilia 2000.

Petrucci F., Verri D., Tuzet F., Pincelli G., Pavani P., Balboni C., Palombo D., *Sistema territoriale. Carta del rischio archeologico. Relazione di progetto*, in Piano Strutturale Comunale Associato. Quadro conoscitivo, Associazione altoferrarese, Ferrara.

Ricci Lucchi F., Ciabatti M., Pellegrini M., Veggiani A., *Evoluzione geologica della pianura*, in *Il mondo della natura in Emilia Romagna*, vol. II, *La pianura e la costa*, Pizzi Editori, Milano 1990.

WEBSITES

https://geoportale.regione.emilia-romagna.it/it

https://landsat.usgs.gov/landsat-8-l8-data-users-handbook-section-1

https://sentinel.esa.int/web/sentinel/missions/sentinel-1/data-products

https://sentinel.esa.int/web/sentinel/radiometric-calibration-of-level-1-products

https://sentinel.esa.int/web/sentinel/user-guides/sentinel-1-sar/acquisition-modes

https://sentinel.esa.int/web/sentinel/toolboxes/sentinel-1/tutorials

https://sentinel.esa.int/web/sentinel/toolboxes/sentinel-1/tutorials

http://www.esa.int/SPECIALS/Eduspace_IT/SEML7ZKXB1G_0.html

http://www.esa.int/SPECIALS/Eduspace_IT/SEMTZSZRA0G_0.html

http://www.intelligence-airbusds.com/en/4572-pleiades-technical-documents

http://www.ist.edu.pk/about

http://www.terramarapilastri.com/wp/

MULTITEMPORAL LANDSCAPE PATTERN ANALYSIS: A QUANTITATIVE APPROACH TO SUPPORT SUSTAINABLE LAND MANAGEMENT

G. Chirici [1]*, P. Rossi[1], D. Fanfani [2], D. Poli [2], M. Rossi[2], B. Mariolle[3]

[1] DAGRI, Università degli Studi di Firenze, Firenze, Italy – (gherardo.chirici; patrizia.rossi)@unifi.it
[2] DIDA, Università degli Studi di Firenze, Firenze, Italy – (david.fanfani; daniela.poli; maddalena.rossi)@unifi.it
[3] Ecole Nationale Supérieure d'Architecture et de Paysage de Lille – agence@bresmariolle.fr

KEY WORDS: Ecosystem service, Land use, Land cover, Time trend analysis

ABSTRACT:

Remotely sensed images are an essential component for the analysis of landscape trends. In this contribution we introduce the analysis of a large study area in the Bassin Minier Nord-Pas-de-Calais (France) were we reconstructed a Corine Land Cover map for the year 1954 on the basis of historical aerial orthophotos. On such a basis we were able to analyse land use/land cover changes and their relative impact on landscape pattern. Whereas the main driver revealed being the urban sprawl in areas dominated in 1954 by agriculture, the study shown how quantitative approach in landscape pattern analysis can provide possible innovative tools to support patrimonial landscape mapping and the identification of possible future projects for territorial development

1. INTRODUCTION

Ecosystem services (ES) represent the goods and services derived from the functions of ecosystems utilized by humanity (Costanza et al. 1997). Human wellbeing is tightly connected to the provision of these services. Ecosystem services represent an high relevant issue that should be included in multi-level land policies and planning activities (Frank et al., 2015, Kangas et al. 2018).
Policy makers are increasingly recognizing the potential of ecosystem service mapping in strategic planning (Vorstius and Spray 2015).
The ecosystem services are operationalized through a selected set of indicators. The purpose of the indicators is to support management of the ecosystems and communicate the condition of ecosystems themselves. Indicators can be estimated under a quantitative approach with different approaches. See for example the pan-European project related to Mapping Ecosystem Services (Maes et al., 2012).
The territorialist approach to land management is an integrated and multi-scale way oriented to take into consideration several thematic elements in defining large interconnected bioregions. In this kind of planning approach the ways for designing territories is aimed to achieve several targets: interconnecting different local territorial systems by networking urban areas and taking into consideration morphological and social elements; recovery and enhancing the relationships between urban systems and natural/rural surroundings areas heading towards a balanced ecosystem; recreating circular matter and goods balances in water basins; regenerating ecological networks at landscape scale level.
This approach was applied and unfolded in a large study site of the Bassin Minier Nord-Pas-de-Calais (France) in the area of Lens, where the Università degli Studi di Firenze and the Ecole Nationale Supérieure d'Architecture et de Paysage de Lille are cooperating for both scientific and didactical purposes. The current area condition was shaped after three centuries of coal extraction from 18th century to 20th century and is now object of several restoration and valorization policies and projects.

In the contribution we present some examples of the use of multitemporal landscape pattern analysis based on diachronic land cover maps acquired from remotely sensed technologies. We produced quantitative analyses which demonstrated the potential benefits that may arise by the use of multitemporal aerial imagery and historical maps for producing a detailed reconstruction of the historical evolution of urban areas. Remotely sensed-based landscape maps may be used for the analysis of different components of the landscape (for example for the analysis of ecological networks) which are the basis for the estimation of the temporal changes in ecosystem service provisioning. Results may be used for supporting the reconstruction of the patrimonial landscape values and the identification of possible future projects for territorial development.

2. METHODS

Following the European Mapping Ecosystem Services approach developed by a large international research group coordinated by the Joint Research Centre of the European Commission, the first step for the spatial assessment of ecosystem services is to create a multitemporal land-use / land-cover map (Maes et al., 2012).
The study area is defined as the administrative region of Bassin Minier Nord-Pas-de-Calais for a total of 1812 km^2. Around the area we created a buffer zone of 10 km in order to take into consideration land use/land cover changes occurred on the border of the investigated area. The total area included within the French border reaches a total of 4563 km^2 (Figure 1).

* Corresponding author

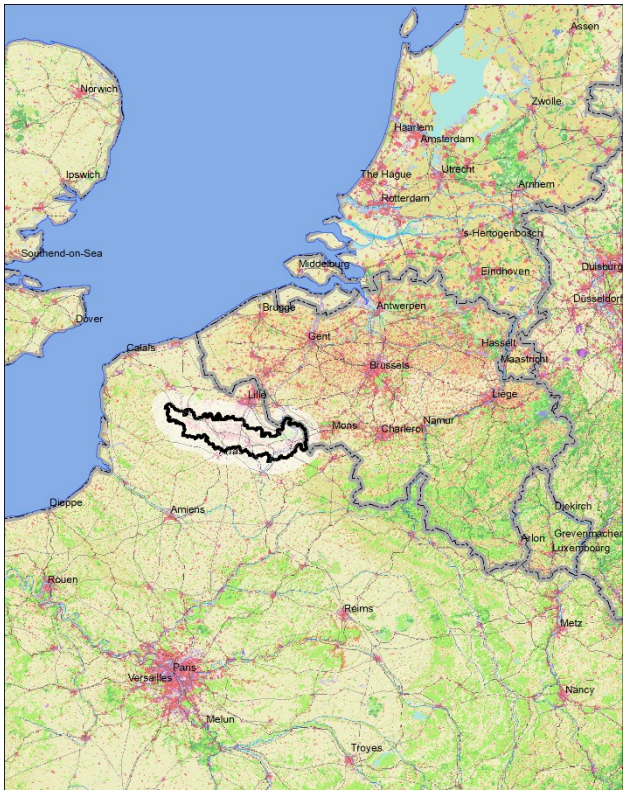

Figure 1. location of the study area and its buffer zone on the basis of Corine Land Cover 2012.

Following the procedure originally proposed by Chirici et al. (2006), we used the oldest Corine Land Cover (CLC) map (year 1990) available for the whole Europe from the European Environmental Agency and jointly the historical photos BD ORTHO® HISTORIQUE available from the Institute National de l'Information Geographique et Forestiére (http://professionnels.ign.fr/bdorthohisto) to create an historic new version of the CLC map denominated CLC1955.
In doing that the students of Università degli Studi di Firenze used the same mapping rules and definitions officially adopted for the CLC project.
The CLC1955 was then crosstabulated with an overlay approach in a GIS environment with the official CLC2012 map in order to analyses spatial dynamics. Change analysis were carried out with a pixel resolution of 20 m.

In the last decades remote sensing technologies from multiple platforms (satellite, aerial, UAV) and from different passive (optical) or active (radar and LiDAR) technologies have augmented their penetration in earth observation applications. This is due to the increased numbers of data sources available, to the fact that this data are nowadays most commonly distributed open-access on line, and that the technologies for their use in producing high added-value information have become more easy to use and powerful.
Designing territories in land management following the territorialist approach requires the elaboration of a vast amount of spatial information that in most of the cases can be derived from multiple earth observation tools. Remote sensing technologies, under this point of view, can contribute in overpassing thematic and rigid visions enabling a more integrated and cross-disciplinary approach.

3. RESULTS

On the basis of the analyses carried out we were able to calculate for each pixel in the study area the transition vector between the land use in 1954 to the new land use in 2018. It turned out how the study area is strongly dominated by anthropogenic land uses (agriculture and urban) (Figure 2).

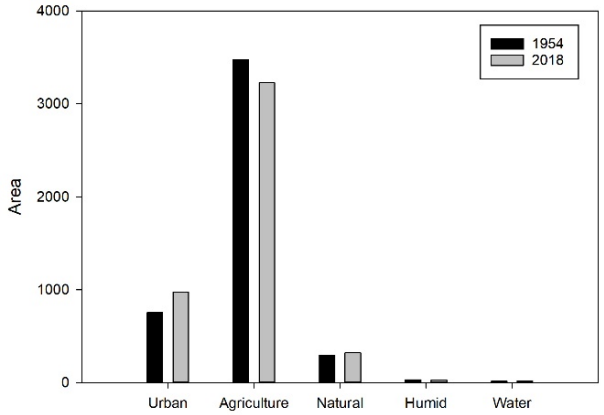

Figure 2. first level CLC classes spatial consistency at the two investigated period in the study area.

Accordingly we present below the analyses for the most important transition classes.
In the analyzed period the 7.7% (351 km^2) of the landscape changed in terms of first level CLC class.
The vast majority of this change (75% of changed areas) is determined by the urban sprawl. Mainly it happened for a transition from agriculture (72%) and just for the 2.7% from natural areas and some 0.5% from humid areas and water bodies Figure 3).

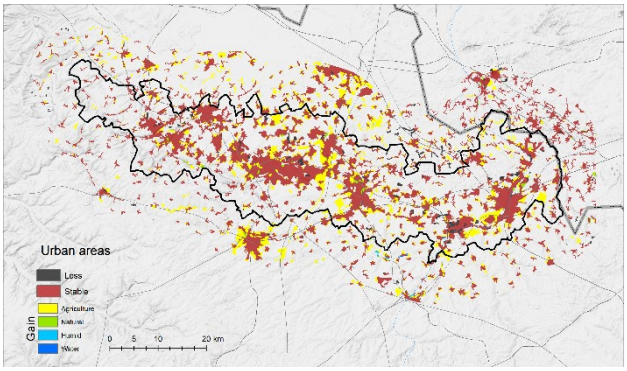

Figure 3. development of urban areas in the period 1954-2018.

New urban areas in the period 1954-2018 increased mainly as evolution from existing urban areas in 1954. The average distance of new urban areas was in fact 345 m from existing urban areas at 1954 (with a maximum of 2474 m (Figure 4).

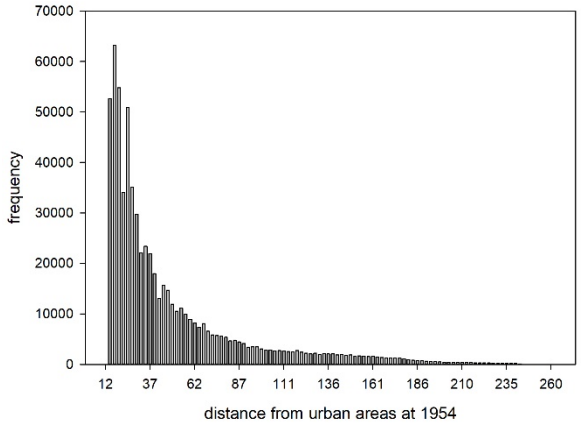

Figure 4: new urban areas created in the period 1954 – 2018 as a distance from existing urban areas in 1954. Frequency in number of pixels, distance in meters.

The increased urban area determined a reduction of more than 10% in the fragmentation of urban areas, the number of continuous urban patches moved from 580 patches in 1954 to 520 patches in 2018. With an average dimension of 1.3 km^2 in 1954 and 1.9 in 2018. The areas with the largest change in patch dimension are those in Lens and Valenciennes. Followed by Douai, which is very close to be connected with Lens, Arras and the western polycentric areas of Auchel / Bethune / Lillers / Bruay-La-Buissière (Figure 5).

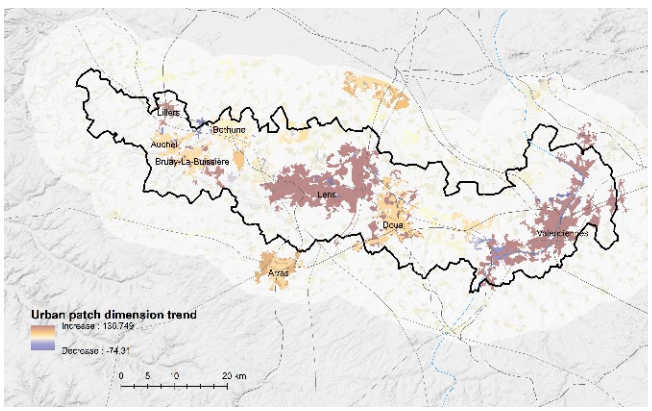

Figure 5: changes in the dimension of continuous urban areas in the period 1954-2018.

The second most important landscape change in the study area (12.2% of all changes) is the increased coverage of areas with natural and semi-natural vegetation. Mainly evolved from the abandonment of agriculture. Since the total increased area of these environments was limited to only 0.1 km^2 the impact on the connectivity of the ecological network was very limited.

4. CONCLUSIONS

In this contribution we applied a method for the analyses of landscape trend in a large study site of the Bassin Minier Nord-Pas-de-Calais (France). On the basis of the reconstruction of the land use land cover at the year 1954 and of of historical orthophotos.

The area resulted mainly dominated by a transition from agriculture areas to urban areas. Changes originated mainly from existing urban areas and determined a consistent change in the spatial pattern of landscape patches. With an augmented area of continuous urban and impervious areas.

We demonstrated that the information that can be obtained from the analysis of historical remotely sensed images can be useful to produce information that may support a multi-temporal and dynamic approach to landscape planning. A method that contributes to enhance the inherited map overlay approach in supporting the reconstruction of the enduring structures of territories and of the related patrimonial landscape values. That aiming to the identification of the key issues to underpin possible future projects for territorial place focused development.

ACKNOWLEDGEMENTS

The work was carried out in the framework of the cooperation project between Ecole Nationale Supérieure d'Architecture et de Paysage de Lille and the Università degli Studi di Firenze "HABITER LE BASSIN MINIER AU XXIÈME SIÈCLE".

REFERENCES

Chirici, G., Corona, P., & Koehl, M. (2006). Earth observation techniques and GIS as tools for assessing land use/cover changes in a landscape context. In M. Agnoletti (Ed.), The conservation of cultural landscapes (pp. 57-70): CAB International

Costanza, R., d'Arge, R., de Groot, R., Farber, S., Grasso, M., Hannon, B., Limburg, K., Naeem, S., O'Neill, R.V., Paruelo, J., Raskin, R.G., Sutton, P., & van den Belt, M., 1997. The value of the world's ecosystem services and natural capital. Nature, 387, pp. 253-260.

Kangas, A., Korhonen, K.T., Packalen, T., & Vauhkonen, J., 2018. Sources and types of uncertainties in the information on forest-related ecosystem services. Forest Ecology and Management, 427, pp. 7-16.

Frank, S., Fürst, C., & Pietzsch, F., 2015. Cross-Sectoral Resource Management: How Forest Management Alternatives Affect the Provision of Biomass and Other Ecosystem Services. Forests, 6, 533-560.

Maes, J., B. Egoh, L. Willemen, C. Liquete, P. Vihervaara, J.P. Schägner, B. Grizzetti, E.G. Drakou, A. LaNotte, G. Zulian, F. Bouraoui, M.L. Paracchini, L. Braat, G. Bidoglio, 2012. Mapping ecosystem services for policy support and decision making in the European Union, Ecosyst. Serv., 1, pp. 31-39.

Vorstius, Anne C., & Spray, C.J., 2015. A comparison of ecosystem services mapping tools for their potential to support planning and decision-making on a local scale. Ecosystem Services, 15, pp. 75-83.

Earth observation advancements in a changing world

Edited by Chirici G. and Gianinetto M. "***Earth observation advancements in a changing world***" is the first volume of "***Trends in Earth observation***", a new series published by the Italian Society of Remote Sensing (AIT).

This volume, organized in 6 thematic chapters, includes 47 contributions from colleagues belonging to 10 different countries. Compared to similar volumes which often focus on the techniques and methods, ***Trends in Earth observation*** also describes case histories. In this sense, it provides the present state-of-the-art of many real-world remote sensing applications.

Edited by Chirici G. and Gianinetto M.

Gherardo Chirici is Professor of Remote Sensing and Forest Inventory and Director of geoLAB – Laboratory of Forest Geomatics at the Department of Agriculture, Food, Environment and Forestry of the Università degli Studi di Firenze. His main research interests are the application of spatial analysis technology for environmental applications and forest ecosystems monitoring. He is member of the Board of the Italian Society of Remote Sensing, of the Italian Academy of Forest Sciences, responsible for the Forest Geomatics working group of the Italian Society of Forest Ecology and Silviculture and coordinator of IUFRO Unit 4.02.04 – Geographic and management information systems. Co Editor-in-Chief of the European Journal of Remote Sensing, editor of Remote Sensing and Sensors. Prof. Chirici authored more than 200 scientific papers and 3 books.

Marco Gianinetto is Professor of Remote Sensing and Geomatics and head of L@RS – Laboratory of Remote Sensing at the Department of Architecture, Built Environment and Construction Engineering of Politecnico di Milano. His main research interests are in the field of Earth Observation and Spatial Information Technologies for environmental monitoring and land mapping. He is member of the Board of the Italian Society of Remote Sensing. Co Editor-in-Chief of the European Journal of Remote Sensing, Editor for International Journal of Remote Sensing and Journal of Applied Remote Sensing. He was also Editor for International Journal of Navigation and Observation from 2007 to 2018.
Prof. Gianinetto published more than 100 scientific papers and co-authored the study 'Space Market Uptake in Europe' for the European Parliament.

ISSN 2612-7148

9 772612 714859

ISBN 978-88-944687-0-0

9 788894 468700